TUTORIALS IN BIOPHYSICS

WILEY-VCH

Thomas Heimburg

Thermal Biophysics of Membranes

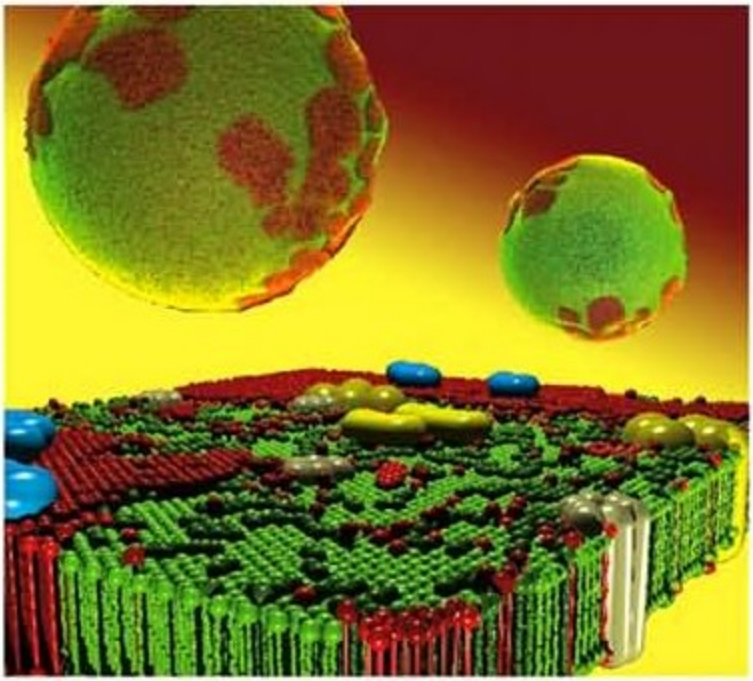

Thomas Heimburg

Thermal Biophysics of Membranes

Thomas Heimburg

Thermal Biophysics of Membranes

WILEY-VCH Verlag GmbH & Co. KGaA

The Author

Prof. Dr. Thomas Heimburg
Niels Bohr Institute
University of Copenhagen
Blegdamsvej 17
2100 Copenhagen
Dänemark

Cover

The cover picture shows confocal microscopy images of giant lipid vesicles containing domains of ordered and disordered lipid (in red and green). The bottom shows the snapshot of a Monte-Carlo simulation describing the same lipid system. The large objects represent proteins.

Library of Congress Card No.:
applied for

British Library Cataloguing-in-Publication Data
A catalogue record for this book is available from the British Library.

Bibliographic information published by the Deutsche Nationalbibliothek
The Deutsche Nationalbibliothek lists this publication in the Deutsche Nationalbibliografie; detailed bibliographic data are available in the Internet at <http://dnb.d-nb.de>.

Typesetting Uwe Krieg, Berlin
Printing betz-Druck GmbH, Darmstadt
Binding Litges & Dopf GmbH, Heppenheim
Wiley Bicentennial Logo Richard J. Pacifico

Printed in the Federal Republic of Germany
Printed on acid-free paper

ISBN-13: 978-3-527-40471-1
ISBN-10: 3-527-40471-6

Contents

Preface

Biological membranes display a wealth of physical phenomena including phase transitions, propagating voltage pulses, variable permeability, structural transitions (as seen in endo- and exocytosis), and domain formation that is thought to have an important influence on signal cascades. The title of this book "Thermal Physics of Membranes" indicates that it deals in particular with the thermodynamics of such systems. Thermodynamics is always true because it is based on only two basic and intuitive laws: the conservation of energy and the maximum entropy principle. Beyond that it is free of any approximations and assumptions. One therefore finds thermodynamics as a basis for physics on all length scales from atomic dimensions up to cosmological scales. Naturally, thermodynamics is also true on the level of biological membranes. We wish to introduce the reader to some of these principles and their consequences concerning the behavior of membranes. Important topics in this book are "phase diagrams" including domain formation and rafts, elasticity and the related changes in vesicular shape, pulse propagation, permeability as well as protein binding and electrostatics.

Biology deals with complex ensembles of organic molecules including proteins, nucleic acids, and lipids, but also salts and water. Proteins often display unique molecular surfaces that give rise to specific interactions. Much of biophysical research therefore has been dedicated to the study of structures and interactions between individual molecules. Cells and their compartments are defined by a large variety of membranes that not only surround the cell as a whole but also each organelle as the nucleus, mitochondria, or the endoplasmic reticulum. On average 50% of the biomembrane mass stems from proteins. The human genome contains about 30,000 genes encoding at least as many proteins, many or most of those being membrane proteins.

The major building blocks of membranes, however, are hundreds or thousands of different lipid species. The human body contains several kg of membrane lipids with a total surface on the order of 0.4 km^2 per kg. The plasma membranes of one eucariot cell contains about 10^{10} lipid molecules. Although

the diversity of lipids is seemingly smaller than that of proteins, lipid membranes contain many molecules and are thus large ensembles.

Biological molecules usually do not only interact with one specific binding partner but also with the abundant lipid surfaces, with protons (because macromolecules contain protonable groups), ions and, very importantly, with water. Therefore one typically deals not with one interaction but rather with many. Even if only a few of these interactions have a strength that is of interest and even if one takes into account that one cell usually does not express all the proteins that are encoded in the genome, it is immediately obvious that it is a impossible to investigate all possible interactions. One further has to take into account that the molecules may have different orientations and different conformations further increasing the complexity. We leave it to the reader to figure out how many different arrangements of, say, 200 lipid species in variable concentrations and conformations in an ensemble of 10^{10} molecules are possible—but the number is beyond any range that can ever be accessed by computers. One must come to the conclusion that life will never be understood on the basis of binary molecular interactions alone. In particular, many cooperative phenomena such as the melting of lipid membranes are beyond the scope of single molecule physics.

Thermodynamics is a fundamental discipline of physics that describes the behavior of assemblies of molecules. It solely relies on two basic principles: the law of the conservation of energy (first law) and the seemingly tautological principle that a most likely state exists that is assumed with the highest probability (second law). The latter principle is also known as the principle of maximum entropy. These two principles are so general and universal that the thermodynamic relations that are derived from them are also fundamentally true. In the case of biological systems, the variety of proteins, lipids, and ions is taken into account by their chemical potentials that are a function of the concentrations of other molecules as well as of temperature, pressure, voltage, or other intensive variables. In thermal equilibrium a multimolecular ensemble like a membrane fluctuates around the state of maximum entropy. If the system is not in equilibrium, the first derivative of the entropy constitutes the thermodynamic forces, which are the forces that drive a system back to equilibrium. The second derivatives of the entropy are related to susceptibilities, for example, to the heat capacity or the elastic constants of membranes. These properties of membranes are often easier to measure, for example with calorimeters (heat capacity), ultrasonic velocity measurements (volume compressibility) or by vesicular shape fluctuations (bending elasticity). Even though in thermal equilibrium the thermodynamics forces are zero, the susceptibilities generally assume nonzero values. Since the different susceptibilities are all second derivatives of the same thermodynamic function (the entropy), they are not independent of each other, but one can find surprising

relationships between various thermodynamic susceptibilities that can provide insights into the behavior of membranes that one would never be able to predict on the basis of single molecule interactions. Many such relations stem from the so-called Maxwell relation. We show two examples:

$$\left(\frac{dS}{dp}\right)_{T,n_i} = -\left(\frac{dV}{dT}\right)_{p,n_i} \tag{0.1}$$

where S and V are the entropy and the volume of an ensemble, respectively, including all their proteins and lipids—and all their conformations. This equation implies that the term on the left-hand side that is experimentally difficult to access is identical to the volume expansion coefficient that is very easy to measure. A second example is

$$\left(\frac{d\mu_i}{dn_j}\right)_{S,V,n_{i\neq j}} = \left(\frac{d\mu_j}{dn_i}\right)_{S,V,n_{j\neq i}} \tag{0.2}$$

This relation couples the chemical potential of one component to the variation of another and demonstrates the symmetry of the coupling. In biochemical textbooks such couplings usually do not play a role. This implies that the findings shown in such books are not necessarily incorrect but definitely incomplete. However, there are also examples where the molecular textbook models are clearly in conflict with the laws of thermodynamics. The application of thermodynamics therefore should not be considered as a method averaging out the molecular details (and thereby losing information) but rather as a means to gain considerable insight into all the couplings between seemingly different processes.

In this textbook we will introduce the reader to the thermodynamic concepts. Overall, our intention is to show the beautiful manner by which thermodynamics can link seemingly unrelated membrane processes resulting in a unified picture of the behavior of membranes as a whole. Our aim therefore is to present a coherent concept rather than achieving a complete presentation of the field. This approach takes the risk that important results of respected colleagues are not presented to the extent that they deserve.

Copenhagen, April 2007 *Thomas Heimburg*

1
Membranes—An Introduction

In the second half of the 19th century it became evident that an osmotic barrier separates the inside and the outside of cells (Nägeli and Cramer, 1855; de Vries, 1871, 1884; Pfeffer, 1877). Plant cell protoplasts were permeable to water but not to larger macromolecules like sucrose (de Vries, 1871). Pfeffer was the first to study the osmotic pressure within cells and formulated the idea that the protoplasm of cells is surrounded by a thin layer, which he called the plasma membrane. In fact, Pfeffer proposed that this membrane does not only cover the outer surface of cells but also separates all aqueous environments of different composition from each other. One may therefore consider Pfeffer as the father of membrane theory. The developments in biology and botany coincided with a rapid development in the theory of thermodynamics of solutions. In particular, based on Pfeffer's work van't Hoff found the formal analogy of concentrations of solutes in water and the partial pressures of ideal gases (van't Hoff, 1887). Ostwald formulated descriptions for the osmotic pressure across semipermeable walls and the related electrical properties (Ostwald, 1887, 1890).[1]

1.1
Overton (1895)

Charles Ernest Overton is a very important figure in the development of a picture of cell membranes. He investigated the osmotic properties of cells and noticed in the late 19th century that the permeation of molecules through membranes is related to their partition coefficient between water and oil (Overton, 1895). Overton's findings led to the hypothesis that the thin membranes surrounding cells have the properties of oil. In his book on anesthesia (Overton, 1901. Jena, Germany. English translation: Studies of Narcosis, Chapman and Hall, 1991, R. Lipnick, Ed., 1991) he called the layers surrounding cells "lipoids" made from lipids and cholesterol. The properties of lipids are described in detail in Chapter 3 and theory of anesthesia is treated in Chapter 19.

1) The history of biomembrane research is nicely reviewed in Ling (2001).

1.2
Langmuir (1917) and Gorter and Grendel (1925)

Langmuir (1917) developed an apparatus in which molecular layers of lipids were spread at the air–water interface. With this monolayer trough (see Section 6.7 and Fig. 6.14) the lateral pressure of the monolayer films could be measured. Langmuir proposed that in the molecular film the polar head groups were directed toward the water whereas the hydrophobic hydrocarbons are pointed toward the air phase.

Gorter and Grendel (1925) experimentally investigated the surface area of lipids. For this purpose they extracted the lipids from red blood cells of man, dog, rabbit, sheep, guinea pig, and goat in acetone. The lipids were spread on a water surface and the area was measured using a Langmuir film balance. From the same blood preparations they measured the surface area of the red blood cells from the microscopic images. They found that the surface area of the monofilms was within error exactly two times that of the cells. They concluded that cell membranes are made of two opposing thin molecular layers, and they proposed that this double layer is constructed such that two lipid layers form a bilayer with the polar head groups pointing toward the aqueous environment (Fig. 1.1). This is the picture of the lipid membrane we know today. As Robertson (1959) noted later, the attractive simplicity of Gorter's and Grendel's pictures is also its greatest weakness since it fails to account for the manifold of functions attributed to cell membranes.

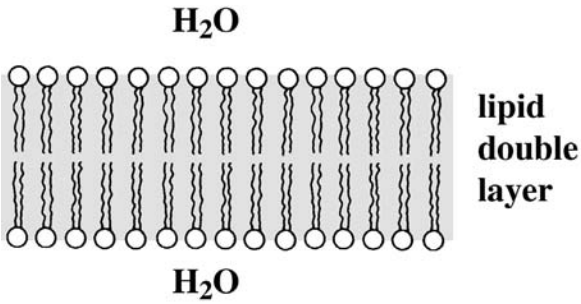

Fig. 1.1 The cell membrane according to Gorter and Grendel (1925). They proposed the lipid bilayer structure.

1.3
Danielli and Davson (1935)

The earliest molecular model for the biomembrane structure including proteins was the model from Danielli and Davson (1935). They took into account that the layers surrounding cells had a significant content of proteins adsorbed

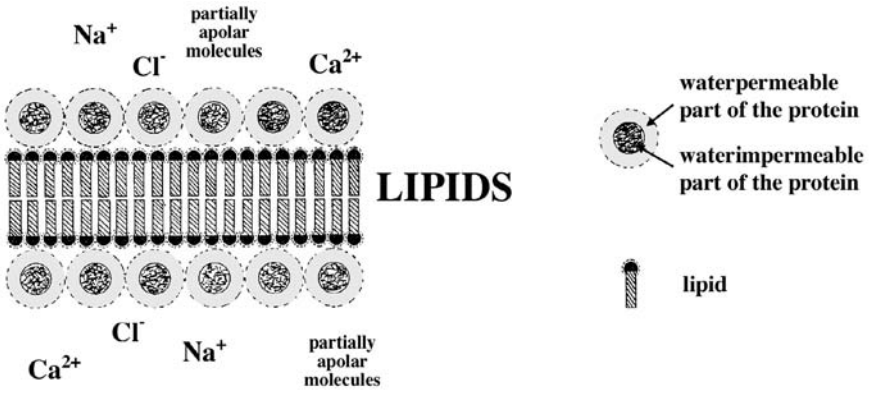

Fig. 1.2 Danielli and Davson (1935) proposed a membrane model including proteins. They used their model to interpret the observation of different membrane permeabilities of ions and hydrocarbons. In particular, they assumed that the membrane has both a lipophilic and a hydrophilic character. Water-containing regions in the membrane give rise to ion transport depending on water content of the membrane and its charge; lipophilic parts are responsible for the transport of water-insoluble molecules. Figure adapted from Danielli and Davson (1935) with permission.

to the layers. It was known that phospholipids have an amphiphilic nature. Furthermore, proteins investigated were mostly water soluble but nevertheless often adsorbed to membranes. Jim Danielli and Hugh Davson thus proposed a model of the cell membrane consisting of a lipid bilayer, with which a protein layer is tightly associated (Fig. 1.2, left). As in earlier membrane studies (e.g., by Overton) they were in particular interested in the permeation properties of membranes. In a theoretical paper they made the following consideration.

- Proteins are adsorbed to the lipophilic layers surrounding cells. The proteins possess hydrophobic interiors and a water-containing outer layer.
- The lipid layer possesses amphiphilic or charged head groups. This implies that the lipid membrane also contains some water.
- The water-containing regions of protein layers adsorped on lipid layers are permeable for charged solutes, e.g., ions.
- Divalent cations as calcium form complexes with lipids or proteins that reduce their interaction with water. Therefore membranes containing calcium are less permeable for ions.
- Hydrophobic molecules such as ether penetrate the membranes through their lipophilic lipid part.

They included some theoretical considerations about the different dependencies of the permeabilities of membranes to ions and hydrophobic molecules as a function of temperature.

> Danielli and Davson concluded that the permeabilities of membranes for solutes are explainable within the concepts of the physical chemistry of the hydrophilic and lipophilic regions of the cell membranes and that no particular chemical reactions including the solutes are needed to explain the transport properties.

Unfortunately, this very sober view is nowadays not in the focus of much of the biochemical membrane research due to the emphasis of the localized function of ion- and solute-specific transport channel proteins. In the chapter on permeability (Chapter 17) we will return to the quite realistic physical view of Danielli and Davson.

Danielli and Davson did not exclude the possibility that the proteins may span the membrane such that a "mosaic" of protein-rich and lipid-rich regions is formed. However, they did restrain themselves from speculating about such a structure due to the lack of experimental evidence. The term "mosaic membrane" was later used again by Singer and Nicolson (1972).

1.4 Robertson (1958)

So far most evidence about the structure of cell membranes was indirect. The resolution of light microscopy is restricted to the regime above 200 nm, which is not sufficient for revealing the bimolecular structure of the biological membrane that is between 5 and 10 nm thick. This changed with the progresses in electron microscopy. In 1959, J. David Robertson wrote a review in which

Fig. 1.3 Two opposing plasma membranes showing the double-layer character of the membranes. Picture taken from Bloom and Fawcett (1994) © Springer. Such images support the view of Gorter and Grendel (1925) and of Danielli and Davson (1935).

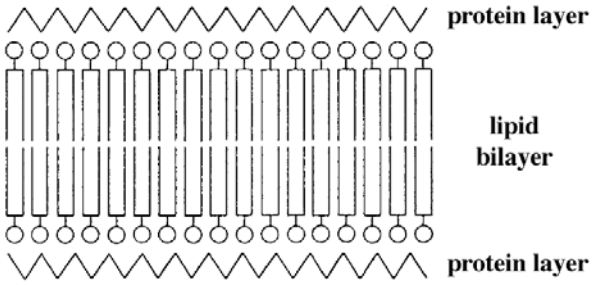

Fig. 1.4 Robertson (1959) collected electron microscopy images of many cells and organelles. His picture of a biological membrane resembles that of Danielli and Davson (1935). However, it is now based on microscopic evidence. Reproduced with permission from Robertson (1959) © The Biochemical Society.

he collected his evidence for a unique membrane structure obtained from the then advanced electron microscopy (Robertson, 1959). He basically confirmed the models of Gorter and Grendel (1925) and Danielli and Davson (1935). In his review he carefully described the membrane structures of the different organelles including the double membrane layers of mitochondria and the cell nucleus (Fig. 1.3). He also described the membranes of nerve cells and recognized that the Schwann cells form membrane layers surrounding the nerve membranes. Robertson's conclusion was that all evidence points at a common construction principle for all membranes of biological cells. They form a three-layered structure and are about 7.5 nm thick. In Robertson's view two protein layers are adsorbed to the lipid bilayer (see Fig. 1.4). As he noted himself this picture is in agreement with that of Danielli and Davson (1935). Remember, however, that the aim of Danielli was rather to explain selective transport of ions and apolar molecules. Robertson's model was sometimes incorrectly interpreted as that all membranes have the same composition. However, Robertson's statement was merely meant to describe a common structure.

1.5 The Fluid Mosaic Model of Singer and Nicolson (1972)

In the 1960s, the structures of a number of soluble proteins were solved by X-ray crystallography. Lenard and Singer (1966) found that many membrane proteins have a high α-helical content. Also, electron micrographs revealed that labeled proteins form isolated spots in some membranes. Furthermore, they considered the role of hydrophobic amino acids in α-helices. From this Singer and Nicolson concluded that proteins may also span through mem-

branes. This led to the famous Singer–Nicolson model (Singer and Nicolson, 1972) also known as the "fluid mosaic model." This model can be summarized as follows: Membranes are constructed from lipids and proteins. The proteins form mainly two classes. Peripheral proteins are those proteins that are only loosely attached to the membrane surface and can easily be separated from the membrane by mild treatment (e.g., cytochrome c in mitochondria or spectrin in erythrocytes). Integral proteins, in contrast, cannot easily be separated from the lipids. They form the major fraction of membrane proteins. The structure forming unit (matrix) is the lipid double layer (bilayer). Proteins may be either adsorbed to the membrane surface or span through the membrane (Fig. 1.5). The term "fluid mosaic model" used by Singer and Nicolson probably originates from Danielli and Davson (1935) although their paper was not cited.

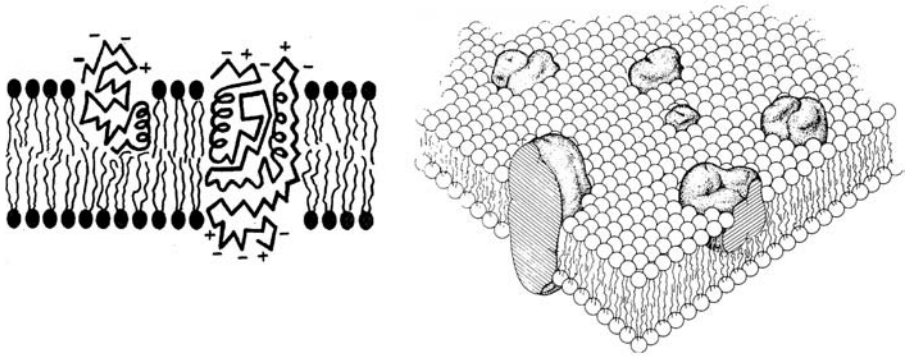

Fig. 1.5 The "fluid mosaic model" of Singer and Nicolson (1972). The left side shows the lipid bilayer including globular proteins intercalated with the membrane, and transmembrane proteins. The membrane proteins are not all distributed homogeneously. Reprinted with permission from AAAS.

Singer and Nicolson (1972) underlined that some proteins seem to interact with the surrounding lipids and that protein function may depend on the presence of specific lipids (see Fig. 1.6). They proposed that the proteins are surrounded by a layer of strongly interacting lipids while most of the remaining lipids are hardly influenced by the presence of proteins. This implies that the lipids form a matrix and no long-range order of proteins exists within the matrix. Short range order due to protein–protein interactions (possibly mediated by specific lipids) was considered as a possibility (see Fig. 1.6). Such interactions are discussed in Chapter 9. It was postulated that the lipid membranes of biological cells are in the fluid lipid state (with exceptions, e.g., the myelin) in which proteins can freely diffuse. In this respect an interesting paper by Frye and Edidin (1970) showed that when two different cells with different proteins are forced to fuse, the proteins redistribute over the whole surface within 40 min. This finding supports the view of freely diffusing pro-

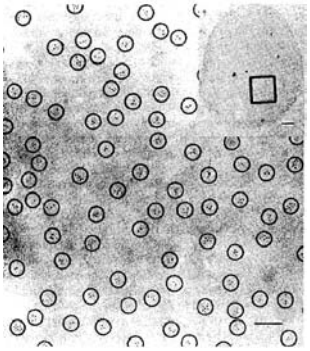

Fig. 1.6 Protein distribution in erythrocyte membranes from Singer and Nicolson (1972). Specific proteins were labeled with antibodies. The circles indicate protein clusters with a diameter of about 30 nm. Reprinted with permission from AAAS.

teins in cell membranes. Singer and Nicolson also noted that the fluid mosaic membrane is most likely asymmetric and displays distinctly different features on the inside and the outside of cells. Asymmetry of membrane lipids has in fact been found in experiments (Rothman and Lenard, 1977; Rothman and Kennedy, 1977). Also, proteins are now known to display preferential orientations in membranes.

The Singer–Nicolson model still is the widely accepted model. In particular, due to progresses in the crystallization of membrane proteins it is nowadays known that membrane proteins display α-helical or β-barrel-like membrane spanning segments of predominantly apolar amino acids.

1.6 The Mattress Model by Mouritsen and Bloom (1984)

The fluid mosaic model of Singer–Nicolson has nowadays experienced some refinement, which takes into account that lipids and proteins may distribute inhomogeneously and that domains and clusters may form within the membrane. Without explicitly saying so, the Singer–Nicolson model considered the lipid membrane as a homogeneous fluid in which the proteins diffuse in two dimensions. In 1984, Mouritsen and Bloom (1984) proposed the mattress model (Fig. 1.7) that suggests that proteins and lipids display interactions with a positive free energy content due to variations in the hydrophobic length of the molecules (see Section 9.1). The typical thickness of a lipid bilayer is about 5 nm. If the hydrophobic core of a membrane protein is longer or shorter than this length, either some hydrophobic protein or lipid segments are exposed to water, or the lipid membrane has to be deformed to compensate for the

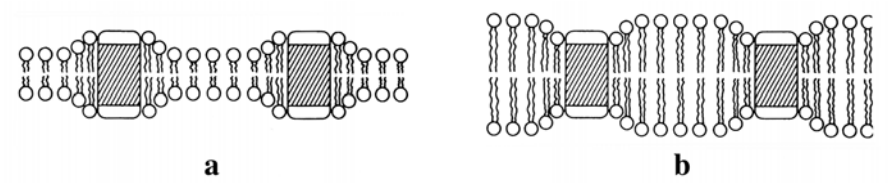

Fig. 1.7 The mattress model from Mouritsen and Bloom (1984). This model takes into account that the hydrophobic core of proteins may not match the bilayer thickness. This leads to interfacial tensions and capillary forces between protein and lipids. With permission from Biophys. J.

unfavorable hydrophobic interactions. This effect is called the "hydrophobic matching." The hydrophobic matching gives rise to interfacial tensions between lipids and proteins. These tensions may result in the accumulation of certain lipid species around the proteins (see Fig. 1.8), and in the mutual attraction of proteins due to capillary forces, leading to aggregation and clustering of proteins.

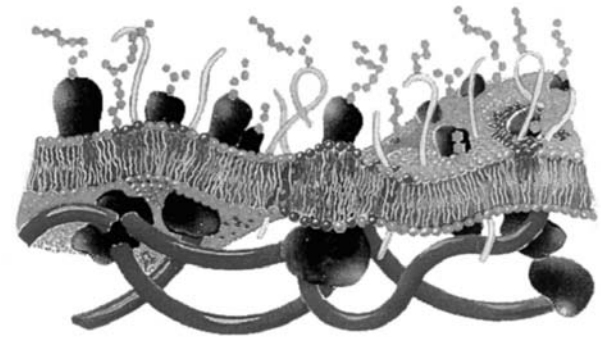

Fig. 1.8 In the mattress model the proteins may influence the lipids in their vicinity. Picture courtesy to O. G. Mouritsen.

1.7 Domain Formation and Protein Clusters

Similar arguments as for the matching of lipids and proteins lead to the assumption that also different lipid species may not match perfectly. Biological membranes contain hundreds of different lipid species with variable head group and chain composition (Chapter 3). Most lipids possess two apolar hydrocarbon chains with variable length. Furthermore, lipid membranes undergo melting transitions, which are accompanied by changes in the effective

lipid chain length (Chapter 6). Thus, also the lipids within the membrane plain can form various clusters, domains, and aggregates. A modern view of biological membranes has to include the phase behavior of the lipid and protein components (Chapters 7–9).

The phase behavior of membranes becomes especially interesting if one considers cooperative transitions in the biological membrane. Native membranes show several cooperative events in direct proximity of growth or body temperature. As an example a calorimetric experiment on native *E. coli* membranes grown at 37° is shown in Fig. 1.9. Slightly below growth temperature a cooperative lipid melting peak is found. Above growth temperature several protein unfolding peaks can be seen.

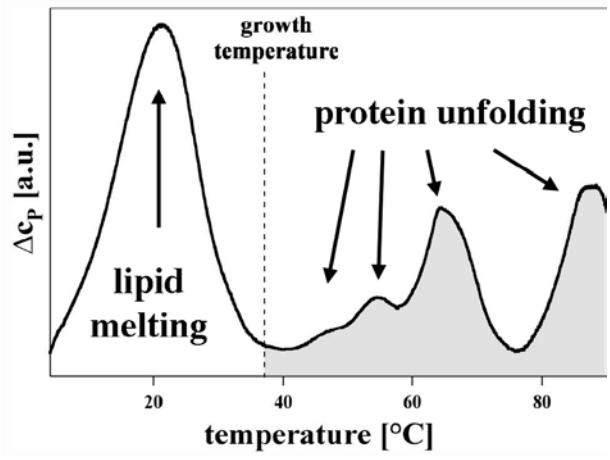

Fig. 1.9 A calorimetric experiment on a native *E. coli* membrane shows that lipid melting events take place slightly below growth temperature. Above growth temperature a number of protein unfolding events take place. Adapted from Heimburg and Jackson (2007a).

During lipid melting transitions the thickness of lipid membranes and the lateral lipid distribution changes. This is of extreme interest for regulation and signal transduction purposes in such membranes (Section 9.5 and Chapter 10). The mattress model implied that the matching of the dimensions of lipids and proteins influences the lipid recruiting around proteins and the lateral arrangement of proteins due to attractive forces from capillary effects. Thus, such transitions are linked to the formation of domains and clusters. Some examples are shown in Fig. 1.10. The left-hand panel shows a fluorescence microscopy image of a monolayer consisting of one single lipid. The dark regions represent ordered lipid domains while the bright regions represent disordered chains. The center panel shows domain formation phenomena in the fluorescence microscopy image of a giant lipid vesicle made from a lipid mixture. Giant vesicles are lipid bilayer vesicles that have similar dimensions to

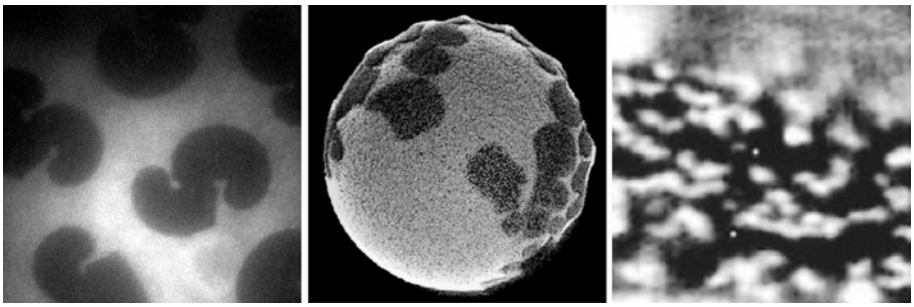

Fig. 1.10 Domain formation in lipid monolayers, bilayers, and in biological cells. Left: Domain formation in the phase coexistence regime of DPPC monolayers. The dimension of the panel is about 100 μm. From Gudmand/Heimburg, NBI Copenhagen. Center: Confocal fluorescence microscopy image of domain formation in a giant lipid vesicle (DLPC:DPPC = 30:70 at room temperature). The size of the vesicle is about 30 μm in diameter. From Fidorra/Heimburg, NBI Copenhagen. Right: Placental alkaline phosphatase distribution in fibroblast. The size of the segment is about 4 μm. From Harder et al. (1998).

biological cells. The right-hand panel shows the formation of protein clusters (placental alkaline phosphatase=PLAP) in a fibroblast cell form (Harder et al., 1998). In this paper it was shown that different proteins species tend to colocalize in different regions of the cell membrane. In biomembranes a special kind of domain called "raft" is presently highly discussed. Rafts are thought to be microdomains consisting predominantly of sphingolipids, cholesterol and certain GPI-anchored proteins. These phenomena are discussed in much more detail in Chapters 8 and 9.

Domain formation is also interesting for the electrostatic properties of membranes. Many membrane components carry charges. Thus, domain formation leads to inhomogeneities in electrostatic potential and to the preferential binding of proteins.

1.8 Perspectives of this Book

The biological membrane resembles the picture in Fig. 1.11, showing variations in the membrane thickness, the presence of peripheral and transmembrane proteins, as well as the formation of lipid and protein domains (Chapters 8 and 9). The thermodynamics of such phenomena is an essential part of this book. Cooperative transitions also influence the elastic constants (Chapter 14). Thus, rearrangement of proteins and lipids is also generally linked to alterations of membrane elasticity and compressibility. Due to the couplings in the thermodynamic equations these relations go in both directions meaning that changes in the membrane curvature by necessity have to change

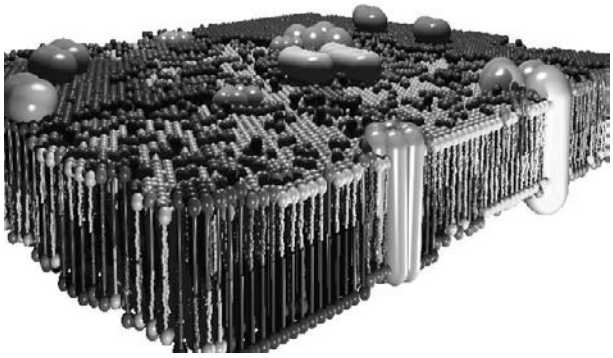

Fig. 1.11 The modern picture of membranes allows for lateral heterogeneities, cluster and domain formation within the membrane plane. Picture generated by H. Seeger, NBI Copenhagen.

lipid distributions. If the melting of membranes leads to the rearrangement of proteins and a related change of the elastic constants, then conversely a change in protein distribution will lead to a change in the physical state of the membrane, and bending will influence melting and protein distributions. The elastic constants are responsible for many changes in the geometry of membranes (Chapter 15), for the possibility of mechanical excitations propagating in membranes (Chapter 18), and for changes in permeability (Chapter 17). Since some of the membrane components carry charges, generally domain formation also leads to heterogeneities in the electrostatic potential and to a coupling of electrostatic fields to the phase behavior of membranes.

The subjects treated in this book include

- composition and structure of biological membranes (Chapters 2 and 3),
- the role of water and the hydrophobic effect (Chapter 5),
- phase behavior and domain formation (Chapters 6–9),
- lipid–protein interactions (Chapter 9) and protein binding to surfaces (Chapter 12),
- diffusion in membranes containing domains (Chapter 10),
- electrostatics and its influence on protein binding (Chapter 11),
- the elastic constants and how they are influenced by temperature, pressure, protein binding, and other thermodynamic variables (Chapters 13 and 14),

- changes in membrane geometry due to changes in the elastic constants (Chapter 15),
- relaxation phenomena (Chapter 16),
- some considerations on the permeability of membranes for ions and larger molecules and how it is related to the thermodynamics of the membrane (Chapter 17).
- the propagation of density pulses and a related thermodynamic theory for the propagation of nerve pulses (Chapter 18),
- a thermodynamic theory for anesthesia (Chapter 19),

The function of the biological membrane cannot be understood without consideration of its thermodynamics. It is a multicomponent system that sensitively responds to changes in temperature, pressure, and the chemical potentials of its components. Therefore, this book also contains a basic introduction into thermodynamics (Chapter 4). The purpose of this book is to describe the concepts of thermodynamic couplings of seemingly independent properties of membranes. It will be shown that all of the above phenomena are intimately related and fit into a coherent thermodynamic picture.

1.9 Summary: Key Ideas of Chapter 1

- Biomembranes mainly consist of lipids and proteins. They are macroscopic ensembles.
- Lipids are amphiphilic molecules with polar head groups and apolar chains. Lipids spontaneously form bilayers in water.
- Proteins may be peripherally adsorbed to the lipid bilayer surface, or they may be integral proteins spanning through the bilayer core.
- The thickness of biological membranes is on the order of about 5–8 nm.
- Due to differences in the size of the different molecules in membranes capillary forces can exist that influence the distribution of molecules in the membranes.
- As a consequence, proteins and lipids are not homogeneously distributed within membranes but form domains, clusters, and aggregates.
- The lateral distribution of the molecules is altered when the thermodynamic variables of the system change.
- Biological membranes can undergo order transitions.
- These order transitions are coupled to changes in the elastic constants of the membranes.

2
Membrane Structure

2.1
Lipid Membrane Structure

Lipids consist of a polar head group and an apolar chain region (Fig. 2.1). While the head groups usually contain charged groups (phosphate and choline groups in phosphatidylcholines) and thus like to interact with water, the chains are hydrocarbons which do not like to interact with water due to the hydrophobic effect described in Chapter 5. Lipids therefore tend to form aggregates that shield the hydrocarbon chains from water and expose the head groups to water. Lipid dispersions also tend to maximize distributional entropy. If it were not for the hydrophobic effect distributional entropy would favor monomeric lipids dissolved in the water phase. The lower the lipid concentration the larger the entropy contribution per molecule. The hydrophobic contact of water with hydrocarbon chains results in an entropy decrease that is not dependent on lipid concentration (Chapter 5). In other words, the formation of lipid aggregates releases some water and increases

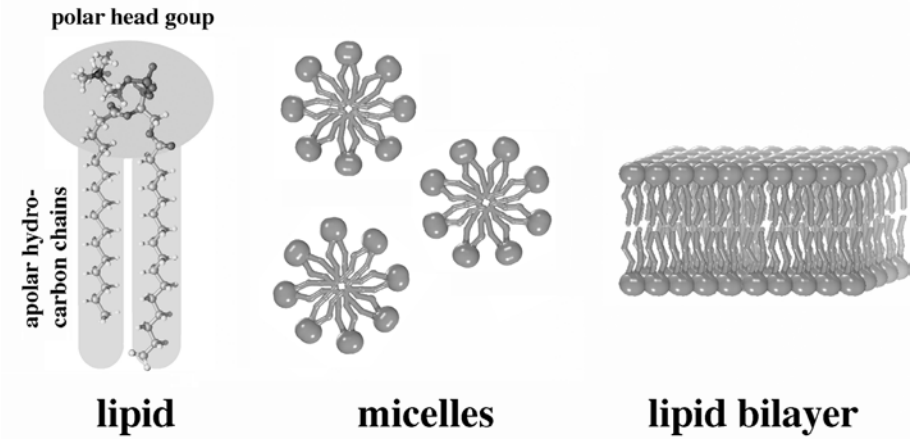

Fig. 2.1 Left: Monomeric lipid showing head group and hydrocarbon chains. Center: Lipid micelles. Right: Lipid bilayer consisting of two opposing monolayers..

the entropy per chain, independent of lipid concentration. From this we have to conclude that the formation of lipid aggregates must be strongly concentration dependent, and that the formation of larger aggregates becomes more favorable at higher lipid concentration. Since the hydrophobic effect is highly temperature dependent one would also expect that the nature of the lipid aggregate is temperature dependent.

Various lipid phases are found in lipid–water systems. The most prominent are as follows.

- *Monomeric lipids*. As a consequence of entropic considerations lipids have a finite probability to be found as monomers, in particular at very high dilutions (Fig. 2.1, left).

- *Micelles*. Above a critical concentration (critical micelle concentration) the lipids aggregate into micelles. These micelles may have all kinds of shapes. For a simple spherically symmetric micelle (Fig. 2.1, center) one may approximate the micelle formation process by a mass action law:

$$\frac{[L_n]}{[L]^n} = K \tag{2.1}$$

  where $[L_n]$ is the concentration of micelle consisting of n lipids and $[L]$ is the monomeric lipid concentration.

- *Lamellar phases* (Fig. 2.1, right): At even higher lipid concentrations, micelles grow into extended two-dimensional sheets, called bilayers. The bilayer phases can exist in different states listed in the following in order of their occurrence at increasing temperature (Fig. 2.2, Janiak et al., 1979):
  - L_c *phase*. This is the crystalline lipid phase with order in three dimensions. The lipids form bilayers which are not separated by a water layer. The lipid chains are ordered into all-trans chains (Fig. 2.2).
  - $L_{\beta'}$ *phase*. This is the so-called gel phase. The lipids arrange in bilayers. Lipid chains are mostly ordered into the all-trans configuration (see Chapter 6). The prime index "′" indicates that the lipids are tilted with respect to the membrane normal. The presence of a tilt depends on the head group of the lipid species (McIntosh, 1980). Phosphatidylcholines display a tilt angle of about 30° while phosphatidylethanolamines do not display a tilt at all. The lipids are arranged on a two-dimensional triangular lattice in the membrane plane (Janiak et al., 1979). This phase is also called the solid-ordered phase (Figs. 2.2 and 6.3).

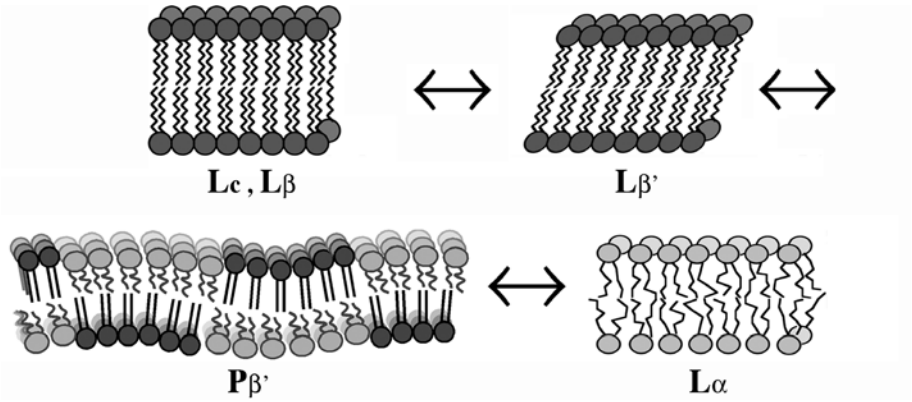

Fig. 2.2 The lipid membrane phases that occur in lipid membranes with increasing temperature display a decreasing order of the chains: L_c phase, $L_{\beta'}$ phase, $P_{\beta'}$ phase, and L_α phase.

  - *$P_{\beta'}$ phase*. This is the ripple phase, showing periodic one-dimensional ripples on the membrane surface (Janiak et al., 1979). This phase forms prior to main chain melting and consists most likely of a partially melted lipid phase with lower average degree of chain ordering than in the $L_{\beta'}$ phase. The ripples are probably formed by periodic arrangements of linear gel ($L_{\beta'}$) and fluid (L_α) lipid domains (Fig. 2.2, (Heimburg, 2000a; de Vries et al., 2005)). The ripple phase will be discussed in more detail in Chapter 15.
  - *L_α phase*. This phase is the so-called fluid phase. The chains are mostly disordered and the lattice order is lost. This phase is also called the liquid-disordered phase (Figs. 2.2 and 6.3) since both chain order and the arrangement on the triangular lattice are lost.

- *Cubic phases*. The cubic lipid phases are mostly bicontinuous lipid bilayer phases with periodic three-dimensional order (Lindblom and Rilfors, 1989). They are unilamellar structures. There are in principle 36 possible cubic space groups allowing for the related phases, but only six cubic phases have been found in crystallographic experiments on lipid membranes. A cubic phase is shown in Fig. 2.10.

- *Inverse hexagonal phase*. The inverse hexagonal phase is a high temperature lipid phase. Due to the associated increase in entropy the chain volume increases and the lipids form cylinders with the chains directed to the outside. Since the chains tend to avoid water the cylinders arrange into two-dimensional hexagonal crystals (Caffrey et al., 1990). Such a pattern can be seen in Fig. 2.8.

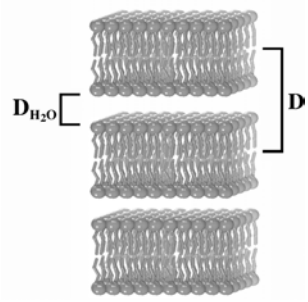

Fig. 2.3 Multilamellar membranes represents a periodic stacking of membranes with a repeat spacing of D separated by a water layer $D_{H_2O} \approx 20$ Å.

In this context one should mention that the tendency to form planar bilayers is most pronounced in the lipid phases with ordered chains. Cubic phases or inverse hexagonal phases display disordered lipid chains and are therefore phases typically occurring at higher temperatures.

How does one know how these structures look like? The most common methods to determine lipid membrane structures are X-ray and neutron diffraction. In the following we briefly outline some principles of X-ray diffraction.

2.2 X-Ray Diffraction

One of the most important methods to determine the structures of membranes is X-ray diffraction (Franks and Levine, 1981).

Let us consider a planar coherent wave of X-rays (or neutrons) with wavelength λ and wave vector $\underline{k}$ with $|k| = 1/\lambda$ along the direction of wave propagation. X-rays are predominantly scattered by electrons because they display a high charge and simultaneously a small mass. Neutron, in contrast, are scattered by the atomic nuclei. The incoming wave shall be scattered by two different points within the sample with a spatial separation described by the vector $\underline{r}$. The incoming wave is described by the wave vector $\underline{k}_i$, and the scattered wave by $\underline{k}_s$. This is schematically shown in Fig. 2.4 (left). Incoming and scattered wave display phase differences [1] that can be determined with the help of Fig. 2.4. This phase difference creates constructive or destructive interference in the diffraction pattern:

$$\text{phase difference} = 2\pi\underline{r} \cdot (\underline{k}_s - \underline{k}_i) \equiv 2\pi\underline{r} \cdot \underline{R} \qquad \text{with} \qquad \underline{R} \equiv \underline{k}_s - \underline{k}_i \quad (2.2)$$

1) Note that in this section the term 'phase' is used in two different contexts.

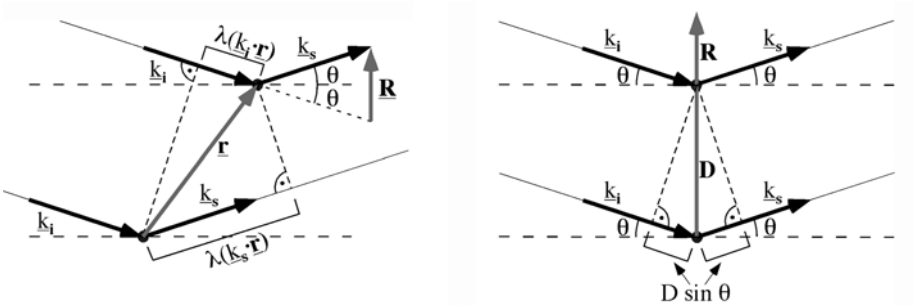

Fig. 2.4 X-ray or neutron scattering by two points (left) and by two planar surfaces (right).

The phase difference of the two scattered waves now is $|R| = 2\sin\theta/\lambda$. Constructive interference is given if $\underline{r} \cdot \underline{R}$ is a multiple of 1. For Bragg diffraction from two planes with distance D (see Fig. 2.3 and Fig. 2.4, right) one obtains $\underline{r}||\underline{R}$, or

$$\begin{aligned} \underline{r} \cdot \underline{R} &= |\underline{r}| \cdot |\underline{R}| \\ &= 2\,D \cdot \frac{\sin\theta}{\lambda} = n \qquad \text{with} \quad n = 1, 2, 3, \ldots \quad \text{and} \quad |\underline{r}| = D \end{aligned} \tag{2.3}$$

The vector $\underline{R}$ is the reciprocal spatial vector ($|\underline{R}| = n/D$), and θ is half the scattering angle. For a general electron distribution $\rho(\underline{r})$ one obtains for the amplitude of the scattered wave with reciprocal vector $\underline{R}$

$$F(\underline{R}) = \int_{\underline{r}} \rho(\underline{r}) \exp(2\pi i\, \underline{r} \cdot \underline{R})\, d\underline{r} \tag{2.4}$$

Let us now consider a membrane: for the two spatial coordinates within the plane it displays a near continuous electron distribution (y- and z-direction). Only perpendicular to the membrane (x-direction) one can resolve the electron distribution. One therefore obtains

$$F(R) = \int_x \rho(x) \exp(2\pi i x\, R)\, dx \tag{2.5}$$

$F(R)$ is the structure factor (or structure amplitude). It is the Fourier transform of the electron density distribution

$$\rho(x) = \int_R F(R) \exp(-2\pi i x R)\, dR \tag{2.6}$$

In experiments one often finds multilayers (Fig. 2.3). Multilayers display a periodic repeat spacing. Here we obtain

$$\rho(x + nD) = \rho(x) \qquad 0 \le x \le D \qquad \text{and} \qquad n = 1, 2, 3, \ldots \tag{2.7}$$

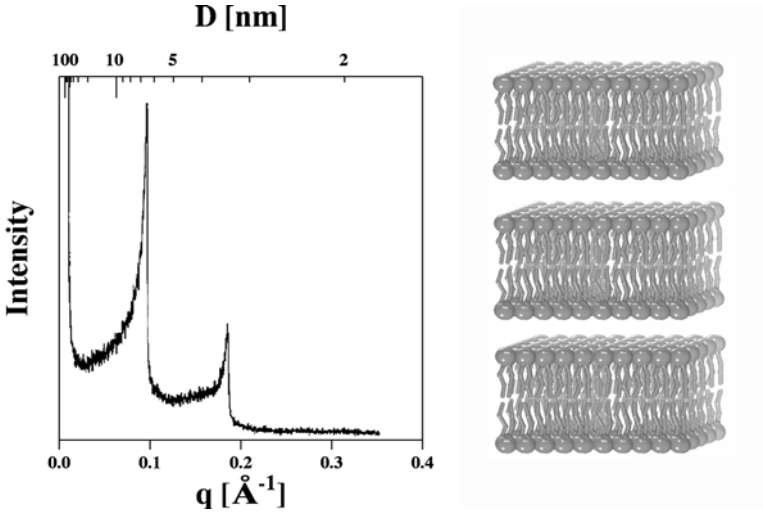

Fig. 2.5 Diffraction pattern of multilamellar DMPC lipid membrane adapted from Heimburg et al. (1990).

For multilayers one can reformulate Eq. (2.5):

$$F(R) = \underbrace{\left(\sum_{n=0}^{N-1} \exp(2\pi i\, R\, n\, D)\right)}_{G(R)} \underbrace{\int_{x=0}^{D} \rho(x) \exp(2\pi\, i\, xR)\, dx}_{F_u(R)} \tag{2.8}$$

The term $F_u(R)$ is the structure factor for an individual isolated membrane. $G(R)$ is the so-called interference function. It is a geometrical series and can (after short calculation) be written as

$$G(R) = \sum_{n=0}^{N-1} \exp(2\pi i\, R\, n\, D) = \exp(\pi\, i\, R\, (N-1)\, D) \frac{\sin(N\pi RD)}{\sin(\pi RD)} \tag{2.9}$$

The interference function displays extrema when $RD = m$ ($m = 0, \pm 1, \pm 2, \ldots$). This corresponds to Bragg's law. The amplitude of the interference function $G(R)$ at the location of the maxima is given by $|G(R)| = \left|\frac{\sin(N\pi RD)}{\sin(\pi RD)}\right| = N$. One obtains sharp maxima of the interference function for $R = m/D$, where $G(R)$is a real function.

In experiments the intensity of a scattered wave is measured:

$$I(R) = F^*(R)F(R) = |F(R)|^2 \tag{2.10}$$

In the experiment one therefore only obtains the amplitude of the structure factor. The phase information is lost. This is a general problem in the scattering techniques. With this reduced information one therefore cannot deduce

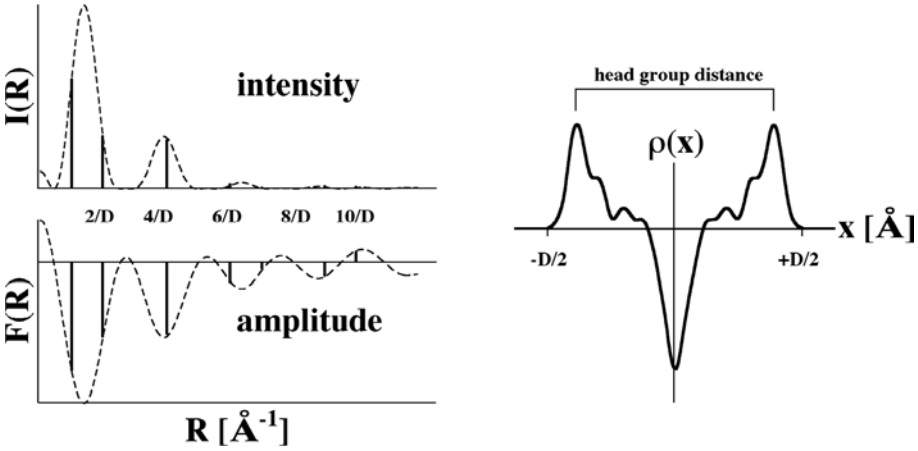

Fig. 2.6 Left: Diffraction intensities and amplitudes of an experiment on multilayers. Right: Electron density calculated from the diffraction experiment. Data adapted from Franks and Levine (1981).

the electron distribution from the experiment. One needs additional information.

Let us consider the special case of a symmetric membrane for which the phase problem is relatively simple. The membrane is symmetrical with respect to its center (very reasonable assumption). Then one obtains for the structure factor of an isolated membrane:

$$F_u(R) = \int_{-D/2}^{+D/2} \rho(x) \exp(2\pi i R x)\, dx$$
$$= \int_{-D/2}^{+D/2} \rho(x) \cos(2\pi R x)\, dx + i \int_{-D/2}^{+D/2} \rho(x) \sin(2\pi R x)\, dx \qquad (2.11)$$

The term containing the sine function is equal to zero (since $\sin(x) = -\sin(-x)$). The structure factor now is a real function.

We also obtain $F_u(R) = |F_u(R)| \cdot \exp(i\alpha) = |F_u(R)| \cdot \cos(\alpha) + i|F_u(R)| \cdot \sin(\alpha)$. Since the imaginary part is equal to zero, $\alpha = n \cdot \pi$. The phase factors therefore display values of ± 1. Whether the structure factor has a positive or negative value cannot be deduced from the data of one single diffraction experiment. The sign has to be found by "reasonable guess." This is possible, e.g., by making a series of experiments where the D-spacing is altered by changing the water layer between the layers using osmotic agents. A typical X-ray experiment performed on a linear probe (in a capillary) is shown in Fig. 2.5. The asymmetric shape of the diffraction peaks is caused by the linear nature of the probe. One obtains diffraction peaks with periodic distances $1 : 2 : 3 : 4 : \ldots$ on the q-axis (where $q = 2\pi R$).

From the intensities of the diffraction peaks and the proper assignment of phase factors one can calculate the electron densities along the membrane normal. Such an electron density profile is shown in Fig. 2.6. One can see that the electron density is much larger in the outer headgroup region than in the membrane interior. From such results one can deduce the membrane thickness.

Why are the electron densities at the outer edge of a membrane (adjacent to the water layer) so different from the electron density in the center of a membrane? This can be explained by the different electron densities of the chemical groups within the lipid, e.g., phosphates and hydrocarbons:

- electron density in the head groups: ≈ 0.45 electrons/Å^3
- electron density of a $-CH_3$-group of lipid chains: ≈ 0.17 electrons/Å^3

Apolar hydrocarbon groups display a much lower electron density than lipid head groups that contain many oxygen atoms.

Thus, the electron density distribution can help to locate the different chemical groups of the lipids along the bilayer normal. In a more advanced study combining X-ray and neutron diffraction Wiener and White (1992) explored the location of different groups in the membrane. As neutrons are scattered

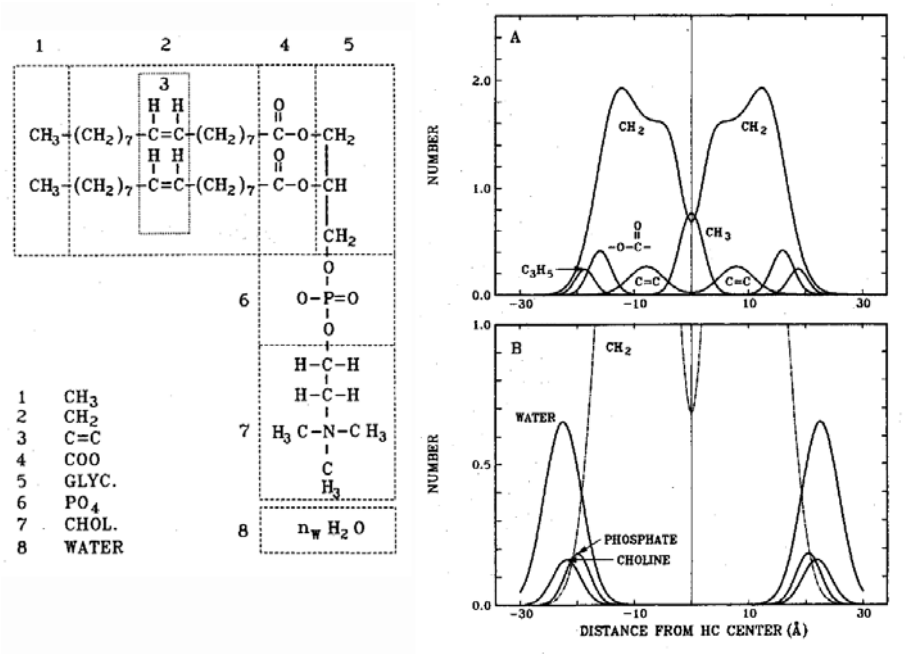

Fig. 2.7 Distribution of different chemical groups of a DOPC membrane obtained from X-ray and neutron diffraction. From Wiener and White (1992). with permission from Biophys. J.

differently by different isotopes, chemical modifications using e.g. the exchange of hydrogen with deuterium can be used to determine the distribution of the labeled groups in the membrane. Wiener and White (1992) could give very good account of the distribution of the different parts of the lipids within the lipid membrane. This is shown in Fig. 2.7.

2.3 Nonlamellar Lipid Phases

2.3.1 Inverse Hexagonal Phase (H_{II}-Phase)

Some lipid phases do not yield periodic Bragg diffraction peaks as in the above example. In Fig. 2.8 (left) an example is shown where the diffraction peaks along the q-axis are not evenly spaced as in the case of multilayered membranes. This corresponds to the inverse hexagonal phase (H_{II}-phase). The H_{II}-phase consists of cylindrical lipid tubes with water inside and lipid chains directed toward the outside (Fig. 2.8, right). Those cylinders arrange into hexagonal two-dimensional lattices. X-ray reflexes can be found at positions with relative spacings of

$$\frac{2(h^2+k^2-hk)^{0.5}}{\sqrt{3a}} \qquad \text{i.e. at} \quad 1, \sqrt{3}, 2, \sqrt{7}, 3, \ldots \tag{2.12}$$

where a is the distance between the centers of the cylinders.

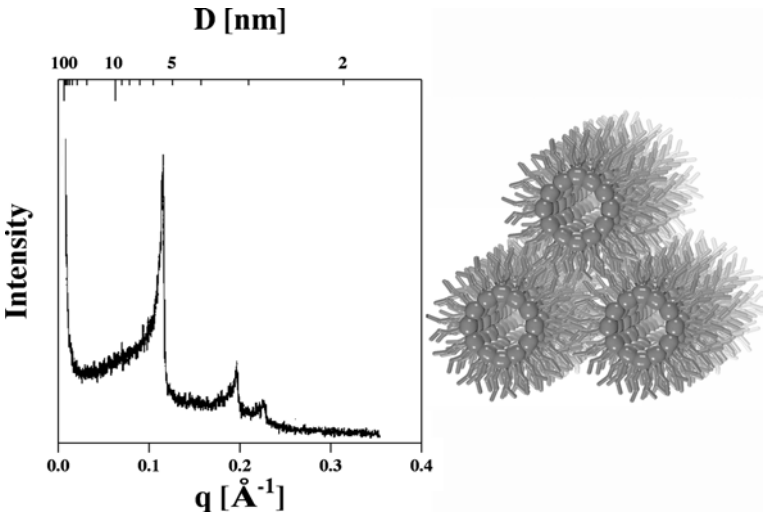

Fig. 2.8 Left: Diffraction pattern of an inverse hexagonal phase in a DMPC–myristic acid 1:2 mixture at 80°, adapted from Heimburg et al. (1990). Right: Schematic picture of an inverse hexagonal phase.

In Fig. 2.9 the layers yielding the first two peaks are shown. Due to the triangular/hexagonal arrangement of the lipid cylinders the two peaks display a $1:\sqrt{3}$ spacing. The further reflexes can be found using the above formula, where h and k are integer numbers ($h,k = 0,1,2,3,\ldots$). Inverse hexagonal phases are typically high temperature phases because only with unordered chains one can find a reasonable packing into cylindrical structures. One finds such cases, for e.g., phosphatidylethanolamines at high temperatures, but also in lipid mixtures as in Fig. 2.8 (Heimburg et al., 1990).

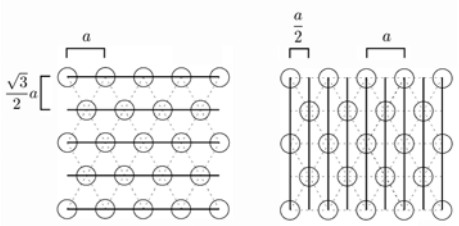

Fig. 2.9 The first and the second diffraction peaks of an inverse hexagonal phase are generated by the layers shown on the left and the right.

2.3.2 Cubic Phases

In cubic phases the membranes arrange in three-dimensional lattices. Diffraction peaks are found at ratios of

$$\frac{(h^2+k^2+l^2)^{0.5}}{a} \qquad \text{i.e. at} \quad 1,\sqrt{2},\sqrt{3},2,\sqrt{5},\sqrt{6},\sqrt{8},3,\ldots \tag{2.13}$$

where h,k and l are integer numbers ($h,k,l = 0,1,2,3,\ldots$). There are several different cubic phases. In Fig. 2.10 a cubic phase of the space group "$Im3m$" is shown. The different cubic space groups differ in peak intensity and the lack of a few reflections is due to symmetry considerations. In general 36 space groups of cubic lattices are possible. They correspond to defined arrangements of lipid compartments on a cubic lattice. In lipid systems so far six different cubic phases have been identified (Lindblom and Rilfors, 1989). Many cubic lipid phases are bicontinuous, i.e., they have two independent connected water volumes. The phase shown in Fig. 2.10 can be imagined as a cubic packing of lipid vesicles that are connected at points where they have closest contact. This phase also has two disconnected continuous water volumes.

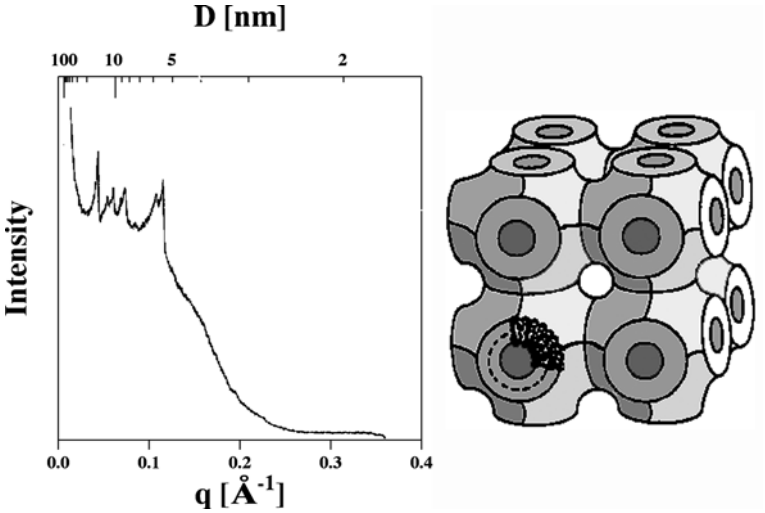

Fig. 2.10 Left: Diffraction pattern of a cubic phase in a DMPC–myristic acid 1:2 mixture at 49°, adapted from Heimburg et al. (1990). Right: Schematic picture of one of the possible cubic phases (space group $Im3m$, adapted from Lindblom and Rilfors (1989) with permission from Elsevier).

2.3.3 Sponge Phases

Topologically sponge phases resemble cubic phases, but they lack the periodic three-dimensional structure (Fig. 2.11). For this reason the sponge phase does not display Bragg peaks. Sponge phases usually display a very high water content and have first been identified in detergent systems (Strey et al., 1990a,b). They are optically transparent and viscous, in contrast to vesicular structures that are opalescent and of low viscosity. It has been proposed that

Fig. 2.11 Schematic drawing of a sponge phase (from Schneider et al. (1999)).

the extended lipid phases occurring in the phase transitions of charged lipid membranes (e.g., dimyristoyl phosphatidylglycerol, DMPG) may be sponge phases. They are discussed further in Chapter 15.

2.4 Summary: Key Ideas of Chapter 2

1. Lipids form many different phases, e.g., micelles, bilayers, and multilayers.

2. The geometry and the distribution of chemical groups within the phase can be investigated using X-ray or neutron diffraction that yields information on electron densities.

3. Together with neutron diffraction one can localize the phosphate groups at the interface with water while the hydrocarbon tails are located in the membrane interior.

4. In multilayers the individual bilayers are separated by a water layer that in the case of phosphatidylcholines is about 2 nm thick. Multilayers display a periodic diffraction peak spacing typical for such lamellar structures with periodicity in only one dimension.

5. In X-ray diffraction one also finds phases that do not display periodic spacings in one dimension, for example the inverse hexagonal phase that consists of inverted lipid cylinders. These cylinders pack into a two-dimensional triangular lattice.

6. Cubic phases display crystal packing in three dimensions and yield typical diffraction peaks. In total 36 cubic space groups exist but only six different cubic lipid phases have been found so far. They often display very large spacings corresponding to the packing of vesicle-like subunits.

7. Some cubic phases are bicontinuous. The continuous lipid membrane surface separates two different continuous water volumes.

8. In detergent systems and possibly in some lipid membrane systems sponge phases exist. Topologically, they resemble cubic phases. However, they do not display crystal symmetry and sharp diffraction peaks in X-ray or neutron experiments.

3
The Composition of Biological Membranes

Biological membranes display complex compositions with hundreds of different lipids and proteins. This chapter introduces the chemical nature of the lipids and some principles of their distribution. It will be shown that the lipid composition varies between different cells and even between different organelles of the same cell. They are also distributed asymmetrically between the two monolayers. It will also be demonstrated that the lipid composition changes as a function of growth conditions, i.e., if ambient temperature, pressure, or the polarity of the aqueous medium are changed.

3.1
Composition of Membranes

Lipids are small amphiphilic molecules with a hydrophobic hydrocarbon region and a hydrophilic head group (Fig. 3.1). In water they spontaneously

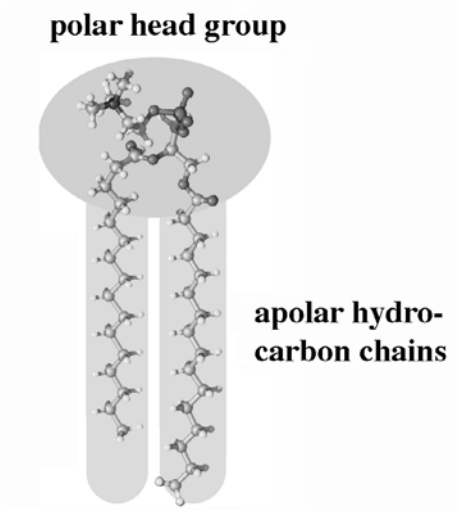

Fig. 3.1 Most lipids possess a polar head group that is exposed to water and an apolar chain region forming the membrane interior.

form aggregates, mostly bilayer membranes. The structure of membranes was introduced in more detail in Chapter 2. The lipids of biological organelles display a rich wealth of chemical structures. Even though most lipids possess two hydrocarbon chains and one hydrophilic head group, the composition of the chains and the head group can vary significantly. Interestingly, the lipid composition is very different in different cell types of the same organism, or even in different organelles of the same cell. Seemingly, the lipid composition responds to changes in intensive thermodynamic variables (see Chapter 4) such as temperature, pressure, pH, or the concentration of solvents. The reason for this is not completely clear. However, the physical rationale is a key issue of this tutorial.

3.2 Head Group Composition

In Figs. 3.2 and 3.3 various lipids with different head groups are shown. Figure 3.2 shows the phospholipids that are the most abundant kind of lipids.

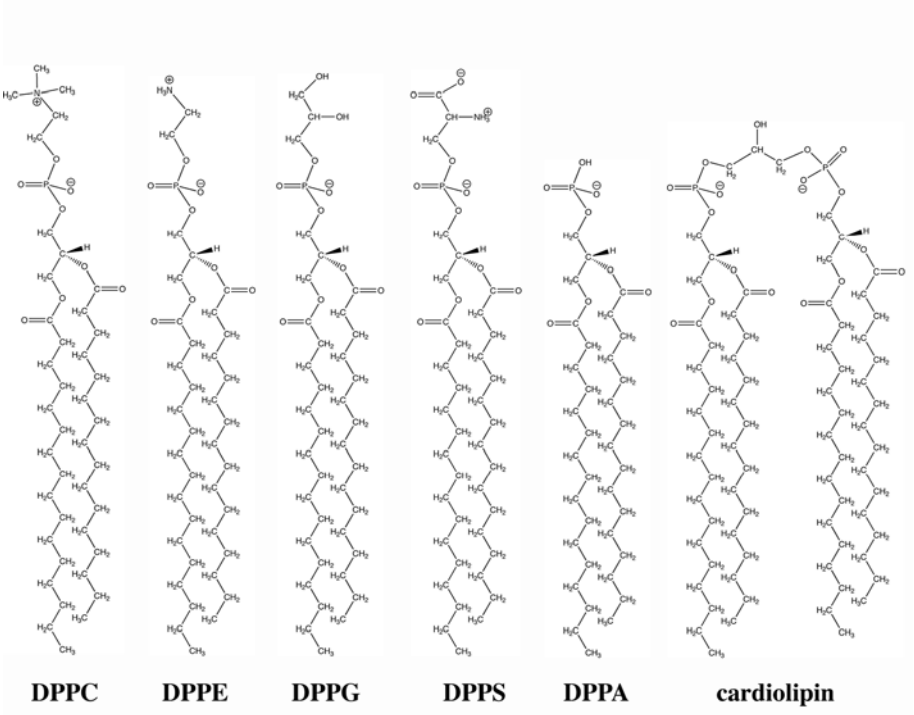

Fig. 3.2 Head group structures of some phospholipids with palmitic fatty acid chains: phosphatidylcholine (DPPC), phosphatidylethanolamine (DPPE), phosphatidylglycerol (DPPG), phosphatidylserine (DPPS), phosphatidic acid (DPPA), and cardiolipin (with four chains and two phosphate groups).

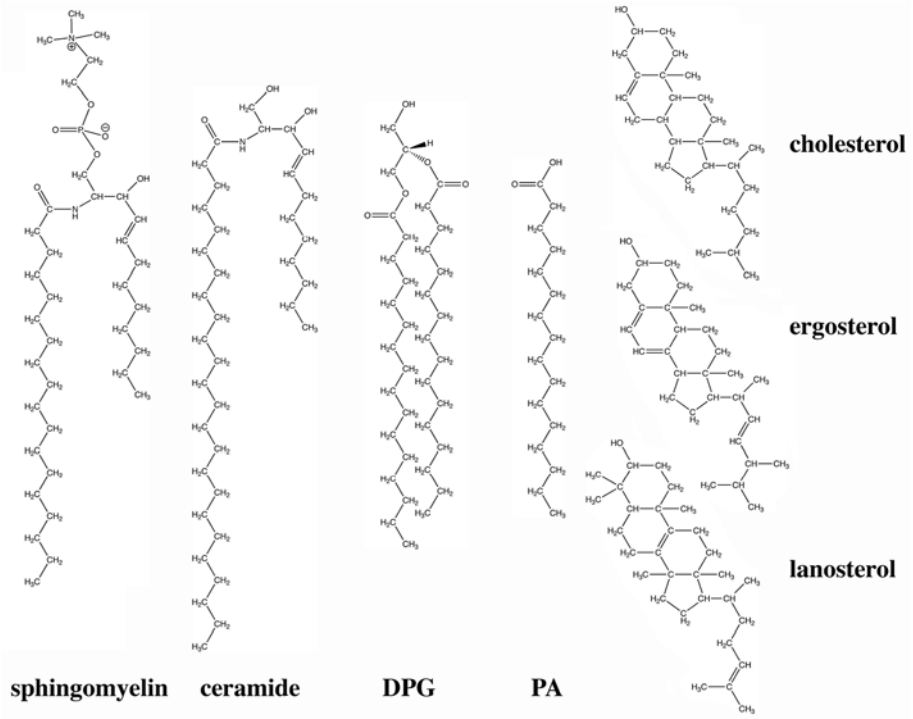

Fig. 3.3 Some lipids without phosphate groups: sphingomyelin, ceramide, dipalmitoylglycerol (DPG), palmitic acid (PA), and the three sterols cholesterol, ergosterol, and lanosterol.

Phospholipids are typically glycero lipids, i.e., they have two fatty acids bound to the first and second positions of a glycerol molecule, while the phosphate-containing head group is bound to the third position. Therefore, a lipid with a phosphatidylcholine head group and two palmitoyl chains is called 1,2 palmitoyl-glycero-sn-3-phosphocholine—or simpler—dipalmitoyl phosphatidylcholine (DPPC). Most lipids display chirality and the chiral center is the center carbon of the glycerol backbone. In monolayers, this chirality leads to the formation of chiral domains that can be seen in light microscopy (see Chapter 6, Fig. 13.6). Among the lipids shown in Fig. 3.2, cardiolipin is special because it is a dimer of two phospholipids. It is found in high concentrations in mitochondrial membranes. While phosphatidylcholine and phosphatidylethanolamine are zwitterionic (i.e., they do not carry a net charge at neutral pH) the other four lipid species are negatively charged. Cardiolipin even carries two negative charges. Positively charged lipids do not occur in nature. However, some synthesized positively charged lipids are used for drug delivery purposes since they bind DNA (Rädler et al., 1997) and other negatively charged molecules.

The lipids shown in Fig. 3.3 are not phospholipids. Sphingomyelin and ceramide do not have a glycerol backbone. These lipids often occur with long saturated chains and are claimed to be relevant for the formation of microdomains in biological cells (rafts, see Section 9.5). Diacyl glycerols have only a very small head group consisting of an –OH group. Such lipids seem to play a role in tumor growth activation. Membranes also contain small fraction of monomeric fatty acids of which palmitic acid is shown. Further important lipids not shown in Figs. 3.2 and 3.3 are glycolipids, gangliosides and lipopolysaccharides.

Very important are the sterols. Shown here is cholesterol that forms up to 20 wt.% of erythrocyte membranes and other plasma membranes. Ergosterol and lanosterol are very similar to cholesterol. While cholesterol is mainly found in animal cells, ergosterol is an important component in fungal plasma membranes (Hsueh et al., 2005), and lanosterol is the sterol of procaryotes and the chemical precursor of the other two sterols (Henriksen et al., 2006). The sex hormones,, e.g., testosterone and progesterone, are derivatives of cholesterol (not shown).

The lipid head group distribution of various cells and organelles is given in Table 3.1 (Jamieson and Robinson, 1977). It can be seen that different membranes also display different lipid compositions. One of the main themes of this book is to show that these differences influence the physical features of membranes. For instance, mitochondria contain about 14% cardiolipin (with two net negative charges) while no other organelle contains more than minute amounts of this lipid. This makes mitochondrial membranes highly charged (Chapter 11). The myelin sheet of nerves has a three times larger cholesterol concentration than the neuronal membranes. Cholesterol is known to abolish chain melting transitions above about 10–15 mol% while up to 10 mol% the influence is very small (see Chapter 7)

Tab. 3.1 Head group composition of the membranes of some mammalian liver cells, erythrocytes , and nerve cells in weight percent. Adapted from Jamieson and Robinson (1977). Abbreviations: PC = phosphatidylcholines, PE = phosphatidylethanolamines, PS = phosphatidylserines, PI = phosphatidylinositols, SM = sphingomyelin, CL = cardiolipin.

Membrane	PC	PE	PS	PI	SM	CL	Glycolipid	Cholesterol	Others
Erythrocyte (human)	20	18	7	3	18	–	3	20	11
Plasma (rat liver)	18	12	7	3	12	–	8	19	21
ER	48	19	4	8	5	–	tr	6	10
Golgi	25	9	3	5	7	–	0	8	43
Lysosome	23	13	–	6	23	≈ 5	–	14	16
Nuclear membrane	44	17	4	6	3	1	tr	10	15
Mitochondria	38	29	0	3	0	14	tr	3	13
Neurons	48	21	5	7	4	–	3	11	1
Myelin	11	17	9	1	8	–	20	28	6

3.3
Hydrocarbon Chain Composition

The hydrocarbon chain composition of lipid membranes is also very diverse. They vary in chain length and the degree of saturation. The most abundant fatty acids are shown in Fig. 3.4. The corresponding trivial names are explained in Table 3.2. A chain denoted with 18:1 denotes a chain with 18 carbons with one double bond, while 18:0 denotes a chain without double bond. Lipids containing double bonds in their chains are called unsaturated lipids and lipids without double bonds are saturated lipids.

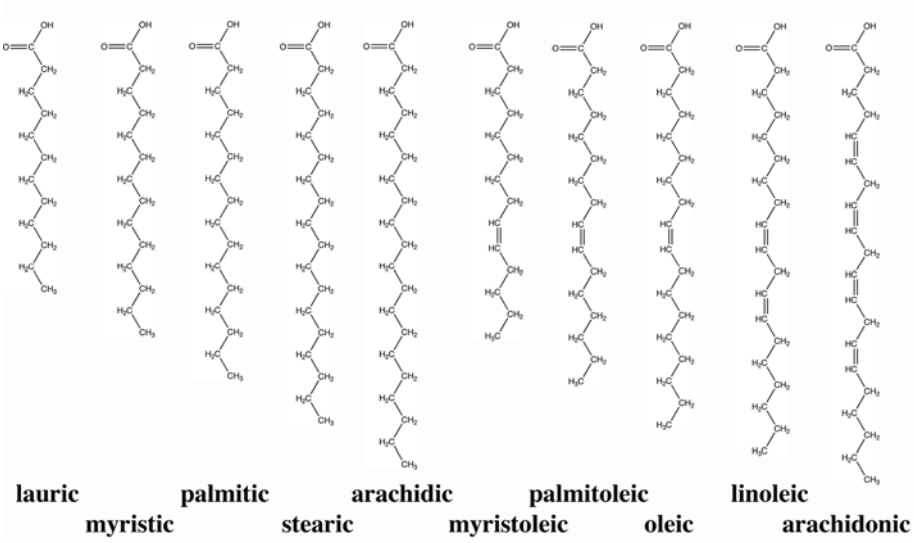

Fig. 3.4 A selection of saturated and unsaturated fatty acids that form the hydrocarbon chains of lipids.

Tab. 3.2 Trivial names of some common fatty acids.

Trivial name	Chain length: number of double bonds	Position of unsaturations
Lauric	12:0	
Myristic	14:0	
Myristoleic	14:1	
Palmitic	16:0	
Palmitoleic	16:1	9-cis
Stearic	18:0	
Oleic	18:1	9-cis
Linoleic	18:3	6-cis, 9-cis, 12-cis
Arachidic	20:0	
Aracidonic	20:4	5-cis, 8-cis, 11-cis, 14-cis

In biological membranes, the chain composition is different for lipids with different head groups. In Table 3.3 we show the distribution of different hydrocarbon chains among lipids of erythrocytes with different head groups (Jamieson and Robinson, 1977). It can be seen, for instance, that in this cell type phosphatidylcholines tend to have relatively short chains between 16 and 18 carbons. The sphingomyelins tend to have long chains with 24 carbons.

Tab. 3.3 Distribution of fatty acid chains of erythrocyte for different head group lipids given in weight percent. Taken from Jamieson and Robinson (1977).

Lipid head group	16:0	18:0	18:1	18:2	20:3	20:4	22:0	22:4	22:5	22:6	24:0	24:1
PC	31	12	19	22	2	7	–	–	2	–	–	–
PE	13	12	18	7	2	24	2	8	4	8	–	–
PS+PI	3	37	8	–	3	24	3	4	3.5	10	–	–
SPHM	24	6	–	3	–	1.4	9.5	–	–	–	23	24
Total	20	17	13	9	1.5	13	2	3	2	4	5	4

The chain composition is also different in different organelles of the same cell. In Table 3.4 this is shown for liver cells (White, 1973). It can be seen that the abundance of 15:0 carbon chains is about 37 wt.% in the plasma membrane while it is about 27% in the mitochondrial membranes. 16:1 chains form about 31% of the chains in the plasma membrane and only 18% of the mitochondrial membranes. Lipid compositions of subcellular membranes have also been studied by Zinser et al. (1991). The relation between composition and function has been reviewed by Spector and Yorek (1985). For further reading the article by Sackmann (1995) is recommended.

Tab. 3.4 Fatty acid compositions of the membranes of some organelles from rat liver in weight percent. Taken from White (1973) and Gennis (1989).

Membrane	14:0	15:0	16:0	16:1	17:0	18:0	18:1	18:2	20:3	22:4	22:6
Mitochondria (outer)	0.4	27.0	4.1	21.0	13.5	13.5	–	–	1.1	15.7	3.5
Mitochondria (inner)	0.3	27.1	3.6	18.0	16.2	15.8	–	–	1.0	18.5	3.8
Plasma	0.9	36.9	–	31.2	6.4	12.9	tr	tr	–	11.1	–
Smooth ER	0.4	28.6	3.1	26.5	10.6	14.9	–	–	1.4	14.0	0.7
Rough ER	0.5	22.7	3.6	22.0	11.1	16.1	–	–	1.8	19.7	2.9
Golgi	0.9	34.7	–	22.5	8.7	18.1	tr	tr	–	14.5	–

3.4 Asymmetry Across Membranes

The lipid composition is not only different in different cell types and organelles but also within the two leaflets of the same membrane. This is shown

in Fig. 3.5 for erythrocyte membranes (Rothman and Lenard, 1977). Many cells display voltage or pH gradients across their plasma membranes. The resting potential of a nerve cell is around −70 mV. These voltage differences are reflected in the distribution of the charged lipid on the inner and outer membrane. Further, there are ATP-consuming active processes that influence the lipid distribution. In Fig. 3.5 it can be seen that negatively charged phosphatidylserines are predominantly located on the inner leaflet of the erythrocytes. The same is true for the phosphatidylethanolamine. Phosphatidylcholines and sphingomyelins are rather found on the outer leaflet. This indicates that physical properties are different on the two sides of the membranes and that thermodynamic forces act across membranes, e.g., by electrostatic field gradients or by differences in chemical potential.

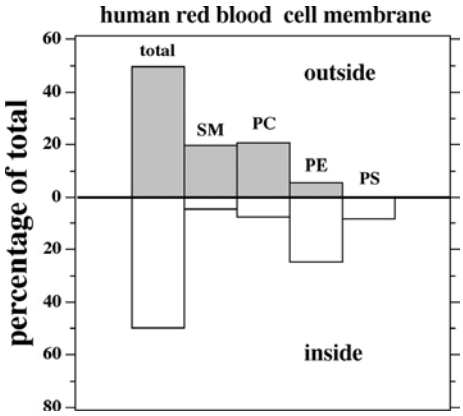

Fig. 3.5 The composition of membranes may be different in the outer and the inner leaflet of the membrane. In erythrocytes phosphatidylcholines and sphingomyelin are found mostly on the outside (exoplasmic) leaflet while phosphatidylethanolamine and phosphatidylserine are found on the inside (cytoplasmic) leaflet. Data adapted from Rothman and Lenard (1977).

It will be shown later that the lipid composition is not even homogeneous within one monolayer leaflet. Lipids tend to segregate into domains due to phase separation phenomena (see Chapters 7 and 8).

3.5 Dependence of Lipid Composition on Growth Temperature

Lipid membranes display melting transitions. Such transitions depend on the chain length and the degree of saturation (i.e., the number of double bonds in the chain). The longer the chains the higher the melting point. However, double bonds in a chain drastically lower the melting temperature. DOPC has

a melting temperature around $-20\,^{\circ}$C while DSPC has a melting temperature of about $53\,^{\circ}$C. The only difference between these lipids is a double bond between carbons 9 and 10 in the oleoyl chains of DOPC. Much of this book is dedicated to the melting phenomenon. It is assumed that many biological phenomena can be understood on the basis of such transitions—including nerve pulse propagation (Chapter 18), anesthesia (Chapter 19), and membrane permeability (Chapter 17).

The likely important role of temperature-dependent transitions leads immediately to the question how cells and organisms respond to changes in physical conditions that influence such transitions. In fact, the lipid composition of biomembranes responds sensitively to changes in temperature and pressure (see the next section). This is shown in Table 3.5 for the example of trouts raised at two different temperatures, $5\,^{\circ}$C and $20\,^{\circ}$C. The data in this table are a selection of much more detailed data from Hazel (1979). The lipid composition of trout livers changes with growth temperature. The general trend in the data is that saturated chains are more abundant in trout livers from the $20\,^{\circ}$C experiment, while the poly-unsaturated chains are more abundant in the $5\,^{\circ}$C experiments. This reflects the trend of the melting temperatures of such lipids. Unsaturated lipids melt at significantly lower temperatures than lipids with saturated chains.

Tab. 3.5 Lipid composition as a function of growth temperature: Fatty acid compositions of the membranes of trout livers are given in weight percent of the respective head group species. The trouts were acclimated at $5\,^{\circ}$C and $20\,^{\circ}$C. Some especially strong changes are highlighted in bold letters. Data are a selection from Hazel (1979).

Fatty Acid	Total 5°C	Total 20°C	PC 5 °C	PC 20 °C	PE 5 °C	PE 20 °C	SM 5 °C	SM 20 °C	CL 5 °C	CL 20 °C
16:0	**16.52**	**22.37**	**18.19**	**27.50**	9.57	11.09	**18.15**	**26.34**	**16.58**	**23.90**
18:0	7.62	6.10	3.86	3.51	**5.81**	**9.66**	5.44	4.72	4.55	5.22
18:1	12.75	14.67	12.39	14.26	18.01	18.74	**9.21**	**13.56**	12.96	12.15
20:5	4.06	2.24	3.35	2.72	**8.46**	**2.34**	**25.76**	**0.77**	1.27	0.12
22:6	35.20	33.43	**40.95**	**32.83**	32.90	32.41	**3.17**	**9.04**	**15.38**	**5.54**

Avery et al. (1995) reported changes in lipid composition of amoebae upon changes in growth temperature. They found that the order within the membrane chains correlated with the changes in composition. A further study on temperature effects in *bacillus subtilis* membranes was made by van de Vossenberg et al. (1999). In these experiments the lipid composition changed significantly with the growth temperature. Simultaneously the chain melting transition of the extracted lipids changed such that bacteria grown at lower temperatures also display melting transitions of their lipids at lower temperatures (data not shown). A very similar observation can be made when investigating the membranes of *E. coli*. In Fig. 3.6 the melting profiles of the

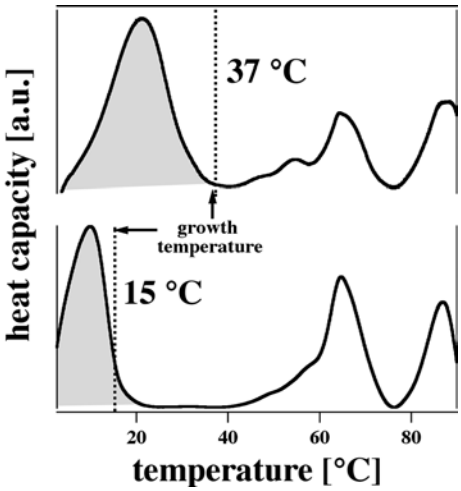

Fig. 3.6 The membranes of *E. coli* display different lipid melting properties when grown at different temperatures. The lipid melting transition, shaded gray in this heat capacity profile, is always found slightly below growth temperature. The peaks at high temperature are protein unfolding peaks. Unpublished data from T. Heimburg, D. Pollakowski and M. Konrad/MPI Göttingen.

isolated membranes of *E. coli* grown at 37 °C and at 15 °C are shown. The native membranes are intact, i.e., they contain all their proteins and are not lipid extracts from those membranes. It can be seen that the melting transition in such membranes can be found slightly below growth temperature. The lipid composition in these membranes has changed in order to accommodate for new environmental conditions. This is very similar to the above case with *bacillus subtilis* membranes. It therefore seems as if the changes in membrane composition follow a very rational purpose in adjusting the physical state of the membrane to the ambient environmental conditions.

The thermal adaptation of lipid composition and its possible physicochemical role has also been reviewed in Hazel (1995).

3.6 Dependence of Lipid Composition on Pressure

Phase transitions in membranes depend on more variables than just temperature. Among those are also pressure, pH, and the chemical potentials of ions such as Ca^{2+}. Pressure, as an example, shifts melting temperatures towards higher temperatures (see Chapter 6). Changes in pressure change the physical state of lipid membranes (Chapter 6) and it seems likely that the membranes of the organisms have to adapt to pressure changes.

Tab. 3.6 Lipid composition in weight% as a function of growth pressure: fatty acid compositions of membranes from the barophilic marine bacterium CNPT3 at 2 °C. Growth pressures were 1, 172, 345, 517, and 690 bar, respectively. Data are a selection from DeLong and Yayanos (1985).

Fatty acid	1 bar	172 bar	345 bar	517 bar	690 bar
14:1	20.0	19.6	17.4	13.7	11.5
14:0	7.5	5.7	5.2	4.8	3.5
16:1	40.2	44.0	47.9	46.8	56.3
16:0	25.2	22.2	20.7	18.7	18.5
18:1	5.5	5.9	6.6	11.0	7.3
18:0	1.5	2.5	2.1	4.9	2.8

In an experiment by DeLong and Yayanos (1985) the dependence of the lipid composition of deep-sea bacteria on the hydrostatic pressure during growth has been investigated. The pressure dependence of lipid membrane states is not very pronounced and it needs relatively high pressures to see reasonable changes. Typically, 40 bar of pressure changes melting transitions by about 1 K (see Section 6.3). Therefore, to see similar changes as in the trout experiment above (15 K temperature difference) one requires about 600 bar. This is the pressure range investigated by DeLong and Yayanos (1985). In Table 3.6 the results of the pressure study are shown. The result is most clearly seen when comparing the abundance of 16:0 chains and 16:1 chains at different pressures. While increasing pressure is accompanied by an increase of the concentration

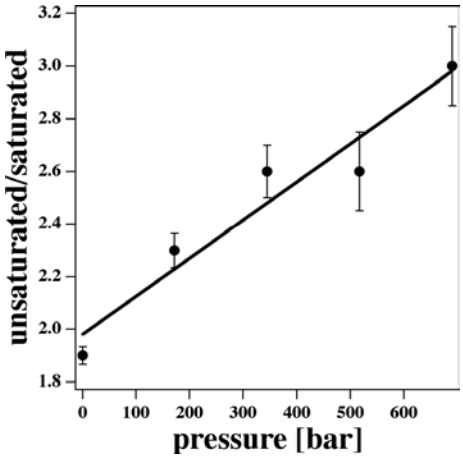

Fig. 3.7 The ratio of unsaturated to saturated fatty acid chains of the deep sea bacterium CNPT3 is linearly dependent on the hydrostatic pressure at which they were cultivated (cf. also values in Table 3.6). Adapted from DeLong and Yayanos (1985).

of unsaturated chains, the abundance of saturated chains is lowered. This is also reflected in Fig. 3.7 where the pressure dependence of the ratio between unsaturated and saturated chains is given. As mentioned above unsaturated chains lower melting point (thus compensating the pressure increase) while saturated chains increase melting points and are predominantly found at low pressures.

A comparable study by Kaneshiro and Clark (1995) came to the conclusion that pressure shifted the temperature dependence of lipid fluidity by ca. 10 K/500 bar toward more ordered states. This corresponds well with the above-mentioned pressure dependence of transitions of about 1 K/40 bar.

3.7 Dependence of Lipid Composition on Changes in Other Thermodynamic Variables

Pressure and temperature are not the only intensive variables in thermodynamics. There are also other variables such as the electrostatic potential, and the chemical potentials of all components of the biological systems. The presence of ethanol lowers melting temperatures (see Chapter 19) Therefore ethanol should result in a similar change in lipid composition to those caused by temperature increase. In a careful study Ingram (1977) investigated the influence of a large number of solvents and other chemicals present in the growth medium (in total 23 substances) on the lipid composition of *E. coli* membranes. It was shown that both head group and chain composition are affected. When grown in a medium containing 48 mM acetone the cardiolipin concentration changes 5-fold from 1.3% to 8.4%. When grown in 38 mM aniline the concentration of 18:1 chains drops from 31.9% to 6.7%. In the presence of 20 mM sodium benzoate the fraction of 12:0 chains increased from 4% to 52% while simultaneously the fraction of 16:1 chains drops from 34.1% to 5.9%. These are drastic changes. Interestingly, the effect of anesthetics follows the same dependences on changes in the thermodynamic variables as does the lipid composition, meaning the increase in solvent concentration and increase in hydrostatic pressure act on the anesthetic potency in the opposite direction. This will be used in Chapter 19 to put forward a thermodynamic explanation of anesthesia.

It is likely that changes in other thermodynamic variables will result in comparable changes. The lowering of ambient pH is expected to result in changes similar to those of pressure increase. This is because a certain fraction of the lipids are negatively charged and can be protonated. Protonation of charged lipids increases their melting temperature (this is explained in detail in Chapter 11).

3.8 Summary: Key Ideas of Chapter 3

- Most lipids in biological membranes are phospholipids with glycerol backbone that possess a phosphate-containing head group and two hydrocarbon chains. One also finds sphingomyelin, ceramide, fatty acids, and other lipids in smaller quantities. A special case is the sterols, e.g., cholesterol and lanosterol. Their abundance in some membranes can be up to 20 wt.%.
- Lipid head groups differ in their net charge, their size, and their polarity.
- Lipid chains differ in length and the degree of unsaturation, i.e., in the number of double bonds. Lipid chains are apolar.
- The lipid composition (and also the protein composition) of different biological membranes is specific for different cell types and even for the different organelles within one cell and it varies considerably. This is true for both head group composition and the chain composition.
- The lipid composition is strongly influenced by growth temperature and by ambient pressure. The chain composition adapts such that the melting point of membranes shift in the same direction as the change in either temperature or pressure.
- The change in other thermodynamic variables also influences the lipid composition, e.g., the chemical potentials of solvents.
- Lipid compositions change in a coherent manner as a response to changes in the environmental conditions that can be expressed in terms of intensive thermodynamic variables. Even though this is not understood so far in all aspects, this book provides numerous examples that demonstrate the physical rationale behind such changes.

4
Introduction Into Thermodynamics

Thermodynamics is one of the fundamental disciplines in physics. It provides the basic definition of functions of state, e.g., internal energy and entropy, or intensive or extensive variables such as temperature, pressure, and volume. One can divide thermodynamics into subdisciplines, which are equilibrium thermodynamics, and linear and nonlinear nonequilibrium thermodynamics. Equilibrium thermodynamics defines relationships between functions of state and the variables, which are strictly true in all fields of physics of equilibrated systems, from particle physics and quantum mechanics to cosmology. Naturally it is also true for all biological matter that does not undergo rapid changes. Since it is a theory based on first principles without approximations, one can derive surprising relations between various observables.

Thermodynamics is a macroscopic theory and is therefore in particular constructed to describe the behavior of ensembles of many molecules, or of single molecules observed over long time intervals. The latter case relies on the ergodic theorem stating that averages over long time are similar to averages over many identical systems. Practically this means that instead of observing, for instance, many lipid vesicles of identical size at a given time (as it is usually done in most experiments), one can also observe one single vesicle over a long period of time, as it is usually done in simulations of membranes. We will make use of the ergodic theorem in Chapter 8 when we introduce Monte Carlo simulations.

Below we will provide an introduction those thermodynamic terms that are important for membranes and the topics discussed in this book.

4.1
Functions of State

A common experience of everyday lab work is that the preparation of samples for experiments requires experience and the knowledge of experts. Many lipid membrane preparations require organic solvents in the preparation process, which are removed in a later stage of the sample preparation by drying the sample in a desiccator. Sometimes, result seems to depend on the use of

a specific solvent during the preparation, and another solvent seems less suitable. Now it is a fundamental requirement of physics that the outcome of an experiment should neither depend on the person who is performing the experiment, nor on the preparation history of the sample, as long as the samples are identical. This fundamental requirement is expressed in thermodynamics by the introduction of the term "function of state." Let us assume a function, Z, that describes the state of the membrane system at given values of the thermodynamic variables. Z is called a function of state if the following relation is fulfilled:

$$\int_a^b dZ \qquad \text{independent of integration path} \tag{4.1}$$

meaning that the integral over dZ only depends on the start and the end points, a and b, but not on the particular way how the system shifted from a to b. In practical terms this means that if we start with a dry powder of lipids and we end with vesicles of this lipid in an aqueous dispersion, the value of the function Z should not depend on which organic solvent was used during an intermediate process of the sample preparation. Equation (4.1) can also be expressed as

$$\oint dZ = 0 \qquad \text{independent of integration path} \tag{4.2}$$

One of the most important functions of state is the internal energy, E.

4.2 First Law of Thermodynamics

Thermodynamics relies on two fundamental laws of physics. The first is conservation of the internal energy, E, expressed through the relation

$$dE = dQ + dW \tag{4.3}$$

where dE is the change of internal energy, dQ is the change of heat of the system, and dW is the work performed on the system. Heat and work are the only two contributions to the internal energy. The work can act on a system in many ways, e.g.,

$$-p\,dV \qquad \text{work to change the volume} \tag{4.4}$$

is the work needed to change the volume, for instance of a lipid membrane, against the bulk pressure, p. This term becomes important later when the compressibility of a membrane is introduced. Very similar contributions are

$$-\Pi\,dA \qquad \text{work to change the area} \tag{4.5}$$

with membrane area, A, and lateral pressure, Π, and

$$-f\,dl \qquad \text{work to change the length of a spring} \tag{4.6}$$

with the force, f, and the length, l. Expression 4.5 relates to the work necessary to change the area, which becomes important in the lateral compressibility and the bending elasticity, and expression (4.6) relates to the work necessary to stretch, for instance, a membrane cylinder.

A further contribution to the work performed on a system is

$$\Psi\,dq \qquad \text{work to charge a capacitor} \tag{4.7}$$

with Ψ being the electrostatic potential of a membrane, and dq being the change of the charge on the membrane. This term is important in electrostatic theory, but also in the theory of nerves, where the membrane is considered to be a capacitor that is charged in a time-dependent electrostatic field. There are many other contributions to the work, like dipolar orientation in electric or magnetic fields, etc., which do not play an important role here.

We can summarize that the work performed on a thermodynamics system (e.g., a membrane) is

$$dW = -p\,dV - \Pi\,dA - f\,dl + \Psi\,dq + \cdots \tag{4.8}$$

In the epochal work of Carnot (1796–1832) (Carnot, 1824) it was shown that neither the heat Q nor the work W are functions of state. This leads to the possibility of the construction of heat engines that transform heat into work, and it is probably not by accident that Carnot's work was written after the revolutionary success of the heat engines first built by Henry Watt. The fact that heat and work are not functions of state leads to the finding that the efficiency of a heat engine (or a motor) depends on the construction principle of the engine. Carnot could derive that the efficiency of the heat engine only depends on the temperature differences, making engines with large temperature differences more efficient than engines with small temperature differences. This maximum efficiency, however, is only obtained when every single step in the Carnot cycle is fully reversible. This is generally not the case, due to friction or losses of heat into the environment. Many processes in biology convert the free energy contained in ATP into biological function, e.g., into the movement of myosin molecules on actin filaments in a muscle. This conversion of the free energy in ATP into physical work can also be considered as an engine with an efficiency that depends on the experimental conditions.

The differential of the internal energy is the sum of the products of intensive variables with the differentials of extensive variables. Intensive variables are those thermodynamics variables that are independent of system size (e.g., pressure p, temperature T, electrostatic field Ψ, ...) while extensive variables

are defined as being proportional to system size (e.g., entropy S, volume V, charge $q, \ldots$).

4.3 Second Law of Thermodynamics

A major step in understanding the fundamental functions of thermodynamics was made by Rudolf Clausius (1822–1888) by stating that for the fully reversible steps in the heat engine

$$dS_r \equiv \frac{dQ}{T} \tag{4.9}$$

is a function of state meaning that

$$\oint dS_r \equiv \oint \frac{dQ}{T} = 0 \tag{4.10}$$

The function S_r was called the entropy (the index r stands for reversibility). In other words, the entropy is the function of state that relates the changes of heat, dQ, to the temperature, T. As W. Thompson (Lord Kelvin, 1824–1907)) later indicated, the above statement also involves a fundamental definition of the nature of temperature. To his honor, the absolute temperature scale now carries the unit K (Kelvin).

As mentioned, the efficiency of a realistic heat engine is usually smaller than that of the ideal engine due to losses of heat that cannot be used to reversibly perform work. These losses must always be larger than zero. The part of the entropy change of a system that cannot be used to perform work is now defined to be dS_i (the index i stands for irreversible). Equation (4.9) can now be rewritten as

$$dS_r + dS_i \geq \frac{dQ}{T} \qquad \text{with} \qquad dS_i \geq 0 \tag{4.11}$$

The irreversible part of the entropy induces changes in the state of the system until no further spontaneous changes occur. This final state is called the thermodynamic equilibrium. In thermal equilibrium the function S is in a maximum, and $dS_i = 0$. The irreversible part of the entropy is linked to all spontaneous processes inside a system, which do not lead to heat exchange with the environment or the performance of work on an external system.

With the help of Eq. (4.9) the first law of thermodynamics (for reversible changes) of the system can now be rewritten as

$$dE = T\,dS_r - p\,dV \quad (-\Pi\,dA - f\,dl + \Psi\,dq + \cdots) \tag{4.12}$$

In most parts of this book we will consider reversible processes and omit the index "r." Reversible means that a process that converts heat into work can

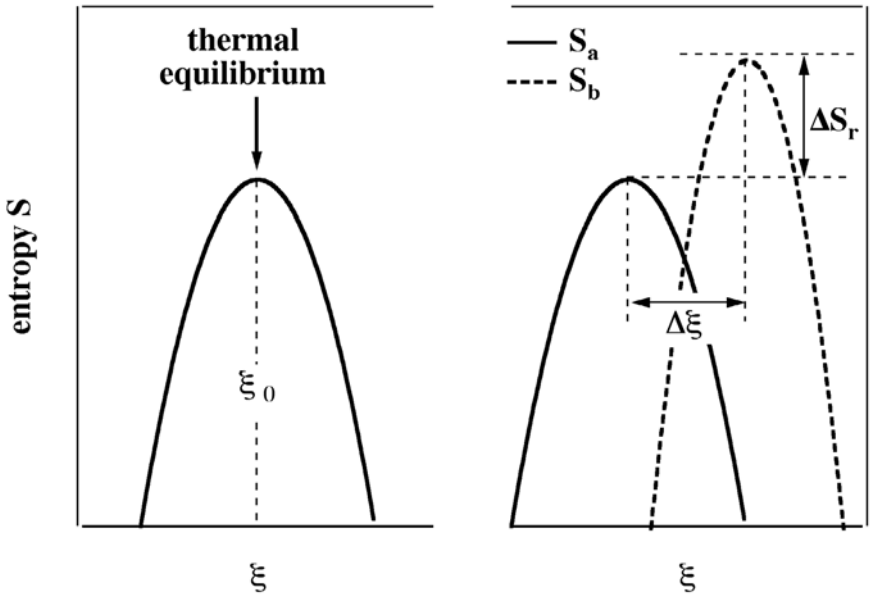

Fig. 4.1 Left: The entropy, S, depends on the irreversible contribution, S_i, that displays close to the thermal equilibrium approximately a quadratic dependence on a reaction variable. The maximum of this function corresponds to thermal equilibrium. Right: If one considers two states of the system, a and b, they may display different maxima of the entropy at different values of the reaction variable, ξ.

be reversed such that the application of the same amount of work leads to a heat release of identical magnitude. Also, to simplify the writing we will often denote the differential of the internal energy as $dE = TdS - pdV$ and tacitly omit all the other contributions to the work (i.e. the terms in brackets in Eq. (4.12)). But it goes without saying the all the contributions to the work have to be taken into account.

4.4 Other Functions of State

The internal energy, E and the entropy, S, are functions of state. The products pV and the TS are also functions of state. Now, the following combinations are also functions of state:

$$\begin{aligned} F &\equiv E - TS && \text{Helmholtz free energy} \\ H &\equiv E + pV && \text{enthalpy} \\ G &\equiv E + pV - TS && \text{Gibbs free energy} \end{aligned} \tag{4.13}$$

Of course, there are many more functions of state that could be defined, but the three functions above are especially useful. The differentials of these functions are

$$\begin{aligned} dF &= dE - d(TS) &&= \cdots = -S\,dT - p\,dV \\ dH &= dE + d(pV) &&= \cdots = T\,dS + V\,dp \\ dG &= dE + d(pV) - d(TS) &&= \cdots = -S\,dT + V\,dp \end{aligned} \tag{4.14}$$

Now it can be immediately seen that

$$\begin{aligned} dF &= 0 \quad \text{for} \quad T, V = \text{const.} \\ dG &= 0 \quad \text{for} \quad T, p = \text{const.} \end{aligned} \tag{4.15}$$

This means that under conditions of constant temperature and constant volume the Helmholtz free energy is either in a minimum or in a maximum. Since the entropy in thermal equilibrium is in a maximum, the Helmholtz free energy is in a minimum. Thus, the introduction of the Helmholtz free energy is a very useful tool to determine the thermodynamic equilibrium under conditions of constant volume and constant temperature.

Similarly, in thermal equilibrium the Gibbs free energy is in a minimum under conditions of constant pressure and constant temperature. The free energies describe the directions of spontaneous processes. The internal energy does not do that. Reactions in general approach free energy minima and not internal energy minima. The internal energy under no conditions can indicate the direction of a spontaneous process. Therefore, the physical contents of the first law and the second law are very different.

In contrast to the internal energy E and the enthalpy H the two free energies F and G can be used to determine where the thermal equilibrium can be found. If one is undecided which of the two free energies to use for calculations related to a given experiment, one has to look at what kind of experiment one intends to perform. In biophysics, under nearly all conditions the experiments are performed at constant temperature (e.g., room temperature) and at constant pressure (usually at atmospheric pressure). Under these circumstances, the Gibbs free energy is the function that determines the thermal equilibrium. The enthalpy H plays a similar role for the Gibbs free energy, as the internal energy E does for the Helmholtz free energy.

The Helmholtz free energy is a useful quantity for experiments performed under conditions of constant temperature and volume, for example in a closed container. Usually, this is not the case in biophysical experiments.

But what if during an experiment temperature and pressure do not stay constant? Well, under these conditions the Gibbs free energy is no useful property and cannot be used to determine the thermal equilibrium. Thus, one should always be careful to define experimental conditions properly, for example by

using an external temperature control (water bath) and by not closing reaction chambers.

4.5 The Chemical Potential

Equation (4.12) showed that the internal energy changes depend on changes in entropy, volume, area, etc. No mention was so far of the number of particles. Let us consider a systems with many different particle species (e.g., different lipids in a membrane) with quantity n_i. One should expect that the internal energy also depends on the number of particles, or the size of the system. To account for the system size, the chemical potential has been introduced such that

$$\mu_i = \left(\frac{\partial E}{\partial n_i}\right)_{S,V,n_j,\ldots} \tag{4.16}$$

The chemical potential thus is an intensive quantity while the number of particles is an extensive variable. It follows that the full expression for the differential of the internal energy and the free energies is

$$\begin{aligned} dE &= T\,dS - p\,dV + \cdots + \sum_i \mu_i dn_i \\ dF &= -S\,dT - p\,dV + \cdots + \sum_i \mu_i dn_i \\ dG &= -S\,dT + V\,dp + \cdots + \sum_i \mu_i dn_i \end{aligned} \tag{4.17}$$

and

$$\mu_i = \left(\frac{\partial E}{\partial n_i}\right)_{S,V,n_j\ldots} = \left(\frac{\partial F}{\partial n_i}\right)_{T,V,n_j,\ldots} = \left(\frac{\partial G}{\partial n_i}\right)_{T,p,n_j,\ldots} \tag{4.18}$$

The chemical potential is a quantity that is very important in chemical reactions where the number of particles does not stay constant (Section 4.7). The number of particles of a given species (or state) also changes in lipid melting (Chapter 7) and in protein unfolding. Under conditions of constant pressure and constant temperature the chemical potential is identical to the Gibbs free energy of a standard amount of substance (in chemistry one usually takes a quantity of 1 mol). It should be added that the chemical potential is a function of pressure, temperature, and other intensive variables.

4.6 The Gibbs–Duhem Equation

As mentioned in the previous section, during chemical reaction the number of particles changes.

The Gibbs free energy is, as entropy S, volume V, enthalpy H, and internal energy E an extensive quantity (they depend on the system size). For given values of the intensive variables it is proportional to the size of the system, e.g., to volume and to the number of particles. Let us now consider a system with many species of particles of quantity n_i, which is the number of moles of the substance with index i. From integration of Eq. (4.17) at constant pressure and temperature we obtain

$$G(p,T,n) = \sum_i n_i \cdot \mu_i(p,T) \tag{4.19}$$

One can see that the chemical potential μ is identical to the Gibbs free energy at constant pressure and temperature for 1 mol of substance. The chemical potential therefore depends on pressure and temperature (and the other intensive variables that have been omitted), but is independent of the number of particles. The differential of the Gibbs free energy is now given by

$$dG(p,T,n) = \sum_i n_i \cdot d\mu_i(p,T) + \sum_i \mu_i(p,T) \cdot dn_i \tag{4.20}$$

Since at constant pressure and temperature $dG = \sum_i \mu_i dn_i$ (Eq. (4.17)) it follows that

$$\sum_i n_i d\mu_i = 0 \tag{4.21}$$

This is the Gibbs–Duhem relation. This relation will be used in Section 7.2.1 to derive Gibbs' phase rule.

4.7 Chemical Equilibrium in Solutions

For 1 mol of noninteracting particles of species i the ideal gas law holds: $p_i \cdot V = R \cdot T$. A pressure change (as induced by a change in volume per particle) at constant temperature and constant number of particles results in a change of the chemical potential (i.e., the Gibbs free energy for 1 mol of particles):

$$\mu_i = \mu_{i,0} + \int_{p_{i,0}}^{p_i} V dp_i = \mu_{i,0} + RT \ln \frac{p_i}{p_{i,0}} \equiv \mu_{i,0} + RT \ln \frac{c_i}{c_{i,0}} \tag{4.22}$$

(cf. Eq. (4.17)). Here the concentrations $c_i = n_i/V = (n_i p_i/RT)$ were introduced. The equivalence of partial pressures, p_i, and concentrations in solutions, c_i, has first been expressed by van't Hoff (1887). The standard state potential μ_0 is the Gibbs free energy of 1 mol of particles under standard conditions ($c_0 = 1$ mol/l). In thermal equilibrium the Gibbs free energy at constant pressure and constant temperature is at minimum,

$$\sum_i \mu_i dn_i = 0 \tag{4.23}$$

In a unimolecular reaction of the form $A \rightleftharpoons B$, with $dn_A = -dn_B$, we obtain the following equilibrium:

$$\mu_A dn_A + \mu_B dn_B = (\mu_A - \mu_B)\, dn_A = 0 \qquad \longrightarrow \qquad \mu_A = \mu_B \tag{4.24}$$

Such a unimolecular reaction could for instance be the thermal unfolding of a protein. In thermal equilibrium the chemical potentials of species A and B are therefore equal. From this follows

$$\mu_{A,0} + RT \ln \frac{c_A}{c_0} = \mu_{B,0} + RT \ln \frac{c_B}{c_0} \quad \rightarrow \quad \frac{c_B}{c_A} = \exp\left(-\frac{\overbrace{\mu_{B,0} - \mu_{A,0}}^{\Delta\mu_0}}{RT} \right) \tag{4.25}$$

In chemical reactions the probability that a randomly chosen particle belongs to a given species can now be linearly related to the concentration.

Similarly, for a bimolecular reaction $A + B \rightleftharpoons C$

$$\frac{c_C}{c_A \cdot c_B} = \frac{1}{c_0} \exp\left(-\frac{\overbrace{\mu_{C,0} - \mu_{A,0} - \mu_{B,0}}^{\Delta\mu_0}}{RT} \right) = \frac{1}{c_0} \exp\left(-\frac{\Delta\mu_0}{RT} \right) \tag{4.26}$$

Another way of writing this equation is

$$\frac{[C]}{[A] \cdot [B]} = \frac{1}{c_0} \exp\left(-\frac{\Delta G^0}{RT} \right) \tag{4.27}$$

where c_0 is the standard state concentration of 1 mol/l. The chemical equilibria treated in the section are also known as "mass action law." With ΔG^0 we always mean the difference between the standard chemical potentials $\Delta\mu_0$ after and before the reaction. The standard potentials cannot be derived. They are material properties, which must be obtained experimentally.

4.8 Statistical Interpretation of Entropy

The statistical interpretation of the entropy is one of the most profound progresses in the development of physics. The first to point out the relationship between entropy and statistics was Ludwig Boltzmann (1866).

Let us consider the canonical ensemble. The canonical ensemble consists of a thermally isolated system with N compartments containing an identical number of molecules (Fig. 4.2). The compartments are in thermal contact. However, no molecules may exchange between the compartments. Furthermore, the system is supposed to be in thermal equilibrium, assuming that thermal equilibrium corresponds to the most likely state of the system. A further constraint shall be that either the volume or the pressure of each compartment shall be a constant. Which of the two variables is constant depends on the choice of experimental conditions. If, as usual in biophysics, the pressure is constant, then we choose a constant pressure condition. Under such conditions, each compartment possesses a defined enthalpy, H_i.

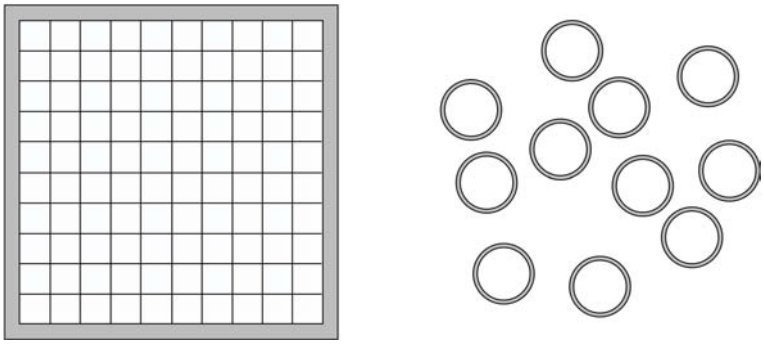

Fig. 4.2 Left: Schematic picture of a thermally isolated canonical ensemble with $N = 100$. Right: A dispersion of equally sized unilamellar vesicles can also be considered as a canonical ensemble.

Typical canonical ensembles are

- a dispersion of equally sized unilamellar vesicles,
- a diluted solution of noninteracting proteins of one species, and
- a series of simulation matrices of Monte Carlo simulation (see Section 8.1)

In the canonical ensemble at constant pressure there shall be n_i compartments with identical enthalpy, H_i. Due to the overall boundary conditions of constant total enthalpy (at constant pressure this is identical to constant total heat)

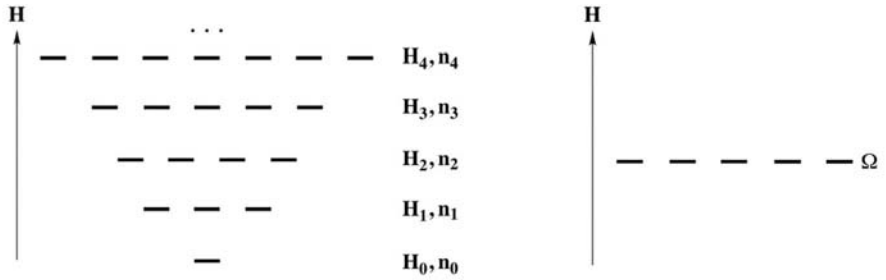

Fig. 4.3 Left: Enthalpy states of the canonical ensemble. The numbers n_i denote the degeneracy of each enthalpy state, H_i. Right: In the microcanonical there is only one enthalpy state, with degeneracy $n \equiv \Omega$.

we find

$$\begin{aligned} \sum n_i H_i &= H_{\text{tot}} \\ \sum n_i &= N \end{aligned} \tag{4.28}$$

This situation is shown in Fig. 4.3 (left panel). For the canonical ensemble it is possible to derive a relation for the probability P_1 of finding a compartment with enthalpy H_1, relative to the probability P_0 of finding it in the ground state with enthalpy H_0,

$$p_1 = \frac{P_1}{P_0} = \exp\left(-\frac{H_1 - H_0}{kT}\right) \tag{4.29}$$

This is the famous Boltzmann distribution. We do not derive it here, but derivations can be found in standard statistical thermodynamics books, e.g., in Hill (1960). The derivation is exclusively based on the assumptions in Eq. (4.28) and the search for that distribution of the n_i that has the highest degeneracy ($\equiv$ probability). The probabilities in Eq. (4.29) are given relative to the ground state with index "0." The absolute probabilities, P_i, are given by

$$P_i = \frac{p_i}{\sum_i p_i} = \frac{\exp\left(-(H_i - H_0)/kT\right)}{\sum_i \exp\left(-(H_i - H_0)/kT\right)} \tag{4.30}$$

The denominator $\sum_i \exp\left(-(H_i - H_0)/kT\right)$ is called the partition function, Q. The absolute probabilities fulfill the necessary requirement that $\sum_i P_i = 1$.

If there are many different enthalpy states (see Fig. 4.3, left), the entropy is given by

$$S = -k \sum_i P_i \ln P_i \tag{4.31}$$

This is also not derived here. It follows from the above considerations and correspondence considerations with classical thermodynamics (Hill (1960)).

Here, the index i refers to summation over each of the N individual compartments.

In the microcanonical ensemble there is only one enthalpy state, H, and the probability for each of the individual states is $P = 1/N \equiv 1/\Omega$, where Ω is the degeneracy of the state. The entropy is now given by

$$S = -k\sum_i P_i \ln P_i = -k\sum \frac{1}{\Omega}\ln\frac{1}{\Omega} = k\ln\Omega \tag{4.32}$$

using the Boltzmann constant $k = 1.381 \times 10^{-23}\, J/K$. This formula is written on Boltzmann's gravestone (even though it was first formulated in this form by Planck). If there is a situation where there are only two enthalpy states with different degeneracies, Ω_0 and Ω_1, one can calculate the entropy difference of the two microcanonical ensembles

$$\Delta S = k\ln\frac{\Omega_1}{\Omega_0} \tag{4.33}$$

4.9 Statistical Averages

In a biophysical experiment one usually cannot directly measure the volumes, V_i, areas, A_i, and enthalpies, H_i, of the individual states, but rather the thermodynamics averages over all states, each of them weighted by its Boltzmann probability given by Eq. (4.29). We obtain for the mean enthalpy

$$\langle H\rangle = \sum_i H_i P_i = \frac{\sum_i H_i \exp\left(-H_i/RT\right)}{\sum_i \exp\left(-H_i/RT\right)} \tag{4.34}$$

Similarly, if one wants to measure the specific volume of the lipids in a vesicle dispersion, or the area per vesicle, one in fact measures the thermodynamic averages for volume and area given by

$$\begin{aligned}\langle V\rangle &= \sum_i V_i P_i = \frac{\sum_i V_i \exp\left(-H_i/RT\right)}{\sum_i \exp\left(-H_i/RT\right)}\\ \langle A\rangle &= \sum_i A_i P_i = \frac{\sum_i A_i \exp\left(-H_i/RT\right)}{\sum_i \exp\left(-H_i/RT\right)}\end{aligned} \tag{4.35}$$

For every observable, $\mathcal{X}$, we can therefore write

$$\langle \mathcal{X}\rangle = \sum_i \mathcal{X}_i P_i \tag{4.36}$$

4.10 Heat Capacity and Elastic Constants

Two thermodynamic quantities that are relatively easy to measure are the heat capacity and the compressibility. These functions can in fact be used to experimentally determine enthalpy and entropy changes.

4.10.1 Heat Capacity

The most direct way to measure the enthalpy of an experimental sample is calorimetry (see Fig. 6.1 and Section 6.1.1). In a calorimeter, the heat capacity of the sample is measured, which is defined as the uptake of heat per temperature increment, usually obtained under constant pressure conditions,

$$c_p = \left(\frac{dQ}{dT}\right)_p \tag{4.37}$$

Since $dH = dQ + Vdp$, we obtain at constant pressure

$$c_p = \left(\frac{dH}{dT}\right)_p \tag{4.38}$$

Since also $dQ = TdS$, the heat capacity at constant pressure is given by

$$c_p = T\left(\frac{dS}{dT}\right)_p \tag{4.39}$$

From this it follows that one can determine changes in enthalpy, ΔH, and entropy, ΔS, with temperature from the heat capacity:

$$\Delta H = \int_{T_0}^{T_1} c_p dT \tag{4.40}$$

$$\Delta S = \int_{T_0}^{T_1} \frac{c_p}{T} dT \tag{4.41}$$

This is very nice since now the calorimetric determination of the heat capacities provides us with the necessary information to determine a lot of important properties of thermodynamics systems. In this book these are basically lipid membranes.

In the next chapters we will intensively treat lipid melting transitions. These are transitions in membranes where a lot of enthalpy is absorbed over a temperature interval much smaller than 1 K. Such transitions are described by

their transition temperature, T_m, and the melting enthalpy. One can approximate the entropy change in such sharp transitions by

$$\Delta S = \int_{T_m-\Delta}^{T_m+\Delta} \frac{c_p}{T} dT \approx \frac{1}{T_m} \int_{T_m-\Delta}^{T_m+\Delta} c_p dT = \frac{\Delta H}{T_m} \tag{4.42}$$

where Δ is a small interval below and above the melting transition. This relation will be used frequently in many chapters in this book.

The heat capacity, c_p, is the temperature derivative of the enthalpy at constant pressure. If we perform experiments with a 10 mM (concentration of single lipids) dispersion containing large unilamellar lipid vesicles (each vesicle containing about 10^5 lipids), we have about 10^{13} vesicles/cm^3. This is a macroscopic number. Each vesicle and even each lipid will display a fixed enthalpy at a given moment. The average enthalpy is given by Eq. (4.34), and therefore the heat capacity is given by

$$c_p = \frac{d\langle H\rangle}{dT} = \ldots \text{short calculation} \ldots = \frac{\langle H^2\rangle - \langle H\rangle^2}{R\,T^2} \tag{4.43}$$

This important relationship is called the "fluctuation theorem" and is closely related to fluctuation dissipation (Kubo, 1966). It can easily be derived by calculating the analytical derivative of Eq. (4.34). It means that the heat capacity is proportional to the fluctuations in the system. In our example with the lipid vesicles, the heat capacity would be given by the mean square deviation of the vesicle enthalpy from the mean enthalpy. The existence of fluctuations in a state around one most likely state is one of the most fundamental features of thermodynamics. One should therefore more correctly state that the maximum entropy state corresponds to a most likely distribution of states.

4.10.2 Isothermal Volume and Area Compressibility

The heat capacity, c_P, is the response function that describes how much heat a sample takes up upon a small temperature increase at constant pressure. Similarly, the isothermal volume compressibility is the quantity that describes the change of the specific volume as a response of a small change in pressure at constant temperature. It is given by

$$\kappa_T^V = -\frac{1}{\langle V\rangle} \left(\frac{d\langle V\rangle}{d\,p}\right)_T \tag{4.44}$$

The mean volume is given by Eq. (4.35), which can be rewritten as

$$\langle V\rangle = \frac{\sum_i V_i \exp\left(-(E_i + p\,V_i)/RT\right)}{\sum_i \exp\left(-(E_i + p/, V_i)/RT\right)} \tag{4.45}$$

by letting $H_i = E_i + p\,V_i$ at constant pressure. Therefore, the isothermal compressibility is given by

$$\kappa_T^V = \ldots \text{short calculation} \ldots = \frac{\langle V^2 \rangle - \langle V \rangle^2}{\langle V \rangle\, R\, T} \tag{4.46}$$

This means that the isothermal volume compressibility is related to the volume fluctuations. We will later see that this leads to functional relationships between compressibility and heat capacity that can explain a number of interesting phenomena in membranes close to melting transitions, for example ripple phase formation and the formation of extended phases in charged lipid membranes.

Similarly, one finds for the area compressibility

$$\kappa_T^A = -\frac{1}{\langle A \rangle} \left(\frac{d\,\langle A \rangle}{d\,\Pi} \right)_T \tag{4.47}$$

with the lateral pressure, Π. The same arguments as for the volume compressibility can be made for the isothermal area compressibility in two dimensions by letting $H_i = E_i + \Pi\, A_i$ at constant lateral pressure Π. This leads to

$$\kappa_T^A = \ldots \text{short calculation} \ldots = \frac{\langle A^2 \rangle - \langle A \rangle^2}{\langle A \rangle\, R\, T} \tag{4.48}$$

Thus, the isothermal area compressibility of membranes is proportional to the fluctuations in area.

4.11 Maxwell Relations

In the previous section, we have calculated the isothermal compressibilities, κ_T^V and κ_T^A. These are the elastic constants, if the membrane is compressed infinitely slowly, and the heat exchange between the sample and the environment is complete. However, in many important cases, a compression is so fast that no heat exchange can take place. Such conditions are called adiabatic. The adiabatic compressibility is an important quantity in sound propagation. Before we derive the adiabatic compressibility, we first introduce some very useful thermodynamics relations, the so-called Maxwell relations.

Remember that the differentials of the thermodynamic functions of state were given by

$$dE = TdS - pdV + \sum_i \mu_i dn_i \qquad dH = TdS - Vdp + \sum_i \mu_i dn_i$$

$$dF = -SdT - pdV + \sum_i \mu_i dn_i \qquad dG = -SdT + Vdp + \sum_i \mu_i dn_i$$

From the first relation we obtain

$$T = \left(\frac{\partial E}{\partial S}\right)_{V,n_i} \qquad p = -\left(\frac{\partial E}{\partial V}\right)_{S,n_i} \qquad \text{and} \qquad \mu_i = \left(\frac{\partial E}{\partial n_i}\right)_{S,V,n_{j\neq i}}$$

and therefore also

$$\left(\frac{\partial T}{\partial V}\right)_S = \frac{\partial^2 E}{\partial S \partial V} = -\left(\frac{\partial p}{\partial S}\right)_V$$

In a similar way more expressions can be derived from dH, dF, and dG, some of which are

$$\begin{aligned}
\left(\frac{\partial T}{\partial V}\right)_S &= -\left(\frac{\partial p}{\partial S}\right)_V && \text{(a)}\\
\left(\frac{\partial V}{\partial S}\right)_p &= +\left(\frac{\partial T}{\partial p}\right)_S && \text{(b)}\\
\left(\frac{\partial S}{\partial V}\right)_T &= +\left(\frac{\partial p}{\partial T}\right)_V && \text{(c)}\\
\left(\frac{\partial S}{\partial p}\right)_T &= -\left(\frac{\partial V}{\partial T}\right)_p && \text{(d)}
\end{aligned} \tag{4.49}$$

These are the famous Maxwell relations. These equations can be used to replace functions that cannot be measured or are difficult to measure (e.g., $(\partial S/\partial p)_T$) by functions that can be measured (e.g., $(\partial V/\partial T)_p$, which is the volume expansion coefficient).

Some other important Maxwell relations are

$$\left(\frac{d\mu_i}{dn_j}\right)_{S,V,n_{i\neq j}} = \left(\frac{d\mu_j}{dn_i}\right)_{S,V,n_{j\neq i}} \tag{4.50}$$

These relations are also known as the linkage relations (Wyman and Gill, 1990). They imply a symmetric coupling between changes of the chemical potential of species i with the change in the concentration of species j. An example may be the chemical potential of a lipid membrane interacting with a protein. The influence of the protein on the chemical potential of the lipid membrane equals the influence of the lipid membrane on the chemical potential of the proteins. Such relationships can generated between all molecules in biological cells, which indicates the mutual coupling of the activities of all molecular species.

4.12 Adiabatic Compressibility

The adiabatic compressibility is the compressibility in the absence of heat exchange, $dQ = 0$. Since for reversible processes $dQ = SdT$, this also means

$dS = 0$. The adiabatic compressibility, κ_S, therefore is given by

$$\kappa_S = -\frac{1}{V}\left(\frac{\partial V}{\partial p}\right)_S \tag{4.51}$$

In this equation we have two extensive variables, V and S, and two intensive variables, p and T. We can write

$$dV = \left(\frac{\partial V}{\partial p}\right)_T dp + \left(\frac{\partial V}{\partial T}\right)_p dT \tag{4.52}$$

and

$$dS = \left(\frac{\partial S}{\partial p}\right)_T dp + \left(\frac{\partial S}{\partial T}\right)_p dT \tag{4.53}$$

If we consider constant entropy ($dS = 0$), we can eliminate dT from Eq. (4.53)

$$dT = -\frac{\left(\frac{\partial S}{\partial p}\right)_T}{\left(\frac{\partial S}{\partial T}\right)_p} dp \qquad \text{for} \quad S = \text{const} \tag{4.54}$$

which can now be inserted into Eq. (4.52)

$$dV = \left(\frac{\partial V}{\partial p}\right)_T dp - \left(\frac{\partial V}{\partial T}\right)_p \frac{\left(\frac{\partial S}{\partial p}\right)_T}{\left(\frac{\partial S}{\partial T}\right)_p} dp \qquad \text{for } S = \text{const} \tag{4.55}$$

$$\left(\frac{\partial V}{\partial p}\right)_S = \left(\frac{\partial V}{\partial p}\right)_T - \left(\frac{\partial V}{\partial T}\right)_p \frac{\left(\frac{\partial S}{\partial p}\right)_T}{\left(\frac{\partial S}{\partial T}\right)_p} \tag{4.56}$$

Due to one of the Maxwell relations, $(\partial S/\partial p)_T = -(\partial V/\partial T)_p$, and $T \cdot (\partial S/\partial T)_p = c_p$, which can be inserted into Eq. (4.56) and we obtain

$$\left(\frac{\partial V}{\partial p}\right)_S = \left(\frac{\partial V}{\partial p}\right)_T + \frac{T}{c_p}\left(\frac{\partial V}{\partial T}\right)_p^2 \tag{4.57}$$

and the adiabatic compressibility can be written as

$$\begin{aligned} \kappa_S &= -\frac{1}{V}\left[\left(\frac{\partial V}{\partial p}\right)_T + \frac{T}{c_p}\left(\frac{\partial V}{\partial T}\right)_p^2\right] \\ &= \kappa_T - \frac{T}{V \cdot c_p}\left(\frac{\partial V}{\partial T}\right)_p^2 \end{aligned} \tag{4.58}$$

Thus, the adiabatic compressibility can be calculated when isothermal compressibility, heat capacity, and volume expansion coefficient are known. In particular, the adiabatic compressibility is always smaller than the isothermal compressibility: $\kappa_S \leq \kappa_T$. We will make use of these relations in Chapters 14 and 18 in the context of sound propagation in membranes and nerves.

4.13 Thermodynamic Forces and Fluxes

Let us now consider the entropy as a potential that depends on thermodynamic variables, ξ_i. Since the entropy is in a maximum, it can be developed around the maximum as a function of the variables ξ_i,

$$\begin{aligned} S &= S_0 + \sum_i \left(\frac{\partial S}{\partial \xi_i}\right)_{\xi_0} (\xi_i - \xi_i^0) \\ &\quad + \frac{1}{2}\sum_i \sum_j \left(\frac{\partial^2 S}{\partial \xi_i \partial \xi_j}\right)_{\xi_i^0, \xi_j^0} (\xi_i - \xi_i^0)(\xi_j - \xi_j^0) + \cdots \\ &\approx S_0 + \frac{1}{2}\sum_i \sum_j \left(\frac{\partial^2 S}{\partial \xi_i \partial \xi_j}\right)_{\xi_i^0, \xi_j^0} (\xi_i - \xi_i^0)(\xi_j - \xi_j^0) \end{aligned} \tag{4.59}$$

The variable, ξ, could for instance be the reaction variable of a chemical reaction, or the internal energy of the system, E. The terms $\left(\partial^2 S/\partial \xi_i \partial \xi_j\right)_{\xi_i^0, \xi_j^0}$ are constants. The harmonic function given in Eq. (4.12) is shown in Fig. 4.1 (left panel).

Reversible changes in the state of a system are changes between two states, a and b, in thermal equilibrium. The change in entropy between these two states, ΔS_r, is shown in Fig. 4.1 (right panel). It corresponds to a change of the reaction variable, $\Delta\xi$.

If the system is not in thermal equilibrium, the entropy changes spontaneously with time, i.e.,

$$\sigma = \frac{dS}{dt} > 0 \qquad \text{entropy production} \tag{4.60}$$

To be more precise, one typically uses the entropy density rather than the entropy for the definition of the forces. If there are several reaction variables, ξ_i, one can write

$$\frac{dS}{dt} = \sum_i \underbrace{\frac{\partial S}{\partial \xi_i}}_{\text{forces}} \cdot \underbrace{\frac{\partial \xi_i}{\partial t}}_{\text{fluxes}} \equiv \sum_i X_i J_i \tag{4.61}$$

introducing the thermodynamic forces X_i and the thermodynamic fluxes J_i. The fluxes are the time-dependent changes of the variable ξ_i. The forces X_i are derivatives of the entropy with respect to the variables. They correspond to the slope of the entropy profile in Fig. 4.1 (left). This transforms the entropy into a potential. The above approach has been introduced by Lars Onsager. Forces and fluxes play a very important role in nonequilibrium thermodynamics—and later in Chapter 16 on relaxation processes in membranes. Onsager has phenomenologically introduced linear relations of fluxes and forces

$$\begin{aligned} J_1 &= L_{11}X_1 + L_{12}X_2 + \cdots \\ J_2 &= L_{21}X_2 + L_{22}X_2 + \cdots \\ J_3 &= L_{31}X_1 + L_{32}X_2 + \cdots \\ \cdots &= \cdots \end{aligned}$$

where the L_{ij} are phenomenological coefficients that have to be determined by experiment. In Chapter 16 the time course of heat release from a lipid sample (relaxation time) will be calculated on the basis of the above equation.

Onsager found following relations for systems close to equilibrium:

$$\begin{aligned} &L_{ii} > 0 \\ &L_{ij} = L_{ji} \qquad \text{reciprocal relations} \\ &\frac{L_{ij}^2}{L_{ii}L_{jj}} \leq 1 \end{aligned} \tag{4.62}$$

These equations have following important implications:

1. The time dependence of the fluxes can be determined when the entropy potential is known.
2. Fluxes may depend on more than one force.
3. Due to the reciprocal relations, surprising relations between different fluxes can be found.

We will use this kind of treatment in Chapter 16 to determine the relaxation properties of lipid membranes.

4.14 Summary: Key Ideas of Chapter 4

- The first law of thermodynamics states that internal energy changes consist of changes in heat, dQ, and work, dW. It implies that internal energy is conserved.
- Functions of state are those functions that only depend on the values of the thermodynamic variables but not on the way how this state has been obtained. The internal energy, E, is a function of state, but the heat, Q, and the work, W, are not.
- The second law of thermodynamics states that for reversible processes $dQ = TdS_r$ introducing the entropy, S. The entropy is a function of state.
- For irreversible processes the differential entropy is given by $dS = dS_r + dS_i$, where $dS_i \geq 0$. This implies that for closed systems the entropy always increases.
- Other functions of state are the enthalpy $H = E + pV$, the Helmholtz free energy, $F = E - TS$, and the Gibbs free energy $G = H - TS$. In an equilibrated system at constant volume and temperature the Helmholtz free energy assumes a minimum. At constant pressure and temperature the Gibbs free energy assumes a minimum.
- The chemical potential at constant pressure and temperature is equal to the Gibbs free energy of 1 mol of substance.
- The mass action law describes the balance of concentrations at chemical equilibrium. It is related to the differences of the standard state chemical potentials.
- The statistical interpretation of the entropy implies that $S = -k \sum_i P_i \ln P_i$ +const, where the P_i are the probabilities of individual states of the system. The maximum entropy state therefore is identical to the most likely state.
- The most likely state is surrounded by slightly less likely states. Due to thermal collisions, these states have a finite probability to be found. The variance of the states around the most likely state is called fluctuations.
- The heat capacity is the incremental uptake of heat when the temperature is increased. At constant pressure it is proportional to the fluctuations of the enthalpy. The isothermal compressibility is proportional to the fluctuations in volume.

- The Maxwell relations are important couplings between different thermodynamic functions and variables.
- The adiabatic compressibility is the compressibility when heat exchange is forbidden.
- The change of entropy with time in a closed system is called entropy production. The entropy production is related to thermodynamic forces and thermodynamic fluxes that define time-dependent changes of a system. The thermodynamic forces are derivatives of the entropy potential.
- Onsager's phenomenological equations allow us to write the fluxes as a linear combination of the forces.

5
Water

Water is the most abundant molecule in living organisms. The human body consists of about 70% water and the typical water content of cells is between 55% and 90%. At low temperatures water forms ice (Fig. 5.1) that displays crystalline order. The ice structure is a consequence of the formation of hydrogen bonds that are interactions of predominantly dipolar nature. While ice has a perfect hydrogen bonding network, water vapor is a gas and does not possess hydrogen bonds. The intermediate phase is liquid water. In Table 5.1 some water properties are listed. The enthalpy of fusion (i.e. the formation of liquid water from ice at 0 °C) is about 6.01 kJ/mol = 333.5 J/g. The enthalpy of vaporization (formation of water vapor from liquid water at 100 °C) is about 40.66 kJ/mol = 2.256 kJ/g. The enthalpy of sublimation (ice to water vapor at 0 °C) is 51.06 kJ/mol = 2.833 kJ/g. Only about 13.4% of this enthalpy can be attributed to movement of molecules (Tanford, 1980). Since ice or water is kept together by hydrogen bonds one has to conclude that

1. upon melting of ice only about 13% of the hydrogen bonds are broken,
2. about 79% of hydrogen bonds are broken upon vaporization, and

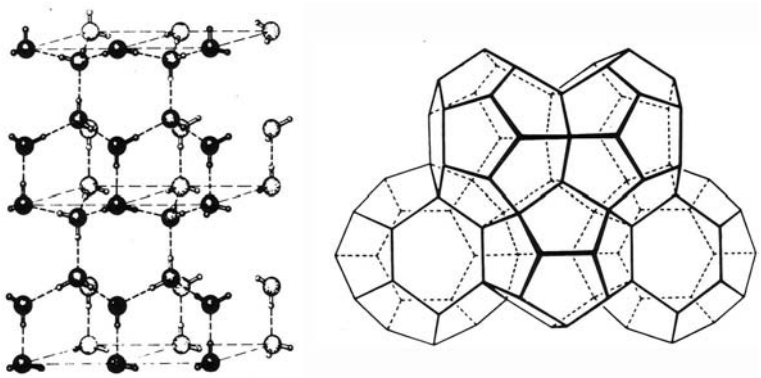

Fig. 5.1 Left: Structure and hydrogen bonds of ice. Right: Hydrogen bonding network around a crystalline Cl_2. Such structures are often called clathrate structures. From Pauling (1939). Copyright © by Cornell University. Used by permission of the publisher, Cornell University Press.

3. the remaining 8% of hydrogen bonds are broken upon heating liquid water from 0 °C to 100 °C.

This means that water still contains most hydrogen bonds (compared to ice) and is highly ordered. The fact that the number of hydrogen bonds changes between 0 °C and 100 °C gives rise to a heat capacity different from zero. At 25 °C it is about 75 J/mol K. Since the heat capacity is always positive, the enthalpy of water is an increasing function of temperature ($H = \int c_P \, dT$, Section 4.10.1). Since the heat capacity is not zero, the entropy also increases upon increasing the temperature (because $S = \int (c_P/T) \, dT$).

Tab. 5.1 Properties of water at standard pressure of 1 bar.

Property	Value
Molar mass	18.02 g/mol
Melting point	0 °C=273.15 K
Boiling point	100 °C=373.15 K
Thermal conductivity	0.610 W/m K (25 °C)
Thermal diffusivity	1.46×10^{-7} m^2/s (25 °C)
Diffusion coeff.	2.272×10^{-9} m^2/s (25 °C)
Density (water)	997.05 kg/m^3 (25 °C)
Density (ice)	916.8 kg/m^3 (0 °C)
Enthalpy of fusion	6.0095 kJ/mol (0 °C)
Enthalpy of vaporization	40.657 kJ/mol (100 °C)
Enthalpy of sublimation	51.059 kJ/mol (0 °C)
Specific heat, c_p	75.327 J/mol K (25 °C)
Speed of sound	1496.7 m/s (25 °C)

5.1 The Electrostatic Potential

The electrostatic potential of a charge, q, in a solvent is given by

$$\Psi(r) = \frac{q}{4\pi\epsilon_0\epsilon \cdot r} \tag{5.1}$$

with the permittivity $\epsilon_0 = 8.854 \times 10^{-12}$ C^2/J m and the dielectric constant (relative permittivity) $\epsilon = 80.4$ for water at 20 °C. Thus, the potential depends on the dielectric constant and the distance r from the charge. In Table 5.2 the dielectric constants for various solvents of different polarity are listed.

The dielectric constant of vacuum is $\epsilon_{\text{vacuum}} = 1$, and that of water at room temperature is $\epsilon_{H_2O} \approx 80$; in oils, fats, and other hydrocarbons one finds $\epsilon_{\text{hc}} \approx$ 2–4.[1]

$$\Psi_{\text{hc}} \approx 20 - 40 \cdot \Psi_{H_2O} \tag{5.2}$$

1) The index "hc" stands for hydrocarbon.

Tab. 5.2 Dielectric constants, ϵ, for various solvents

Solvent	Temperature (°C)	ϵ	Solvent	Temperature (°C)	ϵ
Water	0	88.0	Octanol	20	10.3
	20	80.4	Dichloromethane	20	9.1
	100	55.3	Chloroform	20	4.8
Glycerol	25	42.5	Olive oil	20	3.1
Methanol	25	32.6	Oleic acid	20	2.5
Ethanol	25	24.3	Benzene	20	2.3
Acetone	25	20.7	Petroleum oil	20	2.1
Ammonia	20	16.5	Cyclohexane	20	2.0
Hexanol	25	13.3	Octane	20	2.0

For this reason the free energy ($G_{\mathrm{el}} = \int \Psi dq$) of placing a charge in water is much lower than that in a hydrocarbon (oily) environment. The charged head groups of lipids and the charged amino acids are usually located at the interface with water. Charges can be influenced by pH. Negatively charged lipid can be protonated which naturally drastically changes the free energy of this molecular group.

5.2 The Electrostatic Potential in Electrolytes

In the presence of salts the electrostatic potentials are shielded. This is due to the fact that negatively charged particles display an enhanced likelihood to have positively charged ions in their proximity (and vice versa). Debye and Hückel (1923) derived a famous relation for the electrostatic potential in electrolytes:

$$\Psi(r) = \frac{q}{4\pi\epsilon_0\epsilon \cdot r} \exp\left(-\kappa r\right) \tag{5.3}$$

The underlying theory is called the Debye–Hückel theory. The constant κ in Eq. (5.3) is given by

$$\kappa = \left(2\frac{e^2}{\epsilon_0\epsilon kT}c_0\right)^{0.5} \tag{5.4}$$

It is called the "Debye constant." As apparent from Eq. (5.4), it is a function of the ionic strength, c_0. The ionic strength is given by

$$c_0 \equiv \text{ionic strength} = \frac{1}{2}\sum_i z_i^2 c_{i,0} \tag{5.5}$$

where $c_{i,0}$ is the concentration of ion species i at an infinite distance from the central charge, and z_i is the valency of the respective ion, e.g. $z = +1$ for Na^+,

$z = +2$ for Ca^+, and $z = -1$ for Cl^-. The inverse of the Debye constant is the Debye length. It gives the typical screening length of charges in solutions containing salts. Some values for the Debye length are given in Table 11.1. At 100 mM NaCl it is about 9.7 Å whereas it is about 97 Å at 1 mM. Thus, the length scale of electrostatic screening under physiological conditions is on the same length scale as the typical dimensions of macromolecules (the radius of cytochrome c is about 15 Å and the cross-sectional diameter of a lipid is on the order of 7 Å). Changes in charge (e.g. by protonation or calcium binding) are therefore expected to strongly contribute to the physical state of the macromolecules. It is also expected that divalent ions (e.g. Ca^{2+}) display a much larger influence on the electrostatics than monovalent ions.

We did not derive the above expressions here. However, the theory of charged surfaces (Gouy–Chapman theory) is very similar to the Debye–Hückel theory. The Gouy–Chapman theory is described in detail in Chapter 11. The derivation of the Debye–Hückel theory is analogous and can be found in many textbooks (e.g. Hill (1960)).

5.3 The Hydrophobic Effect

For the understanding of lipid melting, protein folding, and lipid–protein interactions, it is of great importance to understand the principles that determine the Gibbs free energy of the boundary between hydrophobic groups and water. One can measure such free energies by investigating the distribution of hydrophobic substances (e.g. amino acids) between a phase with a low dielectric constant (e.g. octanol or olive oil) and a water phase. One of the first to investigate this carefully was Kauzmann (1959). Table 5.3 shows the Gibbs free energy of the transfer of ethane from an apolar (organic) solvent into a polar solvent (H_2O). This free energy mainly depends on the size of the interface of the apolar molecule with the solvent. Therefore one finds a linear relation between the number of CH_2 and CH_3 groups (Fig. 5.2).

Tab. 5.3 Entropy, enthalpy, and Gibbs free energy of transfer of ethane from an apolar into a polar solvent.

$T = 298$ K	ΔS_{tr} (J/mol K)	ΔH_{tr} (kJ/mol)	ΔG_{tr} (kJ/mol)
C_2H_6 (ethane) from benzine into water	−83.7	−9.4	+15.9
C_2H_6 (ethane) from chloroform into water	−75.3	−7.1	+15.5

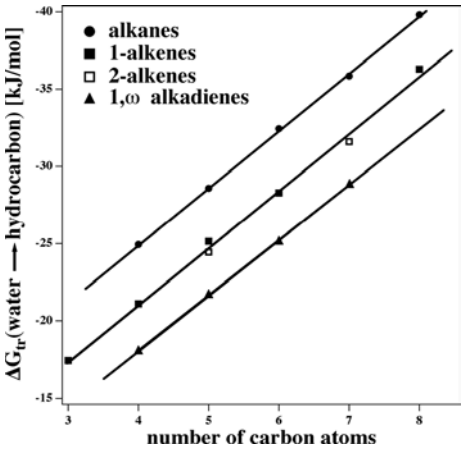

Fig. 5.2 Chain length dependence of the Gibbs free energy of transfer of alkanes, alkenes, and alkadienes from oil into water. Adapted from Tanford (1980).

For hydrocarbons one finds for the transfer from an apolar into a polar environment (Tanford, 1980)

$$\Delta G_{\mathrm{tr}} \approx 105 \frac{\mathrm{J}}{\mathrm{mol\,\AA^2}} \tag{5.6}$$

and following from that for alkanes (CH_3–$(CH_2)_n$–CH_3):

$$\Delta G_{\mathrm{tr}}^{\mathrm{alkane}} \approx 8795 \frac{\mathrm{J}}{\mathrm{mol}} \cdot n_{\mathrm{CH_3}} + 3799 \frac{\mathrm{J}}{\mathrm{mol}} \cdot n_{\mathrm{CH_2}} \tag{5.7}$$

As can be seen in Fig. 5.2 the introduction of double bonds slightly reduces this transfer free energy. Apart from this slight modification the interaction of hydrophobic residues depends mainly on their size or length, respectively.

Correspondingly, one can list experimental values for the transfer of amino acids from oil to water (Table 5.4). This is important for protein folding because upon denaturation hydrophobic residues are exposed to water. Therefore, the hydrophobic effect is a key element of protein stability. Furthermore, the insertion of integral proteins into lipid bilayers is largely dominated by hydrophobic interactions.

5.3.1
Temperature Dependence of the Hydrophobic Effect

The Gibbs free energy ($\Delta G_{\mathrm{tr}} = \Delta H_{\mathrm{tr}} - T\Delta S_{\mathrm{tr}}$) of the transfer from an apolar to a polar solvent has an enthalpic and an entropic contribution. It was experimentally observed that both ΔH and ΔS are very temperature dependent: $\Delta H = \Delta H(T)$ and $\Delta S = \Delta S(T)$.

Tab. 5.4 Gibbs free energy, $\Delta G_{\mathrm{tr}} = G_{\mathrm{H_2O}} - G_{\mathrm{hc}}$, of the transfer of apolar amino acids from hydrocarbon environment to water (given relative to glycine: –HN–CH_2–CO–).

Amino acid side chain	$\Delta G_{\mathrm{tr}} = G_{\mathrm{H_2O}} - G_{hc}$ kJ/mol
Tryptophane	−14.2
Norleucine	−10.9
Phenylalanine	−10.5
Tyrosine	−9.6
Leucine	−7.5
Valine	−6.3
Methionine	−5.4
Alanine	−2.1

Enthalpy and entropy can both be derived from the heat capacity (Section 4.10.1)

$$\Delta H(T) = \int c_P \, dT \qquad \Delta S(T) = \int \frac{c_P}{T} \, dT \tag{5.8}$$

Since both ΔH and ΔS of the transfer are temperature dependent it follows that the heat capacity c_P changes upon the transfer from an apolar to a polar solvent. The interface of an apolar molecule contributes to the heat capacity with $\Delta c_p \neq 0$.

If one develops the temperature dependence of the free energy of the transfer into a Taylor series (Brandts, 1964):

$$\Delta G_{\mathrm{tr}}(T) \approx A_0 + A_1 T + A_2 T^2 + A_3 T^3 + \cdots \tag{5.9}$$

one obtains for entropy and heat capacity changes

$$\begin{aligned} -\Delta S_{\mathrm{tr}} &= \left(\frac{dG_{\mathrm{tr}}}{dT}\right)_p \\ &\approx A_1 + 2 \cdot A_2 T + 3 \cdot A_3 T^2 \quad \rightarrow \quad c_p \approx -2 \cdot A_2 T - 6 \cdot A_3 T^2 \end{aligned} \tag{5.10}$$

The coefficients A_i for some amino acids are given in Table 5.5 and the corresponding free energies of the transfer are given in Fig. 5.3 (left). Similar to the transfer of amino acids (Fig. 5.3, right), the transfer of hydrocarbon also

Tab. 5.5 Transfer of amino acid side chains from an apolar into a polar solvent.

	A_0 (J/mol), $T = 0°$	A_1 (J/mol K)	A_1 (J/mol K^2)	A_3 (J/mol K^3)
Tyrosyl	13305	420.3	−2.247	0.00326
Norleucyl	8075	−104.2	0.849	−0.00130
Valyl	4665	−103.6	0.770	−0.00113
Alanyl	1946	−79.5	0.556	−0.00088

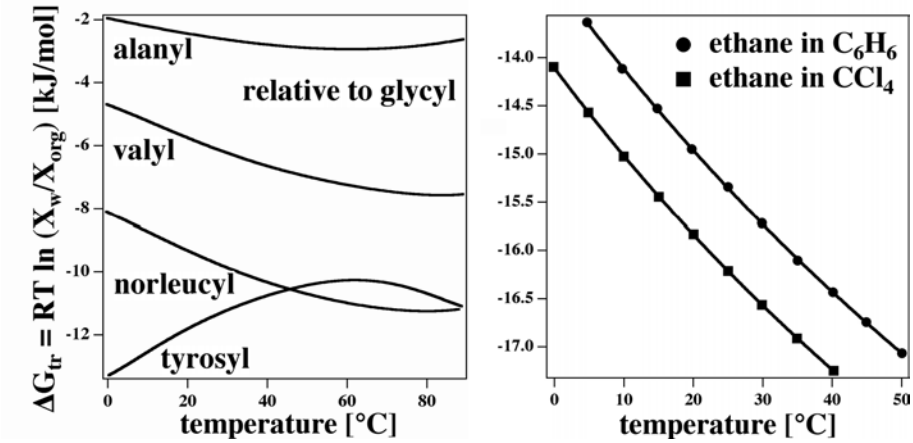

Fig. 5.3 Left: Temperature dependence of the Gibbs free energy of the transfer of the four different amino acid side chains from water to organic solvent (relative to the free energy of the transfer of glycine). Adapted from Brandts (1964). Right: Temperature dependence of the Gibbs free energy of the transfer of ethane from water to either C_6H_6 or CCl_4. Adapted from Tanford (1980).

displays a pronounced temperature dependence. Thus, the transfer of hydrocarbons from oil to water is also linked to an overall increase in the heat capacity.

Why is the above important? Both proteins and lipid membranes display cooperative order transitions. For proteins this is called thermal unfolding or denaturation. In Fig. 5.4 one can see that the unfolding of the globular protein cytochrome c displays a stepwise change in heat capacity from below to above the unfolding transition at $\approx 83\,^{\circ}$C. This step indicates that apolar amino acids were transferred from the inside of the protein into the aqueous solvent upon unfolding. The difference in heat capacity between folded and unfolded proteins causes the interesting phenomenon of cold unfolding. It has been shown that many globular proteins unfold when temperature is lowered from room temperature (Privalov, 1990). A similar effect is found in some detergent solutions where micelles desolve at low and high temperature (Majhi and Blume, 2001).

Lipid melting (see Chapters 2 and 6) is not linked to a change in heat capacity from below to above the melting transition. This indicates that during the melting transition no apolar chain segments were transferred into the aqueous environment and that the interaction of the fluid lipid phase with water is similar to that of the gel phase. We will see later that during melting hydrophobic interactions at phase boundaries are important (Chapter 8).

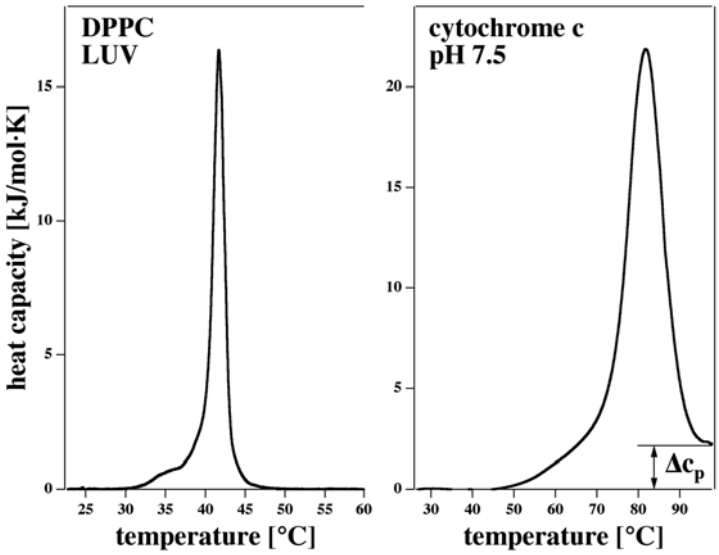

Fig. 5.4 Left: Melting of large unilamellar vesicles of lipid membranes made of DPPC. Right: Denaturation of cytochrome c at pH 7.5. The lipid melting profile does not display a difference in heat capacity below and above the melting temperature. Cytochrome c displays an increase of the heat capacity above the unfolding temperature. This indicates that the hydrophobic effect does not provide a significant contribution to the melting of lipid membranes, but it plays a major role in the unfolding of proteins.

5.4
The Wimley–White Hydrophobicity Scale

The membrane interior mainly consists of hydrocarbon chains. The lipid head groups, in contrast, are polar groups that interact well with water. Peripheral proteins adsorb to lipid membrane surfaces while integral proteins insert to the hydrophobic membrane core. Many peptides exist in an equilibrium between inserted and surface adsorbed species. Such an equilibrium is expected to depend sensitively on hydrophobic interactions and therefore on the amino acid composition. Further, the mode of interaction and the orientation of proteins in the membrane sensitively depend on the arrangement of amino acids along the chain. Some amino acids display affinities towards the hydrophobic membrane core, while others prefer aqueous environments. A third class of amino acids prefers the membrane–water interface. These are in particular the aromatic amino acids (Wimley et al., 1996; Wimley and White, 1996). Wimley and White (1996) showed that the transfer free energies between membrane interfaces and water are a linear function of the transfer free energies between octanol and water.

5.5
Hydrophobic Matching

Hydrophobic matching as a principle regulating lipid–protein interactions was already mentioned by Mouritsen and Bloom (1984) in their paper on the mattress model (Section 1.6). Following the observations outlined above one has to state that

- the transfer of apolar amino acids from the membrane interior into water is unfavorable,
- aromatic amino acids are preferentially located in the membrane head group region (following the hydrophobicity scale shown in Fig. 5.5), and
- polar amino acids prefer the aqueous environment. This is due to huge differences in the dielectric constants of hydrocarbons and water (see Section 5.2).

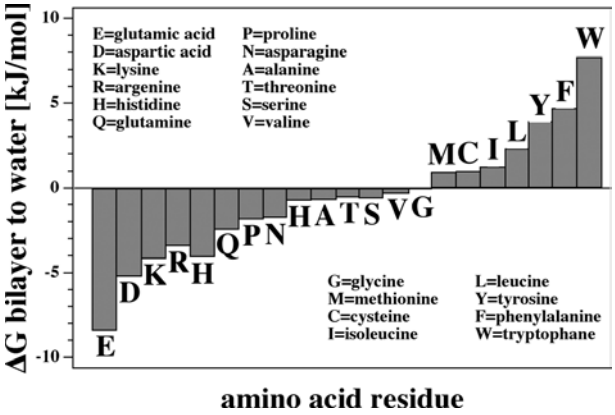

Fig. 5.5 Transfer free energies of amino acids from lipid interfaces into water around neutral pH, adapted from Wimley and White (1996). While the charged residues display a pronounced affinity to the water phase, the aromatic residues (in particular tryptophane) display a preference for the membrane interface. Histidine shows up two times since it has a pK_A close to neutral pH. The charged and the uncharged form display different transfer free energies.

Thus, interactions of integral proteins with membranes are favorable if their primary and tertiary structure allow us to place the respective amino acids in their most preferred environment: chain region, head group region or an aqueous medium. This is shown schematically in Fig. 5.6. If the membrane and protein dimensions do not match, one expects significant free energy contributions due to unfavorable interactions between amino acids and water (or chains).

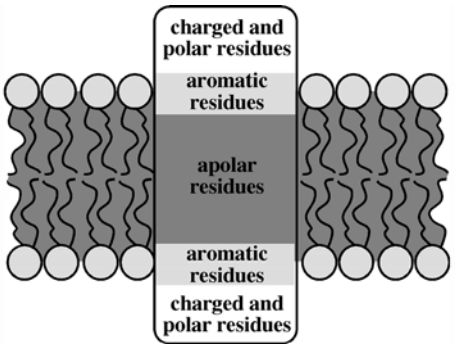

Fig. 5.6 Principle of hydrophobic matching between a membrane and an integral protein. The free energy is minimized when the apolar membrane chain region and the apolar part of the integral protein match. Furthermore, the membrane interface interacts preferentially with the aromatic amino acids.

5.6 Hofmeister Series

Franz Hofmeister was a professor at Prague University in the second half of the 19th century. He and his collaborators published a series of six papers with the collective title "Zur Lehre von der Wirkung der Salze" (About the science of the effect of salts) (Lewith, 1887; Hofmeister, 1888a,b; von Limbeck, 1888; Hofmeister, 1890, 1891). These papers treated the effects of various ions on the precipitation of proteins. Two of these papers were recently translated into English (Kunz et al., 2004b). Hofmeister observed that proteins as lysozyme precipitate in salt solutions, and that this depends on the nature of the ion. Different ions can be ranked according to their ability to precipitate proteins. This so-called Hofmeister series is shown in Fig. 5.7. Today, it is rather measured in terms of their ability to stabilize or destabilize proteins (e.g., on the denaturation temperature).

kosmotropic **stabilizing** (salting-out) **destabilizing** (salting-in) **chaotropic**

Anions: F^- PO_4^{3-} SO_4^{2-} CH_3COO^- Cl^- Br^- I^- SCN^-

Cations: $(CH_3)_4N^+$ $(CH_3)_2NH_2^+$ NH_4^+ K^+ Na^+ Cs^+ Li^+ Mg^{2+} Ca^{2+} Ba^{2+}

Fig. 5.7 Cations and anions display different effects on the ordering of water and the precipitation of proteins. Kosmotropes enhance water structure and precipitate proteins. Chaotropes break water structure and destabilize proteins. The ions are listed in the order of their effect on water from kosmotropic to chaotropic. Adapted from Cacace et al. (1997)

The exact reason of the effect of ions on protein stability is not clear in all details. However, it seems as if it is closely related to the affinity of the ions for water (Hofmeister, 1888b; Kunz et al., 2004a) or their influence on water activity. If the ions bind a lot of water molecules, the effective amount of free water decreases and protein concentrations effectively increase. It is also assumed that the hydrogen-bonding patterns in water (the clathrate structures) are influenced by ions such that some ions can be considered as water-structure enhancers. Such ions are called "kosmotropes." They bind water stronger than other water molecules. Other ions reduce the hydrogen bonding and are called "chaotropes." They interact with water weaker than other water molecules. In some respect the chaotropes make water more liquid (corresponding to a higher temperature state of water). It seems thus clear that all ions affect water properties, in particular at high concentrations. This includes the head groups of lipids and amino acids. Many phenomena in biology seem to be related to the Hofmeister series. The ion conductances of some peptide pores and the permeabilities of the lipid pores described in Chapter 17 (Antonov et al., 2005) seem to follow the Hofmeister series. It should be expected that salts such as KCl, NaCl, and LiCl do not display the same influence on lipid membranes and protein stability since they are found at different positions in the Hofmeister series.

There are speculations that the water-ordering effect of all the macromolecules in cells is so strong (due to the large overall concentration of macromolecules) that effectively no water can be considered as being totally free (Ling, 2001; Pollack, 2001). The cytosol of cells thus may rather be a cytogel (consider, for instance, the egg white of a chicken egg). The competition of macromolecules for water thus introduces all kinds of couplings between seemingly different biochemical or biophysical properties. This is an attractive hypothesis with potentially enormous implications for biological functions. The common investigation of biological molecules at low concentrations may be quite misleading. The notion of a free ion concentrations may be flawed and the chemical potentials of the ions may deviate strongly from $kT \ln(c/c_0)$. Under these conditions, the mass action law derived in Section 4.7 is not valid.

A nice comprehensive Web site on water in general, and Hofmeister series, kosmotropes and chaotropes, is maintained by Martin Chaplin from London South Bank University.[2]

2) http://www.lsbu.ac.uk/water/

5.7 Summary: Key Ideas of Chapter 5

- Charged groups of lipids and proteins prefer aqueous environments because the dielectric constant of water is 20–40 times larger than that of a hydrocarbon environment. Therefore, the electrostatic free energy is lower in water.
- In electrolytes the characteristic length of the electrostatic potential is largely reduced. This is described by the Debye–Hückel theory. At 100 mM NaCl the screening length (Debye length) is about 9.8 Å.
- Apolar groups, e.g., lipid chains and apolar amino acids, prefer an environment with low dielectric constant. Their interaction with water is unfavorable. This is the "hydrophobic effect." The hydrophobic effect (describing the free energy difference of the interface between hydrocarbons and water) is very temperature dependent and increases at higher temperatures. It is proportional to the hydrophobic surfaces of the molecules. For lipid chains it is proportional to their length.
- Apolar amino acids like to partition in the hydrophobic core of lipid membranes, while charged and polar residues prefer the aqueous environment. Aromatic residues (in particular tryptophane) partition preferentially in the head group region of membranes. The amino acid preferences for different membrane regions are described by the Wimley–White hydrophobicity scale.
- These preferences largely determine the interaction and the orientation of proteins in lipid membranes. Proteins have the most favorable interaction with membranes if the hydrophobic lengths of the polypeptide chains and the lipid membrane are similar. This effect is called "hydrophobic matching."
- Charged groups of lipids and proteins interact with water. These interactions depend on the activity of water that is influenced by ions in the aqueous buffer. The effect of ions on water activity is described by the Hofmeister series.

6
Lipid Melting

6.1
Lipid Melting

Lipid membranes may undergo order or melting transitions. This has already been discussed in Chapters 2 and 3. For biological membranes these transitions are typically found in the range 10–25 °C (see Fig. 6.13). Most lipids that are extracted from such membranes melt in the temperature regime between $-20°$ (some lipids with unsaturations in their chains as dioleoyl phosphatidylcholine) and $+60$ °C (lipids with a long saturated long chain, e.g., some sphingolipids and ceramides). Such melting transitions can be measured with many means, including differential scanning calorimetry (DSC) and various spectroscopic methods. Calorimetry has the advantage that it directly yields important thermodynamic information (e.g., enthalpy and entropy changes) not available (without interpretation) from spectroscopy.

6.1.1
Calorimetry and Heat Capacity

Calorimeters record the heat capacity of a sample (Section 4.10). All substances possess a heat capacity and (as shown later in Section 6.4) it always assumes positive values. There are various types of calorimeters that record heat releases under different conditions. Calorimeters that are built for solid state applications usually display a very large range of temperatures. Calorimeters in biosciences only require temperatures between 0 and 100 °C but simultaneously must be very sensitive since material is often precious. The most interesting calorimeter types for biophysicists are differential scanning calorimeters (measuring heat uptake upon temperature increase) and titration calorimeters, measuring the heat release or uptake in binding reactions.

In Fig. 6.1 a schematic drawing of a differential calorimeter is shown. It consists of two cells (one sample cell and one reference cell that usually filled with water or buffer) with a volume of 0.5–1 cm^3. Both cells are heated with

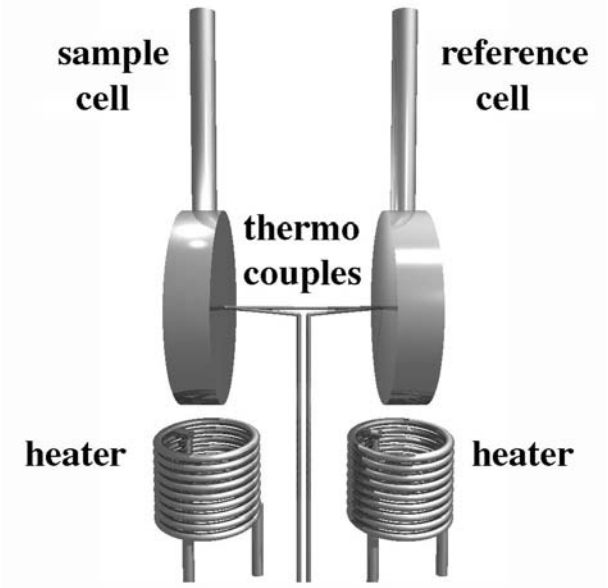

Fig. 6.1 Schematic drawing of a calorimeter containing a sample and a reference cell. Both cells are heated at a constant rate. The power necessary to maintain the rate for both cells is recorded. The heat capacity is obtained by dividing this power with the scan rate.

Peltier heaters at a constant scan rate. The temperature difference between the two cells is kept constant. In a melting transition the sample cells absorb more heat which is compensated by the heaters. The power of the two heaters is finely adjusted such that both the scan rate is constant and the temperature difference of the two cells is zero. The power difference of the two heaters is recorded as a function of temperature. It has the units Watts = J/s. The scan rate has the units K/s. If one divides power by the scan rate one obtains the units J/K, which is the unit of the heat capacity. In a differential scanning calorimeter (DSC) only the difference between the sample and reference cell is recorded, meaning that the heat capacity of the aqueous buffer is subtracted automatically.

The raw heat capacity profiles display an offset and often a slope of the baseline. The primary source of the baseline offset is the different heat capacity of water and lipids. Since the lipid displaces some water volume and water has a very high heat capacity (of 4.183 J/g K at 14 °C), the baseline normally assumes negative values. If the experiment is performed very carefully, from this offset the absolute heat capacity of the lipids outside the transition regime can be obtained. Blume has found it to be of the order of 1600 J/mol K for dipalmitoyl phosphatidylcholine (DPPC) (Blume, 1983). As can be seen in Fig. 6.2 the baseline has approximately the same value below and above the

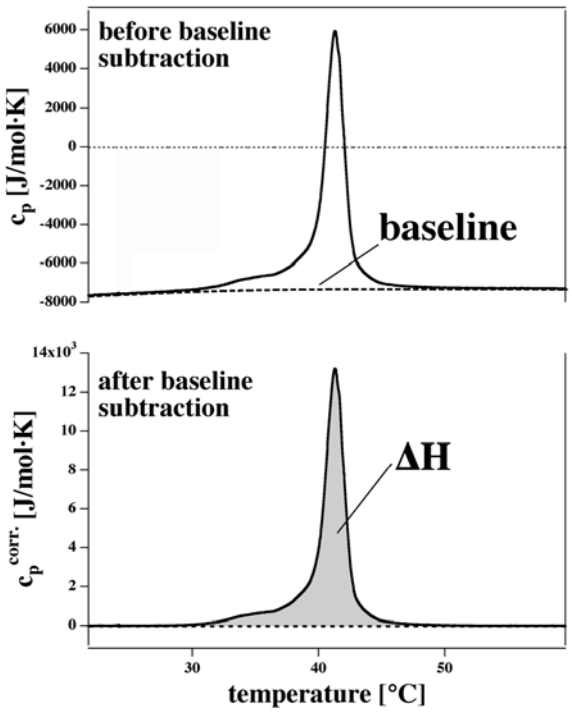

Fig. 6.2 Calorimetric scan of large unilamellar vesicles of dipalmitoyl phosphatidylcholine (DPPC). The top row shows the raw heat capacity data. From these data a suitable baseline can determined (top panel). After subtraction the enthalpy of the transition can be determined by integrating the excess heat capacity profile (bottom panel).

transition. This means that the interaction of the membranes with water stays about constant and that the hydrophobic effect does not play a major role for the melting transition (see Chapter 5). To be more precise, it does not affect the melting point but most likely affects the transition halfwidth due to the hydrophobic matching condition.

The area under the heat capacity peak is the melting enthalpy. The correct determination of the baseline is very important. Sometimes this turns out to be quite difficult if the melting profile is very broad. Then one has to make a somewhat subjective choice of where the limits of the excess melting events are. The accurate determination of the baseline is essential to obtain the correct values for the melting enthalpy. If one compares the literature data of lipid melting enthalpies one finds a large variation in the results. Much of this scattering is related to the different choice of the baseline. Especially the melting enthalpies of broad transitions, e.g., in the presence of cholesterol or proteins, are notoriously underestimated. In the example shown in Fig. 6.2, however, the baseline determination is easy.

6.1.2
Melting of Membranes Consisting of One Lipid Species

At low temperatures lipids are arranged on a triangular lattice (Janiak et al., 1979). At high temperatures, they do not display lateral order. Instead, they are randomly organized and represent a liquid in the language of solid state physics. For this reason the transition is called solid–liquid transition (Fig. 6.3, bottom). Furthermore, the lipid chains of the individual molecules simultaneously also display order–disorder transitions. Whereas at low temperatures the lipids display predominantly all-trans configurations, at high temperatures they show a rather random chain order with many trans-, gauche$^-$, and gauche$^+$ isomerizations in their C–C bonds in the hydrocarbon chain (Fig. 6.3 (top) and Fig. 6.7). Lipid membranes therefore display at least two different phases: the solid-ordered phase often called the "gel phase" and the liquid-disordered phase that is often called the "fluid phase." These terms describe the two different ordering processes in membranes. One may suspect that the solid-liquid transition of the head group arrangement and the order-disorder transition of the chains do not necessarily have to occur at the same temperature, and that possibly solid-disordered and liquid-ordered phases are possible. While the solid-disordered phase has so far not been identified in lipid membranes, the liquid-ordered phase has been proposed to exist in cholesterol-containing membranes (see Fig. 7.14), possibly due to the size of the cholesterol molecule that disturbs the formation of lateral lattices and its hydrogen bonding to carbonyl oxygens. The liquid-ordered phase is a kind of gel phase (i.e., with low enthalpy) without the lateral packing order.

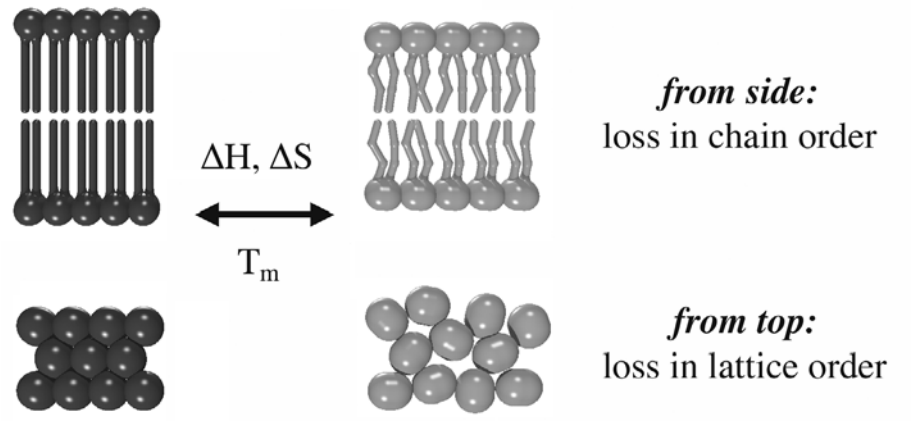

Fig. 6.3 Schematic picture of lipid melting from a solid-ordered to a liquid-disordered phase. Top: The order within the lipid chains is lost upon melting. Bottom: The crystalline order of the lipid head groups is also lost and the matrix undergoes a solid–liquid transition.

A membrane represents a two-dimensional matrix embedded into three-dimensional space, which usually consists of an aqueous medium. While the transitions mentioned above exclusively take place within the plane of the membrane, there is the possibility of the formation of further lipid phases that make use of curvature changes involving the third dimension normal to the bilayer surface. They will play a major role in Chapter 15. Such phenomena are particularly important close to the melting of the lipid membrane because the elastic constants in this temperature regime are largely altered (Chapter 14). One example is the pretransition of lipid membranes (Figs. 6.4 and 6.5), which is discussed in detail in Section 15.6.

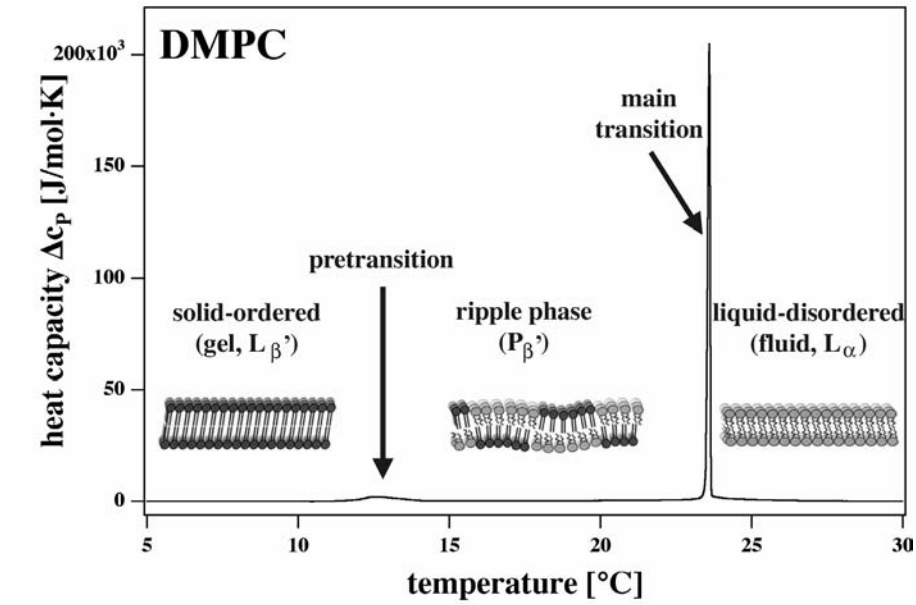

Fig. 6.4 Calorimetric melting profile of dimyristoyl phosphatidylcholine (DMPC). The melting curve displays two peaks called pretransition (T_P) and main transition (T_m). Below the pretransition one finds the solid-ordered phase (gel phase), between pretransition and main transition the ripple phase is found (see the text). Above the main transition one finds the liquid-disordered state (fluid phase). The ripple phase most likely is an intermediate between the gel and fluid phase.

The pretransition is a transition with low cooperativity that is found a few degrees below the main transition. From electron microscopy and atomic force microscopy it is known that between the pretransition and the main transition the membrane surface displays periodical undulations (ripples) with length scales between 13 and 30 nm, in some cases even longer (compare this to the thickness of a membrane of 5 nm, and a typical lipid cross section of 0.7 nm). It will be argued in Chapter 15 that the pretransition and the main transition

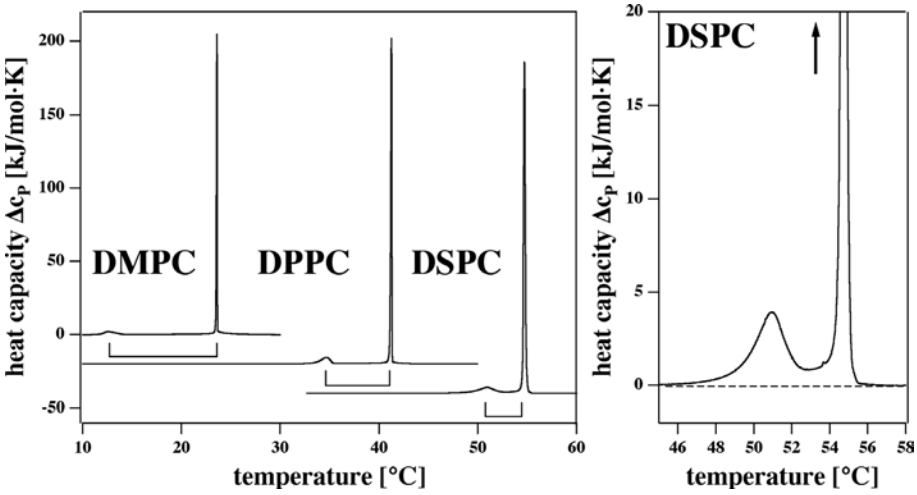

Fig. 6.5 Left: Heat capacity profiles of three different diacyl phosphatidylcholines: dimyristoyl phosphatidylcholine (DMPC), dipalmitoyl phosphatidylcholine (DPPC) , and distearoyl phosphatidylcholine (DSPC). The total area of the melting peak increases with increasing chain length. Simultaneously, the temperature interval between the pretransition and main transition becomes smaller (indicated be the rectangular brackets). Right: Amplified Δc_P profile of DSPC. The excess heat capacity does not return to the baseline between the two transitions. They probably do not represent independent events.

are related phenomena and both are caused by the chain melting process of the lipids. It will be shown that the splitting into two peaks is a consequence of simultaneous changes in the lipid order and membrane curvature. This is the case for the formation of the ripples, too.

Figure 6.5 (left) shows the melting profiles of three different diacyl phosphatidyl cholines, with 14, 16, and 18 carbons in the two hydrocarbon chains, respectively. The trivial names for these lipids are dimyristoyl-, dipalmitoyl, and distearoyl phosphatidyl choline (Table 3.2). It can be seen in Fig. 6.5 that increasing chain length leads to an increase of the melting temperatures, and that the temperature difference between pretransition and main transition decreases. In particular, it can be seen that the heat capacity (actually, here and in the following we talk about the excess heat capacity, Δc_P associated with the cooperative melting events) between the two transitions does not completely return to the baseline such that one has to consider the whole interval between the pretransition and main transition as one continuous melting regime (Fig. 6.5, right). Under such conditions it is obviously difficult to define a melting temperature. The heat capacity is given by $c_P = c_P^0 + \Delta c_P$ where $Deltac_P$ refers to the cooperative melting events. In the literature, the melting temperature is usually defined as the maximum of the Δc_P curve of the main transition. More accurately, one should rather consider the temperature where the excess enthalpy is 50% (and the number of gel and fluid lipids is equal) because there the free energy difference between the two lipid states is zero.

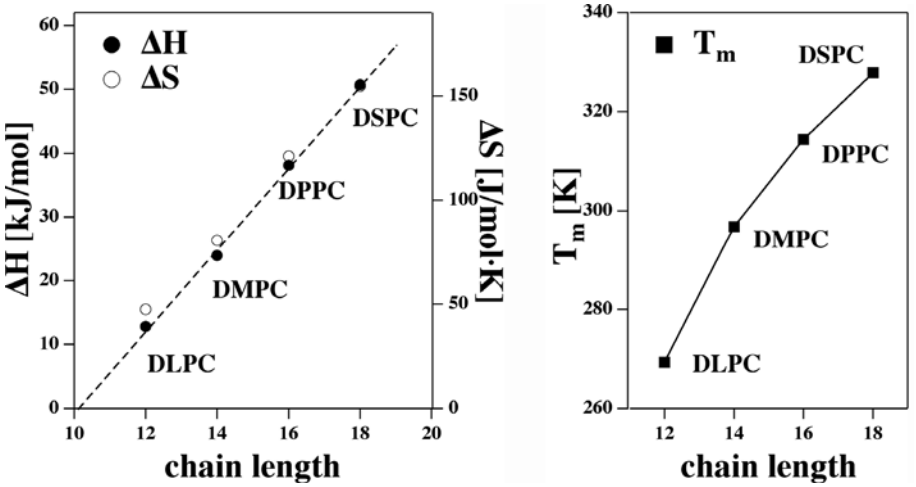

Fig. 6.6 Left: Melting enthalpy, ΔH, and melting entropy, ΔS, as a function of the chain length. Both curves can be approximated by a linear function. Right: Melting temperature, T_m, as a function of the chain length. The relation is not linear. Values are given in Table 6.1.

The enthalpy of the melting curve can be determined from the excess heat capacity by integration.

$$\Delta H = \int_{T_0}^{T_1} \Delta c_P \, dT \tag{6.1}$$

In practice, the excess enthalpy depends on where the integration limits are defined, and how the baseline has been determined. Considering the c_P data in Fig. 6.5 (right), it seems reasonable to integrate from below the pretransition to above the main transition to get one enthalpy value for the whole melting regime. This is not done by most authors, giving rise to a wide spread of different enthalpy values for the different lipids in the databases (e.g., the lipid database "LIPIDAT" that can be found at http://www.lipidat.chemistry.ohio-state.edu/). As discussed earlier in this chapter, incorrect baseline determinations are a significant source of error. For various phosphatidylcholines, the enthalpy values are given in Fig. 6.6. It is recommended to the reader to take the literature values as a recommendation and to cross-check the values in controlled experiments.

The melting entropy is given by

$$\Delta S = \int_{T_0}^{T_1} \frac{\Delta c_P}{T} \, dT \tag{6.2}$$

or, if the melting peak is reasonably sharp (i.e., if $c_P/T \approx c_P/T_m$) one can

simplify to

$$\Delta S = \frac{\Delta H}{T_m} \tag{6.3}$$

These values in molar units are also given in Fig. 6.6 for a series of phosphatidylcholines.

One can recognize that both excess enthalpy and entropy values fall on a straight line that does not pass through the origin. The functional behavior as extracted from Fig. 6.6 is given by

$$\begin{aligned} \Delta H(n_C) &= -64.58 + 2 * n_C \cdot 3.2 \,\frac{\text{kJ}}{\text{mol}} \\ \Delta S(n_C) &= -170.59 + 2 * n_C \cdot 9.053 \,\frac{\text{J}}{\text{mol K}} \end{aligned} \tag{6.4}$$

Let us consider, instead, enthalpy and entropy as functions of the number of bonds n_B in the hydrocarbon chain that is fixed at the glycerol backbone, around which rotations change the chain configuration. In total one finds $n-1$ bonds between n carbons. Rotations around the bond linked to the terminal methyl group do not result in changes of the configuration. Thus, $n_B = n_C - 2$. It follows that

$$\begin{aligned} \Delta H(n_C) &= -51.78 + 2 \cdot (n_C - 2) \cdot 3.20 \,\frac{\text{kJ}}{\text{mol}} \\ \Delta S(n_C) &= -134.38 + 2 \cdot (n_C - 2) \cdot 9.05 \,\frac{\text{J}}{\text{mol K}} \end{aligned} \tag{6.5}$$

In the next paragraph we will explain why it is very reasonable to expect an approximately linear dependence of both functions on the chain length. Surprising, however, is the fact that both curves intersect the chain length axis at a value of $n_C \approx 9$–10. How is this possible? One reason for this may be that not only the lipid chains but also the lipid head groups contribute to the melting enthalpy. In fact, lipids with different head groups, e.g., diacyl ethanolamines, display a similar dependence of the melting entropies and enthalpies on the chain length. However, the absolute numbers are different, and so is the interpolated chain length of zero enthalpy and entropy. This suggests that the interaction of the lipid head groups with the aqueous medium provides a negative contribution to the melting enthalpy and entropy that depends on the head group. For the phosphatidylcholines this is

$$\Delta H_{\text{head group}} = -51.78\,\text{kJ/mol} \qquad \Delta S_{\text{head group}} = -134.38\,\text{J/mol} \tag{6.6}$$

while the contribution from the two chains is given by

$$\begin{aligned} \Delta H_{\text{chain}}(n_C) &= 2 \cdot (n_C - 2) \cdot 3.20 \,\frac{\text{kJ}}{\text{mol}} \\ \Delta S_{\text{chain}}(n_C) &= 2 \cdot (n_C - 2) \cdot 9.05 \,\frac{\text{J}}{\text{mol K}} \end{aligned} \tag{6.7}$$

For DPPC which has 16 carbons and 14 bonds in each chain, this also implies that the total melting enthalpy associated with the chains is 89.6 kJ/mol (rather than the experimentally determined one, 37 kJ/mol), compensated by a head group contribution of −51.78 kJ/mol. Per CH_2 group in a single hydrocarbon chain that corresponds to about 3.2 kJ/mol. Similarly, the total chain entropy of DPPC is 253.50 J/mol K, partially compensated by a head group entropy contribution of −134.38 J/mol K. The numerical values of enthalpy, entropy, and melting temperature given in Table 6.1 are the experimental values that are close to the values above.

Tab. 6.1 Melting enthalpies and entropies, and melting temperatures of some common lipids. Enthalpies are given as the integral of the heat capacity including both pretransition and main transition (see the text). The melting points given are actually the heat capacity maxima. DLPC displays several peaks over a broad range. The two major maxima are given. DMPG shows several peaks if not measured at high ionic strength. Thanks to Heiko Seeger and Katrine R. Laub, Copenhagen.

Lipid	ΔH (kJ/mol)	ΔS (J/mol K)	T_m (°C)	Comments
DLPC	12.8	47.5	−3.8 (+3.9)	Broad transition range (−5 °C and 5 °C)
DMPC	23.9	80.5	23.6	
DPPC	38.1	121.2	41.3	
DSPC	50.7	154.7	54.7	
DMPE	31.5	97.4	49.8	After annihilating metastability
DPPE			63.9	
DMPG	23.0	77.4	23.8	At 500 mM NaCl, pH 7
DPPG	32.5	103.6	40.3	At 500 mM NaCl, pH 7

Equation (6.4) leads to the prediction of negative values for the melting enthalpy for chain lengths smaller than 10 carbons. Negative melting enthalpies, however, are thermodynamically not possible (for a proof see Section 6.4). One has to conclude that lipids do not display transitions at all for those chain lengths. Also, melting entropies must always be larger than zero. This can be easily concluded from the fluctuation theorem. In Chapter 19 we show that only alcohols with chain length shorter than 10 carbons act as anesthetics. Only those molecules are expected to not display phase behavior of their own in lipid membranes which is a requirement for anesthesia.

6.1.3 Some Simple Considerations on the Melting Enthalpies and Entropies

There are several factors that contribute to the enthalpy increase during the transition. Marcalja (Marcelja, 1974a,b) pointed out that dispersion forces between adjacent lipids contribute to the chain melting in a manner comparable to rigid molecules in a liquid crystal. Such forces partially determine the cooperativity of the transition.

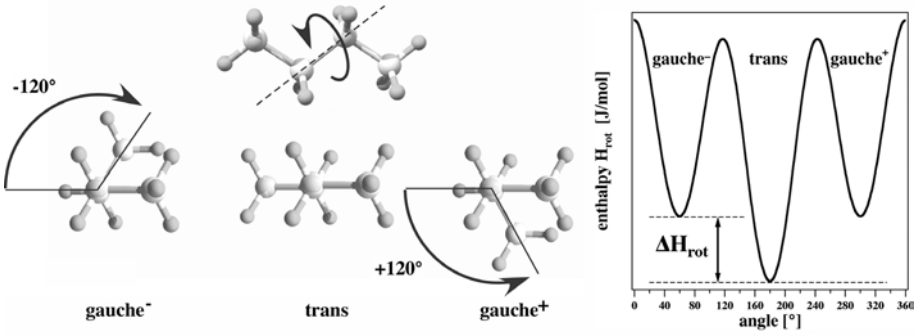

Fig. 6.7 The rotation of hydrocarbon chains with at least 4 carbons by multiples of 120° leads to nonequivalent conformations as demonstrated here for butane. Shown are the side view and the view along the central C–C bond. Rotation around the central bond leads to three enthalpy minima: gauche$^-$, trans, and gauche$^+$. The two gauche conformations are identical mirror images.The trans-configuration represents the lowest enthalpy conformation.

For steric reasons, the all-trans configuration of the lipid chains is favored. Via rotations around carbon–carbon bonds in the hydrocarbon chain one can generate other conformations, so-called gauche$^-$ and gauche$^+$ conformations (Fig. 6.7). Let us now simplify the assumptions about the formation of different chain conformations. The chain conformation with the maximum distance between the carbon at position i and the carbon at $i+3$ shall be called the trans-configuration. We assume that each rotation of a chain away from a trans-conformation around the bond between carbons $i+1$ and $i+2$ (see Fig. 6.7) by $\pm 120^\circ$ into either a gauche$^-$ or a gauche$^+$ configuration leads to the change in enthalpy of ΔH_{rot}. The enthalpy of the hydrocarbon chain is a function of the angle of rotation as shown in Fig. 6.7. The equilibrium between a trans and the two gauche conformations is given by a Boltzmann law

$$\frac{[\mathrm{gauche}^- + \mathrm{gauche}^+]}{[\mathrm{trans}]} = 2 \cdot \exp\left(-\frac{\Delta H_{\mathrm{rot}}}{RT}\right) \equiv \exp\left(-\frac{\Delta H_{\mathrm{rot}} - T \cdot \overbrace{R \ln 2}^{\Delta S_{\mathrm{rot}}}}{RT}\right)$$

$$= \exp\left(-\frac{\Delta G_{\mathrm{rot}}}{RT}\right) \tag{6.8}$$

with $\Delta G_{\mathrm{rot}} = \Delta H_{\mathrm{rot}} - T \cdot \Delta S_{\mathrm{rot}}$. One can see that for high temperatures ($T \to \infty$) each of the two gauche states and the trans state are equally populated. This means that at high temperatures 2/3 of all states are gauche conformers and the mean enthalpy is

$$H_{\mathrm{bond}} = \frac{2}{3}\Delta H_{\mathrm{rot}} \tag{6.9}$$

At high temperatures, the entropy difference between a random configuration and a trans-configuration associated with the rotation around one bond (assuming equal probabilities of gauche$^-$, trans, and gauche$^+$ of 1/3) is given by

$$\Delta S_{\text{bond}} = R \ln 3 = 9.134\,\text{J/mol K} \tag{6.10}$$

This is nearly exactly the value found experimentally in Eq. (6.7) for the contribution of one carbon to the transition entropy (in this equation a value of 9.05 J/mol K was found). The experimental value for the chain enthalpy from one bond from Eq. (6.7) was

$$\Delta H_{\text{bond}} = 3.2\ \text{kJ/mol} \tag{6.11}$$

This corresponds to

$$\Delta H_{\text{rot}} = \frac{3}{2}\Delta H_{\text{bond}} = 4.8\ \text{kJ/mol} \tag{6.12}$$

For the equilibrium between a two-chain lipid with completely ordered (all-trans) and totally disordered chains with $(n-2)$ relevant bonds, we obtain

$$\frac{[\text{disordered}]}{[\text{ordered}]} = \exp\left(-\frac{2(n-2)\cdot(\Delta H_{\text{bond}} - T\Delta S_{\text{bond}})}{RT}\right) \tag{6.13}$$

Thus, one can see that one expects a linear relationship between both melting enthalpy and melting entropy, and the chain length. This was found experimentally (Fig. 6.6). Of course, this is only a rough estimate because within a lipid membrane not all lipid conformations can be assumed and the excess enthalpy and the entropy will be somewhat smaller than for the case where all conformation can be assumed. However, the values from this rough calculation are on a very reasonable scale.

6.2
Cooperativity and Cooperative Unit Size

Melting transitions of lipid membranes occur over a very narrow temperature regime. For instance, DPPC multilayers display a transition half-width of about 0.05 K while the unfolding of proteins displays a typical half-width of about 10 K (see Fig. 5.4). The narrow half-width of lipid transitions is surprising as the following little calculation shows.

Let us assume that all lipids within the membrane melt independently of each other. The free energy difference of the fluid state lipid and the gel state lipid, ΔG, describes the equilibrium between the two states of the lipid.

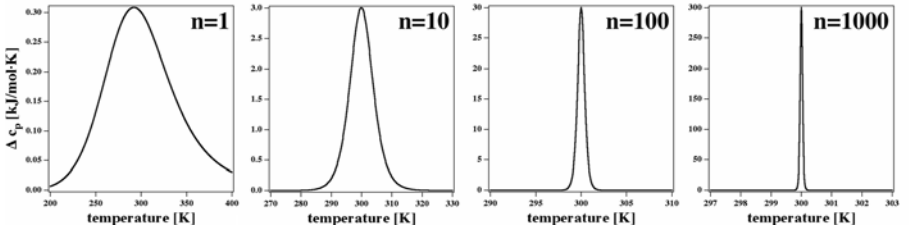

Fig. 6.8 From left to right: Calculated calorimetric melting profile of lipid membranes with a melting enthalpy of 30 kJ/mol and a melting temperature of $T_m = 300$ K, assuming increasing cooperative unit sizes (1, 10, 100, and 1000 lipids). Note the different scaling of the two axes in the four panels.

The equilibrium constant $K = \exp(-\Delta G/RT)$ is a function of temperature and depends on ΔH. Van't Hoff described the temperature dependence of the equilibrium constant by the following law:

$$\ln K(T) = -\frac{\Delta H}{RT} + \frac{\Delta S}{R} \quad \longrightarrow \quad RT^2 \frac{d \ln K}{dT} = \Delta H \tag{6.14}$$

that is called van't Hoff's law. The probability of finding a gel state lipid is given by $1/(1+K)$ and the probability of finding a fluid state lipid is $K/(1+K)$. The mean enthalpy change per mole of lipid is therefore given by

$$\langle \Delta H(T) \rangle = \Delta H \frac{K(T)}{1+K(T)} \tag{6.15}$$

From this one obtains a heat capacity $c_P = d\langle \Delta H \rangle / dT$ of

$$c_P = \left(\frac{\langle \Delta H \rangle}{dT} \right)_P = \frac{K(T)}{(1+K(T))^2} \frac{\Delta H^2}{RT^2} \tag{6.16}$$

For $\Delta H = 35$ kJ/mol one obtains a melting profile with a half width of about 60°. This is not in agreement with experimental data. In experiments transition profiles are significantly narrower—less than 1° (cf. Fig. 6.8). What could be the reason for this?

The Boltzmann factor above is given per mole of the unit that undergoes a transition. Let us assume that lipids do not melt independently of each other but rather simultaneously in clusters of n lipids. Then we have to consider these n lipids as the cooperative unit size. We have to replace enthalpy, entropy, and free energy in the above equations by

$$\begin{aligned} \Delta H &\longrightarrow n\Delta H \\ \Delta S &\longrightarrow n\Delta S \\ \Delta G &\longrightarrow n\Delta G \\ K = \exp(-\Delta G/RT) &\longrightarrow K = \exp(-n \cdot \Delta G/RT) \end{aligned} \tag{6.17}$$

These values have to be used in Eq. (6.16). In Fig. 6.8 the resulting heat capacity profiles are shown for different cooperative unit sizes. The larger the cooperative unit size the narrower the transition peak. To explain the transition half with of DPPC MLV one needs a cooperative unit size of at least 1000 lipids. If the cooperative unit size approaches an infinite number of molecules, the transition half width also becomes infinitely small. This is the limit of a first-order transition. Since lipid vesicles always have a finite size, transition peaks in real systems are never infinitely sharp. Large multilamellar vesicles display generally much narrower transition preaks than unilamellar vesicles.

The above naturally is based on the somewhat arbitrary assumption that the cooperative unit size is independent of temperature. This is actually not the case. A much more sophisticated analysis of such clusters is given in Chapter 8. However, already here is seems obvious that melting of lipid membranes must be a cooperative phenomenon. The cooperative clusters can actually often be seen under the microscope as domains (see, e.g., Fig. 8.3).

6.3 Influence of Pressure

The application of pressure has pronounced effects on lipid melting as shown in Fig. 6.9. In this example we show dimyristoyl phosphatidylcholine (DMPC) multilamellar vesicles at atmospheric pressure and with applied pressure. The main transition of DMPC is very cooperative. The transition half width is less than 0.1 K (slightly depending on buffer conditions). The application of 40 bars bulk pressure leads to a shift of the transition of about 0.92 K. Now

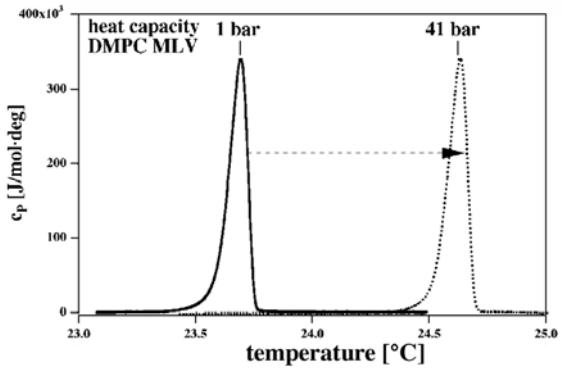

Fig. 6.9 Upon application of pressure heat capacity profiles of lipid membranes shift to higher temperatures. From this volume changes can be calculated. Shown is the heat capacity profile of DMPC MLV. Adapted from Ebel et al. (2001).

the melting temperature T_m for a given constant pressure p_0 is given by (cf. Eq. (6.3))

$$T_m = \frac{\Delta H_0}{\Delta S} = \frac{\Delta E_0 + p_0 \Delta V}{\Delta S} \tag{6.18}$$

Upon an increase of pressure by Δp the change of the melting enthalpy is

$$\Delta\left(\Delta H\right) = \Delta p \Delta V \tag{6.19}$$

It is reasonable to assume that the entropy change in the melting transitions upon an increase of pressure is unchanged if we consider the same low and high temperature states outside the transition regime. The resulting change in melting temperature is

$$\Delta T_m = \frac{\Delta\left(\Delta H\right)}{\Delta S} = \frac{\Delta p\, \Delta V}{\Delta S} = \Delta p\, T_m \frac{\Delta V}{\Delta H_0} \tag{6.20}$$

In Fig. 6.9 it is shown that the application of an excess pressure of $\Delta p = 40\,\text{bar} = 4 \times 10^6$ Pa results in a shift of the melting transition of DMPC membranes by 0.92°. From this shift the volume change in the transition can be calculated:

$$\Delta V = \frac{\Delta T_m\, \Delta H_0}{T_m\, \Delta p} \tag{6.21}$$

where ΔH_0 and T_m are the values at atmospheric pressure. The pressure dependence of lipid phase behavior has been investigated in much detail by Winter and colleagues (Winter and Pilgrim, 1989; Landwehr and Winter, 1994; Czeslik et al., 1998). They found that the shift of the melting temperature as a function of pressure is linear up to more than 1000–2000 bar (Böttner et al. (1994)).

It has been found experimentally by Ebel et al. (2001) that $\Delta T_m / T_m$ at a given pressure change Δp, is within experimental error, the same for various lipids. This also means that $\Delta V / \Delta H_0$ is roughly independent of the nature of the lipid. Let us consider the earlier result that the melting enthalpy depends approximately linearly on the chain length. In the next section we further show that melting enthalpies can never become negative. It therefore follows that for lipid membranes the volume change is also never negative.

Volume changes can be indirectly measured in a pressure calorimetry (Fig. 6.9). More directly they can be obtained from differential densitometry (see the Kratky balance in Fig. 14.3). In such an experiment the lipid dispersion is filled into a vibrating capillary The eigen-frequency of the capillary is related to the density of the dispersion. The specific volume of the dispersion can be deduced from careful measurement of the vibrational frequency. A densitometry experiment is shown in Fig. 6.10. Here, density,

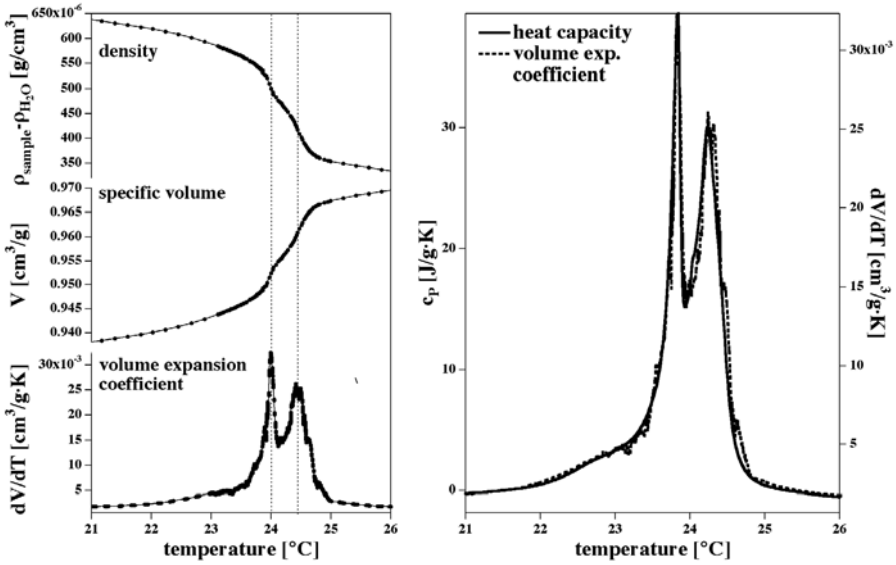

Fig. 6.10 Some thermodynamic functions of a 10mM DMPC LUV dispersion. Left: Density, ρ, obtained in a differential densitometer, specific volume, V, and volume expansion coefficient, dV/dT, as a function of temperature. Right: The volume expansion coefficient is proportional to the heat capacity. The profile shown displays two maxima. This is probably a consequence of shape changes of the vesicles in the melting regime. Adapted from Ebel et al. (2001).

specific volume, and volume expansion coefficient (defined as the temperature dependence of the specific volume, dV/dT) are plotted as a function of temperature. Interestingly, the volume expansion coefficient and excess heat capacity are proportional functions. This statement is much stronger than that made above in Eq. (6.20). The proportional relation between the heat capacity and volume expansion coefficient will play an important role in Chapters 14 and 15, where we will use this fact to calculate elastic constants from the heat capacity.

The melting of the lipid membrane depends on the lateral pressure, $\Delta\Pi$, in a similar manner as on the bulk hydrostatic pressure:

$$\begin{aligned} T_m &= \frac{\Delta H_0}{\Delta S} \qquad \text{and} \qquad \Delta H_0 = \Delta\Pi\,\Delta A \\ \Delta T_m &= \frac{\Delta\Pi\,\Delta A}{\Delta S} = \Pi\, T_m \frac{\Delta A}{\Delta H_0} \end{aligned} \tag{6.22}$$

This will be discussed below in the context of monolayer experiments.

6.4 Metastable States

According to (4.43) the heat capacity is given by

$$c_P = \frac{d\langle H\rangle}{dT} = \frac{\langle H^2\rangle - \langle H\rangle^2}{R\,T^2} = \frac{\langle H - \langle H\rangle\rangle^2}{R\,T^2} \geq 0 \tag{6.23}$$

The heat capacity therefore can never assume negative values. Making use of Eq. (6.23) this implies that the enthalpy is a monotonically increasing function of temperature:

$$\Delta H = \int_{T_1}^{T_2} c_P dT \geq 0 \qquad \text{if} \qquad T_2 > T_2 \tag{6.24}$$

The same is generally true for the entropy:

$$\Delta S = \int_{T_1}^{T_2} \frac{c_P}{T} dT \geq 0 \qquad \text{if} \qquad T_2 > T_2 \tag{6.25}$$

Therefore, during a heat capacity up-scan the enthalpy can never decrease. However, examples can be found where exactly this happens. How is this possible? The example in Fig. 6.11 shows a mixture of dimyristoyl phosphatidyl-

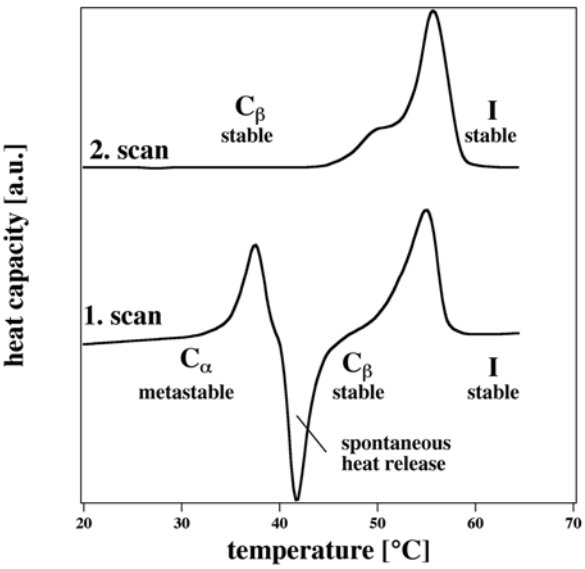

Fig. 6.11 Calorimetric scan of a mixture of DMPC and dimyristoyl glycerol (10:90 mol%:mol%). The first scan and the second scan display a very different shape. In the first scan a transition from a metastable state C_α to a stable state C_β with a lower enthalpy occurs. Adapted from Heimburg et al. (1992).

choline (DMPC) and dimyristoyl glycerol (DMG). DMG does not form membranes on its own but rather forms crystals. At high temperatures it forms an oil melt. Two different crystal structures exist. The lower enthalpy crystal structure, C_β, has a much lower rate of formation. The higher enthalpy crystal structure, C_α, displays a fast rate of formation. Thus, upon cooling usually the C_α phase forms, although the C_β phase is thermodynamically stable. The two crystal structures display different melting points. The C_α phase melts at about 37 °C, whereas the C_β phase rather melts at about 55 °C. Therefore, if the C_α phase is present after cooling the oil phase, at 37 °C it spontaneously converts into the more stable C_β phase. This means that in fact the C_α phase is a metastable phase. During this process heat is released. If the sample is cooled from 37 °C to lower temperatures and the scan is performed again, the spontaneous process at 37 °C disappears. Similar behavior can be found in the heating scans of dimyristoyl phosphatidylethanolamine (DMPE).

One should always be suspicious if one observes spontaneous heat releases upon heating a lipid sample. Usually such processes indicate that the sample is not in thermodynamic equilibrium. The sample can, however, often be equilibrated by partial heating or by storing the sample for a long time.

6.5
Melting of Membranes Consisting of Lipid Mixtures

Biological membranes consist of a complex mixture of lipids with very different melting enthalpies and different melting points. How does melting occur in such mixtures?

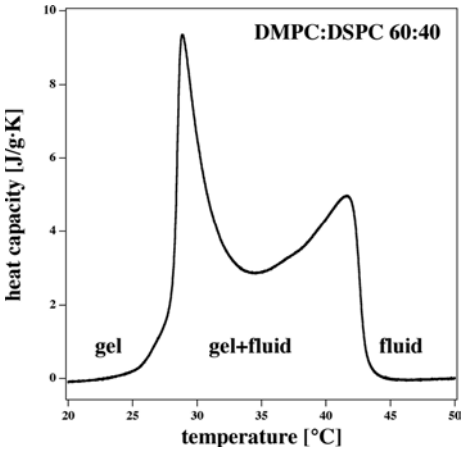

Fig. 6.12 Melting of a 60:40 mixture of DMPC and DSPC. The melting regime displays a half width on the order of 15 K.

In Fig. 6.12 the melting of a mixture of DMPC and DSPC is shown. It shows a melting regime with a half width of about 15 K. The profile displays two maxima, at 28.8 °C and 41.6 °C, respectively. These values are different from the melting points of the individual lipid components (23.6 °C and 54.7 °C, respectively). From this it has to be concluded that the different lipid species do not melt independently but rather influence each other in the melting process. In the next chapter (Chap. 7) we will investigate the phase behavior of lipid mixtures in much more detail.

6.6 Melting in Biological Membranes

All of the above is likely to play an important role in biology because biological membranes can also melt. Typically, such melting transitions are found 10–15 K below body or growth temperature. In Fig. 6.13 three biological samples are shown, which are as follows.

1. *Bovine lung surfactant*. This is a lipid film containing in particular the surfactant protein C (SP-C). It exists in a monolayer–bilayer equilibrium on the lung surface. Its purpose is to reduce the surface tension of the air–water interface of the lungs. Since the lung possesses a total surface area corresponding to the size of a tennis court the lung would collapse without the surface tension reduction caused by lung surfactant. Lung surfactant displays a lipid melting peak about 10–15 °C below body temperature. At higher temperatures above body temperature one can recognize the unfolding peak of the SP-C protein.

2. *E. coli membranes*. The isolated membranes of these cells display a pronounced lipid melting peak about 10–15 °C below growth temperature. Above growth temperature one can recognize a number of different protein unfolding peaks.

3. *Bacillus subtilis membranes*. As the membranes of *E.coli* the isolated membranes of *bacillus subtilis* display a pronounced lipid melting peak about 10–15 °C below growth temperature. Above growth temperature one finds protein unfolding events.

It has been shown that these membranes respond in a similar manner to pressure changes as the artificial membranes in Section 6.3 (Ebel et al., 2001; Heimburg and Jackson, 2007b).

It seems that biological membranes adapt their lipid composition such that the temperature distance between ambient temperature and melting transition is maintained (Chapter 3). When such organisms are grown at different temperature, different pressure, or in the presence of solvents they change

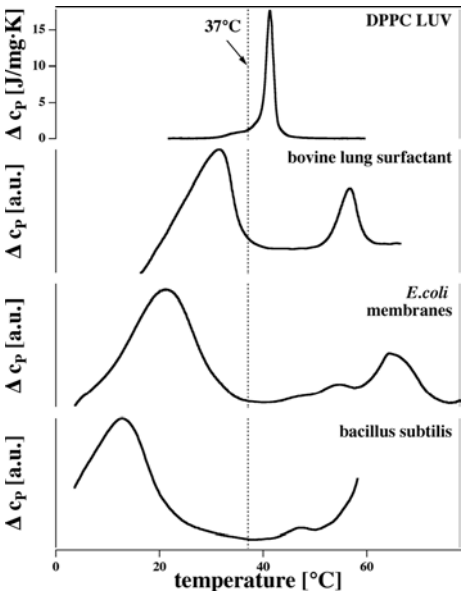

Fig. 6.13 Melting of artificial and biological membranes. From top to bottom: DPPC unilamellar vesicles, bovine lung surfactant, *E. coli* membranes, and *bacillus subtilis* membranes (from Heimburg and Jackson (2005)). The three biological samples also display protein unfolding peaks above body (or growth) temperature. The lipid melting in these membranes is represented by the broad peak below 37 °C.

their lipid composition. In Chapter 14 we derive that the heat capacity maxima are closely coupled to maxima in the elastic constants such that structural changes are easier (Chapter 15). Also, there is the possibility of mechanical excitations (Chapter 18). Thus, it seems likely that such transitions serve a purpose in the biological cell. Slight variation of the thermodynamic variables can move the membranes transiently into the transition regime. Variation of pH is possibly the easiest way to achieve this.

6.7 Lipid Monolayers

Many scientific groups investigate the phase behavior of lipid monofilms on water surfaces. This method has been introduced by Langmuir (1917) and is schematically shown in Fig. 6.14. Lipids spread on an air–water interface with the hydrocarbon tails being exposed to air and the lipid head groups being exposed to water. The area of the film can be altered by moving some teflon barriers and the lateral pressure is measured with a Wilhelmy balance that practically is a little metal rod (or thin paper sheet) sensing the surface tension of the film.

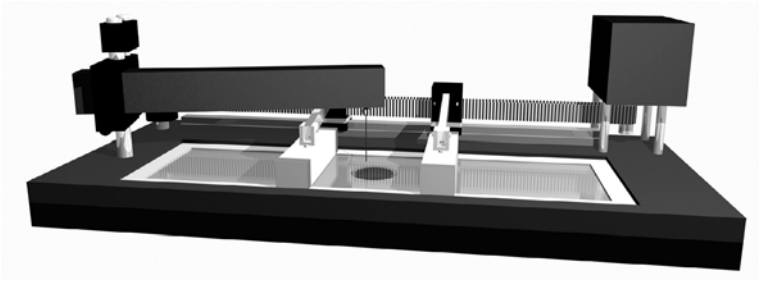

Fig. 6.14 Schematic drawing of a Langmuir trough with which the pressure in a lipid monofilm can be measured. A lipid monofilm spreads on the air-water interface. The area of the film can be altered moving two teflon barriers. The lateral pressure is recorded via the force acting on the metal rod hanging in the center. Domain formation can be imaged through a microscope objective from below. Image courtesy Martin Gudmand, NBI Copenhagen.

For two-dimensional systems at constant number of molecules the differential of the Helmholtz free energy is given by

$$dF = -SdT - \Pi dA \tag{6.26}$$

Thus, it follows that at constant temperature

$$\left(\frac{dF}{dA}\right)_T = -\Pi \tag{6.27}$$

The lateral pressure can be plotted as a function of the molecular area of the monofilm. Figure 6.15 (left) shows four isotherms of DPPC monofilms recorded at different temperatures. At three of those temperatures one can recognize a plateau region in the range about 50–75 ^{2}. This region displays a different width at different temperatures and completely disappears above 40 °C. The isotherms where area changes as a function of pressure have a formal correspondence to the change of enthalpy with respect to temperature. The region where small pressure changes result in large area changes corresponds to the chain melting regime. The two phases at low and high pressure are called the liquid-expanded and liquid-condensed phase. In the plateau region of the pressure-area isotherms the monolayer is very compressible and one finds co-existence of liquid and solid state domains (Fig. 6.16). This become more obvious if we consider the isothermal area compressibility, κ_T^A, that is defined by

$$\kappa_T^A = -\frac{1}{A}\left(\frac{dA}{d\Pi}\right)_T \tag{6.28}$$

The compressibilities are shown in Fig. 6.15 (right). In the chain melting regime one finds pronounced maxima of the compressibility as a function of

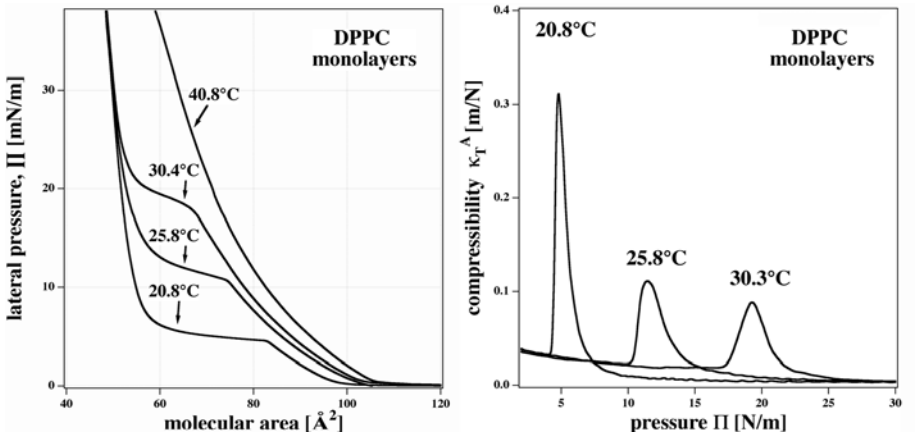

Fig. 6.15 Langmuir isotherms of DPPC monofilms recorded at four different temperatures. Left: Isotherms displaying plateau regime around a molecular area of 65 Å. Right: The lateral compressibility calculated from the data in the left-hand panel. They display pronounced maxima that shift with increasing ambient temperature. Compare this to the pressure-dependent heat capacity data shown in Fig. 6.9. Data by Gudmand and Heimburg, NBI Copenhagen.

pressure. These maxima are shifted toward higher pressures and higher temperatures.

The formal correspondence with the heat capacity profiles is obvious:

- The heat capacity displays maxima in the chain melting regime.
- The heat capacity maxima shift to higher temperatures if the bulk (or the lateral) pressure increases.
- The lateral compressibility displays a maximum in the chain melting regime.
- The compressibility maxima shift to higher pressures if the ambient temperature increases.

The similarity is also evident when comparing the right-hand panel of Fig. 6.15 with Fig. 6.9. For this reason heat capacity measurements and monolayer experiments are complementary. The two figures show distinct aspects of the same membrane phenomena by variation of different intensive variables (temperature and lateral pressure, respectively). In contrast to the heat capacity measurements, where hydrostatic pressure is maintained while the membrane area and volume are allowed to change, in monolayer experiments the area is kept constant and lateral pressure is allowed to vary. This makes monolayer experiments suitable for protein and drug adsorption experiments.

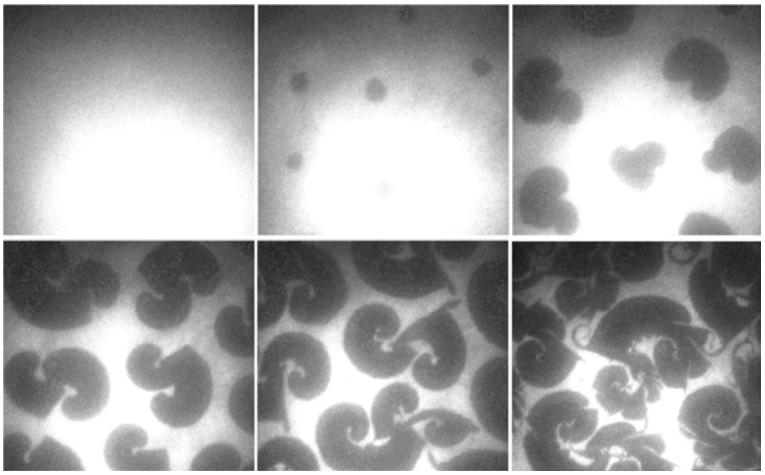

Fig. 6.16 Monolayer during compression through the plateau region (the region of high compressibility) of DPPC at room temperature showing domain formation. Bright regions are liquid regions containing a fluorescence marker. The dark regions are liquid-condensed domains without fluorescence marker. Data by Gudmand and Heimburg, NBI Copenhagen.

The transition in the lipid monolayers can be monitored by using fluorescence microscopy. Figure 6.16 shows a series of images of DPPC monofilms recorded at increasing monolayer pressure. The liquid-condensed domains (corresponding approximately to gel regions) show up in dark shades, while liquid-expanded regions (corresponding approximately to fluid regimes) show up as bright areas. The domains display chirality and increasingly complex shapes. Such chiral shapes are typically not found in bilayer vesicles (compare with Fig. 8.8).

6.8 Summary: Key Ideas of Chapter 6

- Lipid bilayers display melting transitions. Typically, the lipid membranes change their state from solid ordered to liquid disordered. One good way to measure such transitions is the calorimetric determination of the heat capacity, $c_P = (dH/dT)_P$.
- These transitions are associated with a change in enthalpy and entropy.
- The melting transition consists of a pretransition of low enthalpy and a main transition of high enthalpy. Between pretransition and main transition the membrane is periodically undulated (ripple phase). The pretransition and main transition probably represent one single continuous melting event (explained in more detail in Chapter 15).
- Enthalpy and entropy changes depend on both the head group and the chain length of the lipid. The head groups give a constant head-group specific negative contribution to the enthalpy while the chains add a positive enthalpy and entropy contribution that depends linearly on the chain length.
- The linear dependence on the chain length can be understood on the basis of chain isomerizations between trans and gauche configurations.
- Lipid membrane melting occurs over a very narrow temperature regime. This can only be understood if single lipids do not melt independently but in cooperative units. This will lead to cluster and domain formation.
- Hydrostatic pressure shifts melting points toward higher temperatures.
- Heat capacity peaks cannot be negative for equilibrated systems. Negative peaks are generally an indication for metastability or a nonequilibrated system. Such events can be found in the melting of DMG and DMPE membranes.
- Lipid melting transitions are also found in lipid mixtures and in biological membranes. In such systems they typically span over a larger temperature interval.
- Lipid melting can also be investigated by compressing lipid monofilms. Here, the lateral pressure is recorded as a function of area. This corresponds to the measurement of the compressibility as a function of pressure.

7
Phase Diagrams

In the previous chapter we have shown that single lipid membranes can melt and lipid melting depends on chain length, head group, protonation (charge), and pressure. However, biological membranes consist of many, probably hundreds of different lipids (see Chapter 3). In the Introduction we have seen that biological membranes show melting reactions slightly below body temperature that display a broad transition half-width. How can one understand the melting of complex lipid mixtures?

Since biological membranes are complex mixtures of many lipids with individually different melting temperatures and different melting enthalpies, a complex melting behavior is expected. The various lipid species in mixtures are not likely to melt independently. First—as already mentioned in Section 6.2, lipid melting displays cooperativity, i.e., the individual molecules do not melt independently. In mixtures they are influenced by the melting behavior of neighboring lipids of different chemical nature. Furthermore, since the lipids are all dissolved in a matrix (the membrane), they possess chemical potentials closely related to the concentrations (or molar fractions) of the respective lipids. The chemical potentials of the various lipids will be different in the gel and the fluid phase. Thus, a more advanced description of mixing and melting has to be developed.

In the following sections we introduce the theory of lipid phase diagrams, in particular ideal and regular solution theory. The interested reader may also consider reading the excellent article by Lee (1977).

7.1
Ideal Mixture

We will first treat the special case that the free energy of the interaction between all lipids in a phase is the same. Exchanging lipids within the gel phase or the fluid phase will not change the free energy of the lipid matrix. This means that the lipids will randomly distribute in each of the lipid phases. This is called “ideal mixing.”

Let us assume two lipid species, A and B. The interaction free energy of each lipid of species A with each lipid of species B is the same as with another lipid of species A. Furthermore, the lipid membrane shall exist in two states: gel state (g) and fluid state (f). The melting points, $T_{m,A}$ and $T_{m,B}$ of the individual components, as well as the corresponding melting enthalpies, ΔH_A and ΔH_B, are allowed to be different. What happens when the two lipids mix well and the temperature is in between $T_{m,A}$ and $T_{m,B}$?

The melting of a lipid resembles a unimolecular reaction of kind: gel $\rightleftharpoons$ fluid. The differential of the free energy can be written as (see Section 4.7)

$$dG = (\mu_f - \mu_g) dn_f \tag{7.1}$$

where μ_g and μ_f are the chemical potentials of gel and fluid phase lipids, respectively, and n_f is the fraction of fluid lipids. Since in thermal equilibrium $dG/dn_f = 0$ it follows that

$$\mu_\mathrm{g} = \mu_\mathrm{f} \tag{7.2}$$

For each of the components we can therefore write

$$\mu_A^g = \mu_A^f \qquad \text{and} \qquad \mu_B^g = \mu_B^f \tag{7.3}$$

where the index g denotes the gel state, and the index f denotes the fluid state.

In membranes we consider the distribution of lipids in two dimensions. The aqueous buffer is the three-dimensional medium into which the membrane is embedded. Therefore, it is convenient to use relative fractions of the individual components instead of concentrations. Instead of writing the chemical potential as $\mu = \mu_0 + RT \ln(c/c_0)$, we will now write it as $\mu = \mu_0 + RT \ln(x/x_0)$ with $x_0 = 1$. This means that now our standard state is a lipid fraction of x_0. x_i is the fraction of lipid species i, and $\sum x_i = 1$.

Let us now consider two lipids that display different melting temperatures, $T_{m,A}$ and $T_{m,B}$. In a temperature interval between the two melting points one may expect that some of the lipids are in the gel phase and some are in the fluid phase. Due to the different melting points one further expects that the concentration of the different lipid species in gel and fluid phase are different. Thus, the chemical potentials of the components in the gel and the fluid phase may assume different values.

The chemical potentials of the lipids of species A and B in gel and fluid phase are given by:

$$\begin{aligned} \mu_A^g &= \mu_{A,0}^g + RT \ln x_A^g \qquad \text{and} \qquad \mu_A^f = \mu_{A,0}^f + RT \ln x_A^f \\ \mu_B^g &= \mu_{B,0}^g + RT \ln x_B^g \qquad \text{and} \qquad \mu_B^f = \mu_{B,0}^f + RT \ln x_B^f \end{aligned} \tag{7.4}$$

where x_A^g is the fraction of species A in the gel phase (similarly for x_A^f, x_B^g, and x_B^f). It follows that

$$\frac{x_A^f}{x_A^g} = \exp\left(-\frac{\mu_{A,0}^f - \mu_{A,0}^g}{RT}\right) = \exp\left(-\frac{\Delta H_{A,0}}{R}\left(\frac{1}{T} - \frac{1}{T_{m,A}}\right)\right) \equiv e^{-A} \tag{7.5}$$

where it has been used that $\Delta\mu_A = \Delta H_{A,0} - T\Delta S_{A,0}$ and $\Delta S_{A,0} = \Delta H_{A,0}/T_{m,A}$. Correspondingly, one obtains for lipid species B

$$\frac{x_B^f}{x_B^g} = \exp\left(-\frac{\mu_{B,0}^f - \mu_{B,0}^g}{RT}\right) = \exp\left(-\frac{\Delta H_{B,0}}{R}\left(\frac{1}{T} - \frac{1}{T_{m,B}}\right)\right) \equiv e^{-B} \tag{7.6}$$

Furthermore, the fractions of the different lipids in each phase must add to one:

$$x_A^g + x_B^g = 1 \qquad \text{and} \qquad x_A^f + x_B^f = 1 \tag{7.7}$$

One has four unknowns, x_A^g, x_A^f, x_B^g, and x_B^f, and four equations, Eqs. (7.5), (7.6), and (7.7). The composition of the fluid and the gel phase are therefore uniquely defined.

If one solves these equations for the fractions of the two lipid species in the gel and the fluid phase, one obtains the following relations:

$$\begin{aligned} x_A^g &= \frac{e^{-B} - 1}{e^{-B} - e^{-A}} \\ x_B^g &= \frac{e^{-A} - 1}{e^{-A} - e^{-B}} \end{aligned} \tag{7.8}$$

and

$$\begin{aligned} x_A^f &= \frac{e^{-A}(e^{-B} - 1)}{e^{-B} - e^{-A}} \\ x_B^f &= \frac{e^{-B}(e^{-A} - 1)}{e^{-A} - e^{-B}} \end{aligned} \tag{7.9}$$

Some examples for the phase boundaries given by Eqs. (7.8) and (7.9) are shown in (see Fig. 7.1). Of course, for all fractions $0 \leq x_A^g, x_A^f, x_B^g, x_B^f \leq 1$ has to be fulfilled. Equations (7.8) and (7.9) therefore are only meaningful in a temperature interval $T_{m,A}$ and $T_{m,B}$. Below this temperature interval one finds all lipids in the gel phase, whereas above this interval all lipids are in the fluid phase.

The amounts of the gel phase, x^g, and the fluid phase, x^f, depend on the relative amounts of the lipid of species A, x_A, and of species B, x_B. Furthermore, $x^g + x^f = 1$ and

$$x_B = x^f \cdot x_B^f + x^g \cdot x_B^g = x^f \cdot x_B^f + (1 - x^f) \cdot x_B^g = x_f(x_B^f - x_B^g) + x_B^g \tag{7.10}$$

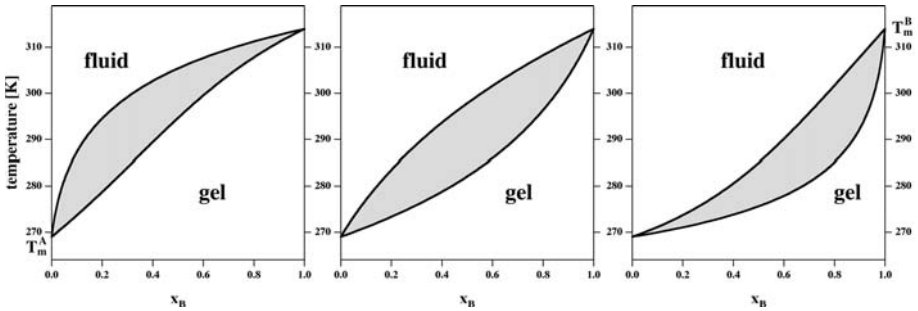

Fig. 7.1 Phase diagrams of ideal mixtures: The profiles of the functions x_B^g and x_B^f are plotted versus temperature for different sets of parameters. Left: $T_{m,A} = 296$ K, $T_{m,B} = 314$ K, $\Delta H_A = 12$ kJ/mol, and $\Delta H_B = 36$ kJ/mol. Center: $T_{m,A} = 296$ K, $T_{m,B} = 314$ K, $\Delta H_A = 24$ kJ/mol, and $\Delta H_B = 24$ kJ/mol. Right: $T_{m,A} = 296$ K, $T_{m,B} = 314$ K, $\Delta H_A = 36$ kJ/mol, and $\Delta H_B = 12$ kJ/mol. The shaded gray regions are gel/fluid phase coexistence regions.

$$x^f = \frac{x_B^g - x_B}{x_B^g - x_B^f} \qquad \text{and} \qquad x^g = 1 - x^f \qquad \text{lever rule} \tag{7.11}$$

This equation can also be written as

$$\frac{x^f}{x^g} = \frac{x_B^g - x_B}{x_B - x_B^f} \tag{7.12}$$

In this equation the linguistic origin of the term "lever rule" can easily be recognized (compare also Fig. 7.2). The lever rule (see Fig. 7.2) allows us to calculate the fractions of gel and fluid phase as a function of the fraction of component B and the temperature.

Now we can also calculate the enthalpy and the heat capacity as a function of temperature:

$$\Delta H(T) = \frac{x_B^g - x_B}{x_B^g - x_B^f} \cdot (x_B^f \cdot \Delta H_B + (1 - x_B^f) \cdot \Delta H_A) \tag{7.13}$$

and the heat capacity is given by $c_p = d\,\Delta H(T)/d\,T$. For the phase diagram in Fig. 7.2 and a molar fraction of lipid B of $x_B = 0.5$ enthalpy and heat capacity are shown in Fig. 7.3. The sharp peaks at the upper and lower temperature limits of the heat capacity profile are due to the assumption that the pure components display an infinitely sharp transition. In real lipid mixtures the edges of the profiles are smoother.

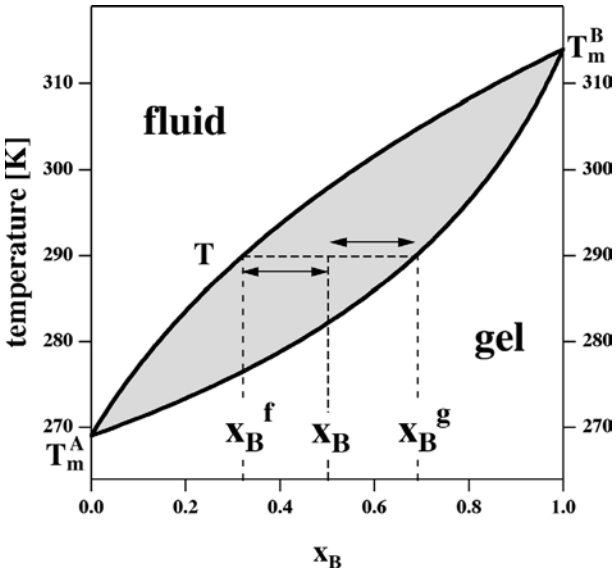

Fig. 7.2 The relative amounts and the compositions of gel phase, x_B^g, and fluid phase, x_B^f for given x_B and temperature can be obtained from using the lever rule. The diagram was calculated for $T_{m,A} = 296$ K, $T_{m,B} = 314$ K, $\Delta H_A = 24$ kJ/mol and $\Delta H_B = 24$ kJ/mol.

In analogy with this calculated melting profile one can determine phase boundaries from experimental profiles. The calculated heat capacity profile in Fig. 7.3 displays sharp edges that correspond to the phase boundaries for this particular lipid mixture. Experimental profiles hardly ever show such sharp

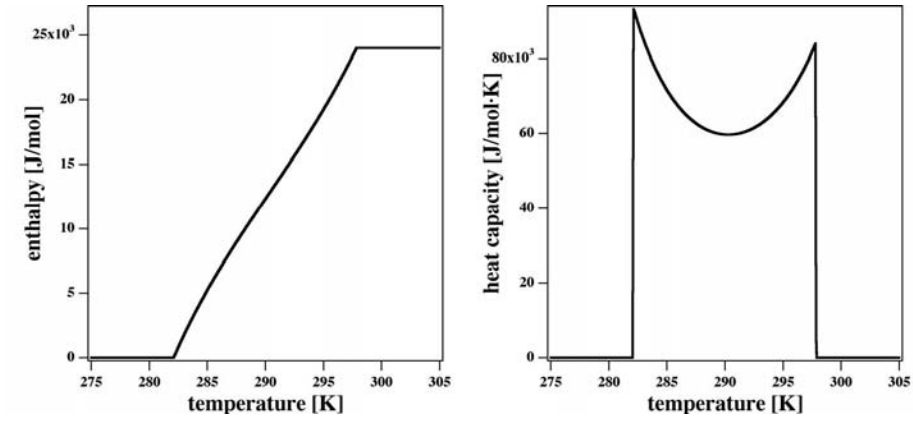

Fig. 7.3 Enthalpy and heat capacity as a function of temperature calculated for $x_B = 0.5$. The diagram was calculated for $T_{m,A} = 296$ K, $T_{m,B} = 314$ K, $\Delta H_A = 24$ kJ/mol and $\Delta H_B = 24$ kJ/mol.

edges because they are not infinitely cooperative. Therefore, one often uses a tangent construction where the intersections of tangents to the profile and the baseline are considered as phase boundaries (see Fig. 7.4). One should, however, be aware that this is an analogy that is based on the fact that the assumptions made for the construction of the theoretical phase diagram are also true for the real system. One of these assumptions is that the melting process is infinitely cooperative, i.e. phase separation is macroscopic. In many real systems, however, one finds finite size domains. The choice of the tangents is also somewhat subjective and therefore not a precise measure.

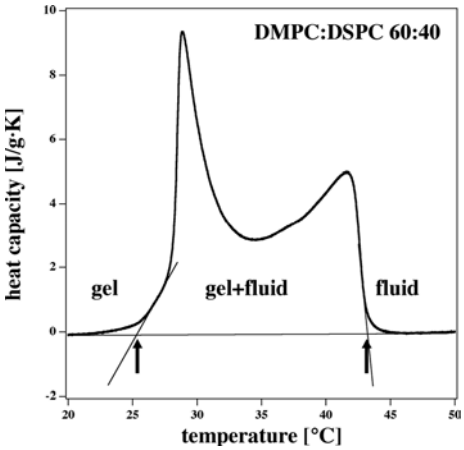

Fig. 7.4 Tangent construction to determine the phase boundaries from an experimental heat capacity profile. Such a construction is made in analogy with the calculated heat capacity profile in Fig. 7.3 (right). The experimental sample shown is a DMPC:DSPC (60:40) mixture.

7.2 On the Number of Coexisting Phases

By investigation of the phase diagram in Fig. 7.2, one can identify three different regions

1. Only one gel phase exists. One can freely vary the concentration and the temperature without leaving this region of the phase diagram.

2. A coexistence of the gel and fluid phase is found. One can only vary either temperature or composition freely. The respective other variable is determined by the lever rule (7.11).

3. Only one fluid phase exists. One can freely vary the concentration and the temperature without leaving this region of the phase diagram.

One therefore only finds one- and two-phase coexistence regions. However, that has been already assumed during the derivation of the equations for one- and two-phase regions. Could there also be more phases?

Question: How many phases can exist simultaneously?

7.2.1 Gibbs' Phase Rule

To consider systems with more than two lipids let us start with some general thermodynamical consideration. Let us assume a lipid mixture in which we find

- K different components (e.g., different lipid species)
- J different phases that coexist (e.g., in different gel and fluid phases, but also inverse hexagonal or other phases)

According to Eq. (4.21) one obtains in the thermal equilibrium

$$\sum_{k=1}^{K} n_{jk} d\mu_{jk} = 0 \qquad \text{Gibbs–Duhem} \tag{7.14}$$

for each phase with index j. In this equation k is the running index for the different components. There are j such equations. The chemical potential of a component is the same in all coexisting phases. Therefore one obtains K different chemical potentials, and the concentrations of these components are variables. The pressure, p, and the temperature, T, are also system variables. In total we therefore have $K + 2$ variables. They are not all independent. Since there are J Gibbs–Duhem equations, one finds

$$F = K + 2 - J \qquad \text{Gibbs' phase rule} \tag{7.15}$$

independent variables. At constant pressure one obtains

$$F = K + 1 - J \qquad \text{Gibbs' phase rule at constant pressure} \tag{7.16}$$

F can be considered as the number of degrees of freedom. The number of degrees of freedom is the number of parameters that we can change externally and thereby influence the state of the phases. For the ideal mixture at constant pressure that means

- In the fluid phase, $J = 1$ and $K = 2$, therefore $F = 2$. This means that variables x_B and T can be freely varied without leaving the fluid phase regime.

- In the coexistence region, $J = 2$ and $K = 2$, therefore $F = 1$. x_B^f and T cannot be varied independently from each other. One therefore obtains phase boundaries. If the temperature is fixed, we cannot influence the composition of the fluid and the gel phase by changing the fraction of the lipid B. The composition of the two phases is also fixed.
- In the gel phase one again finds $J = 1$, $K = 2$, and $F = 2$.

In principle, however, it is possible that at one point within the phase diagram ($F = 0$) and therefore $J = 3$. In the ideal solution, however, this never happens.

In general, the number of the degrees of freedom can never be smaller than zero. Therefore, one has only three different possibilities in two-component mixtures: $J = 1$, $J = 2$, or $J = 3$.

7.2.2 The Role of Water as a Component

So far we have left out one important factor: the role of the aqueous medium. Water also has to be considered as a component. In the previous considerations, however, we have ignored it. Can this generally be done, or if not, are there conditions when this simplification is allowed?

To be precise, the role of water cannot be ignored. Most lipids, in particular the zwitterionic lipids, have a finite interaction with water. Typically, 20–30 water molecules are sufficient to completely hydrate one single uncharged lipid. Thus, any further addition of water does not influence the physical behavior of the lipids. All additional water forms a separated aqueous phase. This means that in Eq. (7.16), we find one more component (water) and one more phase (the aqueous solution). It follows that nothing changes in our considerations about the number of lipid phases.

This line of argument breaks down in the limit of low water concentration. If less water is available than necessary to fully hydrate the lipids, one may induce phase transitions due to changes of the amount of water available. For zwitterionic lipids this happens if the mass ratio between water and lipid is less than 1, i.e., under conditions of extremely high lipid concentrations. In a typical test tube experiment, these conditions are not fulfilled.

Why should one nevertheless worry about the role of water? Seemingly it is abundant in biological cells.

Two factors require a thorough consideration

1. Some lipids, in particular charged lipids such as dimyristoyl phosphatidylglycerol, require large quantities of water to be fully hydrated (cf. Chapter 15). Even if the lipid concentration is as low as 1 mM there is no free water in the system. This can be recognized from calorimet-

ric measurements that demonstrate that the heat capacity profiles are dependent on the lipid concentration even at very low concentrations (Schneider et al., 1999).

2. A growing community of scientists believes that in biological cells all the other macromolecules (proteins, nucleic acids, sugars, and ions) interact so strongly with the water that in fact there is no free water in biological cells. If true, this would strongly influence the phase behavior of lipid membranes (and of all other transitions such as conformational changes of proteins, or their unfolding reactions). For further reading on this topic it is recommended to read the interesting and thought provoking books by Ling (2001) and Pollack (2001) on the role of hydro-gels in biology.

Of course, in the limit of very low lipid concentrations (below the critical micelle concentration) the lipids will form monomers. Thus it is obvious that for the above considerations to be true one should keep the total lipid concentration above the critical micelle concentration.

> The role of water cannot generally be neglected because the amount of water available in biological cells may be small, and because some lipids need high amounts of water to fully hydrate.

In the following, however, we will assume that experiments are done under excess water conditions such that one of the components is water and one of the phases is the aqueous medium.

7.2.3 What Exactly is a Phase?

When deriving the phase boundaries for the ideal mixture and Gibbs' phase rule we tacitly made the assumption that the phase boundaries do not play a role, i.e. they do not contribute to the free energy. This implies that the phases are macroscopically separated. Is that assumption allowed?

In general the interface between two phases always carries a free energy contribution. The interface between water and oil is accompanied by water orientation phenomena that contribute both to enthalpy and entropy of the system (see Chapter 5). However, if the phase is macroscopic, the interfacial area may be small. If the system size x of two macroscopic phases increases, the volume V changes $V \propto x^3$ while the interfacial area A changes by $A \propto x^2$. Thus, the ratio between the interface and volume is $A/V \propto 1/x$. The larger the system size the smaller is the relative contribution of the interface to the free energy of the system as a whole. This argument can easily be translated into

the two-dimensional situation of a membrane containing one-dimensional interfaces between the phases. Therefore, if the phases separate macroscopically, the interface can readily be ignored and all of our above considerations are correct, at least in the limit of infinitely large systems.

What, however, if the phases are not macroscopic? This can happen under different circumstances: The membrane of a biological cell is not infinitely large—thus phase boundaries are unavoidable. Also, under many circumstances microscopic experiments show that domains of finite size exist. If domains have finite sizes, increasing the total membrane area does not change the relative contribution of the domain interface. A system that is 10 times as large just contains 10 times as many domains. The ratio of the domain interface to the domain area is unaffected. Therefore under these conditions the contribution of the domain interface to the free energy of the system cannot be ignored. Further, the length of the domain interface obviously is a system variable. This means that when comparing with the statements made in Section 7.2.1, in the coexistence regime one can change the fraction of lipid *B* and the size of the domains can change. Thus, the physical appearance of the lipid membrane changes and thus the relative contribution of the interface to the free energy. This would also automatically influence the lipid composition within the phases. This has frequently been observed in confocal microscopy images of lipid vesicles. One has to conclude that Gibbs' phase rule cannot be applied for systems containing domains of finite size!

- Gibbs' phase rule can only be applied if the lipid phases separate macroscopically. It is not valid for systems containing small domains.
- A lipid system containing small domains does not necessarily correspond to a phase coexistence regime. They may constitute a one phase regime with microscopic heterogeneities.

Let us try to understand the second statement. An aqueous solution containing lipid micelles is usually considered as one phase. This is because micelles and water do not macroscopically separate. Small domains in a lipid matrix generate a similar situation. But why should one bother about such a distinction between domains and phases? The distinction between domains and phases is important because of the fluctuations in composition and state. This become more obvious in Chapters 8 and 14. In these chapters the difference between first-order and continuous transitions will be discussed. A phase has a fixed and well-defined physical state. Coexisting domains may have fluctuating compositions and sizes. This influences their physical prop-

erties. In particular for the elastic constants of lipid systems this turns out to be a relevant distinction (Chapter 14). This will also be discussed in the context of the ongoing debate on the physical reality of domains in biological membranes called "rafts" (see Section 9.5).

7.3 Regular Solution

In general the mixture between two components is not ideal, i.e., the interaction ϵ_{ij} between two molecules of species A and B cannot be ignored. It shall be given by

$$\epsilon_{AA} \neq \epsilon_{AB} \neq \epsilon_{BB} \tag{7.17}$$

For the *ideal mixture* we had

$$\begin{aligned} G &= x_A \cdot \mu_A + x_B \cdot \mu_B \\ &= x_A \cdot \mu_A^0 + x_A \cdot RT \ln x_A + (1 - x_A) \cdot \mu_B^0 + (1 - x_A) \cdot RT \ln(1 - x_A) \end{aligned} \tag{7.18}$$

The Gibbs free energy of the mixing process therefore was

$$G_{\text{mix}} = RT(x_A \cdot \ln(x_A) + (1 - x_A) \cdot \ln(1 - x_A)) \tag{7.19}$$

Due to Eq. (4.17) the entropy is given by

$$S = -\left(\frac{\partial G}{\partial T}\right)_{p,n_i} \tag{7.20}$$

and consequently the mixing entropy is given by

$$S_{\text{mix}} = -R \cdot (x_A \cdot \ln(x_A) + (1 - x_A) \cdot \ln(1 - x_A)) \quad \text{and} \quad H_{\text{mix}} = 0 \tag{7.21}$$

For a *nonideal mixture (real mixture)* we shall have

$$\mu_A = \mu_A^0 + RT \ln(x_A \cdot j_A) \tag{7.22}$$

where the "activity coefficient" $j_A \neq 1$ describes the nonideality. The nonideality contributes to the chemical potential with μ_A^R (R for regular):

$$\mu_A^R = RT \ln(j_A) \tag{7.23}$$

and the free energy contribution is

$$G^R = x_A \cdot \mu_A^R + x_B \cdot \mu_B^R \tag{7.24}$$

In general the activity coefficient j can be a function of x.

7.3.1 Simple Eutectic Phase Diagram

The most simple example for a nonideal system is an ideal mixture in the fluid phase and immiscibility in the gel phase (this is a limiting case).

One obtains for component A

$$\begin{aligned} \mu_A^g &= \mu_{A,0}^g \\ \mu_A^f &= \mu_{A,0}^f + RT\ln(x_A^f) \end{aligned} \tag{7.25}$$

Since the chemical potentials of component A in the two phases are similar

$$\ln(x_A^f) = -\frac{\mu_{A,0}^f - \mu_{A,0}^g}{RT} = -\frac{\Delta H_{A,0}}{R}\left(\frac{1}{T} - \frac{1}{T_{m,A}}\right) \tag{7.26}$$

and correspondingly for component B ($x_B = 1 - x_A$)

$$\begin{aligned} \mu_B^g &= \mu_{B,0}^g \\ \mu_B^f &= \mu_{B,0}^f + RT\ln(1 - x_A^f) \end{aligned} \tag{7.27}$$

$$\ln(1 - x_A^f) = -\frac{\mu_{B,0}^f - \mu_{B,0}^g}{RT} = -\frac{\Delta H_{B,0}}{R}\left(\frac{1}{T} - \frac{1}{T_{m,B}}\right) \tag{7.28}$$

The two functions for x_A^f can be plotted into a phase diagram (Fig. 7.5). One calls such mixtures *eutectic*. In the center a triple point exists (coexistence of the gel phase of component A, gel phase of component B, and a fluid phase

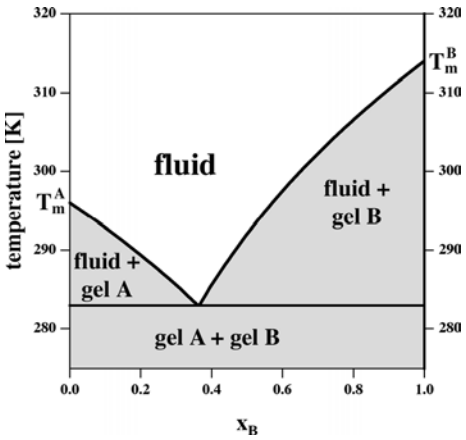

Fig. 7.5 Simple eutectic phase diagram, calculated for $dH_A = dH_B =$ 24 kJ/mol, $T_m^A = 296$ K, and $T_m^A = 314$ K. Note the triple point at $x_B = 0.36$.

which is an ideal mixture of components A and B). The triple point is also called *eutectic point*. At the triple point the number of degrees of freedom is $F = 0$.

7.3.2 Melting Point Depression and the Effect of Anesthetics

Let us assume a small molecule that dissolves in the membrane. It should not display a melting behavior of its own. Furthermore, it should ideally mix with the fluid phase and not mix at all with the gel phase. A typical example for such a behavior would be an anesthetic such as octanol or halothane.

The above problem can be described using Eqs. (7.25) and (7.26).

$$\ln(x_A^f) = -\frac{\mu_{A,0}^f - \mu_{A,0}^g}{RT} = -\frac{\Delta H_{A,0}}{R}\left(\frac{1}{T} - \frac{1}{T_{m,A}}\right)$$

With $x_A^f = 1 - x_B^f = 1 - x_B \quad$ (for $T \geq T_{m,A}$)

$$\ln(1 - x_B) = -\frac{\Delta H_{A,0}}{R}\left(\frac{T_{m,A} - T}{T_{m,A}T}\right) \tag{7.29}$$

If the added amount x_B of the small molecule is small and consequently also the shift in melting point, one can write $\ln(1 - x_B) \approx -x_B$ and $T_{m,A} \cdot T \approx T_{m,A}^2$

$$x_B = \frac{\Delta H_{A,0}}{R}\left(\frac{T_{m,A} - T}{T_{m,A}^2}\right) \tag{7.30}$$

$$\Delta T_m = T_{m,A} - T = \left(\frac{R\,T_{m,A}^2}{\Delta H_{A,0}}\right) x_B \tag{7.31}$$

The phase boundary given by Eq. (7.30) is shown in Fig. 7.6. Again, we can now determine the enthalpy and the heat capacity as a function of temperature through (cf. Eq. (7.13) with $T_{m,B} \to 0$ and therefore $x_B^g = 0$ and $x_B^f = 1 - e^{-A}$)

$$\Delta H(T) = \frac{x_B \exp\left(-\frac{\Delta H_{A,0}}{R}\left(\frac{1}{T} - \frac{1}{T_{m,A}}\right)\right)}{1 - \exp\left(-\frac{\Delta H_{A,0}}{R}\left(\frac{1}{T} - \frac{1}{T_{m,A}}\right)\right)} \cdot \Delta H_{A,0} \tag{7.32}$$

and the heat capacity is given by $c_p = d\,\Delta H_A(T)/d\,T$ (see Fig. 7.7).

Here, it is assumed that the shift is always towards lower temperatures. The melting point depression has been shown for the example of the anesthetic octanol in DPPC membranes in Fig. 19.3, resulting in a lowering of the

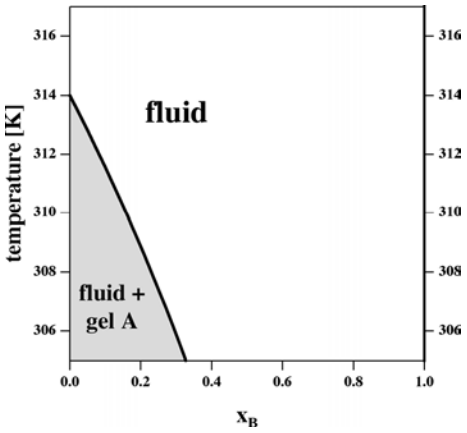

Fig. 7.6 Freezing point depression calculated for a lipid membrane with $T_m = 314$ K and a melting enthalpy of $\Delta H = 35$ kJ/mol. x_B denotes the fraction of a solute without melting behavior, e.g., of anesthetics.

melting temperature of -0.6 K at critical anesthetic dose. Obviously, the action of anesthetics on lipid melting can be well described if one assumes that the anesthetics dissolve well in the fluid phase and that they do not mix at all with the gel phase. Since anesthetics usually have a residual solubility in water, the fraction x_B of anesthetics may change as a function of temperature.

In Chapter 19 we will make use of these relations to explain the action of general anesthetics.

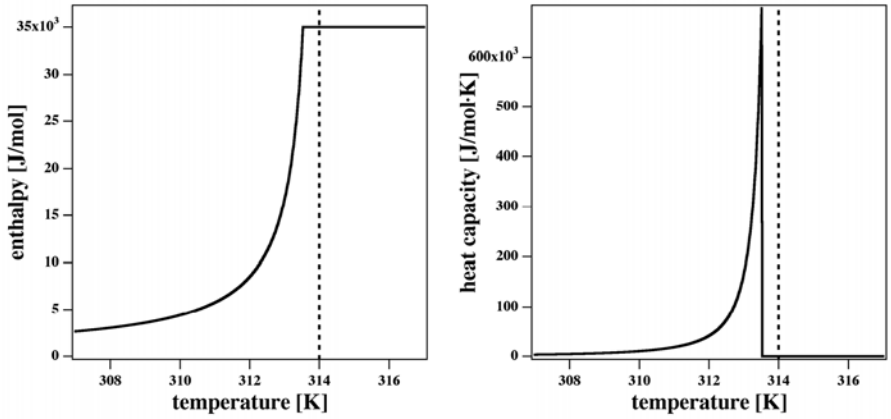

Fig. 7.7 Enthalpy (left) and heat capacity (right) for a lipid membrane with $T_m = 314$ K and $\Delta H = 35$ kJ/mol and a solute (anesthetics) fraction of $x_B = 0.02$ in the membrane. The melting point depression is $\Delta T_m = -0.47$ K. Note that this temperature corresponds to the upper melting temperature and that the whole melting profile extends over a large temperature interval.

7.3.3 Regular Solution Theory

The components in each phase are assumed to mix randomly (ideally) as in the ideal solution theory ($\Delta S^R = 0$). The nearest neighbor interaction shall, however, contribute to the enthalpy:

$$\Delta H^R \equiv \rho_0 \cdot x_A \cdot x_B \tag{7.33}$$

where $\rho_0 = Z \cdot (2\epsilon_{AB} - (\epsilon_{AA} + \epsilon_{BB}))$ describes the energy required to transform ZAA- and BB-pairs into $2ZAB$-pairs. Z is the coordination number (the number of nearest neighbors per lipid). The number of unlike pairs is proportional to x_A and x_B in the phase under consideration. In this (simplified) view we obtain

$$\begin{aligned} \mu_A^R &= \rho_0 \cdot x_B^2 \\ \mu_B^R &= \rho_0 \cdot x_A^2 \end{aligned} \tag{7.34}$$

One can easily test this by inserting Eq. (7.34) into Eq. (7.24). This leads to Eq. (7.33). From this one obtains the chemical potentials of the two components in the two phases

$$\begin{aligned} \mu_A^f &= \mu_{A,0}^f + RT \ln x_A^f + \rho_0^f \cdot (1 - x_A^f)^2 \\ \mu_B^f &= \mu_{B,0}^f + RT \ln(1 - x_A^f) + \rho_0^f \cdot (x_A^f)^2 \\ \mu_A^g &= \mu_{A,0}^g + RT \ln x_A^g + \rho_0^g \cdot (1 - x_A^g)^2 \\ \mu_B^g &= \mu_{B,0}^g + RT \ln(1 - x_A^g) + \rho_0^g \cdot (x_A^g)^2 \end{aligned} \tag{7.35}$$

In thermodynamic equilibrium we furthermore find $\mu_A^g = \mu_A^f$ and $\mu_B^g = \mu_B^f$, and we obtain

$$\begin{aligned} \ln\left(\frac{x_A^f}{x_A^g}\right) + \frac{\rho_0^f \cdot (1 - x_A^f)^2 - \rho_0^g \cdot (1 - x_A^g)^2}{RT} &= -\frac{\Delta H_{A,0}}{R}\left(\frac{1}{T} - \frac{1}{T_{m,A}}\right) \\ \ln\left(\frac{1 - x_A^f}{1 - x_A^g}\right) + \frac{\rho_0^f \cdot (x_A^f)^2 - \rho_0^g \cdot (x_A^g)^2}{RT} &= -\frac{\Delta H_{B,0}}{R}\left(\frac{1}{T} - \frac{1}{T_{m,B}}\right) \end{aligned} \tag{7.36}$$

These are two transcendent equations that can be solved with a computer by iteration. They can have more than one solution (namely two).

The above considerations allow for a calculation of the mixing properties within the gel phase and the fluid phase:

$$\begin{aligned} \Delta G_{\text{mix}}^g &= RT\left(x_A^g \ln(x_A^g) + (1 - x_A^g)\ln(1 - x_A^g)\right) + \rho_0^g x_A^g (1 - x_A^g) \\ \Delta G_{\text{mix}}^f &= RT\left(x_A^f \ln(x_A^f) + (1 - x_A^f)\ln(1 - x_A^f)\right) + \rho_0^f x_A^f (1 - x_A^f) \end{aligned} \tag{7.37}$$

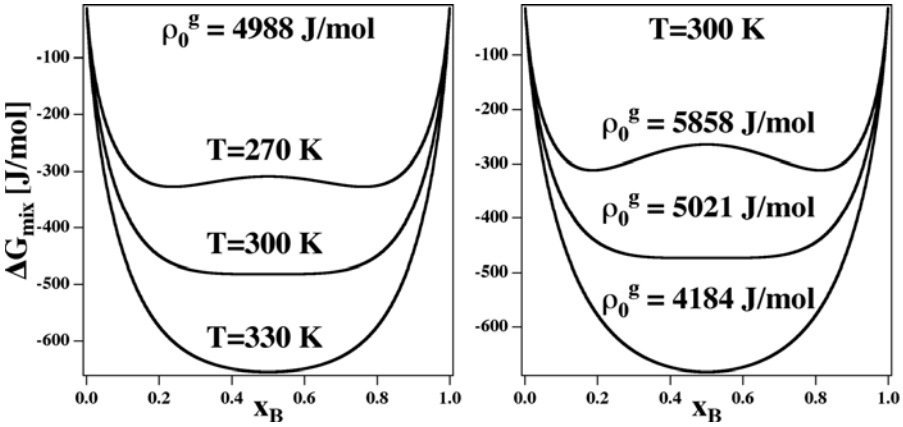

Fig. 7.8 Free energy of mixing in the gel phase. Left: For $\rho_0^g = 1192$ J/mol and various temperatures. Right: For $T = 300$ K and various values for ρ_0^g. With decreasing temperature and increasing ρ_0^g two minima in the mixing free energy form. They correspond to a mixing gap with two gel phases that have the compositions corresponding to the compositions at the minima.

Inspection shows that these two equations may have one or two minima. If there are two minima in the first equation it may be (dependent on lipid mixture and temperature) more favorable if the lipids demix into two gel phases with different compositions. Between these two concentrations a *mixing gap* exists (Fig. 7.8). Depending on the choice of the mixing parameters ρ_0^g and ρ_0^f one can generate a manifold of different phase diagrams (see Fig. 7.9 and 7.10).

With $\rho_0^g = 0$ and $\rho_0^f = 0$ one again obtains the ideal mixture. The fraction of the respective phases can be calculated with the lever rule. The Gibbs phase rule must be obeyed. Mixing gaps can also occur between fluid phases.

The minima of the mixing gap are obtained for

$$\frac{d(\Delta G_{\text{mix}})}{dx_A} = RT\,[\ln x_A - \ln(1 - x_A)] + \rho(1 - x_A) - \rho x_A = 0 \tag{7.38}$$

With increasing temperatures the entropic contribution to ΔG_{mix} dominates, such that the mixing gap closes progressively (Fig. 7.8). At a critical temperature T_c one finds only one gel or one fluid phase. This happens when the minimum of the free energy is a turning point with $d\Delta G_{\text{mix}}/dx_A^2 = 0$:

$$\frac{d^2\Delta G_{\text{mix}}}{dx_A^2} = \frac{RT_c}{x_A(1 - x_A)} - 2\rho_0 = 0 \tag{7.39}$$

Since Eq. (7.39) is symmetric in x_A, one obtains at T_c: $x_A = x_B = 0.5$. Therefore, at

$$T_c = \frac{\rho_0}{2R} \qquad x_A = x_B = 0.5 \tag{7.40}$$

we find a critical point. Practically we find it only if $\rho > 0$.

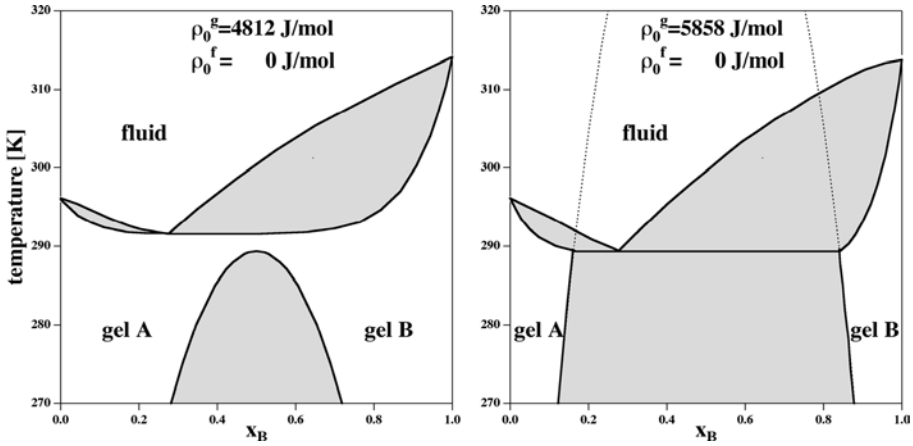

Fig. 7.9 Phase diagrams calculated using the regular solution and $\Delta H_A = 24$ kJ/mol, $\Delta H_B = 36$ kJ/mol, $T_{m,A} = 296$ K, $T_{m,B} = 314$ K. Left: Here a mixing gap at low temperatures (in the gel phase) is found. Right: Eutectic phase diagram. The dotted line corresponds to the phase boundary of the gel phase mixing gap from Eq. (7.37). The regions shaded in gray are phase coexistence regions.

The two phase diagrams shown in Fig. 7.9 are examples for the case of unfavorable mixing in the gel phase and ideal mixing in the fluid phase. In the regions shaded in gray one finds phase separation that obeys the lever rule in Eq. (7.11). The first diagram (Fig. 7.9, left) displays a mixing gap in the gel re-

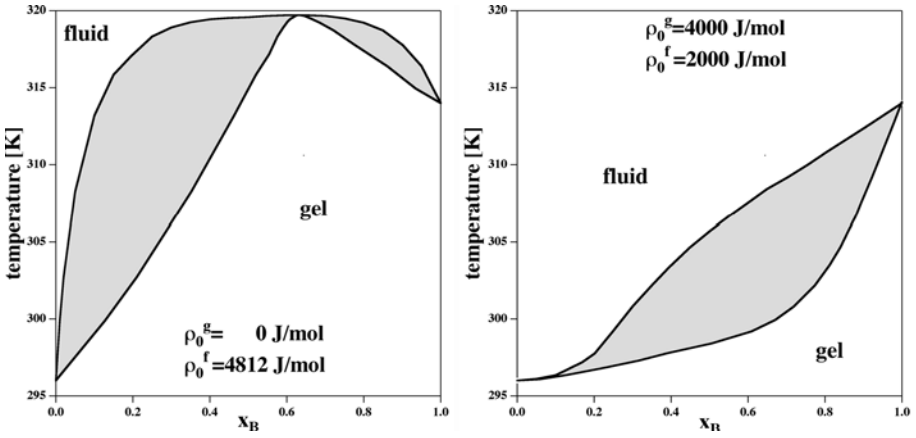

Fig. 7.10 Some other phase diagrams calculated using the regular solution theory using $\Delta H_A = 24$ kJ/mol, $\Delta H_B = 36$ kJ/mol, $T_{m,A} = 296$ K, $T_{m,B} = 314$ K. The nonideality parameters ρ_0^g and ρ_0^f are given in the panels. The gray-shaded regions are phase coexistence regimes.

gions. If the interaction parameter increases, the gel mixing gap overlaps with the gel–fluid coexistence regions (Fig. 7.9, right). Here one obtains a eutectic phase diagram with a eutectic triple point. The dotted line in this diagram shows the hypothetical gel–gel demixing curves from Eq. (7.38) extended to high temperatures.

Summarizing: The theory of the regular solution allows a quantitative description of complicated experimental phase diagrams. However, the assumption is always that the components mix ideally within the respective phases. *In many cases this represents an over-simplification.*

7.4 Experimental Phase Diagrams

The literature is full with experimental phase diagrams of various lipid mixtures. In this section we show a few examples.

7.4.1 Mixtures of Phospholipids

In the following, we show some phase diagrams of phospholipid mixtures. They have been obtained by calorimetry using the tangent construction shown in Fig. 7.4. The heat capacity profiles of two binary mixtures of lipids with phosphatidylcholine head groups are shown in Fig. 7.11. These are DLPC–DPPC and DMPC–DSPC mixtures. The two lipids in both phase diagrams differ in chain length by two carbons. For this reason the two lipids display also different melting points (cf. Fig. 6.6 and table 6.1). Both the phase diagrams display one gel–fluid coexistence region of similar shape. The solidus line is has a smaller slope than the liquidus line indicating that $\omega_0^g > \omega_0^f$. The DMPC–DSPC phase diagram is treated again in Chapter 8.

Figure 7.12 shows the phase diagram of DMPC-DMPE mixtures. Such mixtures are important because about 80% of all lipids in mammalian cells are phosphatidylcholines and phosphatidylethanolamines. DMPC and DMPE possess identical chains but different head groups. The melting points are quite different (Table 6.1). The solidus line is nearly horizontal in most parts of the phase diagram indicating a high numerical value of ω_0^g.

An important special case is the mixtures of DMPC and DMPG (phase diagram not shown). Both lipids have nearly identical melting points and melting enthalpies. The resulting phase diagram at neutral pH consists in a horizontal line just as if two identical lipids are mixed (Garidel et al., 1997). For this reason it is assumed that DMPC and DMPG mix ideally in both phases

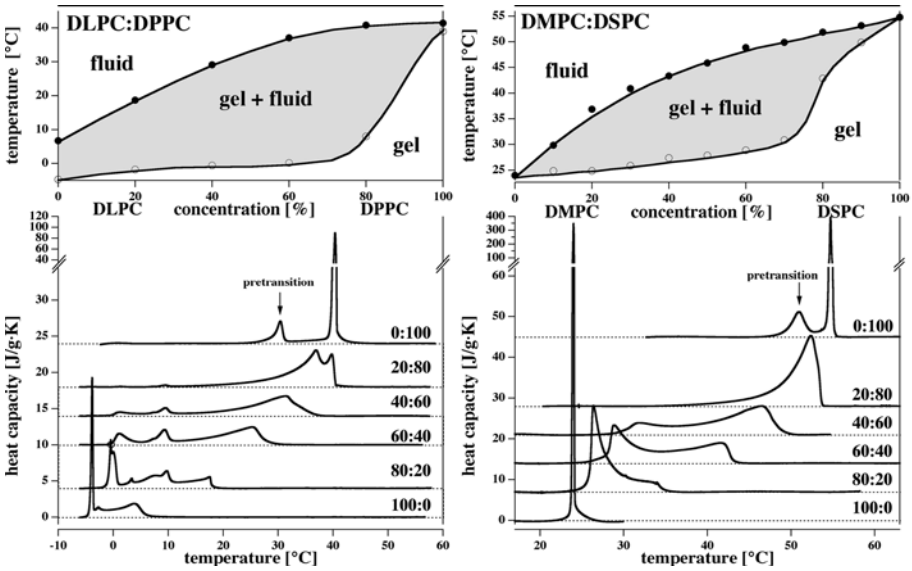

Fig. 7.11 Phase diagrams of DLPC–DPPC mixtures (left) and DMPC–DSPC mixtures (right). The bottom panels show the heat capacity profiles from which the phase boundaries were deduced using the tangent construction. Adapted from Seeger et al. (2005).

and $\rho_0^g = \rho_0^f = 0$. Therefore, these mixtures of PCs and PGs are good model systems for studies involving electrostatic interactions of membranes with ligands. Interestingly, at low pH the phase diagram completely changes. Charged lipids that are protonated display higher melting temperatures than

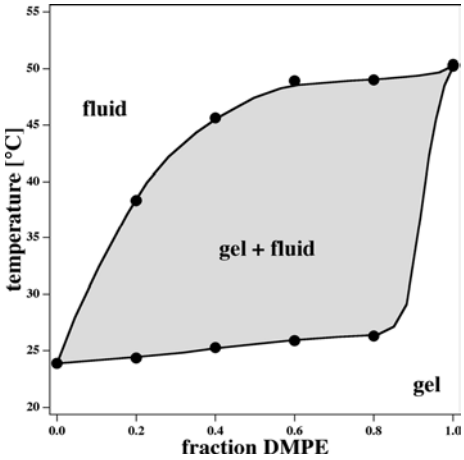

Fig. 7.12 Phase diagram of DMPC–DMPE mixtures. T. Heimburg, unpublished data.

their charged form (see Chapter 11 for an explanation). The very important consequence is that it is very likely that the phase behavior of biological membranes is a very sensitive function of pH.

7.4.2
Mixtures of Phospholipids with Other Lipids

Not all lipids are phospholipids. Mixtures of phospholipids with other lipids are often more complex, probably due to the large difference of the nature of the molecules. Diacylglycerols, for example, have only an –OH group as a head group. Thus, this lipid has a very small head group that is not very polar. Diacylglycerols alone do not form membranes but rather crystals at low temperatures and oil-like isotropics at high temperatures. There are two crystal forms. One of them, the α-form, is metastable but forms very fast while the β-form is thermodynamically stable but forms slowly (see Section 6.4). Diacylglycerols are thought to be second messenger molecules related to the activation of the enzyme protein kinase c (Boni and Rando, 1985).

Figure 7.13 shows the phase diagram of DMPC with dimyristoyl glycerol (DMG) (Heimburg et al., 1992). It displays four different solid phases: a pure DMPC gel phase, a lamellar DMPC:DMG=1:1 complex, a lamellar DMPC:DMG=1:2 complex and pure DMG crystals. Furthermore, it shows three different liquid phases: a fluid L_α phase, an inverse hexagonal phase (H_{II}), and an isotropic oily phase. The identification of the phases was made using solid state NMR and X-ray diffraction.

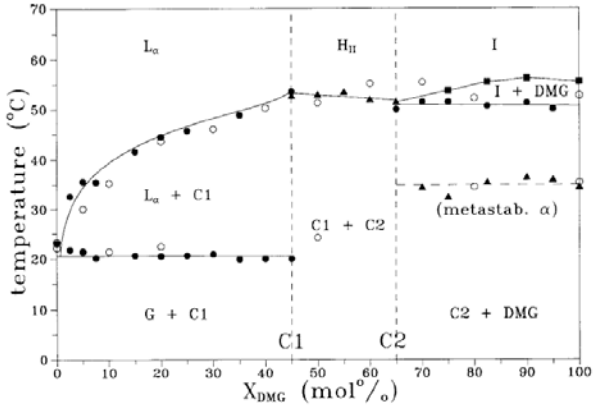

Fig. 7.13 Mixtures of DMPC with dimyristoylglycerol (DMG). There are three solid bilayer phases: G, C_1, and C_2. Pure DMG forms metastable α and stable β crystals. In the high temperature regime one finds the lamellar L_α phase, inverse hexagonal H_{II} phase , and an oily isotropic I phase. From Heimburg et al. (1992).

Up to 30% of the lipids of some membranes (e.g., erythrocyte membranes, cf. Chapter 3) consist of cholesterol. Like diacylglycerols cholesterol does not form bilayers on its own but rather forms crystals. It is a highly important sterol that is different from most other lipid types. It is quite apolar and has a very rigid hydrophobic part with only a short chain segment. Cholesterol has generally the effect of increasing the chain order parameters. In Fig. 7.14 we show the binary phase diagram of DPPC–cholesterol mixtures. This is a good example for eutectic phase diagrams. In the left-hand panel the experimental diagram is shown (Sankaram and Thompson, 1991). One can recognize a large liquid–liquid coexistence regime (LD and LO phases) ranging up to about 35% cholesterol. The right-hand panel shows an earlier theoretical prediction of the phase diagram (Ipsen et al., 1989). This diagram qualitatively looks very similar to the experimental diagram, but the absolute number are different. This theoretical diagram was used to interpret the experimental diagram. Interestingly, the influence of cholesterol on the melting transition of DPPC is quite small at low concentrations, but is huge at 30%. The calorimetric phase transitions are nearly impossible to detect at these high cholesterol contents. Therefore it is often reported that cholesterol lowers the transition enthalpy of phospholipids. This is probably not true. It rather seems that the baseline of the transition cannot accurately be determined.

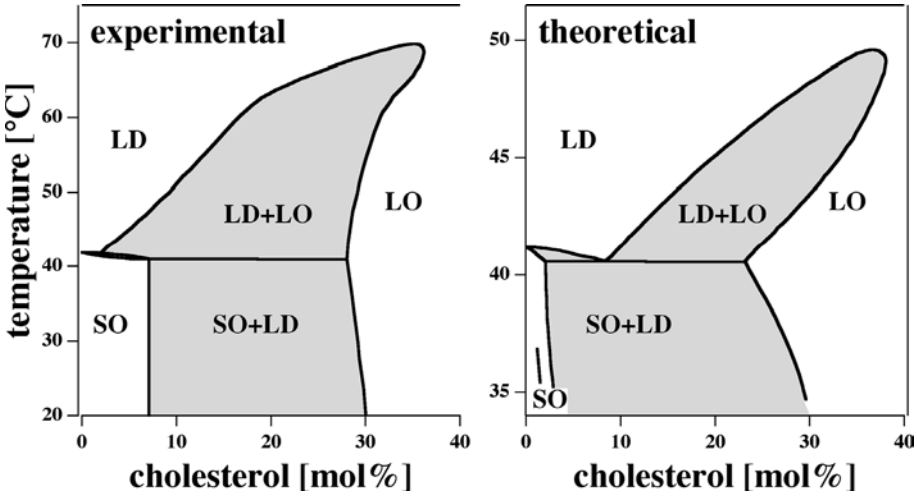

Fig. 7.14 Phase diagram of binary mixtures of DPPC with cholesterol. Left: Experimental phase diagram from Sankaram and Thompson (1991). Right: Theoretical prediction from Ipsen et al. (1989). SO is the solid-ordered phase, LO the liquid-ordered phase and LD the liquid disordered phase.

7.4.3
Ternary Phase Diagrams: Mixtures of Three Lipids

In Section 9.5 we discuss the formation of domains in biological membranes that are often called rafts. Using a somewhat dubious method called "detergent extraction" one often finds detergent insoluble lipid–protein complexes rich in sphingomyelin and cholesterol after treating biological membranes with detergents such as triton (cf. Section 9.5). It is speculated that domains in biological membranes are also rich in these lipids (Simons and Ikonen, 1997). Therefore in the recent decade ternary lipid mixtures of phosphatidylcholines, sphingolipids, and cholesterol have often been investigated. Ternary lipid phase diagrams are much more difficult to investigate. First of all, they typically display a larger variety of phases. According to the phase rule, in excess water at constant pressure up to four phases can coexist simultaneously. Second, the phase diagrams are more difficult to display on paper because they possess two concentration axis and one temperature axis. Third, it is less obvious how to apply the lever rule. To apply the lever rule the orientation of the levers along the so-called tie-lines has to be known. This is clearly an additional complication.

In Fig. 7.15 the phase diagram of N-palmitoyl-D- sphingomyelin, POPC and cholesterol is shown (de Almeida et al., 2003) in cross-sections at two temperatures. One can recognize different liquid-ordered (LO) and liquid-disordered (LD) phases and phase boundaries that change as a function of temperature. The tie-lines in these diagrams (along which the lever rule can be applied) are shown as solid lines. For the purposes of this book it is not important to go into the details of the interpretation of this particular phase diagram. The interested reader may consider reading the original article.

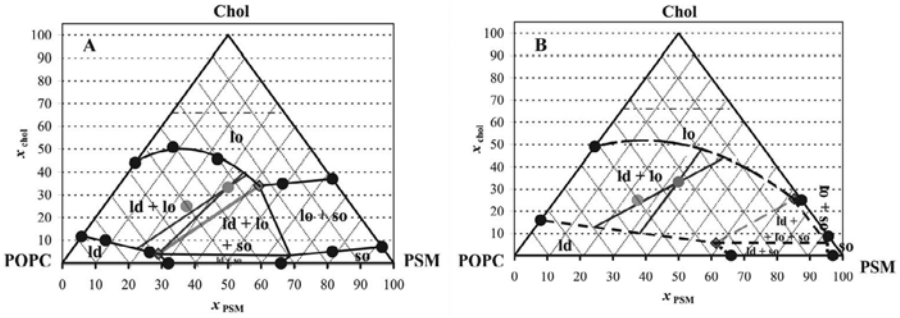

Fig. 7.15 Cross sections through the ternary phase diagrams of mixtures of N-palmitoyl-D-sphingomyelin, POPC , and cholesterol at two different temperatures. From de Almeida et al. (2003). The solid lines represent tentative tie-lines. For details see the original article. Reprinted with permission from Biophys. J.

7.5 Conclusions

Summarizing, it must be concluded that finding the phase diagram of a ternary mixture is already a difficult and time consuming undertaking. The phase diagrams of real biological membranes containing hundreds of different lipids and proteins (of course, proteins are also components in phase diagrams) will probably always be impossible to find. But, of course, biological membranes possess phase behavior and the macroscopic behavior of such membranes cannot be understood without taking this into account! One further has to realize that the assumption of macroscopic phase separation is not true in biological systems and one can therefore wonder whether the concept of phase separation is a meaningful concept for biological membranes. In Chapter 14 we will therefore rather work with the concept of fluctuations that allow more general statements on membranes even when the composition of the membrane and its phase behavior are not known. This concept will turn out to be very useful.

In the next chapter, we will try to extend the theory of phase behavior to the case where phases (domains) do not macroscopically separate.

7.6 Summary: Key Ideas of Chapter 7

- In lipid mixtures various phases may coexist. The diagrams showing the phases as a function of concentration and temperature are called phase diagrams
- In the phase coexistence regime one can find a geometrical construction (lever rule) that allows us to calculate the compositions and the relative quantities of each phase.
- The simplest way to understand phase diagrams consists of the ideal solution theory where lipid–lipid interactions are ignored but the entropy of mixing of two components is taken into account. This theory correctly predicts that there are concentration and temperature regimes where two different phases may coexist.
- Gibbs' phase rule allows us to calculate the number of phases that can coexist. At constant pressure and excess water one finds $F = K + 1 - J$, where K is the number of components, J is the number of coexisting phases, and F is the number of degrees of freedom (i.e., the number of independent variables).
- Under many conditions water has to be counted as one of the components, and the aqueous medium has to be counted as a phase. At low water concentrations this has a significant influence on many phase diagrams.
- In regular solution theory one takes the interactions of lipids in each phase into account. This allows us to describe more complex phase diagrams, including eutectic mixtures with coexistence of three phases.
- The addition of small molecules to lipid mixtures lowers their melting points. This effect is called "freezing point depression'.
- In contrast to ideal solution theory, regular solution theory allows us to calculate phase separation in the gel and in the fluid regimes.
- In regular solution theory the mixing behavior of the lipids in each phase is still considered to be ideal. This is not generally correct.
- Many experimental phase diagrams can at least qualitatively be understood on the basis of regular solution theory.

8
Statistical Models for Lipid Melting

In the models for melting of lipid chains discussed so far we tacitly assumed that lipids are either in gel or fluid state and that no intermediate states exist. Furthermore, it was assumed that there is no interface between gel and fluid lipids, because the equations for the regular solution do not contain the possibility of interfaces. Instead, it was assumed that a fluid lipid is always in fluid environment, and that a gel lipid is always in a gel environment. What, if this is not true? Let us assume the possibility that with a finite possibility a fluid state lipid may be located in a gel environment and vice versa. Then, the models for melting of mixed lipid systems from the previous chapter must be modified. A further shortcoming of the regular solution theory described in Chapter 7 is that the entropy of component mixing is not taken into account correctly. In the derivation of the regular solution theory it was assumed that in a lipid mixture the lipids in the two phases mix ideally, meaning that the interaction of the lipids does not change the entropy. This resulted in a purely enthalpic contribution of the nonideality (see Eq. (7.33)) expressed by

$$\Delta H^R \equiv \rho_0 \cdot x_A \cdot x_B \tag{8.1}$$

In the following we will employ an extension of the regular solution theory that correctly treats the presence of interfaces and the entropic contributions in nonideal mixtures. This will be done on the basis of computer models in which each lipid is placed on a lattice site.

Lattice models are models like the famous "Ising" model (Ising, 1925) for transitions in ferromagnets. In such models molecules are placed on an lattice. Each lipid has a defined state at a given time. Lipids interact via nearest neighbor (and sometimes next-nearest neighbor) interactions. The statistical properties of such models usually are numerically calculated with the help of Monte Carlo simulations. These simulations can yield solutions for relatively complex problems. Since they are based on equilibrium thermodynamics they do generally not contain information on the time scales of the investigated processes. For some problems (such as the one-dimensional Ising model, or the two-dimensional Ising model in the absence of a field) one can find analytical solutions. As a simplification, the Ising model (and its applications

to membranes) only considers two states of each molecule. Such models are sometimes also called "coarse grain" models, because they do not consider the atomistic detail of the molecules.

8.1 Monte Carlo Simulations

The complete description of a problem (e.g., the determination of the state of a membrane) requires that all possible states of a system are generated, the Gibbs free energy is determined, and the probability of this configuration is determined using the respective Boltzmann factors and a statistical thermodynamics averaging. Problem: there are quite many configurations.

The chain of a single lipid with N carbons has 3^{N-2} configurations; each lipid therefore has $3^{2(N-2)}$ configurations. A typical lipid vesicle with radius 100 nm consists of 10^5 lipids. A vesicle of the lipid dimyristoyl phosphatidylcholine (DMPC, chain length $N = 14$) in total has

$$n = \left(3^{2(N-2)}\right)^{100000} = 10^{2400000} \text{ configurations} \tag{8.2}$$

It will never be possible to generate all these configurations in a computer. For this reason one can in principle never exactly determine the partition function. The same problem arises if one wants to calculate protein folding. The problem is dramatically increased if one wants to use a time evolution in an MD simulation, where all the atomic details are taken into account.

In computer simulations one tries to approximate the partition function by only averaging over some representative configurations. The question remains, however, how a representative configuration is defined.

8.1.1 Simple Monte Carlo Procedure

One simple-minded approach may be to determine some random configurations using a random number generator. Of each of these configurations the enthalpy is determined and weighted with a Boltzmann factor $\exp(-H/kT)$. Then, statistical averages are calculated. The disadvantage of this procedure is that most randomly chosen configurations are very unlikely. In a large ensemble (as the lipid membrane) it is very unlikely to find the relevant configurations by random choice . Therefore, it cannot be expected that one can obtain reasonable mean values for a complex system.

If one wants to calculate statistical averages, one needs a method to select only relevant configurations of the thermodynamic system. Such a method is the Metropolis algorithm.

8.1.2 Metropolis Algorithm

The Metropolis algorithm is named after the first author of the paper by Metropolis et al. (1953). This procedure works differently from the previous method. One begins with a random start configuration (in our case, random positions and states of lipids on a lattice). This configuration is saved in a computer. If for each lipid the location and conformation are known, one can also calculate the enthalpy of the membrane. Now one allows the system to undergo a small change, e.g., by changing the state of one single lipid. This alters the enthalpy of the system. The system undergoes a change from state A into state B. The enthalpy difference is $\Delta H = H_B - H_A$. With the probability

$$P_B = \frac{\exp(-\Delta H/RT)}{1+\exp(-\Delta H/RT)} \equiv \frac{K}{1+K} \tag{8.3}$$

the new configuration is accepted, and with the probability

$$P_A = \frac{1}{1+\exp(-\Delta H)/RT} \equiv \frac{1}{1+K} \tag{8.4}$$

the new configuration is rejected. $K = \exp(-\Delta H/RT)$ is a Boltzmann factor This is practically done by using the random number generator of the computer program. The random numbers typically assume values between 0 and 1, as do the probabilities P_A and P_B. Thus, if the random number is larger than P_B, the new configuration is rejected and otherwise it is accepted. Since this is based on an equilibrium constant between two states, the total number of changes from A to B and backwards from B to A is equal. The rate from A to B shall be given by k_{AB}, and the rate of changes from B to A shall be k_{BA}. Then $P_A \cdot k_{AB} = P_B \cdot k_{BA}$. This principle is called the "detailed balance," with $k_{BA}/k_{AB} \equiv K$. It expresses that all substates of the system are in equilibrium with each other.

The equilibrium between the old and the new configuration is now determined by

$$\frac{P_B}{P_A} = \exp\left(-\frac{\Delta H}{kT}\right) \tag{8.5}$$

exactly as expected from a Boltzmann distribution. Thus, the change of the configuration of the membrane is more likely if the new state has a higher likelihood according to the Boltzmann distribution.

The ordered and the disordered state of a lipid display a very different degeneracy, i.e. a very different number of states with equal enthalpy. This can be taken into account by including the entropy difference of each state such that $K = \exp(-\Delta G/RT)$. As indicated by the use of the gas constant, R,

the enthalpy and the Gibbs free energy differences are given per mole of the system under consideration (e.g., per mole of a membrane). The simulations using the Metropolis algorithm are called "Monte Carlo" simulations. Each decision to accept or reject a new configuration is called a Monte Carlo step.

After the first Monte Carlo step a new configuration is determined using the random number generator. Now, one chooses a new lipid with a random number generator and generates a new configuration, repeating the steps described above. Each new configuration is generated (accepted) with a probability $K/(1+K)$. This means that states with a lower Gibbs free energy occur more often than states with a high Gibbs free energy. In general, after infinite time each state occurs with its intrinsic probability. In a Monte Carlo simulation one therefore generates in principle all states of the phase space. However, the more likely states are generated with much larger probability such that after finite time only the "most relevant" configurations are generated.

Definition: A system that accesses all states of the phase space after infinitely large time is called *ergodic*. In an ergodic system all configurations are assumed with their respective probability.

Ergodic theorem: The averaging over very long times ($t \rightarrow \infty$) leads to the same statistical average value as the averaging over a very large system ($N \rightarrow \infty$). This means that instead of averaging over a large number of systems one can also average one single system over long times.

This statement is not trivial, because one can easily imagine situations where different states of the system are separated by large free energy barriers such that only a part of the system is sampled.

A thorough description of computer simulations and their application to phase transitions is given in Mouritsen (1984).

8.2 Magnitude of Fluctuations

During a Monte Carlo simulation the enthalpy of a system does not stay constant but fluctuates around an average value (Fig. 8.1). This is obvious because at each Monte Carlo step a decision between two states of different enthalpy is made.

The average value of the enthalpy (of the membrane) can be calculated by averaging over all configurations:

$$\begin{aligned}\langle H\rangle &= \frac{\sum_i H_i \exp\left(-\frac{G_i}{RT}\right)}{\sum_i \exp\left(-\frac{G_i}{RT}\right)} \\ &= \frac{1}{Q}\sum_i H_i \exp\left(-\frac{G_i}{RT}\right) \qquad p = \text{const.}, \Pi = \text{const.}\end{aligned} \tag{8.6}$$

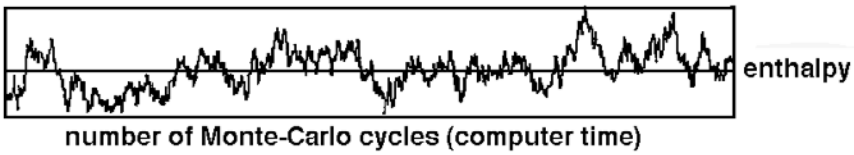

Fig. 8.1 Enthalpy fluctuations during a simulation around the mean enthalpy value.

where $G_i = E_i + pV_i(+\Pi A_i) - TS_i$, with the volume V_i, the area A_i of the state i, the bulk pressure p and the lateral pressure Π. $Q = \sum \exp(-G_i/RT)$ is called the *partition function*.

The heat capacity at constant pressure is defined as

$$c_p = \left(\frac{\langle H \rangle}{dT}\right)_p \tag{8.7}$$

From Eq. (8.6) it follows that

$$\begin{aligned} \frac{d\langle H \rangle}{dT} &= \frac{d}{dT}\left(\frac{1}{Q}\sum_i H_i \exp\left(-\frac{G_i}{RT}\right)\right) \\ &= \ldots \text{some algebra} \ldots \\ &= \frac{1}{RT^2}\left(\frac{1}{Q}\sum_i H_i^2 \exp\left(-\frac{G_i}{RT}\right) - \left[\frac{1}{Q}\sum_i H_i \exp\left(-\frac{G_i}{RT}\right)\right]^2\right) \end{aligned} \tag{8.8}$$

or

$$c_p = \frac{\langle H^2 \rangle - \langle H \rangle^2}{RT^2} \qquad \text{fluctuation theorem} \tag{8.9}$$

This equation also follows from fluctuation dissipation theory (Kubo, 1966). It should be noted that $\langle (H - \langle H \rangle)^2 \rangle = \langle H^2 \rangle - \langle H \rangle^2$, such that the statement of the fluctuation theorem is that the magnitude of the heat capacity is proportional to the mean square deviation of the enthalpy from its mean value. This theorem is generally true (not only for membranes). This also means that the heat capacity at constant pressure can be determined from the mean square fluctuations around the mean value from Monte Carlo simulations.

Similarly one obtains in analogy with Eq. (8.9) for constant volume conditions

$$c_V = \frac{d\langle E \rangle}{dT} = \frac{\langle E^2 \rangle - \langle E \rangle^2}{RT^2} \tag{8.10}$$

It will be shown in Chapter 14 that the elastic constants can also be expressed by similar fluctuation relations.

8.3 Simple Statistical Thermodynamics Model

Transitions in solid state physics are often well described by a simple class of models named after Ernst Ising and his model for ferromagnetism that he used in his Ph.D. thesis (Ising, 1925). With slight modifications this model can also be used to describe transitions in lipids (Sugar et al., 1994; Heimburg and Biltonen, 1996; Ivanova and Heimburg, 2001).

The assumptions are essentially the following: each lipid molecule shall only possess two states:

- a gel state with enthalpy H_g and low entropy S_g and
- a fluid state with enthalpy H_f and high entropy S_f.

Additionally there are interactions with neighboring lipids, which are essentially dispersion interactions with a distance dependence of $1/R^5$. However, also pairwise interactions between the lipids and water play a role that depend on the nature of lipid states.

Simplification. In a first approximation only nearest neighbor interactions shall be considered. In a triangular lattice each lipid has $z = 6$ neighboring lipids ($z \equiv$coordination number). It has been shown experimentally that the lipids in gel membranes display triangular packing.

There are now three different interactions between the lipids:

- interactions between two gel lipids with energy ϵ_{gg},
- interactions between a gel lipid and a fluid lipid with energy ϵ_{gf}, and
- interactions between two fluid lipids with energy ϵ_{ff}.

The Gibbs free energy G_g in the gel phase (all lipids are in the gel state) is now given by

$$G_g = N \left[(H_{0,g} - T\, S_{0,g}) + \frac{z}{2} \epsilon_{gg} \right] \tag{8.11}$$

where the enthalpy $H_{0,g}$ and the entropy $S_{0,g}$ are defined per lipid and N is the total number of lipids. Correspondingly, for the fluid phase one obtains

$$G_f = N \left[(H_{0,f} - T\, S_{0,f}) + \frac{z}{2} \epsilon_{ff} \right] \tag{8.12}$$

For a general distribution with N_f fluid lipids and $N_g = N - N_f$ gel lipids one obtains

- N_{gg} contacts between two gel state lipids,

- N_{gf} contacts between gel and fluid state lipids, and
- N_{ff} contacts between two fluid state lipids.

Here also $N_{gg} = (z\,N_g - N_{gf})/2$ and $N_{ff} = (z\,N_f - N_{gf})/2$ hold. The total Gibbs free energy is now given by

$$\begin{aligned} G = {} & N_g(H_{0,g} - T\,S_{0,g}) + N_f(H_{0,f} - T\,S_{0,f}) \\ & + N_{gg}\epsilon_{gg} + N_{gf}\epsilon_{gf} + N_{ff}\epsilon_{ff} \end{aligned} \tag{8.13}$$

$$\begin{aligned} G = {} & N_g(H_{0,g} - T\,S_{0,g}) + N_f(H_{0,f} - T\,S_{0,f}) + \frac{(zN_g - N_{gf})}{2}\epsilon_{gg} \\ & + N_{gf}\epsilon_{gf} + \frac{(zN_f - N_{gf})}{2}\epsilon_{ff} \end{aligned} \tag{8.14}$$

By rearranging the terms, and using the definitions $\Delta H \equiv H_{0,f} - H_{0,g}$ and $\Delta S \equiv S_{0,f} - S_{0,g}$ one obtains

$$\begin{aligned} G &= G_g + N_f(\Delta H - T\Delta S) + N_{gf}\left(\epsilon_{gf} - \frac{\epsilon_{gg} + \epsilon_{ff}}{2}\right) \\ &\equiv G_g + N_f(\Delta H - T\Delta S) + N_{gf}\,\omega_{gf} \end{aligned} \tag{8.15}$$

In this model ω_{gf} is a cooperativity parameter. It is the only free parameter of the system, because the other two parameters, ΔH and ΔS, can be obtained from the calorimetric experiment.

The partition function is now given by

$$Q = \sum_{N_{gf}} \sum_{N_f=0}^{N} \Omega(N_f, N_{gf}) \exp\left(-\frac{N_f(\Delta H - T\Delta S) + N_{gf}\omega_{gf}}{RT}\right) \tag{8.16}$$

It is not possible to calculate the degeneracy factor $\Omega(N_f, N_{gf})$ in two dimensions for the problem formulated above. (For the experts, the above description corresponds formally to the Ising model in an external magnetic field, here set by the temperature. At $T_m = \Delta H/\Delta S$ the field is zero and both lipid states are equally probable. At low temperature, the gel states are favored and at high temperature the fluid states are favored, corresponding to the two field orientations.)

8.4 Monte Carlo Simulations

In practice, a simulation is performed as follows:

1. A matrix with $m \cdot n$ lipids is generated in a computer. Each lipid is either in gel or fluid state. The number and position of gel and fluid lipids

are determined using a random number generator. Periodic boundary conditions are chosen. This means that the lipids at the left edge of the membrane are neighbors to those at the right edge. The lipids at the top are neighbors to those at the bottom.

2. One lipid is selected with a random number generator. Further, the state of the six nearest neighbors is determined.

3. The Gibbs free energy of the lipid matrix is determined and compared to the free energy it would have after changing the state of the selected lipid.

4. The probability that the selected lipid is found in a gel or the fluid state is given by

$$P_{\text{gel}} = \frac{1}{1+K} \qquad K = \exp\left(-\frac{\Delta H - T\Delta S + \Delta n_{gf} \cdot \omega_{gf}}{RT}\right) \tag{8.17}$$

$$P_{\text{fluid}} = \frac{K}{1+K} \tag{8.18}$$

Δn_{gf} is the change in the number of unlike nearest neighbors for the selected lipid when changing its state. With the help of a random number generator the lipid is chosen to be a gel lipid with the probability P_{gel}, and a fluid lipid with the probability P_{fluid}. The enthalpy of the total matrix (sum of the enthalpies of the individual lipids and all nearest neighbor interactions) is saved into an array in the computer.

5. This procedure is repeated from step 2 as often as possible (typically several million times, depending on the size of the matrix and the magnitude of the fluctuations).

During this procedure the enthalpy does not remain constant, but fluctuates around an average value (see Fig. 8.1). With the help of the fluctuation theorem (Eq. (8.9)) one can calculate the heat capacity. If the Monte Carlo simulation is repeated for each temperature one can calculate a heat capacity profile (Fig. 8.2).

p The fluctuations at the melting point are larger when ω_{gf} gets larger. The melting profile gets narrower for small ω_{gf} (Fig. 8.2). Therefore, the parameter ω_{gf} can be determined from the magnitude of experimental heat capacity at the c_P-maximum and the half-width of the c_P-profile.

The values of the lipid states from the computed matrix at a given time can be plotted into a graph. Such a plot is called a Monte Carlo snapshot. In Fig. 8.3 the Monte Carlo snapshot is compared to an atomic force microscopy experiment at the melting point of a DPPC membrane. An important observation is that domains are formed. This means that the lipid matrix is neither in

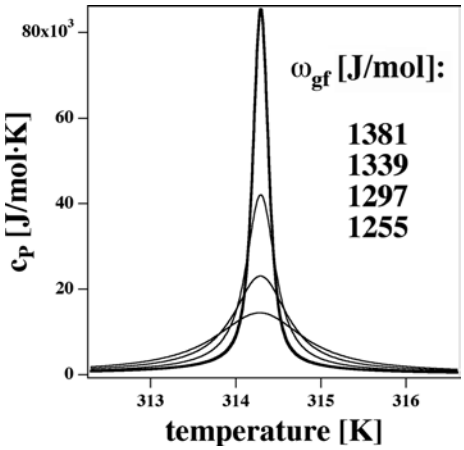

Fig. 8.2 Heat capacity profiles during melting of single lipid membranes for different cooperativity parameters ω_{gf}. The larger is the ω_{gf} the narrower is the melting peak.

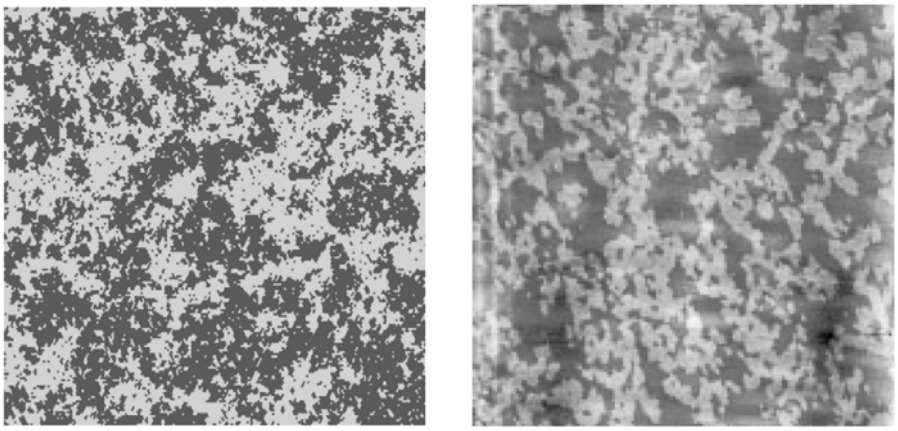

Fig. 8.3 Domain formation in lipid membranes in the melting transition. Left: Snapshot from a Monte Carlo simulation at the melting point of a membrane. Dark points represent gel state lipids, bright points represent fluid lipids. The parameters of the simulation were $\Delta H = 36.4$ kJ/mol, $T_m = 310.3\,^{\circ}$C, $\Delta S = \Delta H/T_m = 0.117$ J/mol K, $\omega_{gf} = 1.3\ \mathrm{kJ/mol} \approx 0.5$ kT. Right: Atomic force microscopy experiments of a DPPC monolayer at the melting point (from Nielsen et al. (2000)). The Monte Carlo simulations are able to correctly reproduce the experimental situation.

the gel phase nor in the fluid phase but there may be coexisting domains of the two states. The larger the cooperativity parameter ω_{gf} the larger the domains at the melting point. Only if ω_{gf} gets very large there are lipid matrices that exclusively are gel or fluid. In this situation one obtains macroscopic phase separation. At low values of the cooperativity parameter, $\omega_{gf} \leq 1/2RT$, one obtains finite size domains and no macroscopic phase separation occurs. Such

phenomena could not be described with the regular solution theory (Chapter 7) where domain boundaries were not considered.

8.5 Derivation of the Partition Function for a Known Distribution of all States: The Ferrenberg–Swendsen Method

The partition function of the model in the two previous sections is

$$Q = \sum_{N_{gf}} \sum_{N_f=0}^{N} \Omega(N_f, N_{gf}) \exp\left(-\frac{N_f(\Delta H - T\Delta S) + N_{gf}\omega_{gf}}{RT}\right) \tag{8.19}$$

Each individual state of the membrane with given N_f and N_{gf} has the probability

$$P(N_f, N_{gf}) = \frac{1}{Q}\Omega(N_f, N_{gf}) \exp\left(-\frac{N_f(\Delta H - T\Delta S) + N_{gf}\omega_{gf}}{RT}\right) \tag{8.20}$$

The unknown quantity in this equation is the degeneracy of each membrane state, $\Omega(N_f, N_{gf})$. It can only be determined by Monte Carlo simulations. It is purely a combinatorial term and thus independent of ΔH, ΔS, ω_{gf}, and T. Therefore one does not have to recalculate it for each set of parameters. If one has performed a simulation for the set of parameters (ΔH, ΔS,ω_{gf}, T), one can derive the distribution of states for a different set of parameters ($\Delta H'$, $\Delta S'$, ω'_{gf}, T'), from the first distribution using the method of Ferrenberg and Swendsen (1988, 1989).

$$\begin{aligned} Q(\Delta H', \Delta S', \omega'_{gf}, T') = {} & Q(\Delta H, \Delta S, \omega_{gf}, T) \\ & \cdot \sum_{N_{gf}} \sum_{N_f} P(N_f, N_{gf}, \Delta H, \Delta S, \omega_{gf}, T) \\ & \cdot \exp\left(-\frac{N_f(\Delta H' - T\Delta S') + N_{gf}\omega'_{gf}}{RT'}\right. \\ & \left. + \frac{N_f(\Delta H - T\Delta S) + N_{gf}\omega_{gf}}{RT}\right) \end{aligned} \tag{8.21}$$

The probability of each state is given by

$$\begin{aligned} P(N_f, N_{gf}, \Delta H', \Delta S', \omega'_{gf}, T') = {} & \frac{P(N_f, N_{gf}, \Delta H, \Delta S, \omega_{gf}, T)}{Q(\Delta H', \Delta S', \omega'_{gf}, T')} \\ & \cdot \exp\left(-\frac{N_f(\Delta H' - T\Delta S') + N_{gf}\omega'_{gf}}{RT'}\right. \\ & \left. + \frac{N_f(\Delta H - T\Delta S) + N_{gf}\omega_{gf}}{RT}\right) \end{aligned} \tag{8.22}$$

In this equation the degeneracy $\Omega(N_f, N_{gf})$ does not show up explicitly (note that the function $Q(\Delta H', \Delta S', \omega'_{gf}, T')$ serves as a normalization constant only). Therefore, if one has determined $P(N_f, N_{gf}, \Delta H, \Delta S, \omega_{gf}, T)$ once, one does not have to repeat the MC simulation for other sets of parameters. Details for the application of this model to lipid membranes are given in Ivanova and Heimburg (2001).

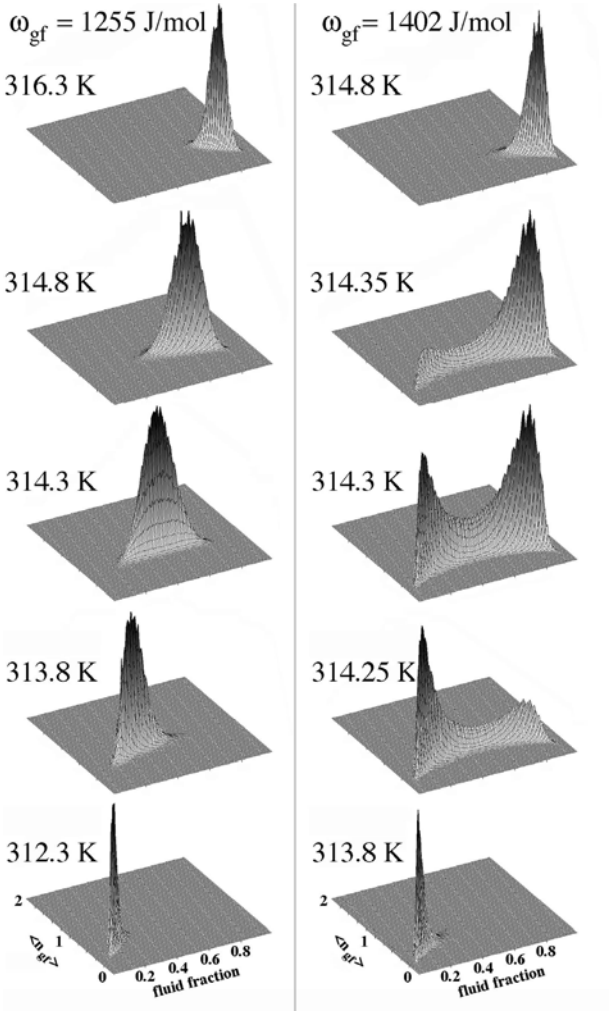

Fig. 8.4 Distribution of states as a function of the fluid fraction, f, and the mean number of unlike nearest neighbor contacts, $\langle n_{gf} \rangle$, for two different values of ω_{gf} at various temperatures. The left-hand side corresponds to a continuous transition, whereas the right-hand side shows first-order behavior. At T_m two maxima of the distribution can be seen, typical for macroscopic phase separation.

In Fig. 8.4 the distribution of states (i.e., the density of states) at the melting point T_m is shown for two different values of ω_{gf} and different temperatures below and above the melting point. These distributions have been calculated using the above formalism. One can easily recognize that this distribution may have one or two maxima at the melting point. If it has two maxima, this is a transition of first order with two coexisting macroscopic phases (corresponding to the two peaks). If the distribution displays only one maximum, this is called a continuous transition and no macroscopic phase transition occurs. For the enthalpy and the melting point of DPPC, the critical point between these two regimes can be found for $\omega_{gf}^{\text{crit}} \approx 1360\ \text{J/mol} = 0.52RT$.

In Fig. 8.5 experimental heat capacity profiles of multilamellar vesicles (MLV) , large unilamellar vesicles (LUV) , and small unilamellar vesicles (SUV) of DPPC are shown. They display different transition half-widths and thus different cooperative behavior. The LUV profiles are theoretically well described by $\omega_{gf} = 1257$ J/mol. This value is smaller than that of $\omega_{gf}^{\text{crit}}$. This finding leads to the notion that unilamellar lipid membrane transitions are close to the critical point but most likely in the continuous regime (not first order). However, so far there is no final agreement about this hypothesis. The melting profile of multilamellar vesicles is much sharper than that of unilamellar vesicles and can be described with $\omega_{gf} = 1595$ J/mol. This is larger than ω_{gf}^{crit}. Such vesicles may therefore be in a first order regime (Ivanova and Heimburg, 2001). There is no doubt that phospholipid vesicles are located very close to critical behavior as found also in Nielsen et al. (2000) (see Fig. 8.3). In this paper it has been shown that the domains display scaling invariance, typical for critical behavior.

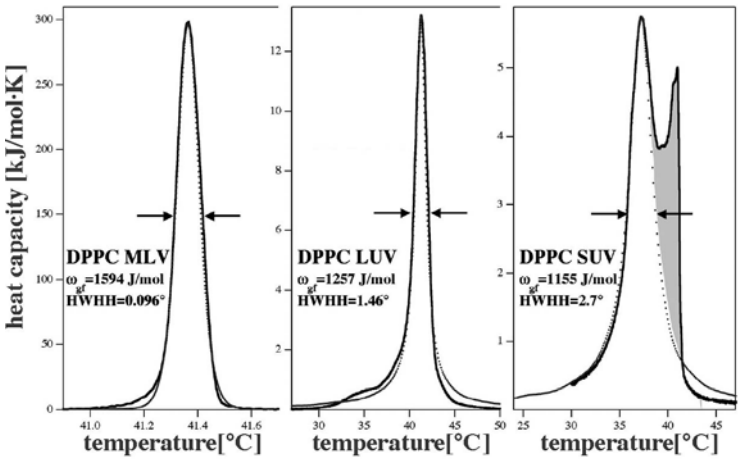

Fig. 8.5 Experimental melting profiles (solid lines) of multilamellar vesicles (MLV), large unilamellar vesicles (LUV), and small unilamellar vesicles (SUV) of DPPC. The simulations are given as dotted lines. Adapted from Ivanova and Heimburg (2001).

8.6
Two-Component Membranes

With Ising models and Monte Carlo simulations one can also describe membranes with several components. In a two-component membrane one has two melting enthalpies and entropies. Furthermore, there are six nearest neighbor interaction parameters: between gel and fluid lipids of species A, between gel and fluid lipids of species B, between gel lipids of species A and B, between fluid lipids of species A and B, between gel A and fluid B, and between gel B and fluid A. The Gibbs free energy of such a configuration is then given by

$$\begin{aligned}\Delta G = {} & N_{f_A}(\Delta H_A - T\Delta S_A) + N_{f_B}(\Delta H_B - T\Delta S_B) \\ & + N_{g_A,f_A}\,\omega_{g_A,f_A} + N_{g_B,f_B}\,\omega_{g_B,f_B} + N_{g_A,g_B}\,\omega_{g_A,g_B} \\ & + N_{f_A,f_B}\,\omega_{f_A,f_B} + N_{g_A,f_B}\,\omega_{g_A,f_B} + N_{f_A,g_B}\,\omega_{f_A,g_B}\end{aligned} \tag{8.23}$$

One can now apply the same Monte Carlo procedure as in the one-component system described in Section 8.3. However, additional to a Monte Carlo step deciding to change a lipid state one has to include a second Monte Carlo step that exchanges the sites of two lipids. This step introduces diffusion. With the help of the fluctuation theorem one can determine the heat capacity during simulation. For the two-component system of dimyristoyl phosphatidylcholine (DMPC) and distearoyl phosphatidylcholine (DSPC) a series of heat capacity profiles from experiment and MC simulations is shown in Fig. 8.6.

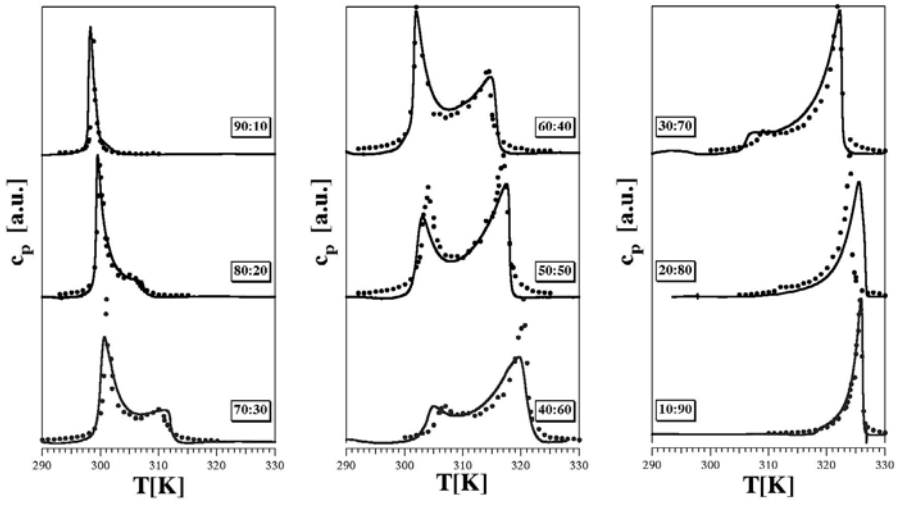

Fig. 8.6 Melting profiles of different mixtures of the two lipids, DMPC and DSPC. The solid lines represent experimental curves, and the symbols are Monte Carlo simulations with properly chosen parameters $\omega_{i,j}$ (Sugar et al., 1999; Seeger, 2002; Hac et al., 2005).

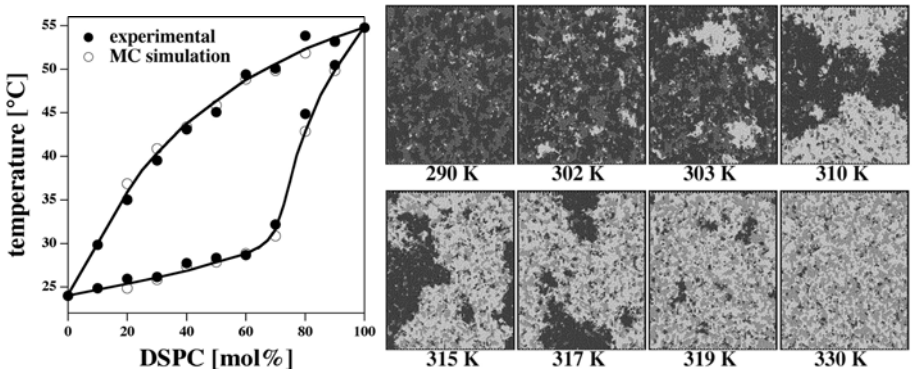

Fig. 8.7 Left: Phase diagram for the melting of DMPC–DSPC mixtures determined from lower and upper limits of the heat capacity anomalies. Filled circles are from experiments and open circles are from Monte Carlo simulations. Right: Snapshots of a Monte Carlo simulation of a DMPC–DSPC mixture at different temperatures. One recognizes the formation of domains.

The nearest neighbor interaction parameters ω_{ij} are determined by fitting the c_P-profiles (see Sugar et al. (1999) and Hac et al. (2005) for details and the choice of parameters).

The upper and lower limits of the heat capacity profile are often used to determine a phase diagram (Fig. 8.7) using the so-called tangent construction (described in Section 7.1 and Fig. 7.4). Such a diagram, however, has to be seen with caution, because as mentioned in Chapter 7, the Gibbs phase rule has been determined without taking possible domain boundaries into account—and if the distribution of states has only one maximum, one may not even have distinguishable phases. During the simulation one also obtains typical snapshots (configurations) that depend on the mixing ratios and on the temperature (Fig. 8.7). One often finds in such simulations that no macroscopic

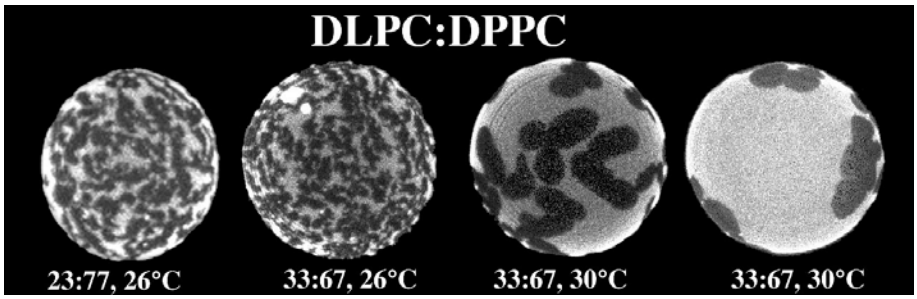

Fig. 8.8 Confocal fluorescence microscopy images of giant lipid vesicles (GUV) of various lipid mixtures showing the formation of domains. Adapted from Seeger et al. (2005).

phase separation occurs, but that one rather obtains many domains of various sizes and compositions. This is also found in experiments. In Fig. 8.8 several confocal fluorescence microscopy images of two lipid mixtures are shown that display domain formation in the lipid melting regime. The sizes of the domains range from small to very large. Small domains are an indication for that the nature of the transition is not of first order.

8.7 Local Fluctuations at Domain Boundaries

The simulations can be used to improve the intuition for the behavior of real lipid membranes. One obvious prediction from the simulations is that of domain formation. Domains have been found in simulations long before they have been seen in experiments (see e.g., Mouritsen and Jorgensen (1995)). The simulations can also be used to visualize the local nature of fluctuations in membranes. This can be done by introducing a local state variable S_{xy}, where x and y are the lateral coordinates of the lipid. If $S = 0$ for a gel lipid and $S = 1$ for a fluid lipid, one can also define a local fluctuation strength, Φ:

$$\Phi_{xy} = \left\langle S_{xy}^2 \right\rangle - \left\langle S_{xy} \right\rangle^2 \tag{8.24}$$

It can easily been shown that the largest value of $\Phi_{xy} = 0.25$. In the pure fluid and pure gel domains Φ_{xy} approaches zero. In Fig. 8.9 the snapshots from Fig. 8.7 are shown in the top panel and are compared with images showing the local fluctuations. It can be seen, that such fluctuations are maximum at

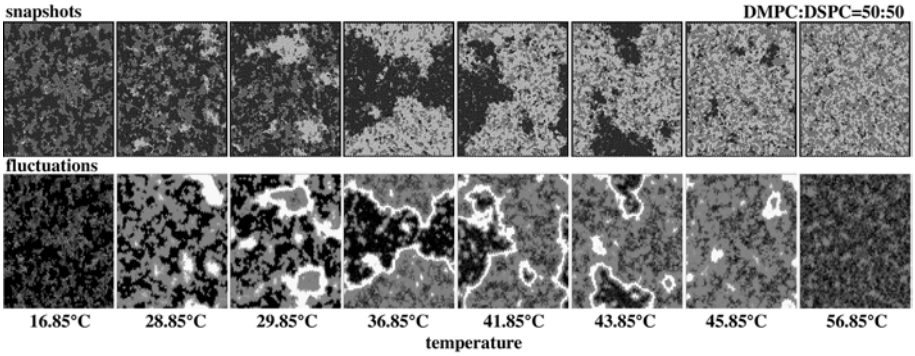

Fig. 8.9 Melting of a DMPC:DSPC=50:50 mixtures as obtained by Monte-Carlo simulations that are based on parameters from experimental heat capacity profiles. Top row: Melting of the membranes. Dark region correspond to gel state domains while grey regions correspond to fluid state domains. Bottom row: Local fluctuation calculated for the simulation snapshots show in the top row. Bright regions correspond to large fluctuations while dark regions corrspond to small fluctuations. The largest fluctuations are found at the domain interfaces. Adapted from Seeger et al. (2005).

the domain interfaces, as one might have expected. Later in this book it will be shown that the degree of fluctuations is closely related to the elastic constants, relaxation times, and permeability (see Chapters 14, 16, and 17). Therefore, it has to be expected that the domain boundaries display very pronounced maxima in the response functions. For example, one expects that the membranes are very permeable at the domain interfaces.

8.8 The 10-State Pink Model

The two-state model is very successful in describing phase behavior and cooperative fluctuations. However, it is clearly an over-simplification at the molecular level. Lipid molecules consist of a head group and hydrocarbon chains with internal degrees of freedom. The implicit assumption of the Ising model is that intermediate lipid states can be neglected. This assumption is, to a certain degree, reasonable if one looks at large scale domain formation. Furthermore, in the thermal average, intermediate values for enthalpy of a molecule are of course possible (e.g., a lipid at a domain boundary being 50% of the time in the fluid state).

If one wants to make statements on the molecular level, e.g., if one wants to calculate the order parameter profile along a lipid chain, one needs models with more states.

In 1980, Pink and collaborators (Pink and Chapman, 1979; Pink et al., 1980) developed a model to describe order parameters and Raman scattering data obtained from lipid membranes in the melting transition. They, too, used a simplified model with 10 lipid states (rather than $\approx 3^{2\cdot(N-2)}$ states). Here, 1 state is the ground state and 1 state is the completely fluid state, whereas the 8 other states are intermediate states with partially ordered chains. This model has been excessively used and extended by Mouritsen (University of Southern Denmark, Odense) and his group, and Zuckermann (Simon Fraser University, Vancouver) (Mouritsen et al., 1983) and has been applied to lipid–cholesterol mixtures (Ipsen et al., 1989; Mouritsen, 1990; Mouritsen et al., 1992), lipid mixtures (Mouritsen and Jorgensen, 1995), and lipid–protein mixtures (Sperotto et al., 1989). With this model, order parameter profiles (corresponding to mean orientations of chain segments along the lipid chain) can be described. In agreement with experiments it was found that the chains become more and more disordered toward the center of the membrane.

Overall, however, the outcomes of two-state Ising models and 10-state Pink models are very similar as discussed in detail in Mouritsen et al. (1983). The reason is that the molecular details, which are clearly relevant on molecular dimensions, are not of major importance on the length scale of domains. Thus, increasing detail in simulations must not necessarily be an advantage. This

applies in particular to the molecular dynamics simulations discussed briefly in the next section.

8.9 Molecular Dynamics

In "molecular dynamics (MD)" the vibrations of the atoms of molecules are calculated on the basis of Newton's laws of motion. Bond elongations and rotations are modeled as springs and approximated by Hooke's law. For each degree of freedom and each kind of chemical bond the force constants are obtained, e.g., by quantum-chemical calculations. The set of parameters needed to make an MD simulation is called a "force field." The correct determination of force fields is crucial.

If the force fields are determined accurately, MD simulations lead to the most accurate molecular information on the membrane structure, e.g., on order parameters and even on local diffusion, and is clearly useful. The method has, however, an important disadvantage: it is very slow. A simulation that reflects the time evolution of states of a membrane with several 100 lipids over about 100 ns may take several weeks to months on an up-to-date computer cluster (2006). Most biological processes take significantly longer (μs to s). In particular, cooperative processes such as lipid melting and the related domain formation takes place on large length and time scales (many μm and milliseconds). For instance, the relaxation time scales in lipid melting transitions may be up to 1 min (Chapter 16). Thus, in the foreseeable future such processes have to be calculated using different methods, e.g., by the lattice models described here.

8.10 Summary: Key Ideas of Chapter 8

1. The regular solution theory, described in Chapter 7, describes the mixing entropy of components in a phase incorrectly and does not allow for finite-size domain.

2. One can extend regular solution theory by applying statistical thermodynamics simulations that include nearest neighbor interactions of individual lipids. These simulations are called Monte Carlo simulations. They correctly predict the occurrence of finite size domains.

3. Monte-Carlo simulations are a valuable tool to interpret heat capacity profiles.

4. Simulations indicate that the melting of lipid membranes is close to critical behavior. However, in unilamellar systems most likely no discontinuity in the thermodynamics occurs, meaning that the melting is probably not of first-order nature.

5. First-order transitions and continuous melting can be distinguished in the distribution of states obtained from Monte-Carlo simulations in the melting regime.

6. Phase diagrams of lipid mixtures can be described with Monte Carlo methods. They lead to a self-consistent picture that links the heat capacity profiles with the sizes of domains. The findings are in agreement with confocal fluorescence microscopy measurements.

7. Statistical thermodynamic simulations can be used to determine the fluctuations at the domain boundaries. In Chapter 14 it will be shown that large fluctuations correspond to high bending elasticity and compressibility. The values of these functions are enhanced at domain boundaries, leading, e.g., to higher permeabilities in these regions.

9
Lipid–Protein Interactions

9.1
Hydrophobic Matching

Many proteins called integral proteins or transmembrane proteins span through the lipid membrane. Some examples are rhodopsin, bacteriorhodopsin, cytochrome c oxidase, but also pore-forming peptides as alamethicin or gramicidin A. The integral part of the proteins typically contains a large fraction of hydrophobic amino acids. The contact of hydrophobic surfaces with water is unfavorable both for entropic and enthalpic reasons (cf. Chapter 5). Thus, the lipid–protein system tries to minimize the contact between hydrophobic regions of both lipids and proteins with water.

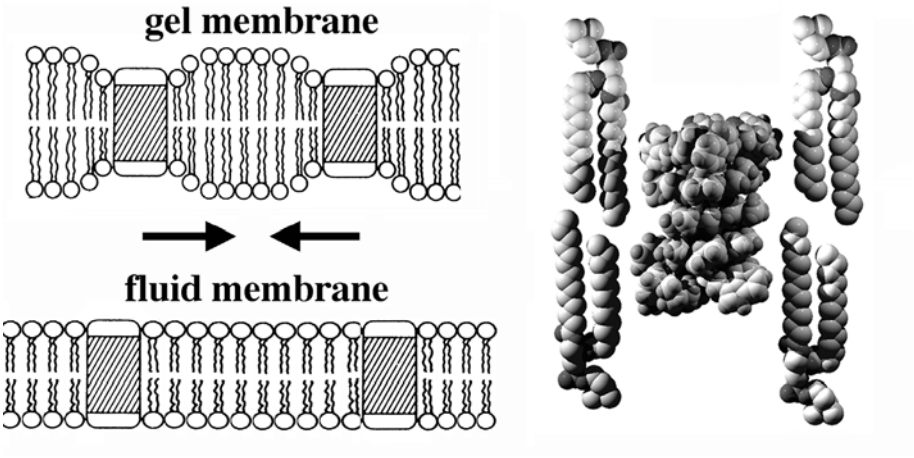

Fig. 9.1 Left: Hydrophobic matching illustrated for integral proteins. If the protein has a different hydrophobic length than the lipid membrane one finds attractive forces between them that resemble capillary forces. After Mouritsen et al. (1983). Right: An example for unfavorable hydrophobic matching is gramicidin A in DPPC membranes (Ivanova et al., 2003).

Lipids may have very different chain lengths. Membranes consisting of different lipids therefore have different hydrophobic thicknesses. If proteins are embedded into membranes of different hydrophobic thicknesses one may expect that some of the hydrophobic lipid of protein surface may get exposed to water. As an example, in Fig. 9.1 (right) we show the antimicrobial peptide gramicidin A that is short as compared to the hydrophobic thickness of a DMPC membrane in the gel phase. In this image one would expect some of the lipid surface close to the peptide to get exposed to water. However, this is not likely to happen. The lipid–protein system has some possibilities to reduce the free energy costs of the hydrophobic mismatch:

- Protein molecules may aggregate such that only molecules of similar hydrophobic length are in contact. Only the interface between protein clusters and the lipid membrane would contribute to the free energy costs. The overall distributional entropy of the proteins is reduced and thus, aggregation is linked to an increase of the free energy.

- The membrane can melt into a fluid annulus surrounding the proteins. The fluid membrane is thinner than the gel membrane. Therefore, the hydrophobic matching is more favorable. However, there is some compensating free energy cost for local melting some lipids. Such a behavior has been reported for bacteriorhodopsin in lipid membranes (Harroun et al., 1999).

- In a mixed lipid membrane, the proteins can recruit lipids of similar hydrophobic length around them. An example is bacteriorhodopsin in lipids of various lengths (Dumas et al., 1997). This will result in a reduction of the entropy of the lipids and an increase in free energy. If there is domain formation in mixed systems, which is very likely, the hydrophobic matching will lead to a segregation of the proteins into different regions of the membrane. This will result in a major influence on signal cascades between various membrane proteins, and thus in a change of the overall function of the biological membrane.

- Proteins can change their conformation to adjust to the hydrophobic thickness of the membrane. Typically, a change in protein structure is also linked to changes in their function. It has been shown that the light-activated bacteriorhodopsin mixes differently with lipid membranes than the dark non-activated form (Kahya et al., 2002).

All of these phenomena occur in real membranes. The hydrophobic matching principle has been shown to be of quite some relevance for lipid–protein interactions (Dumas et al., 1999). Here, we will show examples for aggregation, changes in function, and changes in lipid state below. There is a sub-

tle balance between increasing distributional entropy, the configurational entropy of the molecules, and the hydrophobic effect. Since the hydrophobic effect is very temperature dependent, all of these effects will also display a pronounced temperature dependence.

9.2 Integral Proteins

In the following section we will introduce into the statistical thermodynamics of integral proteins embedded into the membrane. The contact of molecules (including the hydrophobic effect) can be taken into account by considering nearest neighbor interactions. We will consider the interaction of integral proteins with lipid membranes consisting of one species and allow for lipid melting. The simulations will yield insights into the distribution of proteins in the matrix and how it is influenced by lipid melting.

9.2.1 Ising Model for the Interaction with Integral Proteins

One can describe the melting of lipid membranes in the presence of integral proteins in a manner similar to that of the two-component lipid membrane described by Eq. (8.23). If one considers peptides with a cross-sectional area similar to that of a lipid one can consider the protein as the second component in this equation, with the difference that it does not display melting transitions comparable to those of lipids (Ivanova et al., 2003). This reduces the number of unlike nearest neighbor interactions from six to three. The free energy can be written as

$$\Delta G = N_f(\Delta H - T\Delta S) + N_{gf}\,\omega_{gf} + N_{gp}\,\omega_{gp} + N_{fp}\,\omega_{fp} \tag{9.1}$$

where ω_{gf} is the interaction parameter for gel–fluid contacts of the lipid, ω_{gp} and ω_{fp} are the interaction parameters for the contact of a gel lipid with a peptide, and of a fluid lipid with a peptide. The N_{gf}, N_{gp}, and N_{fp} are the respective number of contacts. The phase space can be explored by the Monte Carlo simulations as introduced in the previous chapter.

In the following we will consider some special cases that demonstrate some principles of the interaction of peptides with lipid membranes.

9.2.1.1 Integral proteins that mix ideally with fluid lipid phases

Let us assume that the peptides mix ideally with the fluid state lipids, but unfavorably with the gel state membrane. In such a case one may expect that the peptides aggregate in the gel membrane but not in the fluid phase. This

case is very similar to that discussed in the context of freezing point depression in Section 7.4.

As an example we have chosen DPPC membranes ($\Delta H = 36.4$ kJ/mol, $T_m = 41.2\,^\circ$C and $\omega_{gf} = 1326$ J/mol). We further assume that $\omega_{fp} = 0$ (i.e., the interaction between fluid lipids and peptides is ideal), and the gel–peptide interaction is $\omega_{gp} = 1673$ J/mol), i.e., it is less favorable than gel–fluid contacts.

In Fig. 9.2 we show the outcome of Monte Carlo simulation (described in more detail in Ivanova et al. (2003)). In the left-hand panel one can see the calculated heat capacity profiles in the absence of peptides, and in the presence of 5 mol% and 10 mol% of peptides. One can see that the heat capacity maximum shifts to lower temperatures and that the profile is asymmetrically broadened toward the low temperature end of the c_P-profile. The Monte Carlo snapshots indicate that the peptides aggregate below the heat capacity maximum in the remaining fluid lipid domains. Above the heat capacity maximum the peptides mix ideally and do not aggregate. A shift of c_P-profiles to lower temperatures, in general, has to be taken as an evidence for better miscibility of the peptide in the fluid phase.

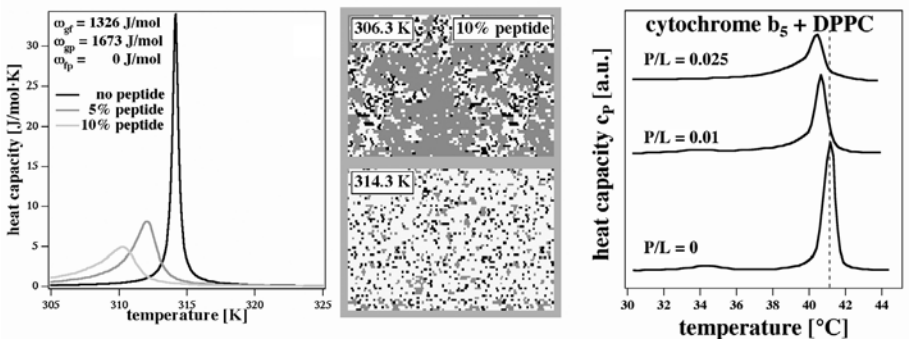

Fig. 9.2 Left: Heat capacity profiles in the absence of peptides, and in the presence of two different concentrations of a peptide that mixes ideally with the fluid lipid phase only. Center: Monte Carlo snapshots of two temperatures below and above the heat capacity maximum. Light points represent fluid lipids, gray dots are gel lipids, and black dots represent peptides. It can be seen that the peptides aggregate at low temperatures in the remaining fluid domains. Monte Carlo data adapted from Ivanova et al. (2003) (see text for parameters). Right: An experimental example for the behavior of the left-hand panels is cytochrome b_5 in DPPC membranes (adapted from Freire et al. (1983)).

One experimental example stems from Freire et al. (1983) who described the calorimetric profiles of cytochrome b_5 embedded in DPPC membranes. Here, one can nicely recognize the shift of the c_P-profile to lower temperatures, accompanied by an asymmetric broadening toward the low temperature side of the profile. One has to expect in this case that cytochrome b_5 mixes reasonably well with the fluid membranes, but aggregates in the gel phase. The reason for the shift in the c_P-profile lies in the difference in the entropy of the protein distribution in the two lipid phases.

9.2.1.2 **Integral proteins that mix ideally with gel lipid phases**

The case when proteins dissolve ideally into gel phases but display unfavorable interactions with the fluid phase is just the mirror image of the previous case.

As an example serves again DPPC membranes ($\Delta H = 36.4$ kJ/mol, $T_m = 41.2\,^{\circ}$C and $\omega_{gf} = 1326$ J/mol). We assume that $\omega_{gp} = 0$ J/mol (i.e., the interaction between gel lipids and peptides is ideal), and the fluid–peptide interaction is $\omega_{fp} = 1673$ J/mol.

In Fig. 9.3 the results of Monte Carlo simulations are shown. In contrast to the previous figure the heat capacity profiles shift to higher temperatures. The profiles are asymmetrically broadened toward the high temperature end. The Monte Carlo snapshots show that the proteins aggregate in the fluid phase.

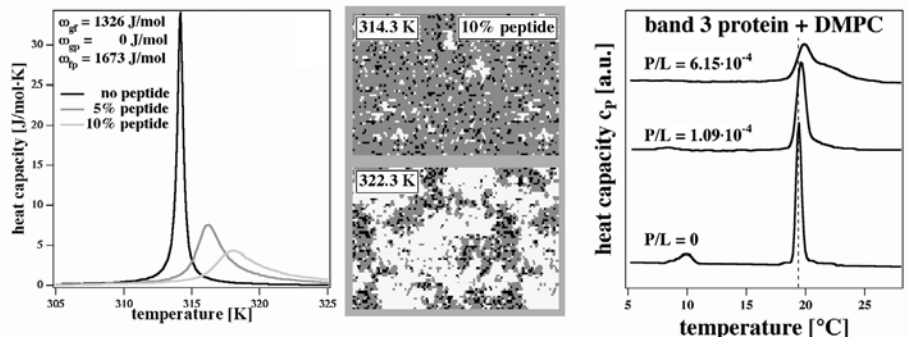

Fig. 9.3 Left: Heat capacity profiles in the absence of peptides, and in the presence of two different concentrations of a peptide that mixes ideally with the gel lipid phase only. Center: Monte Carlo snapshots of two temperatures below and above the heat capacity maximum. Light points represent fluid lipids, gray dots are gel lipids, and black dots represent peptides. It can be seen that the peptides aggregate at high temperatures in the remaining gel domains. Monte Carlo data adapted from Ivanova et al. (2003) (see text for parameters). Right: An experimental example is band 3 protein of erythrocytes reconstituted into DMPC. Data adapted from Morrow et al. (1986).

Such a behavior can for example be found in the interaction of the band 3 protein of erythrocytes with DMPC membranes described by Morrow et al. (1986).

One would expect that this behavior is rather an exception. The gel membrane is crystalline with triangular packing. Typically, molecules of different sizes do not mix well in crystals. The fluid membrane, in contrast, is a liquid (no crystalline packing) and it seems more likely that proteins may mix well with fluid phases, if hydrophobic matching is favorable.

9.2.1.3 **Integral proteins that mix ideally with both gel and fluid lipid phases**

Another limiting case is when peptides mix ideally with both lipid phases. This is an unlikely scenario since the hydrophobic matching of a peptide

would be different in both phases due to different hydrophobic lengths of the lipids. Let us assume, however, that such a situation is possible. The nearest neighbor interaction parameters between peptides and lipids are zero for both gel and fluid. This leads to an accumulation of peptides at the gel–fluid domain interfaces because there the interfacial free energy can be lowered. An effective lowering of the interfacial tension of the domains leads to a decrease in cooperativity and thereby a broadening of the heat capacity profiles. As an example serve DPPC membranes ($\Delta H = 36.4$ kJ/mol, $T_m = 41.2\,^\circ$C, and $\omega_{gf} = 1326$ J/mol). We further assume that $\omega_{gp} = \omega_{fp} = 0$ J/mol. Results of the Monte Carlo simulations are shown in Fig. 9.4. Since the interaction of the peptides is identical with both lipid states, the c_P-maxima are not shifted.

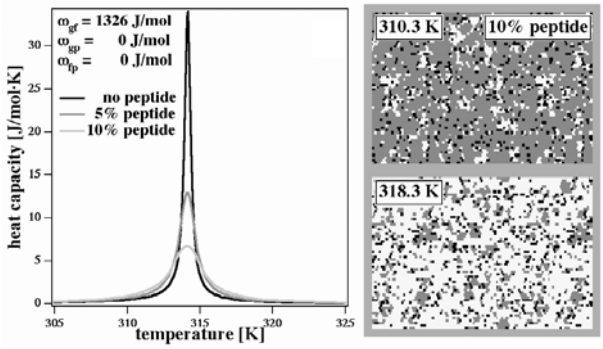

Fig. 9.4 Proteins that mix ideally with both lipid phases (see text for parameters). Left: Heat capacity in the absence and in the presence of two different concentrations of peptides. Right: Monte Carlo snapshots at two temperatures below and above the c_P-maximum. The mean domain sizes are reduced because the peptides effectively lower the tension at the domain interfaces. Monte Carlo data adapted from Ivanova et al. (2003). Light points represent fluid lipids, gray dots are gel lipids, and black dots represent peptides. It can be seen that the peptides aggregate at low temperatures in the remaining fluid domains.

9.2.1.4 **Integral proteins that have unfavorable interactions with both gel and fluid lipid phases**

A fourth limiting case is found when peptides (proteins) do not mix with both lipid phases. This results in the aggregation of peptides in both gel and fluid phase. Since a macroscopic clustering of peptides leads to a reduction of the overall interface between peptides and lipids, the effect of the peptides on the heat capacity profiles is very small. As an example we again chose DPPC membranes ($\Delta H = 36.4$ kJ/mol, $T_m = 41.2\,^\circ$C and $\omega_{gf} = 1326$ J/mol). We further assume that $\omega_{gp} = \omega_{fp} = 2029$ J/mol. Results of the Monte Carlo simulations are shown in Fig. 9.5. Since the interaction of the peptides is identical with both lipid states, the c_P-maxima are not shifted. The effect of the peptides on the melting profiles is very similar to the previous case of ideal

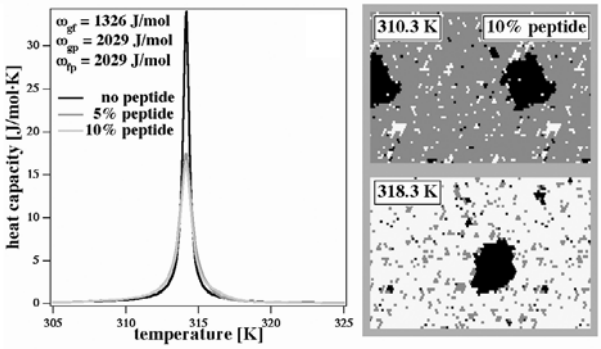

Fig. 9.5 Proteins with unfavorable lipid–proteins interactions in both lipid phases (see text for parameters). Left: Heat capacity in the absence and in the presence of two different concentrations of peptides. Right: Monte Carlo snapshots at two temperatures below and above the c_P-maximum. The peptides aggregate into macroscopic peptide clusters in both lipid phases, thereby reducing the overall interface between peptides and lipids. Monte Carlo data adapted from Ivanova et al. (2003). Light points represent fluid lipids, gray dots are gel lipids, and black dots represent peptides. It can be seen that the peptides aggregate at low temperatures in the remaining fluid domains.

miscibility of peptides in both phases. An example for this behavior is gramicidin A described below in Section 9.2.1.6.

9.2.1.5 **Experimental example 1: Lipid chain length dependence of peptide–lipid interactions**

The hydrophobic matching depends on the hydrophobic length of both peptides and lipids. It therefore has to be expected that the mixing of peptides in lipid membranes and their effect on heat capacity profiles depends on the number of hydrocarbons of the lipid chains. Zhang et al. (1995) made a careful study of the artificial peptide Ac-K_2-$(LA)_{12}$-K_2-amide. This peptide forms transmembrane helices in membranes consisting of short chain lipids. The heat capacity profiles shown in Fig. 9.6 indicate that the effect of this peptide on heat capacity profiles of membranes of different phosphatidylcholines is a function of lipid chain length. The maximum shift in T_m caused by the reference amount of peptide was 7.1 K toward lower temperatures in DPPC membranes. For di-(C_{13}) phosphatidylcholine the shift was only -2.4 K. For di-(C_{22}) phosphatidylcholine $\Delta T_m \approx -1.3$ K was found. Thus, clearly the interactions of the lipid with the peptides are a function of chain length. The largest shift is expected when the interaction with the fluid membrane is close to zero (perfect hydrophobic matching with the fluid phase) and the degree of peptide redistribution upon going through the phase transition is maximum. Zhang et al. (1995) found evidence that for the very long chain lipids the peptide conformation deviated from the simple α-helical conformation. The hydrophobic length of the peptide (31–32 Å) corresponds approximately

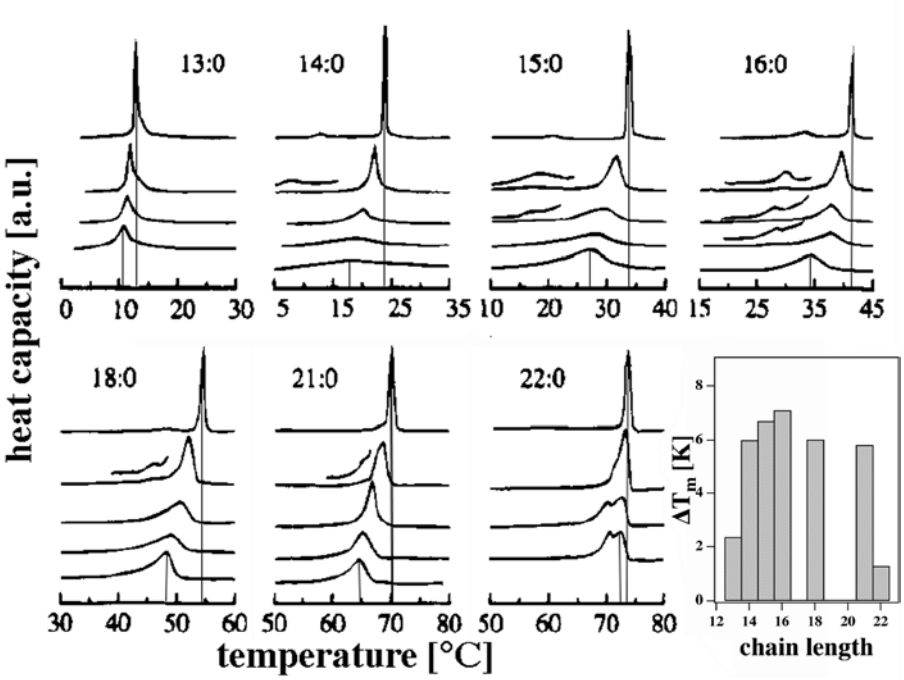

Fig. 9.6 Heat capacity profiles of the artificial peptide Ac-K_2-$(LA)_{12}$-K_2-amide in lipid membranes of different chain lengths, ranging from C_{13} to C_{22}. Heat capacity profiles for various peptide fractions between 0 and 0.17 are shown. They resemble the theoretical profiles described in the previous section. This plot demonstrates the importance of the hydrophobic matching concept. Data adapted from Zhang et al. (1995). With permission.

to the thickness of the gel phase of di-(C_{15}) phosphatidylcholine and to the fluid phase of somewhat longer lipids. For the long chain lipids, both fluid and gel phase of the lipids display larger hydrophobic cores than the length of the peptide. Thus, it is not surprising that for di-(C_{22}) phosphatidylcholine the heat capacity profiles approach the behavior described in Section 9.2.1.4, while it is close to that described in Section 9.2.1.1 for lipids with C_{16} or C_{17} chains. The right bottom panel shows the shift of the c_P-maximum at the highest peptide concentrations as a function of lipid chain length.

9.2.1.6 **Experimental example 2: Gramicidin A in lipid membranes**

Another experimental example is gramicidin A embedded into DMPC membranes. This antimicrobial transmembrane peptide has a very short hydrophobic length (cf. Fig. 9.1). It is shorter than DMPC in both, gel and fluid phase. Thus, one may expect a mixing behavior similar to that described in Section 9.2.1.4, where the peptides segregate into clusters and aggregates in

both lipid phases. One would further expect that mixing is more unfavorable in the gel phase than in the fluid phase due to larger hydrophobic mismatch of gel lipids and gramicidin A. In Fig. 9.7 heat capacity profiles of gramicidin A in DPPC membranes are shown. Increasing amounts of peptide have only a minor impact on the c_P-profiles. This is typical for peptide aggregation in both lipid phases as described in Section 9.2.1.4 and in Fig. 9.5. If the heat capacity profiles are fitted with the use of Monte Carlo simulations one obtains Monte Carlo snapshots that indicate large scale aggregation of peptides in the gel phase and small aggregates in the fluid phase (Fig. 9.7, right top). The slight preference of gel phase aggregation results from the minor shift and asymmetric broadening of the heat capacity profiles toward lower temperatures. In fact, aggregation of gramicidin A in DPPC gel membranes and DMPC fluid membranes is found by atomic force microscopy. In the gel phase of DPPC membranes gramicidin A forms line-like aggregates, highlighted by the arrows in Fig. 9.7 (right, bottom). The same line like pattern of peptide aggregates (WALP peptides) was described by Rinia et al. (2000). In this publication the peptides even formed well-ordered striated patterns. In the fluid phase of DMPC gramicidin A forms small aggregates with diameter of ≈5–10 nm, corresponding to 40–160 gramicidin molecules. The line-like

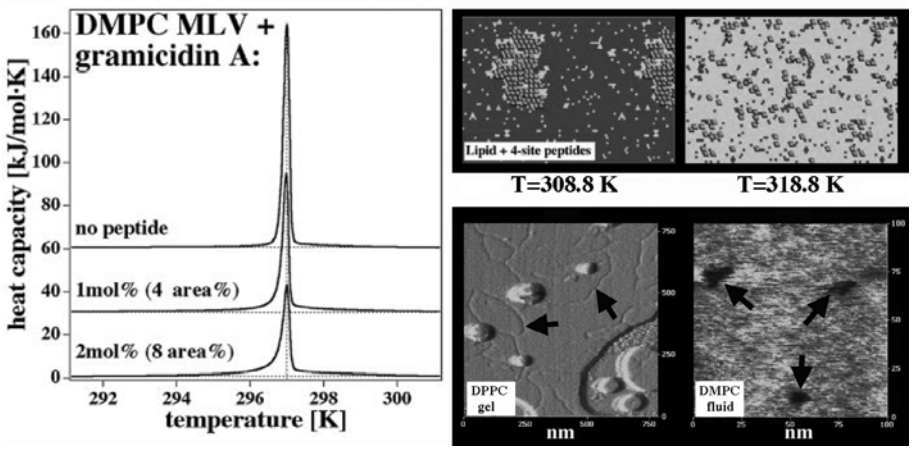

Fig. 9.7 Gramicidin A embedded into DMPC bilayers. Left: Heat capacity profiles in the absence and the presence of two different concentrations of gramicidin A. The profiles resemble those in Fig. 9.5. Right, top: Monte Carlo snapshots below and above the melting transition. The large gray dots represent peptides occupying four lipid sites each (see Ivanova et al. (2003) for details). The peptides aggregate in both phases. However, peptide clusters are big in the gel phase and small in the fluid phase. Monte Carlo snapshots have been obtained by fitting the experimental c_P-profiles. Bottom: AFM experiments show that peptide aggregates can be found in both gel and fluid phase membranes (see arrows). In the gel phase they form line-like aggregates, whereas they form small spherical clusters in the fluid phase (see text for details).

pattern of the peptide aggregates in the gel-phase was not predicted by the Monte Carlo simulation. The simulations cannot do that when it is not built-in into the algorithm. Nevertheless, one has to conclude that the thermodynamic analysis of the heat capacity profiles by simulations correctly predicted the aggregation of peptides in both phases, and that aggregates would tend to be small in the fluid phase.

9.2.2 Lipid Fluctuations at Protein Interfaces

In Section 8.7, we defined the local fluctuations in the lipid matrix. These are the fluctuations in lipid state between gel and fluid lipid state at each point of the lipid matrix (defined by $\Phi_{xy} = \langle S_{xy}^2 \rangle - \langle S_{xy} \rangle^2$). Large fluctuations correspond, e.g., to increased permeability (see Chapter 17) and higher elasticity (Chapter 14). The Monte Carlo simulations provide such information. If the nearest-neighbor interactions are different from zero, the lipid states will be influenced by the presence of proteins. In Fig. 9.8 it is shown that gramicidin A aggregates influence the fluctuations in the proximity of the protein clusters. Considerations of this kind suggest that parts of the function of transmembrane proteins could consist in their local influence on the elastic constants of the surrounding lipid membrane.

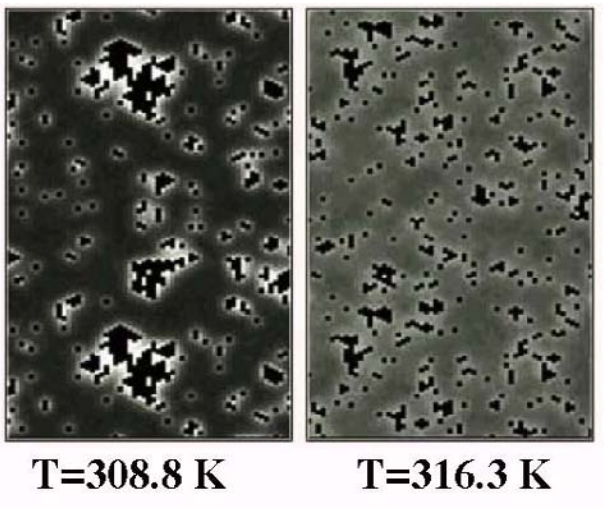

Fig. 9.8 Local fluctuations as defined in Section 8.7 for the DPPC–gramicidin A mixtures simulated in the previous figure. Close to the peptide aggregates one can recognize regions of larger fluctuations (indicated by the bright regions). Such regions tend to be softer and more permeable. Data from Ivanova et al. (2003).

9.2.3
Pore Formation

Some amphiphilic peptides form pores in membranes. Examples are alamethicin, melittin , and margainin. The modes of interaction are discussed in more detail in Chapter 12. Typically, they expose their hydrophilic side to the aqueous inside of the pore whereas the hydrophobic side of the peptide is exposed to the membrane interior. Here, as an example we show the peptide alamethicin dissolved in DPPC membranes in the gel phase (Fig. 9.9) as measured by atomic force microscopy (AFM). While in the literature alamethicin pores are typically thought to consist only of some 10 lipids (Gennis, 1989), it can be seen here that the peptide can also induce large defects in the membrane that are of the order of 100 nm in diameter. The size of such pores roughly depends on the peptide content of the membrane. The height difference at the pore interfaces corresponds to the thickness of one DPPC membrane.

The structure of membranes can also be analyzed by using the tapping mode of the AFM. In this mode one monitors the oscillations of a vibrating AFM cantilever and the corresponding phase shifts between the cantilever ex-

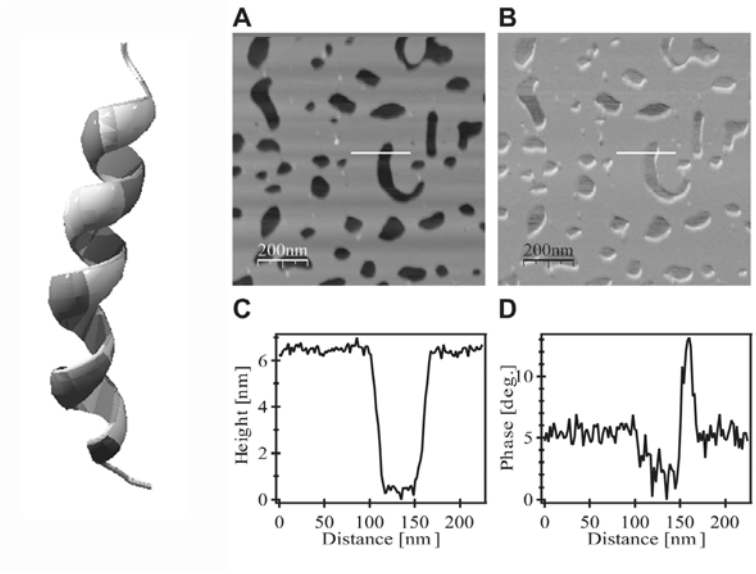

Fig. 9.9 Pore formation by alamethicin in lipid membranes adsorbed on mica. Left: Crystal structure of alamethicin (cf. Fox and Richards (1982)). Center: Surface height AFM plot of alamethicin pores in gel phase DPPC membranes. Dark regions correspond to the mica surface. The height profile at the bottom shows the membrane thickness measured along with the line in the surface plot. Right: The same region of the membrane in a phase image. Bright regions represent especially soft membranes segments. They occur at the pore interface close to the peptides. Data adapted from Oliynyk et al. (2006).

citation and the actual movement of the response. If the surface consists of a viscoelastic fluid a large phase shift would correspond to the softer material while the phase shift on hard surfaces is small. The details of the coupling between phases and the properties of surfaces are not well explored. Thus, we can use phase images here only to demonstrate relative changes in the elastic constants of the surface. Phase images of membranes with alamethicin pores can be seen in Fig. 9.9 (right). The mica surface shows up in dark gray shades indicating that this part of the surface is hard. The lipids show up in light gray shades. They are softer than the mica surface. Interestingly, the interface between the pores induced by alamethicin and the lipid membrane appears as white shades, indicating that the softest part of the membrane can be found close to the alamethicin peptides. This suggests that peptides can in fact change the elastic properties in the vicinity, as theoretically predicted in Section 9.2.2. Details of the alamethicin study can be found in Oliynyk et al. (2006).

9.2.4
Hydrophobic Matching and Integral Protein Function

We have shown above that peptides and proteins can influence the physical state of the lipid membranes. However, each thermodynamic force acting between lipids and proteins has the potential to alter the state of proteins as well. There are numerous examples in the literature for the influence of lipids on protein function. Here, we show the results of experiments on melibiose permease investigated by Dumas et al. (2000). Melibiose permease is a cation/sugar symporter from *E. coli* which catalyzes the cell accumulation of α-galactosides as melibiose.

In Fig. 9.10 the activity (measured by counterflow or $\Delta\Psi$ driven transport) of melibiose permease is shown as a function of the chain length of the surrounding phosphatidylcholine lipids. It can be clearly seen that maximum activity is achieved for C16:1 chains. Taking all data together Dumas et al. (2000) concluded that maximum activity of the sugar symporter was achieved when the hydrophobic thickness of the protein matched that of the lipid membrane.

9.3
Binding of Peripheral Proteins to One-Component Membranes

9.3.1
Ising Model for the Interaction with Peripheral Proteins

Peripheral proteins are proteins that bind to the surfaces of membranes. Often, the binding of peripheral proteins is supported by electrostatic interactions.

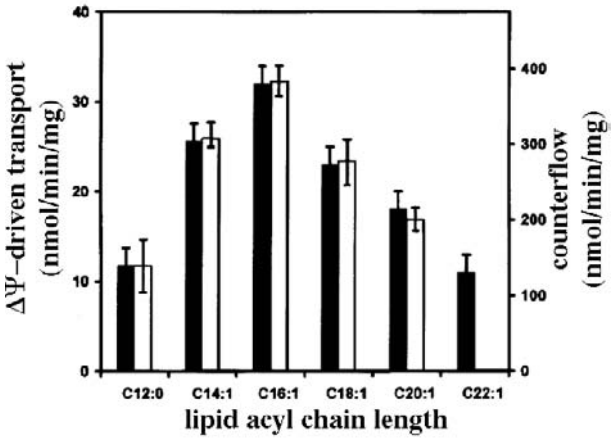

Fig. 9.10 Melibiose permease activity measured by voltage-driven transport or counterflow activity in lipid membranes of various chain compositions. The activity shows a clear maximum for phosphatidylcholines with C16:1 chains. For these chains the hydrophobic matching between lipids and proteins is optimum. Figures adapted from Dumas et al. (2000). With permission.

Such interactions are described, in detail, in Chapters 11 and 12. Upon protein binding one observes that the melting profiles of lipid membranes change. Usually, the heat capacity profiles shift to higher or lower temperatures (depending on the nature of the proteins). If the interaction is of purely electrostatic origin (between a basic protein and a negatively charged membrane) the shift will generally be toward higher temperatures because the charge density of gel membranes is higher than that of the fluid membrane. Therefore, electrostatic binding to gel phases is stronger.

An example for this is the binding of cytochrome c to dimyristoyl phosphatidylglycerol (DMPG, which is charged at neutral pH). Cytochrome c is a protein of 12.384 kDa (1 kilo Dalton = 1000 proton masses). It is positively charged and binds to negatively charged surfaces. When it binds to DMPG membranes, the transition peak shifts by about 5° to higher temperatures (see Fig. 9.11).

Let us consider the binding of peripheral proteins to gel or fluid lipid membranes. This implies four different states: a free gel binding site (G) and free protein (P), a gel binding site occupied by a bound protein (GP), a free fluid binding site (F), and a fluid binding site occupied by a bound protein (FP).

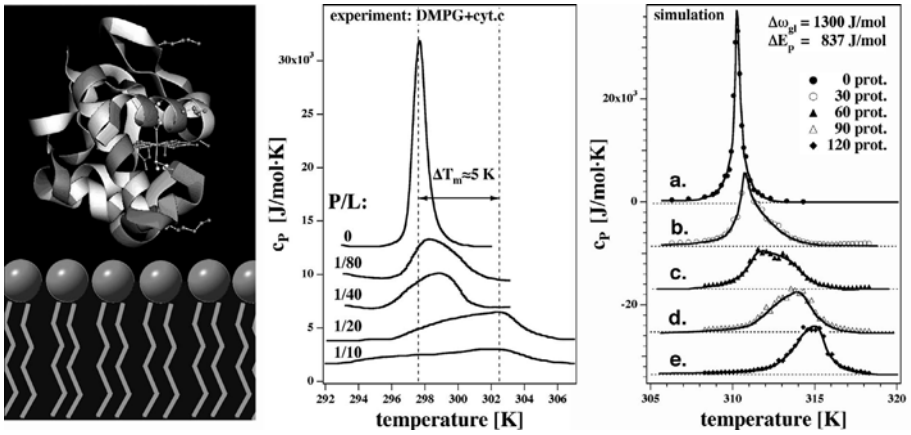

Fig. 9.11 Binding of cytochrome c to a charged lipid membrane. Left: Schematic image using the crystal structure of cytochrome c from Bushnell et al. (1990). Center: Calorimetric profiles, showing the cytochrome c-induced shift of the heat capacity profiles toward higher temperatures. Right: Monte Carlo simulations reproducing a similar behavior.

One obtains the following binding scheme:

$$\begin{array}{ccc} \mathrm{G}+\mathrm{P} & \overset{K_1,\Delta G_1}{\rightleftharpoons} & \mathrm{F}+\mathrm{P} \\ {\scriptstyle K_2,\Delta G_2}\ \uparrow\downarrow & & \uparrow\downarrow\ {\scriptstyle K_3,\Delta G_3} \\ \mathrm{GP} & \underset{K_4,\Delta G_4}{\rightleftharpoons} & \mathrm{FP} \end{array} \tag{9.2}$$

K_1 and K_4 are the melting equilibrium constants, whereas K_2 and K_3 describe the binding equilibria. Since the Gibbs free energy is a function of state, it follows:

$$\Delta G_1 + \Delta G_3 = \Delta G_2 + \Delta G_4 \tag{9.3}$$

meaning that in a cyclic process through the above diagram the total free energy change is zero. This implies that

$$K_1 \cdot K_3 = K_2 \cdot K_4 \tag{9.4}$$

Upon binding of proteins the melting equilibria change because the c_P profiles change. Therefore,

$$K_1 \neq K_4 \tag{9.5}$$

From Eq. (9.3) it immediately follows

$$K_2 \neq K_3 \qquad \text{or} \qquad \Delta G_2 \neq \Delta G_3 \tag{9.6}$$

One has to conclude that the shift in the melting profile implies that the protein binds with a different affinity to the two lipid phases.

We obtain

$$\Delta G_4 - \Delta G_1 = \Delta G_3 - \Delta G_2 \equiv \Delta G_P = \Delta H_P - T\Delta S_P \tag{9.7}$$

This is the difference of the Gibbs free energy of the protein interaction with the fluid and gel membrane. The shift of the melting point can be calculated as follows:

$$\Delta T_m = \frac{\Delta H + \Delta H_p}{\Delta S + \Delta S_P} - \frac{\Delta H}{\Delta S} \tag{9.8}$$

The experiment also allows us to determine both the binding enthalpy difference ΔH_P and the binding entropy difference ΔS_P. ΔH, $\Delta S = \Delta H/T_m$ and ΔH_P are directly obtained from experiment.

9.3.2 Monte Carlo Simulations on the Binding of Proteins to Membranes

We outline here a model described in detail in Heimburg and Biltonen (1996). One can perform Monte Carlo simulations if one assumes two lattices:

- One lattice containing the lipids.
- A second lattice on top of the first lattice contains the proteins. The proteins are allowed to diffuse.

The state of each lipid is determined from the enthalpy and entropy of the lipid transition, the nearest neighbor interactions with other lipids, and the interaction with adjacent proteins. For each lipid one has (following the derivation of the Ising model in the absence of proteins in Chapter 8) the following equilibrium constant for a transition of a lipid assuming that a protein is located on top of the lipid:

$$K = \exp\left(-\frac{\Delta H - T\Delta S + \Delta n_{gf} + \Delta G_P}{RT}\right) \tag{9.9}$$

and

$$K = \exp\left(-\frac{\Delta H - T\Delta S + \Delta n_{gf}}{RT}\right) \tag{9.10}$$

if there is no protein on top of the lipid. The probability to find a fluid lipid is

$$P_f = \frac{K}{1+K} \tag{9.11}$$

and the probability to find a gel state lipid is

$$P_g = \frac{1}{1+K} \tag{9.12}$$

With these probabilities the states of the lipids are simulated along the lines described in Chapter 8.

In a second Monte Carlo step, the proteins are allowed to move on the second lattice. Depending on whether the proteins are located on top of gel or fluid lipids, they have different Gibbs free energies. During the Monte Carlo simulation it is now allowed that the proteins can move by one lattice site in one of the six directions, i, on a triangular lattice. If the number of fluid lipids under the protein changes, this influences the probability to diffuse. The decision to move in one of the six directions on the lattice is governed by

$$P_m(i) = \frac{K_m(i)}{1+K_m(i)} \qquad K_m(i) = \exp\left(-\frac{\Delta n_f(i)\Delta G_p}{RT}\right) \tag{9.13}$$

where $\Delta n_f(i)$ is the change in the number of fluid lipids underneath the protein upon moving in direction i ($i = 1, 2, \ldots, 6$). With such a model one can calculated the c_P-profiles for a peripheral protein with similar parameters as cytochrome c and DMPG lipids (see Fig. 9.11, right). One can also plot snapshot from the simulation from below, within and above the melting transition (Fig. 9.12).

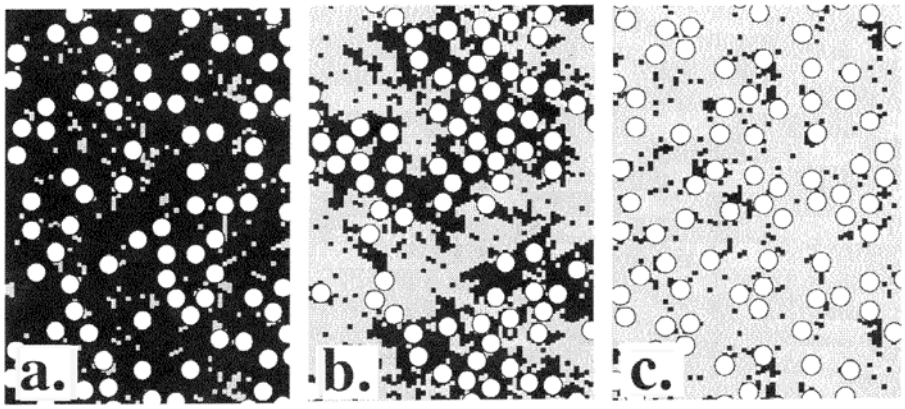

Fig. 9.12 Monte Carlo snapshots for protein distributions at three different temperatures, below, within and above the transition. The lipid–protein parameter ΔG_P was determined such that the effect of cytochrome c binding to DMPC membranes found in calometry is reproduced. One recognizes the aggregation of proteins in the transition regime. Adapted from Heimburg and Biltonen (1996).

From Fig. 9.12 one can see that the proteins tend to aggregate within the lipid melting transition, because they have different affinities to gel and fluid

domains. Since the binding of cytochrome c to gel lipids is stronger, the proteins accumulate on the shrinking gel domains with increasing temperature. At high temperatures, gel domains completely disappear and the proteins are again statistically arranged. Therefore, the proteins are distributed statistically in both gel and fluid phases and only accumulate in the transition regime. This behavior is distinctly different from the integral proteins described in Section 9.2. Interestingly, both tertiary structure and the redox potential of membrane-associated cytochrome c changes in the membrane melting regime (Heimburg et al., 1991; Heimburg and Marsh, 1993) indicating that the lipid state is important for the protein function.

9.4 Action of Phospholipases on Membrane Domains

Phospholipase A_2 (PLA_2) is an enzyme from pancreas and from bee or snake venoms that hydrolyzes the hydrocarbon chains of phospholipids at the sn-2 position. The hydrolysis products of PLA_2 action are lysolipids and fatty acids and protons (Fig. 9.13, left). The action of the enzyme can easily be monitored by keeping the pH constant by adding measurable quantities of bases. The action of phospholipases, and in particular that of PLA_2, is strongly dependent on the phase state of the membrane. Typically, after addition of the enzyme to phospholipid membranes, some time progresses before the enzyme reaches maximum activity. This time is called the lag time (Biltonen, 1990). The shorter the lag time the larger the activity of the protein. If the lag times are plotted as a function of temperature one finds that the enzyme activity is strongly correlated with the heat capacity of the membrane. At the c_P-maximum of DPPC membranes the lag times display a pronounced minimum indicating maximum activity.

The reason for this activity maximum is only partially understood but it seems clear that it is related to the degree of fluctuations in the membrane plane and the presence of lateral phase separation (Burack et al., 1993). Possibly, in the presence of large fluctuations in state and position it is easier for the enzyme to get access to the hydrolysis site on the lipid that is typically buried within the membrane surface. Such a behavior seems evident in monolayer experiments of DPPC lipids in the phase coexistence regime. In Fig. 9.14 the activity of the enzyme at gel–fluid domain interfaces can be followed easily. The dark domains are slowly hydrolyzed by PLA_2 at the domain interfaces. Such studies have been first performed by Grainger et al. (1989). It can also be seen in Fig. 9.15 that the proteins sit preferentially at the domain interfaces. One can recognize bright edges of the domains originating from fluorescently labeled PLA_2 (Dahmen-Levison et al., 1998).

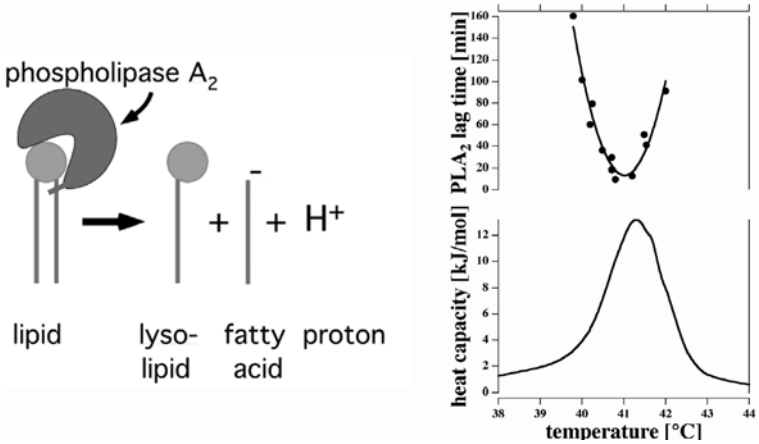

Fig. 9.13 Left: Schematic action of phospholipase A_2 (PLA_2), which hydrolyzes phospholipids at the sn-2 position of the glycerol backbone. Right: The time until maximum activity (lag time) plotted as a function of temperature for two different PLA_2 concentrations acting on DPPC membranes ($T_m \approx 314.2$ K). At the heat capacity maximum the enzyme activity is also maximum. Adapted from Biltonen (1990).

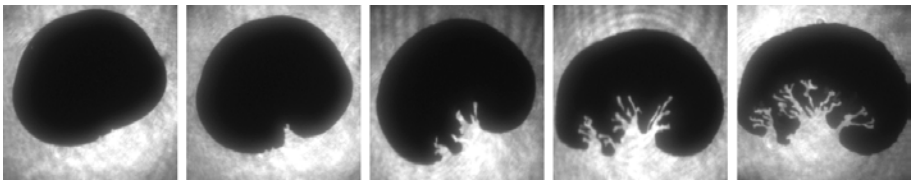

Fig. 9.14 Action of PLA_2 on DPPC monolayers monitored by fluorescence microscopy. The image diameters are of the order of 20 μm. Dark shades correspond to gel domains. Bright regions correspond to fluid regimes. The different snapshots were taken after different time. The increased hydrolysis activity of the enzyme at the domain interfaces can be clearly seen. Data from M. Gudmand and T. Heimburg, NBI Copenhagen. For reference see also Grainger et al. (1989).

9.5 Domains and "Rafts" in Biological Membranes

Biological cell membranes are multicomponent systems made of a variety of lipids and proteins. Naturally, both lipids and proteins display phase behavior. The examples in this chapter also indicate that proteins are components in the phase diagram and contribute to domain formation. The phase behavior of such systems, however, is not well understood. While it is practically unavoidable that domains and aggregation phenomena are present in biomembranes there are many unanswered questions.

Presently, the investigation of domains in membranes is a hot topic in biophysics and cell biology. In particular, the investigation of a very specific kind

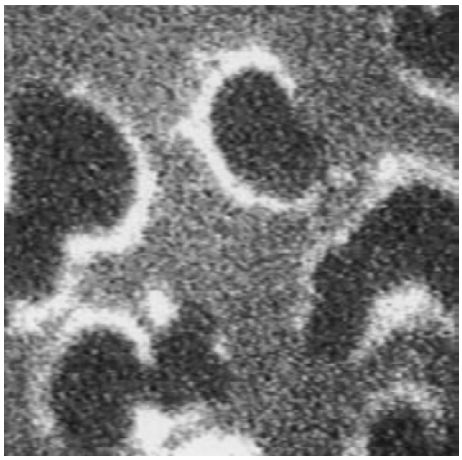

Fig. 9.15 Domains on DPPC monolayers in the phase coexistence regime in the presence of fluorescently labeled PLA_2. The protein is preferentially located at the domain interfaces as obvious from the bright shades. Image from Dahmen-Levison et al. (1998).

of domains, called rafts, caught some interest. Rafts are thought to be isolated domains consisting of predominantly cholesterol, saturated long-chain sphingolipids , and some proteins (see Fig. 9.16). It is believed that this domain formation influences signaling cascades and trafficking within biomembranes (Simons and Ikonen, 1997; Bagnat et al., 2000). If one assumes that for signalling several proteins have to interact, it is obvious that the efficiency of the signal exchange depends on whether the proteins are found in the same or in different domains. A number of good reviews exist on this topic (Brown and London, 1998; Simons and Toomre, 2000; Simons and Ikonen, 2000; London, 2002; Edidin, 2003a,b; Simons and Vaz, 2004). The sphingolipids will predominantly form ordered or gel-phases. Since artificial lipids in the presence of high fractions of cholesterol form liquid-ordered phases it is also believed that rafts may be of liquid-ordered nature. However, one should not imagine these domains as fluids. A liquid-ordered domain is rather a glass state, i.e., rigid but without crystalline order. Glasses typically melt gradually with temperature and do not display well-defined melting points. The existence of such "rafts" has been postulated because one can isolate the respective lipid and protein fractions when washing the biomembranes with detergents (e.g., triton) at low temperature (4 °C). One obtains detergent-resistant domains (DRMs) or lipid–protein aggregates that are enriched in cholesterol, sphingolipids , and some proteins. All other proteins and lipids are washed away by the detergent.

The detergent-extraction method has to be considered with high scepticism. From all that has been written in Chapters 7 and 8 the phase behavior is a

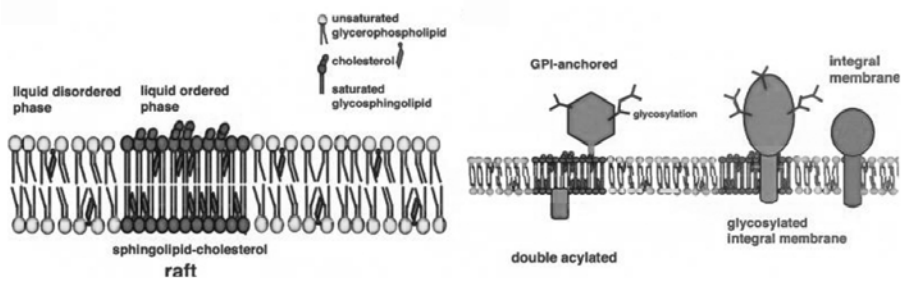

Fig. 9.16 Schematic drawing of raft formation in biological membranes as imagined by Bagnat and Simons (2002). Left: Organization of saturated glycosphingolipids and cholesterol into lipid rafts lipids in a fluid environment of unsaturated lipids. Right: Proposed preferential association of some proteins to lipid rafts.

pronounced function of temperature, in particular if lipids with high melting points are present (here the sphingolipids). Thus, at 4 °C one expects a very different phase behavior than at 37 °C and it is not a surprise that long chain lipids and cholesterol remain in the DRMs at low temperature. This, however, is no indication that this would also happen at physiological temperature. Similarly important is that detergents are also components in the phase diagrams and it seems obvious that high quantities of such detergents do not leave the mixing properties of the other components untouched. In a beautiful paper by Heerklotz (2002) it has been shown that triton can produce phase separation phenomena that are not present or much less likely in the absence of the detergent. It has to be concluded that the detergent-extraction method cannot serve as a reliable tool to draw conclusions upon the formation of domains of rafts in biomembranes. Domain formation can be influenced by temperature, pH, calcium, and other thermodynamic variables. It seems, therefore, unavoidable that the phase behavior of biomembranes is studied under physiological conditions, i.e., on the intact biomembranes at natural pH, temperature, and buffer conditions. No components (neither lipids nor proteins) shall be extracted and detergents should be avoided. However, under physiological conditions it does not seem certain whether "rafts" actually exist. If they exist they are smaller than microscope resolution, i.e., they are probably smaller than 100 nm.

The discussion on raft is closely related to domain formation, which is the more general phenomenon. As said above, domain formation generally has to be expected in multicomponent systems. Only very few membrane systems actually display ideal mixing. Mixtures of phosphatidylcholines and phosphatidylglycerols mix near ideally (Garidel et al., 1997). In Chapter 19 it will be shown that anesthetics mix nearly ideally with fluid lipid membranes and that this forms the basis for the famous Meyer–Overton rule. Such cases, however, have to be considered as exceptions. Clearly, domain formation phe-

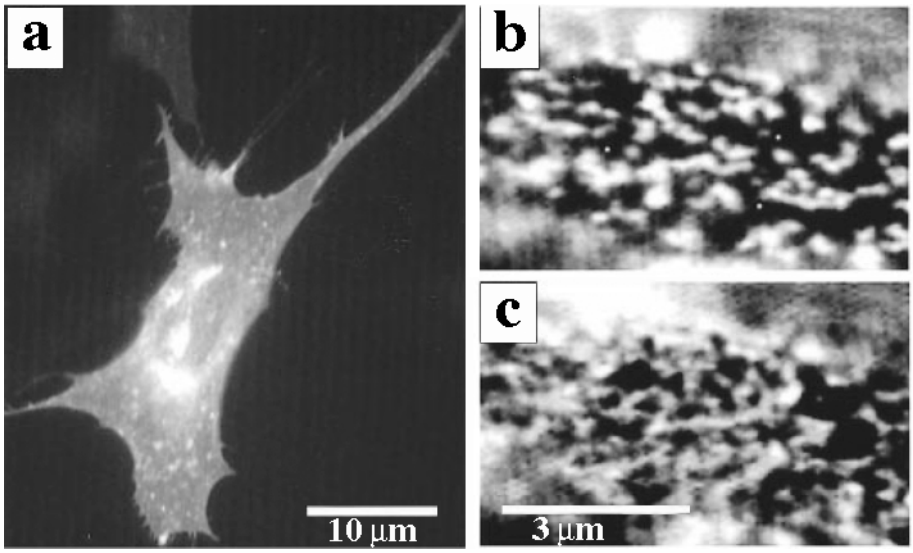

Fig. 9.17 Protein distribution in fibroblast BHK cells adapted from Harder et al. (1998). Left: Fibroblast BHK cell. Right, top: Segment of the cell in the left-hand panel showing the distribution of placental alkaline phosphatase (PLAP) in BHK cells. Right, bottom: distribution of human transferrin receptor (hTfR) in the same membrane segment. Bright regions contain the fluorescently labeled proteins. One can recognize that the proteins are not homogeneously distributed and that PLAP and hTfR are not colocalized.

nomena must take place. Cholesterol shows interesting phase behavior with saturated phospholipids (cf. Chapter 7). It is likely to be an important player but it must not be the only one. Most saturated long-chain lipids are putatively forming ordered domains. Such domains are not expected to generally display well-defined compositions and sizes. More likely, a large diversity of fluctuating domain compositions and sizes have to be expected. In this respect it is interesting to consider segregation of proteins. Protein clustering could already be seen in the classical paper on the fluid mosaic model by Singer and Nicolson (1972) (cf. Fig. 1.6). In the sections above we have discussed the general principles of protein clustering for both integral and peripheral proteins in ordered and disordered lipid phases. Harder et al. (1998) have shown that one can obtain lateral segregation of proteins in fibroblast cell membranes. More specifically, they labeled over expressed and crosslinked glycosyl-phosphatidylinositol (GPI)-anchored proteins, placental alkaline phosphatase (PLAP), hemagglutinin, human transferrin receptor (hTfR) and other proteins with fluorescence markers (Fig. 9.17). It was seen that these proteins were not found at the same positions in the membranes; indicating phase separation phenomena and clustering. In this figure the distributions of PLAP and hTfR are shown. The crosslinking of proteins was necessary to obtain domains of detectable size.

9.6 Summary: Key Ideas of Chapter 9

1. Integral proteins possess a hydrophobic core that may or may not match the thickness of the hydrocarbon region of the lipid membranes. In the latter case the unfavorable hydrophobic matching leads to capillary effects and long-range protein–protein interactions resulting in aggregation.

2. Hydrophobic matching is different in the gel and the fluid lipid phase. Therefore, the lateral distribution of proteins may be different in gel and fluid membranes. Such differences can be detected in heat capacity profiles of lipid–protein mixtures. An example is bacteriorhodopsin in different membranes.

3. Heat capacity profiles shifted to lower temperatures indicate a favorable interaction of proteins with the fluid phase. Proteins will aggregate in the gel phase but mix much better with the fluid phase. The shift of the c_P-profile reflects the changes in protein mixing entropy. An example is cytochrome b_5 in DPPC membranes.

4. Heat capacity profiles shifted to higher temperatures indicate a favorable interaction with the gel phase. Proteins will aggregate in the fluid phase but mix much better with the gel phase. An example is the band 3 protein of erythrocytes in DMPC membranes.

5. Proteins that mix ideally with both lipid phases do not shift heat capacity profiles. They accumulate at the domain interfaces and effectively lower the surface tension of the domains. Thereby they lower the cooperativity. This case is not likely to exist in real membranes because hydrophobic matching cannot be ideal with both lipid phases.

6. Proteins with unfavorable hydrophobic matching with both gel and fluid membranes will always tend to aggregate. In this case the proteins hardly influence calorimetric melting profiles due to the largely reduced interface between proteins and lipids. An example for this case is gramicidin A in DMPC and DPPC membranes.

7. The enzymatic function of integral proteins can be influenced by the degree of hydrophobic matching with the surrounding lipid matrix. An example is melibiose permease.

8. When binding of peripheral proteins is dominated by electrostatic interactions proteins tend to aggregate in the phase coexistence regime. Due to the higher charge density in the gel phase, protein binding is stronger to gel lipids. In the melting regime peripheral proteins accumulate on

gel domains. An example for this behavior is cytochrome c binding to charged lipid membranes.

9. Some peripherally bound enzymes display maximum activity in the lipid melting regime. An example is phospholipase A_2 activity on phosphatidylcholine membranes. This enzymes preferentially hydrolyzes domain interfaces.

10. In biological membranes the coupling between protein localization and the formation of cholesterol-sphingolipid domains has been proposed. Such domains are called 'rafts'. The nature of these rafts is yet under debate. Phase separation phenomena in biomembranes are still not well understood.

11. Detergent extraction leads to an accumulation of raft lipids and some proteins in DRMs (detergent resistant membranes). Such a preparation method, however, is unlikely to yield reliable information on domain formation in biological membranes.

10
Diffusion

Much of this book is dedicated to membranes in thermal equilibrium. Dynamic behavior is treated in Chapters 16 and 18 where the relaxation kinetics and the propagation of density pulses (solitons) are discussed—both are features of nonequilibrated systems. Even though diffusion describes the change of particle positions over time it nevertheless can be considered as a property of equilibrium systems. Thermodynamics considers the most likely state of an ensemble and the thermal fluctuations around this state. In fact, the thermal equilibrium rather describes the most likely distribution of states rather than just one most likely state.

The concept of fluctuations is intimately related to diffusion as shown in the classic paper of Albert Einstein on Brownian motion (Einstein, 1905). Brownian motion is the stochastic motion of objects in viscous fluids due to thermal collisions with the solvent particles. Based on statistical thermodynamics Einstein showed that this motion is well described by

$$\left\langle r^2 \right\rangle \propto Dt \tag{10.1}$$

This law states that the mean square of the translation distance of a particle is linear in time. This law can be verified by following the trajectory of one particle over time, or by averaging the diffusion paths of many particles. The constant D is the diffusion constant and it is inversely related to the viscosity of the surrounding fluid. In two dimensions the diffusion law assumes the form

$$\left\langle r^2 \right\rangle = 4Dt \tag{10.2}$$

The basic concepts for diffusion are well understood for homogeneous and continuous systems. In artificial and biological membranes, however, the matrix is not necessarily homogeneous. Due to domain and possibly "raft" formation (Chapter 9) the viscosity of the lipid matrix will display local variations that must influence the diffusion of both lipids and proteins. The concept of domains in biological membranes is in particular interesting because they influence diffusion pathways and thereby reaction kinetics. Since domain formation can be affected by changing the intensive thermodynamic variables

of the system (temperature, composition, pressure, pH, ...), reaction kinetics will now be sensitively linked to the physics of the membrane. It is very likely that nature makes use of this putatively very powerful control mechanism (that cannot be understood on the single molecule level).

10.1 Percolation

Let us assume a matrix that contains regions with high diffusion constant (e.g., a liquid) and other regions where diffusion is strongly inhibited (e.g., a solid). Then it is obvious that the diffusion of the overall system is influenced by the heterogeneity of the matrix.

Let us consider a triangular lattice and occupy some of the sites with hard particles by using a random number generator. Such a situation is shown in Fig. 10.1. The left-hand panel is 40% filled, the center panel is 50% filled while the right-hand panel is 70% filled. It is easy to see that in the left-hand panel a continuous path of empty sites from one side of the panel to the other can be found, while in the right-hand panel continuous paths of solid particles are seen. This indicates that the first matrix would be permeable for, say, water, while the second may be electrically conducting due to a continuous path of conducting particles. Such connected paths are also called percolating paths. Percolation theory is an important field in mathematics that finds a wide range of applications. For example it is used to predict whether forest fires can propagate and how many trees one has to cut to prevent spreading of fires. It can also be applied to problems where signals propagate in membranes via diffusion.

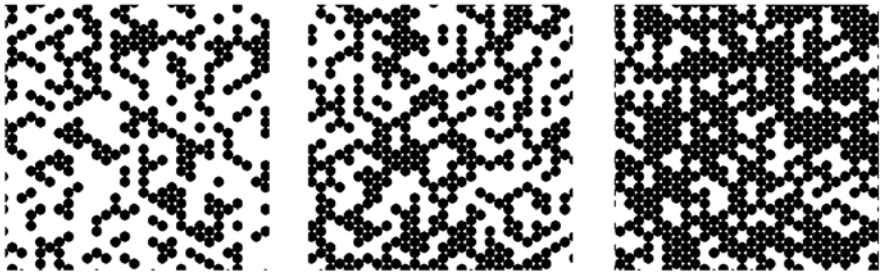

Fig. 10.1 Triangular lattices with different fractions of occupied lattice sites. The sites were randomly filled. Left: 40%. Center: 50%, Right: 70%. The left-hand panel displays a connected (percolating) path of empty sites from one side of the lattice to the other. The right-hand panel, in contrast, shows a continuous path of occupied sites. The center panel is close to the "percolation threshold" between the two other cases. Courtesy Andreas Blicher, NBI Copenhagen.

The center panel of Fig. 10.1 is close to the situation where both the white and the black networks get disconnected. This point is called the percolation threshold. For randomly filled triangular lattices it is found when 50% of the sites are filled. For different lattices one also finds other values.

If we consider a case where diffusion of small particles is possible in the white regions of this matrix but not possible in the black regions one immediately recognizes the importance of percolation theory and percolating paths for diffusion. Close to the percolation threshold one finds continuous paths through the whole matrix but they may be difficult to find and the diffusion time will approach very large values.

Diffusion in the gel phase of lipid membranes is much slower than in the fluid phase (see Table 10.1). Typically, the diffusion constants are different by 2–3 orders of magnitude (as judged from fluorescence correlation spectroscopy). Thus, membranes with coexisting domains can display features resembling the percolation problem in Fig. 10.1. Artificial and biological membranes, however, are not randomly filled lattices. Gel molecules can be changed into fluid molecules by changing temperature (or other variables). Due to cooperative interactions one finds domain formation. Such a situation has been described by Monte Carlo simulations in the previous two chapters and a result of such simulations is shown in Fig. 10.2. Even though the situation in Fig. 10.2 is different from that in Fig. 10.1 one also finds percolating paths. In the left-hand panel of Fig. 10.2 a percolating path of gel lipids can be found, while the right-hand panel displays a near continuous fluid matrix without obstacles. It should also be mentioned that about 50 wt.% of biological membranes are proteins which naturally can also create diffusion obstacles or percolating paths.

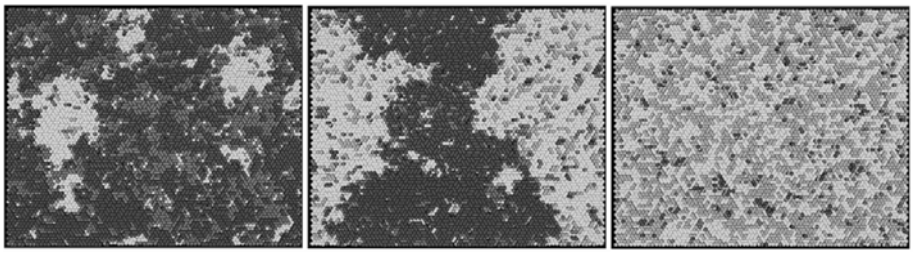

Fig. 10.2 Monte Carlo snapshots of the simulation of DMPC-DSPC membranes at different temperatures, extracted from Fig. 8.7 (details are given in the legend to that figure). In the left-hand panel there is no percolating path of fluid regions. Thus, diffusion is partially confined.

10.2 Diffusion Models

Diffusion in membranes has been described theoretically by various authors. In single component membranes one has used hydrodynamic theory (Saffman and Delbrück, 1975) and free volume theory (Galla et al., 1979). These models make predictions about numerical values of diffusion constants in membranes. Here, we will use experimental values and refer the reader to the two articles above for technical details of the individual diffusion steps.

As long as the matrix is laterally homogeneous diffusion is described by Eq. (10.1). The situation is more complicated when lateral heterogeneities are expected. Some simple cases are shown in Fig. 10.3. Besides diffusion in a pure fluid, the lipid matrix can contain spherical or odd-shaped diffusion obstacles, or the membrane can contain finite regions where diffusion follows normal diffusion behavior. Many such cases have been investigated by M. Saxton. (Saxton, 1987, 1990, 1993, 1994, 1995, 1999, 2001). Below we list the three most relevant examples.

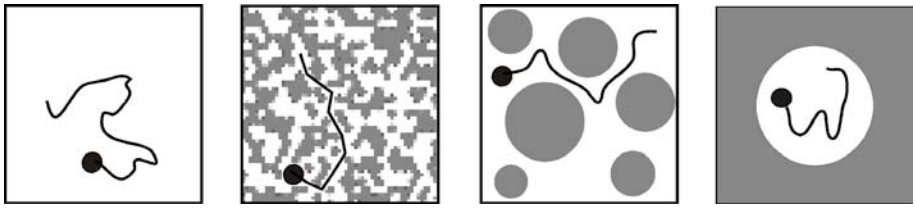

Fig. 10.3 Four limiting cases for diffusion. Left: Homogeneous surface. Center, left: Heterogeneous system close to percolation point. Center, right: Matrix with spherical domains serving as diffusion obstacles. Right: Confined diffusion in local fluid domains. Grey shades indicate regions where diffusion is not possible (diffusion obstacles).

Complex cases as shown in the two center panels of Fig. 10.3 are often described well by the so-called anomalous subdiffusion:

$$\left\langle r^2 \right\rangle = 4Dt^{\alpha} \qquad \alpha < 1 \tag{10.3}$$

In the diffusion equation one finds a critical exponent, $\alpha < 1$. This equation could be written as

$$\left\langle r^2 \right\rangle = 4\left(Dt^{\alpha-1}\right) t = 4\,\widetilde{D}\,(t)\,t \qquad \alpha < 1 \tag{10.4}$$

with $\widetilde{D}\,(t) = Dt^{\alpha-1}$ being a time-dependent diffusion constant. One way to interpret this equation is that the diffusion constant depends on length and time scales and thereby on the characteristic length of the method that is used to determine it. If one finds diffusion behavior that follows this equation one can conclude that the matrix is not laterally homogeneous and that it may

contain obstacles of some kind. The diffusion experiment alone cannot predict the nature of the obstacles. It has been shown by Hac et al. (2005) that the exponent α has no physically clear meaning as long as the microscopic details of the diffusion process are not known. Nevertheless, the finding of $\alpha < 1$ can help to characterize the membrane system.

If diffusion takes place in a membrane in which a steady molecular flow of velocity v exists one obtains

$$\left\langle r^2 \right\rangle = 4Dt + (vt)^2 \tag{10.5}$$

Such cases can happen when directed transport takes place in the membrane. It can also be the consequence of experimental artifacts when the membrane sample is floating. In fluorescence correlation spectroscopy, directed transport leads to autocorrelation curves that strongly differ from the correlation profile of a random walk.

A very important case is that of isolated regions in which diffusion is normal surrounded by connected diffusion obstacles (e.g., in Fig. 10.2, left, or Fig. 10.3, right). Such a case is called corralled diffusion or confinement. The mean square displacement can never be larger than the dimension of the corral. For spherical corrals one finds

$$\left\langle r^2 \right\rangle = \left\langle r_c^2 \right\rangle \left[1 - \exp\left(-\frac{4Dt}{\langle r_c^2 \rangle} \right) \right] \tag{10.6}$$

For short time scales, $4Dt \ll \langle r_c^2 \rangle$, one can expand the exponential term and Eq. (10.6) simplifies to Eq. (10.1). This is expected as long as the mean diffusion path r is shorter than the radius r_c of the corral.

Some further examples for percolating and corraled lipid membranes are shown in Figs. 8.3, 8.7, and 8.8.

10.3 Diffusion of Lipids and Proteins

The diffusion behavior of various molecules have been studied by many methods. The most important are:

- *Fluorescence recovery after photobleaching (FRAP).* In this method the diffusion of labeled particles is monitored in a microscope. Fluorescent markers can be bleached by high intensities of light in their absorption frequency regime. In FRAP, the fluorescence intensity is bleached in the microscope focus, and the recovery of the signal due to particle diffusion back into the focal spot is monitored. FRAP has in particular been used by Almeida, Vaz, and Thompson to study phase behavior

in membranes. FRAP has been especially useful to investigate diffusion in the melting regime of lipid mixtures (Vaz et al., 1989, 1990; Vaz and Almeida, 1991; Almeida et al., 1992; Almeida and Vaz, 1995). One can show that FRAP often is not complete when measured in the melting regime of binary or ternary lipid mixtures. From this one concludes that the diffusion obstacles in such membranes percolate such that one obtains corralled diffusion (Eq. 10.6). Under such conditions, diffusion does not lead to a complete recovery of the fluorescence. The diffusion obstacles in this case are percolating gel domains, while the matrix in which the lipids diffuse are the fluid domains. In FRAP, the diffusion constants within the gel phase are found to be so small that it practically can be ignored. Incomplete FRAP indicates that the fluid domains must be smaller than the fluorescence focus.

- *Fluorescence correlation spectroscopy (FCS).* When fluorescent particles diffuse through an illuminated spot they emit a light pulse that displays a characteristic time scale on the order of the mean dwell time of the label in the focus. An ensemble of diffusing particles generates fluorescent noise. The mean dwell time that is related to the diffusion constant can be obtained from an autocorrelation analysis of the fluorescence noise (Eigen and Rigler, 1994). FCS has been used by many authors to determine diffusion constants in artificial and biological membranes (Korlach et al., 1999; Schwille et al., 1999b,a; Pramanik et al., 2000; Feigenson and Buboltz, 2001; Böckmann et al., 2003). It has been shown by Hac et al. (2005) that in lipid mixtures in the phase coexistence regime one finds anomalous diffusion that can be explained on the basis of statistical thermodynamic simulations. While diffusion constants in fluid lipid phases are very similar to those found by FRAP, diffusion in the gel phase yields larger values. This may be due to some confined motion that cannot be resolved by this method.

- *Single particle tracking (SPT).* Instead of studying ensemble fluctuations one can also follow the diffusion behavior of individual particles labeled with fluorescence or gold markers (Schmidt et al., 1995, 1996; Schütz et al., 1997; Sonnleitner et al., 1999; Harms et al., 1999, 2001). With this method one can actually see the diffusion path and the corralled structure of the membranes. In biological membranes one finds confined diffusion of proteins (Kusumi et al., 1993).

- *Nuclear magnetic resonance in field gradients*. Here, the diffusion can be seen when the particles diffuse out of the regime of their resonance frequency (Fisher, 1978; Kuo and Wade, 1999; Oradd et al., 2002).

- *Neutron scattering*. (Tabony and Perly, 1990; König et al., 1992, 1995). Since the scattering time scale is in the picosecond regime, neutron scattering can only see particle movements on length scales much shorter than the lipid or protein diameters. The diffusion constants measured by this method are usually much larger than those found by other methods (Vaz and Almeida, 1991). On the length scale of domains in membranes, the diffusion constants obtained by neutron scattering cannot be applied.

In Table 10.1 some representative numbers for protein and lipid diffusion are shown. For a more detailed overview see the reviews by Saxton and Jacobson (1997); Saxton (1999).

Tab. 10.1 Diffusion constants of selected lipids and proteins in artificial and biological membranes. Data partially taken from a collection in Saxton and Jacobson (1997). References: 1—Fries et al. (1998), 2—Hac et al. (2005), 3—Korlach et al. (1999), 4—Fein et al. (1993), 5—Lee et al. (1993), 6—Scheets and Jacobson (1996). Methods were FCS (fluorescence correlation spectroscopy), SPT (single particle tracking) and FRAP (fluorescence recovery after photobleaching.)

Diffusing component	System	D (10^{-10} cm^2/s)	Technique	Reference
Rhodamine 6G	Water	30000	FCS	1
Lipids artificial membranes				
Di18	Fluid DMPC	400 (390)	FCS	2 (3)
Di18	Gel DMPC	5 (2)	FCS	2 (3)
Biotin-PE	80% egg PC 20% cholest.	25	SPT	4
GPI-linked proteins artificial membranes				
DAF (CD55)	80% egg PC 20% cholesterol	25	SPT FCS	4
FcγRIIIB (CD16)	Same	56	SPT	4
Lipids biological membranes				
Fi-PE	Fibroblasts	12 (54)	SPT (FRAP)	5
GPI-linked proteins biological membranes				
Thy-1	Fibroblasts	Fast (69%):7.2	SPT	6
		Slow (31%): 0.2	SPT	6
MHCI (Qa2)	HEPA-OVA	2.1(2–4)	SPT (FRAP)	6

10.4 Summary: Key Ideas of Chapter 10

- Diffusion in a homogenous two- dimensional membrane is described by $\langle r^2 \rangle = 4Dt$.
- In the presence of diffusion obstacles the diffusion laws are less simple. Such obstacles can be protein networks, gel lipid domains or rafts. Connected obstacles may form percolating paths. Diffusion pathways are disrupted and diffusion laws change.
- In the presence of obstacles one often finds "anomalous diffusion" described by $\langle r^2 \rangle = 4Dt^{\alpha}$.
- When obstacles are connected and isolated regions are formed, one finds confined diffusion. This is a frequent situation in lipid phase transition regimes were the fluid domains become disconnected.
- Confined diffusion influences reaction and signalling networks.

11
Electrostatics

Approximately 10–40% of the naturally occurring lipids carry a charge (depending on the nature of the membrane)—usually one or two negative charges. The rest of the lipids is neutral or zwitterionic. Positively charged lipids are not found in nature. They can, however, be chemically synthesized for gene delivery purposes and for studies on the interactions between DNA and membranes (Rädler et al., 1997; Salditt et al., 1997). Lipid membranes strongly interact with proteins many of which also carry charges. The water soluble protein cytochrome c carries nine positive charges. Thus, proteins may bind to the negatively charged lipid membranes. A typical value for the ion concentration in biological cells is 150 mM NaCl, but it varies largely. Inside the squid axon one finds about 400 mM KCl.

In this chapter we address the following questions:

- What is the influence of the ionic strength on the electrostatic potentials?
- What is the spatial distribution of ions?
- What is the electrostatic free energy of the membrane?
- How is the binding of proteins influenced by the ionic strength and the charge density of the membrane?
- What is the lateral pressure induced by charging the membrane?

11.1
Diffuse Double Layer—Gouy–Chapman Theory

The electrostatic potential $\Psi(\underline{r})$ of a charge distribution $\rho(\underline{r})$ at location $\underline{r}$ is given by a Poisson equation:

$$\Delta\Psi(\underline{r}) = -\frac{\rho(\underline{r})}{\epsilon_0\epsilon} \tag{11.1}$$

with the permittivity $\epsilon_0 = 8.854 \times 10^{-12}\mathrm{C}^2/\mathrm{J\,m}$ and the relative permittivity (dielectric constant) $\epsilon = 80.4$ for water at $20\,^{\circ}\mathrm{C}$ (see Table 5.2 for a list of

dielectric constants). The concentration c_i of an ion of species i with charge $z_i \cdot e$ ($e = 1.602 \times 10^{-19}$C) at location $\underline{r}$ is given according to the Boltzmann distribution:

$$c_i(\underline{r}) = c_{i,0} \exp\left(-\frac{z_i \cdot e\Psi(\underline{r})}{kT}\right) \tag{11.2}$$

Here, $c_{0,i}$ is the concentration of ion species i at the location with the zero potential $\Psi = 0$ (at infinite distance from the membrane). z_i may be positive or negative. The charge density is given by

$$\rho(\underline{r}) = \sum_i z_i \cdot e \cdot c_i(\underline{r}) \tag{11.3}$$

To be consistent with the units, the concentrations $c_{i,0}$ have to be given in molecules/m^3. If Eq. (11.2) is inserted into Eq. (11.3), and the result is then inserted into Eq. (11.1), one obtains

$$\Delta\Psi(\underline{r}) = -\frac{1}{\epsilon_0\epsilon} \sum_i z_i \cdot e \cdot c_{i,0} \exp\left(-\frac{z_i \cdot e \cdot \Psi(\underline{r})}{kT}\right) \tag{11.4}$$

This equation is called the "Poisson–Boltzmann equation." One can solve it numerically for given boundary conditions, e.g., with fixed charges on a membrane surface. For this there are programs available in the Internet[1], which have now also been implemented into some protein viewer programs.

For the simple geometry of a planar membrane one can simplify this equation such that it can be solved analytically. This will be shown in the following paragraphs.

At infinite distance from the charged surface (potential $\Psi = 0$) the charge density must be zero (electro-neutrality). This leads to the boundary condition:

$$\sum_i z_i \cdot e \cdot c_{i,0} = 0 \tag{11.5}$$

For small potentials Ψ (i.e., for $z_i e\Psi \ll kT$) one can develop Eq. (11.4) into a Taylor series and linearize

$$\begin{aligned} \Delta\Psi(\underline{r}) &= \left(2\frac{e^2}{\epsilon_0\epsilon kT}\left[\frac{1}{2}\sum_i z_i^2 c_{i,0}\right]\right) \cdot \Psi(\underline{r}) \\ &\equiv \left(2\frac{e^2}{\epsilon_0\epsilon kT} c_0\right) \cdot \Psi(\underline{r}) \equiv \kappa^2 \cdot \Psi(\underline{r}) \end{aligned} \tag{11.6}$$

1) Delphi by Barry Honig and collaborators (http://lipid.bioc.columbia.edu/~xu/).

In this equation we have introduced the ionic strength, c_0 and the Debye constant, κ. The ionic strength is defined as

$$c_0 \equiv \text{ionic strength} = \frac{1}{2}\sum_i z_i^2 c_{i,0} \tag{11.7}$$

For a monovalent salt like NaCl the ionic strength is identical to the salt concentration. $1/\kappa$ is called the Debye length. It can be considered as the screening distance of an electrostatic charge. It depends on the ionic strength. The Debye constant κ is given by

$$\kappa = \left(2\frac{e^2}{\epsilon_0 \epsilon kT} c_0\right)^{0.5} \tag{11.8}$$

κ has units of an inverse length (1/m). The concentrations in this and the previous equations carry the units "molecules/m^3" (i.e., 1 M $\equiv$ 6.0223 $\times$ 10^{26}/m^3).

The inverse of the Debye constant, $1/\kappa$, has the units of a distance. It is called the *Debye length*. It can be considered as the screening distance of an electrostatic charge. This becomes obvious in Eq. (11.10), given below. It depends on the ionic strength such that the electrostatic screening length decreases if the ionic strength is increased.

If the ionic strength, c_0, is given in units of (mol/l), then at $T = 300$ K

$$\text{Debye length (nm)} = \kappa^{-1} = 0.3082/\sqrt{c_0} \tag{11.9}$$

Some values are given in Table 11.1.

It is interesting to note that the typical screening length at biological ionic strength ($\approx$ 150 mM) is on the order of a lipid diameter or the diameter of

Tab. 11.1 Debye length for various NaCl concentrations at $T = 300$ K. The Debye length is the screening length of the electrostatic potential, cf. Eq. (11.10).

Ionic strength	Debye length κ^{-1} (nm)	Ionic strength	Debye length κ^{-1} (nm)
100 µM	30.82	20 mM	2.18
200 µM	21.79	50 mM	1.38
500 µM	13.78	100 mM	0.97
1 mM	9.75	200 mM	0.69
2 mM	6.89	500 mM	0.44
5 mM	4.36	1 M	0.31
10 mM	3.08	2 M	0.22

an α-helix. Thus, it is on the order of the length scale of biological macromolecules. Changes in ionic strength (or pH) therefore significantly influence the electrostatic forces within charged macromolecules under physiological conditions. The Debye length has already been used in Section 5.2 to describe the electrostatic screening of a central charge but was not derived there.

Let us now consider an infinitely extended planar membrane with homogeneous charge density. Then, there is only an ion concentration gradient along the x-axis (defined here as being perpendicular to the membrane plane), and the Laplace operator can be replaced by $\Delta \rightarrow d^2/dx^2$. Under such conditions the differential equation (11.6) that has been obtained for low potentials has the simple solution

$$\Psi(x) = \Psi_0 \exp(-\kappa x) \tag{11.10}$$

Obviously, the potential decreases at increasing distance from the membrane and is maximum at its surface (see Fig. 11.1). In the following we determine the surface potential, Ψ_0. After multiplying Eq. (11.4) with $2d\Psi/dx$ we obtain

$$\left(2\frac{d\Psi(x)}{dx}\right)\frac{d^2\Psi(x)}{dx^2} = -\left(2\frac{d\Psi(x)}{dx}\right)\cdot\frac{1}{\epsilon_0\epsilon}\sum_i z_i\cdot e\cdot c_{i,0}\exp\left(-\frac{z_i e\Psi(x)}{kT}\right) \tag{11.11}$$

Using the boundary conditions ($\Psi \rightarrow 0$ and $d\Psi/dx \rightarrow 0$ for $x \rightarrow \infty$) this can be easily integrated from ∞ to x and one obtains

$$\left(\frac{d\Psi(x)}{dx}\right)^2 = \frac{2kT}{\epsilon_0\epsilon}\sum_i c_{i,0}\left[\exp\left(-\frac{z_i e\Psi(x)}{kT}\right) - 1\right] \tag{11.12}$$

In the simplifying case of an electrolyte solution (salt solution) of univalent ions ($z = \pm 1$, e.g., NaCl $\rightarrow$ $Na^+ + Cl^-$, but not $CaCl_2 \rightarrow Ca^{2+} + 2Cl^-$). Equation (11.12) becomes

$$\frac{d\Psi(x)}{dx} = -\sqrt{\frac{2kT\cdot c_0}{\epsilon_0\epsilon}}\left[\exp\left(\frac{e\Psi(x)}{2kT}\right) - \exp\left(-\frac{e\Psi(x)}{2kT}\right)\right] \tag{11.13}$$

The membrane surface shall carry a surface charge density of σ. Due to electro neutrality one finds

$$\sigma = -\int_0^\infty \rho(x)dx \overset{\text{Eq.(11.1)}}{=} +\int_0^\infty \epsilon_0\epsilon\frac{d^2\Psi(x)}{dx^2}dx = -\epsilon_0\epsilon\left(\frac{d\Psi(x)}{dx}\right)_{x=0} \tag{11.14}$$

By using Eq. (11.13) $(d\Psi/dx)_{x=0}$ can be expressed as a function of $\Psi(0) \equiv \Psi_0$, which is the potential at the membrane surface. Using Eq. (11.13), Eq. (11.14)

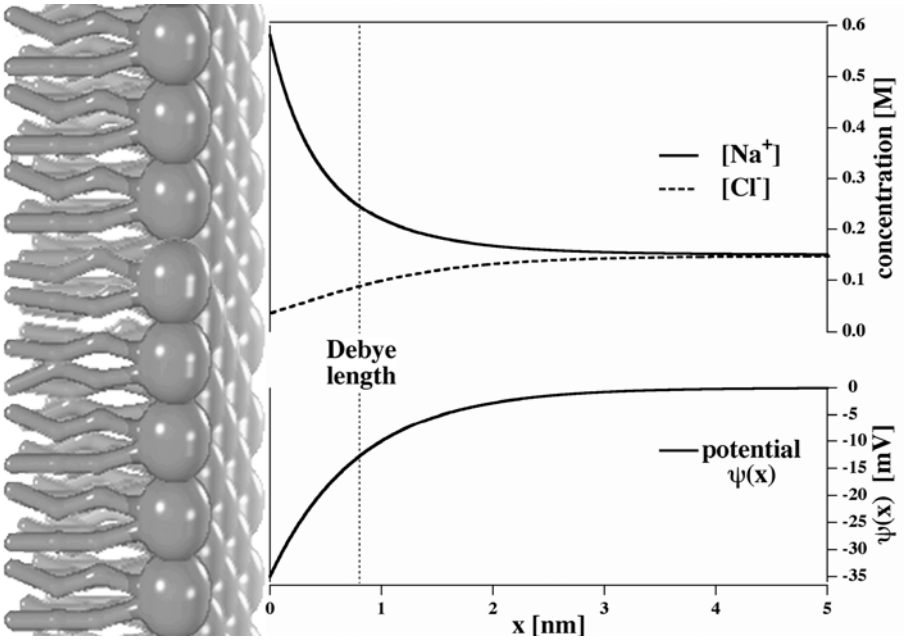

Fig. 11.1 Distribution of sodium and chloride ions and the electrostatic potential close a lipid surface with 10% charged lipids and an ionic strength corresponding to 150 mM NaCl. Under these conditions, the surface potential is -36 mV and the Debye length is 0.8 nm. The sodium concentration is increased close to the lipid head groups. Calculated using Eqs. (11.10) and (11.16). The lipid size in this graph is on realistic scale.

transforms into

$$\begin{aligned}\sigma &= \sqrt{2\epsilon_0\epsilon\, c_0 kT}\cdot\left[\exp\left(\frac{e\Psi_0}{2kT}\right)-\exp\left(-\frac{e\Psi_0}{2kT}\right)\right]\\ &= \sqrt{8\epsilon_0\epsilon\, c_0 kT}\sinh\left(\frac{e\Psi_0}{2kT}\right)\end{aligned} \tag{11.15}$$

or

$$\Psi_0 = \frac{2kT}{e}\sinh^{-1}\left(\sqrt{\left(\frac{1}{8\epsilon_0\epsilon kT}\right)}\frac{\sigma}{\sqrt{c_0}}\right) \tag{11.16}$$

The surface potential for three different charge densities is shown in Fig. 11.2 as a function of ionic strength. At physiological conditions ($c_0 \approx 150$ mM) it is not very dependent on the ionic strength. The potential varies significantly at low ionic strength. Scientists measuring at low ionic strength or in distilled water should be warned! A membrane similar to a biological membrane with about 10% negatively charged lipids (area per lipid $\approx 0.5\,\mathrm{nm}^2$,

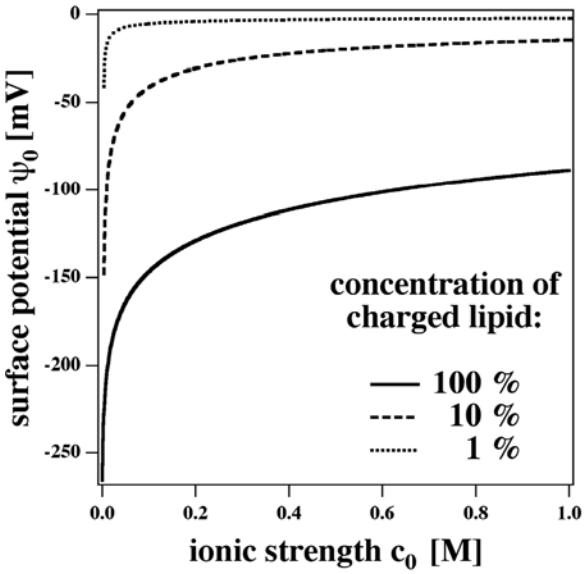

Fig. 11.2 Surface potential of a planar membrane as a function of ionic strength with 100%, with 10% and with 1% of the lipids being negatively charged. Calculated using Eq. (11.16).

charge density $\approx 0.32\text{C}/\text{m}^2$) displays a surface potential of $\Psi_0 = -36$ mV. This is the order of magnitude that has been found experimentally. Biological membranes are usually asymmetrically charged. While the outer monolayer contains high amounts of uncharged lipids, the inner monolayer is enriched in charged lipids. Nerve membranes typically possess potential differences of -70 mV between inside and outside Johnston and Wu (1995).

For low surface potentials ($|e\Psi_0| \ll 2kT$, i.e., $|\Psi| < 50$ mV) this can be approximated by

$$\sigma = \sqrt{2\epsilon_0\epsilon\, c_0 kT} \cdot \frac{e\Psi_0}{kT} = \epsilon_0\epsilon\kappa\Psi_0 \qquad \text{cf. Eq. (11.8)} \tag{11.17}$$

or

$$\Psi_0 = \frac{1}{\epsilon_0\epsilon\kappa}\sigma \qquad \text{low potential approximation} \tag{11.18}$$

using the Debye constant κ. As can be seen in Fig. 11.3 the conditions for low potentials are only fulfilled at very high ionic strength and low fractions of charged lipid.

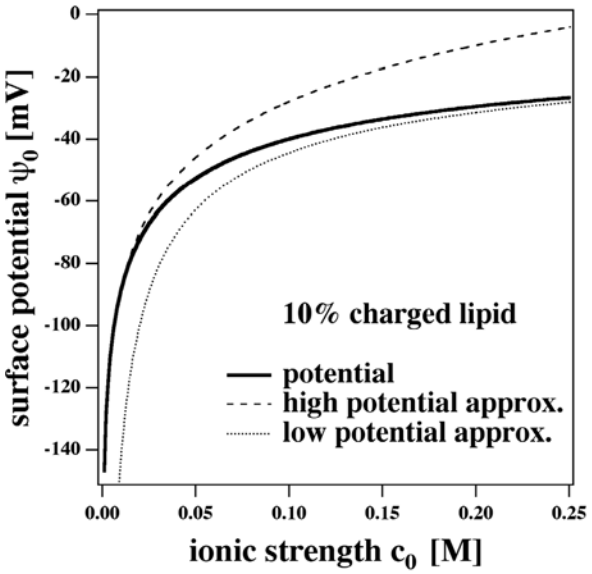

Fig. 11.3 Surface potential of a planar membrane as a function of ionic strength in the case where 10% of the lipids are negatively charged. Also shown are the high and low potential approximations. The high potential approximation yields good values above $|\Psi_0| = 50$ mV and fails at lower potentials. The low potential approximation yields good values for $|\Psi_0| < 50$ mV.

For large surface potentials ($|e\Psi_0| \gg 2kT$ or $|\Psi_0| > 50$ mV) one can approximate Eq. (11.15) by

$$\Psi_0 = \frac{2kT}{e} \ln\left(\sqrt{\frac{1}{2\epsilon_0\epsilon\, c_0 kT}}\,\sigma\right) \qquad \text{for} \qquad \sigma > 0 \qquad \text{high potential approx.}$$

$$\Psi_0 = -\frac{2kT}{e} \ln\left(-\sqrt{\frac{1}{2\epsilon_0\epsilon\, c_0 kT}}\,\sigma\right) \qquad \text{for} \qquad \sigma < 0 \tag{11.19}$$

For the example of an lipid membrane with 10% charged lipid the low and high potential approximations are plotted as a function of ionic strength in Fig. 11.3. The high potential approximation leads to good values only if $|\Psi_0| > 50$ mV. The low potential approximation leads to reasonable values for $|\Psi_0| < 50$ mV.

11.2
Potential and Free Energy of Membranes

A lipid membrane with N negatively charged lipids has the charge $q = -N \cdot e$. A single lipid has an area of A_L, taken here as $A_L \approx 0.5$ nm^2. For a fully charged membrane the charge density is then given by $\sigma = -e/A_L$. Let us assume the membrane as a two-dimensional system under conditions of constant area, i.e., $A_L = \text{const}$. For such systems the equilibrium is described by the Helmholtz free energy, F.

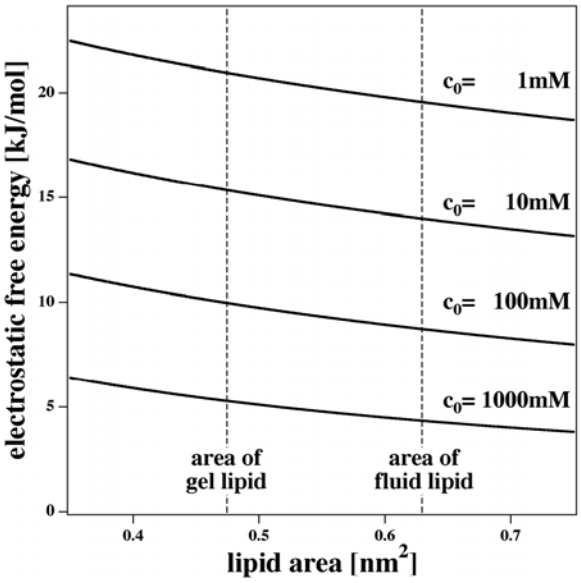

Fig. 11.4 Electrostatic free energy of a lipid membrane consisting of 100% negatively charged lipids as a function of lipid area. Calculation for four different ionic strengths using Eq. (11.22)

The differential of the Helmholtz free energy of a charged system is given by

$$dF = -SdT + \Pi dA + \Psi dq \overset{A,T=\text{const.}}{=} \Psi dq \tag{11.20}$$

The contribution of electrostatics to the free energy per mole of lipid is then given by

$$F_{\text{el},L} = \int_{q=0}^{e} \Psi_0 dq = A_L \int_{\sigma'=0}^{\sigma} \Psi_0 d\sigma' \tag{11.21}$$

By integrating Eq. (11.16) one obtains for the free energy

$$\begin{aligned} F_{\mathrm{el},L} &= A_L \int_{\sigma'=0}^{\sigma} \Psi_0 \, d\sigma' \\ &= A_L \left(\sigma\Psi_0 - (4\epsilon_0\epsilon) \left(\frac{kT}{e}\right)^2 \kappa \left[\cosh\left(\frac{e\Psi_0}{2kT}\right) - 1 \right] \right) \end{aligned} \tag{11.22}$$

This expression can be checked by inspection: differentiation of the term in brackets yields Ψ_0. The molar electrostatic free energy is obtained by multiplying with Avogadro's number.

The electrostatic contribution to the free energy is dependent on the area per lipid and on the ionic strength. F_{el} is shown as a function of lipid area in Fig. 11.4.

11.3 Influence of Electrostatics on Melting Temperatures of Membranes

Upon lipid melting the area per lipid increases. Therefore, the electrostatic potential of a charged membrane will also change. In the following we want to determine the influence of the potential on the melting points of membranes.

The areas of gel and fluid lipids shall be given by $A_{L,\mathrm{gel}}$ and $A_{L,\mathrm{fluid}}$, respectively. ΔA_L is the area difference between gel and fluid lipids. Let us take the areas of DPPC as an example. The parameters for this lipids are given in Table 11.2. The area of the lipid membrane increases upon melting, thus the electrostatic free energy decreases. Since we talk about constant area conditions, in the following we will use the internal energy of lipids rather than the enthalpy. The values for ΔE and ΔS can be assumed to be constant.

Tab. 11.2 Internal energy, entropy, and T_m of a lipid without electrostatics (values are those of DPPC). Further, the electrostatic free energy found under the assumption that the lipids carry one net negative charge is given.

ΔE^0	35 kJ/mol
ΔS^0	111.3 J/mol· K
ΔT_m^0	314.3 K
$A_{L,\mathrm{gel}}$	0.474 nm^2
$A_{L,\mathrm{fluid}}$	0.629 nm^2

Ionic strength (mM)	$F_{\mathrm{el},L}^{\mathrm{gel}}$ (kJ/mol)	$F_{\mathrm{el},L}^{\mathrm{fluid}}$ (kJ/mol)	$\Delta F_{\mathrm{el},L}$ (kJ/mol)
1	20.9708	19.577	−1.394
10	15.3444	13.9888	−1.356
100	9.96519	8.72326	−1.242
1000	5.28414	4.33364	−0.950

Intuitively one would predict that the melting temperature of a charged lipid membrane is lower than that of a neutral membrane, since the charges on the head groups repel each other, favoring the fluid state with larger area.

Let us assume that the membrane undergoes a change from gel to fluid. In the absence of electrostatics one finds

$$\begin{aligned} F^0_{\text{gel}} &= E^0_{\text{gel}} - T \cdot S^0_{\text{gel}} \\ F^0_{\text{fluid}} &= E^0_{\text{fluid}} - T \cdot S^0_{\text{fluid}} \\ \Delta F^0 &= \Delta E^0 - T\Delta S^0 \end{aligned} \tag{11.23}$$

At the melting temperature, T_m, $\Delta F^0 = 0$ and we obtain

$$T^0_m = \frac{\Delta E^0}{\Delta S^0} \tag{11.24}$$

In the presence of electrostatics we obtain

$$\begin{aligned} F_{\text{gel}} &= E^0_{\text{gel}} - T \cdot S^0_{\text{gel}} + F^{\text{gel}}_{\text{el},L} \\ F_{\text{fluid}} &= E^0_{\text{fluid}} - T \cdot S^0_{\text{fluid}} + F^{\text{fluid}}_{\text{el},L} \end{aligned} \tag{11.25}$$

Again, at the melting temperature, T_m the free energies of the two phases are equal. This leads to

$$\Delta E^0 - T_m \Delta S^0 = -\Delta F_{\text{el},L} \tag{11.26}$$

and the melting temperature, T_m is given by

$$T_m = \underbrace{\frac{\Delta E^0}{\Delta S^0}}_{T^0_m} + \frac{\Delta F_{\text{el},L}}{\Delta S^0} = T^0_m \left(1 + \frac{\Delta F_{\text{el},L}}{\Delta E^0}\right) \tag{11.27}$$

using $\Delta S^0 = \Delta E^0 / T^0_m$. Thus, in the presence of electrostatics the transition shifts by

$$\Delta T_m = T^0_m \frac{\Delta F_{\text{el},L}}{\Delta E^0} \tag{11.28}$$

Inserting the values from Table 11.2 one obtains the shifts of transition temperatures given in Table 11.3.

At low ionic strength the shift is $\Delta T_m \approx -12.5$ K. For lipids with shorter chains and lower transition enthalpies, the shift would be significantly higher. The change in transition temperature of MPA (methylphosphatidic acid) shown in Fig. 11.5 was induced by protonation (lowering of pH). It was found to be about $\Delta T_m \approx -14$ K. One can further see that the melting temperature

Tab. 11.3 Shift in transition temperature of a lipid upon charging with the parameters of Table 11.2 at four different ionic strengths.

Ionic strength (mM)	ΔT_m (K)
1	−12.5
10	−12.2
100	−11.2
1000	−8.5

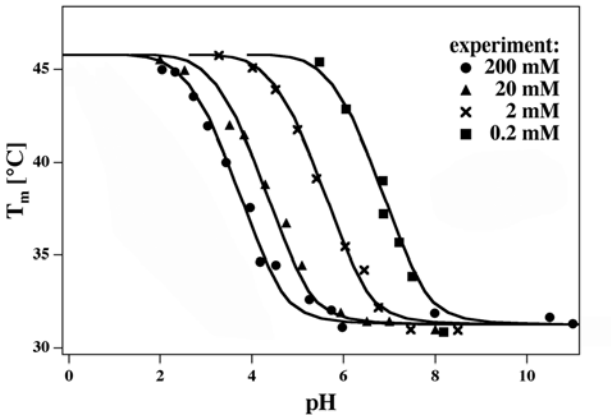

Fig. 11.5 Titration of methylphosphatidic acid (MPA) membranes with protons at different ionic strength conditions. Lower ionic strength leads to larger surface potentials and a shift of the titration profile to higher pH values. At low ionic strength the membranes are right in the transition regime at neutral pH. Data adapted from Träuble et al. (1976)

of charged lipids shows a slight dependence on ionic strength. At 100 mM salt the transition temperature is about 1.3 K higher than at 1 mM.

11.4 Titration of Charged Lipid Membranes with Protons

The pK_A of a charged membrane corresponds to that pH value at which 50% of all charged head groups are protonated. Figure 11.5 demonstrates that the pK_A of the membrane increases for lower ionic strengths. This is discussed below. The effect has been carefully investigated by Träuble, Jähnig, and collaborators (Träuble et al., 1976; Jähnig, 1976).

On the basis of calculations similar to those in the previous paragraph, Träuble and coworkers calculated the ionic strength dependence of the protonation of a charged lipid membrane with a protonable head group. At low pH the free proton concentration is high, and the charges on the lipids are neutralized by binding of protons. At high pH, the free proton concentration is low, the

protons dissociate and the lipids are charged. In Fig. 11.5 it can be seen that an uncharged membrane of methyl phosphoric acid (MPA) has a melting point of about 32 °C at low pH. If the pH is increased the melting point is about 46 °C. When going from low to high pH one can see that the melting point decreases with pH. For zwitterionic lipids this happens at a pH of about 1.5. The half value of the titration curve is called the pK_A of the membrane.

When the ionic strength is increased, the pK_A shifts to lower values. At an ionic strength of 200 mM the pK_A is at about 5. This means that at physiological ionic strength the membrane is close to the pK_A. At low ionic strength the pK_A may well be at neutral pH. Therefore, one should be very careful when investigating charged lipids. At low ionic strength one may be in a two-phase coexistence regime. Therefore, experimental pH and ionic strength should be chosen with care.

11.5 Binding of Charged Proteins

When positively charged (basic) proteins bind to negatively charged membranes, they reduce the effective charge on the surface in a way comparable to the protonation of the surface. The protein cytochrome c possesses a net effective positive charge of $+4e$ and covers about 12 lipids. At complete saturation of a lipid surface consisting of negatively charged lipids with a charge of $q = -e$, the charge density is therefore reduced by 33%. Under these conditions and taking the parameters in Table 11.2 one arrives at $\Delta F_{\mathrm{el},L} = 0.885$ kJ/mol at 10 mM salt. Without the adsorption of protein, $\Delta F_{el,L} = -1.356$ kJ/mol, respectively.

Thus, the binding of cytochrome c to a negatively charged lipid membrane changes the transition temperature by

$$\Delta T_m = T_m^0 \frac{\Delta F_{\mathrm{el},L}}{\Delta E^0} \approx 4.2 \text{ K} \tag{11.29}$$

This shift compares well with that seen in the calorimetric experiment with cytochrome c and DMPG membranes (Heimburg and Biltonen, 1996) (see Fig. 11.6). Therefore, the electrostatics of membranes and of protein binding can be reasonably well understood on the basis of relatively simple approximations, i.e., the Gouy–Chapman equations.

The adsorption of proteins to membranes will be studied in more detail in Chapter 12.

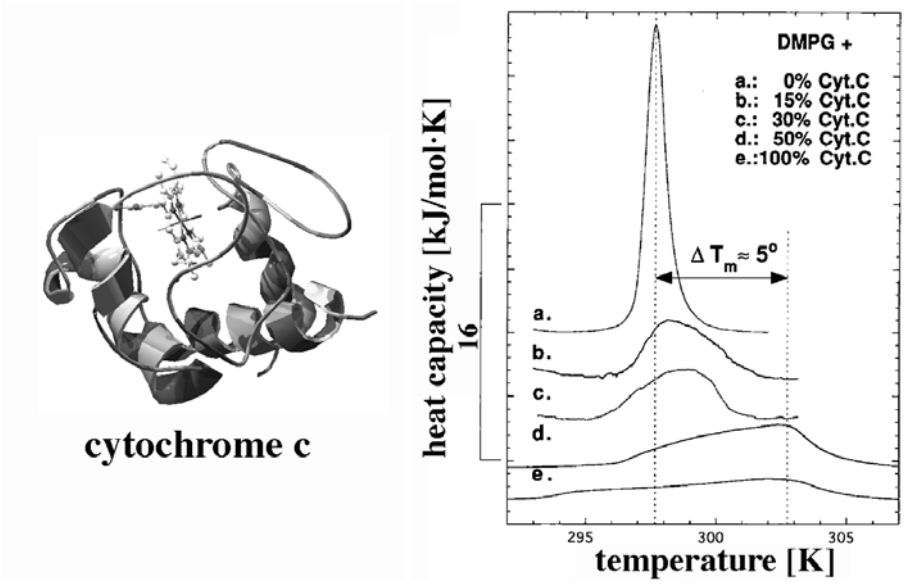

Fig. 11.6 Influence of the binding of cytochrome c (net charge ≈ 4) to DMPG membres at high lipid concentrations. The transition maximum shifts to higher temperatures. Data adapted from Heimburg and Biltonen (1996)

11.6 Lateral Pressure Induced by Charges

One can interpret the influence of an electrostatic field on a membrane transition also in terms of a lateral pressure generated by the field. This implies that lateral pressure changes must not necessarily be caused by external mechanical forces. In Chapter 18 the propagation of lateral density pulses is described. They can in principle be generated by changes in the field.

We now want to calculate the lateral pressure generated by the electrostatics of the membrane.

$$\Pi_{\mathrm{el}} = -\left(\frac{dF_{\mathrm{el},L}}{dA_L}\right)_{T,q} \tag{11.30}$$

From Eq. (11.22) it follows that[2]

$$\Pi_{\mathrm{el}} = \sigma\Psi_0 - \frac{F_{\mathrm{el},L}}{A_L} \tag{11.31}$$

2) Let us abbreviate the free energy given in Eq. (11.22) as $F_{\mathrm{el},L} = A_L \cdot Y$. Then $dF_{\mathrm{el},L}/dA_L = A_L \cdot dY/dA_L + Y$. dY/dA_L can be written as $dY/d\sigma \cdot d\sigma/dA_L$. $dY/d\sigma$, however, is equal to Ψ_0. From this follows Eq. (11.31).

Tab. 11.4 Pressure created by the electrostatics for a fully charged membrane with the parameters in Table 11.2.

Ionic strength (mM)	Π_g (N/m)	Π_f (N/m)	ΔT_m (K)
1	0.0907	0.0646	−12.64
10	0.0706	0.0495	−12.64
100	0.0157	0.0081	−12.55
1000	0.0124	0.0059	−11.73

Taking $A_L = 0.5$ nm^2 and $\Psi_0 = -150$ mV (for $c_0 = 100$ mM and a fully charged membrane) one obtains a lateral pressure of 0.0481 N/m (see Table 11.4).

To get a feeling for what these pressures mean it is helpful to relate them to the membrane cross section, which is about 5 nm. A lateral pressure of 0.0907 N/m then corresponds to 181 bar. These pressures are significant.

From Chapter 6 it is known that melting temperatures change upon pressure. One can also calculate the resulting shift in transition temperature using

$$\Delta T_m = T_m \frac{\Delta(\Pi A_L)}{\Delta H_0} = T_m \frac{(\Pi_f A_f - \Pi_g A_g)}{\Delta H_0} \tag{11.32}$$

where ΔH_0 is the enthalpy change in the absence of electrostatics. Values calculated with this approximation are given in Table 11.4. They are nearly identical to those from Table 11.3 calculated from the electrostatics directly. Thus, the changes in electrostatic free energy correspond to the work done against a lateral pressure created by the charging of the membrane.

11.7 Summary: Key Ideas of Chapter 11

1. A charged lipid membrane creates an electrostatic potential that can be calculated using the Gouy–Chapman theory.
2. The potential contributes to the free energy of the membrane.
3. The electrostatic free energy is lower in the fluid phase than in the gel phase of a lipid membrane. As a consequence the charged membrane displays lower melting points. The shift is on the order of $\Delta T_m = -15\,\mathrm{K}$, depending on the chain melting enthalpy and the lipid areas.
4. Negatively charged membranes become neutral upon protonation. For this reason lowering of the pH has a significant influence on the melting temperatures, typically leading to an increase of the melting point by $\approx 15\,\mathrm{K}$.
5. The $\mathrm{p}K_A$ of a charged membrane is strongly influenced by ionic strength. The lower the ionic strength the higher the $\mathrm{p}K_A$. At an ionic strength of 1 mM the $\mathrm{p}K_A$ of a fully charged membrane is in the neutral pH regime.
6. Similarly, when basic proteins bind to negatively charged membranes the melting temperatures increase.
7. From the area dependence of the electrostatic free energy a lateral pressure can be calculated.

12
Adsorption, Binding, and Insertion of Proteins

As discussed in Chapter 11 biological membranes are negatively charged. Therefore, there are many basic proteins that bind to membranes, e.g., the mitochondrial protein cytochrome c that was already discussed in Chapter 11. This protein is a prototypical globular protein of nearly exactly spherical shape. Its binding properties are well studied. Other proteins also bind to uncharged membranes. Examples include some pore-forming peptides as alamethicin, margainin, and melittin. At low concentrations, these proteins bind peripherally to the membranes, while they insert into the membranes at higher concentrations. In the following, we will first introduce into surface adsorption of global proteins. Further, we discuss the electrostatics of protein binding. Later, we will also treat elongated proteins and their insertion into membranes, as well as protein binding to mixed lipid membranes.

12.1
The Langmuir Isotherm

The simplest case of surface adsorption is binding to independent lattice sites.

Let us first consider a vesicle with only one binding site (Fig. 12.1, left). The binding equilibrium between one binding site and a free protein is given by

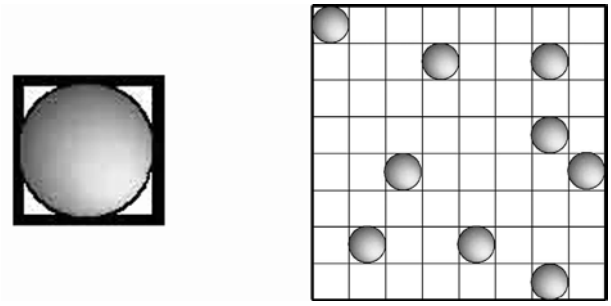

Fig. 12.1 Binding of spherical proteins to a lattice. Left: The lattice has only one site ($n = 1$). Right: This lattice has 64 binding sites ($n = 64$). Nine of these sites are occupied ($i = 9$).

the mass action law (Section 4.7):

$$\frac{[P_b]}{[P_f][S_f]} = K_0 \qquad \text{or} \qquad \frac{[P_b]}{[S_f]} = [P_f] \cdot K_0 \tag{12.1}$$

where $[P_b]$ is the concentration of bound protein, $[P_f]$ is the concentration of free protein, and $[S_f]$ is the concentration of free binding sites. Let us rename the concentration of bound proteins by $[P_b] \equiv [S_1]$, the concentration of vesicles with one protein bound. The concentration of free sites shall be renamed by $[S_f] \equiv [S_0]$, the concentration of vesicles without any bound proteins.

$$\frac{[S_1]}{[S_0]} = [P_f] \cdot K_0 \tag{12.2}$$

Let us now consider a vesicle with two binding sites. Two facts must be accounted for:

1. There are two possibilities to bind one ligand. We will therefore introduce the degeneracy Ω_i, the number of ways to arrange i bound proteins on the surface with n binding sites. For two sites it is equal to two.

2. There is one case where two proteins bind and one possibility of having zero proteins bound.

To take the binding of the second ligand into account, one can consider the equilibrium between a vesicle with one protein bound and a vesicle with two proteins bound

$$\frac{[S_2]}{[P_f][S_1]} = K_0 \qquad \text{or} \qquad [S_2] = [P_f] \cdot K_0 \cdot [S_1] \tag{12.3}$$

or by using Eq. (12.2)

$$[S_2] = [P_f] \cdot K_0 [S_1] = [P_f]^2 \cdot K_0^2 [S_0] \qquad \text{or} \qquad \frac{[S_2]}{[S_0]} = [P_f]^2 \cdot K_0^2 \tag{12.4}$$

The mean number of bound ligands, $\langle i \rangle$, is now given by

$$\langle i \rangle = \frac{\sum_{i=1}^{2} i \cdot \Omega_i [S_i]/[S_0]}{\sum_{i=0}^{2} \Omega_i [S_i]/[S_0]} = \frac{\sum_{i=1}^{2} i \cdot \Omega_i [P_f]^i K_0^i}{\sum_{i=0}^{2} \Omega_i [P_f]^i K_0^i} \tag{12.5}$$

where Ω_i is the degeneracy. For a vesicle with $n = 2$, $\Omega_0 = 1$, $\Omega_1 = 2$, and $\Omega_2 = 1$.

For a membrane with a total of n binding sites and $(n - i)$ free binding sites, we obtain

$$\langle i \rangle = \frac{\sum_{i=1}^{n} i \cdot \Omega_i [P_f]^i K_0^i}{\sum_{i=0}^{n} \Omega_i [P_f]^i K_0^i} \tag{12.6}$$

with the degeneracy Ω_i

$$\Omega_i = \frac{n!}{(n-i)! \cdot i!} \tag{12.7}$$

To make the degeneracy more transparent, let us consider the drawing in Fig. 12.1 (right), where we have $n = 64$ binding sites and $i = 9$ bound proteins. For the first protein we have 64 possible binding sites, for the second protein $64 - 1 = 63$ sites, and so on. For the nine proteins we therefore have $64 \cdot 63 \cdot 62 \cdot \ldots \cdot 57 \cdot 56 = 64!/55! = 64!/(64-9)!$ possibilities. However, of these configurations, $9 \cdot 8 \cdot 7 \cdot \cdots \cdot 2 \cdot 1 = 9!$ are identical, because in any given arrangement one can exchange bound proteins with each other without creating a new configuration. Therefore the number of different configurations is $\Omega_9 = 64!/(55! \cdot 9!)$. The number of distinguishable configurations, $\Omega_i = n!/(n-i)! \cdot i!)$, is called the *binomial coefficient*.

Let us abbreviate the denominator of Eq. (12.6) with

$$Q \equiv \sum_{i=0}^{n} \frac{n!}{(n-i)! \cdot i!} [P_f]^i K_0^i \tag{12.8}$$

This function is called the partition function. Equation (12.5) can be rewritten as:

$$\begin{aligned}
\langle i \rangle &= \frac{1}{Q} \sum_{i=1}^{n} i \cdot \frac{n!}{(n-i)! \cdot i!} [P_f]^i K_0^i \\
&= [P_f] K_0 \frac{1}{Q} \cdot \sum_{i=1}^{n} (n-i+1) \cdot \frac{n!}{(n-i+1)! \cdot (i-1)!} [P_f]^{i-1} K_0^{i-1} \\
&\overset{j \equiv (i-1)}{=} [P_f] K_0 \underbrace{\frac{1}{Q} \cdot \sum_{j=1}^{n} (n-j) \cdot \frac{n!}{(n-j)! \cdot j!} [P_f]^j K_0^j}_{n - \langle i \rangle} \\
&= [P_f] K_0 (n - \langle i \rangle)
\end{aligned} \tag{12.9}$$

or finally:

$$\frac{\langle i \rangle}{[P_f] \cdot (n - \langle i \rangle)} = K_0 \tag{12.10}$$

which corresponds to the mass action law in Eqs. (12.1) and (12.2). It can be seen that it is independent of the number of binding sites on the membrane. This is not surprising, since the binding sites are independent, and basically do not "know" that they are all on the same surface. If one defines the fractional occupancy $\theta = \langle i \rangle / n$, Eq. (12.10) becomes

$$[P_f] = \frac{1}{K_0}\frac{\theta}{(1-\theta)} \qquad \text{Langmuir isotherm} \tag{12.11}$$

This binding equilibrium is called the Langmuir isotherm. The constant K_0 has to be determined by experiment. Since the Langmuir isotherm basically corresponds to a mass action law, it seems as if Eq. (12.11) is trivial and the effort to derive this equation was not necessary. However, this was a good exercise for the derivation of the more general isotherms in the next section. The constant K_0 has to be determined by experiment.

12.2 The Adsorption to a Continuous Surface

Proteins are usually significantly larger than lipids. Therefore one can consider the biological membrane surface as a continuous plane. Proteins may bind to any point on the surface. No defined binding sites exist (Fig. 12.2). For such a system, the Langmuir isotherm is not a good description. It rather applies to macromolecules with locally separated binding sites (e.g., oxygen binding sites in hemoglobin). If a membrane is continuous, each protein has an excluded volume (Fig. 12.2, right). Consider a surface with area A_{tot}. A protein with area A_P can bind anywhere on that surface. However, a second protein has only $A_{\text{tot}} - 4 \cdot A_P$ available, which means that in contrast to the Langmuir isotherm the surface available for the binding of proteins is smaller than the total surface minus the occupied surface. Therefore, one needs to make a better model.

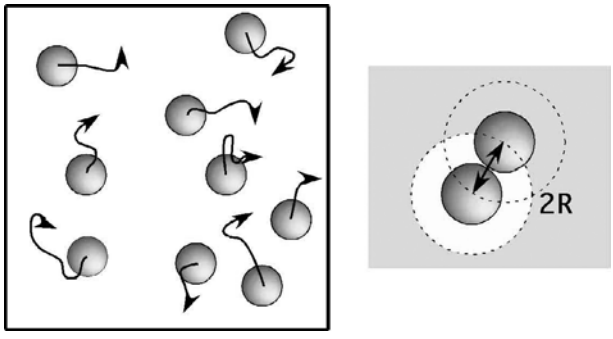

Fig. 12.2 Left: Binding of spherical proteins to a surface without localized binding sites. Instead, the surface is continuous. Right: Each bound protein displays an excluded volume of 4 times the protein cross-sectional area.

12.2.1 The Protein Adsorbate as a Two-Dimensional Gas

Let us assume that the adsorbed proteins form a two-dimensional gas. If more proteins bind to the surface, the gas has to be compressed, and work has to be performed

$$\Delta F(i) = \Delta W(i) = -\int_{A_0}^{A} \Pi(i)\, dA \tag{12.12}$$

using a lateral pressure Π of the 2D gas. Similarly to Eq. (12.9) one can calculate the adsorption isotherm for an adsorbed lateral gas

$$\langle i \rangle = \frac{\sum_{i=1}^{n} i \cdot \frac{1}{i!}[P_f]^i K_0^i \exp\left(-\frac{\Delta F(i)}{kT}\right)}{\sum_{i=0}^{n} \frac{1}{i!}[P_f]^i K_0^i \exp\left(-\frac{\Delta F(i)}{kT}\right)} \tag{12.13}$$

where the term $\frac{n!}{(n-i)!}$ is now replaced by $\exp(-\frac{\Delta F(i)}{kT})$. We do not know yet what function of the number of bound proteins ΔF is. For this we will use a model below. For now, we will simplify Eq. (12.13) using an approach similar to that in Eq. (12.9).

$$\begin{aligned}\langle i \rangle &= [P_f]K_0 \frac{\sum_{i=1}^{n} \frac{1}{(i-1)!}[P_f]^{i-1} K_0^{i-1} \exp\left(-\frac{\Delta F(i-1)}{kT}\right) \exp\left(-\frac{\Delta F(i)-\Delta F(i)}{kT}\right)}{\sum_{i=0}^{n} \frac{1}{i!}[P_f]^i K_0^i \exp\left(-\frac{\Delta F(i)}{kT}\right)} \\ &= [P_f]K_0 \frac{\sum_{i=0}^{n-1} \frac{1}{i!}[P_f]^i K_0^i \exp\left(-\frac{\Delta F(i)}{kT}\right) \exp\left(-\frac{d}{di}\frac{\Delta F(i)}{kT}\right)}{\sum_{i=0}^{n} \frac{1}{i!}[P_f]^i K_0^i \exp\left(-\frac{\Delta F(i)}{kT}\right)}\end{aligned} \tag{12.14}$$

If the vesicle is very large ($n \longrightarrow \infty$), one of the terms in the sum represents a pronounced maximum (for $i \approx \langle i \rangle$), and Eq. (12.14) can be simplified to (Heimburg and Marsh, 1995)

$$\langle i \rangle = [P_f]K_0 \exp\left(-\frac{d}{di}\frac{\Delta F(i)}{kT}\right) \tag{12.15}$$

This equation is important, because it generally describes the binding of ligands to surfaces for all possible forms of $\Delta F(i)$. We call this equation the "Gibbs" isotherm and will make heavy use of it in the following. The function $d\Delta F/di$ is equal to the chemical potential of the surface adsorbed proteins, $\Delta\mu_{\text{surf}}$. Equation (12.15) could therefore also be written as

$$\langle i \rangle = [P_f]K_0 \exp\left(-\frac{\Delta\mu_{\text{surf}}(i)}{kT}\right) \tag{12.16}$$

However, let us stick to the first version of this equation.

12.2.2
The van der Waals Adsorption Isotherm

To calculate the value for $\langle i \rangle$ in Eq. (12.15) one needs to find an expression for the lateral pressure in Eq. (12.12). As a first approximation let us take the van der Waals equation of state for a real gas. If the proteins do not interact, the equation of state is given by

$$\Pi(i) \cdot (n \cdot \Delta A - i \cdot \Delta A) = ikT \qquad \longrightarrow \qquad \Pi(i) = \frac{ikT}{(n-i)\Delta A} \tag{12.17}$$

where ΔA is the hard core area of one protein, $n \cdot \Delta A$ is the total area of the membrane and $i \cdot \Delta A$ is the area occupied by proteins. Therefore, $\Delta F(i)$ is given by

$$\Delta F = -\int \frac{ikT}{(n-i)\Delta A}\, dA = -\int \frac{ikT}{(n-i)}\, d\, n = -ikT \ln(n-i) \tag{12.18}$$

using $dA = \Delta A dn$.

$$\frac{d}{di}\frac{\Delta F(i)}{kT} = -kT \ln(n-i) + \frac{ikT}{n-i} \tag{12.19}$$

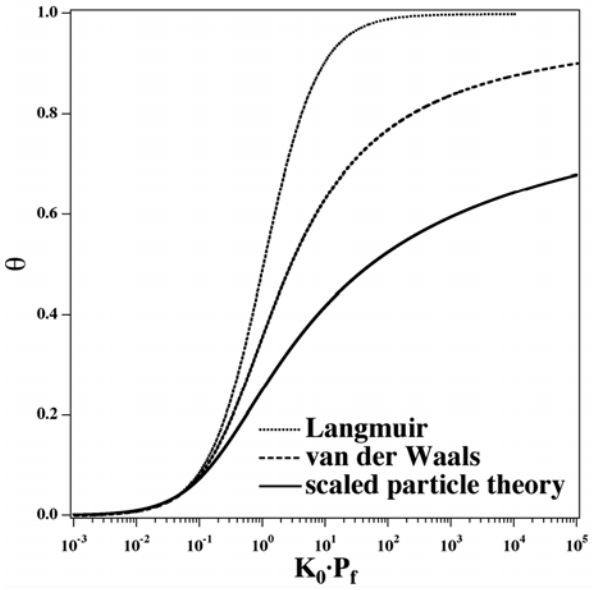

Fig. 12.3 Comparison of Langmuir isotherm, van der Waals isotherm and the isotherm derived from the scaled particle theory (SPT). The scaled particle isotherm is most realistic. It can be seen that binding is strongly suppressed at higher degrees of surface coverage.

Now the binding isotherm is given by

$$\langle i \rangle = [P_f] K_0 (n - i) \exp\left(-\frac{i}{n-i}\right) \tag{12.20}$$

$$[P_f] = \frac{1}{K_0} \frac{\theta}{1-\theta} \exp\left(\frac{\theta}{1-\theta}\right) \tag{12.21}$$

This isotherm we shall call the "van der Waals" isotherm (Fig. 12.3).

12.2.3 Scaled Particle Theory

The van der Waals equation of state (Eq. (12.17)) is a pretty rough approximation for a two-dimensional gas. A better approximation for the lateral pressure of the two-dimensional protein gas is derived from the scaled particle theory. If one assumes proteins that are hard spheres in cross section, the free energy of compressing the lateral gas (work performed) is

$$\Delta F^{\mathrm{SPT}}(i) = -ikT[\ln(n-i) + 1] + \frac{inkT}{n-i} \tag{12.22}$$

We did not derive this expression here. For details the reader should refer to Helfand et al. (1961) and Chatelier and Minton (1996). The resulting binding isotherm has the form

$$[P_f] = \frac{1}{K_0} \frac{\theta}{1-\theta} \exp\left(\frac{3\theta}{1-\theta} + \left(\frac{\theta}{1-\theta}\right)^2\right) \tag{12.23}$$

This isotherm is the most realistic one for spherical proteins that do not interact, i.e., it compares very well with Monte Carlo simulations for that situation. One can see that the Langmuir isotherm, the van der Waals (vdW) isotherm and the scaled-particle (SPT) isotherm are similar only at low degrees of surface coverage (Fig. 12.3). At higher degrees of surface coverage, further binding is strongly suppressed in both, vdW and SPT isotherm. Practically, it is impossible to fill the complete available surface. The Langmuir isotherm, in contrast, allows for a practically complete surface coverage if $K_0 \cdot P_f > 10^2$. One has to conclude that the Langmuir isotherm is not suitable to describe binding of proteins to surfaces. The entropic "costs" are too high. Unfortunately the Langmuir isotherm is still often used in the literature.

It should be mentioned that the work to compress a gas is very small at low surface coverage, such that in the limit of very low degrees of binding one has the approximate result

$$\frac{\theta}{[P_f]} \approx K_0 \tag{12.24}$$

which implies that the degree of binding is simply proportional to the free protein concentration. From experiments at low protein concentrations one can thereby determine the intrinsic binding constant, K_0.

12.3 Aggregation Equilibria of Adsorbed Proteins

The van der Waals equation of state for a real gas allows for the interaction of particles with finite volume. In two dimensions, the expression for the lateral pressure is (cf. Eq. (12.17)).

$$\Pi(i) = \frac{ikT}{(n-i)\Delta A} - a\left(\frac{kT}{\Delta A}\right)\left(\frac{i}{n}\right)^2 \tag{12.25}$$

where a is a parameter describing interactions between proteins on the surface. Insertion of the result in Eqs. (12.12) and (12.15) yields

$$[P_f] = \frac{1}{K_0} \cdot \frac{\theta}{1-\theta} \exp\left(\frac{\theta}{1-\theta} - 2a\theta\right) \tag{12.26}$$

This isotherm has been derived originally by Hill (1946).

In analogy, one can insert the phenomenological interaction term of the van der Waals equation of state, $-2a\theta$, into the SPT isotherm (Eq. (12.27))

$$[P_f] = \frac{1}{K_0}\frac{\theta}{1-\theta} \exp\left(\frac{3\theta}{1-\theta} + \left(\frac{\theta}{1-\theta}\right)^2 - 2a\theta\right) \tag{12.27}$$

If the parameter a is positive, attractive interactions between proteins are present and aggregation may occur. This can be seen in Fig. 12.4. In the right-hand panel of this figure it can be seen that the binding isotherms may become biphasic. This indicates an equilibrium between monomeric and aggregated proteins in a defined regime of protein concentrations. The tendency of a protein to aggregate on surfaces can drastically increase the binding capacity of the membrane for this protein, because protein aggregation creates free connected surface area.

One of the cases where such an aggregation equilibrium has been observed is the denaturation of surface adsorbed cytochrome c (Heimburg and Marsh,

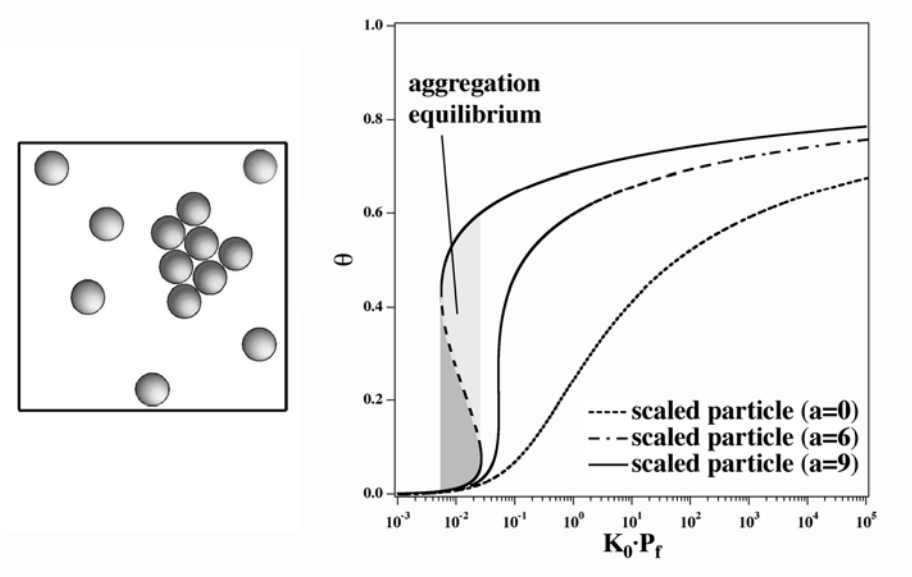

Fig. 12.4 Left: Schematic drawing of an aggregation equilibrium on a membrane surface. Right: Comparison of the scaled particle isotherm in the absence and in the presence of protein–protein interactions (Eqs. (12.23) and (12.27)). If aggregation occurs, the binding isotherms become biphasic. The interaction parameter was chosen to be $a = 0$, $a = 6$ and $a = 9$, respectively.

1995). Unfolded proteins tend to aggregate to avoid the contact of hydrophobic amino acids with water. Other cases are the aggregation of lytic peptides into pores, described in a later section.

12.4 Binding of Asymmetric Proteins

But what happens for nonspherical proteins? In Fig. 12.5 it is shown that elongated proteins may hinder each other in rotation, thereby affecting the free energy. In 1996, Chatelier and Minton (1996) derived an isotherm that takes the shape of a ligand into account:

$$[P_f] = \frac{1}{K_0} \cdot \frac{\theta}{1-\theta} \exp\left(\frac{\theta}{1-\theta} - \epsilon + \frac{\epsilon}{(1-\theta)^2}\right) \tag{12.28}$$

Here, ϵ is a parameter that depends on shape. For instance, $\epsilon = 1$ for a hard sphere, and $\epsilon = \frac{25}{4\pi}$ for a rectangular protein cross section with axial ratio of four (Chatelier and Minton, 1996). For the spherical case, Eq. (12.28) reduces to Eq. (12.23).

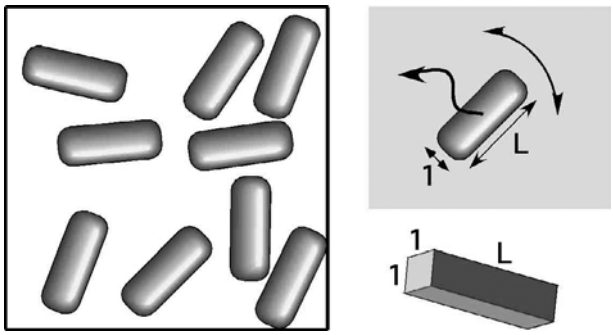

Fig. 12.5 In the case of elongated proteins bound to the surface, the spacial dimensions of the protein start playing a role. At high concentrations the rotation of the ligands is restricted.

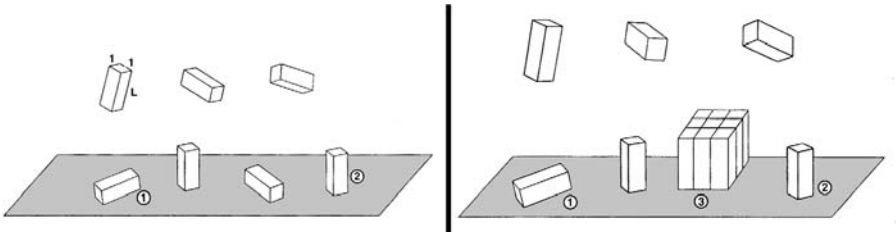

Fig. 12.6 Left: Asymmetric proteins may adsorb in different orientations on the surface (states 1 and 2). Which orientation dominates depends on the surface concentration of proteins. Right: If there are aggregation equilibria, one of the orientations may aggregate preferentially. Thus, there are three different states on the protein on the surface. Figures from Minton (1999) with permission from Biophys. J.

Tab. 12.1 Values for ϵ used in Eq. (12.28) for different shapes of the protein cross section. From Chatelier and Minton (1996).

Shape	ϵ
circle	1
Regular polygon (n sides)	$(n/\pi)\cdot\tan(\pi/n)$
Rectangle (axial ratio $L \geq 1$)	$(L/\pi)\cdot(1+1/L)^2$
Ellipse (axial ratio $L \geq 1$)	$\frac{4L}{\pi^2}\cdot\left[\int_0^{\pi/2}\left(\frac{\sin^2\theta}{L^2}+\cos^2\theta\right)^{0.5}d\theta\right]^2$

Minton (1999) also discussed the case that asymmetric proteins may adsorb with different orientations, and how the equilibrium is affected by surface coverage (Fig. 12.6, left). Clearly, at higher occupancy the protein orientation with the smaller cross section is favored. Also, aggregation equilibria may be influenced by the orientational rearrangements.

12.5
Binding in the Presence of Electrostatic Interactions

In Chapter 11 we derived expressions for the electrostatic free energy. Let us consider the binding of positively charged proteins to negatively charged lipid membranes at low ionic strength. In this case we can use the high potential approximation for the electrostatic free energy per lipid (Eq. (11.22)).

$$\begin{aligned} F_{\mathrm{el,L}} &= A_L\left(\sigma\Psi_0 - (4\epsilon_0\epsilon)\left(\frac{kT}{e}\right)^2\kappa\left[\cosh\left(\frac{e\Psi_0}{2kT}\right)-1\right]\right) \\ &\overset{\text{high pot.}}{=} A_L\left(-\frac{2kT}{e}\sigma\left[\ln\left(-\sqrt{\frac{1}{2\epsilon_0\epsilon KTc_0}}\sigma\right)+1\right]\right) \\ &\quad +4\epsilon_0\epsilon\left(\frac{kT}{e}\right)^2\sqrt{\frac{2e^2}{\epsilon_0\epsilon kT}c_0} \end{aligned} \tag{12.29}$$

The last term is independent of σ.

Let us consider a positively charged protein with cross-sectional area A_P, corresponding to the molecular area of α lipids, such that $\alpha \cdot A_L = A_P$. Let us further assume that the effective charge of the protein is $+Z \cdot e$. The membrane is defined to have a total area corresponding to the n protein areas, i.e., $n \cdot A_P = n \cdot \alpha A_L$. Each lipid carries one negative charge. This means that protein binding reduces the mean charge density of the membrane. A membrane with i protein molecules bound displays a charge density of

$$\sigma = -\frac{(n\,\alpha - iZ)}{n\,A_P}e \tag{12.30}$$

After inserting Eq. (12.30) into Eq. (12.29) one obtains the electrostatic free energy for the total membrane, F_{el}

$$F_{\mathrm{el}}(i) = n\alpha F_{el,L} = -2kT(n\alpha - iZ)\ln\left(\sqrt{\frac{e^2}{2\epsilon_0\epsilon kTc_0}}\left(\frac{n\alpha - iZ}{nA_p}\right)+1\right) \tag{12.31}$$

According to Eq. (12.15) we can generally write the binding isotherm as

$$\langle i\rangle = [P_f]K_0\exp\left(-\frac{d}{di}\left[\frac{\Delta F_{\mathrm{SPT}}(i)+\Delta F_{\mathrm{el}}(i)}{kT}\right]\right) \tag{12.32}$$

where $\Delta F_{\mathrm{SPT}}(i)$ refers to the compression of the uncharged 2D protein gas on the surface, and $\Delta F_{\mathrm{el}}(i) = F_{\mathrm{el}}(i) - F_{\mathrm{el}}(0)$ is the additional change of the electrostatic free energy resulting from protein binding.

Differentiation of $\Delta F_{\mathrm{el}}(i)/kT$ (see Eq. (12.31)) with respect to i yields

$$\frac{1}{kT}\frac{d\,\Delta F_{\mathrm{el}}(i)}{di} = -2Z\ln\left(\frac{1}{A_L}\sqrt{\frac{e^2}{2\epsilon_0\epsilon kT\,c_0}}\right) - 2Z\ln\left(1-\frac{iZ}{n\alpha}\right) \tag{12.33}$$

Let us now first describe the limit of very low surface coverage with $i/n \to 0$. Combining Eq. (12.33) in this limit with Eq. (12.24) leads to

$$\frac{\theta}{[P_f]} \approx K_0 \left(\frac{1}{A_L} \sqrt{\frac{e^2}{2\epsilon_0 \epsilon k T\, c_0}} \right)^{2Z} \equiv K(0) \tag{12.34}$$

where $\theta = i/n$ is the fractional coverage of the lipid surface with protein. Thus, we can define an intrinsic binding constant $K(0)$ which is a function of the ionic strength, c_0. Equation (12.34) describes the binding at very low protein concentrations. The intrinsic binding constant can easily be determined experimentally, for example by ultracentrifugation assays (Heimburg and Marsh, 1995). In such experiments, lipid vesicles are added to an aqueous buffer containing proteins. Some of the proteins bind to the membranes. The membranes with the bound proteins are removed by ultracentrifugation and the remaining proteins in solution can be obtained by determination of the spectral absorption coefficient in a photospectrometer. From Eq. (12.34) it is obvious that at very low degrees of surface coverage

$$\ln K(0) = -Z \ln(c_0) + \text{const.} \tag{12.35}$$

If one measures the initial degree of binding as a function of ionic strength, c_0, one can now determine the charge of the protein, Z. This is shown in Fig. 12.7 for the example of cytochrome c binding to dimyristoyl phosphatidylglycerol membranes.

Combining Eqs. (12.23), and (12.32)–(12.34) one arrives at the overall binding isotherm in the presence of electrostatics:

$$[P_f] = \frac{1}{K(0)} \left(1 - \theta \frac{Z}{\alpha}\right)^{-2Z} \frac{\theta}{1-\theta} \exp\left(\frac{3\theta}{1-\theta} + \left(\frac{\theta}{1-\theta} \right)^2 \right) \tag{12.36}$$

This means that a determination of the binding isotherms as a function of ionic strength requires three parameters to be known: the ionic strength dependent intrinsic binding constant, $K(0)$, the effective charge of the protein, Z, and the number of lipids covered by one protein, α. A good example of how to use this formalism is the binding of the water-soluble protein cytochrome c to charged lipid membranes (Heimburg and Marsh, 1995) and (Heimburg et al., 1999).

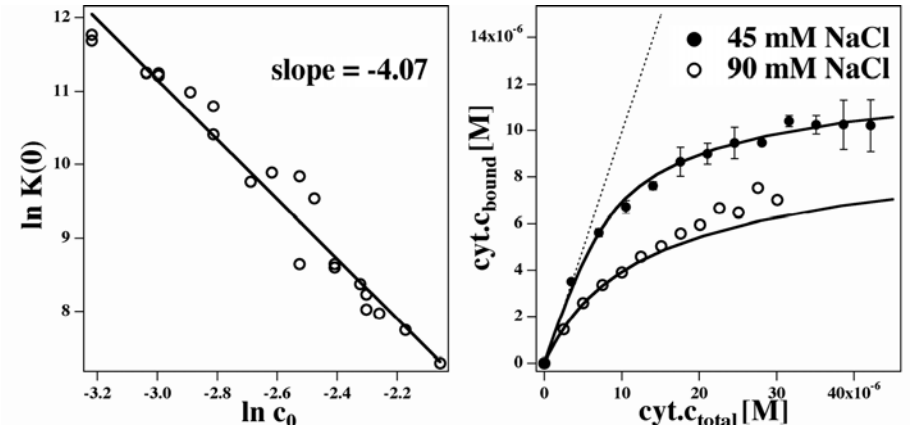

Fig. 12.7 Binding of cytochrome c to dioleoyl phosphatidylglycerol (DOPG) membranes. Left: Double-logarithmic plot of the intrinsic binding constant versus the ionic strength ($K(0)$ in (l/mol) and c_0 in (mol/l)). One obtains a straight line with slope -4. Therefore, the effective charge of the protein is $Z = 4$. Right: Binding isotherms for cytochrome c binding to DOPG membranes at two different ionic strengths. The solid lines are fits using Eq. (12.36) and the $K(0)$ values of the straight line in the left-hand panel. Data adapted from (Heimburg et al., 1999)

12.6 Lateral Pressure Changes Induced by Protein Binding

Let us now go back one step and consider the binding in the absence of electrostatic interactions. If we consider the adsorbed proteins on a membrane surface as a two-dimensional gas with a lateral pressure it would be interesting to calculate the pressure generated by absorption. The free energy of the protein gas is given in Eq. (12.22). The lateral pressure is given by $\Pi = -dF/dA$. If we let $dA = \alpha A_L dn$, i.e., we express the area in terms of lipid areas, then

$$\Pi = \frac{1}{\alpha A_L} \frac{\theta}{(1-\theta)^2} kT \tag{12.37}$$

We considered a very similar problem in Section 11.6. The lateral pressure of the protein gas as a function of fractional occupancy of the membrane surface is shown in Fig. 12.8. To give a better feeling for the numbers we relate it to a pressure per membrane cross section in units of bars. Thus, at 70% surface coverage and $\alpha = 1$ the lateral pressure corresponds to $0.0193\,\mathrm{N/m} \equiv 38.7$ bar. This pressure can shift lipid transitions to lower temperatures, cf. Eq. (11.32). Taking the values of DPPC ($\Delta H = 35$ kJ/mol, $T_m = 314.2$ K, the area difference between gel and fluid lipid $\Delta A_L = 1.5 \times 10^{-19}$ m^2) the shift of T_m is on the order $\Delta T_m = -7$ K. It is significant.

Protein binding to charged membranes has two opposing effects on the melting temperature of membranes. The shielding of the electrostatics moves melting temperatures to higher values. The lateral pressure of the protein gas

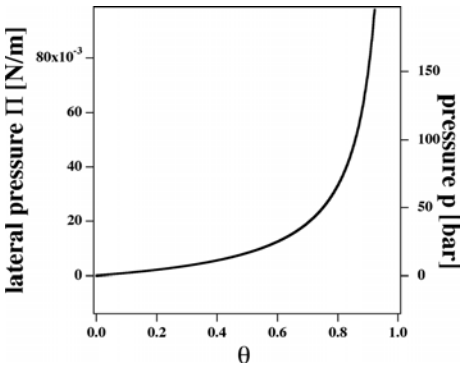

Fig. 12.8 Lateral pressure of a two-dimensional protein gas with $\alpha = 1$ as a function of the fractional occupancy of the membrane, θ. On the right-hand axis, the corresponding pressure on the membrane cross section is given.

moves the transition temperature to lower temperatures. It can therefore be expected that binding of proteins to surfaces raises the transition temperature at low degrees of binding and lowers it at higher degrees of binding.

12.7 Protein Insertion and Pore Formation

The fact the adsorbed proteins generate a lateral pressure on lipid membranes can lead to protein insertion. Let us assume that a protein binds strongly to membrane surfaces. Then the protein generates a large lateral pressure. If one takes a look at the derivation of the isotherms in the previous sections one can see that such a pressure is also generated if proteins do not bind to surfaces but rather penetrate the membrane. There is, however, one major difference between a surface adsorbed protein and an inserted protein: Upon protein adsorption the total membrane surface stays constants, whereas it increases upon protein insertion. On the other hand, protein insertion leads to interactions between the hydrophobic lipid chains and the peptides and may thus be less favorable than insertion at low concentrations.

Based on what has been said so far one can predict that peptides that adsorb to surfaces at low concentrations but insert into the membranes at higher concentrations may exist. Such adsorption insertion equilibria therefore occur mostly with peptides that are partially hydrophobic and partially hydrophilic, i.e., amphiphilic. Many of such polypeptides form pores. These pores are aggregates of several peptides. Prominent examples are melittin, alamethicin (Fig. 12.9), margainin, the α5-helix of endotoxin and pardaxin (see Zuckermann and Heimburg (2001) for a discussion). The alamethicin pore is thought

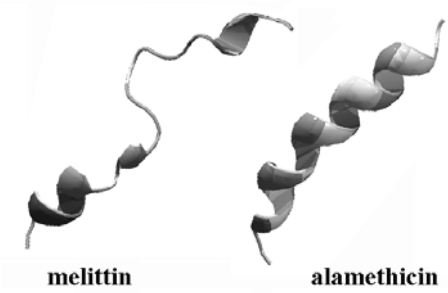

Fig. 12.9 Crystal structures of two pore-forming lytic peptides. Left: Melittin from bee venom. Right: Alamethicin.

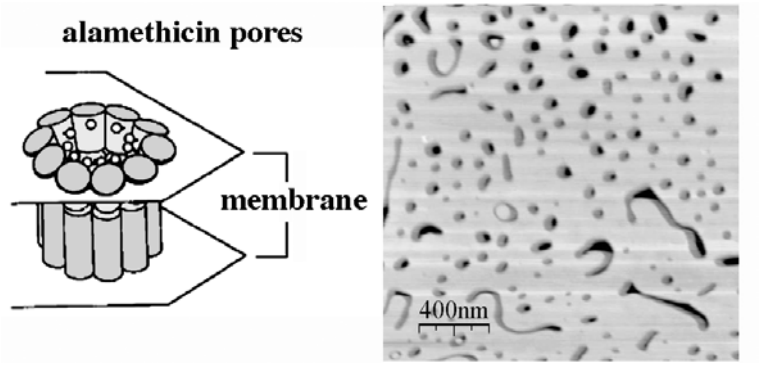

Fig. 12.10 Left: An alamethicin pore, after Fox and Richards (1982). Right: AFM image of 1% alamethicin in DMPC membranes, showing pores on the length scale of several 10 nm. From Oliynyk et al. (2006)

to consist of about 10 peptides (Gennis, 1989), but AFM images indicate that such pores can also be much larger (Fig. 12.10).

In principle, both adsorption and insertion can be described using a formalism similar to that described above (Zuckermann and Heimburg, 2001). For both surface adsorbed proteins and inserted proteins, the free energies and therefore also the equilibria between the two adsorption states can be determined. We will not do this here because the calculation is somewhat lengthy. We will, however, outline the essential features of such thermodynamic considerations. Upon adsorption of proteins the following chain of events is found:

1. Soluble proteins adsorb to the lipid membrane interface and form a two-dimensional gas on the surface.

2. This gas exerts a lateral pressure on the membrane. If the intrinsic binding constant is large these pressures can be substantial. This pressure

could ultimately lead to the rupture of the membrane at a critical pressure.

3. Instead of membrane rupture it may be favorable that proteins insert in the membrane. Insertion has two consequences: 1. The surface concentration of proteins is reduced leading to a lowering of the lateral pressure. 2. The total area increase leads to a further reduction in pressure of the protein gas. Therefore, insertion of proteins lowers the free energy of the protein gas.

4. Inserted proteins display an interaction with the hydrophobic core of the lipid membrane. If these interactions are unfavorable, protein insertion will only happen at very high protein concentrations (or never). If the interaction is favorable, the proteins may readily insert into the membrane.

5. The most interesting case is obviously the intermediate situation where the interactions between proteins (or peptides) and lipid chains are neither favorable nor especially unfavorable, i.e., for amphiphilic peptides like melittin. For such proteins one expects that the proteins adsorb to the membrane surface at lower concentrations to avoid contact with the chains. At high concentrations the proteins insert into the membrane to reduce the lateral pressure of the protein gas. Such a case has been found for the α5-helix of endotoxin and for pardaxin (Fig. 12.12) discussed below.

In the previous section we have outlined most of what is necessary in order to calculate such a situation. However, such a calculation requires a number of additional parameters describing for example shape of the proteins, lipid–protein interactions and number of peptides in a pore. The interested reader should therefore refer to Zuckermann and Heimburg (2001). The following description is rather meant to describe the principle, which is outlined in Fig. 12.11.

Proteins accumulate on the surface and generate a lateral pressure. This leads to insertion of proteins, either monomeric (Fig. 12.11, left) or as pores (Fig. 12.11, center). The corresponding isotherms take a form that resembles the profiles in Fig. 12.11 (right). In the example shown proteins start to insert at a critical fraction of $\theta = 0.3$. The binding isotherm displays a drastic increase in binding. Below that surface coverage the proteins just adsorb to the surface and look like the SPT isotherm given in Fig. 12.3. The dotted line in this figure shows how binding would progress if proteins would only adsorb to the surface.

Such kind of adsorption behavior has in fact been found experimentally. Shai and coworkers (Rapaport and Shai, 1991; Gazit et al., 1998; Shai, 1999)

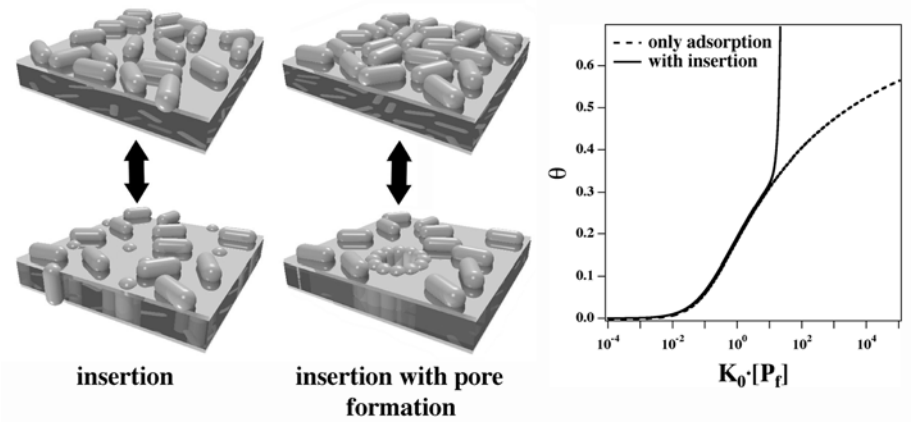

Fig. 12.11 Two scenarios for protein insertion. Left: Proteins first adsorb to the surface. At a critical protein concentration some proteins insert into the membrane. Center: Same situation but proteins consequently form pores within the membrane. Right: Binding isotherm of a pore-forming peptide. The dotted line is the isotherm calculated without insertion. If insertion occurs the binding isotherm shows a largely increased protein association at a critical free peptide concentration. This sudden increase is due to pore formation. This is a cooperative process. Figures adapted from Zuckermann and Heimburg (2001) with permission.

have shown for different antimicrobial peptides as δ-endotoxin or pardaxin. δ-endotoxin is a highly potent pore-forming insecticidal toxin produced by *bacillus thuringiensis*. Gazit et al. (1998) especially investigated the central α5-helix. Pardaxin is a neurotoxic peptide acting as shark repellant in certain fish. Both peptides form pores and display binding isotherms to zwitterionic membranes as described in Fig. 12.12. Such binding isotherms can be described by using an equilibrium between surface adsorbed peptides and inserted peptides that shifts toward the inserted pore-forming fraction at higher concentrations of peptide as described in Fig. 12.12 for the case of pardaxin.

To summarize, one can state that if peptides tend to increase their binding affinity drastically above a certain value of surface coverage, θ, this is an indication for protein insertion. Further, if this increase in affinity is very steep it also indicates pore formation or other types of aggregation of the inserted peptides.

12.7.1 Insertion Triggered by the Binding of Secondary Proteins

The description of binding processes given in this chapter relies on thermodynamics of the adsorbed protein gas and, in particular, on its lateral pressure. The pressure depends on the number and size of the proteins but not on their chemical nature. Therefore, it is also interesting to consider the case where

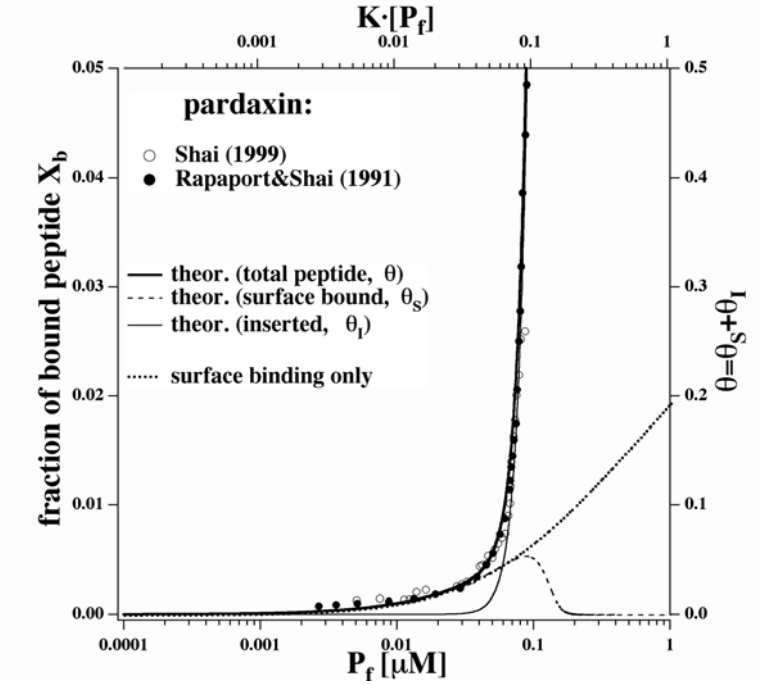

Fig. 12.12 An experimental example for the insertion of peptides into membranes is the binding of pardaxin to phosphatidylcholine membranes. The solid line represents the theoretical description including surface adsorption and insertion of the peptides. The individual contributions of surface adsorption and inserted proteins are given as dotted lines. The data are taken from Shai (1999) and were analyzed by Zuckermann and Heimburg (2001). Reproduced with permission.

a second species of proteins adsorbs to the surface. Further, we assume that this second species does not insert into the membrane because it displays an unfavorable interaction with the membrane core. This protein, nevertheless, contributes to the lateral pressure of the surface protein gas (now consisting of two species). Thus, it has the potential of affecting the surface-insertion equilibrium of the first protein species, even if the two protein species do not interact at all! Such a situation is schematically shown in Fig. 12.13.

It can generally be stated that thermodynamics often creates a coupling between seemingly independent variables, as for example the concentrations of two noninteraction protein species that both contribute to the pressure.

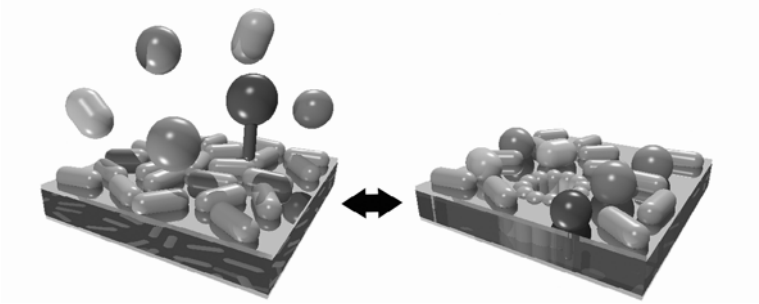

Fig. 12.13 The equilibrium between surface adsorbed and inserted species depends on the lateral pressure of the surface adsorbed gas. It can therefore be altered when other proteins adsorb to the membrane that cannot insert. This means that pore formation of peptides can be triggered by other proteins that have no direct connection to the insertion process. Adapted from Zuckermann and Heimburg (2001) with permission.

12.8 Binding to Mixed Lipid Membranes

Biological membranes are made of many lipid species, some of which are charged and others that are uncharged. As we have learned in a previous chapter, lipids are not in general distributed homogeneously within the membrane plane (Chapter 7). Typically, lipids can diffuse and rearrange after perturbations. They may form domains and clusters. How would the response of the lipid distribution to protein binding look like and what influence does this redistribution have on the binding constant of the protein?

In the following we discuss three limiting cases of a membrane composed of two different lipid species with molar fractions f_A and f_B:

1. The two lipid species are homogeneously distributed in the membrane. Their distribution does not change upon protein binding (Fig. 12.14, top). This could happen when both lipids have the same affinity to the protein, or when the lipids are linked to each other. A further possibility is that the diffusion constant is so low that the lipids do not redistribute within the experimental time frame.

2. The two lipids are homogeneously distributed and mix ideally. They are, however, free to diffuse. If one lipid species binds stronger to the protein than the second species, lipids will redistribute and the lipid with stronger affinity will accumulate within the binding site of the protein. This scenario is fulfilled when one of the two lipids is charged and the protein binds primarily by electrostatic interactions (Fig. 12.14, center).

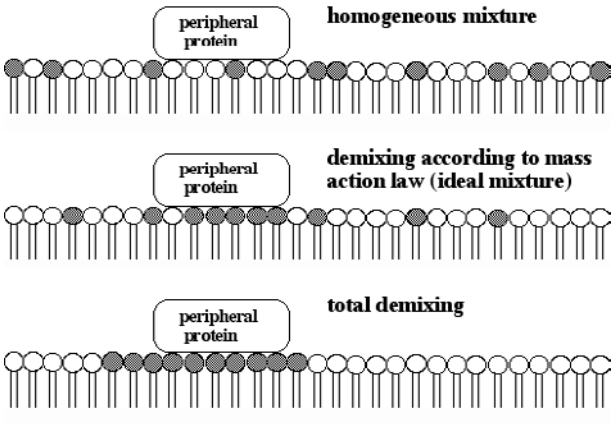

Fig. 12.14 Protein binding to two-component lipid membranes. If the protein has different affinities to two lipid species several binding modes may result. Top: For rigid membranes with no diffusion the lipid distribution does not alter when the protein binds. Center: The lipids with higher affinity to the protein accumulate underneath the protein binding site. This in turn alters the binding affinity of the protein. Bottom: If the two lipids macroscopically phase separate the binding to the two different domain types is independent of the presence of the second species.

3. The two lipid species do not mix at all and phase separate (Fig. 12.14, bottom).

Cases 1 and 3 can be treated very easily with the equations in the previous sections.

Case 1 describes a homogenous membrane and all binding sites are equivalent. If the binding is dominated by electrostatics the charge density has to adjusted accordingly in Eq. (12.30). Taking f_A to be the charged lipid fraction, the charge density of a membrane with n lipids and i proteins bound is now

$$\sigma = -\frac{(n\,\alpha\, f_A - iZ)}{n\,A_P} e \tag{12.38}$$

This has to be considered in the derivations of Section 12.5.

Case 3 is even simpler. Since the two lipid phases separate macroscopically one can consider the two lipid systems as independent and just treat them according to Eqs. (12.23) or (12.36).

Case 2 is a bit more complicated. When a positively charged protein binds to a mixture of negatively charged and uncharged lipids, the charged lipids will have a tendency to accumulate underneath the protein. To what degree this occurs depends on the number of adsorbed protein molecules and the fraction of charged lipids. Such a case has been treated by Heimburg et al. (1999). They have considered the binding of the positively charged protein cytochrome c to mixtures of dioleoyl phosphatidylcholine and dioleoyl phosphatidylglycerol.

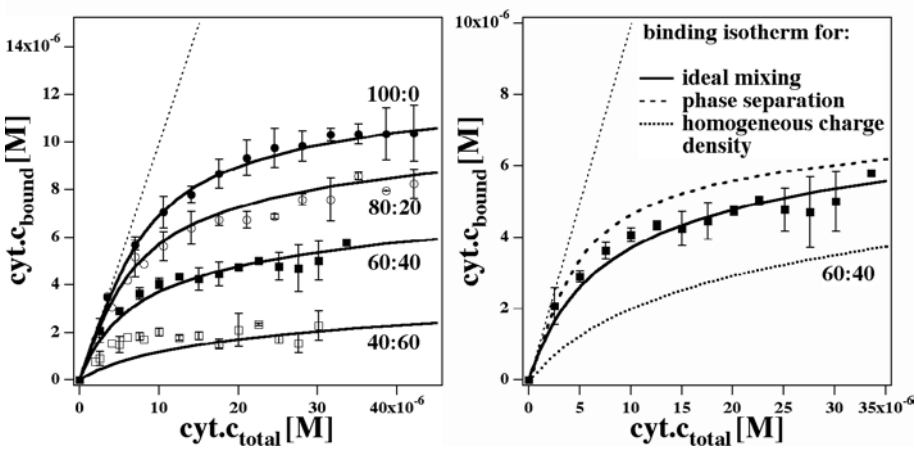

Fig. 12.15 Binding of cytochrome c to ideal mixtures of the negatively charged lipid DOPG and the uncharged lipid DOPC. Left: Binding isotherms to four different mixing ratios. The solid lines represent the theoretical description outlined in Heimburg et al. (1999) assuming that the charged lipids can accumulate underneath the bound proteins (Fig. 12.14, center). Right: Binding to the 60:40 mixture. The solid and dotted curves show how the isotherms would look like assuming the three different cases described in Fig. 12.14. Adapted from Heimburg et al. (1999).

The latter lipid carries one net negative charge. Further, diacyl phosphatidylcholines and diacyl phosphatidylglycerols are known to mix ideally at neutral pH (Garidel et al., 1997). Some results of membranes with different fractions of charged lipid are shown in Fig. 12.15 (left). Since the charge density is smaller, the initial binding constant, $K(0)$, must obviously be smaller. The binding isotherms are shown in Fig. 12.15. The solid lines are the theoretical curves using a refined binding model that takes lipid reordering into account, cf. Heimburg et al. (1999). In the right panel of Fig. 12.15 the isotherm for the 60:40 DOPG/DOPC mixture is shown again. Additionally, the calculated isotherms for cases 1 (no lipid rearrangements) and 3 (macroscopic phase separation) are displayed. It can be seen that the diffusion properties and the lateral organization of the lipids is important for the binding properties.

Under most conditions, binding of proteins will lead to reordering of lipid molecules. Since the neutralization of charges can lead to changes in the phase behavior of lipids (Garidel et al., 1997) one can expect that protein binding in general will influence the mixing behavior of lipids, too. Protein binding leads to changes of lipid composition in the binding site. If lipids mix ideally, however, protein binding cannot induce domains larger than the binding site.

12.9 Summary: Key Ideas of Chapter 12

1. The binding of ligands to independent binding sites is described by the Langmuir isotherm. It basically corresponds to a mass action law. It consists of an equilibrium between free binding sites, occupied binding sites, and free ligands.

2. The Langmuir adsorption isotherm is not a good description of the binding process of ligands to continuous surfaces. The binding sites are not independent of each other and hard core interactions between ligands start playing a role. One has to consider the adsorbed proteins as a two-dimensional gas. Such a binding behavior can generally be described by using a "Gibbs" isotherm.

3. When the lateral pressure of a protein gas is approximated by a real gas as described by the "van der Waals" equation of state one obtains the "van der Waals" isotherm. This isotherm can also describe aggregation equilibria of bound proteins.

4. Better is the use of an equation of state from the scaled particle theory (SPT). Here, the corresponding binding isotherm is called the "SPT" isotherm.

5. The general description of binding processes by a "Gibbs" isotherm can also include the electrostatics of the binding process as introduced in Chapter 11.

6. The lateral pressure of the protein gas exerts a lateral pressure on the membrane.

7. From the area dependence of the electrostatic free energy a lateral pressure can be calculated. At 70% surface coverage the lateral pressure corresponds to 0.0193 N/m which is equivalent to 38.7 bar relative to the cross section of the membrane.

8. This pressure can be sufficient to rupture the membrane or to facilitate the insertion of proteins. Thus, proteins that adsorb to membrane surfaces tend to insert into the membrane at higher degrees of surface coverage.

9. Pore formation processes of a number of antimicrobial peptides can be understood that way.

10. When proteins bind to mixed lipid membranes, lipid rearrangement takes place that influences the binding process.

13
Elasticity and Curvature

13.1
Liquid Crystalline Phases

Lipid membranes are closely related to liquid crystals. Liquid crystals are phases of axial molecules that influence each other in their orientation. This is clearly the case for a lipid membrane since the lipid molecules display a preferential orientation within the membrane.

Before we describe the theory of membrane elasticity, we start by describing the more general case of liquid crystals in three dimensions. One can mainly distinguish four different classes of liquid crystals:

1. *Nematic liquid crystals*.
   Most cylindrical molecules do not display spacial order, but an order in orientation since next nearest neighbor molecules influence each other in orientation (Fig. 13.1, left).

2. *Smectic liquid crystals*.
   Additional to a preferential orientation of molecules one finds an arrangement of molecules in layers. Smectic phases are more ordered than the nematic phases and therefore in most cases display a higher viscosity. (Fig. 13.1, center left).

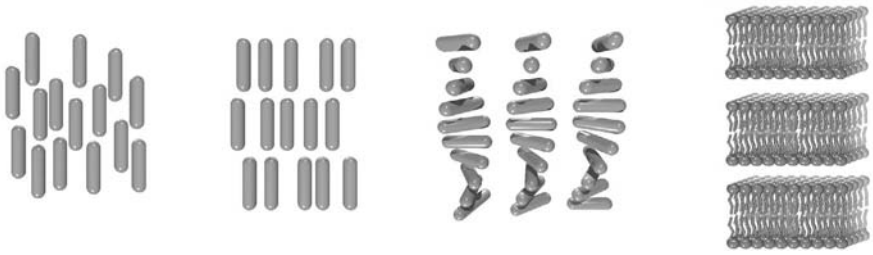

Fig. 13.1 Different liquid crystalline phases. Left: nematic. Center, left: smectic. Center, right: cholesteric. Right: lyotropic.

3. *Cholesteric liquid crystals*.
   Such phases occur in derivatives of cholesterol. One finds a rotation (twist) of the molecules perpendicular to the molecular axis. All nematic phases with strong twist are called cholesteric (Fig. 13.1, center right).

4. *Lyotropic liquid crystals*.
   Polar molecules with one hydrophilic and one hydrophobic side form membranes. The lyotropic liquid crystals are related to smectic phases (Fig. 13.1, right). Lipid multilayers are lyotropic liquid crystals.

A multilayered lipid membrane is a lyotropic liquid crystal (Fig. 13.1, right). A single lipid membrane can be considered as liquid crystal in two dimensions.

13.2 Elastic Theory of Incompressible Liquid Crystalline Phases

In the following we outline the theory of liquid crystals by Frank (1958) who himself based his work on earlier publications by Friedel (1922) and Oseen (1933). In liquid crystalline phases an equilibrium order of molecules exists, which can be altered by performing work. This leads to a distortion of the liquid crystal (Fig. 13.2). The distortion is usually given in relation to a unit vector $\underline{L}(x, y, z)$ that indicates the preferred orientation at a given point (x, y, z). One can distinguish between different distortions.

- Splay: $s_1 = \partial L_x/\partial x \qquad s_2 = \partial L_y/\partial y$ (Fig. 13.3, left)
  Splay describes curvature as one finds it for instance on the surface of a balloon.

- Twist: $t_1 = -\partial L_y/\partial x \qquad t_2 = \partial L_x/\partial y$ (Fig. 13.3, center)
  Twist rather describes torsion within the surface in the x–y plane.

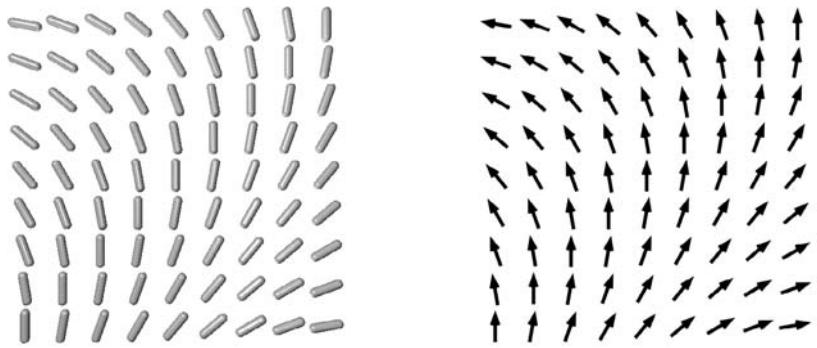

Fig. 13.2 Vector field of the orientation of molecules in a liquid crystal.

- Bending: $b_1 = \partial L_x/\partial z \qquad b_2 = \partial L_y/\partial z$ (Fig. 13.3, right)

  Bending would then be a property only occurring in a three-dimensional medium that extends into the z-direction. Thus, bending (as defined by Frank (1958)) applies to lipid multilayers, but not to purely two-dimensional systems.

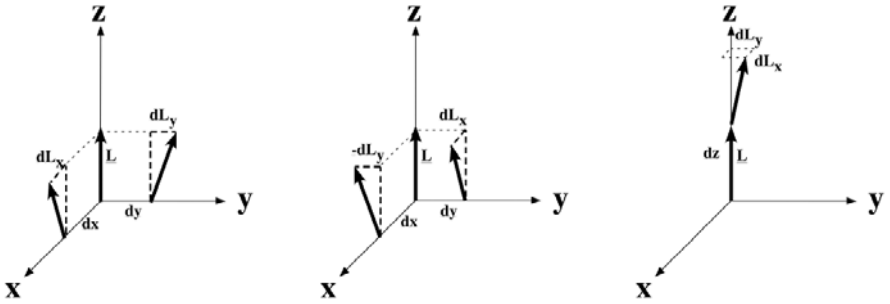

Fig. 13.3 Different distortions in a vector field. Left: splay. Center: twist. Right: bending.

Let us now define: $a_1 \equiv s_1$, $a_2 \equiv t_2$, $a_3 \equiv b_1$, $a_4 \equiv -t_1$, $a_5 \equiv s_2$, $a_6 \equiv b_2$.

We now introduce a vector $\underline{L}(x, y, z)$ of unit length 1 that describes the orientation of molecules in the liquid crystal (see Fig. 13.2). We choose a local coordinate system such that $\underline{L}(0, 0, 0)$ shall be parallel to the z-axis ($\underline{L}(0, 0, 0) = (0, 0, 1)$). The distortion of the liquid crystalline matrix at a small distance (x, y, z) from the origin is now described by

$$\begin{aligned} L_x &= a_1 x + a_2 y + a_3 z + O(r^2) \\ L_y &= a_4 x + a_5 y + a_6 z + O(r^2) \\ L_z &= 1 + O(r^2) \qquad r^2 = x^2 + y^2 + z^2 \end{aligned} \tag{13.1}$$

This is a linearization of the distortion valid at small x, y and z.

To deform the liquid crystal one has to change its free energy. Let us assume that the Gibbs free energy G of a liquid crystal in a configuration deviating from equilibrium is given by

$$G = \int_v g \, dv \tag{13.2}$$

with a free energy density $g = g(x, y, z)$. For small distortions of the liquid crystal one can approximate the free energy density by a harmonic potential:

$$g = \sum_i k_i a_i + \frac{1}{2} \sum_i \sum_j k_{ij} a_i a_j \qquad i, j, = 1, 2, \ldots, 6 \qquad k_{ij} = k_{ji} \tag{13.3}$$

where k_i and k_{ij} are the elastic constants. This is done in analogy to Hooke's law in the mechanics of springs. The first linear terms are due to the fact that in the minimum free energy configuration molecules do not necessarily have to be all parallel. The cholesteric phase in Fig. 13.1 is an example, but the orientational distribution shown in Fig. 13.2 could also represent an undistorted crystal. For a liquid crystal where all molecules are parallel in the configuration of lowest free energy, the constants $k_1, k_2, \ldots, k_6 = 0$. In the next paragraph we will relate the linear constants a_i to the "spontaneous curvature."

Equation (13.3) yields six constants k_i and 36 constants k_{ij}. Since $a_i a_j = a_j a_i$ it follows that $k_{ij} = k_{ji}$. Thus, one only has 21 different k_{ij}. The total number of elastic constants from linear and quadratic terms is therefore 27.

In the following it shall be demonstrated that many of these constants are not independent of each other.

13.2.1 Using Symmetries

The free energy density is a scalar (it has no "direction") and may therefore not depend on the orientation of the coordinate system. One can therefore choose another coordinate system (x', y', z') (letting here $z = z'$, resulting in an effective rotation or the rotation of the mirror image around the z-axis), in which one finds

$$g = \sum_i k_i a_i' + \frac{1}{2} \sum_i \sum_j k_{ij} a_i' a_j' \tag{13.4}$$

It has been shown by Frank (1958) that by rotating the coordinate system by an arbitrary angle around the z-axis one can significantly reduce the number of independent moduli k_i and k_{ij} (see Fig. 13.4). We do not perform the lengthy calculation here. Of the six constants k_i two are equal to zero and only two are independent (k_1 and k_2) such that the vector (k_i) is given by

$$(k_i) = (k_1 \quad k_2 \quad 0 \quad -k_2 \quad k_1 \quad 0) \tag{13.5}$$

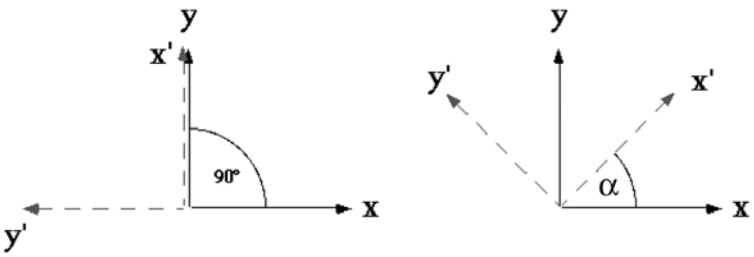

Fig. 13.4 Symmetry operations in a vector field: Rotation of the coordinate system around the z-axis by an angle α.

Only five of the k_{ij} are independent (which are k_{11}, k_{22}, k_{33}, k_{12}, and k_{24}) and the matrix (k_{ij}) is given by

$$(k_{ij}) = \begin{pmatrix} k_{11} & k_{12} & 0 & -k_{12} & (k_{11}-k_{22}-k_{24}) & 0 \\ k_{12} & k_{22} & 0 & k_{24} & k_{12} & 0 \\ 0 & 0 & k_{33} & 0 & 0 & 0 \\ -k_{12} & k_{24} & 0 & k_{22} & -k_{12} & 0 \\ (k_{11}-k_{22}-k_{24}) & k_{12} & 0 & -k_{12} & k_{11} & 0 \\ 0 & 0 & 0 & 0 & 0 & k_{33} \end{pmatrix} \tag{13.6}$$

This is the general case of a three-dimensional liquid crystal with molecules of arbitrary shape. It is described by seven constants.

For special classes of molecules one can apply further symmetry operation if molecules display certain properties.

13.2.2
Apolar Molecules

If the molecules are apolar (in respect to a favored orientation) or polar with an equal probability of both orientations (this case is given in the case of a symmetric membrane), one can apply further symmetry arguments. One obtains

$$(k_i) = (0 \quad k_2 \quad 0 \quad -k_2 \quad 0 \quad 0) \tag{13.7}$$

and for (k_{ij}) one finds

$$(k_{ij}) = \begin{pmatrix} k_{11} & 0 & 0 & 0 & (k_{11}-k_{22}-k_{24}) & 0 \\ 0 & k_{22} & 0 & k_{24} & 0 & 0 \\ 0 & 0 & k_{33} & 0 & 0 & 0 \\ 0 & k_{24} & 0 & k_{22} & 0 & 0 \\ (k_{11}-k_{22}-k_{24}) & 0 & 0 & 0 & k_{11} & 0 \\ 0 & 0 & 0 & 0 & 0 & k_{33} \end{pmatrix} \tag{13.8}$$

Thus, the total number of constants is further reduced to five (k_2, k_{11}, k_{22}, k_{33}, and k_{24}).

13.2.3
Achiral and Apolar Molecules

Chirality is the handedness of molecules. It implies that a molecule is different from its mirror image. If a molecule is identical to its mirror image one can apply further symmetry operations and obtains

$$(k_i) = (0 \quad 0 \quad 0 \quad 0 \quad 0 \quad 0) \tag{13.9}$$

and the matrix (k_{ij}) is identical to that in Eq. (13.8). The total number of remaining constants is four (k_{11}, k_{22}, k_{33}, and k_{24}). Most lipid molecules are chiral. However, if one uses racemates in which right-handed and left-handed molecules are equally probable one can apply these simplifications.

13.2.4 Spontaneous Curvature

The case described in Section 13.2.1 is the general case, whereas the cases described in Sections 13.2.2 and 13.2.3 are special cases.

Remember that $a_1 \equiv s_1$, $a_2 \equiv t_2$, $a_3 \equiv b_1$, $a_4 \equiv -t_1$, $a_5 \equiv s_2$, and $a_6 \equiv b_2$.

Using the information contained in Eqs. (13.5) and (13.6) of the general liquid crystal one can write

$$\begin{aligned} g = {} & k_1(s_1 + s_2) + k_2(t_1 + t_2) \\ & + \frac{1}{2}k_{11}(s_1 + s_2)^2 + \frac{1}{2}k_{22}(t_1 + t_2)^2 + \frac{1}{2}k_{33}(b_1^2 + b_2^2) \\ & + k_{12}(s_1 + s_2)(t_1 + t_2) - \frac{1}{2}(k_{22} + k_{24})(s_1 s_2 + t_1 t_2) \end{aligned} \tag{13.10}$$

If one additionally introduces the abbreviations

$$s_0 \equiv -\frac{k_1}{k_{11}} \qquad t_0 \equiv -\frac{k_2}{k_{22}} \qquad g' = g + \frac{1}{2}k_{11}s_0^2 + \frac{1}{2}k_{22}t_0^2 \tag{13.11}$$

where s_0 and t_0 are called the spontaneous splay and the spontaneous twist, respectively. They are intrinsic properties of the liquid crystal molecules. $\frac{1}{2}k_{11}s_0^2 + \frac{1}{2}k_{22}t_0^2$ only defines a constant offset of the Gibbs free energy. Since one is usually only interested in Gibbs free energy differences, this choice of an offset can always be done without affecting free energy differences. Therefore, g and g' are equivalent.

Using the definitions in Eq. (13.11) one can transform Eq. (13.10) into

$$\begin{aligned} g' = {} & +\frac{1}{2}k_{11}(s_1 + s_2 - s_0)^2 + \frac{1}{2}k_{22}(t_1 + t_2 - t_0)^2 + \frac{1}{2}k_{33}(b_1^2 + b_2^2) \\ & + k_{12}(s_1 + s_2)(t_1 + t_2) - \frac{1}{2}(k_{22} + k_{24})(s_1 s_2 + t_1 t_2) \end{aligned} \tag{13.12}$$

The meaning of the spontaneous splay and the spontaneous tilt now become obvious: If $s_1 + s_2 = s_0$, and $t_1 + t_2 = t_0$, the Gibbs free energy density is in its minimum. Thus, in equilibrium the crystal displays a natural splay and tilt. For apolar molecules the spontaneous splay is zero. For apolar and achiral molecules the spontaneous twist is also zero.

13.3
Elastic Theory of Membrane Bending

We will now apply the elastic theory to a planar membrane. Let us consider a single membrane. Let us also assume that the membrane can be considered as a (nearly) infinitely thin film such that it has no extension into the z-direction. We can therefore omit the terms containing the z-axes (b_1 and b_2). The free energy density can therefore be written as

$$g' = \frac{1}{2}k_{11}(s_1 + s_2 - s_0)^2 + \frac{1}{2}k_{22}(t_1 + t_2 - t_0)^2 + k_{12}(s_1 + s_2)(t_1 + t_2) - \frac{1}{2}(k_{22} + k_{24})(s_1 s_2 + t_1 t_2) \tag{13.13}$$

This equation contains four elastic constant (k_{11}, k_{22}, k_{12}, and k_{24}). Spontaneous twist is a consequence of chirality of molecules. Typically, lipid molecules are chiral. This, as a consequence, leads to twist distortions of membranes and chirality within the membrane.

13.3.1
Membranes Without Twist

Let us now discuss a special case of this equation: L shall be parallel to the membrane normal and the spontaneous twist shall be zero (see Fig. 13.5). This can be achieved by either using racemic mixtures of lipids (with equal amounts of left- and right-handed molecules) or by considering molecules

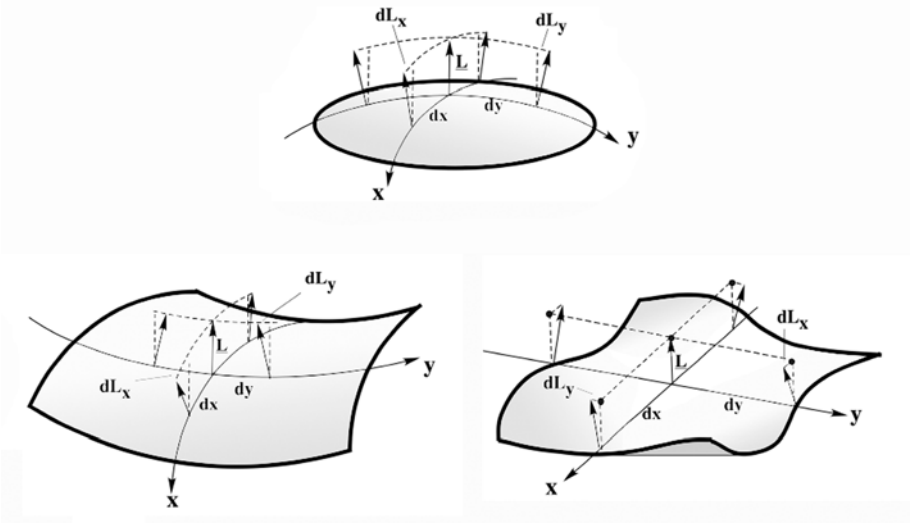

Fig. 13.5 Top: curved membrane with splay. Bottom, left: saddle point structure. Bottom, right: Membrane surface with twist.

without chirality. Further, let us ignore twist distortions all together. The above equation for the free energy (Eq. (13.13)) then simplifies to

$$g' = \frac{1}{2} K_B \, (s_1 + s_2 - s_0)^2 + K_G \, s_1 s_2 \tag{13.14}$$

with $K_B \equiv k_{11}$ and $K_G \equiv -(k_{22} + k_{24})$. This equation contains only two constants: K_B, which is often called "bending modulus" even though it is technically rather a "splay modulus." K_G is called the "Gaussian modulus." In the following we will denote K_B as the bending modulus.

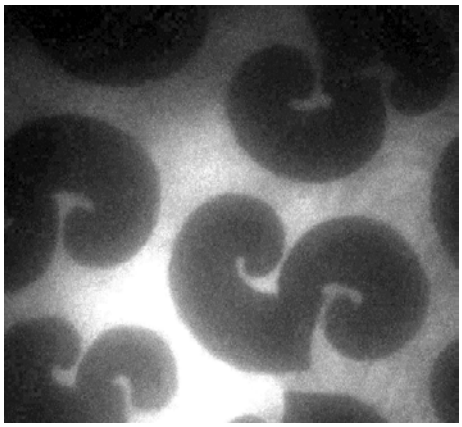

Fig. 13.6 In monolayer experiments on a water surface one can see that chirality of lipids plays a role on long length scales. This image shows a section of 100 µm × 100 µm in the liquid-expanded (fluid)/liquid-condensed (gel) coexistence regime of a DPPC monolayer. Domains can be distinguished due to a tiny concentration of fluorescence markers that dissolve better in the fluid phase. The gel domains, shown in dark shades, show a distinct handedness. Gel-like domains display chiral shapes indicating twist of the molecules. Courtesy M. Gudmand, NBI Copenhagen.

Equation 13.14 was derived by Wolfgang Helfrich in a highly cited paper. He used a somewhat more elegant differential geometry approach (Helfrich, 1973).

Monolayer experiments as shown in Fig. 13.6, indicate, however, that chirality of lipids cannot generally be ignored, in particular not in the solid-ordered (gel) phase. Liquid condensed domains in monolayers display a pronounced handedness on length scale of a few 10 µm. Equation (13.14) is very often used, but one should be aware of its limitations and the underlying assumptions.

13.3.2 Radii of Curvature

The splay of the membrane surface is related to the radius of curvature of the membrane segment. Let us consider a curved surface with a curvature in the

x-direction described by a radius of curvature, R_x. Similarly, the radius of curvature in the y-direction shall be described by the radius R_y. In Fig. 13.7 this is demonstrated. If one considers a displacement dx of the vector $|L|$ along the x-axis of the membrane surface and the surface displays curvature, one also obtains a relative change of the angle α. This change can also be expressed in a change of the x-component of the vector $|L|$, dL_x:

$$\frac{dx}{R_x} = \sin(\alpha) \qquad \text{and} \qquad \frac{dL_x}{|L|} = \sin(\alpha) \tag{13.15}$$

with $|L| = 1$. From this follows that

$$\frac{1}{R_x} = \frac{dL_x}{dx} = s_x \,(= s_1) \tag{13.16}$$

This situation is shown in Fig. 13.7 (left). An equivalent situation is shown in Fig. 13.7 (right) with the only difference that the curvature points in the other direction. For this situation, the displacement dL_x points in the opposite direction, such that

$$-\frac{1}{R_x} = \frac{-|dL_x|}{dx} = s_x \tag{13.17}$$

Thus, one obtains a radius of curvature that carries a negative sign. The choice of the sign of the radius of curvature depends on the arbitrary choice of the direction of the membrane normal. Similarly, the radius of curvature in the y-direction can be related to the splay in the y-direction

$$\pm\frac{1}{R_y} = \frac{dL_y}{dy} = s_y \,(= s_2) \tag{13.18}$$

The arbitrary choice of the direction of the membrane normal only plays a role when the two radii of curvature, R_x and R_y point in the opposite direction.

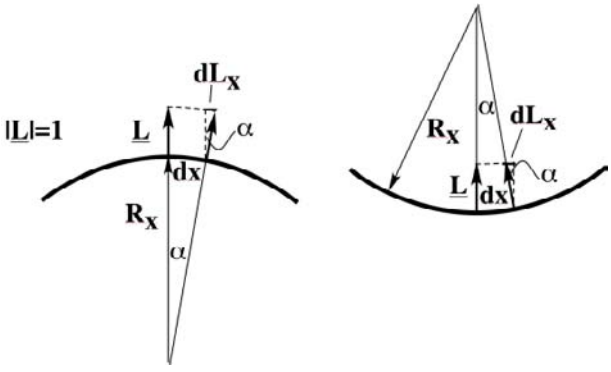

Fig. 13.7 Illustration of the connection of splay distortions with the radius of curvature.

13.3.3 Topology of Vesicles and Saddle Points

A vesicle is a closed structure in itself. Since this creates a topological boundary condition, the elastic free energy must not be necessarily in a free energy minimum. If the vesicle is spherical $|R_x| = |R_y| = |R|$. If the membrane itself is made of the same lipids on both sides and is thus symmetric, the spontaneous radius of curvature is zero. The total elastic free energy is then given by

$$G_{\text{vesicle}} = \frac{K_B}{2} \oint_A \left(\frac{4}{R^2} \right) dA + K_G \oint \frac{1}{R^2} dA \tag{13.19}$$

Since the surface of a spherical vesicle is $4\pi R^2$, we obtain

$$G_{\text{vesicle}} = 8\pi K_B + 4\pi K_G \tag{13.20}$$

independent of the radius of the vesicle.

A typical value for the bending modulus in a fluid phase lipid membrane is $K_B = 10^{-19}$ J and the Gaussian modulus is of similar magnitude. These values differ slightly depending on the method used. A careful review on measurements of both quantities as obtained by different methods is given by Marsh (2006). The elastic free energy of a vesicle is independent of radius but not independent of shape. If the vesicle is deformed, G_{vesicle} changes.

One can show that the integrated Gaussian term is independent of vesicular shape such that generally one obtains for a closed vesicle without topological defects

$$K_G \oint_A s_1 s_2 dA = 4\pi \cdot K_G \tag{13.21}$$

Thus, when calculating the changes of the integrated curvature free energy of vesicle deformation one can ignore the Gaussian term.

The Gaussian term becomes especially important for saddle point structures as shown in Fig. 13.5. Such saddle points can be found in cubic phases and in sponge phases, but also in fusion pores of vesicles.

Let us first make the simplifying assumption that in the saddle point the two radii of curvature have the same value but opposite sign ($R_1 = -R_2$). Let us furthermore assume a symmetric membrane where the spontaneous radius of curvature, s_0, is zero. Then we find for the "bending" term $1/2\, K_B(s_1 + s_2)^2 = 0$. Surfaces where $(s_1 + s_2)^2$ is zero at any point of the surface are called minimal surfaces. Cubic lipid phases are often considered to represent minimal surfaces. However, the Gaussian term $K_G s_1 s_2$ assumes a value different from zero and the entire elastic free energy is described by the Gaussian term.

13.3.4
Vesicles with Fixed Volume/Area Ratio

For closed vesicles the integrated Gaussian term is constant and does not have to be considered. For symmetric membranes the "bending" term obviously approaches a minimum if the vesicle is spherical, because the curvature terms enter the equation quadratically. The volume-to-area ratio is given by $V/A = R/3$.

Membranes display a water permeability that is highly dependent on the excess heat capacity of the membranes (see Chapter 17). Outside of the transition regime one may assume that for short periods of time the membrane can be considered as impermeable for water. This implies that a spherical vesicle cannot be deformed, because the volume-to-area ratio would decrease. This is impossible for a water-impermeable membrane. On the other hand, if $V/A < R/3$ the vesicles cannot assume spherical shapes because no water can flow into the vesicles. For such situations one has to find the minimum of the elastic free energy of a vesicle by assuming a fixed volume/area ratio. In Fig. 13.8 this is shown both experimentally and theoretically for a series of different volume/area ratios.

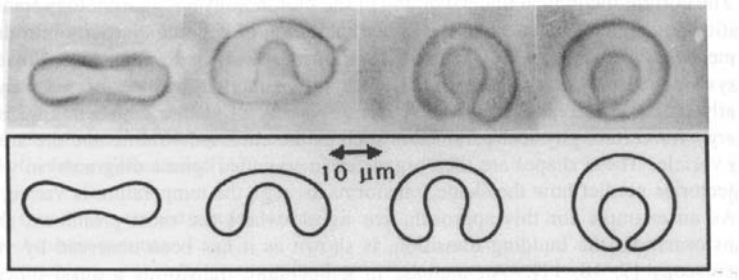

Fig. 13.8 Shapes of lipid vesicles different ambient temperatures, as found in a light microscope. Top row: experimentally found vesicle shapes for various volume/area ratios of the vesicles. Bottom: Calculated vesicle shapes for different ratios reproducing the shapes from the experiment. From Lipowsky (1995) with permission from Elsevier.

13.3.5
Fusion Pores

In biological cells one of the most frequent membrane processes is secretion, meaning the fusion or fission of vesicular membranes. In exocytosis, for instance, synaptic vesicles are thought to fuse with the presynaptic membrane with the subsequent release of neurotransmitters into the synaptic gap. During the fusion process so-called fusion pores are formed that display regions of high curvature. Since such fusion pores contain saddle point structures and

display a bending and a Gaussian term. Since two vesicles fuse to one vesicle, the Gaussian contribution to the free energy reduces from $2 \times 4\pi K_G$ to $4\pi K_G$ (Fig. 13.9). Thus, the Gaussian contribution cannot be neglected when calculating the elastic free energy of a fusion pore. Values for the Gaussian bending modulus K_G are on the order of 10^{-19}J (Marsh, 2006). It is not unreasonable to assume that there are particular lipids or lipid mixtures that have elastic constants that stabilize fusion pores. The cubic phase shown in Fig. 2.10 can be seen as a network of vesicles linked by fusion pores.

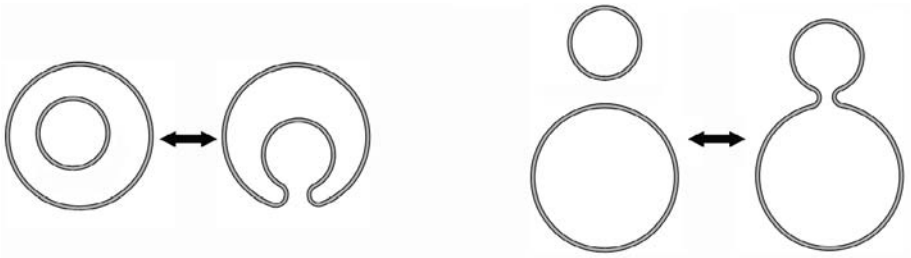

Fig. 13.9 Two membrane fusion events that change the Gaussian contribution to the total elastic free energy. Events of this nature are thought to play a role in synaptic exo- and endocytosis, and in many secretion processes.

Kozlovsky and Kozlov (2002) have calculated the elastic free energy of fusion pores to find out whether such pores can spontaneously be created on the basis of thermal fluctuations (which are on the order of kT). During this calculation they assumed that the membrane is homogeneous and isotropic. They further assumed that the bending modulus κ is a constant with a value on the order of 10^{-19} J, and they neglected the contribution of Gaussian curvature. With such calculations they arrived at an elastic free energy on the order of $40kT$ for one fusion pore. This is a very high value which makes it very unlikely that such a process would occur spontaneously.

Calculating elastic free energies using such simplifying assumptions may be dangerous. It is likely that in curved regions lipid membranes display a different lipid composition because some lipids tend to induce curved structures. Thus, the elastic free energy would couple to the chemical potentials of the membrane components - including the membrane proteins. Furthermore, the elastic constants cannot be considered as universal constants. As shown in Chapter 14 they are highly dependent on temperature, pH, and other system variables that can be influenced by the biological organism.

13.4 Summary: Key Ideas of Chapter 13

1. Liquid crystals are made of elongated molecules that display correlated orientations in space.
2. The elastic free energy can be derived by using quadratic approximations (Hooke's law) for the different distortions that are possible in space.
3. The elastic free energy of incompressible liquid crystals can be described with seven elastic constants, related to the different splay, twist, and bending distortions.
4. If the liquid crystal consists of apolar molecules, the free energy can be described by using five elastic constants.
5. If the liquid crystal consists of apolar and achiral molecules, 4 elastic constants are sufficient to calculate the elastic free energy.
6. If the liquid crystal displays splay and twist in equilibrium (no work performed), it possesses spontaneous splay and twist.
7. A lipid membrane can be considered as a two-dimensional liquid crystal. Thus, bending modes do not have to be considered. If the membrane does not display twist distortions (achiral molecules) three elastic constants are sufficient to calculate the elastic free energy of the membrane: The 'bending' modulus K_B, the Gaussian modulus K_G, and the spontaneous curvature, s_0. Major contributions to the elastic free energy of membranes have been made by Wolfgang Helfrich.
8. The Gaussian contribution to the Gibbs free energy of closed vesicular shapes is a constant.
9. Fusion events imply a change in the Gaussian contribution to the elastic free energy.
10. The elastic theory derived in this chapter is only valid for homogeneous and isotropic membranes. It does not cover membranes with domain formation and lateral heterogeneities.
11. Typically the elastic constants are functions of temperature, pH, ionic strength, and membrane asymmetry (see the next chapter).

14
Thermodynamics of the Elastic Constants

In Chapter 13 we have described the elastic constants for liquid crystals and membranes that are incompressible. This implies that hydrostatic pressure does not change the volume and lateral pressure does not change the area of a membrane. For real membranes this is not the case. Lipid membranes, both of artificial and biological origin are compressible. Further, the elastic constants turn out to be the functions of temperature, pressure, and other intensive system variables.

Liquids usually are not very compressible. On the other hand, in melting transitions lipid membranes change their volume by about 4% and the area by about 25%. At the melting point of a lipid membrane the Gibbs free energy difference between gel- and fluid phase is zero. Therefore, the free energy that has to be provided to melt the membrane is zero. It seems therefore that membranes should be very compressible close to the melting events. In this chapter we show that the elastic constants are highly temperature dependent. Since melting events change as a function of pH, pressure, ionic strength, etc., the elastic constants will be a function of all these intensive variables.

In a population of lipid vesicles with identical number of lipids (a canonical ensemble), each vesicle may display a different internal energy H_i, a different area, A_i, and a different lipid volume, V_i. Following Section 4.9, the enthalpy H_i of vesicle i is given by

$$H_i = E_i + p \cdot V_i + \Pi \cdot A_i \tag{14.1}$$

with the hydrostatic pressure p and the lateral pressure Π. The partition function for a monolayer at constant pressure and constant lateral pressure is given by

$$Q = \sum_i \Omega_i \exp\left(-\frac{H_i}{RT}\right) \tag{14.2}$$

where the sum is over all states of different enthalpy, and Ω_i is the degeneracy of the state with enthalpy H_i The mean enthalpy, averaged over all vesicles, is

given by

$$\langle H \rangle = \frac{1}{Q} \sum_i H_i \Omega_i \exp\left(-\frac{H_i}{RT}\right) \tag{14.3}$$

The mean volume, averaged over all vesicles, is given by

$$\langle V \rangle = \frac{1}{Q} \sum_i V_i \Omega_i \exp\left(-\frac{H_i}{RT}\right) \tag{14.4}$$

The mean area, averaged over all vesicles, is given by

$$\langle A \rangle = \frac{1}{Q} \sum_i A_i \Omega_i \exp\left(-\frac{H_i}{RT}\right) \tag{14.5}$$

14.1 Heat Capacity

The heat capacity of a vesicular dispersion is given by Eq. (4.43)

$$c_p = \frac{d\langle H \rangle}{dT} = \frac{\langle H^2 \rangle - \langle H \rangle^2}{R\,T^2} \tag{14.6}$$

The heat capacity is proportional to the fluctuations in enthalpy. What does this mean? Let us consider a dispersion with large unilamellar vesicles of radius 100 nm. If one assumes a lipid area of about 0.5 nm^2 this corresponds to about 100,000 lipids per vesicle. 1 ml of a 10 mM lipid dispersion then contains about 6×10^{13} vesicles. Enthalpy fluctuations imply that each vesicle has a slightly different enthalpy, and that the values scatter around the mean enthalpy per vesicle. The difference in the enthalpy of individual vesicles can for example arise from slightly different fractions of fluid lipid, or from slightly different vibrational excitations in the lipid chains. Obviously, when the heat capacity is large, also the fluctuations are large. One can easily understand this. At the melting point of the lipid membrane the free energy difference between gel and fluid lipids is zero, meaning the free energy necessary to change the enthalpy of a vesicle is very small. Therefore, thermal fluctuations of order kT are sufficient to cause large changes in vesicle state.

If one separates the intrinsic heat capacity (originating for intramolecular degrees of freedom) of the individual lipid molecules, $c_{p,0}$, from the excess heat capacity related to the cooperative melting events, Δc_p, one can easily show that these two quantities can be added. One finds

$$c_p = c_{p,0} + \Delta c_p = \frac{\langle H_0^2 \rangle - \langle H_0 \rangle^2}{RT^2} + \frac{\langle \Delta H^2 \rangle - \langle \Delta H \rangle^2}{RT^2} \tag{14.7}$$

meaning that the enthalpy fluctuations of different parts of the system are additive and can be considered independently of other. This separation of intrinsic heat capacity and excess heat capacity plays an important role later in this chapter.

14.2 Volume and Area Compressibility

Lipid membranes are to a certain degree compressible. One can distinguish the volume compressibility measured by applying hydrostatic pressure to an aqueous lipid dispersion, and area compressibility measured by compressing or stretching membranes in the membrane plane via the application of lateral pressure or tension.

14.2.1 Volume Compressibility

Volume compressibilities of lipid membranes can be measured with ultrasonic velocity measurements, which are described below. Briefly, the speed of sound in a lipid dispersion depends on the compressibility of the lipid membranes (and the compressibility of water). Thus, in ultrasonic resonators, one can deduce the volume compressibility from the wavelength of a standing wave (Fig. 14.10).

Let us now consider a lipid membrane being compressed at constant temperature. This usually means that the heat released upon compression is absorbed by a large external water bath. For lipid vesicles in an aqueous environment this is fulfilled if the compression is performed very slowly (much slower than the relaxation processes in the membrane). With volume we mean the volume of the lipid membrane, but not the aqueous volume of the lipid vesicles.

The hydrostatic pressure change Δp in the liquid is proportional to the relative change in volume, $\Delta V / V_0$, at constant temperature

$$\Delta p = -K_V \left(\frac{\Delta V}{V_0} \right) \tag{14.8}$$

Here, K_V is the modulus of compression used in a similar manner as the elastic moduli in the previous chapter and V_0 is the volume at zero pressure. At constant temperature the Gibbs free energy density change upon change in volume as the integral $\int V dp$:

$$g_V = \int \frac{\Delta V}{V_0} dp = -K_V \int \frac{\Delta V}{V_0} d\left(\frac{\Delta V}{V_0} \right) = +\frac{1}{2} K_V \left(\frac{\Delta V}{V_0} \right)^2 \tag{14.9}$$

in equivalence to Hooke's law.

On the other hand, the isothermal volume compressibility κ_T^V is given by

$$\kappa_T^V = -\frac{1}{V_0}\left(\frac{dV}{dp}\right)_T \tag{14.10}$$

By comparison with Eq. (14.8) one can see that the compressibility is the inverse of the compression modulus

$$\kappa_T^V = \frac{1}{K_V} \tag{14.11}$$

To be more precise, the compressibility of the membrane is that of the canonical ensemble average (e.g., of the large number of vesicles in a vesicular dispersion). Therefore, the compressibility in Eq. (14.10) should rather be expressed by using the thermal average of the membrane volume.

$$\kappa_T^V = -\frac{1}{\langle V_0\rangle}\left(\frac{d\langle V\rangle}{dp}\right)_T \tag{14.12}$$

In Section 4.10.2 (or by forming the pressure derivative of Eq. (14.4)) we have shown that in fact the isothermal compressibility can be written as

$$\kappa_T^V = \frac{\langle V^2\rangle - \langle V\rangle^2}{\langle V\rangle\, R\, T} \tag{14.13}$$

The volume compressibility is proportional to the fluctuations in volume. The physical origin of this relation is similar to the relation between heat capacity and enthalpy fluctuation.

As for the heat capacity (Eq. (14.7)), one can immediately show that

$$\begin{aligned}\kappa_T^V &= \kappa_{T,0}^V + \Delta\kappa_T^V \\ &= \frac{1}{\langle V\rangle \cdot RT}\left[\left(\left\langle V_0^2\right\rangle - \langle V_0\rangle^2\right) + \left(\left\langle \Delta V^2\right\rangle - \langle \Delta V\rangle^2\right)\right]\end{aligned} \tag{14.14}$$

meaning that the volume compressibility of the chains and that originating from the cooperative fluctuations are additive and can be considered independently of other.

14.2.2 Area Compressibility

While applying hydrostatic pressure is easy applying lateral pressure or lateral tension is much more difficult. One possibility is the pipette aspiration technique schematically shown in Fig. 14.1. In this technique developed by Evans and Kwok (1982) one applies suction to a giant unilamellar vesicle using a very thin glass pipette. During such an experiment the volume/area

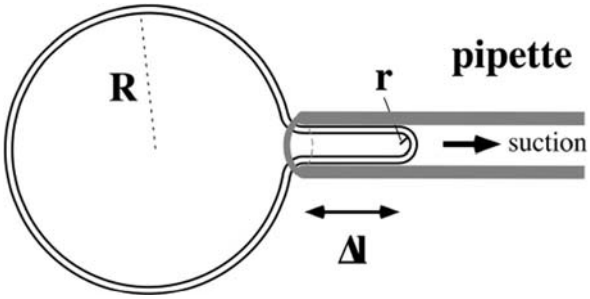

Fig. 14.1 Pipette aspiration technique to measure the lateral compressibility of membranes. From the dimensions of the vesicle, of the pipette, and the pressure difference between the bulk medium and the pipette one can calculate the lateral compressibility.

ratio changes as a function of pressure difference between external medium and the interior of the pipette. By this mean area compressibilities can be measured.

The theoretical considerations for the area compressibility are very similar to those made for the volume compressibility in the previous section. The Gibbs free energy density of area compression is

$$g_A = \frac{1}{2} K_A \left(\frac{\Delta A}{A_0} \right)^2 \tag{14.15}$$

The area compressibility is given by

$$\kappa_T^A = -\frac{1}{\langle A_0 \rangle} \left(\frac{d \langle A \rangle}{d\Pi} \right)_T \tag{14.16}$$

where Π is the lateral pressure. The compressibility is again the inverse of the lateral compression modulus.

$$\kappa_T^A = \frac{1}{K_A} \tag{14.17}$$

The isothermal area compressibility can be written as

$$\kappa_T^A = \frac{\langle A^2 \rangle - \langle A \rangle^2}{\langle A \rangle R T} \tag{14.18}$$

The area compressibility is proportional to the fluctuations in area. Again, following Eq. (14.7)

$$\begin{aligned} \kappa_T^A &= \kappa_{T,0}^A + \Delta\kappa_T^A \\ &= \frac{1}{\langle A \rangle \cdot RT} \left[\left(\left\langle A_0^2 \right\rangle - \langle A_0 \rangle^2 \right) + \left(\left\langle \Delta A^2 \right\rangle - \langle \Delta A \rangle^2 \right) \right] \end{aligned} \tag{14.19}$$

meaning that the lateral compressibility of the chains and that of the cooperative fluctuations are additive and can be considered independently of other.

14.3 The Coupling Between Area Compressibility and Curvature Elasticity

The bending elasticity can be calculated from the lateral area compressibility. Let us assume that the Gibbs free energy density of a bilayer is given by

$$\Delta g_A = \frac{1}{2} K_A \left(\frac{\Delta \langle A \rangle}{\langle A \rangle} \right)^2 \equiv \frac{1}{2\kappa_T^A} \left(\frac{\Delta \langle A \rangle}{\langle A \rangle} \right)^2 \tag{14.20}$$

with the compression modulus $K_A = 1/\kappa_T^A$, and κ_T^A is the area compressibility.

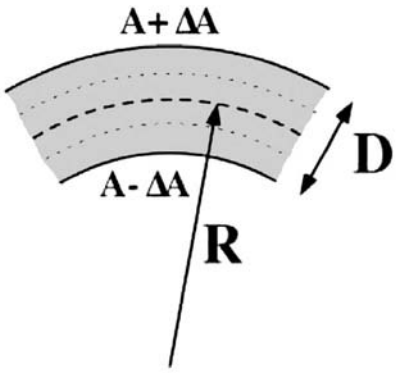

Fig. 14.2 Schematic drawing of a curved membrane. The outer monolayer is stretched and the inner monolayer is compressed. This creates a relation between bending elasticity and lateral compressibility.

If one considers the lipid monolayer as half a bilayer, we obtain

$$\Delta g_{\text{mono}} = \frac{1}{4\kappa_T^A} \left(\frac{\Delta A}{A} \right)^2 \tag{14.21}$$

assuming that the free energy density of a monolayer compressed by ΔA is only half of that of a bilayer.

If we bend a membrane segment along one coordinate with radius of curvature R (assuming that the second principle curvature is zero) the bending free energy density of the curved membrane segment is given by

$$\Delta g_B = \frac{1}{2} K_B \left(\frac{1}{R} \right)^2 \equiv \frac{1}{2\kappa_B} \left(\frac{1}{R} \right)^2 \tag{14.22}$$

If a membrane is curved, the outer monolayer has to be stretched by the area increment ΔA, whereas the inner monolayer is compressed by the area increment ΔA (see Fig. 14.2). The radius R shall be defined from the center of the membrane, the center of the outer monolayer lies at $R + D/4$, where D is the membrane thickness. The center of the inner monolayer lies at $R - D/4$ (cf. Fig. 14.2). Now, for geometrical reasons

$$\frac{A + \Delta A}{R + D/4} = \frac{A - \Delta A}{R - D/4} \tag{14.23}$$

or

$$\frac{1}{R} = \frac{4\Delta A}{A \cdot D} \tag{14.24}$$

Equation (14.24) can be inserted into Eq. (14.22) to yield

$$\Delta g_B = \frac{1}{2\kappa_B} \left(\frac{4\Delta A}{A \cdot D} \right)^2 \tag{14.25}$$

The free energy should also correspond to that of one monolayer expanded by ΔA and a second one compressed by ΔA. Therefore,

$$2 \cdot \Delta g_{\text{mono}} = \Delta g_B \qquad \longrightarrow \qquad \kappa_B = \kappa_T^A \cdot \frac{16}{D^2} \tag{14.26}$$

with the units (J^{-1}). Therefore, one can calculate the bending elasticity (and the bending modulus) from the lateral compressibility. This expression has been derived earlier by Evans (1974). Taking literature values for DMPC membranes ($D = 3.55$ nm (Marsh, 1990), $\kappa_T^A = 7.5$ m/N (Evans and Kwok, 1982)) yields $\kappa_B = 9.52 \times 10^{18}\text{J}^{-1}$ or $K_B = 1.05 \times 10^{-19}$ J, which is close to the experimental value of the bending modulus in the fluid phase ($K_B = 1.1 \times 10^{-19}$ J at $T_m + 2.5K$, (Meleard et al., 1997)).

It can also be concluded that the bending elasticity is a linear function of the curvature fluctuations and that the curvature fluctuations can be related to the area fluctuations.

14.4 The Temperature Dependence of the Elastic Constants

In the following we show that the temperature dependence of enthalpy, volume, and area are intimately related to each other. We show a number of relationships between the various elastic constants that depend on experimental findings.

14.4.1
Proportionality Between Enthalpy and Volume Changes

As mentioned earlier, during melting transitions enthalpy, volume, and area change. While enthalpy changes can be measured by calorimetry, volume changes can be obtained using a so-called Kratky balance (Kratky et al., 1969, 1973). Such a balance consists in a vibrating capillary. The vibration is excited with a small magnet at the tip of the capillary (Fig. 14.3).

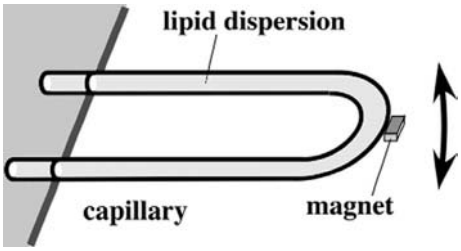

Fig. 14.3 Schematic drawing of a Kratky balance. It consists of a vibrating capillary. The eigenfrequency of the capillary filled with a lipid dispersion depends on the mass of the resonator. Larger frequency corresponds to smaller densities of the dispersion. The little magnet is used to excite the capillary in a feedback loop.

Let us now look at an interesting densitometric experiment (Fig. 14.4). For extruded large unilamellar vesicles of DMPC, the density and the heat capacity were measured as a function of temperature. The specific volume, V, is the inverse of the density, ρ. From the specific volume one can determine the volume expansion coefficient, dV/dT (see Fig. 14.4).

When plotted in the same figure one can see that the change of the volume expansion coefficient, and the excess heat capacity, c_p, are proportional functions in the transition regime. The heat capacity profile in Fig. 14.5 (left panel) displays two sharp maxima for reasons that are discussed in Chapter 15. It is obvious that the volume expansion coefficient displays exactly the same fine structure (Ebel et al., 2001). The same behavior has been found for various lipids, lipid mixtures (Fig. 14.5, right panel), and even biological membranes as bovine lung surfactant (Ebel et al., 2001) or native *E. coli* membranes.

This finding means that

$$\frac{d}{dT}\langle \Delta V(T)\rangle \propto \frac{d}{dT}\langle \Delta H(T)\rangle \tag{14.27}$$

or

$$\frac{d}{dT}\langle \Delta V(T)\rangle = \gamma_V \frac{d}{dT}\langle \Delta H(T)\rangle \tag{14.28}$$

where γ_V is a constant with units m^3/J. It shall be noted that this is only true for the excess volume changes and the excess heat capacity obtained in

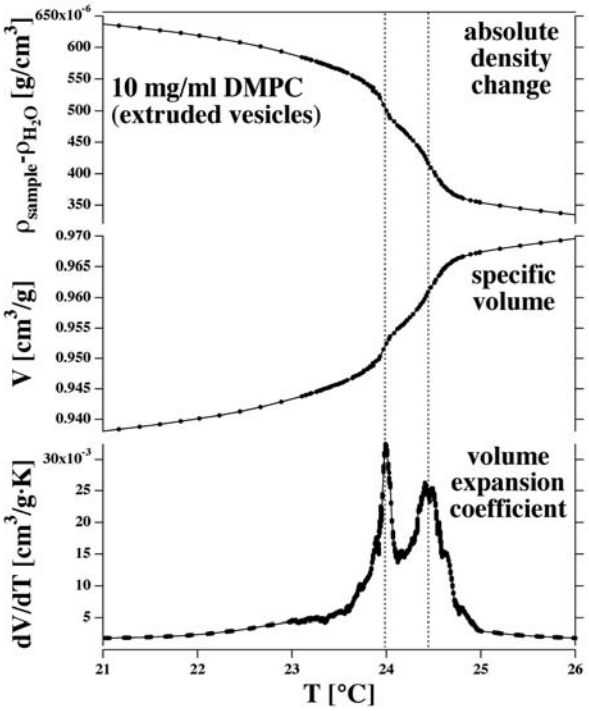

Fig. 14.4 Volume expansion coefficient of extruded DMPC vesicles and heat capacity of the same sample. The two functions are proportional, leading to the relation $\frac{d\Delta V}{dT} = \gamma_V \frac{d\Delta H}{dT}$. From Ebel et al. (2001).

the transition regime. By integrating Eq. (14.28) one easily sees that this also means that

$$\langle \Delta V(T) \rangle = \gamma_V \cdot \langle \Delta H(T) \rangle \tag{14.29}$$

The value of $\gamma_V = 7.8 \pm 0.1 \times 10^{-10}$ m^3/J is within experimental error always the same for different lipids.

Due to Eqs. (14.4) and (14.29) we can now write

$$\langle \Delta V \rangle = \frac{1}{Q} \sum_i \Delta V_i \Omega_i \exp\left(-\frac{H_i}{RT}\right) = \frac{\gamma_V}{Q} \sum_i \Delta H_i \Omega_i \exp\left(-\frac{H_i}{RT}\right) \tag{14.30}$$

$$\langle \Delta V \rangle = \frac{1}{Q} \sum_i \gamma_V \Delta H_i \Omega_i \exp\left(-\frac{H_i}{RT}\right) \tag{14.31}$$

Consequently, we also obtain (Heimburg, 1998)

$$\Delta V_i^2 = (\gamma_V \Delta H_i)^2 \tag{14.32}$$

Our finding means that the proportional relation between volume and enthalpy changes in the transition regime is also true for all available enthalpy

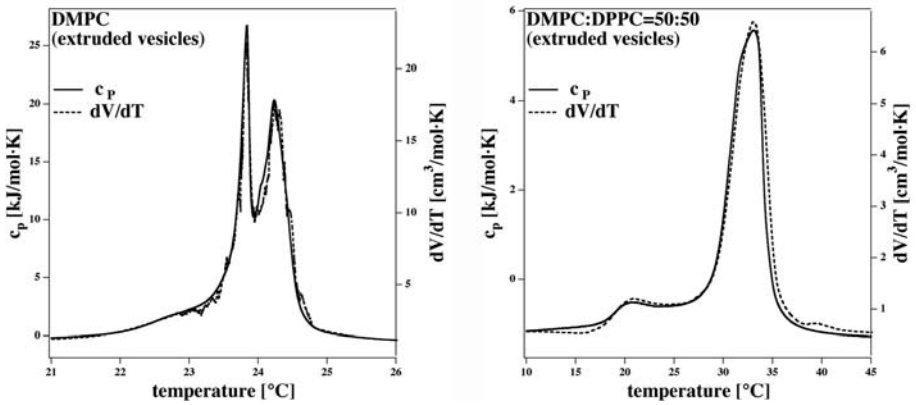

Fig. 14.5 Left: Excess heat capacity and volume expansion coefficient of extruded DMPC vesicles as a function of temperature. Right: Excess heat capacity and volume expansion coefficient for a mixture of DMPC:DPPC = 50:50 mol%. One can see that both functions are superimposable even in minute details of the profile. From Ebel et al. (2001).

substates (with index i) of the lipid system. With this relation we can relate the fluctuations of the volume to the fluctuations in enthalpy

$$\left\langle \Delta V^2 \right\rangle = \frac{1}{Q} \sum (\gamma_V \Delta H_i)^2 \Omega_i \exp\left(-\frac{H_i}{RT}\right) = \gamma_V^2 \left\langle \Delta H^2 \right\rangle \tag{14.33}$$

The fluctuations in volume are proportional to the fluctuations in enthalpy. This finding is not at all trivial. It is exclusively based on the experimental finding that the volume changes of lipid membranes in their melting transition are proportional to the corresponding enthalpy changes. While this is true for lipids, it is not likely to be generally true. The above finding is not based on first principles, and the reason why the heat capacity of lipids changes proportional to the volume expansion coefficient still requires a theoretical justification.

14.4.2
Proportionality Between Enthalpy and Volume Changes by Pressure Calorimetry

The finding that volume fluctuations and enthalpy fluctuations are proportional functions is crucial for everything that follows below.

For some samples densitometric experiments are not easy, in particular not if the sample has a tendency to sediment due to a density that is higher than that of water, or for samples where the changes extend over a large temperature interval. Therefore, we develop in the following an independent and very

sensitive test of the relationship $\Delta V(T) = \gamma_V \Delta H(T)$ that is based on pressure calorimetry.

The calorimetry experiment can be performed with the application of hydrostatic pressure; applied for instance by using high pressure nitrogen. The application of pressure leads to shifts in the transition as shown in Section 6.3 and also in Fig. 14.6.

Let us now assume that the finding $\Delta V(T) = \gamma_V \, \Delta H(T)$ also $\Delta V_i = \gamma_V \, \Delta H_i$ for all available substates is correct.

The enthalpy of each substate at pressure p_0 can be written as

$$\Delta H_{i,0} = \Delta E_{i,0} + p_0 \Delta V_i \tag{14.34}$$

Typically, we will assume that $p_0 = 1$ bar, which corresponds to atmospheric pressure. If an excess hydrostatic pressure of Δp is applied to the lipid dispersion, the enthalpy of each substate changes to

$$\Delta H_{i,\Delta p} = \Delta E_{i,0} + (p_0 + \Delta p) \Delta V_i \tag{14.35}$$

Using $\Delta V_i = \gamma_V \, \Delta H_i$ we obtain from this

$$\Delta H_{i,\Delta p} = (1 + \gamma_V \, \Delta p) \, \Delta H_{i,0} \tag{14.36}$$

Using Eq. (14.3) we obtain for the enthalpy change at pressure $p_0 + \Delta p$

$$\left\langle \Delta H_{\Delta p}(T) \right\rangle = \frac{\sum_i (1 + \gamma_V \, \Delta p) H_{i,0} \Omega_i \exp\left(-(1 + \gamma_V \, \Delta p) H_{i,0}/kT\right)}{\sum_i \Omega_i \exp\left(-(1 + \gamma_V \, \Delta p) H_{i,0}/kT\right)} \tag{14.37}$$

Let us now introduce a new temperature scale

$$T^* = \frac{T}{(1 + \gamma_V \cdot \Delta p)} \tag{14.38}$$

With this definition we can rewrite Eq. (14.37)

$$\left\langle \Delta H_{\Delta p}(T) \right\rangle = (1 + \gamma_V \, \Delta p) \frac{\sum_i H_{i,0} \Omega_i \exp\left(-H_{i,0}/kT^*\right)}{\sum_i \Omega_i \exp\left(-H_{i,0}/kT^*\right)} \tag{14.39}$$

or

$$\left\langle \Delta H_{\Delta p}(T) \right\rangle = (1 + \gamma_V \, \Delta p) \cdot \left\langle \Delta H_0(T^*) \right\rangle \tag{14.40}$$

This equation indicates that one can obtain the profile measured at pressure p_0 from the profile measured at $p_0 + \Delta p$ by rescaling the temperature axis by a factor $(1 + \gamma_V \, \Delta p)$ and dividing the amplitude by the same factor. How this is done can be seen in Fig. 14.6, where this operation has been performed for extruded vesicles of DMPC and for bovine lung surfactant.

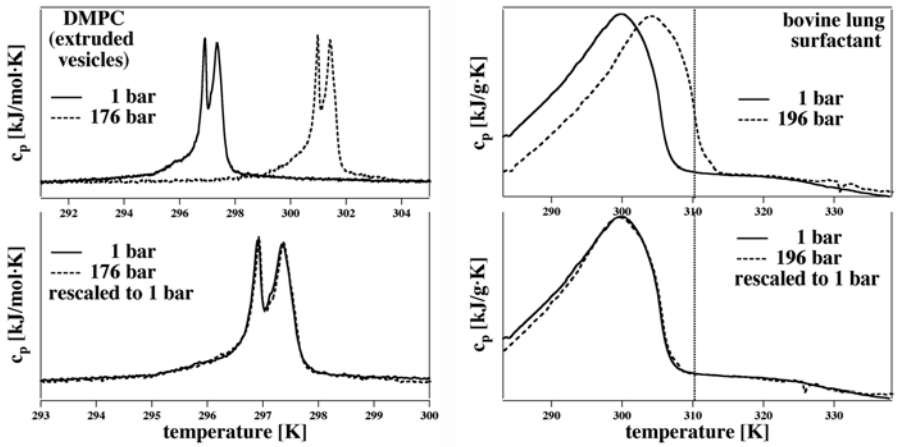

Fig. 14.6 Pressure calorimetry. Left: Heat capacity at 1 bar and at 176 bar hydrostatic pressure (top panel). If the curve obtained at 176 bar is rescaled to 1 bar it is superimposable with the curve measured at 1 bar (bottom panel). Right: The same experiment for bovine lung surfactant measured at 1 bar and at 196 bar hydrostatic pressure. The dotted line indicates bovine body temperature. From Ebel et al. (2001).

Equation (14.40) was derived by assuming that $\Delta V_i = \gamma_V \, \Delta H_i$. Only if this relation is true, one can transform the heat capacities measured at different pressures into each other. Figure 14.6 shows that this can be done to a surprising accuracy. The proportional relation is true even for complex biological systems as lung surfactant.

We obtain the shift in the melting transition from

$$T_m^* = (1 + \gamma_V \, \Delta p) T_m \tag{14.41}$$

This equation is valid for all lipids that have been investigated (different phosphatidylcholines and lung surfactant). Since $\gamma_V = 7.8 \times 10^{-10}$ m^3/J $= 7.8 \times 10^{-10}$ (m^2/N), an applied pressure of 200 bars results in a shift of the transition temperature of DMPC from $T_m = 293.85$ K to $T_m^* = 301.48$ K, or a shift of $\Delta T_m = 4.63$ K. This means that a pressure of 43.2 bar shifts the transition by 1 K.

The above findings are quite remarkable. They mean that one can derive general laws for the elastic constants even if we do not know the exact lipid composition as is usually the case for biological membranes. We can now also immediately relate findings from model lipid mixtures to biological membranes.

14.4.3
Proportionality Between Isothermal Volume Compressibility and Heat Capacity Changes

Let us now accept the finding that both $\langle \Delta V \rangle = \gamma_V \cdot \langle \Delta H \rangle$ and $\Delta V_i = \gamma_V \cdot \Delta H_i$ for all available enthalpy substates with index i. These two relations lead to

$$\left\langle \Delta V^2 \right\rangle - \langle \Delta V \rangle^2 = \gamma_V^2 \left(\left\langle \Delta H^2 \right\rangle - \langle \Delta H \rangle \right) \tag{14.42}$$

meaning that the excess volume fluctuations are exactly proportional to the excess enthalpy fluctuations. This gives us now the possibility to express the relation of the excess volume compressibility, $\Delta\kappa_T^V$, to the heat capacity:

$$\Delta\kappa_T^V = \frac{\gamma_V^2 T}{\langle V \rangle} \Delta c_p \tag{14.43}$$

Our final result is that the isothermal excess volume compressibility is exactly proportional to the excess heat capacity.

14.4.4
Proportionality Between Enthalpy and Area Changes

Let us now assume that the excess area change in the melting transition, $\langle \Delta A \rangle$ and the excess enthalpy change, $\langle \Delta H \rangle$ obey a similar relationship as the volume changes.

$$\langle \Delta A \rangle = \gamma_A \cdot \langle \Delta H \rangle \tag{14.44}$$

There are so far no sufficiently exact experiments that prove that this relationship is true. In the following we can demonstrate, however, that this relationship leads to correct predictions of the bending elasticity modulus. Therefore, we will assume that there is also a proportional relationship between excess area change and excess enthalpy change. For DPPC one finds $\gamma_A = 0.893\ \mathrm{m}^2/\mathrm{J}$. Since the corresponding constant for volume changes was universal, we also assume that γ_A has approximately the same value for all lipids.

14.4.5
Proportionality Between Isothermal Compressibility, Bending Elasticity and Heat Capacity Changes

Based on the previous considerations one can make a similar argument for the relationship between area compressibility and heat capacity,

$$\Delta\kappa_T^A = \frac{\gamma_A^2 T}{\langle A \rangle} \Delta c_p \tag{14.45}$$

In Eq. (14.26) we derived the relation between area compressibility and bending elasticity, $\kappa_B = \kappa_T^A \cdot \frac{16}{D^2}$. Using Eq. (14.45) we can rewrite this into

$$\Delta\kappa_B = \frac{16}{\langle D\rangle^2}\frac{\gamma_A^2 T}{\langle A\rangle}\Delta c_p \tag{14.46}$$

14.4.6 The Relations Between Heat Capacity and the Elastic Constants

We can summarize the findings from above to

$$\begin{aligned}
c_p(T) &= c_{p,0}(T) \;+\; \Delta c_p(T)\\
\kappa_T^V(T) &= \kappa_{T,0}^V(T) \;+\; \frac{\gamma_V^2\, T}{\langle V\rangle}\Delta c_p(T)\\
\kappa_T^A(T) &= \kappa_{T,0}^A(T) \;+\; \frac{\gamma_A^2\, T}{\langle A\rangle}\Delta c_p(T)\\
\kappa_B(T) &= \kappa_{B,0}(T) \;+\; \frac{16}{\langle D\rangle^2}\frac{\gamma_A^2 T}{\langle A\rangle}\Delta c_p(T)
\end{aligned} \tag{14.47}$$

The values for $c_{p,0}$, $\kappa_{T,0}^V$, $\kappa_{T,0}^A$, and $\kappa_{B,0}$ may assume different numerical values for the gel and the fluid lipid phase. It may therefore be a good approximation to assume that

$$\begin{aligned}
c_{p,0}(T) &= (1-f)\cdot c_{p,0}^{\text{gel}} + f\cdot c_{p,0}^{\text{fluid}}\\
\kappa_{T,0}^V(T) &= (1-f)\cdot \kappa_{T,0}^{V,\text{gel}} + f\cdot \kappa_{T,0}^{V,\text{fluid}}\\
\kappa_{T,0}^A(T) &= (1-f)\cdot \kappa_{T,0}^{A,\text{gel}} + f\cdot \kappa_{T,0}^{A,\text{fluid}}\\
\kappa_{B,0}(T) &= (1-f)\cdot \kappa_{B,0}^{\text{gel}} + f\cdot \kappa_{B,0}^{\text{fluid}}
\end{aligned} \tag{14.48}$$

where $f = f(T)$ is the fraction of fluid lipids calculated from the heat capacity

$$f(T) = \frac{\int_{T_a}^{T}\Delta c_p dT}{\int_{T_a}^{T_b}\Delta c_p dT} \tag{14.49}$$

Here, T_a is a temperature far below the melting events, T_b is a temperature far above the melting events, and $T_a < T < T_b$.

The constants in Eq. (14.48) are listed in Table 14.1. Typical changes in the isothermal volume and area compressibilities are given in Fig. 13.7.

The temperature dependence of isothermal volume and area compressibilities for DPPC unilamellar vesicles are shown in Fig. 14.7. Since they are linear functions of the heat capacity they both display pronounced maxima at the transition maximum.

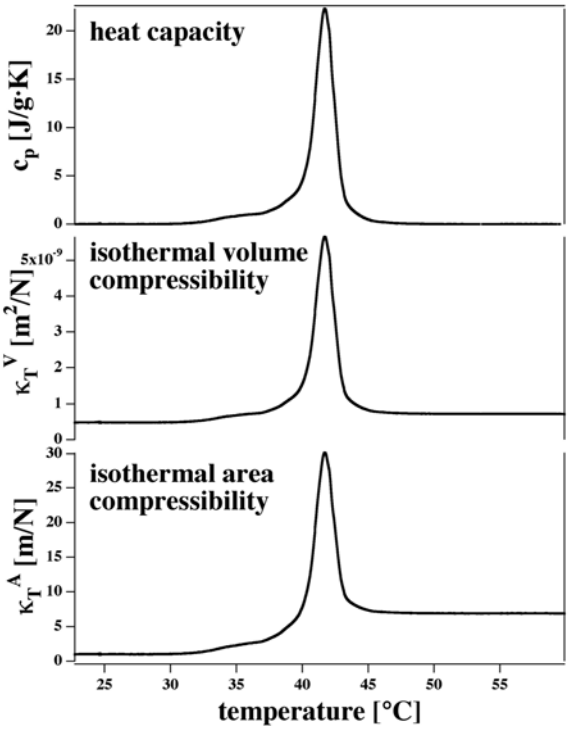

Fig. 14.7 Volume and area compressibility of extruded vesicles, calculated using Eqs. 14.47, and the values in Table 14.1.

14.4.7
Proportionality Between Bending Elasticity and Heat Capacity

In Eq. (14.26) it has been shown that the bending elasticity can be expressed as a simple function of the lateral compressibility, $\kappa_B = \kappa_T^A \cdot \frac{16}{D^2}$. Therefore, it is also a function of the heat capacity. Since lateral area compressibility displays a maximum at the melting transition the bending elasticity also displays a maximum. Membranes in the transition become very elastic. The bending modulus, $K_B = 1/\kappa_B$, displays a pronounced minimum (see Fig. 14.8). The data in Fig. 14.8 have been calculated from the heat capacity profiles of unilamellar DPPC vesicles. They have been compared to experimental data obtained for giant DMPC vesicles by Dimova et al. (2000) using optical tweezers, and by data from Fernandez-Puente et al. (1994) and Meleard et al. (1997). Similar findings were reported by Lee et al. (2001). At the heat capacity maximum the bending rigidity is about a factor of 10 smaller than in the fluid phase. This is a remarkable change and it leads to all kinds of structural rearrangements in the proximity of the chain melting transition, e.g., the formation of the ripple phase and the formation of extended bilayer network. In Chapter 15 we will focus on such transitions.

Tab. 14.1 Constants related to heat capacity, isothermal volume, and area compressibility for DPPC membranes (adapted from the values in Heimburg (1998); Halstenberg et al. (1998); Ebel et al. (2001); Schrader et al. (2002) and references therein.)

Constant	Gel phase	Fluid phase
$c_{p,0}$ (J/mol· K)	1600	1600
κ_T^V (m^3/J)	5.2×10^{-10}	7.8×10^{-10}
κ_T^A (m^2/J)	1	6.9
Specific volume (cm^3/g)	0.947	0.999
Specific area (cm^2/g)	1.9×10^6	2.52×10^6
Area/lipid (nm^2)	0.474	0.629
Volume expansion coefficient $V^{-1}(dV/dT)$ (K^{-1})	0.00088	0.001
Area expansion coefficient $A^{-1}(dA/dT)$ (K^{-1})	0.0026	0.0042
Thickness (nm)	4.79	6.29
γ_V (m^2/N)	7.8×10^{-10}	
γ_A (m/N)	0.893	
$\Delta V/V$	0.0406	($P_{\beta'} \rightarrow L_\alpha$)
$\Delta A/A$	0.246	($P_{\beta'} \rightarrow L_\alpha$)

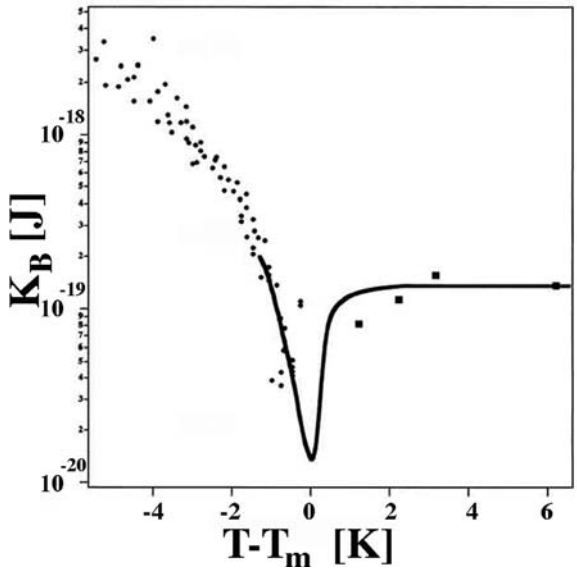

Fig. 14.8 Elastic bending modulus of DPPC LUV, calculated from the heat capacity (solid line) (Heimburg, 2000b), compared to experimental values for DMPC vesicles, from Dimova et al. (2000).

14.5 Adiabatic Volume Compressibility

The adiabatic compressibility is the compressibility under conditions where no heat is exchanged with the environment. Therefore, it is also called isentropic compressibility ($dQ = 0$ is equivalent to $dS = 0$). Typically one considers the adiabatic compressibility for short term phenomena like sound propagation. If a reversible compression lasts only for a short time the heat has no time to dissipate into the bulk environment. In Section 4.12 it has been shown that the adiabatic compressibility is given by

$$\kappa_S = \kappa_T - \frac{T}{V \cdot c_p} \left(\frac{\partial V}{\partial T} \right)_p^2 \tag{14.50}$$

In a homogeneous system this is easy to interpret because the adiabatic compressibility is a function of isothermal compressibility, heat capacity and volume expansion coefficient, all of which can be determined from the heat capacity of a lipid system. Problems arise when the system is heterogeneous. A vesicular lipid dispersion is a mixture of bulk water and lipid membranes. The isothermal compressibility of water and the lipids are additive. A problem arises for the heat capacity that shows up in the denominator on the right-hand side. The reason why a heat capacity shows up in this equation is because the heat that is released during compression is stored in the heat capacity of the system. Now we have to ask the question to what degree the water surrounding the membranes contributes to buffering of the heat during a transient compression.

Let us consider a periodic perturbation of the lipid dispersion, for instance by a sound wave with frequency ω. If the frequency of the excitation is very low, the heat released from the lipid membranes during compression has enough time to be absorbed by a large water volume. Thus, the heat capacity in Eq. (14.50) obviously assumes large values and we obtain in the limit of very low frequencies

$$\lim_{\omega \to 0} \kappa_S^V = \kappa_T^V \tag{14.51}$$

Thus, the adiabatic compressibility approaches the isothermal compressibility for low frequencies. This is the case if the periodic perturbation is slower than the slowest relaxation process. Both isothermal and adiabtic compressibility assume a maximum at the melting point of the membrane (Fig. 14.9).

On the other hand, if the frequency approaches very large values the adiabatic compressibility approaches zero

$$\lim_{\omega \to \infty} \kappa_S^V = 0 \tag{14.52}$$

This is obviously the case if the periodic perturbations are faster than the fastest relaxation process.

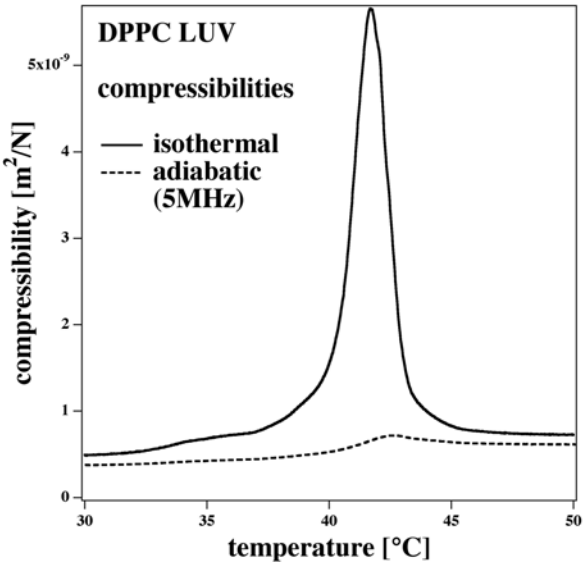

Fig. 14.9 Isothermal and adiabatic volume compressibility calculated from the heat capacity of unilamellar DPPC vesicles.

For lipid systems the sound velocity is often measured with a ultrasonic resonator in a frequency regime of a few MHz. We now make a crucial assumption that can only be justified by its success. Let us assume in the following that in the MHz regime heat can not exchange between the membranes and the bulk water. Under these conditions, one can just add the adiabatic compressibility of water and the lipid membranes

$$\kappa^V_{S,\text{dispersion}} = f_{H_2O} \cdot \kappa^V_{S,\text{lipid}} + f_{\text{lipid}} \cdot \kappa^V_{S,\text{lipid}} \qquad \text{(no heat exchange)} \qquad (14.53)$$

where f_{H_2O} and f_{lipid} are the volume fractions of water and lipids, respectively. The adiabatic compressibility of water can be calculated using the data for isothermal compressibility, heat capacity, and volume expansion coefficients that can be found in the *Handbook of Chemistry and Physics* (Lide and Frederikse, 1996). The adiabatic compressibility of the lipid membranes can be calculated using the heat capacity of the lipid membranes and the values in Table 14.1. We will not address the question how it is possible that no heat is exchanged between lipids and water even though heat conduction is very fast in water. However, we will see in the next section that this approach is quite successful and that therefore the heat exchange between membranes and aqueous environment must be negligible in the Megahertz regime.

14.6
Sound Propagation in Vesicle Dispersions

The sound velocity c_0 of a three-dimensional liquid or gas is given by

$$c_0 = \sqrt{\frac{1}{\kappa_S \cdot \rho}} \tag{14.54}$$

where ρ is the mass density. For lipid dispersions, the sound velocity can be calculated using Eq. (14.53). The sound velocity can also be measured in a resonator experiment (Fig. 14.10). Since the frequency, the wavelength, and the sound velocity are related by

$$\nu \cdot \lambda = c_0 \tag{14.55}$$

one can obtain the sound velocity from an experiment where the wavelength of a standing wave at constant frequency is measured. This usually happens in the 5 MHz regime with wavelength in the 0.3 mm regime. Lipid vesicles typically have sizes between 100 nm and a few μm and are much smaller than the wavelength. The periodic perturbation can be considered to be that of a homogenous medium because the small scale heterogeneities are averaged out over the wavelength of the standing sound wave. In an aqueous solution of lipid vesicles, the sound velocity will depend on the lipid concentration. To

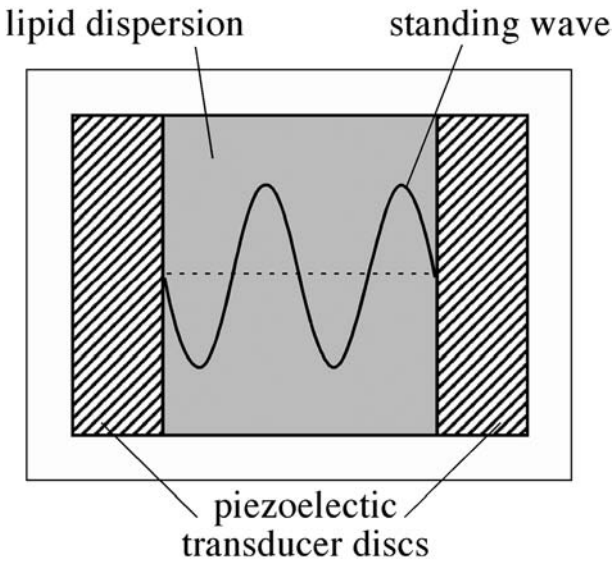

Fig. 14.10 Schematic drawing of an ultra sound cavity. It typical has a resonator length of a few centimeters. Depending on the exact dimensions of the resonator, two piezotransducers generate a standing wave in the lipid dispersion.

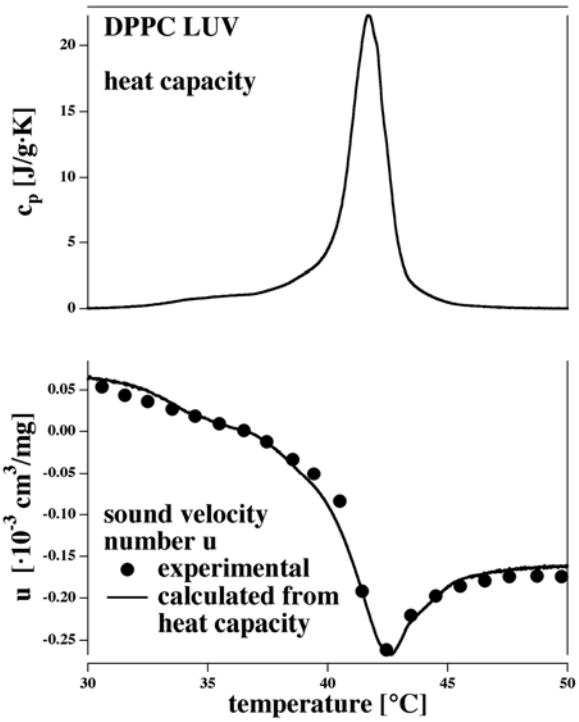

Fig. 14.11 Heat capacity and ultrasonic sound velocity number of large unilamellar vesicles of DPPC. The ultrasound velocity numbers calculated from the heat capacity are in good agreement with the experimental data, measured at 5 MHz.

obtain a normalized value for the sound velocity, the sound velocity number u is introduced,

$$u = \frac{c_0^{\text{dispersion}} - c_0^{H_2O}}{c_0^{H_2O} \cdot [L]} \tag{14.56}$$

where $[L]$ is the lipid concentration in units of (mg/ml). In Fig. 14.11 we show the experimental sound velocity numbers of DPPC LUV, measured in a 5 MHz resonator (Halstenberg et al., 1998; Schrader et al., 2002). The numbers calculated from the heat capacity are nearly identical. From the experimental sound velocity data the adiabatic compressibility can be deduced .

The sound velocity in two dimensions will play a major role in Chapter 18 when we describe density pulse propagation in biomembranes and nerves.

14.7
Curvature Fluctuations and Critical Swelling of Multilayers

14.7.1
Curvature Fluctuations

Close to the melting transitions in lipid bilayers the fluctuations in enthalpy, volume, and area are high. High enthalpy fluctuations lead to a high heat capacity (Eq. (14.7)), high volume fluctuations lead to a high volume compressibility (Eq. (14.13)), and high area fluctuations lead to a high area compressibility (Eq. (14.13)). Furthermore, according to Eq. (14.24) the curvature is related to the area difference between outer and inner monolayers. Therefore by necessity, area fluctuations lead to curvature fluctuations and the bending elasticity can be expressed as a function of the fluctuations in curvature. Let us repeat the calculations in Section 14.3 with a slightly different nomenclature. Let us consider a curved membrane segment with thickness D, an outer monolayer area of A_o and an inner monolayer area of A_i (Fig. 14.12).

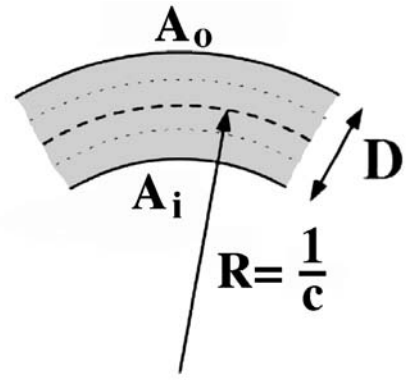

Fig. 14.12 Curved membrane segment with different areas A_o and A_i on outer and inner monolayer, respectively. The two monolayers are assumed to fluctuate independently.

Then the curvature of the membrane segment can be expressed as

$$A_o\left(R-\frac{D}{4}\right)=A_i\left(R+\frac{D}{4}\right) \tag{14.57}$$

$$c=\frac{1}{R}=\frac{4\cdot(A_o-A_i)}{D\cdot(A_o+A_i)}\approx\frac{2\cdot(A_o-A_i)}{D\cdot\langle A\rangle} \tag{14.58}$$

The fluctuations in curvature are consequently given by

$$\begin{aligned}\langle c^2\rangle - \langle c\rangle^2 &= \frac{4}{\left(\langle A\rangle D\right)^2}\cdot\left(\langle (A_o - A_i)^2\rangle - \langle (A_o - A_i)\rangle^2\right)\\ &= \frac{4}{\left(\langle A\rangle D\right)^2}\cdot\left[\left(\langle A_o^2\rangle - \langle A_o\rangle^2\right) + \left(\langle A_i^2\rangle - \langle A_i\rangle^2\right)\right]\\ &= \frac{8}{\left(\langle A\rangle D\right)^2}\cdot\left(\langle A^2\rangle - \langle A\rangle^2\right)\end{aligned} \tag{14.59}$$

assuming that the fluctuations on the outer monolayer have the same value than those on the inner monolayer. The fluctuations in curvature are obviously proportional to the area fluctuations in a monolayer. We can now express the curvature elasticity as a function of curvature fluctuations, if we recall that the area compressibility of a monolayer is given by $\kappa_T^{A,\mathrm{mono}}(\langle A\rangle \cdot kT)^{-1}(\langle A^2\rangle - \langle A\rangle^2)$ and $\kappa_T^{A,\mathrm{mono}} = 2\cdot\kappa_T^A$, and by using Eq. (14.26)

$$\langle c^2\rangle - \langle c\rangle^2 = \frac{16kT}{\langle A\rangle D^2} \tag{14.60}$$

$$\kappa_B = \langle A\rangle\frac{\langle c^2\rangle - \langle c\rangle^2}{kT} \tag{14.61}$$

According to this equation the curvature fluctuations are larger, if larger area segments are considered. Since the bending elasticity is a simple function of the heat capacity, the curvature fluctuations are also a function of the heat capacity, meaning that they are very high close to the chain melting transition.

14.7.2
Critical Swelling of Multilayered Membranes

A free standing bilayer will display curvature fluctuations, and such fluctuations are high close to the chain melting transition (Fig. 14.13 A). If the membrane is multilayered, one may wonder whether the curvature fluctuations will affect the spacing between the membranes. It seems straightforward to expect an increase in the mean distance of the membrane if the vertical height

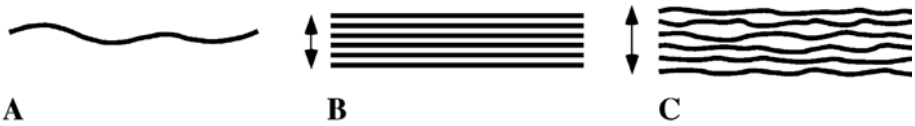

Fig. 14.13 A. Curvature fluctuations in a free standing bilayer segment. B. Multilayer stack of membranes in the absence of curvature fluctuations. C. Multilayer stack of membranes in the presence of curvature fluctuations leading to an increase in the mean bilayer spacing.

fluctuations induced by the curvature fluctuations are on a length scale comparable to the distance.

Such a problem has been considered by Helfrich (1978) who called the curvature fluctuations undulations. Helfrich concluded that the undulation free energy density g_u of a membrane in a bilayer stack takes the form

$$g_u = \frac{3\pi}{128}\frac{(kT)^2\kappa_B}{d^2} \tag{14.62}$$

where d is the spacing between the membranes (for a derivation of this equation refer to Helfrich (1978)). If the membranes are soft and the bending elasticity κ_B assumes a high value, also the undulation free energy density increases. In particular one finds that the free energy density can be lowered by increasing the bilayer spacing in a multilayer stack. Thus an increase in spacing can compensate the increase in κ_B close to the melting transition.

Hønger et al. (1994) observed this effect, which is called critical swelling, by using small angle neutron scattering (SANS) experiments (see Fig. 14.14). In such experiments they find the multilayer stack spacing increases significantly in the proximity of the lipid phase transition.

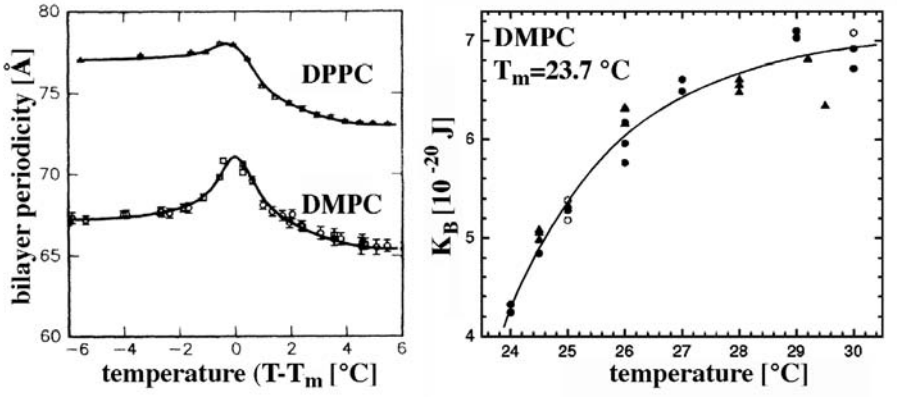

Fig. 14.14 Critical swelling of lipid multilayers. Left: Bilayer repeat distance in DPPC and DMPC multilayers display a maximum in the chain melting regime. Adapted from Hønger et al. (1994). Right: The elastic bending modulus K_B derived from the repeat spacing of DMPC multilayers displays a pronounced minimum at the chain melting temperature (cf. Fig. 14.8). Adapted from Chu et al. (2005).

Helfrich's undulation equation can be used to extract the bending elasticity (or the bending modulus, $K_B = 1/\kappa_B$) as a function of temperature. The bending modulus for DMPC multilayer membranes has been calculated by Chu et al. (2005). They found that the K_B decreases significantly if one approaches the melting temperature, in agreement with the calculations made in Section 14.4.7

14.8
Local Fluctuations at Domain Interfaces

In the following we discuss an interesting consequence of the finding in this chapter. In Chapter 8 we showed by Monte Carlo simulations and by atomic force microscopy that the fluctuations close to domain interfaces may be very high. This is shown again in Fig. 14.15 for gel–fluid interfaces in DMPC–DSPC mixtures (Seeger et al., 2005) and in Fig. 14.16 for the interface between gramicidin A aggregates and DPPC membranes (Ivanova et al., 2003).

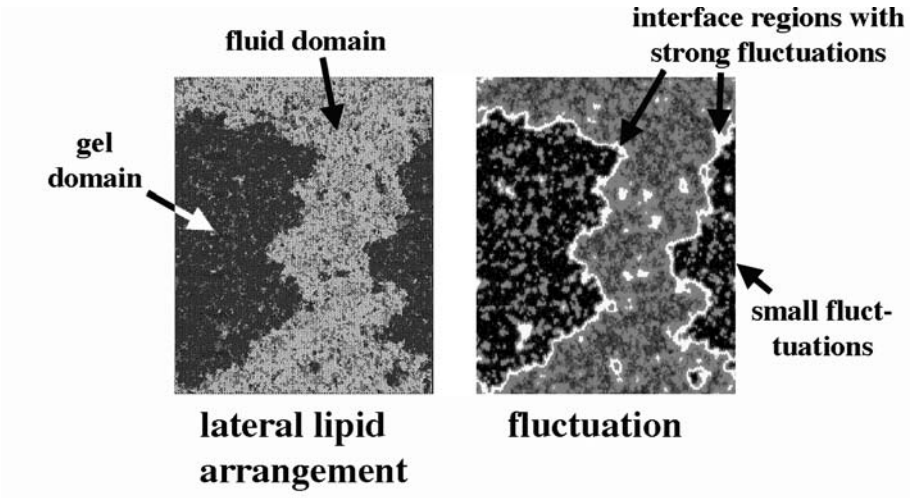

Fig. 14.15 Monte Carlo snapshots of a DMPC:DSPC=50:50 mixture at 36.9 °C. Left: distribution of lipids. Dark gray regions correspond to gel domains and light gray regions to fluid domains. Right: The same snapshot, but now the strength of the local fluctuations is shown. Bright shades correspond to large fluctuations and dark shades to small fluctuations. By comparison with the left-hand panel one can recognize that the fluctuations are especially strong at the domain interface. Adapted from Seeger et al. (2005)

The intensity of the local fluctuations is given in different gray shades. The brightest regions correspond to the regions with the highest fluctuations in enthalpy, volume, and area. In Fig. 14.15 one can see that the fluctuations in the gel domains are lower than in the fluid domains, but that they are by far the strongest directly at the domain interface. Taking into account what has been derived in this chapter it seems as if the domain interfaces are very interesting regions, with the highest lateral area compressibility and the highest bending elasticity. In Chapter 17 we will use this finding to relate the permeability of lipid membranes to the fluctuations at the domain interfaces. In brief one can assume that the likelihood of forming a spontaneous pore increases if the lateral compressibility is higher, because to form a pore in the lipid membrane one has to compress the surrounding lipids environment.

According to the mattress model (Mouritsen and Bloom, 1984) described in Chapter 1, integral proteins may have extensions of the hydrophobic core that

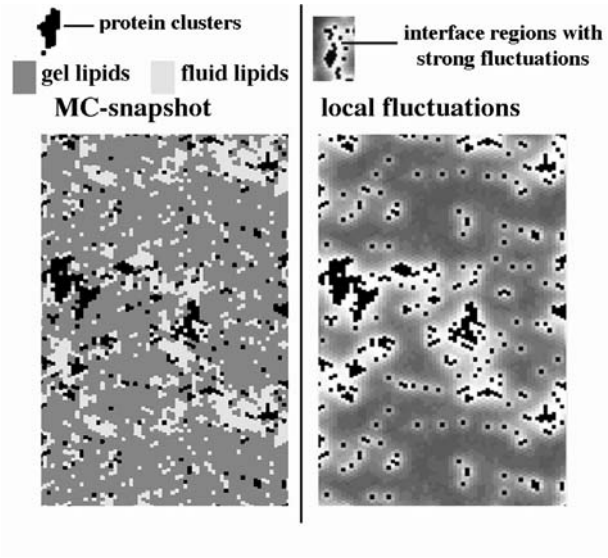

Fig. 14.16 DPPC membrane containing gramicidin A molecules at $T = 40.2\,^{\circ}$C (slightly below the heat capacity maximum). 10% of the lattice sites are filled with peptides. Left: Monte Carlo snapshot showing gel domains (dark gray), fluid domains (light gray), and protein clusters (black). Right: Same snapshot as in the left-hand panel, but now showing local fluctuations in different gray shades. White regions correspond to the strongest fluctuations. Adapted from Ivanova et al. (2003)

are different from the bilayer thickness. Gramicidin A is a pore forming dimer that is much shorter than the typical membrane. This means two things: 1. the hydrophobic matching between the proteins is not ideal and 2. the free energy of the lipid protein interface is affected. Under such conditions one may obtain attractive forces between proteins that lead to aggregation and clusters, but also to altered fluctuations at the protein interface. In Fig. 14.16 one can see gramicidin A aggregates (in black) in a simulated DPPC membrane at 313.3 K. The fluctuations are much stronger close to the proteins than further away. This means that proteins can locally alter the elastic constants if the membranes are close to the chain melting transition. Thus, proteins may not only induce local changes in permeability but also may induce local curvature fluctuations.

The finding that the elastic constants, curvature fluctuations, and permeabilities are affected close to domain boundaries may especially play a role in respect to the ongoing discussion about small domains in biomembranes, called rafts (see discussion in Section 9.5). These rafts are usually rich in sphingolipids with long saturated chains and in cholesterol. Thus, rafts are most likely gel domains and their interfaces with the rest of the membranes must display large fluctuations. Therefore, the existence of small domains of this kind will affect many physical properties of membranes including permeability and curvature fluctuations.

14.9 Summary: Key Ideas of Chapter 14

1. The heat capacity is proportional to the enthalpy fluctuations, the isothermal volume compressibility is proportional to the volume fluctuations, and the area compressibility is proportional to the area fluctuations.
2. One can relate the bending elasticity to the lateral compressibility.
3. The changes in heat capacity close to chain melting transitions are proportional to the changes in both volume and area compressibility. Thus, membranes close to melting transitions are very compressible and are soft.
4. As a consequence, the bending elasticity is very high close to transitions.
5. The adiabatic volume compressibility is a simple function of the heat capacity changes. It is always smaller than the isothermal compressibility.
6. The sound propagation velocities in lipid dispersions (and as we see in Chapter 18) the lateral sound propagation velocity along lipid cylinders can be calculated from the heat capacity changes.
7. Close to melting transitions, the curvature fluctuations and the bending elasticity are high. One can relate the bending elasticity to the fluctuations in curvature.
8. Due to the high curvature fluctuations, membrane multilayers display a critical swelling close to the melting transitions.
9. Fluctuations are generally high close to domain interfaces, e.g., the interfaces between gel and fluid domains in lipid mixtures, or the interface between proteins and lipids.
10. As a consequence biomembranes display altered physical properties close to rafts and to proteins, that may lead among others to changes in permeability or to curvature fluctuations.
11. Elastic constants are strongly coupled to the heat capacity—in fact, they all are just different aspects of the same phenomenon: Fluctuations around the entropy maximum.

15
Structural Transitions

The previous chapter dealt with the changes of the elastic constants in the chain melting regime. It has been shown that these changes can be significant. The bending modulus for unilamellar DPPC vesicles changes by a factor of 10 as compared to the fluid phase. One may ask the question whether these obviously large changes influence the equilibrium of shapes of lipid vesicles. In this chapter we present examples and theoretical considerations concerning transition-induced changes in vesicular shape.

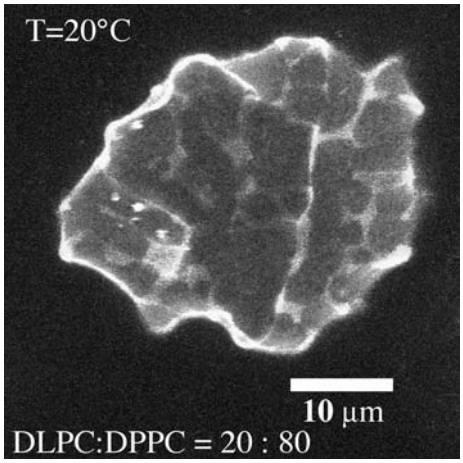

Fig. 15.1 Confocal microscopy image of a giant lipid vesicle (20:80 mixture of DLPC and DPPC at room temperature). Bright regions correspond to fluid domains, dark gray regions to gel domains. It can be seen that the regions of the highest curvature are at the interface between gel and fluid domains. Adapted from Fidorra (2004).

15.1
Coupling of Curvature and Domain Distribution

In Chapter 14 it was concluded that in the chain melting regime the bending elasticity is much higher. Furthermore, it was also discussed that in the

chain melting regime coexistence of gel and fluid domains can be found. We concluded that the fluctuations in enthalpy, area, and curvature must be enhanced at the interface between gel and fluid domains (Section 14.8, Figs. 14.15 and 14.16). If giant vesicles of lipid mixtures are investigated by confocal microscopy one sometimes finds vesicles that adopt crumpled shapes in the chain melting regime (Fig. 15.1). With selected fluorescence markers one can label gel and fluid domains. In Fig. 15.1 the fluid domains appear in brighter shades than the gel domains. The highly curved regions obviously occur at the interface between gel and fluid domains. Thus, it seems as if the chain melting transition can affect the shapes of vesicles and membranes.

15.2
Secretion, Endo- and Exocytosis in the Chain Melting Regime

In biological cells the fusion and fission of vesicles is a very common process. As mentioned earlier (Section 13.3.5), the fusion of a vesicle with a bilayer membrane is linked to the formation of a fusion pore. These pores display relatively high free energies of the intermediate state. Assuming a constant value for the bending modulus Kozlovsky and Kozlov (2002) calculated a free energy on the order of $40kT$. This value for the fusion intermediate is very high and it is thus unlikely that fusion is triggered by thermal activation. However, if the bending modulus changes by a factor of 10 during chain melting, the free energy of a fusion pore would drop to $4kT$, making thermal activation of the fusion pore a relatively likely event. Such processes are shown in Figs. 15.2 and 15.3.

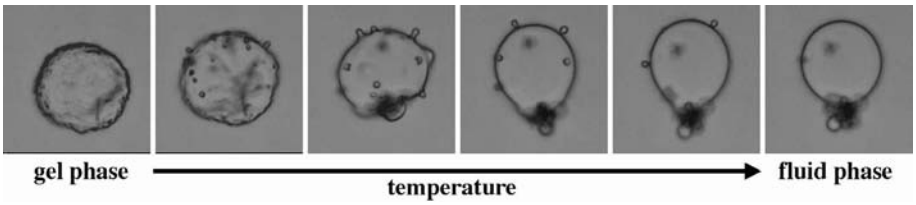

Fig. 15.2 Change in vesicular structure of giant DPPC vesicles during a rapid change of temperature from 30 to 45 °C. One can recognize the transient formation of buds resembling events in secretion. The duration of the whole process was about 10 seconds. Unpublished data, courtesy to C. Leirer and M. Schneider (Augsburg).

Let us consider a giant vesicle made of DPPC with a diameter on the order of 30 µm undergoing a rapid change of temperature from 30 to 40 °C while passing through the chain melting transition. Such a case is shown in Fig. 15.2, where several snapshots during this process are shown. At the lowest temperature one can recognize that during the temperature change some vesic-

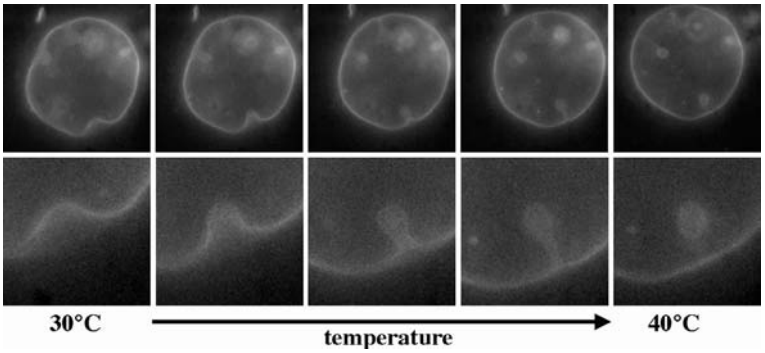

Fig. 15.3 Change in vesicular structure of giant vesicles of a DMPC:DPPC = 50:50 mixture during a rapid change of temperature from 30 to 45 °C. The top row shows the complete vesicle at different times during a rapid change in temperature, whereas the bottom row displays an amplified section showing the formation of a vesicle. Such changes can obviously be triggered by melting transitions. Unpublished data, courtesy to C. Leirer and Dr. M. Schneider (Augsburg).

ular buds appear on the surface, directed toward outside of the vesicle. The vesicular buds mostly disappear again at the highest temperature.

A similar experiment is shown in Fig. 15.3. This time a giant vesicle of a DMPC:DPPC = 50:50 (mol:mol) mixture undergoes the same temperature change. The main difference in appearance is that in this example the vesicular buds form inside of the vesicle. In the bottom row of Fig. 15.3 one can even see a complete endocytotic event involving the formation of a new vesicle.

We can summarize these findings by stating that

- During the passage through a chain melting transition endocytotic and exocytotic fusion and fission events can spontaneously occur without the control by proteins.
- Whether these events occur inside or outside of vesicles depends on their composition.

One should add here that an experiment during a fast change in temperature is not very well controlled. Additional forces occur, in particular caused by the rapid changes in the volume/surface area ratio of the vesicles. Thus, the experiments shown in this section rather serve as a prove of principle.

15.3 Curvature and the Broadening of the Melting Transition

The curvature of a lipid membrane must have an influence in the chain melting profile. Gel and fluid lipids have a surface area that is different by

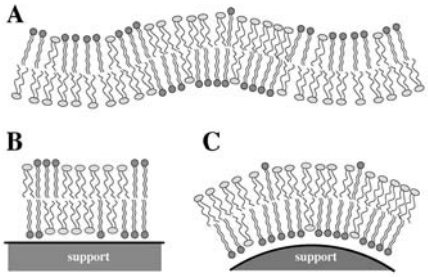

Fig. 15.4 Schematic drawings of bilayers in the chain melting regime. (A) a free standing lipid bilayer with curvature fluctuations. (B) A membrane on a flat support with near equal likelihood of finding fluid lipids on both monolayers. (C) A membrane on a curved support with a higher likelihood to find fluid lipids on the outer monolayer. Adapted from Ivanova and Heimburg (2001).

about 25%. Let us consider a membrane with equal number of lipids on both monolayers at the melting point T_m with a 50% probability to find a fluid lipid. Upon curvature the area of the outer monolayer increases, whereas it decreases on the inner monolayer (cf. Fig. 14.2). Thus, a logical consequence of curvature would be a redistribution of gel and fluid lipid states on the two monolayers. Such redistributions are shown in Fig. 15.4 for different geometries. In particular, for a lipid bilayer on a flat support the likelihood of finding a fluid lipid must be very similar on both monolayers, whereas it should be very different for a membrane on a curved support. In the latter case one expects a higher probability to find fluid lipids on the outer monolayer because their area is larger.

In a very simple-minded manner one may consider the increased likelihood of finding a gel lipids on the inner monolayer as a consequence of compression, whereas the increased likelihood of finding a fluid lipid on the outer monolayer may be seen as a consequence of stretching the monolayer. According to the findings in Section 14.4.2, compression leads to a shift of transition events to higher temperatures whereas stretching would lead to a shift to lower temperatures. Thus one would expect that the melting events on the two monolayers display a different temperature dependence, and thus curvature leads to a broadening of the transition half width.

Figure 15.5 shows the melting profiles of vesicles of three different sizes (this Figure was shown before, Fig. 8.5 in the context of computer simulations of curved membranes). Multilamellar vesicles are typically large with sizes about 500 nm. Due to their multilayer structure and large size they are assumed to have approximately flat bilayers. The transition half width is very narrow and is on the order of less than 0.1 K (in fact, the narrowest transition half width of DPPC in distilled water was found to be about 0.05 K, e.g.,

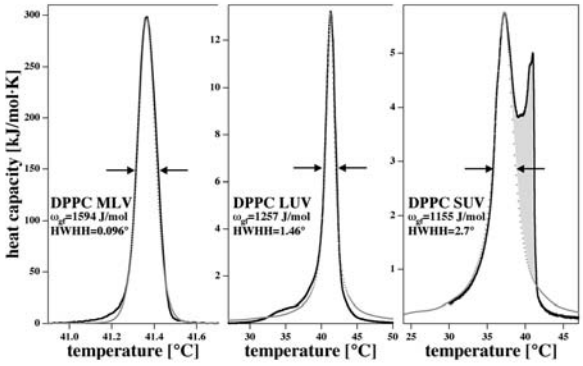

Fig. 15.5 The melting profiles of lipid vesicles from DPPC with different radius display a very different transition half width. Left: The transition half width of multilamellar vesicles is typically below 0.1 K. Center: The transition half width of large unilamellar vesicles (LUV) with diameter on the order of 140 nm (made by ultrasonication and subsequent fusion at low temperatures) is on the order of 1.5 K. Right: The transition half width of small unilamellar vesicles (SUV) with diameter on the order of 20 nm is about 2.7 K. The gray shaded area in this curve represents a small fraction of LUV that form by fusion of the SUV. These changes in transition half width are most likely a consequence of different curvatures. Adapted from Ivanova and Heimburg (2001).

Biltonen (1990)). Unilamellar vesicles of diameters of about 140 nm display a transition half width of about 1.5 K, whereas small unilamellar vesicles display a transition half width of 2.7 K. A consequence of these changes in heat capacity naturally is also a different temperature dependence of the elastic constants for the different vesicular shapes.

Brumm et al. (1996) have measured the melting profiles of membranes supported by glass beads of different diameters. These results are shown in Fig. 15.6 (right panel). It can be seen that the larger the radius of the supporting glass bead the smaller the transition half width. Similar results are obtained using Monte Carlo simulations as described in Chapter 8 for supported membranes with identical number of lipids on both monolayers of the lipid membrane (Fig. 15.6, left panel). These profiles were calculated using the histogram algorithm described in Chapter 8.

In the following we will see that these differences result in the possibility of the transition between vesicular geometries in the chain melting regime.

15.4 Structural Transitions of Vesicles in the Melting Regime

The occurrence of geometry changes in the vicinity of chain melting transitions often results in occurrence of several heat capacity maxima. Examples are the two peaks found in the chain melting regime of extruded DMPC vesi-

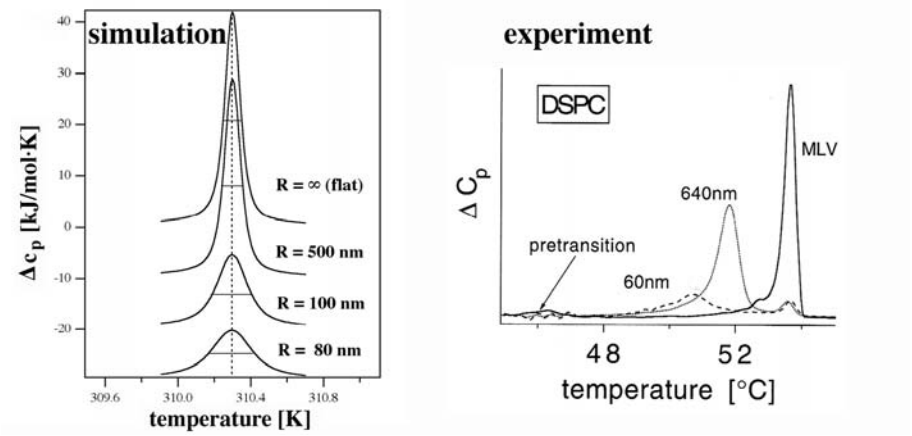

Fig. 15.6 Melting profiles of lipid vesicles of different radius. Left: Transition profiles for supported vesicles of different radius calculated on the basis of Monte Carlo simulations using the histogram algorithm described in Chapter 8 and Ivanova and Heimburg (2001). Left: DPPC membranes on curved supports using silica beads with different radius. The transition profiles broaden and shift to lower temperatures. Adapted from Brumm et al. (1996).

cles, the splitting of the melting transition of multilamellar vesicles into pretransition and main transition, and the complex melting profiles of charged lipid membranes (see Fig. 15.7).

To understand the occurrence of complex melting profiles let us make some general simplifying assumptions. First, let us assume that the melting profile

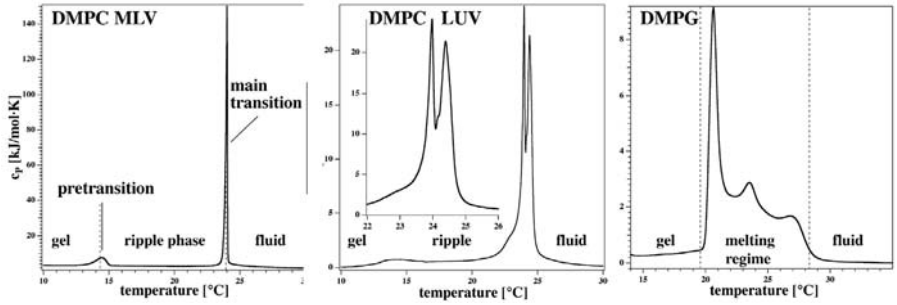

Fig. 15.7 Heat capacity profiles of three different lipid dispersions displaying several heat capacity maxima in the chain melting regime. Left: Multilamellar vesicles of DMPC showing pretransition and main transition. In the temperature regime between the two maxima the ripple phase, $P_{\beta'}$, is found. Center: Extruded lipid vesicles display splitting into two peaks. The origin of this splitting is unknown, but is most likely due to a different vesicular geometry in the regime between the two peaks. Right: Melting profiles of DMPG at low ionic strength. Three maxima can be seen. In the whole transition regime the viscosity of the lipid dispersion is largely increased indicating the formation of connected membrane phase with correlations over large length scales.

is broadened by curvature and that we consider the equilibrium between exactly two geometrical structures of different curvatures, for instance one being flat and the other one being curved with a radius of 60 nm (Fig. 15.8). We use here the melting profiles calculated in Monte Carlo simulations (Chapter 8), but all the following considerations can be made using experimental profiles of vesicles with different radius without loss of generality.

Fig. 15.8 Equilibrium between two membrane segments of different curvatures described by a Gibbs free energy difference, $\Delta(\Delta G)$.

As indicated above, vesicles of different curvatures display different transition half widths. The enthalpy, H, and the entropy, S, as a function of temperature can be calculated by integration of the heat capacity profiles,

$$\begin{aligned} H &= H_0 + \int_{T_m-\Delta T}^{T_m+\Delta T} \Delta c_p dT \\ S &= S_0 + \int_{T_m-\Delta T}^{T_m+\Delta T} \frac{\Delta c_p}{T} dT \end{aligned} \tag{15.1}$$

Since the two different curvatures display different heat capacity profiles they also consequently possess a different temperature dependence of the Gibbs free energy. It is given by

$$G = G_0 + \Delta H - T \cdot \Delta S \tag{15.2}$$

The calculation for two different radii of curvature is shown in Fig. 15.9.

The Gibbs free energy difference between the two geometries yields

$$\begin{aligned} \Delta G = \Delta G_0 + \Delta(\Delta G) \; = \; & \underbrace{\left(G_0^{\text{curv}} - G_0^{\text{flat}}\right)}_{\Delta G_{\text{solv}}} \\ & + \underbrace{\int \left(\Delta c_p^{\text{curv}} - \Delta c_p^{\text{flat}}\right) dT - T \cdot \int \left(\frac{\Delta c_p^{\text{curv}} - \Delta c_p^{\text{flat}}}{T}\right) dT}_{\Delta G_{\text{elast}}} \end{aligned} \tag{15.3}$$

This equation contains two terms, ΔG_0 and ΔG_{bend}. The first term, ΔG_0, reflects that two states of different curvatures may display different interaction with the environment, in particular with the solvent, and may therefore be

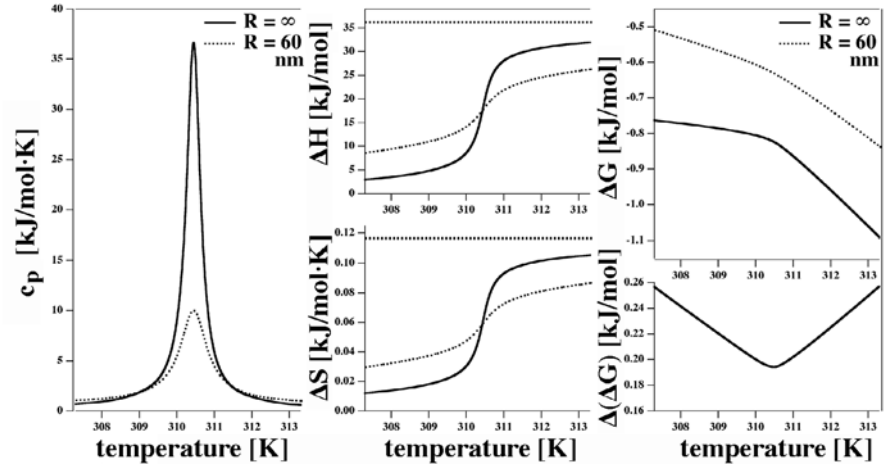

Fig. 15.9 Free energy difference between different curvatures. Left: Heat capacity profiles of flat and of curved lipid membranes obtained in Monte Carlo simulations. Center: Enthalpy and entropy changes, ΔH and ΔS in the transition calculated from the integration of the c_p profiles. Right: Gibbs free energy, ΔG, of the two different curved states and the free energy difference between these two states $\Delta(\Delta G)$. The free energy difference between the two geometries is minimum at the transition maximum.

denoted with ΔG_{solv}. The second term, $\Delta(\Delta G)$ reflects that the temperature dependence of the free energies of states with different curvatures is different. Therefore, the second term yields the Gibbs free energy of bending related to the transition events and may therefore be denoted with ΔG_{bend}.

For symmetric membranes with no spontaneous curvature, ΔG_{bend} is always positive, as shown in Fig. 15.9. The value for ΔG_{solv} depends on the interactions with the solvent, e.g., on ionic strength, and on the charge density of the membrane.

15.5 Charged Lipid Membranes

About 10–40% of the lipids of biological membranes are negatively charged. Positively charged lipids only exist as synthesized chemicals. The main difference between uncharged and charged lipids is the interaction between the membrane, water and the ions. At an ionic strength of 100 mM the screening length of the electrostatic potential is about 0.9 nm, whereas it is about 9 nm at 1 mM ionic strength. In the latter case this is much larger than the typical bilayer spacing in multilayer vesicles (MLV). Repulsive interactions between opposing bilayers that are a function of ionic strength. Therefore, charged lipids usually do not form MLVs at low ionic strength. In the following we show that in charged lipid membranes transitions may occur that couple to the chain melting reaction.

15.5.1 DMPG

During the melting process of charged lipid membranes, in particular of dimyristoyl phosphatidylglycerol (DMPG) membranes, one observes a peculiar melting behavior (Fig. 15.10). The heat capacity profile extends over a width of several degrees and displays three distinct maxima. The optical appearance of the dispersion is opalescent below and above the transition regime, while it is completely transparent in the transition regime. The viscosity of the dispersion is similar to that of the aqueous medium outside of the transition range, while the dispersion becomes very viscous in the chain melting regime. We define the relative viscosity as the ratio between the shear viscosity of the dispersion and that of distilled water at the same temperature.

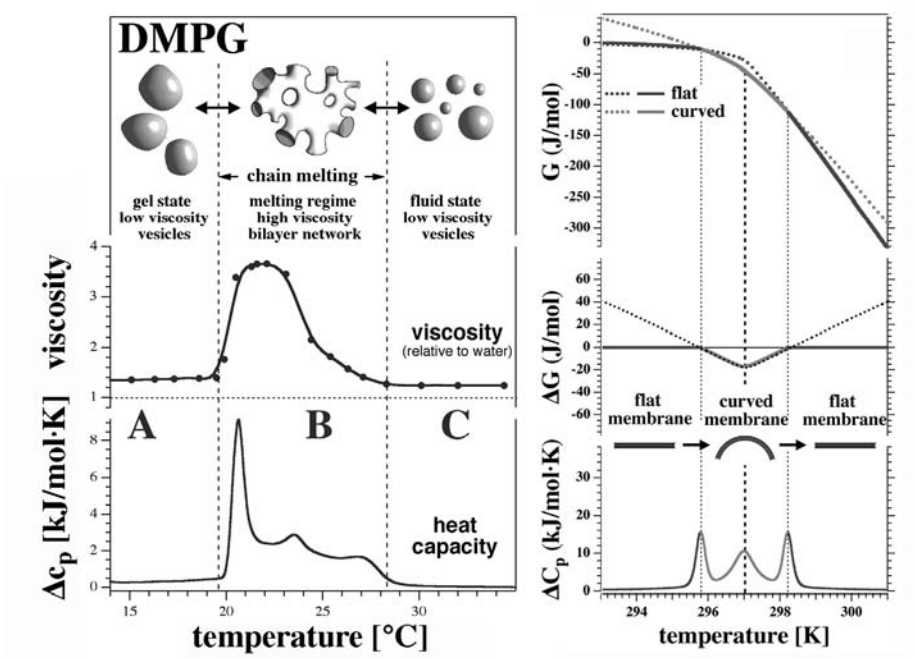

Fig. 15.10 Left: In the melting regime of DMPG one finds a transition profile with three maxima. In this temperature interval the viscosity increases dramatically indicating changes in the bilayer arrangements. According to electron microscopy experiments vesicles are found below and above the melting events, while a 3-dimensionally connected bilayer phase exists in the melting regime (top row). Adapted from Schneider et al. (1999). Right: In Fig. 15.9 one can see the different free energy profiles for different curvatures. If the curved structure has a more favorable interaction with the solvent ($G_{\mathrm{solv}}^{\mathrm{curv}} < G_{\mathrm{solv}}^{\mathrm{flat}}$) the free energy profiles can intersect such that the curved structure is the most probable structure in the phase transition regime. Under these conditions one obtains a chain melting profile with three maxima. Between the two outer peaks the curved structure exists, whereas outside of the melting regime the flat structure can be found.

Shown in Fig. 15.10 (left) is the relative viscosity, given by $\eta_{\text{dispersion}}/\eta_{H_2O}$. The drastic changes in viscosity indicate changes in vesicular geometry. As described in more detail in Heimburg and Biltonen (1994) and Schneider et al. (1999), electron micrographs show that the dispersion undergoes a transition from large vesicles in the gel phase to a continuous bilayer network in the transition regime back to vesicles of smaller size. The change of vesicular size indicates further that membrane fusion events took place in the melting regime. This change in bilayer structure is remarkable because it is completely reversible and obviously solely triggered by temperature changes. As shown above, similar changes already happen to a smaller degree in giant vesicles of uncharged lipids after a temperature jump (Figs. 15.2 and 15.3). Thus, in this case the reversible fusion and fission is controlled by macroscopic thermodynamic parameters rather than by the local action of drugs.

As can be seen in Fig. 15.12 (left) the splitting of the heat capacity profile into several maxima nearly disappears in uncharged membranes of DMPC. Similarly, the width of the splitting and the changes in viscosity for the DMPG dispersion continuously decrease when the ionic strength is increased (Fig. 15.11, left). Also, the increase in chain length weakens the effect, i.e., in a charged lipid with 13 carbons in the fatty acid chains the width of the chain melting regime is larger than in DMPG (C-14) and the effect is practically gone in DPPG (C-16).

Summarizing, factors influencing the probability to find structural changes in the melting regime are

- charge and consequently lowering of ionic strength or increasing pH (cf. Fig. 15.11, left),
- chain length, making the change in geometry more likely with shorter chain length (cf. Fig. 15.11, right),
- as shown in the next paragraph, the adsorption of charged drugs (cf. Fig. 15.12, right),
- temperature, inducing the geometry changes in the chain melting regime where the membranes become soft and flexible (Section 14.9), and
- head group (see the next section).

15.5.2 Geometry Changes Introduced by Charged Drugs

Since the change in vesicular geometry is obviously strongly influenced by the charge of the membrane; it is interesting to note that the binding of charged

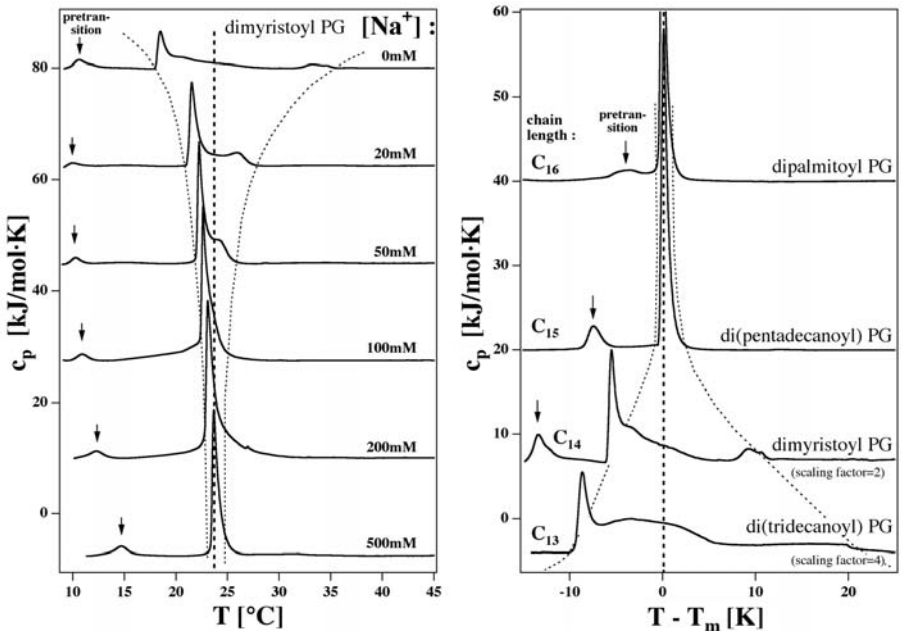

Fig. 15.11 Left: The range of the chain melting transition increases with decreasing ionic strength; indicating that the electrostatic potential plays an important role. Right: The melting range increases with decreasing chain length, quite similar to the findings for the pretransition later in this chapter.

drugs can induce such a behavior. The drug Losartan© (this is a brand name of Merck) is an angiotensin receptor antagonist. This means that it antagonizes the contraction of arteries and thus lowers blood pressure. The chemical structure can be seen in Fig. 15.12 (right). It consists of a number of rings and it carries a net positive charge in solution. Now, from Chapter 5 we know that aromatic amino acids tend to partition well in the bilayer interface. We suspect the same property for the drug Losartan, namely that it binds to the interfacial region of the membrane bilayer. As can be seen in Fig. 15.12 (right) Losartan also broadens the transition, induces three peaks and increases the viscosity in the chain melting regime (see Theodoropoulou and Marsh (1999) and Theodoropoulou and Marsh (2000) for details about the thermal behavior). DMPC membranes in the presence of Losartan (admittedly in a high concentration of 15 mM in the aqueous solution) behave very much the same than DMPG membranes at low ionic strength. Thus, the tendency to change vesicular geometry can be influenced by drugs.

The experiments shown in Fig. 15.12 (right) was in the presence of 15 mM Losartan. Although this seems high one has to consider that the concentra-

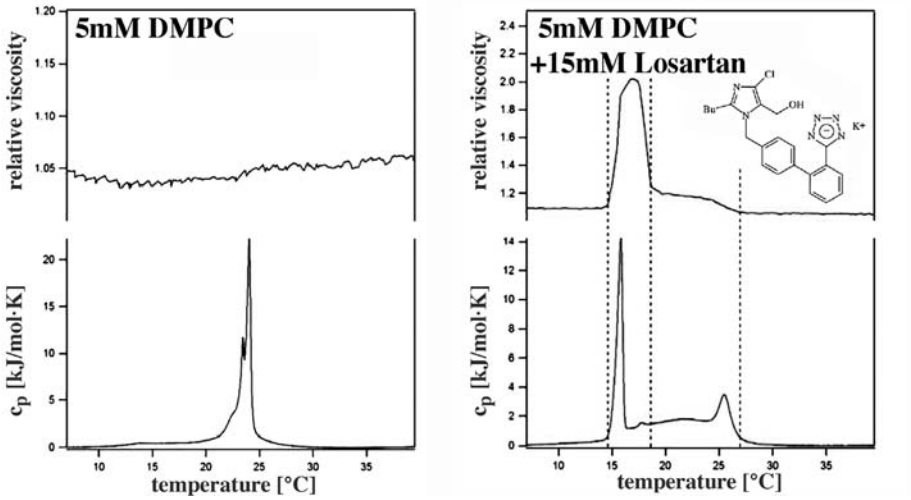

Fig. 15.12 Left: A dispersion of extruded DMPC vesicles shows a narrow melting profile with no significant changes in relative viscosity in the transition regime. Right: The same dispersion in the presence of the drug Losartan (©Merck) changes the heat capacity profile such that it resembles the DMPG profiles of Fig. 15.10. The viscosity similarly shows big changes in the melting regime indicating structural transitions. Adapted from Grabitz et al. (2002).

tion of neurotransmitters in synaptic vesicles is usually in the range of several 100 mM. Therefore, at the site of neurotransmitter release during exocytosis the concentration may transiently be very high. This in fact refers to all concentration changes in biology. Usually they are transient and may be locally very strong even though macroscopically concentration may seem very low. This especially relates to changes in pH that often occur due to the action of enzymes in the local environment of the protein.

Theodoropoulou and Marsh (2000) have shown that the effect of Losartan on phosphatidyl-ethanolamine membrane is much lower indicating that not only charge but also the nature of the head group play a role.

15.6 The Ripple Phase

Another structural transition in the vicinity of the chain melting transition is the pretransition slightly below the main chain melting transition. Between the pretransition and the main transition the ripple phase is found. The ripple phase consists in periodic undulations, as shown in the atomic force microscope images shown in Fig. 15.13 which are taken from Kaasgaard et al. (2003). The pretransition is best described in lipid multilayers but probably also ex-

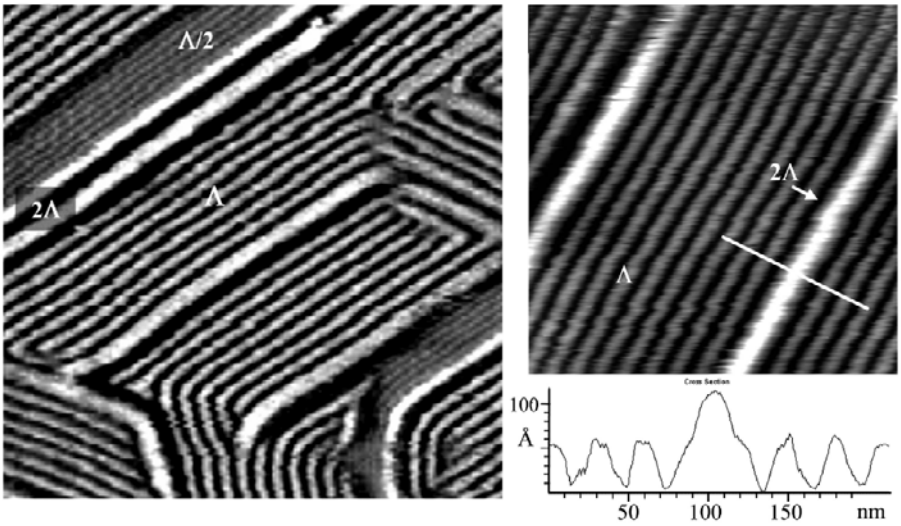

Fig. 15.13 AFM measurements on ripple phase formation in supported DPPC membranes show periodic height undulations. Three different periodicities can be called $\Lambda/2$, Λ, and $2\Lambda/2$. Here, $\Lambda = 28$ nm. From Kaasgaard et al. (2003) with permission from Biophys. J.

ist in single bilayer systems (Lichtenberg et al., 1984; Meyer, 1996) where it is broader and less separated from the main transition.

The pretransition is much less cooperative than the main transition. Its half width typically is on the order of 1–2 °C. The main transition, in contrast, can be as narrow as 0.05 °C in multilamellar DPPC vesicles. The temperature interval between pretransition and main transition is chain length dependence, similar to the multipeak transition in charge lipids (see above). In phosphatidylcholines, it is about 10 °C for DMPC, 7 °C for DPPC, 3.1 °C for DSPC , and 1.2 °C for $DC_{20}PC$ (Jorgensen, 1995), see Fig. 15.21.

The formation of the ripple phase is dependent on the head group. Phosphatidylethanolamines (McIntosh, 1980; Kodama and Miyata, 1996), and glycolipids (Hinz et al., 1985) do not display a pretransition, but is readily found in phosphatidylcholines and phosphatidyl glycerols (Rand et al., 1975). This fact indicates that the interaction with the solvent may play a role in the formation of such phases. More details can be found in Heimburg (2000a).

In this section we explore the possibility that the formation of the ripple phase can be described by the coupling of chain melting and the formation of periodic ripples. In Fig. 15.14 the pretransition, the enthalpy change, the volume change, and the chain mobility as measured in an electron spin resonance are shown. It is obvious that enthalpy, volume and chain mobility change in

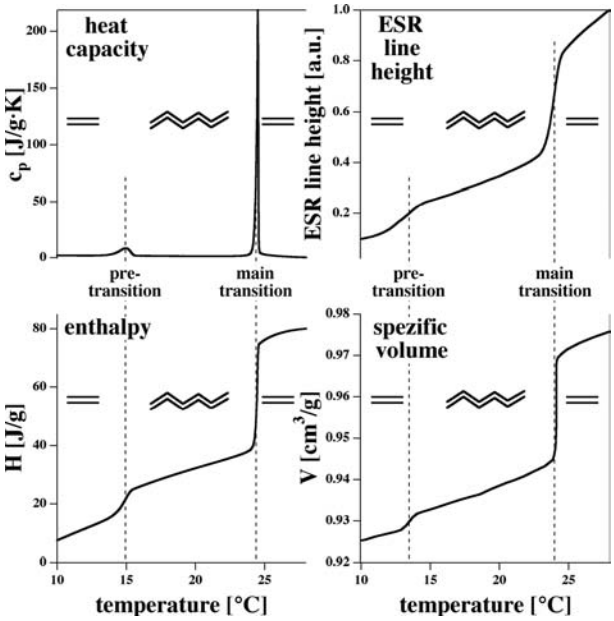

Fig. 15.14 Pretransition and main transition of DMPC in different experiments: Heat capacity, enthalpy, specific volume, and the chain mobility as measure in an electron spin resonance experiment (cf. Heimburg et al. (1992)). One can recognize that enthalpy, volume and mobility change in both, pretransition and main transition, indicating that similar events occur in both transitions.

both, pretransition and main transition to a comparable degree (Heimburg, 2000a). Since both transitions display very similar feature one may indeed wonder whether they are coupled in a similar manner than the complex transition events described in the previous sections. In other words: Pretransition and main transition are both part of the chain melting transition with the splitting into two peaks being the consequence of the change in membrane geometry during the melting events (i.e., transitions between planar membranes and rippled membranes.)

15.6.1 Geometrical Considerations

Heimburg (2000a) described in detail how the formation of the ripple phase can be understood on the basis of Monte Carlo simulations. Even though we do not intend to describe the model here in all details, we will introduce the underlying idea. It has been shown by X-ray crystallography that lipids in the gel and in the ripple phase are packed into a triangular lattice, whereas they are disordered in the fluid phase. Simultaneously, as mentioned already

in previous chapters, the area of lipids increases by about 25% in the chain melting transition. From this a major geometrical problem arises. How is the melting of individual lipids initiated if it happens within a crystal lattice? This situation is shown in Fig. 15.15. Admittedly, the melting of individual lipids in one step from gel to fluid state is a simplification that according to Chapter 8 is useful for cooperative events but nevertheless only a rough approximation to reality on the molecular scale. However, let us for now keep that picture even on small scales. Obviously, each lipid with disordered chains gives rise to a major distortion of the lattice and therefore by necessity is associated with a considerable elastic free energy. However, if the same number of disordered lipids pack along the principle axes of the lattice and form a linear defect, the distortion of the lattice is much reduced.

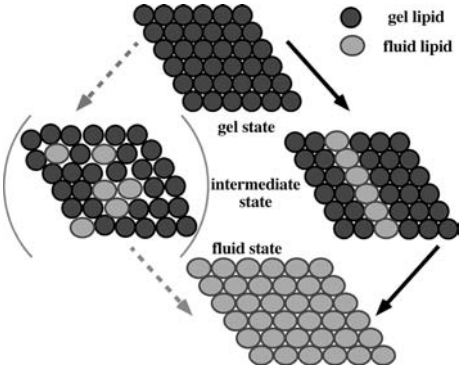

Fig. 15.15 It is known that the lipids in the gel phase adopt a crystalline triangular packing. Since the lipid area increase upon melting, it is much easier to melt the lipids in a linear defect than melting many lipids independently.

Following these considerations, we conclude from the above that the formation of linear defects of disordered lipids is favored over the individual melting of lipids. Therefore, we now assume that the onset of melting in lipid membranes leads to the formation of linear defects consisting of fluid lipids with disordered chains, ignoring the melting of individual lipids for convenience. The occurrence of linear defect of fluid lipids with larger area by necessity lead to curved membranes as shown in Fig. 15.16. We explore in the following whether the formation of the ripple phase in lipid membranes is a consequence of the existence of linear fluid defects in gel membranes. If this would be a good approximation of the truth, it immediately explains why the ripples may form 120° angles (Fig. 15.13) because these angles are the angles between the principle axes in triangular lattices. It also explains why in the pretransition volume and chain order parameter change in a similar manner as in the main transition (Fig. 15.14).

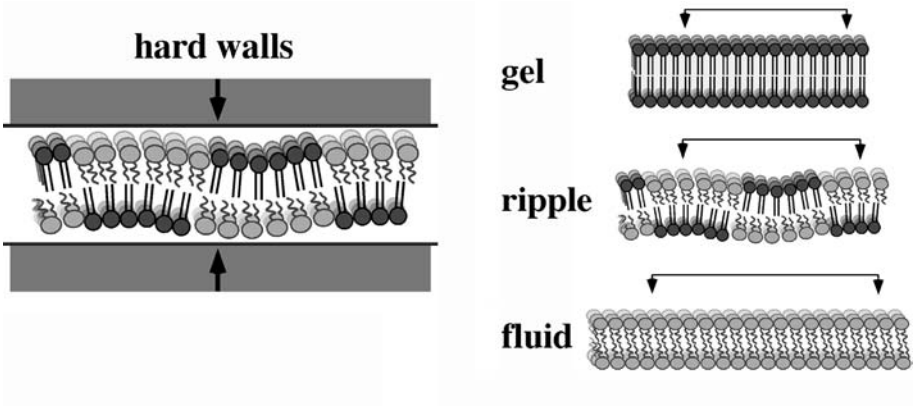

Fig. 15.16 Curved segments arise from different populations of gel and fluid lipids on both sides. In lipid multilayers the bilayers are separated by a water layer of about 2 nm. This means that curved segments can only have a maximum extension that is superimposed by the bilayer spacing. This means that periodic arrangements of curved segments are superimposed when fluid and gel domains become large.

15.6.2 Modeling the Pretransition

We now want to model the ripple formation on the basis of two coupled monolayers. We take into account the following experimental findings:

1. The pretransition is linked to the formation of linear defects of disordered chains.
2. Pretransition and main transition are more cooperative for longer chain lipids.
3. The membrane in the ripple phase is curved. Ripples may be oriented toward each other in 120° angles (Fig. 15.13).
4. Ripple formation is affected by interactions with the solvent.
5. The pretransition is much more pronounced in multilamellar lipid bilayers.
6. The ripples in the $P_{\beta'}$-phase display a periodicity. Typically one finds periods of 15–30 nm length.

Let us assume that the membrane is a $m \times n$ lattice.

Condition 1 is taken into account by approximating the membrane by a one-dimensional array with extension n. Variations of the m lipids in the second

dimension are ignored, i.e., all lipid with given n are assumed to have the same state (see Fig. 15.15).

Condition 2 is considered by introducing nearest neighbor interactions between gel and fluid lipids similar to those used in the Ising models of Chapter 8. This is shown in Fig. 15.17 (left).

Condition 3 is taken into account by considering two opposing lattices, A and B. If the states of the lipids on both sides is different, the membrane is locally curved.

Condition 4 is taken into account by adding an interaction term with the solvent that depends on the local curvature. Gel–fluid contacts are therefore given a different interaction free energy on the outside of a curved segment than on the inside, Fig. 15.17 (right).

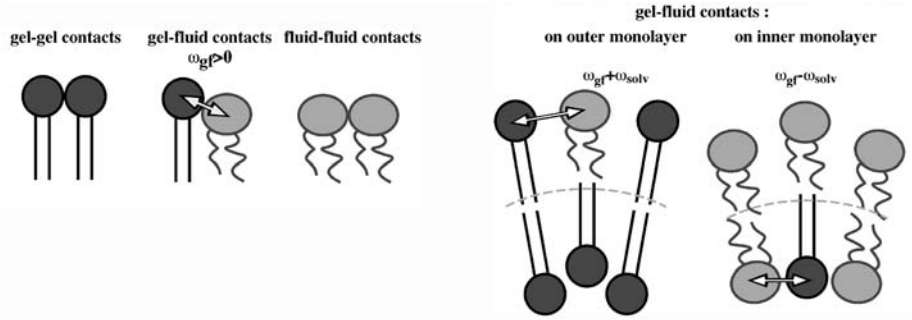

Fig. 15.17 Schematic drawing of the nearest neighbor interactions in the one-dimensional lattice, and how it depends on local curvature. Left: gel-fluid contacts with the interaction parameter ω_{gf}. Right: Unlike nearest neighbor interactions are given a higher value on the outer side of a curved membrane than on the inner side. This difference is due to interaction with the solvent, ω_{solv}. Adapted from Heimburg (2000a).

Condition 5 can be modeled by assuming that in a multilayer stack the neighboring membranes constitute walls that inhibit curvature fluctuations of the membranes. We assume here that this corresponds to a melting in a confined space limited by neighboring bilayers. The neighboring bilayers are approximated by walls.

The periodicity of the ripples (condition 6) originates from the distance of the bilayers (Fig. 15.16). In the model we vary the forces acting on these walls (weak and strong confinement). This will lead to less or more mean deviations from exact periodicities.

The Hamiltonian of such a membrane now consists of the following terms:

$$\mathcal{H} = \mathcal{H}_{\text{chain}} + \mathcal{H}_{\text{NN}} + \mathcal{H}_{\text{solv}} + \mathcal{H}_{\text{geom}} \tag{15.4}$$

where $\mathcal{H}_{\text{chain}}$ is the energy of the chains, $\mathcal{H}_{\text{NN}}$ is the energy in the nearest neighbor interactions, $\mathcal{H}_{\text{solv}}$ is the energy arising from the interaction with the

solvent, and $\mathcal{H}_{\text{geom}}$ represents the geometrical confinement of the membrane and in particular the work done on these walls. These four terms are now described in more detail.

Let us assume that the lipids on the two monolayers carry the indices A and B. A line of m gel lipids at position i shall be associate by a state variable $\sigma_i^A = 0$ or $\sigma_i^B = 0$, and a fluid lipid by $\sigma_i^A = 1$ or $\sigma_i^B = 1$ (depending on whether monolayer A or B is considered). Now

$$\mathcal{H}_{\text{chain}} = m \cdot \Delta H \cdot \sum_i (\sigma_i^A + \sigma_i^B) \tag{15.5}$$

with the melting enthalpy ΔH.

The nearest neighbor interaction part of the Hamiltonian is given by

$$\mathcal{H}_{\text{NN}} = m \cdot \omega_{gf} \cdot \sum_i \left(\left| \sigma_i^A - \sigma_{i-1}^A \right| + \left| \sigma_i^B - \sigma_{i-1}^B \right| \right) \tag{15.6}$$

where ω_{gf} is the nearest neighbor interaction parameter defined as in Chapter 8.

As shown in Fig. 15.17 (right) gel–fluid contacts can be located outside or inside of a curved segment. These configurations are given a different interaction with the solvent such that

$$\begin{aligned} \mathcal{H}_{\text{solv}} &= m \cdot \omega_{\text{solv}} \cdot \sum_i \delta_i^{solv} \\ \delta_i^{\text{solv}} &= \begin{cases} = +1 & \text{if} \quad \sigma_{i-1}^A + \sigma_{i-1}^B + \sigma_i^A + \sigma_i^B = 1 \\ = -1 & \text{if} \quad \sigma_{i-1}^A + \sigma_{i-1}^B + \sigma_i^A + \sigma_i^B = 3 \\ = 0 & \text{else} \end{cases} \end{aligned} \tag{15.7}$$

where ω_{solv} is an interaction parameter describing the interaction of locally curved membrane regions with the solvent and δ_i^{solv} indicates the local curvature state at position i. Only three different curvatures at a site can occur: positive or negative curvature, or a flat membrane. The magnitude of curvature is exclusively determined by the area difference between gel and fluid lipids (about 25% for DPPC), and the thickness of the membrane (about 5 nm).

If one compares with Fig. 15.17 (right) one can recognize that this definition describes gel–fluid contacts on the outer side ($\delta_i^{\text{solv}} = +1$), on the inner side ($\delta_i^{\text{solv}} = -1$) or a flat membrane ($\delta_i^{\text{solv}} = 0$).

The periodicity of the membrane can be superimposed by defining a correlation length $2l + 1$. If the typical ripple period is given by 2.8 nm, and each lipid has a diameter of 0.7 nm, it is convenient to adjust l to a value of 20 (meaning that the ripple period corresponds to 41 lipid diameters). We introduce therefore

$$\mathcal{H}_{\text{geom}} = m \cdot \alpha \cdot \sum_i \left(\sum_{i-l}^{i+l} (\sigma_i^A - \sigma_i^B) \right)^2 \tag{15.8}$$

Here, α is an interaction parameter that describes how energy costly it is to violate the periodicity restriction. One can see immediately that $\mathcal{H}_{\text{geom}} = 0$ if $\sigma_i^A - \sigma_i^B$ is zero in all intervals $i - l$ to $i + l$, indicating perfect periodicity. This condition is fulfilled both for flat gel or fluid membranes, and for perfectly rippled membranes with a period of $2l + 1$.

The Hamiltonian described above can now be used in Monte Carlo simulations as described in Chapter 8. For details on these simulations the reader is also encouraged to refer to Heimburg (2000a). The result of such a simulation as a function of temperature is given in Fig. 15.18. The simulation results in a splitting of the heat capacity profile into two peaks. In between the two transitions the excess heat capacity is slightly larger than zero. In between these two peaks, the membrane displays periodic ripples. Outside of the two peaks, the membrane is a flat gel or fluid lattice. Thus, we identify the two peaks with the pretransition and the main transition, respectively. The ripple phase consists in periodic domains of gel and fluid phase that alternate on both sides and result in periodically curved regions.

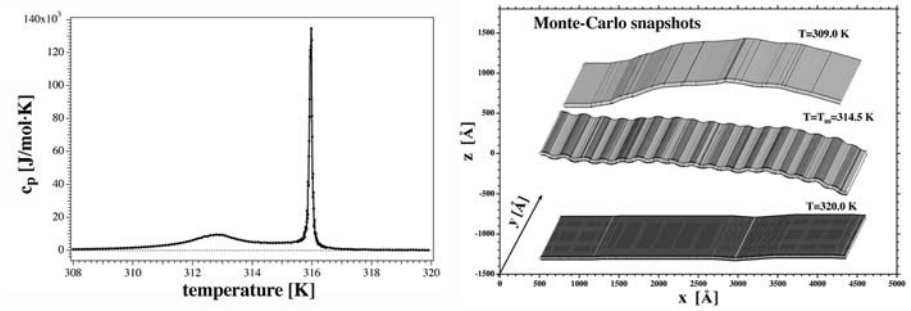

Fig. 15.18 Left: Heat capacity profile calculated using Monte Carlo simulations showing pretransition and main transition. Right: Snapshots of a Monte Carlo simulation showing ripple formation in the temperature regime between pretransition and main transition. Adapted from Heimburg (2000a).

The parameter ω_{gf} affects the sharpness of the transition. The larger its value the sharper both peaks. The parameter ω_{solv} creates an asymmetry in peak width. The larger its value, the broader the pretransition and the narrower the main transition. Changes in α (i.e., the strength of the potential that enforces the periodicity) leads to a fusing of pretransition and main transition if its value becomes smaller. The simulation in Fig. 15.18 has been performed using the following values:

- $m \cdot \Delta H = 209.2$ kJ/mol
- $m \cdot \omega_{gf} = 4.184$ kJ/mol
- $m \cdot \omega_{\text{solv}} = -1.569$ kJ/mol

- 2l+1=41
- $m \cdot \alpha = 40\,kT = 104.6$ kJ/mol

With these parameters one obtains a melting profile very similar to that found in real DPPC membranes. The potential described by the parameter α can be seen as being related to a force acting on two walls, between which the membrane undergoes curvature fluctuations. If that force is zero, the membrane is free to adopt any curvature states. If it is infinite, only periodic solutions are allowed. As mentioned, the periodicity of these solutions is set by the distance between the two walls (Fig. 15.16).

If the strength of the potential is lowered one also lowers the constraint to only allow for periodic solutions. In Fig. 15.19 simulations using different values for α are compared to experiments. It can be seen that in the absence of a constraint ($\alpha = 0kT$) the simulated profile looks very comparable to that of large unilamellar vesicles obtained by sonication (diameter ≈ 140 nm). For $\alpha = 40kT$ the profile resembles that of extruded unilamellar vesicles (diameter ≈ 100 nm) whereas for $\alpha = 50kT$ the c_p profile is similar to that of multilamellar vesicles. Clearly, curvature fluctuations on large unilamellar vesicles are less restricted than in multilamellar vesicles.

From this one may predict the following behavior of the ripple formation:

- ripple formation is more pronounced in multilamellar vesicles. In giant or large unilamellar vesicles the constraint is weaker. It only consists in the existence of a closed spherical geometry. One expects that ripples are less periodic. In the limit of free standing bilayer segments without geometric constraints the curvature undulations are expected to be random.
- The top bilayer in a multilayer stack has a constraint from only one side. It may therefore happen that one ripple segment turns in the opposite direction leading to period doubling (cf. Fig. 15.13).
- molecules that have an affinity to fluid domains, e.g., anesthetics and small peptides, will accumulate in the most highly curved regions of the ripple phase.

15.7 Peculiarities in the Melting of Zwitterionic Lipids

The pretransition is not the only melting peak additional to the main transitions. Both in unilamellar vesicles of short chain diacyl phosphatidylcholines and in multilamellar vesicles of long chain diacyl phosphatidylcholines one finds additional peaks. The origin of these peaks is less obvious than in

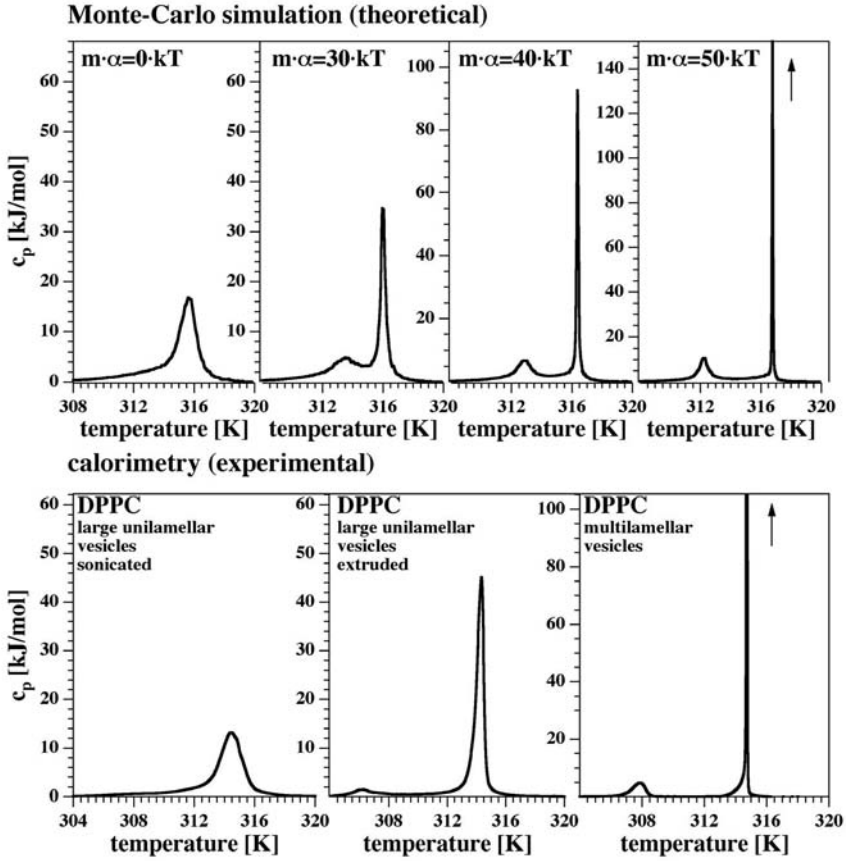

Fig. 15.19 Comparison between theoretical and experimental heat capacity profiles. Top: Heat capacity profiles for four different interactions of the membranes with the neighboring walls. Stronger confinement leads to sharper peaks for pretransition and main transition. Bottom: Experimental heat capacity profiles of DPPC vesicles. From left to right: Large unilamellar vesicles produced by ultrasonication and subsequent equilibration, large unilamellar vesicles produced by extrusion (diameter 100 nm), and multilamellar vesicles. It can be seen that the heat capacity profiles strongly resemble those from simulation. Adapted from Heimburg (2000a).

the case of the ripple phase formation and the extended bilayer networks of charged lipids.

15.7.1 Short Chains

As shown earlier (Section 14.4.1, Fig. 14.5) extruded DMPC vesicles with C-14 chains display two peaks in the chain melting regime. Extruded vesicles of

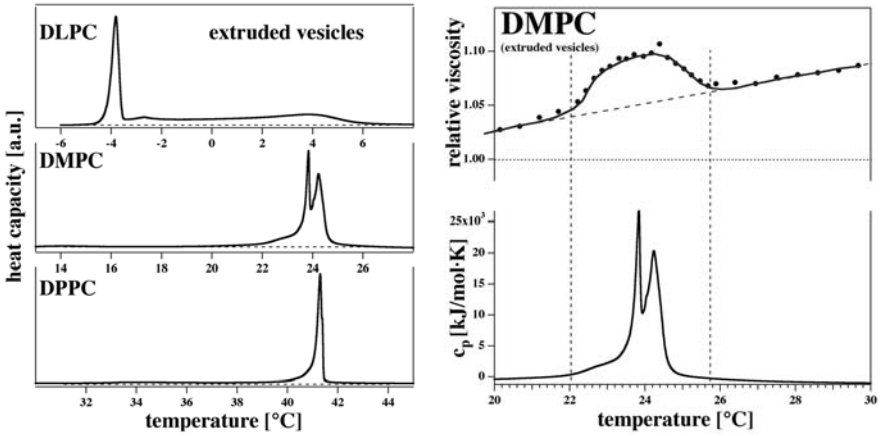

Fig. 15.20 Left: Unilamellar vesicles of diacyl phospholipid vesicles with short chains display two or more peaks. These peaks are more separated with decreasing chain length - similar to the behavior of charge phospholipids but less pronounced. Right: In the melting regime one finds a slightly increased viscosity of the aqueous dispersion. Adapted from Schneider et al. (1999).

DPPC with C-16 chains, in contrast, do not show a similar behavior. Multilamellar vesicles of DLPC with C-12 chains, however, display a melting regime over several degrees with three maxima, much more extended than the DMPC vesicles (Fig. 15.20). The origin of this behavior is unclear. However, following the line of argument of the previous sections, it is likely that changes in local or macroscopic curvature of the membranes is the reason behind these findings. Dispersions of extruded unilamellar vesicles (diameter $\approx$ 100 nm) display a small increase in the relative viscosity in the melting regime. This indicates changes in the vesicular geometry. So far, no electron micrographs of such changes have been reported. However, it seems likely that such changes in vesicular geometry can be found. A further indication that geometry changes are involved is the pronounced chain length dependence that follows the same trend than both, the transition of charged vesicles from vesicles to extended networks, and the pretransition. For all of these transitions the distance between the outer transition peaks increases with decreasing chain length. The same is also true for the sub-main transition described in the next section.

15.7.2 The Sub-Main Transition

In 1995, Jorgensen (1995) described a small enthalpy transition peak in long chain phosphatidylcholines with chain length larger than C-16, which he

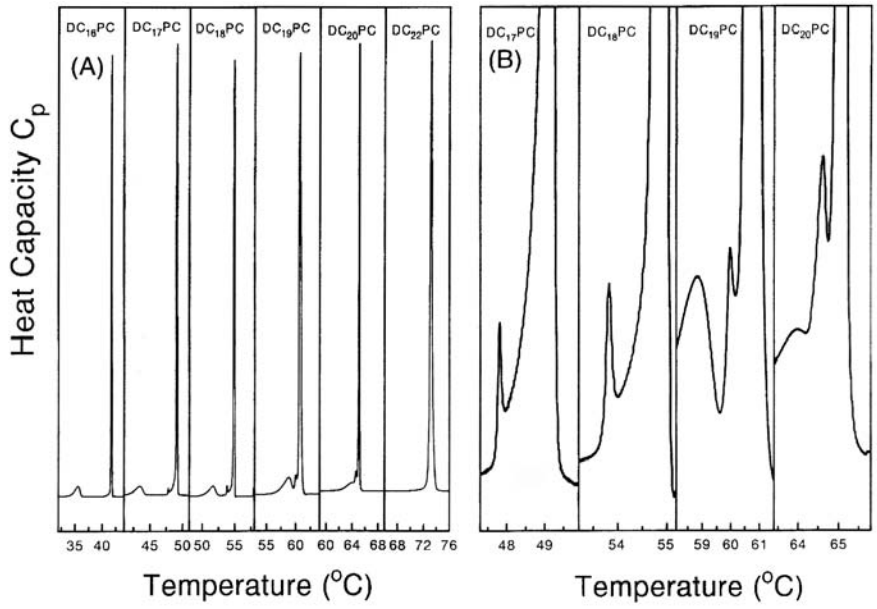

Fig. 15.21 Multilamellar diacyl phosphatidylcholines with chain lengths longer than 16 display a small sharp peak slightly below the main transition, which was called the 'sub-main transition'. At slightly lower temperatures one can recognize the pretransition. Reprinted from Jorgensen (1995) with permission from Elsevier. This figure also shows the chain length dependence of the pretransition.

called the sub-main transition. In Chapter 6 we showed that during chain melting both chain order and lateral order on a lattice is lost (Fig. 6.3). Referring to an earlier paper by Mouritsen and Zuckermann (1985), Jorgensen suggested that the sub-main transition may be due to a transition between a lipid matrix with both lattice order and ordered chains to a phase where lattice order is lost but chain order still persists. The main transition in this picture is then the subsequent loss in chain order. The distance between sub-main transition and main transition decreases with increasing chain length, just as in all other examples in this chapter. There is no direct evidence for whether this interpretation is correct or not. Based on the evidence provided in this chapter, however, we propose another explanation. In this chapter we showed that chain melting is linked to an increase of the elastic constants, and that the likelihood to find membrane states with curvature is increased in this temperature interval. Thus, one obtains the possibility of curvature transitions linked to melting. This generally leads to transitions with three peaks, as shown in Fig. 15.10. The central peak in this chain of events corresponds to the melting of the intermediate phase with different curvatures. Therefore, it

seems reasonable to propose the following chain of events:

$$\text{state 1, gel} \underbrace{\longrightarrow}_{\text{pretransition}} \text{state 2, solid} \underbrace{\longrightarrow}_{\text{sub-main}} \text{state 2, liquid} \underbrace{\longrightarrow}_{\text{main transition}} \text{state 1, fluid}$$

Here, the sub-main transition rather corresponds to a melting transition of the ripple-phase.

It seems very likely that a careful search will reveal many more transitions that couple chain melting and curvature transitions, possibly also induced by secondary components as salts, peptides, and other molecules.

15.8 Summary: Key Ideas of Chapter 15

1. In the melting regime membranes become soft and the possibility of geometry changes of vesicles arises. Thus, structural changes in membrane can be induced by chain melting.
2. Curvature changes are more likely close to domain interfaces.
3. The melting process can induce events that resemble fusion and fission events as in secretion, endo- and exocytosis. The elastic free energy of fusion pores is reduced in the chain melting regime.
4. The coupling of geometry changes with chain melting can lead to transitions that display three peaks in a heat capacity profile.
5. Such changes can be found in charged lipid membranes (in particular DMPG). In both gel and fluid phase lipid vesicles are found. In the chain melting regime one finds a three-dimensionally connected lipid phase with high viscosity.
6. Structural transitions similar to those in charged lipid membranes can be induced in neutral membranes if charged drugs like Losartan©bind to the surface.
7. In many membranes one finds a low enthalpy transition slightly below the main transition, which is called pretransition. The intermediate phase is the ripple phase that consists of periodic undulations of the membrane surface. Typical repeat lengths are 15–30 nm.
8. The pretransition can be explained if one assumes that it is also the consequence of the coupling between geometry changes and chain melting, with the ripple phase being the intermediate phase.
9. In long chain lipids one can resolve a third transition peak additional to pretransition and main transition. It has been called sub-main transition. It is possibly linked to the melting of the ripple phase.
10. The temperature regime of the intermediate phase generally increases with decreasing chain length (for all transitions described in this chapter).

16
Relaxation Processes in Membranes

This chapter is dedicated to relaxation phenomena of membranes. If a system, in our case a biomembrane, is perturbed by a sudden change in one or several of the intensive thermodynamic variables , e.g., temperature, pH, calcium concentration, pressure, ..., it will assume a new equilibrium position within a certain timescale that depends on the nature of the perturbation. Under some conditions the equilibration of the state variables (e.g. enthalpy) occurs as a single exponential function of time, i.e.

$$\frac{d\xi_i}{dt} = \xi_{i,0} \exp\left(-\frac{t}{\tau_i}\right) \tag{16.1}$$

where τ_i is the relaxation time. Generally, however, one finds many relaxation processes. Sometimes they can be seen as independent relaxation processes but usually these processes are coupled and do not follow simple exponential processes.

According to Onsager (1931) each fluctuation of the system, induced by thermal collisions, can also be seen as a perturbation of the equilibrium with a subsequent relaxation process. Therefore, the timescale of the thermal fluctuations and the timescale of relaxation processes after small perturbations are identical. For lipid membranes one finds relaxation processes on all timescales, for example vibrational modes in the femtosecond range, trans-gauche isomerization processes in the nanosecond range, diffusion timescales on the order of 0.1–10 μs for a nearest neighbor exchange between lipids. There are all kinds of other relaxation phenomena, for example head group rearrangements linked to changes in dipole potential and—most importantly for this chapter—relaxation of domain sizes due to fluctuations in enthalpy. Since the fluctuations become large within lipid melting transitions one expects also dramatic changes in the relaxation behavior of membranes in this temperature regime. The relaxation behavior of lipid membranes has been studied by many authors by various techniques (Tsong and Kanehisa, 1977; Elamrani and Blume, 1983; Blume and Hillmann, 1986; van Osdol et al., 1989, 1991). They all found dramatic changes in the phase transition regime. The theory for such changes is outlined below.

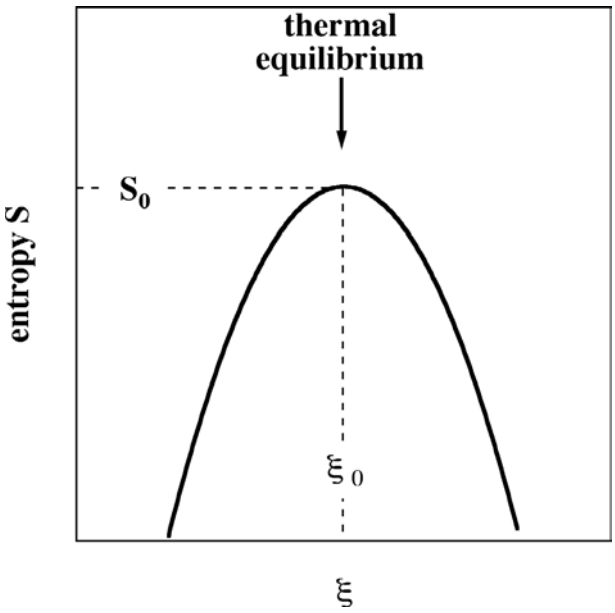

Fig. 16.1 For small deviations of a thermodynamic variable, ξ, from equilibrium the entropy can be approximated by a harmonic potential. At equilibrium the system fluctuates around the maximum of the entropy.

16.1 Thermodynamic Forces and Fluxes and Their Relation to Relaxation

According to Section 4.13 the entropy of any thermodynamic system close to equilibrium can be written as

$$\begin{aligned} S - S_0 &= \frac{1}{2}\sum_i \sum_j \underbrace{\left(\frac{\partial^2 S}{\partial \xi_i \partial \xi_j}\right)_{\xi_i^0, \xi_j^0}}_{\equiv -\alpha_{ij}} (\xi_i - \xi_i^0)(\xi_j - \xi_j^0) + \cdots \\ &\approx -\frac{1}{2}\sum_i \sum_j \alpha_{ij}(\xi_i - \xi_i^0)(\xi_j - \xi_j^0) \end{aligned} \tag{16.2}$$

where the ξ_i are the thermodynamic variables and S_0 is the entropy at equilibrium. The α_{ij} are constants with positive values. This means that the entropy can be seen as a potential which can be approximated by quadratic functions of the thermodynamic variables (see Fig. 16.1). For a spatially homogeneous system the equilibration process is described by the time derivative of the entropy

$$\frac{d(S-S_0)}{dt} = \sum_i \left(\underbrace{\frac{\partial(\xi_i - \xi_i^0)}{\partial t}}_{J_i} \underbrace{\sum_j (-\alpha_{ij}(\xi_j - \xi_j^0))}_{X_i} \right) \equiv \sum_i J_i X_i \tag{16.3}$$

Here, as described earlier (Section 4.13) the thermodynamic fluxes, $J_i = \partial(\xi_i - \xi_i^0)/\partial t$, and the thermodynamic forces, $X_i = \sum_j(-\alpha_{ij}(\xi_i - \xi_i^0))$, have been introduced. The fluxes are defined as the change of the variables in time. The forces are proportional to the deviation from equilibrium. It should be noted that this also applies to the classical mechanical spring. One can also easily see that

$$X_i = \frac{\partial(S-S_0)}{\partial(\xi_i - \xi_i^0)} \qquad \text{and} \qquad \frac{d(S-S_0)}{dt} = \sum_i \frac{\partial(S-S_0)}{\partial(\xi_i - \xi_0)} \frac{\partial(\xi_i - \xi_0)}{\partial t} \tag{16.4}$$

i.e., the thermodynamic force is the derivative of the entropy with respect to the conjugated thermodynamic variable. If we consider a system with only one thermodynamic variable ξ one has to consider only one flux, J, and one thermodynamic force, X.

$$\frac{d(S-S_0)}{dt} = -\frac{\partial(\xi - \xi^0)}{\partial t}\alpha(\xi - \xi^0) = J\,X \tag{16.5}$$

In a viscous medium the fluxes are proportional to the forces (Onsager, 1931). A typical example is Stoke's law where the force on a spherical particle in a viscous solution is proportional to its velocity. Accordingly, one can write the thermodynamic flux as a linear combination of the forces

$$J_i = \sum_j L_{ij} X_j \tag{16.6}$$

where the L_{ij} are constants called the phenomenological coefficients. The set of equations is called the "phenomenological equations." Due to the linearization this approach is called "linear nonequilibrium thermodynamics." It relies on the assumption that the entropy can be approximated by a harmonic potential. Using Eq. (16.3) this can be written as

$$J_i = \frac{\partial(\xi_i - \xi_i^0)}{\partial t} = -\sum_j L_{ij} \sum_k \alpha_{jk}(\xi_k - \xi_k^0) = \sum_j L_{ij} X_j \tag{16.7}$$

For the simple case in Eq. (16.5) one obtains

$$J = \frac{d(\xi - \xi^0)}{dt} = -L\alpha(\xi - \xi^0) = L\,X \tag{16.8}$$

This equation can be solved for ξ

$$(\xi - \xi^0)(t) = (\xi - \xi^0)_0 \exp(-L \cdot \alpha\ t) \equiv (\xi - \xi^0)_0 \exp(-\frac{t}{\tau}) \tag{16.9}$$

where $\tau = (L \cdot \alpha)^{-1}$ is the relaxation time of the equilibration process.

If in Eq. (16.7) all phenomenological coefficients L_{ij} with $i \neq j$ are zero ($L_{ij} = 0$ for $i \neq j$), one obtains a simple exponential relaxation for each thermodynamic variable, with relaxation times $\tau_i = (L_{ii}\alpha_{ii})^{-1}$. For such a system one therefore expects a multi-exponential relaxation process after a perturbation. However, if generally $L_{ij} \neq 0$, relaxation processes can be more complex. Different relaxations processes couple to each other and it becomes less obvious how to assign experimental timescales to individual processes. As an example we may serve the reorientation of lipid head groups after a perturbation, which is a fast process. The lipid head group orientation is different in the gel and the fluid phase. Therefore, a sudden change in temperature or pressure may result in changes in head group orientation. If during head group relaxation simultaneously also the domain sizes change, by necessity the head group relaxation must couple to the domain size relaxations and vice versa.

16.2 Relaxation Times of Domain Formation Processes

In the chain melting transition several variables of the membrane change, including enthalpy, volume, and area. Let us consider phenomenological equations of the relaxation processes in which these three variables change:

$$\begin{aligned} J_H &= L_{HH}X_H + L_{HV}X_V + L_{HA}X_A \\ J_V &= L_{VH}X_H + L_{VV}X_V + L_{VA}X_A \\ J_A &= L_{AH}X_H + L_{AV}X_V + L_{AA}X_A \end{aligned} \tag{16.10}$$

In Chapter 14 we have shown that enthalpy, volume, and area are proportional functions of the temperature, T:

$$\Delta V(T) = \gamma_V \Delta H(T) \qquad \text{and} \qquad \Delta A(T) = \gamma_A \Delta H(T) \tag{16.11}$$

with the constants $\gamma_V = 7.8 \times 10^{-10}$ (m^2/N) and $\gamma_A = 0.893$ m^2/J which have been obtained experimentally from various experiments (cf. Sections 14.4.2 and 14.4.4). Further, the fluctuations in H, V, and A are also proportional functions of the temperature:

$$\begin{aligned} \langle \Delta V(T)^2 \rangle - \langle \Delta V(T) \rangle^2 &= \gamma_V^2 \left(\langle \Delta H(T)^2 \rangle - \langle \Delta H(T) \rangle^2 \right) \\ \langle \Delta A(T)^2 \rangle - \langle \Delta A(T) \rangle^2 &= \gamma_A^2 \left(\langle \Delta H(T)^2 \rangle - \langle \Delta H(T) \rangle^2 \right) \end{aligned} \tag{16.12}$$

It seems obvious that the three thermodynamic variables are so tightly coupled that they cannot be changed independently (at least if the perturbations are small). Therefore, one can reduce the relaxation process described by Eq. (16.10) to one term,

$$\begin{aligned} J_H &= L \cdot X_H \\ \frac{d\,(H - H_0)}{d\,t} &= L \cdot X_H = -L \cdot \alpha\,(H - H_0) \end{aligned} \tag{16.13}$$

In this equation we have not yet determined the thermodynamic force driving the membrane back to equilibrium. It depends on $\alpha = (d^2S/dH^2)_{H_0}$. However, we will show in the following that one can obtain it from the excess heat capacity.

16.2.1
Coupling Between Relaxation Times and Excess Heat Capacity

Grabitz et al. (2002) have shown that the relaxation times can be deduced from the heat capacity profile. Their derivation is demonstrated in the following. The excess heat capacity $c_P = T \cdot dS/dT$ is a function of the entropy. Simultaneously, it is a function of the fluctuations in enthalpy (see Fig. 16.2). As described above, the thermodynamic forces can be derived from the entropy potential.

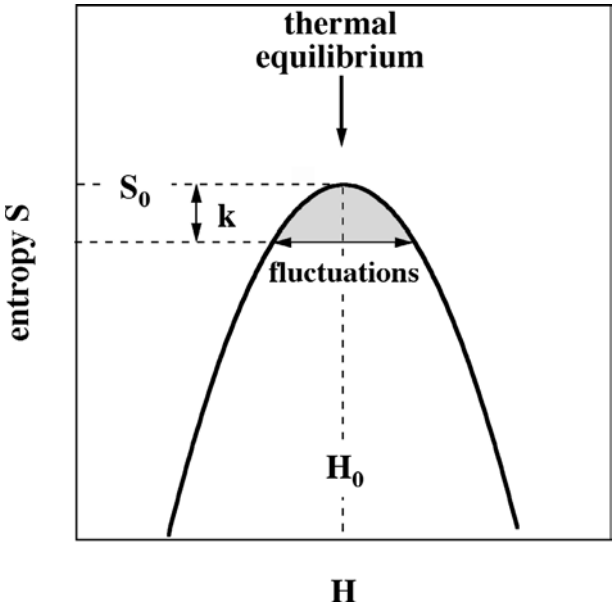

Fig. 16.2 Entropy as a function of the enthalpy of a lipid membrane.

It has been shown in Chapter 8 that in a continuous lipid transition the fluctuations (i.e., the distribution of states) of the enthalpy around the equilibrium assume a Gaussian form. This is not the case for the first-order transitions where distribution of states displays two maxima. Let us assume that our lipid melting transition is not of the first order but rather a continuous transition. Then the distribution of states with enthalpy H and entropy S is given by

$$P(H-H_0) = \frac{1}{\sigma\sqrt{2\pi}} \exp\left(-\frac{(H-H_0)^2}{2\sigma^2}\right) = \frac{1}{Q}\exp\left(-\frac{G}{kT}\right) \tag{16.14}$$

Here, σ is the width of distribution of states and Q is the partition function that serves as a normalization constant. By comparison it follows that the two exponential terms must be equal (except for a constant factor). Therefore,

$$-\frac{(H-H_0)^2}{2\sigma^2} = -\frac{G}{kT} + \text{const.} \tag{16.15}$$

and

$$G(H-H_0) = kT\frac{(H-H_0)^2}{2\sigma^2} + \text{const.} \tag{16.16}$$

The entropy is given by $S = (H-G)/T$ and thus

$$S(H-H_0) = (H-H_0) - k\frac{(H-H_0)^2}{2\sigma^2} - \frac{\text{const.}}{T} \tag{16.17}$$

Since we now know the dependence of the entropy on the enthalpy we conclude that the coefficient α in Eq. (16.13) is given by

$$\alpha = -\left(\frac{d^2\,S}{d(H-H_0)^2}\right)_{H_0} = \frac{k}{\sigma^2} \tag{16.18}$$

We do not yet know the value of σ but we show now that it is a function of the heat capacity. As shown in Chapter 4 the heat capacity is directly related to the fluctuations in enthalpy which correspond to the width of the Gaussian distribution of states:

$$c_P = \frac{\langle H^2\rangle - \langle H\rangle^2}{kT^2} = \frac{\sigma^2}{kT^2} \tag{16.19}$$

Now we can express α as a function of the heat capacity such that

$$\alpha = \frac{1}{T^2 c_P} \tag{16.20}$$

The final kinetic equation follows from combining Eqs. (16.13) and (16.20):

$$\frac{d\,(H-H_0)}{d\,t} = -\frac{L}{T^2 c_P}\,(H-H_0) \tag{16.21}$$

with the solution

$$(H - H_0)(t) = (H - H_0)_0 \exp\left(-\frac{L}{T^2 c_P} t\right) \tag{16.22}$$

The phenomenological constant L is unknown and has to be determined experimentally. The relaxation time is given by

$$\tau = \frac{T^2}{L} c_P \tag{16.23}$$

This result is valid for continuous lipid melting transitions provided that the proportional relations between enthalpy, volume, and, area are fulfilled.

> In lipid melting transitions the relaxation times are proportional to the heat capacity
>
> $\tau \propto c_P$
>
> Relaxation processes are therefore slow close to the heat capacity maximum. This effect is known as "critical slowing down."

Since the excess heat capacity is linked to the fluctuations in domain sizes this relaxation time basically reflects the cooperative processes of domain growth. Other relaxation process not directly linked to the lipid melting process and to large changes in heat are likely to be also present. As mentioned before, many fast relaxation processes have been described in the literature (for reference see Grabitz et al. (2002)).

According to Onsager (1931) the relaxation of thermal fluctuations follows the same thermodynamic forces as those of macroscopic perturbations. Therefore, the analysis of fluctuation noise by autocorrelation also yields relaxation times. In Chapter 8 we have already shown how heat capacity profiles can be determined from the enthalpy fluctuations obtained by Monte Carlo simulations. The very same fluctuations can be used to obtain the relaxation times by autocorrelation

$$\mathcal{G}(\tau) = \frac{\int_0^\infty (H(t) - H_0)(H(t+\tau) - H_0) dt}{\int_0^\infty (H(t) - H_0)^2 dt} \tag{16.24}$$

where $\mathcal{G}(\tau)$ is the autocorrelation function.

The autocorrelation analysis is shown in Fig. 16.3 for a simulated lipid system. In the left-hand panel the enthalpy fluctuations at three different temperatures are shown. At the melting point, T_m, where 50% of the lipids are fluid the fluctuations not only display maximum amplitude (and therefore

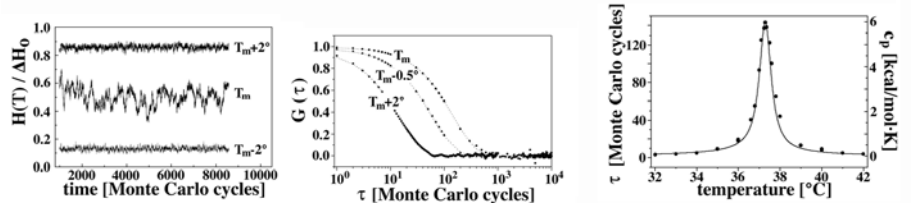

Fig. 16.3 Relaxation times extracted from the fluctuations of the enthalpy. Left: Enthalpy fluctuations at three temperatures below, within, and above T_m. Center: Autocorrelation of the enthalpy fluctuations at three temperatures below, within, and above T_m. At T_m the correlation time is at maximum. Right: Comparison of calculated heat capacities and calculated relaxation times reveal the linear relationship between these two functions. Data adapted from Grabitz et al. (2002)

maximum heat capacity), but also the slowest fluctuation timescale. The autocorrelation curves for such enthalpy traces are shown in the center panel. A fit of these profiles with an exponential function yields the correlation time which corresponds to the relaxation time of the system. In the panel on the right-hand side the heat capacity calculated from the amplitude of the fluctuations is compared with the relaxation time calculated from autocorrelation of the same traces. One can see that the two profiles overlap. Since Monte Carlo simulations are not able to generate physically meaningful timescales, relaxation timescales are given in units of Monte Carlo cycles. This means that the proportional relation between relaxation times and heat capacities are proportional is also found in experiments as shown in the next paragraph. Figure 16.3 serves as a theoretical proof of principle.

16.2.2 Relaxation Experiments

The theoretical prediction that relaxation times are simply related to the heat capacity has been demonstrated in experiments. Figure 16.4 shows the relaxation times of DPPC multilamellar vesicles in comparison to the heat capacity. Since what we describe here are the slow cooperative fluctuations in the melting process that contain a low of heat; the use of calorimetric means is most suitable. With spectroscopic methods that are not quantitative it is often difficult to distinguish molecular and cooperative processes.

At the c_P-maximum the heat capacity is nearly 50 s, i.e., for the very cooperative systems the relaxation times are long. If one adds small amounts of cholesterol to the same lipid system the maximum heat capacity is reduced by about 4-fold and the heat capacity profile is simultaneously broadened. Interestingly, the profile of the relaxation times is also broadened and the maximum relaxation time is reduced by 4-fold. Thus, addition of small molecules

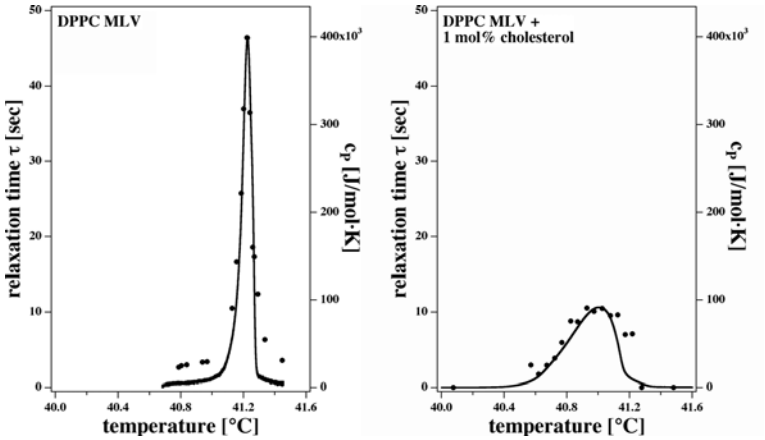

Fig. 16.4 Relaxation times (measured by pressure perturbation calorimetry) and heat capacity for DPPC multilamellar vesicles (left) and DPPC multilamellar vesicles in the presence of 1 ml% cholesterol (right). It can be seen that the changes in the heat capacity are reflected in the changes of the relaxation times. Cholesterol lowers the c_P-maximum by about 4-fold. The same is observed for the relaxation time. The proportional factor between relaxation time and heat capacity is found to be $\frac{T^2}{L} \approx 1.16 \times 10^{-4} \frac{\mathrm{s\,mol\,K}}{\mathrm{J}}$. Data adapted from Grabitz et al. (2002).

to lipid systems may have a significant influence the relaxation times. Most importantly, the proportional factor $\frac{T^2}{L} \approx 1.16 \times 10^{-4} \frac{\mathrm{s\,mol\,K}}{\mathrm{J}}$ in Eq. (16.23) seems to be nearly constant for different membranes.

In Fig. 16.5 further examples for the influence of small molecules on the relaxation process are shown. The heat capacity profiles and simultaneously the relaxation times of multilamellar DMPC membranes (left) are significantly influenced by the anesthetic octanol (right, top), by the neurotransmitter serotonin (right, center) and the antibiotic peptide gramicidin A (right, bottom). These seemingly so different molecules classes all reduce the relaxation times of the pure lipid membrane in a coherent manner, yielding a proportional factor between relaxation time and heat capacity of $\frac{T^2}{L} \approx 1.34 \times 10^{-4} \frac{\mathrm{s\,mol\,K}}{\mathrm{J}}$, roughly identical to the DPPC system in Fig. 16.4.

16.2.3 Relaxation Times of Biomembranes

Little is known about the relaxation times of the cooperative processes in biomembranes. However, let us be courageous and assume that the linear relation between heat capacity and relaxation times is the same for biomembranes as it is for model membranes. Let us further assume that the proportionality factor T^2/L is the same as in model systems ($\approx 1.2 \times 10^{-4} \frac{\mathrm{s\,mol\,K}}{\mathrm{J}}$). Then one can estimate the order of magnitude of the relaxation times in biological membranes. As an example let us take bovine lung surfactant (BLES) that displays a cooperative melting transition just below body temperature.

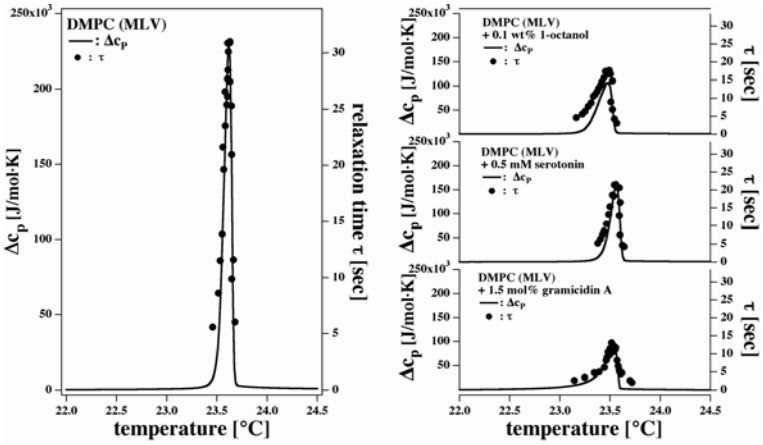

Fig. 16.5 Relaxation times (measured by pressure perturbation calorimetry) and heat capacity for 50 mM DMPC multilamellar vesicles (left) and DMPC multilamellar vesicles in the presence of 0.1 wt.% of the anesthetic octanol (relative to lipid weight) (right, top), 0.5 mM of the neurotransmitter serotonin (right, center) and 1 mol% of the antibiotic peptide gramicidin A. The changes in the heat capacity are again reflected in the changes of the relaxation times. The proportional factor between relaxation time and heat capacity is found to be $\frac{T^2}{L} \approx 1.34 \times 10^{-4} \ \frac{\mathrm{s\,mol\,K}}{\mathrm{J}}$. Data adapted from Seeger (2006).

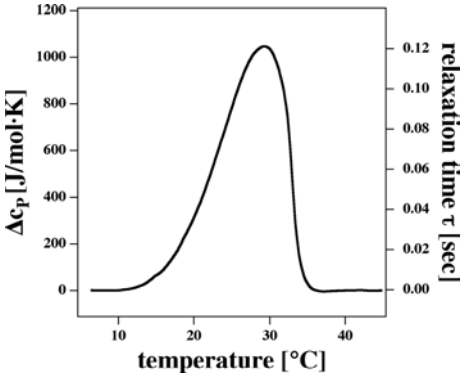

Fig. 16.6 Normalized heat capacity profile of bovine lung surfactant (BLES) with a transition maximum at 29.2 °C and a transition half-width of about 10 K. The relaxation times, τ, are estimated by assuming the same proportionality factor between τ and Δc_P than for the model systems ($T^2/L \approx 1.2 \times 10^{-4} \ \frac{\mathrm{s\,mol\,K}}{\mathrm{J}}$). The estimated relaxation time at maximum is ≈ 120 ms.

The heat capacity profile and the tentative estimates of the relaxation times are given in Fig. 16.6. The melting profiles of biological membranes are significantly broadener than those of pure lipid systems. Therefore, the absolute heat capacities at the c_P-maximum is much lower. For bovine lung surfactant this is about 1 kJ/mol K resulting in a relaxation time of about 120 ms.

Since at physiological temperatures one is typically slightly above the melting point, one expects relaxation times of the cooperative membrane processes of a few milliseconds up to a few 10 ms. This is interestingly exactly the timescale of the opening and closing events of spontaneous ion channels in lipid membranes and those of protein ion channels (cf. Chapter 17). It is very unlikely that this is a coincidence. Rather, it is likely that the physics behind the relaxation of the domain formation and the timescales of important biological function are intimately related to each other.

The relaxation times of cooperative domain forming processes in biomembranes are expected to be of the order of a few milliseconds up to a few 10 ms. This is exactly the timescale of ion channel opening and closing processes.

16.3 Summary: Key Ideas of Chapter 16

1. At equilibrium the entropy is at maximum. A perturbation leads to a lowering of the entropy and the system relaxes back to the equilibrium.

2. The equilibration process can be described by using concepts of thermodynamics fluxes and thermodynamics forces. The fluxes are the changes of a thermodynamic variable in time, and the conjugated forces consist of the derivative of the entropy with respect to the thermodynamics variable. Such variables can, for example, be enthalpy, volume, and heat.

3. In general the different relaxation processes in a thermodynamics system cannot be investigated independently since they are coupled.

4. Close to the lipid melting transition the relaxation time is proportional to the heat capacity. This process is known as critical slowing down. The general finding is that $\tau \approx 1.2 \times 10^{-4}\ \mathrm{s\,mol/J} \cdot \Delta c_P$ for many lipid systems.

5. For multilamellar lipid vesicles the maximum relaxation times are up to one minute.

6. These slow relaxation processes correspond to the fluctuations in domain size (i.e., domain growth). Relaxation processes on molecular scale have also been observed but they are considerably faster.

7. If the heat capacity is affected by the addition of drugs, e.g., steroids, anesthetics, neurotransmitters, or antibiotics, the relaxation times are affected correspondingly. For example, 1 mol% cholesterol lowers the maximum relaxation time by a factor of 4.

8. The estimated relaxation times for biomembranes are on the order of a few milliseconds to a few 10 ms. This is exactly the time scale of many biological processes including the opening and closing of ion channels (see Chapter 17).

17
Permeability

Lipid membranes are very thin. The typical thickness is 5 nm. Nevertheless, in the biological literature the lipid membranes are often considered as perfect isolators. This is in particular true for the nerve conduction theories where the ion conductance is attributed exclusively to protein ion channels (see Chapter 18). This implies the permeability of the membranes for ions and larger molecules is usually neglected. On the other hand, it is obvious that in thermodynamics there is always a finite probability of solutes to cross membranes. For instance, it is known that pure lipid membranes display a significant permeability for water (Fettiplace and Haydon, 1980; Finkelstein, 1987). We will show in the following that the permeability of lipid membranes can be significant, in particular close to phase transitions. One finds ion-channel-like events even in the complete absence of proteins. In this chapter we mainly focus on the permeability of lipid membranes. Some protein conductances that are influenced by the phase behavior of the surrounding lipid membrane are discussed in Section 17.4. The reader interested in the huge literature on protein conductances may rather refer to Hille (1992).

17.1
Permeability of Lipid Membranes in the Melting Transition

Several different permeation mechanisms can play a role in biomembranes:

1. diffusion through the hydrocarbon part of the membrane,
2. permeation through pores within the lipid membrane, and
3. permeation through protein pores, i.e., ion channel proteins.

In a classic paper by Papahadjopoulos et al. (1973) the permeation rate of radioactive sodium, ^{22}Na, through DPPG membranes was investigated. It was shown that the permeability of ions through lipid bilayers largely changes in the phase transition region (Fig. 17.1, left). It was suggested by the same authors that the anomaly in the transition regime is related to the formation of domains. The increase in permeability, P, was suggested to be caused

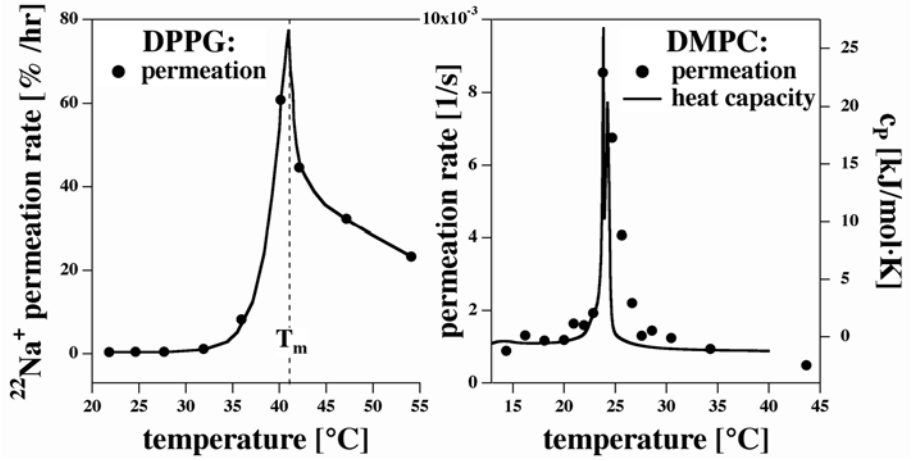

Fig. 17.1 Permeability close to lipid melting transitions. Left: Permeation of ^{22}Na through DPPG lipid membranes with a heat capacity maximum at 41 °C, adapted from Papahadjopoulos et al. (1973). The NaCl concentration was 100 mM. Right: Permeation of a dithionite through DMPC vesicles. Unpublished data from J. S. Andersen, K. Jørgensen, and O. G. Mouritsen (University of Southern Denmark, Odense) with permission. The solid curve represents the heat capacity profile of a dispersion of DMPC LUV.

by defects at the domain boundaries. This view has later been adopted by Cruzeiro-Hansson and Mouritsen (1988) in a publication where the domain boundaries were described in statistical thermodynamics simulations as introduced in Chapter 8. A more general view was taken by Nagle and Scott (1978) by attributing the permeability to the temperature dependent changes in the lateral compressibility, κ_T^A—and to the fluctuations in area, respectively. They semiempirically described the permeability as

$$P = C_0 + C_2 \cdot \kappa_T^A \tag{17.1}$$

where C_0 and C_2 are constants. According to our earlier statements (Eq. (14.47)) the lateral compressibility can be expressed as a linear function of the heat capacity such that one arrives at

$$P = \alpha_0 + \alpha_2 \cdot \Delta c_P \tag{17.2}$$

where α_0 and α_2 are constants that are not significantly influenced by the melting process. Such an understanding of the pore formation process seems to be able to reasonably well describe the experimental observations. In Fig. 17.1 (right) the permeability of a DMPC membrane for dithionite is compared to the heat capacity profile of the lipid dispersions (unpublished data from J. S. Andersen, K. Jørgensen, and O. G. Mouritsen, University of Southern Denmark). The maximum of the heat capacity profile is identical to the maximum in permeability.

17.2 Lipid Pores

Diffusion of solutes through the hydrophobic core of the membrane probably cannot explain the anomaly of the permeation at the transition point that is somehow related to the lateral compressibility of the lipid membrane. Thus, it is more likely that pores in the membrane exist. The formation of pores in the membrane requires that work against the lateral pressure of the bilayer is performed. This work is a function of the lateral compressibility. The formation of spontaneous pores induced by thermal motion is therefore much more likely close to the transition where the compressibility is high. Thus, the work required to form a pore is smaller in the transition range. Pore formation will be especially likely close to domain interfaces and protein clusters (cf. Figs. 14.15 and 14.16).

Ion currents across membrane segments are often measured by using the black lipid membrane technique where a membrane spans over a tiny hole in a teflon film (typically with a diameter of several 10 μm) (Müller et al., 1962). If a voltage across pure lipid membranes is applied one often finds current fluctuations in discrete steps that are mostly of similar time and conductance scales than those found for ion channel proteins (i.e., milliseconds and picoamperes, see Section 17.4).

The first report about conductance fluctuations in pure lipid membranes was by Yafuso et al. (1974). This was prior to the first reports of quantized currents through proteins measured by patch clamp (Neher and Sakmann, 1976). In this paper the authors investigated the conductance of black lipid membranes made of cholesterol (a quite exotic synthetic system). Ever since then there has been a number of reports demonstrating such quantized currents through lipid membranes (Boheim et al., 1980; Antonov et al., 1980; Kaufmann and Silman, 1983a,b; Gögelein and Koepsell, 1984; Antonov et al., 1985; Yoshikawa et al., 1988; Woodbury, 1989; Antonov et al., 2005). In Fig. 17.1 (left) the permeability of sodium through a synthetic lipid membrane is shown. Fig. 17.2 (top) displays some typical data by Antonov et al. (1980). In black lipid membranes made of DSPC, they found quantized conductance steps of about one picoampere close to the melting transition of these membranes. At temperatures different from the melting point no such currents were found. The current histogram shows that the currents occur in discrete steps. In their paper Antonov et al. (1980) also indicated that the conductance of this pure lipid membrane displays some ion specificity. For example, they found that negatively charged membranes are conductors for cations. Figure 17.2 (bottom) shows quantized currents through a soybean lecithin membrane (Gögelein and Koepsell, 1984). The authors of this study suggested that those currents are caused by impurities. However, this must not be the case since such currents can also be found in synthetic lipid membranes as seen in the

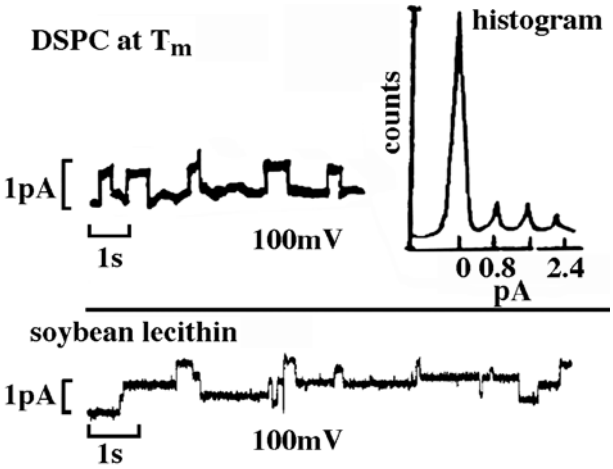

Fig. 17.2 Top, left: Quantized currents through a planar DSPC membrane at 59 °C (close to the phase transition temperature) in 1 M KCl at pH 7.4. The quantized currents disappear above and below the chain melting range. Top, right: Current histogram analysis of the current trace showing the discrete conductance levels. Data from Antonov et al. (1980). Bottom: Quantized currents through a planar bilayer made of soybean phosphatidylcholine and cholesterol (6:1) in 150 mM NaCl at pH 7.4. Data from Gögelein and Koepsell (1984).

top panel of Fig. 17.2. Similar currents were also found through membranes of egg-yolk phosphatidylcholine (Antonov et al., 1980; Gögelein and Koepsell, 1984).

The finding of quantized discrete currents through pure lipid membranes is surprising and so far has not found a convincing explanation. It seems as if in a given membrane pores of very well defined sizes can be formed.

17.3 Quantized Currents in Pure Lipid Membranes and Their Dependence on Thermodynamic Variables

The main theme of this book is the dependence of the physical properties of membranes as a function of the thermodynamic variables. The differential of the internal energy can be written as

$$dE = TdS - p\,dV - \Pi dA - f\,dl + \Psi dq + \cdots + \sum_i \mu_i dn_i \tag{17.3}$$

where T, p, Π, f, Ψ, $\ldots \mu_i$ are the intensive variables. The chemical potentials, μ_i, are related to the concentrations of the components of the membrane. It is important to note that this includes the chemical potentials of the ion channel proteins that are also intensive variables of the membrane system.

Other chemical potentials are related to proton or calcium concentrations. The physics of the system under consideration (i.e., the membrane) will depend on the value of all the variables. Thus, it should generally be the aim in biological studies (including the studies of ion channel proteins) to study the dependence of the effect one wants to investigate on changing these variables. In the following we will show that the spontaneous currents in lipid membranes react on the variation of these variables.

17.3.1 Temperature

In their seminal paper Antonov et al. (1980) found that the conductance increases in the melting transition range of the DSPC lipid membranes. Twenty-five years later, the same authors reported conductance data on DPPC membranes (Fig. 17.3) giving further evidence for the induction of quantized currents in lipid membranes by temperature. In Fig. 17.3 one can see that quantized currents are observed in planar membranes of DPPC when measuring close to the phase transition temperature. At temperatures outside of the transition regime no such events were found. Antonov et al. (2005) showed that upon varying the voltage across the membrane they obtained linear current–voltage relations that depended on the nature of the salt in the aqueous medium:

$$I = g \cdot U \tag{17.4}$$

where I is the current, U is the transmembrane voltage, and g is the conductance of the membrane. They found that the conductance was largest for lithium. For different cations the conductance followed the decreasing series $g_{\mathrm{Li}} > g_{\mathrm{Na}} > g_{\mathrm{K}} > g_{\mathrm{Rb}} > g_{\mathrm{Cs}}$. This order is in agreement with the Hofmeister series indicating the degree to which different ions interact with water (Hofmeister, 1888b; Kunz et al., 2004b,a), see also Section 5.6. It should be noted that the magnitude of the quantized currents in the DPPC transition was higher than in most other lipid membrane preparations (nanoampere regime) and the life times are very long (several seconds).

In Chapter 16 it was shown that fluctuations of domain sizes display a similar time scale in the transition regime. In unilamellar DPPC membranes they are of the order of a few seconds at T_m (Grabitz et al., 2002; Seeger et al., 2007). It is very likely that the time scale of the current fluctuations displays the same dependence on temperature as the relaxation time scales of the domain size (that are proportional to the excess heat capacity, see Chapter 16) and the area fluctuations. The heat capacity of DPPC LUV at T_m is approximately 46 kJ/mol K while the channel lifetimes are about 1–10 s.

The finding that spontaneous currents occur in the phase transition regime was also supported by our lab (Fig. 17.4, unpublished data from Fidorra and

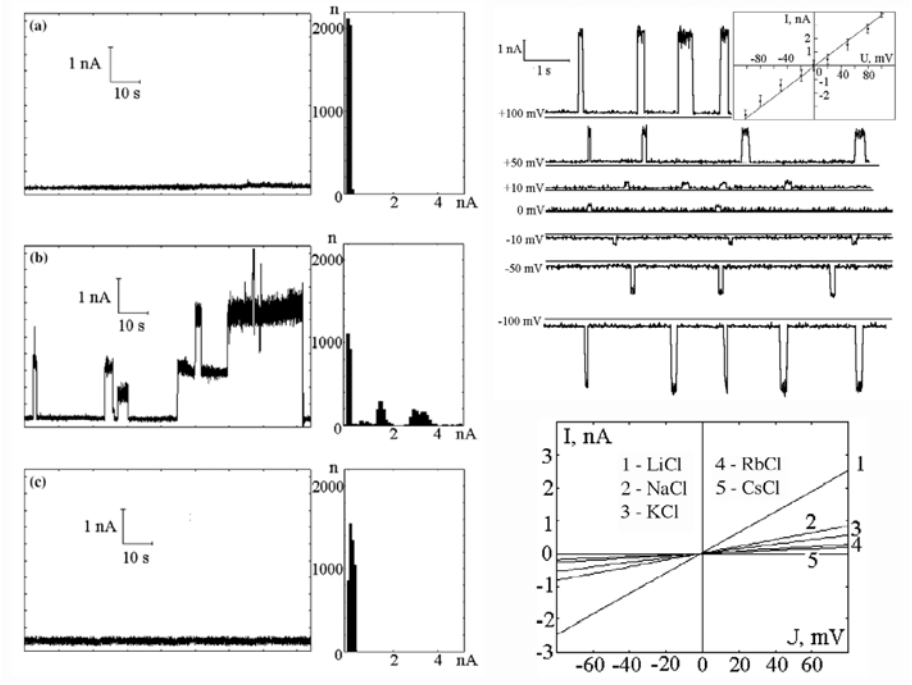

Fig. 17.3 Introduction of quantized currents through planar DPPC membranes by changes in temperature, from Antonov et al. (2005). Left: At three different temperatures (top: 50 °C), Right, top: 43 °C, bottom: 35 °C in 1 M LiCl and 50 mV. The corresponding current histograms are also shown. Center: Quantized currents at different voltages and the characteristic current–voltage relation for 1 M LiCl. Right, bottom: Voltage–current relations for five different monovalent salts (LiCl, NaCl, KCl, RbCl, and CsCl) demonstrate different conductances for different cations. They follow the well known Hofmeister series (Hofmeister, 1888b; Kunz et al., 2004b,a) (see Section 5.6).

Heimburg in collaborations with Professor M. Winterhalter, Bremen). We investigated DOPC:DPPC mixtures at different temperatures and found ion channel-like events at the heat capacity maximum and no spontaneous channels in the fluid phase outside of the transition regime. The heat capacity at this temperature is approximately 2.6 kJ/mol·K. The opening times of the ion channels at 17 °C are on the order of 10–50 ms. They are thus much faster than in the pure lipid system, as expected from the much lower heat capacity.

17.3.2 Calcium and Protons

In Chapter 11 we have shown that the melting temperature of negatively charged lipid membranes increases when neutralizing the charges by protons, proteins, or divalent ions. In fact, melting points are even drastically increased in zwitterionic membranes (unpublished data from our group). Thus,

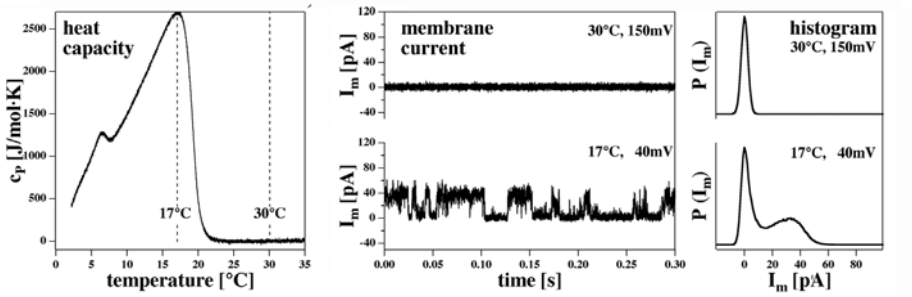

Fig. 17.4 Introduction of quantized currents through DOPC:DPPC=75:25 mixtures (synthetic lipids, 50 mM KCl, pH 7) by changes in temperature. Left: Heat capacity profiles. Center: Currents through planar membranes made of this mixture at temperatures of 30 °C (top trace) and 17 °C (bottom trace). Recordings were performed at 40 mV and 150 mV. Quantized currents occur at the c_P-maximum. No spontaneous currents are seen in the fluid phase. Right: Current histograms of the traces in the center. Unpublished data from M. Fidorra, M. Winterhalter, and T. Heimburg, 2006.

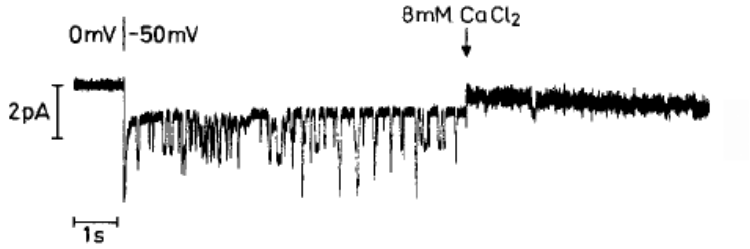

Fig. 17.5 Introduction of quantized currents by changes in calcium concentration. Single channel fluctuations through planar membranes of bovine brain phosphatidylserine and the inhibition by calcium ions. Data from Gögelein and Koepsell (1984).

it is not unexpected that the presence of calcium influences the occurrence of spontaneous currents through lipid membranes. Figure 17.5 shows how the currents through bovine brain phosphatidylserine membranes are blocked by calcium chloride. Since there are no proteins present this cannot be explained by a stoichiometric binding of calcium. In general, one should be very careful in biological studies not to postulate a binding event when the function is altered. As seen in this example this must not be the case. The opposite case—quantized currents being induced by calcium—has been documented by Antonov et al. (1985) using synthetic dipalmitoyl phosphatidic acid (DPPA) membranes. Naturally, if calcium (or another ion or molecule) increases or lowers the permeability depends on the thermodynamic state of the membrane, i.e., on the other thermodynamic variables.

The concentration of protons (i.e., pH) is another variable in a thermodynamic system. Similar to the calcium concentration it influences the melting

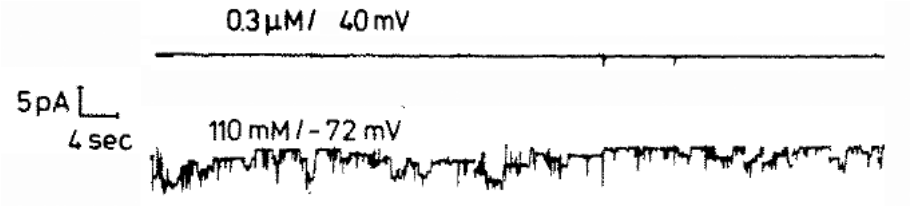

Fig. 17.6 Introduction of quantized currents through soybean phosphatidylcholine membranes by pH changes. Top: Proton concentration on one side adjusted to 0.3 µm ($\approx$ pH 6.5) 1 M KCl, 40 mV . Bottom: Proton concentration on one side adjusted to 110 mM ($\approx$ pH 1), 1 M KCl, -72 mV. Data adapted from Kaufmann and Silman (1983b).

points of lipid membranes by binding to the phosphate groups of the lipids. Kaufmann and Silman (1983b) have reported that the change in pH induces spontaneous fluctuations in lipid membranes (Fig. 17.6). In these experiments planar lipid membranes of soybean phosphatidylcholine were studied and the pH was changed on one side of the membrane from 6.5 to 1. At pH 1 currents through the membrane can be seen that are absent at pH 6.5. This effect was reversible meaning that the membrane staid intact and the channel events disappear after reversing the pH to 6.5.

This book at many places dealt with changes in temperature. Often organisms do not control their temperature in a rapid manner, meaning that temperature is roughly constant over the time scale of molecular processes. However, pH is highly variable in biological cell. While many body liquids have a pH between 6 and 7, in synaptic vesicles it can be below 5, and it is below 2 in the stomach. Many catalytic reactions, in particular hydrolysis reaction including those of ATPases, change the pH locally. These changes have the potential to influence the permeability of membranes.

17.3.3 Lateral Pressure and Mechanosensitivity

Lateral pressure is another of the intensive variables in thermodynamics. Many protein channels are reported to be mechanosensitive (Perozo, 2006). But also ion channels in pure lipid membranes react to changes in lateral pressure. Kaufmann et al. (1989) show how quantized conductance events can be generated in soybean phosphatidylcholine membranes (at the relatively high voltage of 500 mV). In this investigation the lateral pressure was changed by applying suction in patch pipettes (Fig. 17.7).

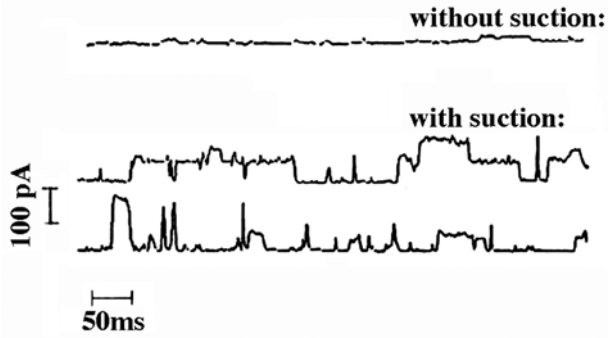

Fig. 17.7 Introduction of quantized currents by changes in lateral pressure, Π. Soybean phosphatidylcholine membranes were investigated by patch clamp (1 M NaCl, 500 mV). Traces without (top) and with applied suction (bottom) are shown. Suction corresponds to a reduction of the lateral pressure in the membrane. Data adapted from Kaufmann et al. (1989).

17.4 The Coupling of Lipid Phase Behavior and Ion Channels Proteins

Much of the permeation of ions through biological membranes has been attributed to proteins called ion channels. Currents through such molecules have been identified by Neher and Sakmann (1976) in patch-clamp recordings (Nobel prize 1991). Figure 17.8 shows the discrete currents related to the acetyl choline receptor from the original paper of Neher and Sakmann (1976).

The conductance of such proteins seems to be highly dependent on the lipid environment. In Fig. 17.9 one can see the conductance of the sarcoplasmic reticulum calcium channel protein reconstituted into different mixtures

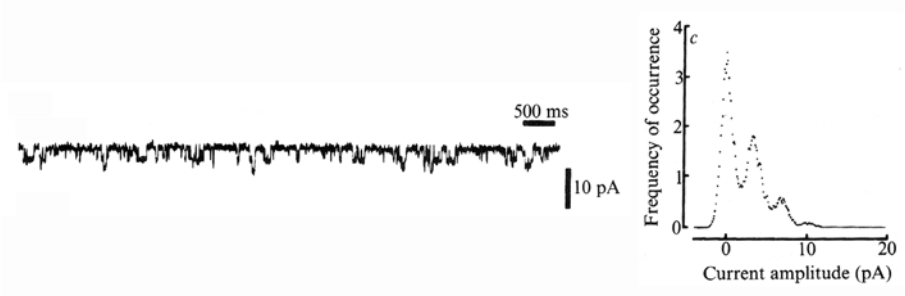

Fig. 17.8 Current recordings from the original paper by Neher and Sakmann (1976) on the channel associated to the acetyl choline receptor measured by patch clamp. Currents into a denervated frog muscle fiber in the presence of suberyldicholine and the corresponding histogram of the distribution of currents are shown. Drug dependent quantized currents on the order of picoamperes were found.

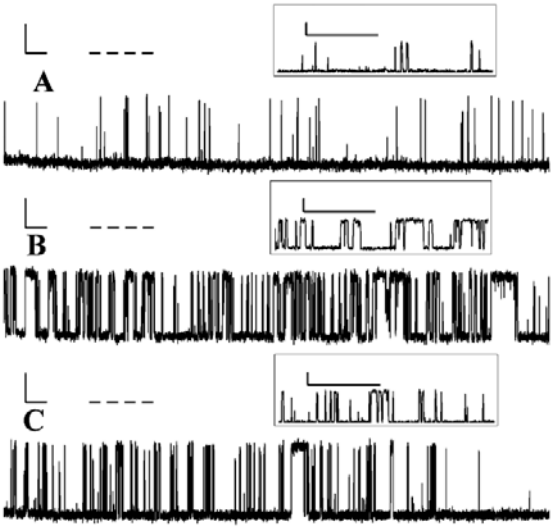

Fig. 17.9 The activity of the sarcoplasmic reticulum calcium channel is strongly influenced by the composition of the lipid membrane. The three panels show the protein reconstituted into mixtures of POPE and POPC. Top: POPE:POPC = 41:59. Center: POPE:POPC = 81:19. Bottom: POPE:POPC = 90:10. The activity displays a pronounced maximum at the phase boundary at about 80% POPE. The open times of the channels reach a maximum. The scale bars for current and time are 10 pA and 50 ms, respectively. From Cannon et al. (2003) with permission from Biophys. J..

of POPE and POPC (Cannon et al., 2003). It was found that the total open time and the dwell time of open events depends on the lipid mixture. They approach maximum values at the phase boundary of the POPE–POPC phase diagram (at 80% POPE) where also the excess heat capacity is expected to be at maximum. The effect of lipid on the potassium channel has been investigated by Turnheim et al. (1999) and Schmidt et al. (2006). Clear dependences of channel activity on the lipid composition have been demonstrated and it has been proposed that lipids regulate the channel gating. Schmidt et al. (2006) showed that the voltage dependent potassium channel (KvAP) displays a conductance in negatively charged lipid membranes but not in positively charged membranes. Thus, the function of such proteins is often not independent of the surrounding lipid matrix and its thermodynamics. The typical current amplitudes and open times are very comparable to those in the lipid mixtures (Fig. 17.4).

Finally it seems worth noting that quantized currents in the picoampere regime and lifetime in the 10 ms range were also found when patch pipettes were brought in contact with silicon rubber surfaces (Sachs and Qin, 1993). The authors of this study found these currents indistinguishable from those found in biological membranes. They further noted that they displayed se-

lectivity for different ions very similar to the nicotinic actylcholine receptor. A similar finding on polyethylene terephthalate filters was reported by Lev et al. (1993). The similarity of currents through proteins, lipid membranes, and at the edge of patch pipettes on hydrophobic surfaces is striking. This may hint at that the spontaneous currents have a relation to organized water at interfaces. Ordered interfacial water is the only feature that proteins embedded in membranes, pure lipid membranes, and rubber surfaces in water have in common. Clearly, there is an urgent need to investigate the origin of such findings.

17.5 Summary: Key Ideas of Chapter 17

1. Lipid membranes display maximum in their conductance for ions and larger molecules close to the lipid melting transition.
2. This increase is possibly directly related to the changes in the lateral compressibility, i.e., to area fluctuations.
3. It is so far not understood how the quantized currents through pure lipid membranes can be explained. Seemingly, pores of well-defined diameter are stable in such membranes.
4. The occurrence of lipid ion channels depends on the relevant intensive thermodynamic variables, e.g., temperature, hydrostatic pressure, lateral pressure, voltage, pH, calcium concentration, ...
5. The opening times of the lipid channels are likely to be related to the relaxation times.
6. Some ion channel proteins are influenced by the thermodynamic behavior of the surrounding lipid matrix, e.g., by the charge of the membrane lipids or the presence of phase boundaries at which the excess heat capacity is high.

18
Nerve Pulse Propagation

The last two chapters of this book are dedicated to two phenomena of biological relevance: nerve pulse propagation and anesthesia. It will be shown that both phenomena are related to the thermodynamics of cell membranes. In particular it will be shown that nerve pulses display mechanical properties that are related to the temperature dependence of the elastic constants. These phenomena find their expression in characteristic heat changes, in thickness and other changes in the state of the nerve membranes. It is shown that the nerve pulse resembles in many aspects of a piezoelectric pulse.

To be able to introduce into the thermodynamics of nerve pulses we first introduce into the textbook model of nerve pulse conduction as formulated by Alan L. Hodgkin and Andrew F. Huxley in 1952.

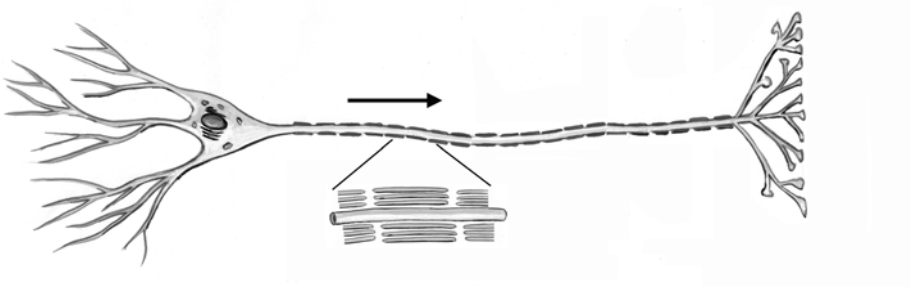

Fig. 18.1 Nerve may assume different shapes and sizes. Some nerves are myelinated whereas others are not. The myelin sheet is formed by Schwann cells that wrap around the axon.

18.1
The Hodgkin–Huxley Model

In Nature one finds about 10,000 different kinds of nerves . In principle nerve cells are not different to other cells, i.e., they have a plasma membrane, a nucleus, mitochondria, and so on (Fig. 18.1). However, they possess long extended regions called axons and dendrites along which voltage pulses can

be transmitted (Fig. 18.2). Some nerves are surrounded by another cell type called Schwann cell. The membranes of the Schwann cell form the so-called myelin layer. Myelinated nerves transmit pulses much faster than nonmyelinated nerves. The conduction velocity in a myelinated nerve is around 100 m/s, whereas it is rather 1–5 m/s in a nonmyelinated nerve. Myelinated nerves can be very long (longer than a meter). In typical nerves the ion concentration of sodium and potassium is very different inside and outside. In the squid axon, one finds 400 mM K^+ inside and only 20 mM K^+ outside. For sodium the ratio is just reversed (400 mM Na^+ outside and only 20 mM Na^+ inside).

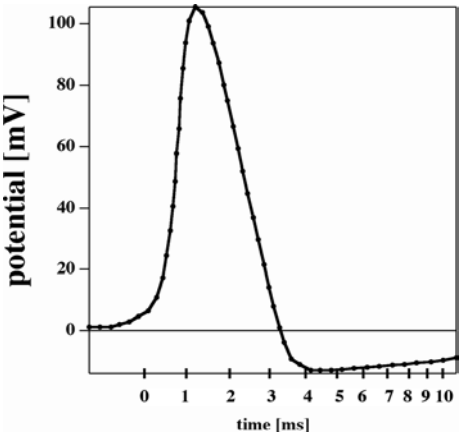

Fig. 18.2 Action potentials are transient voltage changes that propagate along an axon. Shown is the voltage change during the action potential in a squid axon adapted from the original papers of Cole and Curtis (1939) and Hodgkin and Huxley (1952).

The accepted textbook model[1] of nerve pulses (action potential) is the model by Hodgkin and Huxley (1952). In the following we will give a brief introduction into the essentials of the model. We will, however, not review all its details. There are excellent textbooks that can be used as a reference, e.g., Johnston and Wu (1995).

The Hodgkin–Huxley model relies on proteins called ion channels. In fact, the model itself rather speaks abstract about membrane conductances for different ions but it is clear that this aimed at specific protein channels. Ion channels are membrane proteins that open and close in a complex time- and voltage-dependent manner and allow for selective conduction of different ions. If ions flow through the channels they change the voltage across the membrane. In particular, the ion currents influence the charges on the mem-

1) One should in general distinguish between models and theories. While a theory is based on first principles a model is rather a picture that intends to help the intuition.

brane surface. This can be taken into account by considering the membrane as a capacitor with a capacitance of $C_m \approx 1\ \mu\text{F/cm}^2$.

Many early measurements on nerves have been performed on squid axons because they are big (diameter > 1 mm) and it is easy to insert electrodes. Further, it turned out that they only contain two major classes of proteins and the description is therefore simpler. Hodgkin and Huxley described, in much detail, the properties of ion conduction through squid axon membranes. They found complicated time and voltage-dependent currents through the membranes that they attributed to sodium and potassium channels and to capacitive currents. If ion channels open, ions flow from the side of high concentration to the side of low concentration (Fig. 18.3) following the gradient in the electrochemical potential.

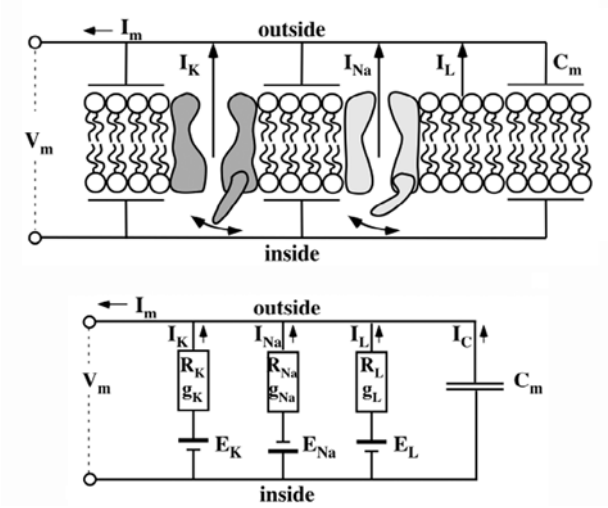

Fig. 18.3 Top: The nerve membrane is thought to be made of proteins (potassium and sodium channel) that conduct ions. Bottom: the picture in the top panel can be translated into equivalent circuits. The ion channel proteins display a resistance R_{K} and R_{Na} (or conductances,g_{K} and g_{Na}, respectively). The membrane is considered as an isolator and simultaneously as a capacitor with capacitance C_m. R_L and g_L indicate leak currents through the membrane.

Experiments on nerves often are voltage clamp experiments meaning that one does not investigate the propagating pulse but rather the conductance through the membrane at constant voltage after a sudden voltage change. The current through a membrane containing Na^+- and K^+-channels is described by

$$I_m = C_m \frac{dU}{dt} + g_{\text{K}}(U - E_{\text{K}}) + g_{\text{Na}}(U - E_{\text{Na}}) \tag{18.1}$$

where $E_K \approx -70$ mV and $E_{Na} \approx +30$ mV are resting potentials for potassium and sodium. At these potentials the flows of the respective ions change direction. They are dependent on the overall concentration differences of the ions across the membrane. g_K and g_{Na} are voltage- and time-dependent conductances for potassium and sodium, respectively.

$$g_K = g_K(U,t) \qquad \text{and} \qquad g_{Na} = g_{Na}(U,t) \tag{18.2}$$

The origins of the complex behavior of the conductances is not known and has rather been determined by empirical fitting of this behavior. This introduces many parameters into the above equation (in total these are 12 empirical parameters only to describe the two channels, for details see Johnston and Wu (1995) or the original paper by Hodgkin and Huxley (1952)). Conductances are the inverse of the resistances R_K and R_{Na} of the membrane. The voltage, U, is a function of time and remains constant a few milliseconds after a sudden voltage change. The first term on the right-hand side is the capacitive current assuming that the membrane surface acts as a capacitor. The charge on a capacitor, Q, is described by

$$Q = C_m \cdot U \tag{18.3}$$

and the capacitive current is the derivative

$$I_c = \frac{dQ}{dt} = C_m \frac{dU}{dt} + U \frac{dC_m}{dt} \tag{18.4}$$

To derive Eq. (18.1) it was assumed by Hodgkin and Huxley that $dC_m/dt = 0$ ($C_m = \text{const.}$). This is an assumption that will be shown to be not quite correct (Section 18.2.2).

The Hodgkin–Huxley picture of the propagating pulse can be summarized as follows: Many sodium and potassium channels are homogeneously distributed in a long nerve membrane (Fig. 18.4). When they locally open after a voltage pulse, they influence the electric potential in their environment and thereby also induce opening of channels in their neighborhood. By these

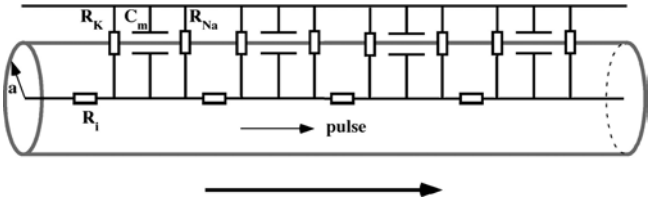

Fig. 18.4 To describe the propagation of a nerve pulse along the nerve axon, many equivalent circuits along the axon membrane are in parallel.

means, the voltage pulse can propagate. The differential equation describing the propagation of the voltage pulse is given by

$$\frac{a}{2R_i} \cdot \frac{\partial^2 U}{\partial x^2} = C_m \frac{\partial U}{\partial t} + g_{\mathrm{K}}(U - E_{\mathrm{K}}) + g_{\mathrm{Na}}(U - E_{\mathrm{Na}}) \tag{18.5}$$

The voltage, U, is now a function of space and time. Here, R_i is the specific intracellular resistivity (of the cytosol inside the axon) and a is the radius of the axon. With this equation, (containing many parameters from the conductances) Hodgkin and Huxley could successfully describe action potentials as shown in Fig. 18.2. However, Hodgkin and Huxley were quite careful in their original publication from 1952. They summarized

> *The agreement must not be taken as evidence that our equations are anything more than an empirical description of the time-course of the changes in permeability to sodium and potassium. An equally satisfactory description of the voltage clamp data could no doubt have been achieved with equations of very different form, which would probably have been equally successful in predicting the electrical behavior of the membrane. . . . the success of the equations is no evidence in favor of the mechanism of permeability change that we tentatively had in mind when formulating them.*

We will show below that one can in fact derive similar propagation equations that are based on completely different physics.

In the mid-70s, Neher and Sakmann developed the patch clamp technique with which they found quantized currents in biological membranes that were equated with these protein ion channels (see e.g., (Neher and Sakmann, 1976) or (Hille, 1992)). This work was rewarded the Nobel prize in 1991. In 1998, MacKinnon and collaborators published the crystal structure of the potassium channel (Doyle et al., 1998) and they proposed a mechanism for how the ions are conducted. The channel-based concepts for the nerve pulse gained considerable respect in the community and are seemingly quite successful. In the next section we will nevertheless discuss some shortcommings of this model.

18.2 Thermodynamics of the Nerve Pulse

Electrophysiology is the discipline of measuring voltage, current, and capacitance changes across biological membranes. The Hodgkin–Huxley model is based on equivalent circuits and on Kirchhoff's laws. Thus, it is not a thermodynamical model since it does not explicitly contain temperature, entropy, pressure, etc. Such data, however, are necessary to make a complete thermodynamic description of the nerve pulse (and, of course, of any other physical

system). The search for thermodynamic data on nerve pulses has not been extensive but there are some data that deserve recognition. Here, we focus on data shown in Figs. 18.5–18.7. They show

1. temperature or heat changes,
2. thickness changes, and
3. forces

generated during the action potential. One also finds changes in the state of lipid membranes in optical experiments, e.g., in fluorescence and turbidity. The Hodgkin–Huxley model does not contain a language for these changes. This does not necessarily mean that it is in conflict with these findings. Resistors dissipate heat in a circuit. Even though heat dissipation is not explicitly mentioned in Ohm's law it does not contradict the electrical description. In the next paragraph, however, we demonstrate that some of the findings in nerves are in fact in a fundamental conflict with the Hodgkin–Huxley model.

18.2.1 Heat Changes During the Action Potential

Several groups have measured temperature and heat changes during the action potential. It has been found that during the action potential the temperature of the nerve increases and decreases back to baseline in the second phase of the action potential. By heat block analysis also the heat changes have been determined. During the action potential the nerve releases heat and reabsorbs it in the second phase such that integrated over the nerve pulse no or only little net heat is dissipated (Fig. 18.5).

One of the first authors studying this effect was A. V. Hill. He was rewarded the Nobel prize in 1922 for his studies on heat production in muscle. He also published a large number of articles on the heat production in nerves under the influence of the action potential (summarized in (Abbott et al., 1958)). Other authors have been Keynes and coworkers (Howarth et al., 1968; Ritchie and Keynes, 1985) and coworkers as well as Tasaki and coworkers (Tasaki, 1988; Tasaki et al., 1989; Tasaki and Byrne, 1992). Further reports are listed in Ritchie and Keynes (1985). Measurements on many nerve systems including nonmyelinated nerves from Maia (crab), rabbit vagus nerves, pike olfactory nerves, and myelinated nerves from bullfrog were performed. It has been clearly demonstrated by control experiments that the reabsorption of heat is not an artifact related to conduction of heat into the aqueous medium (see e.g., (Ritchie and Keynes, 1985)). All authors came to similar conclusions: during the action potential no significant net heat is produced. Transient heat releases are mostly reabsorbed in the second phase of the action potential. These findings have been made for both nonmyelinated and myelinated nerves (Tasaki

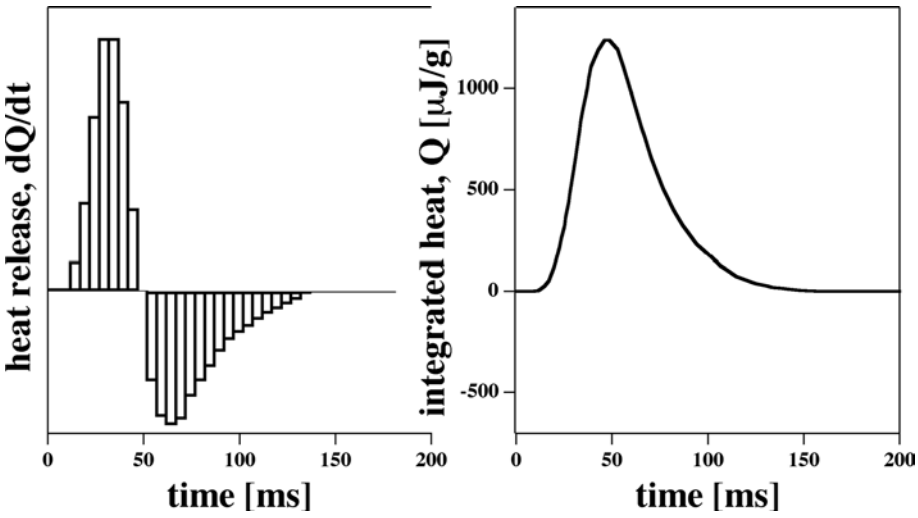

Fig. 18.5 Heat release in garfish olfactory nerve. Left: During the action potential one finds an initial phase of heat release that is followed by a phase of heat absorption. Right: Integration of the rate of heat release reveals that within error no net heat is released. Data adapted from Ritchie and Keynes (1985).

and Byrne, 1992). Abbott et al. (1958) found that the heat release is most like proportional to the area of the nerve membrane indicating that the heat is generated by a physical process related to the membranes themselves. Further, for myelinated nerves they found that the heat release occurs along the whole nerve rather than just at the nodes of Ranvier (which are nonisolated segments of the myelinated nerve). From that they concluded that the whole nerve is active and not just the nonisolated nerve segments as required for the saltatory conduction in the models for myelinated nerves.

One further result concerning the reversible heat uptake is shown in Fig. 18.7 (left). In this figure two curves can be seen: the integrated heat released during the action potential, and the calculated energy of the nerve membrane capacitor ($E_c = 0.5 C_m U^2$). One finds that

$$\Delta Q(t) \propto \frac{1}{2} C_m U(t)^2 \tag{18.6}$$

i.e., the reversible heat release is approximately proportional to the energy of the membrane capacitor. Simultaneously it was found that the heat energy is much larger than the internal energy stored in the capacitor (Howarth et al., 1968; Ritchie and Keynes, 1985). This means that the charging of the membrane during the action potential cannot explain the magnitude of the heat changes. Most importantly, a reversible heat change (no net release of heat) means that the action potential is isentropic (constant total heat also means

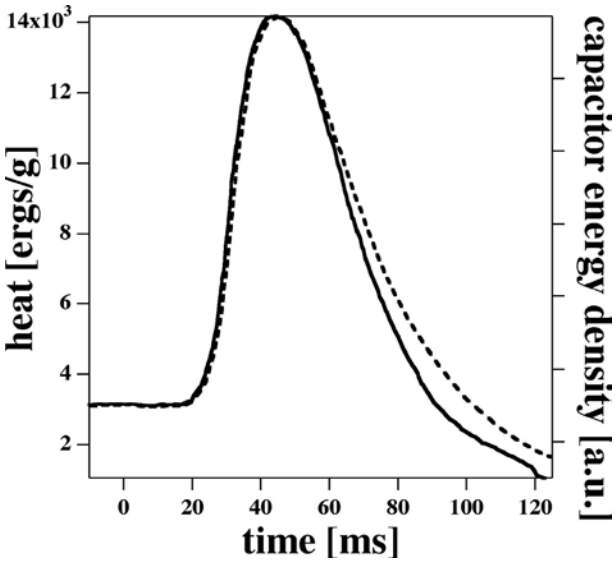

Fig. 18.6 Reversible heat change during the action potential. The square of the voltage (i.e., the energy of charging a capacitor) is proportional to the heat of the nerve pulse. The heat, however, is much larger than the capacitor energy. The heat during the nerve pulse returns to the baseline indicating that the nerve pulse is adiabatic (does not generate net heat after completion of the action potential). Data on garfish olfactory nerve adapted from Ritchie and Keynes (1985).

that the entropy is conserved since $dQ = TdS$). After a careful examination of the origin of the reversible heat Howarth et al. (1968) concluded that

> *It seems probable that the greater part of the initial heat results from changes in the entropy of the nerve membrane when it is depolarized and repolarized.*

Isentropic (or adiabatic) processes imply that the essential physics on which the respective process is based must be reversible. However, the Hodgkin–Huxley theory is not reversible. It is based on the equilibration of ion gradients that increase the entropy of the system. If the equivalent circuit picture of Figs. 18.3 and 18.4 is to be maintained one has to conclude that the conduction of ions through the nerve membrane should produce a heat that is related to the transmembrane voltage and current through

$$\frac{dQ}{dt} = U \cdot I_m = g\, U^2 > 0 \tag{18.7}$$

Additionally, the charging of the capacitor and the currents along the nerve have to be accounted for. According to the model by Hodgkin and Huxley (Hodgkin and Huxley, 1952) the heat generation during the action potential

is a consequence of the currents through resistors. This heat production is always positive since resistors heat up independent of the direction of the current. Heat changes are only reversible if the work performed by the system is also reversible, i.e., the flux of the ions is reversed by the change in capacitance in the second phase of the pulse. This is in fact not the case in the Hodgkin–Huxley model. One has to conclude that

> The finding of a reversible heat release during the action potential of nerves is a striking and very fundamental fact. It is inconsistent with the Hodgkin–Huxley model. The physics underlying the nervous impulse must rather be based on reversible processes.

This has also been noticed by the authors that measured the reversible heats (typically it was mentioned that the heat response lacks a satisfactory explanation). Hodgkin himself wrote in his book "The conduction of the nervous impulse" (Hodgkin, 1964):

> *In thinking about the physical basis of the action potential perhaps the most important thing to do at the present moment is to consider whether there are any unexplained observations which have been neglected in an attempt to make the experiments fit into a tidy pattern. ... perhaps the most puzzling observation is one made by A.V. Hill and his collaborators Abbott and Howarth (1958). ... Hill and his colleagues found that it was diphasic and that an initial phase of heat liberation was followed by one of heat absorption. ... a net cooling on open-circuit was totally unexpected and has so far received no satisfactory explanation.*

18.2.2 Mechanical Changes During the Action Potential

One important researcher in the study of thermodynamic data on nerves is Ishiji Tasaki (NIH, USA). He and his collaborators contributed considerably to measuring of the reversible heat in nerve membranes. He further recorded various mechanical changes in nerves. It was found that during the action potential a dislocation of the membrane surface can be observed that is strictly coupled to the potential changes of the surface (Fig. 18.6, right), (Iwasa and Tasaki, 1980; Iwasa et al., 1980; Tasaki, 1988; Tasaki et al., 1989; Tasaki and Byrne, 1990). Simultaneously, one can also measure a force on a piston that is in contact with the nerve (Fig. 18.7).

A change of the membrane surface during the nerve pulse and the simultaneous change of the thickness must have an influence on the capacitance of the membrane (because $C_m = \varepsilon_0 \varepsilon \frac{A}{D}$). Therefore, one has to conclude that the

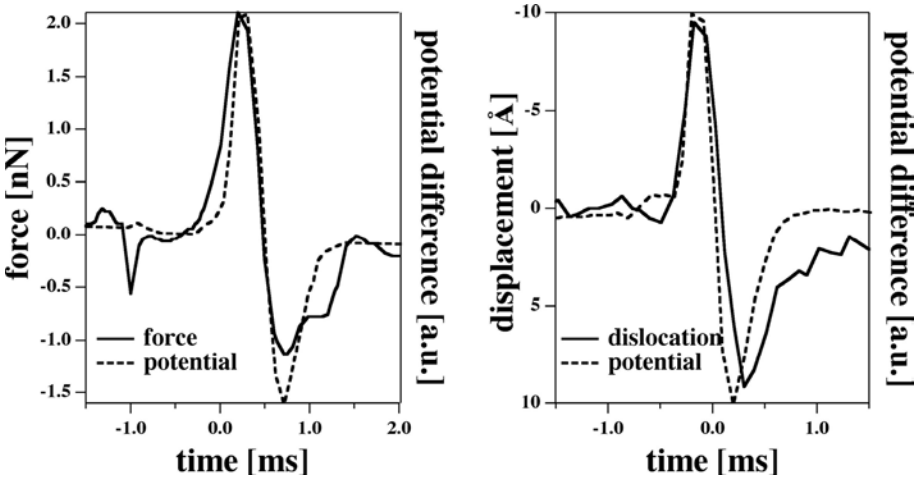

Fig. 18.7 Mechanical changes during the action potential. Left: Force on a piston during the action potential in a squid axon. The solid line represents the voltage changes and the dotted curve the force. Right: During the nerve pulse in a squid axon the thickness of the nerve changes proportional to the voltage. Data adapted from Iwasa and Tasaki (1980).

approximation made to derive Eqs. (18.1) and (18.4), namely that $dC_m/dt = 0$ is probably not correct.

Tasaki and collaborators also reported that during the action potential in nerves various optical properties change, including changes in the lipid membrane fluorescence and turbidity (Tasaki et al., 1968, 1969b,a). It was also shown that the fluorescence anisotropy changes during the action potential (Tasaki et al., 1969b; Kobatake et al., 1971). A change in fluorescence anisotropy indicates changes in the rotational mobility of the fluorescence markers typical for changes in lipid state.

18.2.3 Are There Phase Transitions During the Action Potential?

The changes in fluorescence intensity and anisotropy briefly mentioned in the previous section were taken as evidence for the occurrence of a phase transition during the nerve pulse (Kobatake et al., 1971; Kinnunen and Virtanen, 1986; Tasaki, 1999). If one changes the lipid state from fluid to gel one expects: heat release, increase in membrane thickness, reduction of area, and lowering of rotational mobility of the lipids. If one reversibly goes through the transition one would expect exactly those changes that were reported in the previous section.

If that were so then the thermodynamics of the lipid phase transition should very sensitively affect the action potential, which is in fact the case. Kobatake

et al. (1971) reported that a sudden decrease in temperature can induce nerve pulses, while an increase in temperature does inhibit it. The data mentioned above should be taken as a hint toward the existence of transitions during the nerve pulse but not as a final proof. In the following, however, we explore the possibility that the action potential in nerves is in fact coupled to lipid phase transitions.

18.3 Isentropic Pulse Propagation

In this section we want to outline a description for the propagation of entropic pulses that is based on the thermodynamics of biological membranes as outlined in Chapter 14 and the fact that biomembranes are situated slightly above melting transitions.

Overall, the action potential is isentropic, meaning that the entropy that is a function of state is the same before and after the pulse. Further, no net heat is released means that $\oint dQ = \oint TdS \approx 0$, which is only possible for reversible processes. The action potential is also accompanied by mechanical changes and most likely by changes in lipid state.

The Hodgkin–Huxley model is no thermodynamic model. This means that it does not make a complete treatment of the total energy change, but it only considers closed electrical circuits in cable theory. In the framework of this theory Ohmic currents flow through resistors which dissipates heat due to friction, no matter in which direction the ion currents flow. Both friction and concentration equilibration are irreversible processes! The quantities "entropy" and "temperature" do not play a role in the Hodgkin–Huxley model. The Hodgkin–Huxley model therefore is not based on isentropic (adiabatic) processes. For this reason it is not possible to understand the temperature response of the neuron within the framework of this model. It must at least be incomplete: the thermodynamics is not correctly included. From experiments it is obvious that thickness and density changes occur in nerve membrane, accompanied by changes in lipid state. Reversible processes clearly play a role that are not included in the HH model.

However, there is another phenomenon in physics that shares a lot of similarities with the mechanical pulse accompanying the action potential. This is the propagation of sound. A sound wave is isentropic. Whether a similar process is possible in a two-dimensional membrane depends on whether the energy of a sound wave is dissipated into the aqueous medium (as some people believe) or not. If the energy dissipates a mechanical wave cannot propagate. Experiments like those from Hill, Howarth, Keynes, Tasaki, and others are critical for such a decision. In real systems no process is perfectly adiabatic (completely reversible) and always some of the energy is dissipated.

If the dissipation is small, however, sound propagation can occur over long distances.

In the following we want to outline a model that includes the thermodynamic findings described in the previous paragraphs (Heimburg and Jackson, 2005). In particular, we show that the thermodynamic state of biological membranes in the proximity of the phase transition allows for the propagation of localized isentropic pulses called solitons. We will loosely refer to such pulses as solitons. Since biomembranes are charged the soliton resembles a piezoelectric pulse where voltage is caused by electromechanical coupling.

18.3.1 Solitons

Solitons are localized pulses that propagate without attenuation, and without changes in shape. The formal requirement for the existence of solitons is the existence of nonlinear elastic constants upon density changes. The second requirement is dispersion, i.e., a frequency dependence of the sound velocity.

As mentioned at various places in this textbook biological membranes often display melting transitions slightly below body temperature (Fig. 18.8). This implies that slightly below body temperature the elastic constants also change (see Chapter 14). If one lowers the temperature one moves the physical state of the membrane through the lipid melting transition. During this transition the lateral area of the membrane decreases by about 25%. This in turn means that instead of lowering the temperature one could also increase the lateral pressure to move the system through its melting transition. During this process the lateral compressibility increases. This is indeed a remarkable situation: when membranes under physiological conditions are compressed (until the system is moved into its melting transitions) it becomes softer. They resemble a spring that becomes softer upon compression. If the membrane is compressed further until it is in the gel state, it becomes rigid. This is exactly what was meant by nonlinear elastic constants. Therefore, the first requirement for solitons is fulfilled. Furthermore, it has been found experimentally that the adiabatic compressibility is frequency dependent (Mitaku and Date, 1982), i.e., the membranes display dispersion. Therefore, the second requirement for solitons is also fulfilled. In Fig. 18.9 it is shown that the adiabatic lateral compressibility displays lower values at 5 MHz than at very low frequencies. In fact, at low frequencies, the adiabatic compressibility approaches the isothermal compressibility for a membrane system. This has been justified in Section 14.5 (see also (Heimburg, 1998)). We summarize

$$\begin{aligned} \kappa_S^A(\omega) &< \kappa_T^A \qquad \text{for} \qquad \omega > 0 \\ \kappa_S^A &= \kappa_T^A \qquad \text{for} \qquad \omega = 0 \end{aligned}$$

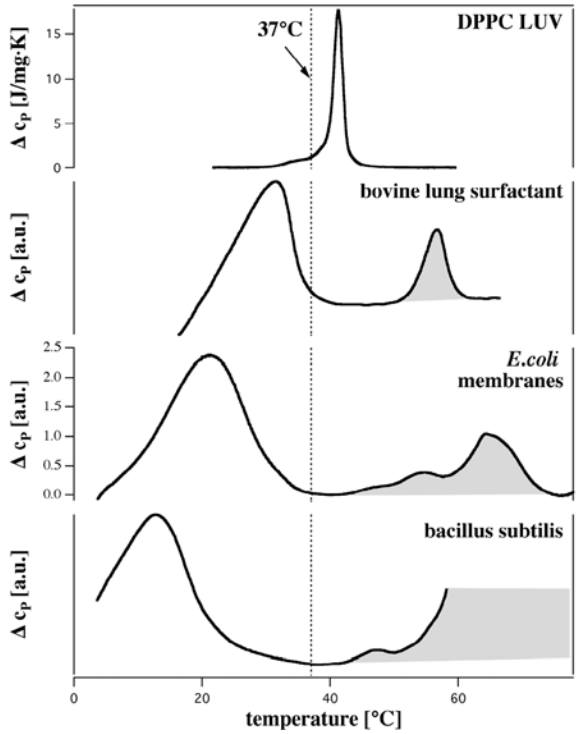

Fig. 18.8 Melting of a lipid membranes in an artificial system and in various biological systems. From Heimburg and Jackson (2005)

where ω is the frequency of a periodic perturbation. It is related to the time scale of the change in area, i.e., on the time scale of a pulse.

In Fig. 18.9, we show the heat capacity for a lipid membrane (DPPC unilamellar vesicles). Following the concepts in Chapter 14 one can calculate the changes in density and in compressibility (left panels in Fig. 18.9). Let us now recall that the speed of sound, c_0, is given by $c_0^2 = (\kappa_S^A \rho)^{-1}$. Thus, using the data in the left-hand panels one can plot the square of the sound velocity versus the change in density as compared to the equilibrium state of the membrane slightly above the transition (Fig. 18.9, right). This figure clearly shows that not only does the heat capacity and the lateral compressibility display a maximum below body temperature, but also the speed of sound displays a minimum (cf. also Fig. 14.11) upon compression. In the following we make use of this.

We now consider one-dimensional sound propagation along a cylindrical membrane with coordinate x that shall represent the long axis of the nerve axon. During a propagating sound pulse the lateral density ρ^A of the membrane changes. Therefore we express the following equations as functions of

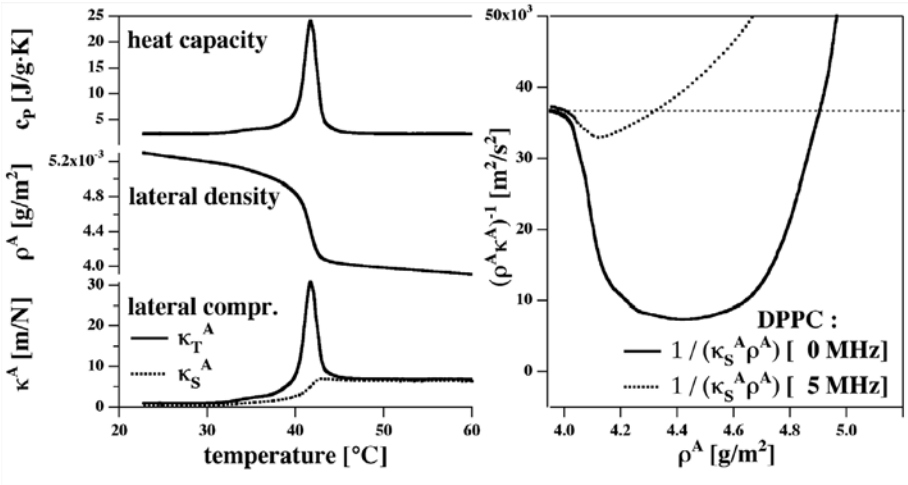

Fig. 18.9 Left: Heat capacity of DPPC LUV (top), the lateral area density, ρ^A, and the corresponding isothermal area compressibility (bottom, solid curve, corresponding to a low frequency case) and adiabatic area compressibility (bottom, dotted line, corresponding to a 5 MHz ultrasonic experiment), as calculated from the heat capacity. Right: The lateral sound velocity $c^2 = 1/\kappa_S^A\rho^A$ $(\mathrm{m}^2/\mathrm{s}^2)$ for the low frequency and the 5 MHz case, as a function of membrane area density, ρ_A $(\mathrm{g}/\mathrm{m}^2)$ at $T = 45\,^\circ$C.

the lateral density. If the membrane is a long and narrow cylinder, we can reduce the problem to propagation in one direction, x. In the absence of dispersion, sound propagation is governed by the equation

$$\frac{\partial^2}{\partial t^2}\Delta\rho^A = \frac{\partial}{\partial x}\left(\frac{1}{\kappa_S^A\cdot\rho^A}\left(\frac{\partial}{\partial x}\Delta\rho^A\right)\right) \tag{18.8}$$

where $\Delta\rho^A = \rho^A - \rho_0^A$ is a function of x and t. This equation originates from the Euler equation in fluid hydrodynamics. If the compressibility is approximately constant and if $\Delta\rho^A \ll \rho_0^A$, this reduces to

$$\frac{\partial^2}{\partial t^2}\Delta\rho^A = c_0^2\frac{\partial^2}{\partial x^2}\left(\Delta\rho^A\right) \tag{18.9}$$

where $c_0 = 1/\sqrt{\rho_0^A\kappa_S^A}$ is the velocity of small amplitude sound. This well-known equation for the propagation of sound governs, for example, the sound propagation in air. Recall, however, that the lateral compressibility κ_S^A depends strongly on $\Delta\rho^A$ if one is close to a transition in the membrane (Fig. 14.7). We thus expand the data shown in Fig. 18.9 (right) for the sound velocity as a function of the density change

$$c^2 = \frac{1}{\rho^A\kappa_S^A} = c_0^2 + p\Delta\rho^A + q(\Delta\rho^A)^2 + \cdots \tag{18.10}$$

where $\Delta\rho^A = \rho^A - \rho_0^A$ with ρ_0^A the equilibrium lateral density. Here we neglected higher orders than quadratic terms. The values for the parameters p and q are obtained by fitting the experimental values of c^2. For the data for unilamellar DPPC vesicles shown in Fig. 18.9 (low frequency case), we obtain $c_0 = 176.6\,\mathrm{m/s}$, $p = -16.6\,c_0^2/\rho_0^A$ and $q = 79.5\,c_0^2/(\rho_0^A)^2$ with $\rho_0^A = 4.035 \times 10^{-3}\,\mathrm{g/m^2}$, assuming a bulk temperature slightly above the melting temperature of $T = 45\,^\circ\mathrm{C}$. In Heimburg and Jackson (2005) the corresponding parameters for biological examples have also been calculated using an equilibrium temperature of $37\,^\circ\mathrm{C}$. The results are comparable to the DPPC model system.

Higher frequencies result in higher propagation velocities, v, because the isentropic compressibility is a decreasing function of frequency as shown in Fig. 18.9. We will approximate the dispersive effects discussed above by introducing a dispersive term, $-h\partial^4\Delta\rho^A/\partial z^4$ with $h > 0$. The introduction of this term is justified by the dispersion relation in Eq. (18.12) that follows from the introduction of this term (see below).

The equation governing sound propagation is then

$$\frac{\partial^2}{\partial t^2}\Delta\rho^A = \frac{\partial}{\partial x}\left[\left(c_0^2 + p\Delta\rho^A + q(\Delta\rho^A)^2\right)\frac{\partial}{\partial x}\Delta\rho^A\right] - h\frac{\partial^4}{\partial x^4}\Delta\rho^A \tag{18.11}$$

(For experts, this equation is closely related to the Boussinesq equation). For periodic low amplitude solutions (i.e., we neglect the nonlinearity of the sound velocity) with $\Delta\rho^A = \rho_0^A \sin(\omega t - k\,x)$, we thus obtain the dispersion relation

$$v^2 = \frac{\omega^2}{k^2} = c_0^2 + hk^2 \approx c_0^2 + \frac{h\omega^2}{c_0^2} \tag{18.12}$$

The sound velocity thus increases with increasing frequency as required by the experimental observation of decreasing compressibility with increasing frequency. It should nevertheless be added that the assumption of the dispersion term is ad hoc because the exact form of the frequency dependence in the millisecond time regime (the time scale of the nerve pulse) is not yet known.

We now consider the possibility of propagating solitons and seek solitonic solutions of the form $\Delta\rho^A(z)$ with $z = x - vt$. Equation (18.11) can now be rewritten as

$$v^2\frac{\partial^2}{\partial z^2}\Delta\rho^A = \frac{\partial}{\partial z}\left[\left(c_0^2 + p\Delta\rho^A + q(\Delta\rho^A)^2\right)\frac{\partial}{\partial z}\Delta\rho^A\right] - h\frac{\partial^4}{\partial z^4}\Delta\rho^A \tag{18.13}$$

It has been shown by Lautrup et al. (2005) that this equation has an exact solution for each given value of the velocity v. This solution has the following

form:

$$\Delta\rho^A = \frac{p}{q}\frac{1-\left(\frac{v^2-v_{min}^2}{c_{0^2}-v_{min}^2}\right)}{1+\left(1+2\sqrt{\frac{v^2-v_{min}^2}{c_{0^2}-v_{min}^2}}\right)\cosh\left(\frac{c_0}{\sqrt{h}}z\sqrt{1-\frac{v^2}{c_0^2}}\right)} \tag{18.14}$$

where

$$v_{\min} = \sqrt{c_0^2 - \frac{p^2}{6q}}$$
$$c_0 \geq v \geq v_{\min} \tag{18.15}$$

is the minimum velocity of a soliton that can propagate in the membrane cylinder (note that the above equation has no solutions for $v < v_{\min}$). For the DPPC system $v_{\min} \approx 0.649851 \times c_0 = 115$ m/s. It turns out that depending on the total energy of the soliton (depending on the strength of the excitation) each soliton has a different velocity. The larger the energy in the pulse the slower the propagation velocity approaching $v_{\min}$. A representative profile is shown in Fig. 18.10. As can be seen from Eq. (18.15) the soliton also approaches a maximum amplitude given by

$$\Delta\rho_{max} = \frac{|p|}{q} \tag{18.16}$$

approaching the minimum velocity, $v_{\min}$.

What can also be seen from the analytical solution in Eq. (18.15) is that the dispersion parameter h does not play a role in the shape of the profile other than defining the length scale in the pulse. If h is four times larger, the pulse width changes by a factor of 2.

18.3.2 Energy of the Solitons

18.3.2.1 Total energy

Each of the solitons has an associated energy. The precise soliton shape depends on the energy of the excitation. For sufficiently large excitation energies, only maximum amplitude solitons will propagate. They correspond to 21% area density change at maximum for both DPPC LUV and lung surfactant (the lung surfactant data have not been shown). The total area change in the transition of DPPC is 24.6% (experimental findings). This means that, at the peak maximum, the soliton forces the membrane about 85% through the lipid melting transition. The energy density of a soliton has both potential and kinetic energy contributions and can be calculated using a Lagrangian formalism. Here, only the result of such a calculation is shown (see (Heimburg and

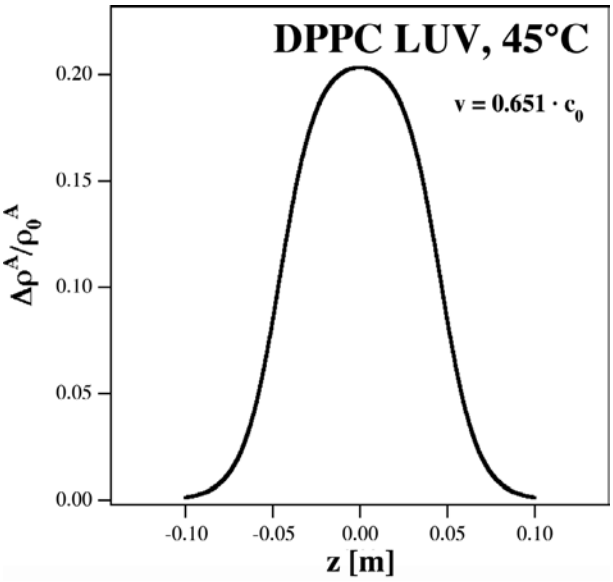

Fig. 18.10 Representative soliton for the DPPC system. The solitons approach a maximum amplitude corresponding to $\approx 0.21\rho_0^A$. This is close to the area density change from fluid to gel.

Jackson, 2007b)). The energy density is given by

$$e_{\text{sol}} = \frac{c_0^2}{\rho_0^A}(\Delta\rho^A)^2 + \frac{p}{3\,\rho_0^A}(\Delta\rho^A)^3 + \frac{q}{6\,\rho_0^A}(\Delta\rho^A)^4 \tag{18.17}$$

The total soliton energy is the integral over dz, i.e., over the length of the pulse. The transient heat release of the soliton during the nerve pulse is equivalent to the potential energy in the pulse, which is about half of the energy change in Eq. (18.17). The other half is the kinetic energy.

18.3.2.2 **Capacitive energy**

Membranes are asymmetrically charged. This gives rise to a transmembrane voltage. At physiological conditions the potential is approximately proportional to the charge density (cf. Eq. (11.17)):

$$\Psi_0 = \frac{1}{\epsilon_0\epsilon\kappa}\sigma = \frac{1}{\epsilon_0\epsilon\kappa}\cdot q_L \cdot \rho^A \tag{18.18}$$

where q_L is the mean number of charges per lipid. This couples the lateral density with the charge density. During the density pulse the charge density changes by about 20% and thus it can be expected that the density pulse is accompanied by a voltage change. This is called electromechanical coupling. This effect has been well described in literature. The membrane behaves like

a piezoelectric crystal. Upon the exertion of a force it changes its transmembrane voltage. The magnitude of this pulse will strongly depend on the value of the charge densities on the two sides of the membrane. It is known that the concentration of negatively charged lipids in the inner membrane layer is larger than in the outer layer (Rothman and Lenard, 1977). This charge imbalance is partially compensated by basic residues of membrane proteins. It is shown in Heimburg and Jackson (2007b) that one can generate voltage changes of the order of 50 mV upon going from fluid to gel phase, assuming that the inner monolayer contains 40% charged lipid and the outer monolayer is uncharged. Thus, the orders of magnitude of the observed voltage changes are close to those obtained by simple electrostatic considerations. There is little known about the exact charge distribution on the two sides of the membrane, and therefore our line of argument in the following will be based on the known transmembrane voltage changes.

The potential difference across the nerve axon membrane is about -70 mV. During the pulse a transient voltage change of about $+100$ mV takes place such that the voltage at the peak maximum is about $+30$ mV.

We assume that the capacitive energy of a membrane is a consequence of compression and the accompanying voltage change. In the low potential limit of the Gouy–Chapman theory (relevant for medium to high ionic strength conditions and a small fraction of charged lipids), the membrane potential is proportional to the charge density and hence to the density change, $\Delta\rho^A$. We assume that the capacitive energy density is given by

$$e_{cap} = \frac{1}{2} C \left(\frac{V_0 \, \Delta\rho^A}{\Delta\rho^A_{\text{max,limit}}} \right)^2 \tag{18.19}$$

The result of a detailed calculation of the total soliton energy and the capacitive energy are given in Fig. 18.11. The result is that the expected reversible heat release from the membrane is expected to be about 20 times larger than the capacitive energy. Experiments on real nerves resulted in similar findings. Howarth et al. (1968) made a careful analysis of the heat release in nerve. They concluded that the observed heat changes cannot be explained by a reversible charging of the membrane capacitor. Further one should mention that the charging of the capacitor in Hodgkin–Huxley is not reversible because the work performed is provided by irreversible fluxes of ions along their gradients.

18.3.3 Thickness Changes

Volume changes in lipid transitions are significantly smaller than area changes. Since the membrane density changes in the soliton, the membrane

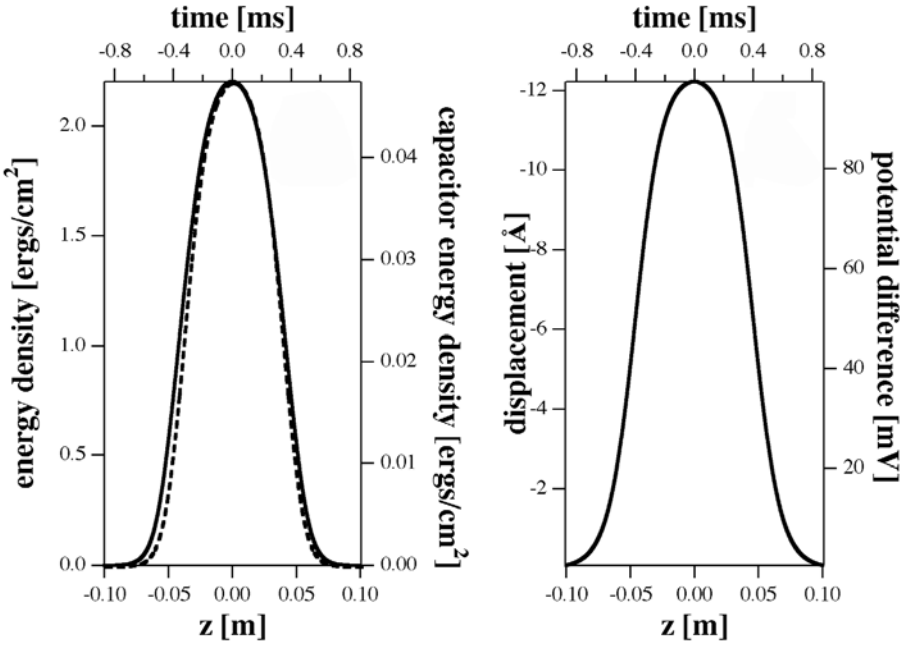

Fig. 18.11 Left: Calculated total energy and capacitive energy densities stored in the soliton during the passage. Both functions display similar time dependence. Compare with the experimental data in Fig. 18.7. Right: Calculated thickness changes of a membrane cylinder (displacement) and corresponding voltage changes. Both functions display identical time dependence. Compare with the experimental data in Fig. 18.7.

thickness must also change. For lipid membranes, the area change is proportional to the volume change and to the thickness change. The volume change when going through the transition is 4.7% for DPPC, the corresponding area change is 24.6%, and the thickness change is -16% (corresponding to -7.4 Å). If the solitons at maximum display a area density change of 21% (corresponding to 85% of the transition) the thickness change must be of order -6.4 Å. This results in a change in the thickness of a membrane cylinder of -12.8 Å. Voltage changes and thickness changes should be proportional.

18.4 Consequences of the Isentropic Theory

We have discussed the influence of the melting transition on the propagation of sound and isentropic waves in the plane of the membrane. If a membrane is slightly above the melting temperature, the response to compression is an

initial lowering of the elastic modulus, followed by a steep increase. Solitons exist as a consequence of a balance between nonlinear and dispersive effects. Nonlinearities are clearly present in the empirical compression modulus (Fig. 18.9). Dispersion effects, approximated here by $-h\partial^4\Delta\rho^A/\partial z^4$, are related to the experimental frequency dependence of sound velocities. Both the form and magnitude of this term can be checked experimentally by investigating the velocity of small amplitude sound. The value of h adopted here and the dispersion relation $\omega^2 = c_0^2k^2 + hk^4$ suggest an increase in the sound velocity of approximately 4% at a frequency of 5 kHz. In 3D experiments, the sound velocity is known to be approximately constant well above and below the transition. Within the transition, the compression modulus at 5 MHz is drastically reduced in comparison with the isothermal (or low frequency) case. While there are propagating mechanical aspects of the nerve pulse that have been found in experiments it has not been discussed here whether there can be dissipation due to friction. The experimental fact that most of the heat is reversible, however, indicates that possible friction effects are small.

Our calculations were performed for a quasi-one-dimensional cylinder slightly above the cooperative melting transition. This is a simplification that does not include possible dependences of the propagation phenomena on the radius of the axon. As biological examples we chose lung surfactant (which exists as a surface film lungs in a bilayer/monolayer equilibrium) as well as *E. coli* and *bacillus subtilis* membranes, which display similar lipid melting features slightly below body or growth temperature. Although we have no direct data on the melting of nerve axon membranes, the biological implications of such a phenomenon seem to be particularly striking regarding the propagation of the action potential. It is of major importance to obtain reliable data on the cooperative behavior of biological membranes, in particular of nerve membranes. Summarizing, the soliton model is able to explain the thermodynamic data obtained from experiments on nerves. In Chapter 19 it will be shown that such a model may also imply a satisfactory model for anesthesia.

18.5 Summary: Key Ideas of Chapter 18

1. The nerve pulse is accompanied by changes in various thermodynamics variables including electrostatic potential (voltage), density and temperature.

2. The Hodgkin–Huxley theory describes the propagation of voltage pulses along nerves on the basis of ion fluxes through ion channel proteins (K^+ and Na^+-channels). The theoretical description is based on electrical circuits. In such a description the currents should produce heat.

3. Experimental data show that during the action potential a transient heat release followed by reabsorption of the heat can be found. Thus, integrated over the nerve pulse no net heat is released. The action potential is a mostly isentropic (adiabatic) phenomenon. This is not in agreement with a picture exclusively based on electrical currents.

4. During the action potential the thickness of the nerve changes and forces are exerted on the environment.

5. Fluorescence changes of lipid membrane markers can be found during the action potential. They indicate that the nerve pulse is accompanied by changes in the physical state of the lipid membrane. Further, turbidity changes are found.

6. Biological membranes exist slightly above the melting temperature of their lipid membranes. Under these conditions in hydrodynamic theory stable density pulses called solitons can propagate. They are consequences of the nonlinear features of the compression modulus close to transitions. Those pulses would be consistent with the finding of a reversible heat, thickness, and state changes.

7. The action potential in nerves shares many similarities with a piezoelectric pulse.

19
Anesthesia

It has long been known that ethanol and certain herbs as opium and cannabis have the ability to reduce pain. In the late 18th century and in the early 19th century nitrous oxide (laughing gas) and carbon dioxide were shown to have anesthetic effects. In the 1840s nitrous oxide (laughing gas) and diethylether were used for painless tooth extraction. On October 1846 the American dentist William T .G. Morton performed the first public surgery on a neck tumor. In a letter to Morton the writer Oliver W. Holmes coined the word anesthesia in 1846. Later in the 19th century also ether, chloroform, and cocaine were used to induce anesthesia. Overton (1901. Jena, Germany. English translation: Studies of Narcosis, Chapman and Hall, 1991, R. Lipnick, Ed.) points out that anesthetics influence all organisms to a similar degree, and that also plants can be anesthetized (as evident from the motion of particles in plant cells).

A surprising variety of different substances cause anesthesia (Fig. 19.1), including noble gases like xenon. The origin of the anesthetic effect is still not understood. In the literature theories one finds competing theories relating anesthesia to their effect on lipid membranes or on their effect on proteins. In particular the local anesthetics are believed to function via their influence on sodium channels. The function of a number of other proteins are influenced by anesthetics including proteins that are probably unrelated to anesthesia as the firefly luciferase. It should also be noted right that anesthetics also alter a number of other properties of lipid membranes as are permeability or hemolysis. This fact indicates that the action of anesthetics may be of much more general origin than just being explained by their effect on nerves. In the following we will mostly discuss lipid models. Since some general physical-chemistry features of the behavior of anesthetics have been found; this is for a very good reason. In the light of Chapter 18 we will especially investigate the effect of anesthetics on the thermodynamic properties of membranes. The fact that anesthesia is caused by a large variety of different molecules including noble gases speak against mechanisms based on the binding of anesthetics to proteins.

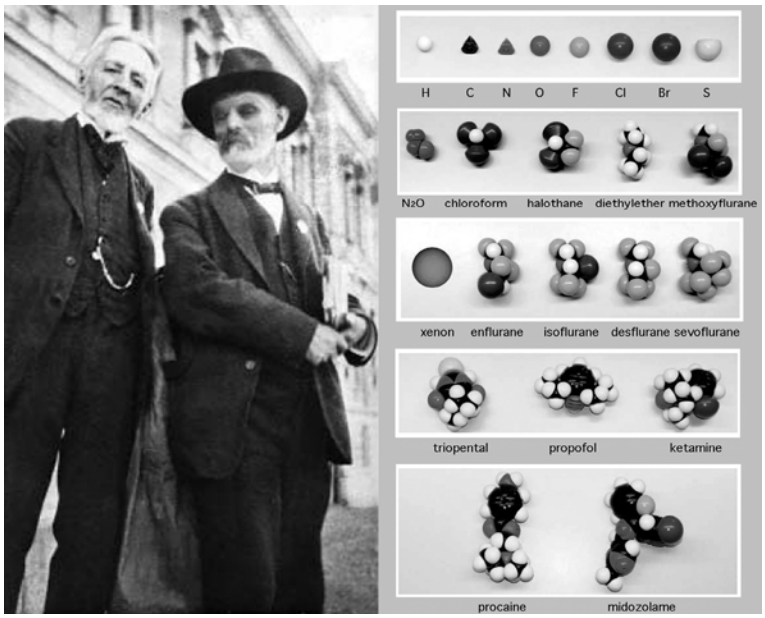

Fig. 19.1 Left: Hans Meyer and Charles E. Overton, 1910. Photo courtesy Dag Lundberg (Lund). Right: Structure of various volatile and liquid anesthetics. From **?** with permission.

19.1 The Meyer–Overton Rule

In 1901 Overton (1901. Jena, Germany. English translation: Studies of Narcosis, Chapman and Hall, 1991, R. Lipnick, Ed.) published a classic monograph written in German with the title "Studien der Narkose (Studies of narcosis)" in which he summarized the findings of his extensive studies on anesthetics. He found that the anesthetic potency is directly proportional to their partition coefficient between water and olive oil. Overton proposed that the solubility of such molecules in olive oil reflects the solubility in the lipid membranes of the cells, in particular of the nerve cells. Overton's book was rated so highly that it was translated into English in 1991. Some of the English quotes below are taken from the translated version. More or less simultaneously with Overton, Meyer (1899) came to very similar conclusions. Meyer summarized his findings as follows:

- All substances that are predominantly chemically nonreactive and that are soluble in fat or fatty substances must have a narcotic effect on living protoplasm to the extent to which they are able to be distributed in it.
- Their action must occur first and strongest within those cells with a chemical composition consisting mainly of fatty substances and which

are particularly good bearers of cell functions: primarily, therefore, the nerve cells.

- The relative strength of action of these narcotics must be dependent upon both their mechanical affinity to fatty substances, and to other cell constituents; i.e., mainly water for the latter. Therefore, it must depend upon the partition coefficient, which determines its distribution in a mixture of water and fatty substance.

Overton added to this a number of further findings and statements that were in agreement with Meyer's ideas, including the additivity of the action of different anesthetics.

The Meyer–Overton can be summarized as follows:

The partition coefficient, P, defined as the ratio of the concentrations of the drug between oil (or the membrane hydrocarbon region) and water is inversely proportional to the critical anesthetic dose (ED_{50}) in water at which anesthesia occurs for this drug,

$$\frac{[C_{H_2O}]}{[C_{membrane}]} \equiv P^{-1} \propto [ED_{50}] \tag{19.1}$$

and

$$P \cdot ED_{50} = \text{const.} \tag{19.2}$$

From this also follows by letting $[C_{H_2O}] = [ED_{50}]$ that the critical anesthetic dose (concentration)

$$[C_{membrane}] = \text{const.} \qquad \begin{array}{l}\text{at critical anesthesia concentration,}\\ \text{independent of drug}\end{array} \tag{19.3}$$

meaning that at critical anesthetic concentration the concentration of the anesthetic dissolved in the membrane is independent of the chemical nature of the anesthetic molecule. These finding are summarized for a number of anesthetic molecules in Fig. 19.2. It is found that both for volatile anesthetics and liquid anesthetics this general rule is obeyed. The slope of the partition coefficient as a function of ED_{50} is -1 within error. It should be noted that (according to van't Hoff) pressures and concentrations are equivalent. In practice, the partition coefficient is often given as the relative concentrations of the anesthetic between octanol and water. The values of the partition coefficient are slightly different for different hydrocarbon reference systems, as are olive oil, octanol, or PC membranes.

In Fig. 19.2 (right) some literature data for anesthesia of tadpoles are given. The partition coefficients are given with respect to three different reference systems: octanol, phosphatidylcholine membranes, and erythrocyte (or other cholesterol-containing) membranes, respectively. If one assumes that the main target of anesthetics are nerve membranes which have a low cholesterol content, one should consider the phosphatidylcholine membranes as the appropriate reference system for determination of the partition coefficient. The experimental finding is that

$$P \cdot \mathrm{ED}_{50} = 0.0341 \frac{\mathrm{mol}}{\mathrm{l}} \qquad \text{for PC membranes} \tag{19.4}$$

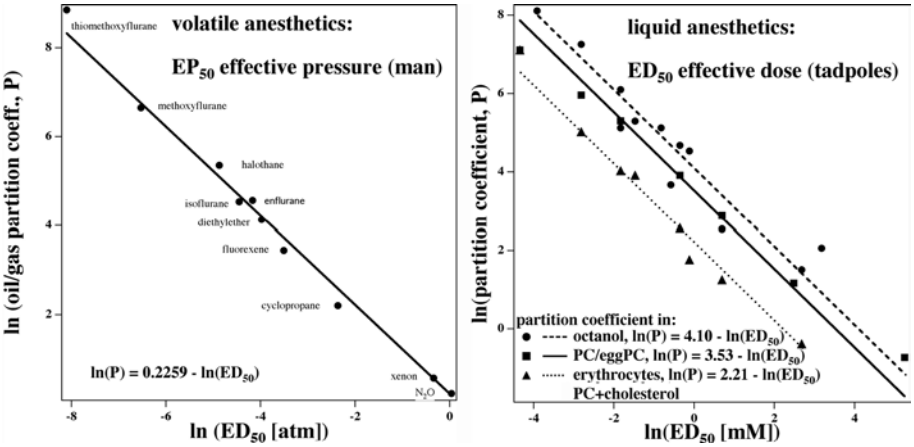

Fig. 19.2 The Meyer–Overton rule: The partition coefficient is inversely related to the effective anesthetic dose $[\mathrm{ED}_{50}]$. Data adapted from Overton (1991). Left: For volatile anesthetics. Instead of a critical concentration a critical partial pressure is given. According to van't Hoff partial pressure and concentration are equivalent. Right: For a number of different liquid anesthetics, shown for three different reference systems—octanol, PC membranes, and cholesterol containing membranes/erythrocytes, respectively. Under all conditions one finds a linear relationship with slope -1. Data taken from Firestone et al. (1987)

The concluding statements of Overton (1901. Jena, Germany. English translation: Studies of Narcosis, Chapman and Hall, 1991, R. Lipnick, Ed.)

- ...there can hardly be any doubt that the action of nonspecific narcotics depends upon the fact that these compounds dissolve in the brain lipoids. This property generally leads to the accumulation of ...narcotics in the brain with changes in the physical state of the brain lipoids induced by their presence. The brain lipoids can no longer fulfill their functions in the nerve cell ...or they somehow disturb the functions of other components of the neurons.

- It is not unlikely that the brain lipoids have a role in defining the physical properties of the protoplasm that is equal to or even greater than that of the cell proteins themselves. The modification in the physical state of brain lipoids in response to the absorption of foreign compounds, occurs in addition, regardless of how this change affects the normal workings of the cell.

These statements by Overton are still valid. In the following we are therefore in search for physical mechanisms of anesthesia.

19.2 The Effect of Anesthetics on the Lipid Melting Points

In the previous chapter we have learned about a mechanism of the nerve pulse that is intimately related to the melting of lipid membranes. It is therefore of interest to investigate the effect that such anesthetics have on melting transitions.

Let us assume the following: Small molecules like anesthetics dissolve perfectly in fluid lipid membranes but do not dissolve at all in gel lipid membranes. We will see below that this seems to be a valid assumption. What influence will this have on the melting points of lipid membranes? In Section 7.4 we have already treated this case. We have shown there that one obtains an effect called freezing point depression. It is a consequence of the mixing entropy of anesthetics in the fluid phase. We obtained the following equation of the freezing point depression:

$$\Delta T_m = \left(\frac{R\, T_m^2}{\Delta H} \right) x_A \tag{19.5}$$

where ΔH and T_m are enthalpy and melting temperature of the lipid membranes, respectively, and x_A is the molar fraction of the anesthetic molecules.

In Section 7.4 (Eqs. (7.31) and (7.32)) it was also shown how to calculate the corresponding heat capacity profiles. In Fig. 19.3 we show a further example for the anesthetic octanol (all simple alcohols from ethanol to decanol have to be considered as anesthetics). It can be seen that the experimental profiles are well reproduced using simple regular solution theory.

In fact, the linear dependence of the melting point on anesthetics concentration is a general feature that can be linked to the critical anesthetic dose. Kharakoz (2001) has collected data for various organisms and many anesthetics. In Fig. 19.4 the dependence of the melting point on the anesthetic concentration (a series of alkanols) in the bulk medium has been plotted as a function of temperature. One obtains a straight line in a double-log plot with the slope

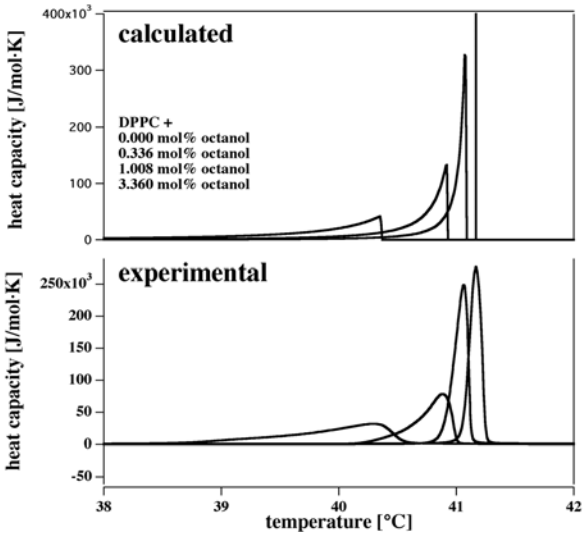

Fig. 19.3 Influence of anesthetics on the melting transition of DPPC membranes. Bottom: Experimental profiles at four different octanol concentrations in the fluid bilayer. Top: Calculated heat capacity profiles for the same concentrations as in the experiment (using Eqs. (7.31) and (7.32)). For the calculation it was assumed that the aqueous phase is small and the total amount of anesthetics in the membrane stays approximately constant during melting.

of -1, meaning that

$$\ln \frac{dT_m}{dC_{\text{anesth}}} = \alpha - \ln \text{ED}_{50} \tag{19.6}$$

with $\alpha = -0.627$. Since the shift of the melting temperature is a linear function of the amount of anesthetic in the membrane, which is again a linear function of the partition coefficient it follows that

$$\frac{\Delta T_m}{\Delta C_{\text{anesth}}} = \frac{\beta}{\text{ED}_{50}} \tag{19.7}$$

with $\beta = \exp(\alpha) = -0.534$ K. If the free concentration of anesthetics, C_{anesth} is equal to the critical anesthetic dose, ED_{50}, one obtains from Fig. 19.4 that the empirical shift of T_m at ED_{50} is given by

$$\Delta T_m = -0.53\,\text{K} \tag{19.8}$$

Thus, the result is that the shift of the melting point of lipid membranes at critical anesthetic dose is always the same and it is independent of the drug. One can also calculate this from the data in Fig. 19.2. The critical molar fraction

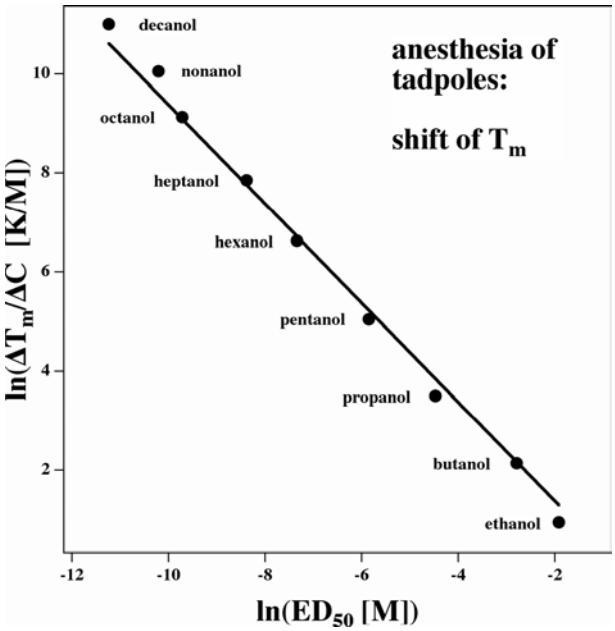

Fig. 19.4 Concentration dependence of the melting point of DPPC membranes plotted versus the critical anesthetic dose, ED_{50}. Data show a series of alkanols and the anesthesia of tadpoles. Adapted from Kharakoz (2001).

of anesthetics in the membrane is

$$x_A = P \cdot \mathrm{ED}_{50} \cdot \mathrm{V_L} \tag{19.9}$$

where V_L is the molar volume of the lipids. For a DPPC membrane $V_L = 0.734$ l/mol and we take this value as being close to the mean value in biological membranes. From the data in Fig. 19.2 we show that $P \cdot \mathrm{ED}_{50} = 0.0341$ (Eq. (19.4)) and as a consequence the molar fraction of anesthetics in the membrane is

$$x_A = 0.026 \qquad \text{independent of drug} \tag{19.10}$$

Inserting this into Eq. (19.5) one finally obtains

$$\Delta T_m = -0.6 \text{ K} \tag{19.11}$$

very similar to the data of Kharakoz given in Eq. (19.8).

> The molar fraction of anesthetics at critical dose is $x_A \approx 0.026$. The corresponding shift of the melting transition is $\Delta T_m \approx -0.6$ K, independent of the chemical nature of the anesthetic drug.

The thermodynamic theory of anesthesia has been treated in detail in Heimburg and Jackson (2007b) and the connection with nerve pulse propagation is reviewed in Heimburg and Jackson (2007a).

19.3 The Lateral Pressure Profile

We have seen in previous chapters that the melting transition is dependent on pressure. One may therefore wonder whether the shift of the transition temperature caused by anesthetics can be translated into a lateral pressure.

As above we assume that the anesthetics molecules are readily soluble in the fluid phase but insoluble in the gel phase. The free energy is related to the concentration of molecules in the fluid phase, given per total area of the fluid membrane, $f \cdot A_f$. This concentration changes as the molar fraction of fluid phase, f, changes in the transition regime.

$$F = F_0 + nkT \ln x_A^f \qquad x_A^f = \frac{n}{f \cdot A_f} \tag{19.12}$$

where n is here the number of anesthetics molecules per lipid (which can be smaller than one). The x_A^0 and x_A^f are molar fractions of anesthetics. The lateral pressure in the membrane induced by anesthetics is given by

$$\Pi = -\frac{dF}{dA} = -\frac{dF}{A_f df} = -kT\frac{n}{f \cdot A_f} = -kT\, x_A^f \tag{19.13}$$

The pressure in the fluid phase is

$$\begin{aligned} \Pi &= -kT\frac{n}{A_f} \\ &= -0.00723 \cdot x_A^f \left[\frac{\mathrm{N}}{\mathrm{m}}\right] \qquad T = 314\ \mathrm{K},\ A_f = 0.6 \times 10^{-18}\,\mathrm{m}^2 \end{aligned} \tag{19.14}$$

The pressure approaches ∞ if $f \to 0$. Therefore, it is impossible under the above assumptions to move the system completely into the gel phase. This is in agreement with the heat capacity profiles shown in Fig. 19.3. The melting temperature in the presence of anesthetics, T_m^A, is given by

$$\begin{aligned} T_m^A &= \frac{\Delta H + \Pi A_f}{\Delta S} = T_m + \frac{\Pi A_f}{\Delta H} T_m \\ \Delta T_m &= \frac{\Pi A_f}{\Delta H} T_m = -\frac{0.00723 A_f \cdot x_A^f}{\Delta H} T_m \end{aligned} \tag{19.15}$$

At the critical anesthetic concentration $x_A^0 = 0.026$ (see Eq. (19.10)). Taking the parameters of a DPPC membrane ($T_m = 314.2$ K, $\Delta H = 35$ kJ/mol) one

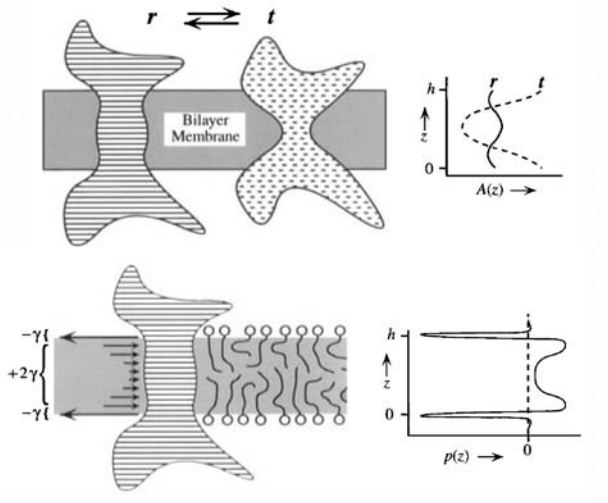

Fig. 19.5 Lateral pressure profile across the membrane, adapted from Cantor (1997a). Bottom, left: A membrane protein may experience different lateral pressures (indicated by arrows) at different depth in the membrane. Bottom, right: Calculated lateral pressure $p(z)$ as a function of position z in the membrane. Top, left: Schematic picture of how the lateral pressure can influence the equilibrium of two conformations of a protein. To, right: Cross-sectional area $A(z)$ of the two protein conformations as a function of position z in the membrane.

arrives at

$$\Delta T_m = -0.6 \text{ K} \tag{19.16}$$

which is exactly the number obtained in Eq. (19.11). Thus, it is completely reasonable to consider the effect of anesthetics as the generation of a lateral pressure within the membrane plane.

> Anesthetics change the lateral pressure distribution within the membrane. Thereby, they lower melting points and simultaneously potentially influence protein structures.

Since in equilibrium the area assumes a constant value the net lateral pressure (surface tension), of course, is zero. This means that the different contributions to the surface tension by lipid chains, head groups, electrostatics, anesthetics ... add to a net zero tension. The repulsive pressure term caused by the anesthetics must be compensated by attractive terms such that integrated over the membrane diameter the net pressure is zero. Cantor (1997a,b, 1999a) applied statistical thermodynamics means in a lattice model to calculate the attractive and the repulsive pressure contributions in the membrane as

a function of the depth in the membrane. He arrived at a lateral pressure profiles that is shown in Fig. 19.5. It can be seen that the repulsive forces within the membrane are compensated by attractive forces in the head group region such that the integral over the lateral pressure amounts to zero, which is the equilibrium condition. Cantor pointed out that this pressure may well influence conformational equilibria of membrane proteins (Cantor, 1997b, 1999b). Since anesthetics influence the lateral pressure profile Cantor argues that this may be the mechanism by which anesthetics regulate protein function.

19.4
Dependence of Anesthesia on Hydrostatic Pressure

Hydrostatic pressure shifts transitions to higher temperatures according to

$$\Delta T_m = \gamma_V \Delta p T_m \qquad \gamma_V = 7.8 \times 10^{-10} \frac{\mathrm{m}^2}{\mathrm{N}} \tag{19.17}$$

If we assume that the shift in the transition temperature is of biological relevance, the application of hydrostatic pressure should have the potential to reverse anesthesia. As mentioned above, the lowering of the transition temperature at critical anesthetic dose is of the order $\Delta T_m = -0.6$ K. Using Eq. (19.17) one can calculate the pressure necessary to reverse anesthesia. One obtains that

$$\Delta p = 24.6 \cdot 10^5 \frac{N}{m^2} = 24.6\,\mathrm{bar} \tag{19.18}$$

> Anesthesia can be reversed by hydrostatic pressure on the order larger than 25 bar.

This has in fact be measured. Johnson and Flagler (1950) have reported that tadpoles anesthetized in $3-6$ vol% ethanol solutions awake upon application of 140–350 bar of hydrostatic pressure. The critical anesthetic concentration for ethanol in water is 1.1 vol%. Thus, Johnson and Flagler used 3–6 times the anesthetic dose. To reverse the effect of such high amounts of anesthetics one obviously needs 3–6 times the bulk pressure of 25 bar, i.e., 75–150 bar. That is relatively close to the range of pressures found by Johnson and Flagler (1950). Thus, the pressure reversal of anesthesia is in agreement with the picture that explains anesthesia by the thermodynamic effects of anesthetic drugs.

19.5
pH Dependence of Anesthesia

In Chapter 11, we have shown that pH changes can significantly change the melting points of charged lipid membranes. Lowering of pH typically increases the melting temperature due to protonation of negatively charged phosphate groups. In Fig. 19.6 the effect of pH changes on *E. coli* membranes is shown. The change in transition temperature of these native biological membranes (including all proteins) is quite significant, i.e., the shift of pH from 9 to 5 changes the transition midpoint by about 7.3 K to higher temperatures, approximately linear in pH. Lacking other reliable data for the time being, let us assume that this is a behavior typical for biological membranes. We thus conclude that the shift in T_m is $\Delta T_m \approx -1.8$ K/pH unit. To reverse the effect of anesthetics one therefore requires a lowering of the pH by $\Delta\text{pH} = -0.33$. Interestingly, it is known that inflamed tissue cannot be anesthetized with the typical dose. Some groups believe that this is somehow related to the observed lowering of the pH observed in inflamed tissue, which is on the order of 0.5 pH units (Punnia-Moorthy, 1987). This is exactly the range of pH changes required for the above considerations.

> Inflamed tissue cannot be anesthetized. Simultaneously, the pH in such tissue is by about 0.5 pH units lower than in healthy tissue. This pH change is sufficient to reverse anesthesia.

In general, all salts that increase melting temperatures should display the potency to reverse anesthesia, in particular divalent cations as Ca^{2+}.

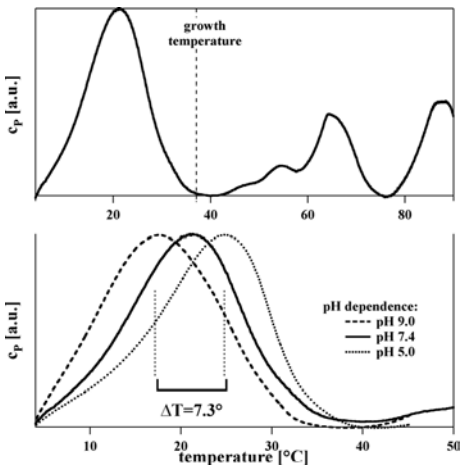

Fig. 19.6 pH dependence of the melting transition of native *E. coli* membranes. Adapted from Heimburg and Jackson (2007b).

19.6
Neurotransmitters

Neurotransmitters are substances that are believed to regulate the signal transmission in across the synapses by binding to specific receptor proteins. They are not typically recognized as anesthetics. However, anesthetics also bind to lipid membranes and lower their melting points. Remember the statement by Meyer (1899) that all substances soluble in membranes act as anesthetics.

In Fig. 19.7 the action of the neurotransmitter serotonin on DMPC vesicles is shown. The lipid concentration is 50 mM and the total neurotransmitter concentration was 0 mM, 1 mM, and 2.5 mM. Total means that the free and bound concentration counted together. These concentrations are much lower than the concentration of neurotransmitters in synaptic vesicles, which is of the order of 100 mM. It can be seen that such relatively low neurotransmitter concentrations have a significant effect on the melting behavior that is of the same order than that of anesthetics. Other neurotransmitters as dopamine have similar effects. Findings of such kind have lead to the question first asked by Cantor (2003) on whether neurotransmitters besides their specific properties also display unspecific anesthetic effects.

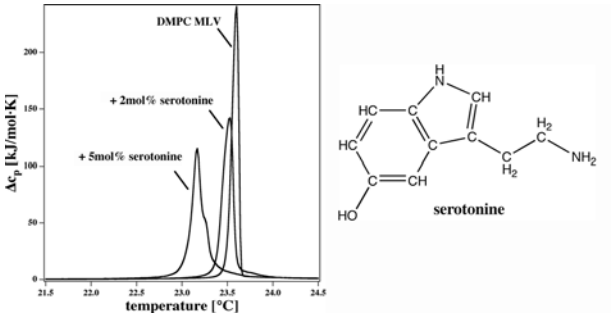

Fig. 19.7 Influence of the neurotransmitter serotonin on DMPC membranes (50 mM) at three concentrations: 0 mol%, 2 mol% and 5 mol% (referring to the overall molar ratio of neurotransmitter and lipids, i.e., 0, 1, and 2.5 mM total serotonin concentration). From Seeger (2006).

Due to the findings of Meyer and Overton one has to ask this question quite generally about all membrane interacting substances that lower melting temperatures including neurotransmitters and peptides. Everything that increases melting temperatures has the potential to reverse anesthesia, including protons and divalent cations.

19.7 Summary: Key Ideas of Chapter 19

1. The partition coefficient, P, and the potency of an anesthetic are directly proportional to each other for a large class of molecules. Even noble gases can act as anesthetics. If the critical anesthetic concentration is [ED_{50}], then $P \cdot [ED_{50}]$ = const. This empirical finding is called the Meyer–Overton rule.

2. This means that the molar fraction, x_A, of all anesthetics in the membrane at critical concentration is generally the same. It is $x_A = 0.026$.

3. Anesthetics lower the melting points of lipid membranes in a simple linear manner. At [ED_{50}] the lowering of T_m is 0.6 K for all anesthetics (that obey the Meyer–Overton rule).

4. The effect of anesthetics on the melting temperatures can be explained by "freezing-point depression." The anesthetics dissolve ideally in the fluid lipid membrane but are insoluble in the gel membrane. The lowering of the melting point is a consequence of the solution entropy of the anesthetic in the fluid phase.

5. The effect of anesthetics can also be understood in terms of a lateral pressure that is induced within the fluid membrane. Such pressures have a putative effect on conformational equilibria of membrane proteins.

6. Anesthesia can be reversed by hydrostatic pressure. A pressure of 25 bars is necessary to completely reverse the effect at [ED_{50}]. The pressure reversal can be quantitatively explained by the pressure effect on phase transitions.

7. Similarly, divalent cations should have the potency to reverse anesthesia since they increase melting temperatures.

Appendix A
Abbreviations Used in this Book

Abbreviations of Lipid Names

CL	cardiolipin
DLPC	1,2-dilauroyl-sn-3-phosphatidylcholine
DMG	1,2-dimyristoyl-sn-3-glycerol
DMPC	1,2-dimyristoyl-sn-3-phosphatidylcholine
DMPE	1,2-dimyristoyl-sn-3-phosphatidylethanolamine
DMPG	1,2-dimyristoyl-sn-3-phosphatidylglycerol
DOPC	1,2-dioleoyl-sn-3-phosphatidylcholine
DPPA	1,2-dipalmitoyl-sn-3-phosphatidic acid
DPPC	1,2-dipalmitoyl-sn-3-phosphatidylcholine
DPPE	1,2-dipalmitoyl-sn-3-phosphatidylethanolamine
DPPG	1,2-dipalmitoyl-sn-3-phosphatidylglycerol
DSPC	1,2-distearoyl-sn-3-phosphatidylcholine
POPC	1-palmitoyl-2-oleoyl-sn-3-phosphatidylcholine
SM	sphingomyelin

Abbreviations of Techniques

DSC	differential scanning calorimetry
FCS	fluorescence correlation spectroscopy
FRAP	fluorescence recovery after photobleaching
ITC	isothermal titration calorimetry
NMR	nuclear magnetic resonance

References

B. C. Abbott, A. V. Hill, and J. V. Howarth. The positive and negative heat production associated with a nerve impulse. *Proc. R. Soc. London. B*, 148:149–187, 1958.

P. F. F. Almeida and W. L. C. Vaz. Lateral diffusion in membranes. In R. Lipowsky and E. Sackmann, editors, *Structure and Dynamics of Membranes: From Cells to Vesicles*, pages 305–357. Elsevier, Amsterdam, 1995.

P. F. F. Almeida, W. L. C. Vaz, and T. E. Thompson. Lateral diffusion and percolation in two-phase, two-component lipid bilayers. Topology of the solid-phase domains in-plane and across the lipid bilayer. *Biochemistry*, 31:7198–7210, 1992.

V. F. Antonov, V. V. Petrov, A. A. Molnar, D. A. Predvoditelev, and A. S. Ivanov. The appearance of single-ion channels in unmodified lipid bilayer membranes at the phase transition temperature. *Nature*, 283:585–586, 1980.

V. F. Antonov, E. V. Shevchenko, E. T. Kozhomkulov, A. A. Molnar, and E. Y. Smirnova. Capacitive and ionic currents in BLM from phosphatidic acid in Ca^{2+}-induced phase transition. *Biochem. Biophys. Research Comm.*, 133:1098–1103, 1985.

V. F. Antonov, A. A. Anosov, V. P. Norik, and E. Y. Smirnova. Soft perforation of planar bilayer lipid membranes of dipalmitoylphosphatidylcholine at the temperature of the phase transition from the liquid crystalline to gel state. *Eur. Biophys. J.*, 34: 155–162, 2005.

S. V. Avery, D. Lloyd, and J. L. Harwood. Temperature-dependent changes in plasma-membrane lipid order and the phagocytic activity of the amoeba acanthamoeba castellanii are closely correlated. *Biochem. J.*, 312:811–816, 1995.

M. Bagnat and K. Simons. Lipid rafts in protein sorting and cell polarity in budding yeast saccharomyces cerevisiae. *Biol. Chem.*, 383:1475–1480, 2002.

M. Bagnat, S. Keranen, A. Shevchenko, and K. Simons. Lipid rafts function in biosynthetic delivery of proteins to the cell surface in yeast. *Proc. Natl. Acad. Sci. USA*, 97:3254–3259, 2000.

R. L. Biltonen. A statistical-thermodynamic view of cooperative structural changes in phospholipid bilayer membranes: their potential role in biological function. *J. Chem. Thermodynamics*, 220:1–19, 1990.

Bloom and Fawcett. *A Textbook of Histology*. Chapman and Hall, N.Y., 12th edition edition, 1994.

A. Blume. Apparent molar heat capacities of phospholipids in aqueous dispersion. *Biochemistry*, 22:5436–5442, 1983.

A. Blume and M. Hillmann. Dimyristoylphosphatidic acid/cholesterol bilayers. thermodynamic properties and kinetics of the phase transition as studied by the pressure jump relaxation technique. *Europ. Biophys. J.*, 13:343–353, 1986.

R. A. Böckmann, A. Hac, T. Heimburg, and H. Grubmüller. Effect of sodium chloride on a lipid bilayer. *Biophys. J.*, 858:1647–1655, 2003.

G. Boheim, W. Hanke, and H. Eibl. Lipid phase transition in planar bilayer membrane and its effect on carrier- and pore-mediated ion transport. *Proc. Natl. Acad. Sci. USA*, 77:3403–3407, 1980.

L. Boltzmann. Über die mechanische bedeutung des zweiten hauptsatzes der wärmetheorie. *Wien. Ber.*, 53:195–220, 1866.

L. T. Boni and R. R. Rando. The nature of protein kinase c activation by physically defined phospholipid vesicles and diacylglycerols. *J. Biol. Chem.*, 260:10819–10825, 1985.

M. Böttner, D. Ceh, U. Jacobs, and R. Winter. High pressure volumetric measurements on phospholipid bilayers. *Z. Phys. Chem.*, 184: 205–218, 1994.

J. F. Brandts. The thermodynamics of protein denaturation. II. A model of reversible denaturation and interpretations regarding the stability of chymotrypsinogen. *J. Am. Chem. Soc.*, 86:4302–4314, 1964.

D. A. Brown and E. London. Functions of lipid rafts in biological membranes. *Ann. Rev. Cell Develop. Biol.*, 14:111–136, 1998.

T. Brumm, K. Jorgensen, O. G. Mouritsen, and T. M. Bayerl. The effect of increasing membrane curvature on the phase transition and mixing behavior of a dimyristoyl-sn-glycero-3-phosphatidylcholine/ distearoyl-sn-glycero-3-phosphatidyl-choline lipid mixture as studied by fourier transform infrared spectroscopy and differential scanning calorimetry. *Biophys. J.*, 70:1373–1379, 1996.

W.R. Burack, Q. Yuan, and R.L. Biltonen. Role of lateral phase separation in the modulation of phospholipase a2 activity. *Biochemistry*, 32:583–589, 1993.

G. W. Bushnell, G. V. Louie, and G. D. Brayer. High-resolution three-dimensional structure of horse heart cytochrome c. *J. Mol. Biol.*, 214:585–595, 1990.

M. G. Cacace, E. M. Landau, and J. J. Ramsden. The hofmeister series: salt and solvent effects on interfacial phenomena. *Quart. Rev. Biophys.*, 30:241–277, 1997.

M. Caffrey, R. L. Magin, B. Hummel, and J. Zhang. Kinetics of the lamellar and hexagonal phase transition in phosphatidylethanolamine. Time-resolved x-ray diffraction study using a microwave-induced temperature jump. *Biophys. J.*, 58: 21–29, 1990.

B. Cannon, M. Hermansson, S. Györke, P. Somerharju, and J. A. Virtanen. Regulation of calcium channel activity by lipid domain formation in planar lipid bilayers. *Biophys. J.*, 85:933–942, 2003.

R. S. Cantor. Lateral pressures in cell membranes: a mechanism for modulation of protein function. *J. Phys. Chem. B*, 101:1723–1725, 1997a.

R. S. Cantor. The lateral pressure profile in membranes: a physical mechanism of general anesthesia. *Biochemistry*, 36:2339–2344, 1997b.

R. S. Cantor. Lipid composition and the lateral presure profile in bilayer. *Biophys. J.*, 76: 2625–2639, 1999a.

R. S. Cantor. Solute modulation of conformational equilibria in intrinsic membrane proteins: Apparent "cooperativity" without binding. *Biophys. J.*, 77(2643-2647), 1999b.

R. S. Cantor. Receptor desensitization by neurotransmitters in membranes: are neurotransmitters the endogenous anesthetics? *Biochemistry*, 42:11891–11897, 2003.

N. L. S. Carnot. *Réflexions sur la puissance motrice du feu et sur les machines propres à développer cette puissance*. Bachelier, Paris, 1824.

R. C. Chatelier and A. P. Minton. Adsorption of globular proteins on locally planar surfaces -Models for the excluded surface area and aggregation of adsorbed protein on adsorption equilibria. *Biophys. J.*, 71: 2367–2374, 1996.

N. Chu, N. Kucerka, Y. Liu, S. Tristam-Nagle, and J.F.Nagle. Anomalous swelling of lipid bilayer stacks is caused by softening of the bending modulus. *Phys. Rev. E*, 71:041904–1 to 4, 2005.

K. S. Cole and H. J. Curtis. Electrical impedance of the squid giant axon during activity. *J. Gen. Physiol.*, 220:649–670, 1939.

L. Cruzeiro-Hansson and O. G. Mouritsen. Passive ion permeability of lipid membranes modelled via lipid-domain interfacial area. *Biochim. Biophys. Acta*, 944:63–72, 1988.

C. Czeslik, O. Reis, R. Winter, and G. Rapp. Effect of high pressure on the structure of dipalmitoylphosphatidylcholine bilayer membranes: a synchroton-x-ray diffraction and ft-ir spectroscopy study using the diamond anvil technique. *Chem. Phys. Lett.*, 91: 135–144, 1998.

U. Dahmen-Levison, G. Brezesinski, and H. Möhwald. Specific adsorption of PLA_2 at monolayers. *Thin Solid Films*, 327–329: 616–620, 1998.

J. F. Danielli and H. Davson. A contribution to the theory of permeability of thin films. *J. Cell Comp. Physiol.*, 5:495–508, 1935.

R. F. M. de Almeida, A. Fedorov, and M. Prieto. Sphingomyelin/phosphatidylcholine/cholesterol phase diagram: Boundaries and composition of lipid rafts. *Biophys. J.*, 85:2406–2416, 2003.

A. H. de Vries, S. Yefimov, A. E. Mark, and S. J. Marrink. Molecular structure of the lecithin ripple phase. *Proc. Natl. Acad. Sci. USA*, 102: 5392–5396, 2005.

H. de Vries. Sur la permeabilite du protoplasma des betteraves rouges. *Arch. Neerl. Sci. Exactes Nat.*, 61:117–126, 1871.

H. de Vries. Eine Methode zur Analyse der Turgorcraft. *Jahrb. Wiss. Bot.*, 14:429–601, 1884.

P. Debye and E. Hückel. Zur Theorie der Elektrolyte. I. Gefrierpunktserniedrigung und verwandte Erscheinungen. *Physik. Z.*, 24: 185–206, 1923.

E. F. DeLong and A. A. Yayanos. Adaptation of the membrane lipids of a deep-sea bacterium to changes in hydrostatic pressure. *Science*, 228:1101–1103, 1985.

R. Dimova, B. Pouligny, and C. Dietrich. Pretransitional effects in dimyristoylphosphatidylcholine vesicle membranes: Optical dynamometry study. *Biophys. J.*, 79:340–356, 2000.

D. A. Doyle, J. Morais, J. M. Gulbis, A. L. Cohen, B. T. Chait, and R. MacKinnon. The structure of the potassium channel: Molecular basis of k+ conduction and selectivity. *Science*, 280:69, 1998.

F. Dumas, M. M. Sperotto, M. C. Lebrun, J. F. Tocanne, and O. G. Mouritsen. Molecular sorting of lipids by bacteriorhodopsin in dilauroylphosphatidylcholine/distearoylphosphatidylcholine lipid bilayers. *Biophys. J.*, 73:1940–1953, 1997.

F. Dumas, M. C. Lebrun, and J. F. Tocanne. Is the protein/lipid hydrophobic matching principle relevant to membrane organization and functions? *FEBS Lett.*, 458:271–277, 1999.

F. Dumas, J. F. Tocanne, G. Leblanc, and M. C. Lebrun. Consequences of hydrophobic mismatch between lipids and melibiose permease on melibiose transport. *Biochemistry*, 39:4846–4854, 2000.

H. Ebel, P. Grabitz, and T. Heimburg. Enthalpy and volume changes in lipid membranes. i. the proportionality of heat and volume changes in the lipid melting transition and its implication for the elastic constants. *J. Phys. Chem. B*, 105:7353–7360, 2001.

M. Edidin. The state of lipid rafts: From model membranes to cells. *Ann. Rev. Biophys. Biomol. Struct.*, 32:257–283, 2003a.

M. Edidin. Lipids on the frontier: A century of cell-membrane bilayers. *Nat. Rev. Mol. Cell Biol.*, 4:414–418, 2003b.

M. Eigen and R. Rigler. Sorting single molecules: Application to diagnostic and evolutionary biotechnology. *Proc. Natl. Acad. Sci. USA*, 91:5740–5747, 1994.

A. Einstein. Über die von der molekularkinetischen Theorie der Wärme geforderte Bewegung von in ruhenden Flüssigkeiten suspendierten Teilchen. *Ann. Phys. (Leipzig)*, 17 (532):549–560, 1905.

K. Elamrani and A. Blume. Phase transition kinetics of phosphatidic acid bilayers. a pressure-jump relaxation study. *Biochemistry*, 22:3305 – 3311, 1983.

E. Evans and R. Kwok. Mechanical calorimetry of large dimyristoylphosphatidylcholine vesicles in the phase transition region. *Biochemistry*, 210(4874 - 4879), 1982.

E. A. Evans. Bending resistance and chemically induced moments in membrane bilayers. *Biophys. J.*, 14:923–931, 1974.

G. W. Feigenson and J. T. Buboltz. Ternary phase diagram of dipalmitoyl-pc/dilauroyl-pc/ cholesterol: Nanoscopic domain formation driven by cholesterol. *Biophys. J.*, 80:2775–2788, 2001.

M. Fein, J. Unkeless, F. Y. S. Chuang, M. Sassaroli, R. da Costa, and et al. Lateral mobility of lipid analogues and gpi-anchored proteins in supported bilayers determined by fluorescent bead tracking. *J. Membr. Biol.*, 135:83–92, 1993.

L. Fernandez-Puente, I. Bivas, M. D. Mitov, and P.Meleard. Temperature and chain length effects on bending elasticity of phosphatidylcholine bilayers. *Europhys. Lett.*, 28: 181–186, 1994.

A. M. Ferrenberg and R. H. Swendsen. New Monte Carlo technique for studying phase transitions. *Phys. Rev. Lett.*, 61:2635–2638, 1988.

A. M. Ferrenberg and R. H. Swendsen. Optimized Monte Carlo data analysis. *Phys. Rev. Lett.*, 63:1195–1198, 1989.

R. Fettiplace and D. A. Haydon. Water permeability of lipid membranes. *Physiol. Reviews*, 60:510–550, 1980.

M. Fidorra. Untersuchung des Phasenverhaltens von Membranen durch konfokale Mikroskopie und Kalorimetrie. Master's thesis, University of Göttingen, 2004.

A. Finkelstein. *Water movement through lipid bilayers, pores, and plasma membranes. Theory and reality*, volume 4 of *Distinguished lecture series of the society of general physiologists*. Wiley, 1987.

L. L. Firestone, A. S. Janoff, and K. Miller. Lipid-dependent differential effects of stereoisomers of anesthetic alcohols. *Biochim. Biophys. Acta*, 1987.

R. W. Fisher. Lateral diffusion of the phospholipid molecule in dipalmitoylphosphatidylcholine bilayers. an investigation using nuclear spin–lattice relaxation in the rotating frame. *Biochemistry*, 17:1177–1183, 1978.

R. O. Fox and F. M. Richards. A voltage-gated ion channel model inferred from the crystal structure of alamethicin at 1.5 Å resolution. *Nature*, 300:325–330, 1982.

F. C. Frank. 1. liquid crystals - On the theory of liquid crystals. *Discuss. Faraday Soc.*, 25: 19–28, 1958.

N. P. Franks and Y. K. Levine. Low-angle x-ray diffraction. In E. Grell, editor, *Membrane Spectroscopy*, pages 437–487, Berlin, Heidelberg, New York, 1981. Springer.

E. Freire, T. Markello, C. Rigell, and P. W. Holloway. Calorimetric and fluorescence characterization of interactions between cytochrome b_5 and phosphatidylcholine bilayers. *Biochemistry*, 28:5634–5643, 1983.

G. Friedel. Les etats mesomorphes de la matiere. *Ann. Physique*, 18:409–465, 1922.

J. R. Fries, L. Brand, C. Eggeling, M. Kölner, and C. A. M. Seidel. Quantitative identification of different single molecules by selective time-resolved confocal fluorescence spectroscopy. *J. Phys. Chem.*, 102: 6601–6613, 1998.

L. D. Frye and M. Edidin. The rapid intermixing of cell surface antigens after formation of mouse-human heterokaryons. *J. Cell Sci.*, 7:319–335, 1970.

H. J. Galla, W. Hartmann, U. Theilen, and E. Sackmann. On two-dimensional passive random walk in lipid bilayers and fluid pathways in biomembranes. *J. Membr. Biol.*, 48:215–236, 1979.

P. Garidel, C. Johann, L. Mennicke, and A. Blume. The mixing behavior of pseudobinary phosphatidylcholine-phosphatidylglycerol mixtures as a function of ph and chain length. *Eur. Biophys. J.*, 263:447–459, 1997.

E. Gazit, P. La Rocca, M. S. P. Sansom, and Y. Shai. The structure and organization within the membrane of the helices composing the pore-forming domain of Bacillus Thuringiensis δ-endotoxin are consistent with an "umbrella" structure of the pore. *Proc. Natl. Acad. Sci. USA*, 95:12289–12294, 1998.

R. B. Gennis. *Biomembranes. Molecular structure and function*. Springer, New York, 1989.

H. Gögelein and H. Koepsell. Channels in planar bilayers made from commercially available lipids. *Pflügers Arch.*, 401:433–434, 1984.

E. Gorter and F. Grendel. On bimolecular layers of lipid on the chromacytes of the blood. *J. Exp. Med.*, 41:439–443, 1925.

P. Grabitz, V. P. Ivanova, and T. Heimburg. Relaxation kinetics of lipid membranes and its relation to the heat capacity. *Biophys. J.*, 82: 299–309, 2002.

D. W. Grainger, A. Reichert, H. Ringsdorf, and C. Salesse. An enzyme caught in action: Direct imaging of hydrolytic function and domain formation of phospholipase A2 in phosphatidyl choline monolayers. *FEBS Lett.*, 252:73–82, 1989.

A. Hac, H. Seeger, M. Fidorra, and T. Heimburg. Diffusion in two-component lipid membranes—a fluorescence correlation spectroscopy and monte carlo simulation study. *Biophys. J.*, 88:317–333, 2005.

S. Halstenberg, T. Heimburg, T. Hianik, U. Kaatze, and R. Krivanek. Cholesterol-induced variations in the volume and enthalpy fluctuations of lipid bilayers. *Biophys. J.*, 75:264–271, 1998.

T. Harder, P. Scheiffele, P. Verkade, and K. Simons. Lipid domain structure of the plasma membrane revealed by patching of membrane components. *J. Cell Biol.*, 141: 929–942, 1998.

G. S. Harms, M. Sonnleitner, G. J. Schütz, H. J. Gruber, and T. Schmidt. Single-molecule anisotropy imaging. *Biophys. J.*, 77:2864–2870, 1999.

G. S. Harms, L. Cognet, P. H. M. Lommerse, G. A. Blab, H. Kahr, R. Gamsjager, H. P. Spaink, N. M. Soldatov, C. Romanin, and T. Schmidt. Single-molecule imaging of L-type Ca2+ channels in live cells. *Biophys. J.*, 81:2639–2646, 2001.

T. A. Harroun, W. T. Heller, T. M. Weiss, L. Yang, and H. H. Huang. Experimental evidence for hydrophobic matching and membrane-mediated interactions in lipid bilayers containing gramicidin. *Biophys. J.*, 76:937–945, 1999.

J. R. Hazel. Influence of thermal acclimation on membrane lipid composition of rainbow trout liver. *Am. J. Physiol. Regulatory Integrative Comp. Physiol.*, 287:R633–R641, 1979.

J. R. Hazel. Thermal adaptation in biological membranes: Is homeoviscous adaptation the explanation? *Ann. Rev. Physiol.*, 57: 19–42, 1995.

H. Heerklotz. Triton promotes domain formation in lipid raft mixtures. *Biophys. J.*, 83: 2693–2701, 2002.

T. Heimburg. Mechanical aspects of membrane thermodynamics. Estimation of the mechanical properties of lipid membranes close to the chain melting transition from calorimetry. *Biochim. Biophys. Acta*, 1415: 147–162, 1998.

T. Heimburg. A model for the lipid pretransition: Coupling of ripple formation with the chain-melting transition. *Biophys. J.*, 78: 1154–1165, 2000a.

T. Heimburg. Monte Carlo simulations of lipid bilayers and lipid protein interactions in the light of recent experiment. *Curr. Opin. Colloid Interface Sci.*, 5:224–231, 2000b.

T. Heimburg and R. L. Biltonen. Thermotropic behavior of dimyristoylphosphatidylglycerol and its interaction with cytochrome c. *Biochemistry*, 33:9477–9488, 1994.

T. Heimburg and R. L. Biltonen. A Monte Carlo simulation study of protein-induced heat capacity changes. *Biophys. J.*, 70:84–96, 1996.

T. Heimburg and A. D. Jackson. On soliton propagation in biomembranes and nerves. *Proc. Natl. Acad. Sci. USA*, 102:9790–9795, 2005.

T. Heimburg and A. D. Jackson. On the action potential as a propagating density pulse and the role of anesthetics. *Biophys. Rev. Lett.*, 2:57–78, 2007a.

T. Heimburg and A. D. Jackson. The thermodynamics of general anesthesia. *Biophys. J.*, May 2007b.

T. Heimburg and D. Marsh. Investigation of secondary and tertiary structural changes of cytochrome c in complexes with anionic lipids using hydrogen exchange measurements: An FTIR study. *Biophys. J.*, 65:2408–2417, 1993.

T. Heimburg and D. Marsh. Protein surface-distribution and protein-protein interactions in the binding of peripheral proteins to charged lipid membranes. *Biophys. J.*, 68: 536 – 546, 1995.

T. Heimburg, N. J. P. Ryba, U. Würz, and D. Marsh. Phase transition from gel to a fluid phase of cubic symmetry in dimyristoylphosphatidylcholine/ myristic acid 1:2 (mole/mole) bilayers. *Biochim. Biophys. Acta*, 1025:77–81, 1990.

T. Heimburg, P. Hildebrandt, and D. Marsh. Cytochrome c-lipid interactions studied by resonance Raman and ^{31}P-NMR spectroscopy. correlation between the conformational changes of the protein and the lipid bilayer. *Biochemistry*, 30:9084–9089, 1991.

T. Heimburg, U. Würz, and D. Marsh. Binary phase diagram of hydrated dimyristoylglycerol- dimyristoylphosphatidylcholine mixtures. *Biophys. J.*, 63: 1369–1378, 1992.

T. Heimburg, B. Angerstein, and D. Marsh. Binding of peripheral proteins to mixed lipid membranes: Effect of lipid demixing upon binding. *Biophys. J.*, 76:2575–2586, 1999.

E. Helfand, H. L. Frisch, and J. L. Lebowitz. Theory of the two- and one-dimensional rigid sphere fluids. *J. Chem. Phys.*, 14:1037–1042, 1961.

W. Helfrich. Elastic properties of lipid bilayers: Theory and possible experiments. *Z. Naturforsch.*, 28c:693–703, 1973.

W. Helfrich. Steric interaction of fluid membranes in multilayer systems. *Z. Naturforsch.*, 33c:305–315, 1978.

J. Henriksen, A. C. Rowat, E. Brief, Y.-W. Hsueh, J. L. Thewalt, M. J. Zuckermann, and J. H. Ipsen. Universal behavior of membranes with sterols. *Biophys. J.*, 90: 1639–1649, 2006.

T. L. Hill. Statistical mechanics of multimolecular absorption. ii. localized and mobile adsorption and absorption. *J. Chem. Phys.*, 14:441–453, 1946.

T. L. Hill. *An introduction to statistical thermodynamics*. Sinauer Associates Inc., Sunderland, Ma, 1960.

B. Hille. *Ionic channels of excitable membranes*. Cambridge University Press, Cambridge, 1992.

H. J. Hinz, L. Six, K. P. Ruess, and M. Lieflander. Head-group contributions to bilayer stability: monolayer and calorimetric studies on synthetic, stereochemically uniform glucolipids. *Biochemistry*, 240:806–813, 1985.

A. L. Hodgkin. *The conduction of the nervous impulse*. Liverpool University Press, Liverpool, UK, 1964.

A. L. Hodgkin and A. F. Huxley. A quantitative description of membrane current and its application to conduction and excitation in nerve. *J. Physiol.*, 117:500–544, 1952.

F. Hofmeister. Zur Lehre von der Wirkung der Salze: Zweite Mittheilung. Ueber Regelmässigkeiten in der eiweissfällenden Wirkung der Salze und ihre Beziehung zum physiologischen Verhalten derselben. *Arch. Exp. Pathol. Pharmakol.*, 24:247–260, 1888a.

F. Hofmeister. Zur Lehre von der Wirkung der Salze. Dritte Mittheilung. Ueber die wasserentziehende Wirkung der Salze. *Arch. Exp. Pathol. Pharmakol.*, 25:1–30, 1888b.

F. Hofmeister. Zur Lehre von der Wirkung der Salze. Fünfte Mittheilung. Untersuchungen über den Quellvorgang. *Arch. Exp. Pathol. Pharmakol.*, 27:395–413, 1890.

F. Hofmeister. Zur Lehre von der Wirkung der Salze. Sechste Mittheilung. Die Betheiligung gelöster Stoffe an Quellungsvorgängen. *Arch. Exp. Pathol. Pharmakol.*, 28:210–238, 1891.

T. Hønger, K. Mortensen, J. H. Ipsen, J. Lemmich, R. Bauer, and O. G. Mouritsen. Anomalous swelling of multilamellar lipid bilayers in the transition region by renormalization of curvature elasticity. *Phys. Rev. Lett.*, 72:3911–3914, 1994.

J. V. Howarth, R.D. Keynes, and J. M. Ritchie. The origin of the initial heat associated with a single impulse in mammalian nonmyelinated nerve fibres. *J. Physiol.*, 194: 745–793, 1968.

Y.-W. Hsueh, K. Gilbert, C. Trandum, M. J. Zuckermann, and J. Thewalt. The effect of ergosterol on dipalmitoylphosphatidylcholine bilayers: A deuterium NMR and calorimetry study. *Biophys. J.*, 88:1799–1808, 2005.

L. O. Ingram. Changes in lipid composition of escherichia coli resulting from growth with organic solvents and with food additives. *Appl. Environ. Microbiol.*, 33:1233–1236, 1977.

J. H. Ipsen, O. G. Mouritsen, and M. J. Zuckermann. Theory of thermal anomalies in the specific heat of lipid bilayers containing cholesterol. *Biophys. J.*, 56:661–667, 1989.

E. Ising. Beitrag zur Theorie des Ferromagnetismus. *Z. Phys.*, 31:253–258, 1925.

V. P. Ivanova and T. Heimburg. A histogram method to obtain heat capacities in lipid monolayers, curved bilayers and membranes containing peptides. *Phys. Rev. E*, 63: 1914–1925, 2001.

V. P. Ivanova, I. M. Makarov, T. E. Schäffer, and T. Heimburg. Analizing heat capacity profiles of peptide-containing membranes: Cluster formation of gramicidin A. *Biophys. J.*, 84:2427–2439, 2003.

K. Iwasa and I. Tasaki. Mechanical changes in squid giant-axons associated with production of action potentials. *Biochem. Biophys. Research Comm.*, 95:1328–1331, 1980.

K. Iwasa, I. Tasaki, and R. C. Gibbons. Swelling of nerve fibres associated with action potentials. *Science*, 210(338–339), 1980.

F. Jähnig. Electrostatic free energy and shift of the phase transition for charged lipid membranes. *Biophys. Chem.*, 4:309–318, 1976.

G. A. Jamieson and D. M. Robinson. *Mammalian cell membranes*, volume 2. Butterworth, London, 1977.

M. J. Janiak, D. M. Small, and G. G. Shipley. Temperature and compositional depen-

dence of the structure of hydrated dimyristoyl lecithin. *J. Biol. Chem.*, 254:6068–6078, 1979.

F. H. Johnson and E. A. Flagler. Hydrostatic pressure reversal of narcosis in tadpoles. *Science*, 112:91–92, 1950.

D. Johnston and S. M. S. Wu. *Cellular Neurophysiology*. MIT Press, Boston, 1995.

K. Jorgensen. Calorimetric detection of a sub-main transition in long-chain phosphatidylcholine lipid bilayers. *Biochim. Biophys. Acta*, 1240:111–114, 1995.

T. Kaasgaard, C. Leidy, J. H. Crowe, O. G. Mouritsen, and K. Jorgensen. Temperature-controlled structure and kinetics of ripple phases in one- and two-component supported lipid bilayers. *Biophys. J.*, 58:350–360, 2003.

N. Kahya, D. A. Wiersma, B. Poolman, and D. Hoekstra. Spatial organization of bacteriorhodopsin in model membranes: Light induced mobility changes. *J. Biol. Chem.*, 277:39304–39311, 2002.

S. M. Kaneshiro and D. S. Clark. Pressure effects on the composition and thermal behavior of lipids from the deep-sea thermophile methanococcus Jannaschi. *J. Bacteriol.*, 177:3668–3672, 1995.

K. Kaufmann and I. Silman. Proton-induced ion channels through lipid bilayer membranes. *Naturwissenschaften*, 70:147–149, 1983a.

K. Kaufmann and I. Silman. The induction by protons of ion channels through lipid bilayer membranes. *Biophys. Chem.*, 18:89–99, 1983b.

K. Kaufmann, W. Hanke, and A. Corcia. Ion channels. download webpage: "http://membranes.nbi.dk/Kaufmann/pdf/", Caruaru, 1989.

W. Kauzmann. Factors in interpretation of protein denaturation. *Adv. Prot. Chem.*, 14:1, 1959.

D. P. Kharakoz. Phase-transition-driven synaptic exocytosis: A hypothesis and its physiological and evolutionary implications. *Biosci. Rep.*, 210:801–830, 2001.

P. K. J. Kinnunen and J. A. Virtanen. A qualitative, molecular model of the nerve pulse. Conductive properties of unsaturated lyotropic liquid crystals. In F. Gutmann and H. Keyzer, editors, *Modern Bioelectrochemistry*, pages 457–479. Plenum Press, New York, 1986.

Y. Kobatake, I. Tasaki, and A. Watanabe. Phase transition in membrane with reference to nerve excitation. *Adv. Biophys.*, 208:1–31, 1971.

M. Kodama and T. Miyata. Effect of the head group of phospholipids in the acyl-chain packing and structure of their assemblies as revealed by microcalorimetry and electron microscopy. *Colloids Surf. A*, 109:283–289, 1996.

S. König, W. Pfeiffer, T. Bayerl, D. Richter, and E. Sackmann. Molecular dynamics of lipid bilayers studied by incoherent quasi-elastic neutron scattering. *J. Phys.II France*, 2:1589–1615, 1992.

S. König, T. Bayerl, G. Coddens, D. Richter, and E. Sackmann. Hydration dependence of chain dynamics and local diffusion in l-alpha-dipalmitoylphosphtidylcholine multilayers studied by incoherent quasi-elastic neutron scattering. *Biophys. J.*, 68: 1871–1880, 1995.

J. Korlach, J., P. Schwille, W. W. Webb, and G. W. Feigenson. Characterization of lipid bilayer phases by confocal microscopy and fluorescence correlation spectroscopy. *Proc. Natl. Acad. Sci. USA*, 96:8461–8466, 1999.

Y. Kozlovsky and M. M. Kozlov. Stalk model of membrane fusion: Solution of energy crisis. *Biophys. J.*, 82:882–895, 2002.

O. Kratky, H. Leopold, and H. Stabinger. Determination of density of liquids and gases to an accuracy of $10^{-}6g/cm^3$. *Z. Angew. Phys.*, 27:273–277, 1969.

O. Kratky, H. Leopold, and H. Stabinger. The determination of the partial specific volume of proteins by the mechanical oscillator technique. *Methods Enzymol.*, 27:98–110, 1973.

R. Kubo. The fluctuation-dissipation theorem. *Rep. Prog. Phys.*, 29:255–284, 1966.

W. Kunz, J. Henle, and B. W. Ninham. 'Zur Lehre von der Wirkung der Salze' (about the science of the effect of salts): Franz Hofmeister's historic papers. *Curr. Opin. Colloid Interface Sci.*, 9:19–37, 2004a.

W. Kunz, P. Lo Nostro, and B. W. Ninham. The present state of affairs with hofmeister effects. *Curr. Opin. Colloid Interface Sci.*, 9: 1–18, 2004b.

A. L. Kuo and C. G. Wade. Lipid lateral diffusion by pulsed nuclear magnetic resonance. *Biophys. J.*, 77:2300–2308, 1999.

A. Kusumi, Y. Sako, and M. Yamamoto. Confined lateral diffusion of membrane receptors as studied by single particle tracking (nanovivid microscopy). Effect of calcium-induced differentiation. *Biophys. J.*, 65: 2021–2040, 1993.

A. Landwehr and R. Winter. The t,x,p-phase diagram of binary phospholipid mixtures. *Ber. Bunsenges. Phys. Chem.*, 98:1585–1589, 1994.

I. Langmuir. The constitution and fundamental properties of solids and liquids. *J. Am. Chem. Soc.*, 39:1848–1906, 1917.

B. Lautrup, A. D. Jackson, and T. Heimburg. The stability of solitons in biomembranes and nerves. *arXiv:physics/0510106*, 2005.

A. G. Lee. Lipid phase transitions and phase diagrams. II. Mixtures involving lipids. *Biochim. Biophys. Acta*, 472:285–344, 1977.

C.-H. Lee, W.-C. Lin, and J. Wang. All-optical measurement of the bending rigidity of lipid-vesicle membranes across structural phase transitions. *Phys. Rev. E*, 64:020901, 1–4, 2001.

G. M. Lee, F. Zhang, A. Ishihara, C. L. McNeil, and K. A. Jacobson. Unconfined lateral diffusion and an estimate of pericellular matrix viscosity revealed by measuring the mobility of gold-tagged lipids. *J. Cell Biol.*, 120:25–35, 1993.

J. Lenard and S. J. Singer. Protein conformation in cell membrane preparations as studied by optical rotatory dispersion and circular dichroism. *Proc. Natl. Acad. Sci. USA*, 56:1828–1835, 1966.

A. A. Lev, Y. E. Korchev, T. K. Rostovtseva, C. L. Bashford, D. T. Edmonds, and C. A. Pasternak. Rapid switching of ion current in narrow pores: implications for biological ion channels. *Proc. Biol. Sci.*, 252:187–192, 1993.

S. Lewith. Zur Lehre von der Wirkung der Salze. Erste Mittheilung. *Arch. Exp. Pathol. Pharmakol.*, 24:1–16, 1887.

D. Lichtenberg, M. Menashe, S. Donaldson, and R. L. Biltonen. Thermodynamic characterization of the pretransition of unilamellar dipalmitoyl- phosphatidylcholine vesicles. *Lipids*, 19:395– 400, 1984.

D. R. Lide and H. P. R. Frederikse. *Handbook of chemistry and physics 77th ed.* CRC Press, Boca Raton, 1996.

G. Lindblom and L. Rilfors. Cubic phases and isotropic structures formed by membrane lipids - possible biological relevance. *Biochim. Biophys. Acta*, 988:221–256, 1989.

G. N. Ling. *Life at the Cell and Below-Cell Level. The Hidden History of a Fundamental Revolution in Biology*. Pacific Press, New York, 2001.

R. Lipowsky. The morphology of lipid membranes. *Curr. Opin. Struct. Biol.*, 5:531–540, 1995.

E. London. Insights into lipid raft structure and formation from experiments in model membranes. *Curr. Opin. Struct. Biol.*, 12: 480–486, 2002.

P. R. Majhi and A. Blume. Thermodynamic characterization of temperature-induced micellization and demicellization of detergents studied by differential scanning calorimetry. *Langmuir*, 17:3844–3851, 2001.

S. Marcelja. Chain ordering in liquid crystals. 1. Even-odd effect. *J. Chem. Phys.*, 60: 3599–3604, 1974a.

S. Marcelja. Chain ordering in liquid crystals. II. Structure of bilayer membranes. *Biochim. Biophys. Acta*, 367:165–176, 1974b.

D. Marsh. *CRC Handbook of Lipid Bilayers*. CRC Press, Boca Raton, FL, 1990.

D. Marsh. Elastic curvature constants of lipid monolayers and bilayers. *Chem. Phys. Lipids*, 144:146–159, 2006.

T. J. McIntosh. Differences in hydrocarbon chain tilt between hydrated phosphatidylethanolamine and phosphatidylcholine bilayers. a molecular packing model. *Biophys. J.*, 294:237–245, 1980.

P. Meleard, C. Gerbeaud, T. Pott, L. Fernandez-Puente, I. Bivas, M. D. Mitov, J. Dufourcq, and P. Bothorel. Bending elasticities of model membranes. influences of temperature and sterol content. *Biophys. J.*, 72:2616–2629, 1997.

N. Metropolis, A. W. Rosenbluth, N. N. Rosenbluth, A. H. Teller, and E. Teller. Equation of state calculations by fast computing machines. *J. Chem. Phys.*, 21:1087–1092, 1953.

H. Meyer. Zur Theorie der Alkoholnarkose. Erste Mittheilung. Welche Eigenschaft

der Anästhetica bedingt ihre narkotische Wirkung? *Arch. Exp. Pathol. Pharmakol.*, 425: 109–118, 1899.

H. W. Meyer. Pretransition-ripples in bilayers of dipalmitoylphosphatidyl choline - undulation or periodic segments - a freeze fracture study. *Biochim. Biophys. Acta*, 1302: 138–144, 1996.

A. P. Minton. Adsorption of globular proteins on locally planar surfaces. ii. models for the effect of multiple adsorbate conformations on adsorption equilibria and kinetics. *Biophys. J.*, 76:176–187, 1999.

S. Mitaku and T. Date. Anomalies of nanosecond ultrasonic relaxation in the lipid bilayer transition. *Biochim. Biophys. Acta*, 688:411–421, 1982.

M. R. Morrow, J. H. Davis, F. J. Sharom, and M. P. Lamb. Studies of the interaction of human erythroyte band 3 with membrane lipids using deuterium nuclear magnetic resonance and differential scanning calorimetry. *Biochim. Biophys. Acta*, 858: 13–20, 1986.

O. G. Mouritsen. *Computer studies of phase transitions and critical phenomena*. Springer, Berlin, Heidelberg, New York, 1984.

O. G. Mouritsen. Computer simulation of cooperative phenomena in lipid membranes. In R. Brasseur, editor, *Molecular description of biological membrane components by computer aided conformational analysis*, pages 3–83. CRC Press, Boca Raton, 1990.

O. G. Mouritsen and M. Bloom. Mattress model of lipid-protein interactions in membranes. *Biophys. J.*, 46:141–153, 1984.

O. G. Mouritsen and K. Jorgensen. Micro-, nano- and meso-scale heterogeneity of lipid bilayers and its influence on macroscopic membrane properties. *Mol. Membr. Biol.*, 12: 15–20, 1995.

O. G. Mouritsen and M. J. Zuckermann. Softening of lipid bilayers. *Eur. Biophys. J.*, 12: 75–86, 1985.

O. G. Mouritsen, A. Boothroyd, R. Harris, N. Jan, T. Lookman, L. MacDonald, D. A. Pink, and M. J. Zuckermann. Computer simulation of the main gel-fluid phase transition of lipid bilayers. *J. Chem. Phys.*, 79: 2027–2041, 1983.

O. G. Mouritsen, J. H.Ipsen, K. Jorgensen, M. M. Sperotto, Z. Zhang, E. Corvera, D. P. Fraser, and M. J. Zuckermann. Computer simulation of phase transitions in natures preferred liquid crystal: the lipid bilayer membrane. In G. F. Luckhurst, editor, *Computer simulation of liquid crystals*. Kluwer Academic Publishers, The Netherlands, 1992.

P. Müller, D. O. Rudin, H. T. Tien, and W. C. Wescott. Reconstitution of cell membrane structure in vitro and its transformation into an excitable system. *Nature*, 194:979–980, 1962.

C. Nägeli and C. Cramer. *Pflanzenphysiologische Untersuchungen*. Shulthess, Zürich, 1855.

J. F. Nagle and H. L. Scott. Lateral compressibility of lipid mono- and bilayers lateral compressibility of lipid mono- and bilayers. theory of membrane permeability. *Biochim. Biophys. Acta*, 513:236–243, 1978.

E. Neher and B. Sakmann. Single-channel currents recorded from membrane of denervated frog muscle fibres. *Nature*, 260: 779–802, 1976.

L. K. Nielsen, T. Bjørnholm, and O. G. Mouritsen. Critical phenomena - fluctuations caught in the act. *Nature*, 404:352, 2000.

V. Oliynyk, U. Kaatze, and T. Heimburg. Pore formation of lytic peptides in lipid membranes and their influence on the thermodynamic properties of the pore environment. *Biochim. Biophys. Acta*, 2006.

L. Onsager. Reciprocal relations in irreversible processes. I. *Phys. Rev.*, 37:405–426, 1931.

G. Oradd, G. Lindblom, and P. W. Westerman. Lateral diffusion of cholesterol and dimyristoylphosphatidylcholine in a lipid bilayer measured by pulsed field gradient NMR spectroscopy. *Biophys. J.*, 83(1423): 2702–2704, 2002.

C. W. Oseen. The theory of liquid crystals. *Trans. Faraday Soc.*, 29:883–899, 1933.

W. Ostwald. *Lehrbuch der allgemeinen Chemie*. Engelmann, Leipzig, 1887.

W. Ostwald. Elektrische Eigenschaften halbdurchlässiger Scheidewände. *Z. Phys. Chem.*, 6:71–82, 1890.

C. E. Overton. *Studien über die Narkose*. Verlag Gustav Fischer., 1901. Jena, Germany. English translation: Studies of Narcosis, Chapman and Hall, 1991, R. Lipnick, Ed.

C. E. Overton. *Studies of narcosis*. Chapman and Hall, 1991. English version of 'Studien der Narkose' from 1901.

E. Overton. Über die osmotischen Eigenschaften der lebenden Pflanzen und Tierzelle. *Vierteljahresschrift Naturforsch. Ges. Zürich*, 1895.

D. Papahadjopoulos, K. Jacobson, S. Nir, and T. Isac. Phase transitions in phospholipid vesicles. fluorescence polarization and permeability measurements concerning the effect of temperature and cholesterol. *Biochim. Biophys. Acta*, 311:330–340, 1973.

L. Pauling. *The nature of the chemical bond and the structure of molecules and crystals - An introduction to modern structural chemistry*. Cornell University Press, 1939.

E. Perozo. Gating prokaryotic mechanosensitive channels. *Nat. Rev. Mol. Cell Biol.*, 7: 109–119, 2006.

W. Pfeffer. *Osmotische Untersuchungen. Studien zur Zellmechanik*. W. Engelmann, Leipzig, 1877.

D. A. Pink and D. Chapman. Protein-lipid interactions in bilayer lipids: a lattice model. *Proc. Natl. Acad. Sci. USA*, 76:1542–1546, 1979.

D. A. Pink, T. J. Green, and D. Chapman. Raman scattering in bilayers of saturated phosphatidylcholines. Experiment and theory. *Biochemistry*, 19:349–356, 1980.

G. H. Pollack. *Cells, gels and the engines of life. A new, unifying approach to cell function*. Ebner & Sons, Seattle, 2001.

A. Pramanik, P. Thyberg, and R. Rigler. Molecular interactions of peptide with phospholipid vesicle membranes as studied by fluorescence correlation spectroscopy. *Chem. Phys. Lett.*, 104:35–47, 2000.

P. L. Privalov. Cold denaturation of proteins. *Crit. Rev. Biochem. Mol. Biol.*, 25:281–305, 1990.

A. Punnia-Moorthy. Evaluation of ph changes in inflammation of the subcutaneous air pouch linig in the rat, induced by carreenan, dextran and staphylococcus aureus. *J. Oral Pathol.*, 16:36–44, 1987.

J. O. Rädler, I. Koltover, T. Salditt, and C. R. Safinya. Structure of dna-cationic liposome complexes: Dna intercalaction in multilamellar membranes in distinct interhelical packing regimes. *Science*, 275:810–814, 1997.

R. P. Rand, D. Chapman, and K. Larsson. Tilted hydrocarbon chains of dipalmitoyl lecithin become perpendicular to the bilayer before melting. *Biophys. J.*, 155:1117–1124, 1975.

D. Rapaport and Y. Shai. Interaction of fluorescently labeled pardaxin and its analogues with lipid bilayers. *J. Biol. Chem.*, 266:23769–23775, 1991.

H. A. Rinia, R. A. Kik, R. A. Demel, M. M. E. Snel, J. A. Killian, J. P. J. M. Eerden, and B. de Kruijff. Visualization of highly ordered striated domains induced by transmembrane peptides in supported phosphatidylcholine bilayers. *Biochemistry*, 39: 5852–5858, 2000.

J. M. Ritchie and R. D. Keynes. The production and absorption of heat associated with electrical activity in nerve and electric organ. *Quart. Rev. Biophys.*, 392:451–476, 1985.

J. D. Robertson. The ultrastructure of cell membranes and their derivatives. *Biochem. Soc. Symp.*, 16:3–43, 1959.

J. E. Rothman and E. P. Kennedy. Asymmetrical distribution of phospholipids in the membrane of bacillus megaterium. *J. Mol. Biol.*, 110:603–618, 1977.

J. E. Rothman and J. Lenard. Membrane asymmetry. *Science*, 195:743–753, 1977.

F. Sachs and Feng Qin. Gated, ion-selective channels observed with patch pipettes in the absence of membranes: novel properties of a gigaseal. *Biophys. J.*, 65:1101–1107, 1993.

E. Sackmann. Physical basis of self-organization and function of membranes: Physics of vesicles. In R. Lipowsky and E. Sackmann, editors, *Structure and Dynamics of Membranes: From Cells to Vesicles*, pages 213–304. Elsevier, Amsterdam, 1995.

P. G. Saffman and M. Delbrück. Brownian motion in biological membranes. *Proc. Natl. Acad. Sci. USA*, 72:3111–3113, 1975.

T. Salditt, I. Koltover, J. O. Rädler, and C. R. Safinya. Two-dimensional smectic ordering of linear DNA chains in self-assembled DNA-cationic liposome mixtures. *Phys. Rev. Lett.*, 79:2582–2585, 1997.

M. B. Sankaram and T. E. Thompson. Cholesterol-induced fluid-phase immiscibility in membranes. *Proc. Natl. Acad. Sci. USA*, 88:8686–8690, 1991.

M. J. Saxton. Lateral diffusion in an archipelago. the effect of mobile obstacles. *Biophys. J.*, 52:989–997, 1987.

M. J. Saxton. Lateral diffusion in a mixture of mobile and immobile particles: A Monte Carlo study. *Biophys. J.*, 58:1303–1306, 1990.

M. J. Saxton. Single particle tracking: Effects of corrals. *Biophys. J.*, 65:389–398, 1993.

M. J. Saxton. Anomalous diffusion due to obstacles: A Monte Carlo study. *Biophys. J.*, 66: 394–401, 1994.

M. J. Saxton. Single-particle tracking: Effect of corrals. *Biophys. J.*, 69:389–398, 1995.

M. J. Saxton. Lateral diffusion of lipids and proteins. *Curr. Top. Membr.*, 48:229–282, 1999.

M. J. Saxton. Anomalous subdiffusion in fluorescence photobleaching recovery: A Monte Carlo study. *Biophys. J.*, 81:2226–2240, 2001.

M. J. Saxton and K. Jacobson. Single particle tracking: Applications to membrane dynamics. *Ann. Rev. Biophys. Biomol. Struct.*, 26:373–399, 1997.

E. D. Scheets and K. Jacobson. Gpi-anchored proteins and glycosphingolipids exhibit transient lateral confinement to small domains: a single particle tracking study. *Biophys. J.*, 70:A335, 1996.

D. Schmidt, Q.-X. Jiang, and R. MacKinnon. Phospholipids and the origin of cationic gating charges in voltage sensors. *Nature*, 444:775–779, 2006.

T. Schmidt, G. J. Schütz, W. Baumgärtner, H. J. Gruber, and H. Schindler. Characterization of photophysics and mobility of single molecules in a fluid lipid membrane. *J. Phys. Chem.*, 99:17662–17668, 1995.

T. Schmidt, G. J. Schütz, W. Baumgärtner, H. J. Gruber, and H. Schindler. Imaging of single molecule diffusion. *Proc. Natl. Acad. Sci. USA*, 93:2926–2929, 1996.

M. F. Schneider, D. Marsh, W. Jahn, B. Kloesgen, and T. Heimburg. Network formation of lipid membranes: Triggering structural transitions by chain melting. *Proc. Natl. Acad. Sci. USA*, 96:14312–14317, 1999.

W. Schrader, H. Ebel, P. Grabitz, E. Hanke, T. Heimburg, M. Hoeckel, M. Kahle, F. Wente, and U. Kaatze. Compressibility of lipid mixtures studied by calorimetry and ultrasonic velocity measurements. *J. Phys. Chem. B*, 106:6581–6586, 2002.

G. J. Schütz, H. Schindler, and T. Schmidt. Single-molecule microscopy an model membranes reveals anomalous diffusion. *Biophys. J.*, 73:1073–1080, 1997.

P. Schwille, U. Haupts, S. Maiti, and W. W. Webb. Molecular dynamics in living cells observed by fluorescence correlation spectroscopy with one- and two-photon excitation. *Biophys. J.*, 77:2251–2265, 1999a.

P. Schwille, J. Korlach, and W. W. Webb. Fluorescence correlation spectroscopy with single-molecule sensitivity on cell and model membranes. *Cytometry*, 36:176–182, 1999b.

H. Seeger. Theoretische und experimentelle Beschreibung von Diffusionsprozessen in einem zweikomponentigen Lipidsystem. Master's thesis, University of Göttingen, 2002.

H. Seeger. *Kinetics of domain formation processes in lipid membranes*. PhD thesis, University of Göttingen, 2006. URL http://webdoc.sub.gwdg.de/diss/2006/seeger/seeger.pdf.

H. Seeger, M. Fidorra, and T. Heimburg. Domain size and fluctuations at domain interfaces in lipid mixtures. *Macromol. Symposia*, 219:85–96, 2005.

H. M. Seeger, M. L. Gudmundsson, and T. Heimburg. The influence of anesthetics, neurotransmitters and antibiotics on the relaxation processes in lipid membranes. *submitted (arXiv:physics/0703022)*, 2007.

Y. Shai. Mechanism of binding, insertion and destabilization of phospholipid bilayer membranes by α-helical antimicrobial and cell non-selective membrane-lytic peptides. *Biochim. Biophys. Acta*, 1462:55–70, 1999.

K. Simons and E. Ikonen. Functional rafts in cell membranes. *Nature*, 387:569–572, 1997.

K. Simons and E. Ikonen. Cell biology - How cells handle cholesterol. *Science*, 290:1721–1726, 2000.

K. Simons and D. Toomre. Lipid rafts and signal transduction. *Nat. Rev. Mol. Cell Biol.*, 1: 31–39, 2000.

K. Simons and W. L. C. Vaz. Model systems, lipid rafts and cell membranes. *Ann. Rev. Biophys. Biomol. Struct.*, 33:269–295, 2004.

S. J. Singer and G. L. Nicolson. The fluid mosaic model. *Science*, 175:720–731, 1972.

A. Sonnleitner, G. J. Schütz, and T. Schmidt. Free Brownian motion of individual lipid molecules in biomembranes. *Biophys. J.*, 77: 2638–2642, 1999.

A. A. Spector and M. A Yorek. Membrane lipid composition and cellular function. *J. Lipid Res.*, 26:1015–1035, 1985.

M. M. Sperotto, J. H. Ipsen, and O. G. Mouritsen. Theory of protein-induced lateral phase separation in lipid membranes. *Cell Biophys.*, 14:79–95, 1989.

R. Strey, W. Jahn, G. Porte, and P. Bassera. Freeze fracture electron microscopy of dilute lamellar and anomalous isotropics (l3) phase. *Langmuir*, 6:1635–1639, 1990a.

R. Strey, R. Schomäcker, D. Roux, F. Nallet, and U. Olsson. Dilute lamellar and l3 phases in the binary water-c12e15-system. *J. Chem. Soc. Faraday Trans.*, 86:2253–2261, 1990b.

I. P. Sugar, R. L. Biltonen, and N. Mitchard. Monte Carlo simulations of membranes: phase transition of small unilamellar dipalmitoylphosphatidylcholine vesicles. *Methods Enzymol.*, 240:569–593, 1994.

I. P. Sugar, T. E. Thompson, and R. L. Biltonen. Monte Carlo simulation of two-component bilayers: DMPC/DSPC mixtures. *Biophys. J.*, 76:2099–2110, 1999.

J. Tabony and B. Perly. Quasielastic neutron scattering measurements of fast local translational diffusion of lipid molecules in phospholipid bilayers. *Biochim. Biophys. Acta*, 1063:67–72, 1990.

C. Tanford. *The hydrophobic effect: Formation of micelles and biological membranes*. John Wiley & Sons, New York, 1980.

I. Tasaki. A macromolecular approach to excitation phenomena: mechanical and thermal changes in nerve during excitation. [review] [63 refs]. *Physiol. Chem. Phys. Med NMR*, 20:251–268, 1988.

I. Tasaki. Evidence for phase transition in nerve fibers, cells and synapses. *Ferroelectrics*, 220:305–316, 1999.

I. Tasaki and M. Byrne. Volume expansion of nonmyelinated nerve fibers during impulse conduction. *Biophys. J.*, 57:633–635, 1990.

I. Tasaki and P. M. Byrne. Heat production associated with a propagated impulse in bullfrog myelinated nerve fibers. *Jpn. J. Physiol.*, 42:805–813, 1992.

I. Tasaki, A. Watanabe, R. Sandlin, and L. Carnay. Changes in fluorescence, turbidity and birefringence associated with nerve excitation. *Proc. Natl. Acad. Sci. USA*, 61:883–888, 1968.

I. Tasaki, L. Carnay, R. Sandlin, and A. Watanabe. Fluorescence changes during conduction in nerves stained with acridine orange. *Science*, 163:683–685, 1969a.

I. Tasaki, L. Carnay, and A. Watanabe. Transient changes in extrinsic fluorescence of nerve produced by electric stimulation. *Proc. Natl. Acad. Sci. USA*, 64:1362–1368, 1969b.

I. Tasaki, K. Kusano, and M. Byrne. Rapid mechanical and thermal changes in the garfish olfactory nerve associated with a propagated impulse. *Biophys. J.*, 55:1033–1040, 1989.

E. Theodoropoulou and D. Marsh. Interactions of angiotensin II non-peptide AT1 antagonist losartan with phospholipid membranes studied by combined use of differential scanning calorimetry and electron spin resonance spectroscopy. *Biochim. Biophys. Acta*, 1461:135–146, 1999.

E. Theodoropoulou and D. Marsh. Effect of angiotensin II non-peptide AT(1) antagonist losartan o phosphatidylethanolamine membranes. *Biochim. Biophys. Acta*, 1509:346–360, 2000.

H. Träuble, M. Teubner, and H. Eibl. Electrostatic interactions at charged lipid membranes. i. effects of ph and univalent cations on membrane structure. *Biophys. Chem.*, 43: 319–342, 1976.

T. Y. Tsong and M. I Kanehisa. Relaxation phenomena in aqueous dispersions of synthetic lecithins. *Biochemistry*, 16:2674–2680, 1977.

K. Turnheim, J. Gruber, C. Wachter, and V. Ruiz-Gutierrez. Membrane phospholipid composition affects function of potassium channels from rabbit colon epithelium. *Am. J. Physiol. Cell Physiol.*, 277:83–90, 1999.

J. L. C. M. van de Vossenberg, A. J. M. Driessen, M. S. da Costa, and W. N. Konings. Homeostasis of the membrane proton permeability in bacillus subtilis grown at different temperatures. *Biochim. Biophys. Acta*, 1419:97–104, 1999.

W. W. van Osdol, R. L. Biltonen, and M. L. Johnson. Measuring the kinetics of membrane phase transition. *J. Bioener. Biophys. Methods*, 20:1–46, 1989.

W. W. van Osdol, M. L. Johnson, Q. Ye, and R. L. Biltonen. Relaxation dynamics of the gel to liquid crystalline transition of phosphatidylcholine bilayers .effects of chainlength and vesicle size. *Biophys. J.*, 59: 775–785, 1991.

J. H. van't Hoff. The role of osmotic pressure in the analogy between solutions and gases. *Z. Phys. Chem.*, 1:481–508, 1887.

W. L. C. Vaz and P. F. Almeida. Microscopic versus macroscopic diffusion in one-component fluid phase lipid bilayer membranes. *Biophys. J.*, 60:1553–1554, 1991.

W. L. C. Vaz, E. C. C. Melo, and T. E. Thompson. Translational diffusion and fluid domain connectivity in a two-component, two-phase phospholipid bilayer. *Biophys. J.*, 56:869–876, 1989.

W. L. C. Vaz, E. C. C. Melo, and T. E. Thompson. Fluid phase connectivity in an isomorphous,two-component, two-phase phosphatidylcholine bilayer. *Biophys. J.*, 58: 273–275, 1990.

R. von Limbeck. Zur Lehre von der Wirkung der Salze. Vierte Mittheilung. Ueber die diuretische Wirkung der Salze. *Arch. Exp. Pathol. Pharmakol.*, 25:69–86, 1888.

D. A. White. Form and function of phospholipids. In G. B. Ansell, J. N. Hawthorne, and R. M. C. Dawson, editors, *The phospholipid composition of mammalian tissues.*, pages 441–482, New York, 1973. Elsevier.

M. C. Wiener and S. H. White. Structure of a fluid dioleoylphosphatidylcholine bilayer determined by joint refinement of x-ray and neutron diffraction data. iii. Complete structure. *Biophys. J.*, 61:434–447, 1992.

W. C. Wimley and S. H. White. Experimentally determined hydrophobicity scale for proteins at membrane interfaces. *Nat. Struct. Biol.*, 3:842–848, 1996.

W. C. Wimley, T. P. Creamer, and S. H. White. Solvation energies of amino acid side chains and backbone in a family of host-guest pentapeptides. *Biochemistry*, 35:5109–5124, 1996.

R. Winter and W.-C. Pilgrim. A SANS study of high pressure phase transitions in model biomembranes. *Ber. Bunsenges. Phys. Chem.*, 93:708–717, 1989.

D. J. Woodbury. Pure lipid vesicles can induce channel-like conductances in planar bilayers. *J. Membr. Biol.*, 109:145–150, 1989.

J. Wyman and S. J. Gill. *Binding and linkage*. University Science Books, Mill Valley, Ca., 1990.

M. Yafuso, S. J. Kennedy, and A. R. Freeman. Spontaneous conductance changes, multilevel conductance states and negative differential resistance in oxidized cholesterol black lipid membranes. *J. Membr. Biol.*, 17:201–212, 1974.

K. Yoshikawa, T. Fujimoto, T. Shimooka, H. Terada, N. Kumazawa, and T. Ishii. Electrical oscillation and fluctuations in phospholipid membranes. phospholipids can form a channel without protein. *Biophys. Chem.*, 29:293–299, 1988.

Y.-P. Zhang, R. N. A. H. Lewis, R. S. Hodges, and R. N. McElhaney. Peptide models of helical hydrophobic transmembrane segments of membrane proteins. 2. Differential scanning calorimetry and FTIR spectroscopc studies of the interaction of Ac-K2-(LA)12-K2-amide with phosphatidylcholine membranes. *Biochemistry*, 34:2362–2371, 1995.

E. Zinser, C. D. Sperka-Gottlieb, E. V. Fasch, S. D. Kohlwein, F. Paltauf, and G. Daum. Phospholipid synthesis and lipid composition of subcellular membranes in the unicellular eukaryote saccharomyces cerevisiae. *J. Bacteriol.*, 173:2026–2034, 1991.

M. J. Zuckermann and T. Heimburg. Insertion and pore formation driven by adsorption of proteins onto lipid bilayer membrane-water interfaces. *Biophys. J.*, 81:2458–2472, 2001.

Index

Acknowledgments

Several people helped me while preparing this manuscript. Professor Andrew D. Jackson from the Niels Bohr Institute (Copenhagen), Professor Jesper Ferkinghoff-Borg and Professor Kirstine Berg-Sørensen (Technical University of Denmark), and Dr. Thomas Gutberlet (Paul Scherrer Institut, Switzerland) proofread some of the chapters. Hanne Christensen helped to prepare the final form of the manuscript. The editors of this book series, Professor Andreas Herrmann and Professor Klaus-Peter Hofmann from Humboldt University of Berlin carefully proof-read the manuscript and made many helpful suggestions. Several figures and some data were provided by students from my group partially before publication. I thank in particular Dr. Heiko Seeger, Martin Gudmand, and Matthias Fidorra for their support. My student collaborators suffered because my project supervision was sometimes not as intense as it should have been, and the publication of some of their results was delayed. Significant parts of this book were written during my vacation time on the expense of my family and important friends.

I wish to express my gratitude to some of my teachers. In particular I thank Professor Rodney L. Biltonen (University of Virginia, Charlottesville) and Dr. Konrad Kaufmann (Göttingen) who forced me to learn thermodynamics, partially against my own will in hour-long fights at the blackboard, and to appreciate the beauty of thermodynamic treatment of problems in biology. Dr. Kaufmann interested me in the thermodynamics of nerves and permeation phenomena of membranes. Professor Ole Mouritsen (University of Southern Denmark) and Professor Martin Zuckermann (Simon Fraser University, Vancouver) have been an inspiration for many years. They strongly contributed to pave the way for a sober thermodynamic treatment of biomembrane phenomena. Professor Andrew D. Jackson provided lots of encouragement and support when developing the description of the thermodynamics of nerves and anesthesia in a joint effort.